THE APPLICATION OF X-RAY MICROTOMOGRAPHY TO STUDY DAMAGE DEVELOPMENT AND DEFORMATION IN Ti/SiC$_f$ COMPOSITES AND Al FOAMS

A thesis submitted to the University of Manchester for the degree of Ph.D. in the Faculty of Science and Engineering

2004

SAMUEL MCDONALD

MANCHESTER MATERIALS SCIENCE CENTRE

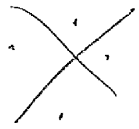

Th 2d 2-3d+

List of Contents

Chapter 2

Investigation of Computerised Tomography System Performance

Chapter 3

Ti/SiC_f MMCs and Composite Micromechanics

Chapter 4

Micromechanics of Load Transfer and Damage Development

Chapter 5

Mechanics and Characterisation of Metallic Foams

List of Figures

Chapter 1

X-ray Microtomography as a Materials Characterisation Technique

Chapter 2

Investigation of Computerised Tomography System Performance

Chapter 3

Ti/SiC$_f$ MMCs and Composite Micromechanics

Chapter 5

Mechanics and Characterisation of Metallic Foams

Chapter 6

Microstructural Characterisation and the Compressive Deformation of Al Foams

Appendix

List of Tables

Chapter 3

Ti/SiC_f MMCs and Composite Micromechanics

Chapter 4

Micromechanics of Load Transfer and Damage Development

Chapter 6

Microstructural Characterisation and the Compressive Deformation of Al Foams

Abstract

X-ray microtomography has been applied to the investigation of damage development and deformation mechanisms occurring in two different microstructured materials, namely silicon carbide fibre reinforced titanium and aluminium foams. Tomography has been used to provide a virtual reconstruction of their 3-D internal structures. A detailed description of the capability of the technique is reviewed, including its physical basis and an overview of laboratory and synchrotron X-ray sources. Both sources were used in this study. The capabilities of each in terms of the output image quality from the reconstruction process are described, while the basis of the algorithms used for reconstruction and the importance of minimising artefacts, is outlined. Image quality is important as it affects the detection of features or details in a reconstructed image, while minimisation of beam hardening artefacts is important when quantitative data is to be obtained. A brief investigation of the performance of a laboratory microtomography system has been carried out to illustrate the capabilities and improvements in image quality that can be obtained. The spatial resolution of the system is defined, and the optimisation of equipment settings is shown to improve the output image quality.

High spatial resolution synchrotron X-ray strain measurements, carried out by diffraction, and X-ray microtomography have been performed on composite samples containing damaged fibres to study damage development in Ti/SiC_f MMCs. Single composite plies containing precisely located fibre defects, induced via laser drilling, were fabricated so that the redistribution of load from damaged fibres to neighbouring ones could be investigated. The distribution of axial strain has been mapped along individual fibres during incremental loading to obtain strain profiles along each fibre. The results obtained show a local load sharing mechanism with load redistribution from a broken fibre increasing that in its nearest neighbours by about 40% of the uniform strain, and that in next nearest fibres by about 20%, causing successive fractures to occur near the original defect. From the build-up of fibre strain around load-induced cracks, interfacial frictional shear strengths of 200-250 MPa are inferred. Values in the range 100-150 MPa are inferred from the pre-induced defects. Synchrotron X-ray microtomography has enhanced the quality of the information that can be obtained in terms of the resolution of the features under inspection, taking advantage of phase sensitive imaging and improving the detection

of small features. The observation of cracking sequences and the accumulation and characteristics of fibre breakages, as a function of applied load, has shown characteristic wedge shaped cracks to occur, which are assumed to originate at a defect on the surface of a fibre. The fracture of a fibre caused by the first high stress fracture event, consisting of a straight crack morphology, is suggested to introduce surface damage from which the wedge cracks form. In a specimen with six plies of unidirectional fibres and containing a matrix fatigue crack, all fibres were observed to bridge the crack. Crack opening displacement measurements were observed to decrease as the crack tip was approached, and an increase in the applied stress resulted in an increase in the magnitude of the CODs.

For the investigation of deformation mechanisms in closed-cell Al foams, laboratory X-ray microtomography has been employed to generate 3-D images of samples of the material, enabling the internal structure, in terms of individual cells, to be characterised in three-dimensions. The effect of the 3-D cellular structure on the local concentration and mechanisms of deformation during compression has revealed not only the position of large cell volumes to be very important in the concentration of stress, but also the immediate surrounding distribution. By performing *in situ* compressive deformation studies, the structural evolution of two types of Al foam was investigated by mapping deformation bands within the 3-D tomographic virtual microstructures. The influence of the production method on the structural performance of the foam materials was observed to be crucial. The calculation of density distributions showed significant gradients through the thickness of the Cymat foam, while the Alporas material was more uniform. Significantly different stress-strain responses between the two were measured as a result, the latter showing a flat plateau stress important for energy absorption efficiency.

Declaration

No portion of the work referred to in the thesis has been submitted in support of an application for another degree or qualification of this or any other university or other institute of learning.

Copyright Statement

(1) Copyright in text of this thesis rests with the Author. Copies (by any process) either in full, or of extracts, may be made **only** in accordance with instructions given by the Author and lodged in the John Rylands University Library of Manchester. Details may be obtained from the Librarian. This page must form part of any such copies made. Further copies (by any process) of copies made in accordance with such instructions may not be made without the permission (in writing) of the Author.

(2) The ownership of any intellectual property rights which may be described in this thesis is vested in the University of Manchester, subject to any prior agreement to the contrary, and may not be made available for use by third parties without the written permission of the University, which will prescribe the terms and conditions of any such agreement.

(3) Further information on the conditions under which disclosures and exploitation may take place is available from the Head of the Department of the Manchester Materials Science Centre.

Dedication and Acknowledgements

In the production of this thesis and the work that has been carried out within, I would like to thank my supervisors, Dr. Paul Mummery and Prof. Philip Withers, for their valuable comments and guidance. For help with the general running of the tomography equipment, Judith Shackleton is acknowledged, and I would like to thank both Steve Burch (AEA Technology) and Greg Johnson for discussions on all things tomography. Greg Johnson is also acknowledged for valuable discussions on image processing and characterisation. Other people I would like to thank are Ivan Easdon for help with mechanical testing, Paul Dewey of the University of Cambridge for help with fabrication of the single-ply composite material, and Dr. Tim Doel of the University of Birmingham for providing the multi-ply fatigue cracked specimens. Dr. Jerry Lord is acknowledged for provision of the foam material. Regarding the experiments at the ESRF, thanks go to Dr. Ann Terry and Dr. Gavin Vaughan for help with the composite strain mapping, and Dr. Peter Cloetens and Dr. Elodie Boller for the tomography measurements.

I would like to dedicate this thesis to my parents and brothers for their constant support during the three years.

Chapter 1

X-Ray Microtomography as a Materials Characterisation Technique

The aim of this chapter is to introduce X-ray microtomography as a powerful characterisation technique for the investigation of the internal structure of, and the deformation mechanisms and damage development in, structural materials. At the moment, the technique, which has been widely used in medicine, is the only one that can provide direct non-destructive images of the interior of a material. A detailed description of the technique will be given, including its physical basis and relationship to conventional radiography, on which it is based. An overview of the relative advantages and disadvantages of laboratory based micro-focus sources and the possibilities offered by third generation synchrotron X-ray sources will be presented. The importance of defining and improving the image quality in both cases will be described, with the latter providing emphasis of the phase contrast technique which considerably extends the field of classical X-ray microtomography. An introduction to the algorithms used for the reconstruction of the numerical images, and the importance of minimising artefacts in these reconstructed images, will also be given. Finally, a brief review of other characterisation techniques will aim to emphasise the many advantages of the X-ray microtomography technique.

1.1. What is X-Ray Microtomography?

1.1.1. Background and applications

X-ray microtomography is a non-destructive technique that allows the internal structure of an object/sample to be imaged by the spatial distribution of its linear X-ray absorption coefficients, providing a cross-sectional view of the interior of the object. In using the technique, quantitative, readily interpretable data are provided, and the inspection of structures that are not suitable to any other non-destructive evaluation technique is enabled. The development of a commercial CT (computed tomography) scanner (or CAT scanner for computed axial tomography or computer-aided tomography) by Hounsfield,

early in the 1970s, revolutionised the field of medical diagnostic imaging (Hounsfield, 1973). This was after Radon had established the underlying mathematics in 1917 (Radon, 1917/1986), and Cormack had demonstrated the feasibility of using X-rays and a finite number of radiographic viewing directions to reconstruct the distribution of X-ray absorptivity within a cross-section of an object (Cormack, 1963). For medical research, the technique has provided, and continues to provide, more detailed and useful information (Engelke *et al*, 1993; Kinney *et al*, 1995) than any previous and subsequent non-invasive imaging technique, such as ultrasonic imaging (Linzer, 1996; White *et al*, 1982) and magnetic resonance imaging (Mansfield and Morris, 1982; Wang and Doddrell, 2002). For the same reason, the method has gained a measure of acceptance for use in industry (Copley *et al*, 1994). A wide variety of applications have arisen over recent years for non-destructive evaluation and testing, including defect detection, dimensional inspection and local characterisation. Reverse engineering is feasible using the information gained from such NDT applications (Schillinger *et al*, 1999). A wide range of object sizes can be inspected, from 1 mm samples to a whole rocket motor several metres in diameter.

Computed tomography (CT) provides a spatially accurate map of the variation of X-ray absorption within an object, regardless of whether there is a well defined substructure of different phases or slowly varying density gradients. High-resolution X-ray computed tomography, where the spatial resolution is of the order of tens of microns, is also termed X-ray microtomography (XMT). Here, the interior of an object/sample can be reconstructed with the spatial and contrast resolution required for many problems of interest in materials science or engineering. The distinction between conventional computed tomography and microtomography is artificial, where the latter is taken to include results obtained with at least 50-100 μm spatial resolution. The actual resolution needed for a particular application depends on the microstructural features of interest and their size and shapes. The spatial resolution obtained with X-ray microtomography can approach that of optical microscopy (typically, with a laboratory X-ray source, no better than 5 μm in samples whose cross-sectional diameter is in the order of 1 mm). It has the major advantage that it is non-invasive, no specimen preparation is required, and the resulting reconstructed image is in three-dimensions, allowing slices to be viewed through the sample volume in different directions.

In terms of applications of X-ray tomography, apart from medical diagnosis in hospitals, medical research has included the study of osteoporosis (Kinney *et al*, 1995; Kirby *et al*, 1997), and the investigation of the interconnectivity, anisotropy and volume

fraction of trabeculae constituting cancellous bone (Cody *et al*, 1996; Engelke *et al*, 1993; Layton *et al*, 1988) and their relation to mechanical properties. For industrial research, many of the main applications have been related to aerospace where the high cost and performance requirements of aeroengine components, for example, justifies the cost of CT inspection (Copley *et al*, 1994). It has been used to further the understanding of damage accumulation and fracture in ceramic and metal matrix composites (Baaklini *et al*, 1995; Breunig *et al*, 1993; Hirano *et al*, 1995; Kinney *et al*, 1990; London *et al*, 1990), and to study fatigue crack closure during a fatigue cycle (Guvenilir and Stock, 1998; Guvenilir *et al*, 1997; Stock *et al*, 1995) allowing the changing pattern of crack openings to be followed as a function of applied load. Use in other industries, including the oil industry, where the role of porosity and pore connectivity in material transport has been researched (Bernard *et al*, 2000; Kinney and Haupt, 1997; Lee *et al*, 1998), continues to grow. Currently, evaluation of castings using radiography is very time consuming because of widely varying thicknesses of components. With accurate three-dimensional tomographic measurements, castings with critical flaws can be detected and eliminated before subsequent costly manufacturing steps (Buffière *et al*, 2000). The study of void and cavity nucleation, growth and coalescence during creep and superplastic deformation, important in high temperature applications such as pressure vessels, has also been aided with the technique (Martin *et al*, 2000). This brief review of medical and industrial applications of X-ray microtomography reveals the increasing importance of the technique to the understanding of the structure and evolution of natural materials, such as bone, and the microstructural and mechanical behaviour of engineering materials and components.

1.1.2. X-ray tomography and conventional radiography

Computed tomography is distinguished from conventional radiography and radioscopy by the different orientation of the image plane, and by the nature of the data that is generated. In conventional radiography, the image plane is approximately normal to the X-ray beam, and the image represents total X-ray attenuation through the object. Figure 1-1 illustrates the common mode of producing an X-ray image (Copley *et al*, 1994).

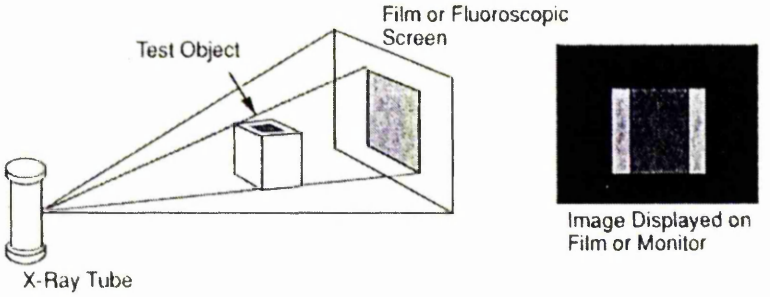

Figure 1-1. A conventional radiograph is formed by projecting an X-ray shadow image onto a plane normal to the X-ray beam. (Copley *et al*, 1994).

The CT method, illustrated by Figure 1-2(a), creates a digital representation of a thin slice of the object parallel to the X-ray beam (Copley *et al*, 1994). This image is reconstructed from multiple X-ray views through the object at different angles, shown by Figure 1-2(b).

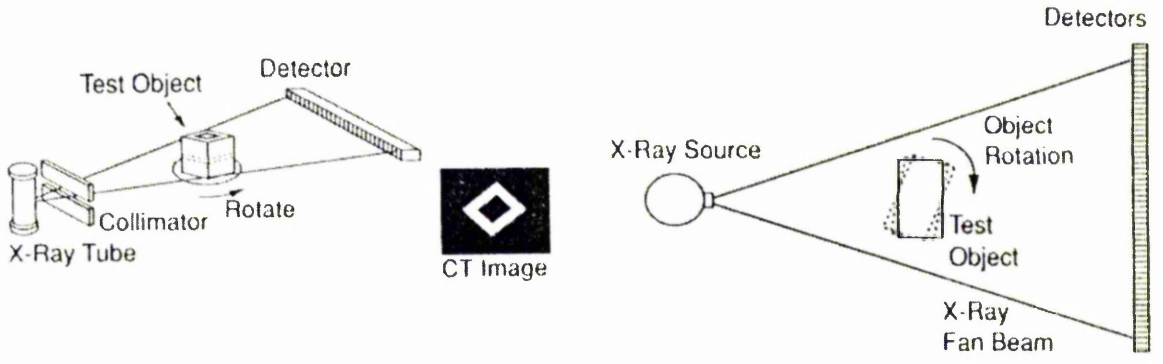

(a) (b)

Figure 1-2. a) Illustrating how computed tomography produces an image of a cross-sectional slice parallel to a collimated X-ray fan beam; b) The X-ray data needed to reconstruct a CT image are acquired from multiple X-ray 'views' with a small rotation of the object between each view. (Copley *et al*, 1994).

The CT slice is stored as an array of numbers representing local X-ray attenuation values for each of the small volume elements (voxels) that make up the slice, and represented in a reconstructed image as a series of grey level values, as illustrated in Figure 1-3 (Copley *et al*, 1994).

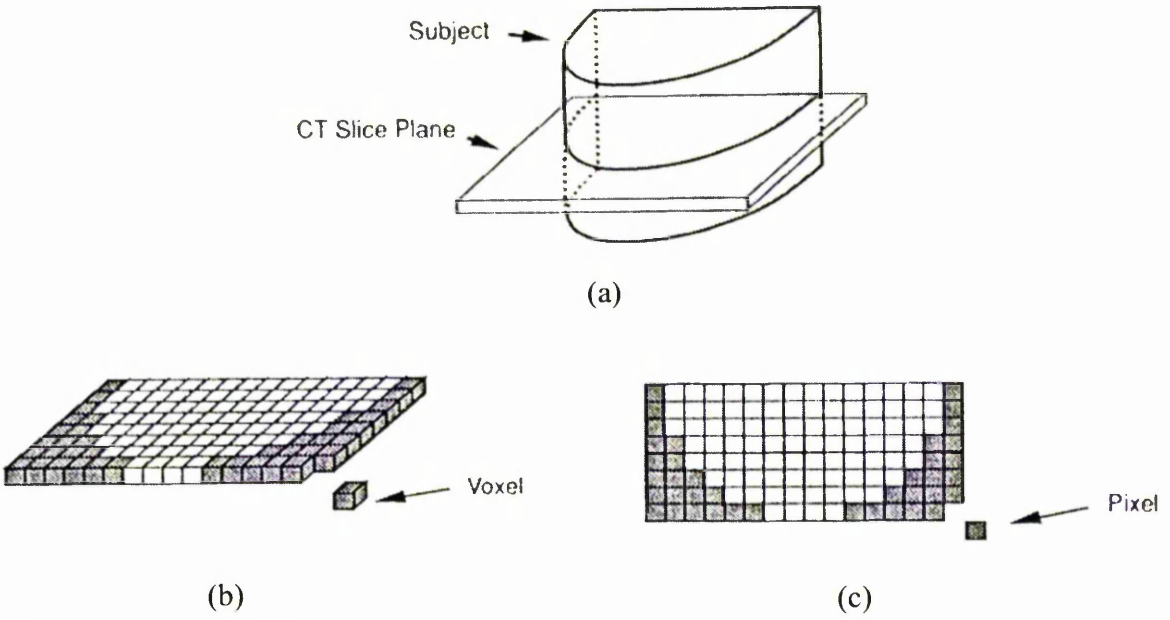

Figure 1-3. a) The CT image represents a thin slice plane within the scanned object; b) For reconstruction and display, the slice plane is represented as consisting of a large number of voxels; c) The 2-D CT image is made up of pixels whose grey level represents the local X-ray attenuation in the corresponding voxel. (Copley *et al*, 1994).

Computed tomography has the advantage over conventional radiography that the image data represents a local material-dependent property, the linear attenuation coefficient (μ), that is largely independent of object geometry. A radiograph only represents an integral of μ along the X-ray path through the object, and represents a projection of a large amount of information on one single plane. The resulting image can be difficult to interpret if the complexity of the microstructural feature along the thickness of the sample is important. Tomography overcomes this drawback by combining the information of many radiographs, each being acquired with a different orientation of the object (incremental steps over a range of 180°). When the angular increment between each radiograph is small enough (~0.5°), it is possible to compute the local value of the attenuation coefficient at each point in the sample from the complete set of radiographs. Thus, tomography, providing more useful and quantitative characterisation of materials, overcomes a major limitation of radiography, the inability to discriminate between thickness and density changes. Radiography, on the other hand, has the benefit of accelerating data acquisition from 2-3 hours for a tomograph (including reconstruction) to less than a minute for a single radiograph. Furthermore, it reduces the amount of data that must be stored and analysed.

1.1.3. Physical basis of X-ray tomography

Three different X-ray tomography setups exist: transmission tomography, scattered photons tomography and emission tomography. Simple diagrams illustrating each of these are shown in Figure 1-4 (Peix *et al*, 2000). It is transmission X-ray tomography that is widely used in both the industrial and medical fields and it delivers a map of μ, the linear attenuation coefficient.

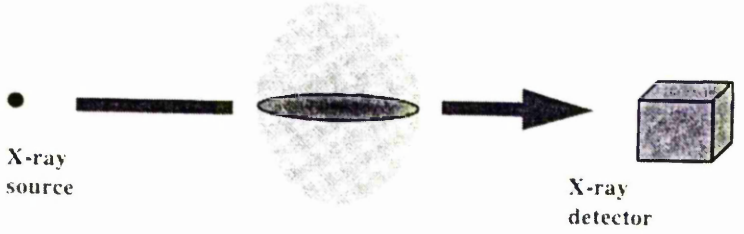

(a)

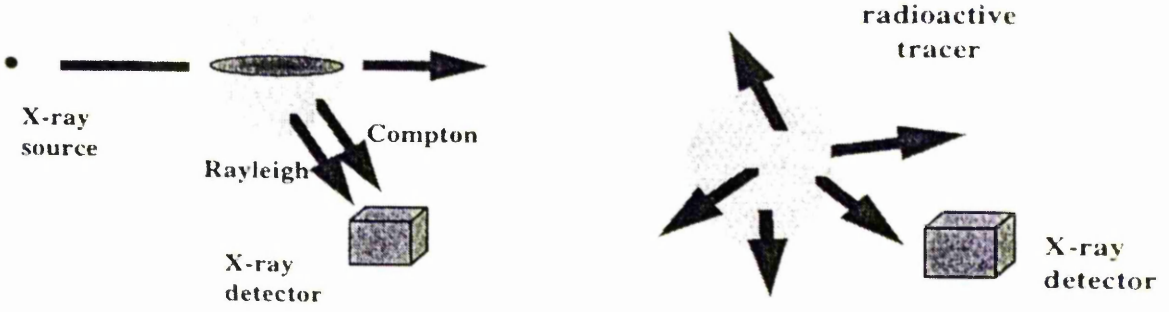

(b) (c)

Figure 1-4. a) X-ray transmission tomography; b) scattered photons tomography; c) emission tomography. (Peix *et al*, 2000).

The basic principle of the technique is that the transmitted intensities, detected using an imaging device with a linear response such as a CCD camera, are related to the integral attenuation of the various materials encountered inside the object, along each individual ray path of the X-ray beam. For a specific photon energy and for every sensitive pixel in the detector, the intensity is given by the Beer-Lambert or attenuation law:

$$I = I_0 \exp\left(- \int \mu(x,y)\, dx \right) \qquad (1\text{-}1)$$

The term $\mu(x,y)$ represents the value of the linear attenuation coefficient at the point (x,y) along the considered ray path of the X-ray beam. Measuring the intensity of the incident photons emitted by the source, I_0, and the intensity of the photons transmitted along a single line or ray path through the sample, I, as illustrated in Figure 1-5, allows the calculation of the integral of μ along the considered path (rearranging Equation (1-1)):

$$\ln\left(\frac{I_0}{I}\right) = \int \mu(x,y)\, dx \qquad (1\text{-}2)$$

Repeating such a measurement along a great number of paths within the same slice delivers the Radon transform of the object (see Section 1.4). Radon demonstrated that it is possible to determine the value of a function over a region of space if the set of line integrals for all ray paths through the region is known (Radon, 1917/1986; Kak and Slaney, 1987; see Section 1.4). He subsequently showed that finding an inverse to the transform enabled the $\mu(x,y)$ map of the slice to be reconstructed.

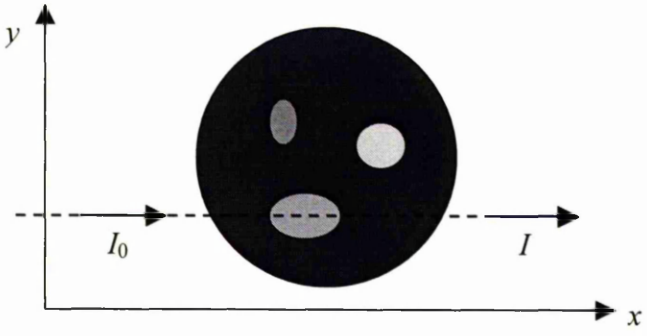

Figure 1-5. Illustrating the physical basis of transmission tomography inside a single slice of an object, for a single ray path through the object. Each point, (x,y), along the path contributes a value of the linear attenuation coefficient, $\mu(x,y)$.

It is important to note that the attenuation coefficient varies along the beam and depends on the local composition of the investigated material/sample (the density, ρ, and atomic number, Z) and the energy of the incident photons, E. In the photoelectric domain, and when the beam is monochromatic, μ typically follows a law of the type:

$$\mu(x,y) = K\rho\frac{Z^4}{E^3} \qquad (1\text{-}3)$$

where K is a constant. For a polychromatic beam, the Beer-Lambert law (Equation (1-1)) has to be integrated over the whole spectrum due to such a beam containing photons of differing energies. The Beer-Lambert or attenuation law is the basic rule used to explain

the contrast observed in an X-ray radiograph of a bulky material because each point in a detector placed behind the sample is situated in front of a different X-ray path.

1.2. X-Ray Microtomography Sources and Geometries

1.2.1. Laboratory based microtomography system geometries

Most laboratory microtomography systems employ one of four geometries. These are illustrated in Figure 1-6 (Stock, 1999). For each of these geometries, P is the X-ray source, C is the collimator, O is the object being imaged, X_1 is the translation axis of the sample, X_2 is the axis about which the sample is rotated to produce successive views or projections required for reconstruction, S is the scatter shield and D is the detector.

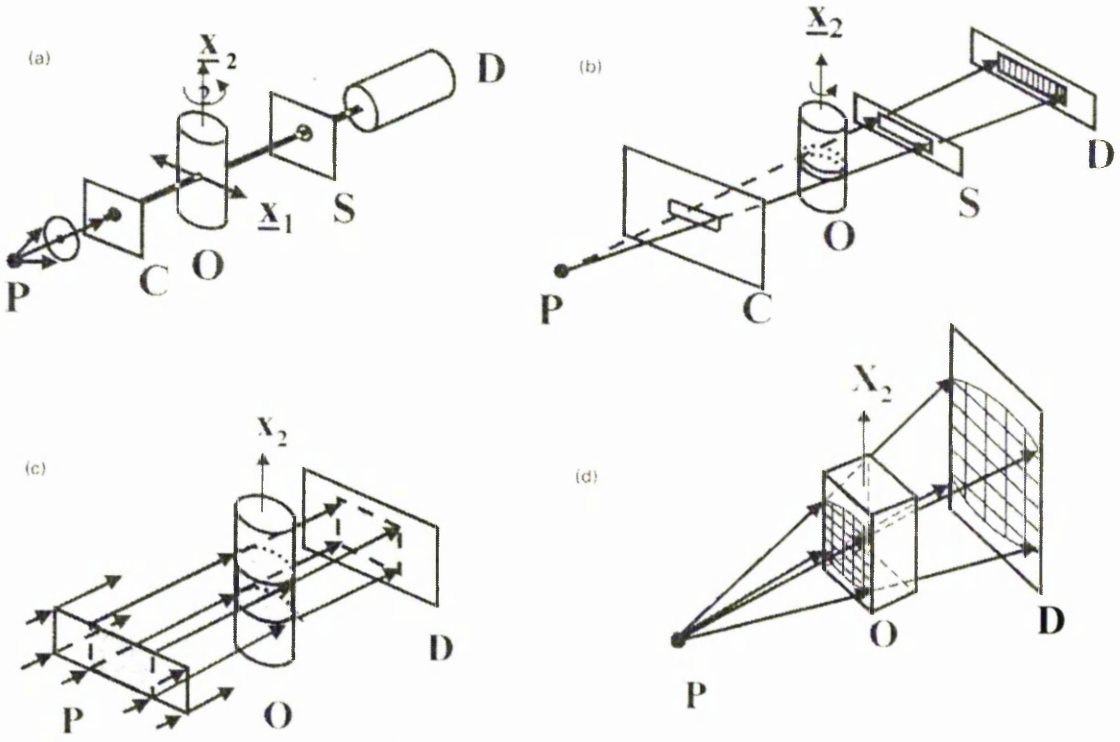

Figure 1-6. Illustration of four experimental approaches to laboratory X-ray microtomography data collection: a) pencil, b) fan, c) parallel and d) cone beam methods. (Stock, 1999).

In first generation or pencil beam systems (Figure 1-6(a)), a pinhole collimator from the point-like source produces a narrow, pencil-like beam that is scanned across the object along X_1 to produce each view; successive views are obtained by rotation of the

object about X_2. Only a simple zero-dimensional X-ray detector is required. Such apparatus is simple and flexible to use, and there is a relatively greater immunity to degradation of contrast due to scatter, compared to the other methods. Pencil beam microtomography has been and continues to be used with laboratory X-ray sources (Elliott and Dover, 1982; Justice *et al*, 2000; Mummery *et al*, 1995), and very high spatial resolution has been achieved in small polymer samples using synchrotron radiation (Ferrero *et al*, 1993).

Fan beam systems (Figure 1-6(b), third generation apparatus) use a rotate-only geometry instead of the translate-rotate geometry of the pencil beam system (London *et al*, 1990). A flat fan of X-rays defined by the collimator and spanning the sample originates at the point-like source, passes through the sample and scatter shield and is collected by the one-dimensional X-ray detector. These systems are often used with laboratory micro-focus generated X-rays. The detector consists of an array of discrete elements that allows the entire view to be collected simultaneously. One to two thousand detector elements are typically in the array, making fan beam systems much more rapid than pencil beam systems, but data for only one slice are recorded at a time. Disadvantages include the necessity of normalising detector response, and ring artefacts (reconstruction artefacts in the resulting images/slices, see Section 1.4.5) can result from various non-uniformities in the calibration and system setup (Schneberk *et al*, 1990).

In situations where a spatially wide, parallel beam of X-rays is available, the parallel beam geometry (Figure 1-6(c)) allows straightforward and very rapid data collection for multiple slices, i.e. a volume, simultaneously. A parallel beam from a source with a certain cross-sectional area shines through the sample and is collected by a two-dimensional detector array. Since the X-ray beam is parallel, the projection of each slice of the object on the detector, i.e. each row of the array, is independent of all other slices. In practice, in order to obtain a highly parallel beam, this must be carried out at storage rings optimised for the production of the hard synchrotron X-rays (see Section 1.2.3). High performance area detectors are required, but there is an enormous increase in data collection rates over the geometries described above. For example, at a synchrotron facility, 900 projection images can be collected in about 1 hour.

The cone beam geometry (Figure 1-6(d)), the three-dimensional analogue of the two-dimensional fan beam arrangement, is especially well suited for volumetric computed tomography employing micro-focus tube sources. The X-rays diverge from the source, pass through the sample, and are recorded on an area detector. With this geometry, each

detector row, except the central row, receives contributions from more than one slice, and the effect becomes greater the farther one moves along the plane perpendicular to the rotation axis. The cone beam reconstruction algorithm is an approximation, however, and some blurring is to be expected in the axial direction for features that do not have significant extent along this direction. With an X-ray source size approaching 5-10 μm, system resolution is limited by that of the X-ray detector array and the sample size.

1.2.2. Setup of laboratory based instrumentation

Typical laboratory X-ray microtomography instrumentation/systems are based on the pencil, fan or cone beam geometries and comprise:

1. An X-ray source based on the classical microfocus X-ray tubes;
2. A motorised manipulation stage for sample handling in order to translate (magnification and horizontal/vertical movement) and rotate the sample relative to the X-ray source and detector;
3. An imaging chain consisting of an image intensifier which transforms the X-rays into visible light via a fluorescent screen, optical lenses and a high resolution digital video CCD camera (consisting of columns and rows of sensitive elements) with typically 1024 × 1024 pixels;
4. An image handling and CT reconstruction software package,
5. A control console consisting of a PC for control of the X-ray source, camera and manipulation stage, a display to view the results, and data storage media.

Figure 1-7 shows a schematic diagram of the typical imaging arrangement in a laboratory based microtomography and digital radiography system (Mangard and Hammersberg, 1998). Of the four system geometries explained in Section 1.2.1, and illustrated in Figure 1-6, it is the cone beam geometry that is well-suited to laboratory microfocus tube sources and has the advantage of being able to perform volumetric data collection. With such a diverging beam geometry (Figure 1-6(d)), the magnification of the sample is easily altered by adjusting the spatial position of the sample between the source and detector. The maximum obtainable resolution is mainly due to the size of the microfocus, which introduces a blur in the projected image. The focus size has to be as small as possible in order to obtain the best resolution. However, the focus size depends largely on the energy delivered by the X-ray tube – the lower the energy, the smaller the focus size. For an acceptable acquisition time, the reconstruction resolution is a trade-off between the focus size and the X-ray energy delivered to the sample to prevent the flux becoming too low to

allow sufficient attenuation. Also, due to the necessity of the sample remaining in the field of view of the detector system during acquisition of the raw data, a compromise is needed between the maximum sample size and the required spatial resolution. In such laboratory setups, the microfocus X-ray source emits X-rays from a metallic target and, owing to the use of a white, polychromatic beam, quantitative analysis requires calibration prior to reconstruction due to the resulting beam hardening artefacts (see Section 1.4.3).

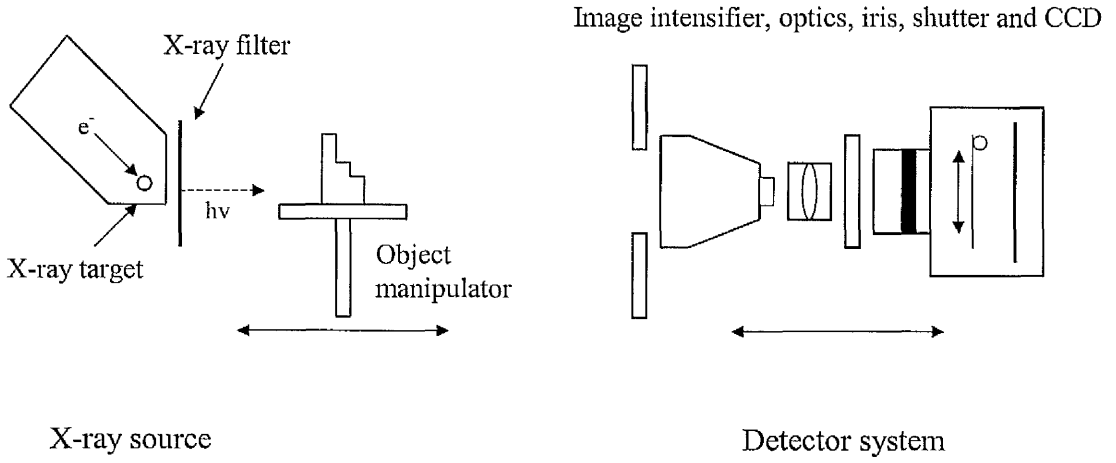

Figure 1-7. Schematic description of the imaging arrangement in a typical laboratory microtomography and digital radiography system.

1.2.3. Microtomography using a synchrotron radiation source

Systems using X-ray tubes are limited due to the flux delivered by this kind of source. Synchrotron sources, however, deliver a very high flux (at least 1000 times larger than X-ray tubes) while using a small source size, allowing high-resolution microtomography and high quality images to be reconstructed in terms of signal-to-noise ratio and spatial resolution. Synchrotron radiation is the electromagnetic radiation produced by ultra-relativistic electrons in a storage ring when they are accelerated by a magnetic field (Hasnain *et al*, 1994). This field is uniform in bending magnets over a portion of the trajectory and oscillates spatially in insertion devices (wigglers and undulators) that can be set on the straight sections between two bending magnets. The X-rays are emitted in a narrow cone tangentially to the curved trajectory of the electrons in the storage ring. Synchrotron radiation sources feature a very high intensity of the emitted beam and, when the source is a bending magnet or a wiggler, a continuous spectrum spanning the whole range from infra-red to X-rays (Hasnain *et al*, 1994; Laclare, 1994).

Figure 1-8 shows the experimental setup used at the ESRF (European Synchrotron Radiation Facility) on beam line ID19 (Buffière *et al*, 1999), which is devoted to high-resolution imaging. The features of this beam line include:

- The high energy of the electrons producing the radiation (6 GeV), leading to an energy-tuneable X-ray beam (7–100 keV);
- A large source-sample distance (~150 m) and the small size of the beam cross-section (<100 μm), leading to high brilliance and a very small angular extension of the source as seen from a point in the specimen, i.e. low divergence (~1 μrad).

These features of the beam make it possible to perform radically improved microtomography experiments, as compared to laboratory sources, through the use of:

- A beam that is very intense, homogeneous, parallel and monochromatic (after passing through a monochromator – a perfect crystal or multilayer). This is compared to the relatively weak, polychromatic and divergent beam used in laboratory microtomography;
- The high lateral coherence properties of the beam, making it possible to obtain phase images by adjusting the sample-detector distance.

Also crucial for microtomography experiments is the availability of a fast, high-resolution detector system. On beam line ID19, this consists of a fluorescent screen (YAG:Ce), which transforms the X-rays into visible light, and microscope optics to project the image onto the cooled 2048^2 CCD camera, displaying at the same time a large dynamic range (14 bits), low dark current (3 electrons/s), and a fast readout (0.22 s/frame). This Fast REadout LOw Noise (FRELON) camera, developed at the ESRF, is fitted with an optical system that leads to effective pixel sizes from 0.2 μm to several microns.

The use of such a synchrotron radiation source has provided new possibilities for microtomographic imaging. The monochromatic character of such a beam suppresses beam hardening effects (Schneberk *et al*, 1990), and, together with its highly parallel nature, gives an 'exact' reconstruction allowing quantitative measurements to be performed (Buffière *et al*, 2000; Martin *et al*, 2000). Such a highly parallel beam, together with a large source-sample distance, contributes to the rapidly increasing field of phase sensitive imaging owing to a partially coherent beam (Cloetens *et al*, 1997). Together with a small sample-detector distance, this leads to an improvement in the detection of phase features (e.g. cracks) due to a 'phase contrast' that is added to the regular attenuation contrast (see Section 1.3.3). The typical wavelength of the beam, and of those used for

phase sensitive imaging, is $\lambda \approx 0.5$ Å, using an X-ray energy of 25 keV. The main drawback of this approach is that no magnification is obtained, and the spatial resolution mainly results from the effective pixel size of the detector, resulting in the need for small samples if very high resolution is required. All of this has lead to the possibility of making sub-micron resolution X-ray tomographic images (Babout *et al*, 2003; Salvo *et al*, 2003).

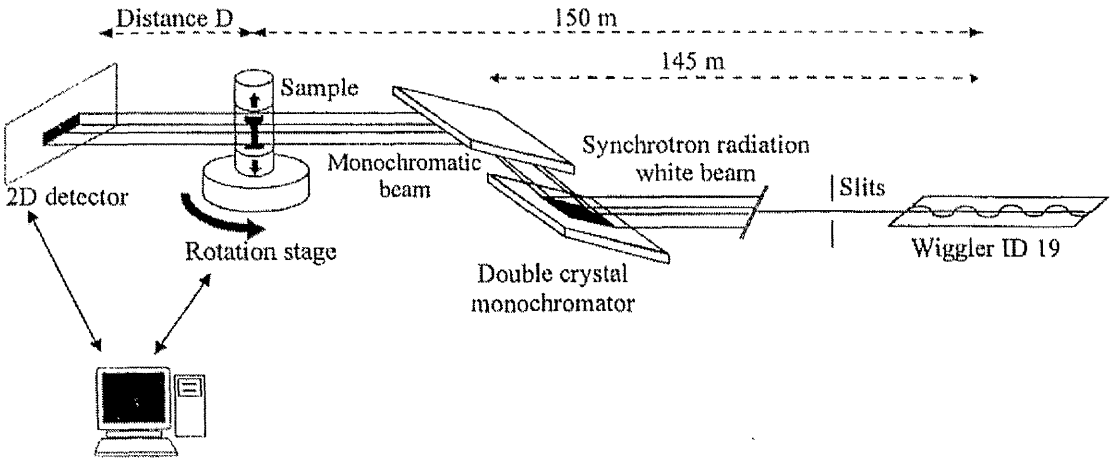

Figure 1-8. Schematic diagram of the experimental setup used at the ESRF on beam line ID19. (Buffière *et al*, 1999).

1.3. Image Quality

1.3.1. Laboratory X-ray tube sources

The image quality of a sample scanned using a laboratory X-ray microtomography system depends on the characteristics of both the sample and the CT-imaging equipment, and it can be defined in terms of contrast, resolution and noise (Dainty and Shaw, 1976):

1. Noise is defined as the uncertainty in a signal due to random fluctuations. Noise originates from the random nature of generating and detecting X-ray photons, quantum noise, and added contributions from the electronic noise in the detector;
2. The contrast in a CT image depends on both the imaged object and the properties of the CT system and originates from the difference in linear X-ray attenuation coefficients between the detail and the surrounding material;
3. The resolution of an X-ray system can be quantified with the modulation transfer function, MTF. The MTF describes how the CT system transfers the input signal, i.e. the raw projection data or radiographs, into the output reconstructed CT image as a function of spatial frequency. Since the MTF can be used to determine the

contrast as a function of spatial frequency, it combines the term contrast and resolution. For example, a CT image of an object with a sharp edge, that contains infinitely high frequencies, will look smoothed due to the damping of these high frequencies, as illustrated by Figure 1-9 (Mangard, 2000).

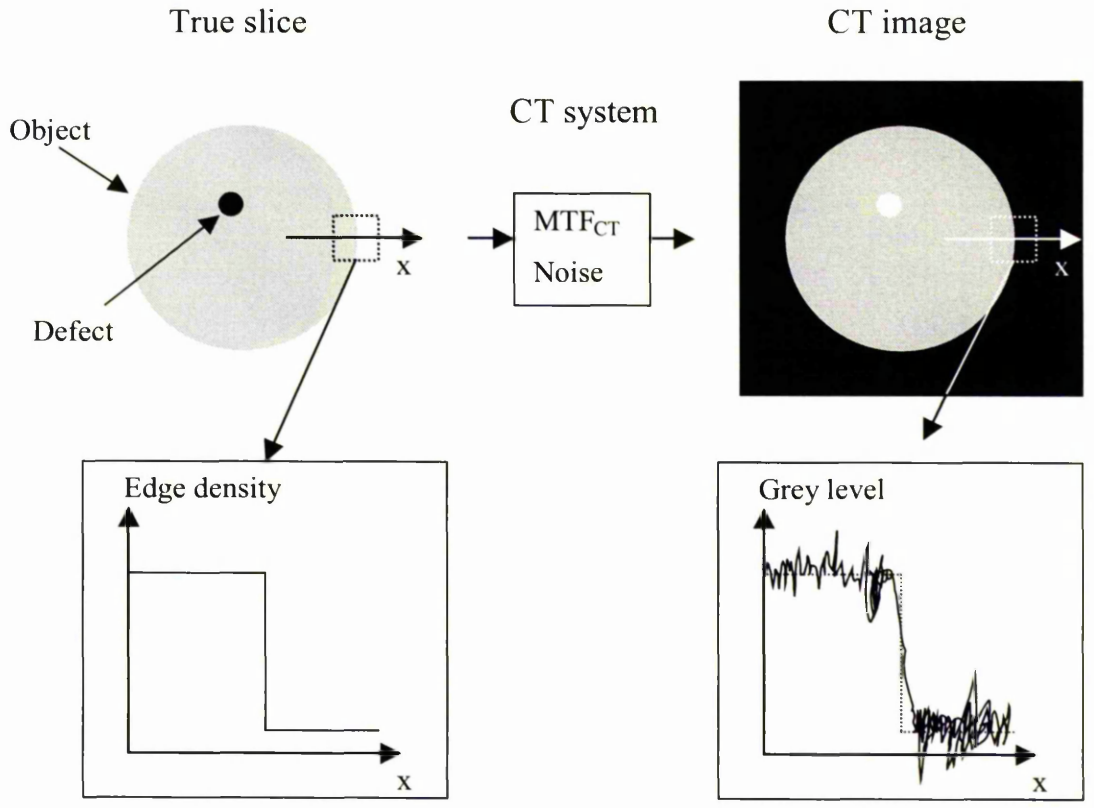

Figure 1-9. The grey level intensity response in a CT image of a cylinder with a sharp edge, as compared to that of a true slice. (Mangard, 2000).

1.3.1.1. Signal-to-noise ratio

The signal-to-noise ratio, SNR, is an important parameter for characterising image quality, combining both contrast and noise. The detail signal-to-noise ratio in a CT image is defined as (Graeff and Engelke, 1991):

$$SNR_{\Delta S,CT} = \frac{\Delta S}{\sigma_{\Delta S}} = \frac{|m_{S2} - m_{S1}|}{\sqrt{(\sigma_1^2 + \sigma_2^2)}} \tag{1-4}$$

where m_{S2}, σ_2^2 and m_{S1}, σ_1^2 are the expected value and variance of the signals in the detail and the surrounding material of the object respectively, as defined by Figure 1-10 (Mangard, 2000). In CT images, the signal, S, is proportional to the effective linear X-ray attenuation coefficient.

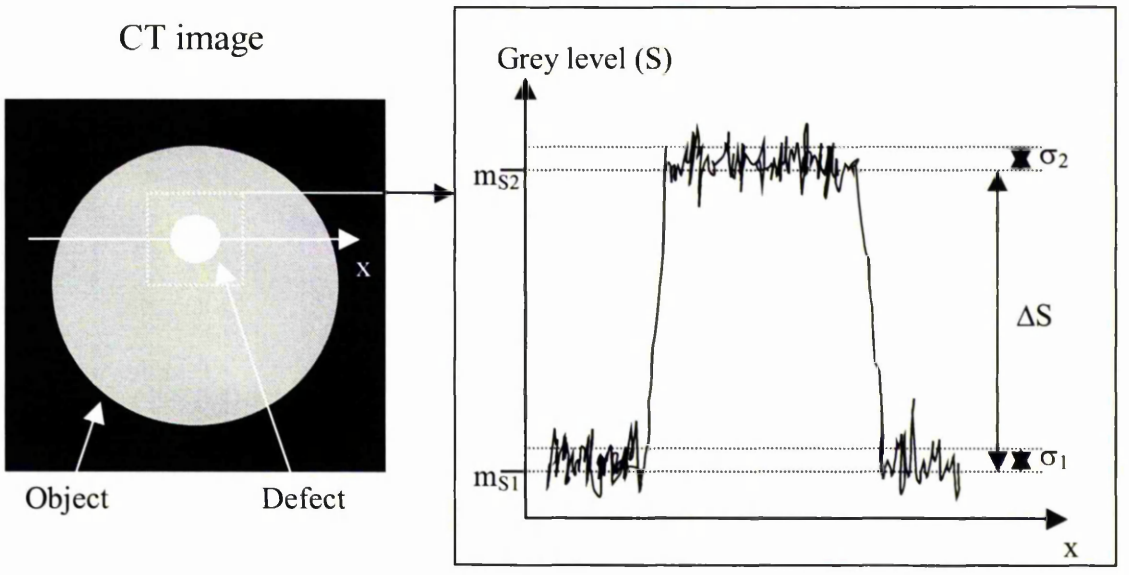

Figure 1-10. Defining the detail signal-to-noise ratio in a CT image. (Mangard, 2000).

The input to the CT-reconstruction algorithms, the raw projection data, represents the negative logarithm of the signal collected after attenuation of the X-rays through the object, P_1, divided by the signal collected with no object attenuating the X-rays, P_0. Analogously, the detail signal-to-noise ratio in the collected projection data, $SNR_{\Delta proj}$, can be defined as (Graeff and Engelke, 1991; Hammersberg *et al*, 1995):

$$SNR_{\Delta proj} = \frac{\left|\ln(m_{P2}) - \ln(m_{P1})\right|}{\sigma_{\Delta proj}} \tag{1-5}$$

where

$$\sigma_{\Delta proj}{}^2 = V\left[\ln\left(\frac{P_2}{P_0}\right) - \ln\left(\frac{P_1}{P_0}\right)\right] \approx \frac{\sigma_{P2}{}^2}{m_{P2}{}^2} + \frac{\sigma_{P1}{}^2}{m_{P1}{}^2} + \frac{2\sigma_{P0}{}^2}{m_{P0}{}^2} \tag{1-6}$$

P_0 is defined as the collected signal generated from an X-ray path passing beside the object. P_1 is the signal generated from the X-ray path passing through the object and slightly besides the detail. The signal P_2 is defined as that generated from the X-ray path passing through the object and a detail in the centre of the object. These signals are defined in Figure 1-11. m_P and $\sigma_P{}^2$ denote the expected value and variance respectively of the corresponding signal. V is the number of views or projections acquired during CT data collection.

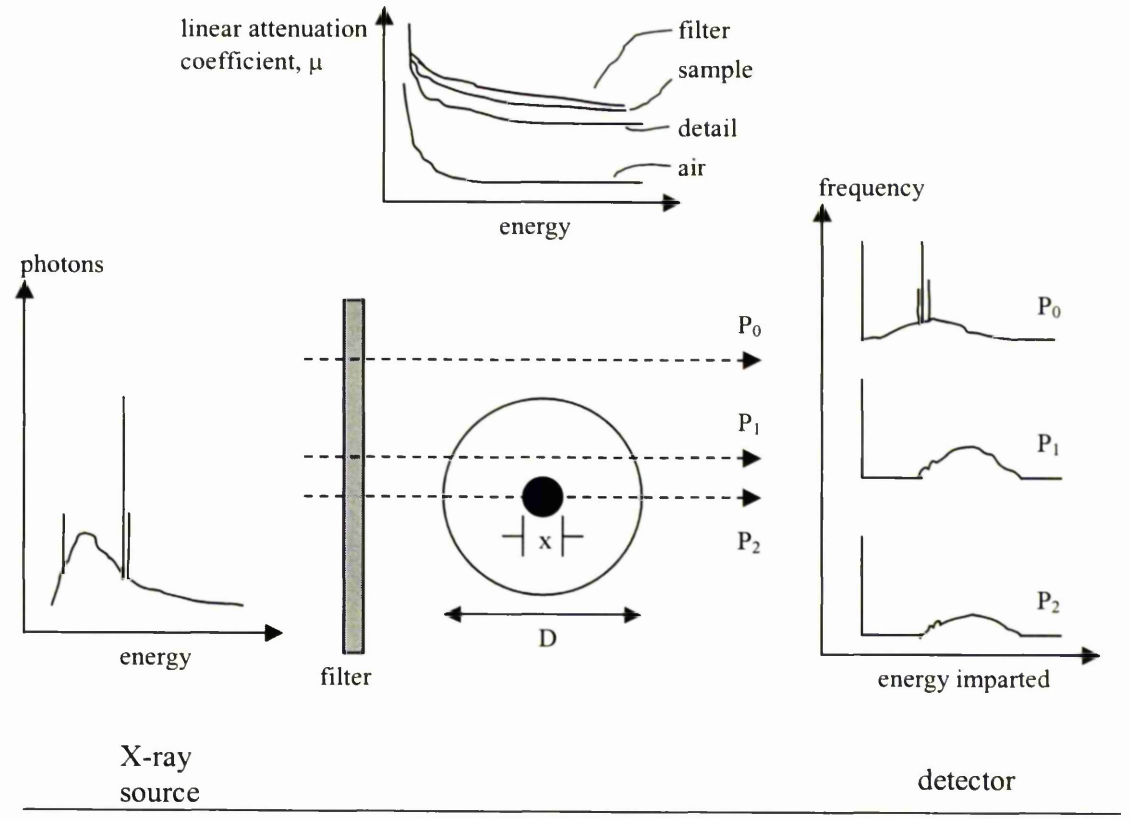

Figure 1-11. Definition of the signals P_0, P_1 and P_2 with respect to the object and detail. Schematically, the X-ray spectrum, attenuation coefficients and the differential energy response of the detector are shown for the different ray paths. D is the sample diameter and x is the detail thickness. (Graeff and Engelke, 1991).

1.3.1.2. Maximising the detail signal-to-noise ratio

To maximise the detail signal-to-noise ratio in the raw projection data, $SNR_{\Delta proj}$, the difference between signals P_1 and P_2 should be as large as possible, combined with a low noise-level of the signals. To be able to reconstruct a CT image from the projection data, it is necessary to know the signal level beside the object, P_0. This signal has therefore to be within the dynamic range of the detector system (see Figure 1-12) such that the detector is not saturated by the X-rays, which constrains the maximisation of the detail signal-to-noise ratio (Graeff and Engelke, 1991).

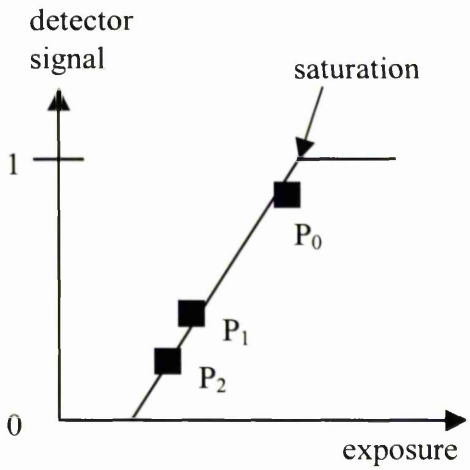

Figure 1-12. The difference between signals P_1 and P_2 should be as large as possible without saturating the detector with signal P_0. (Graeff and Engelke, 1991).

The relationship between the signal-to-noise ratio in the projection data for a detail, $SNR_{\Delta proj}$, the size of a pixel in the CT image in the centre of the object and the detail signal-to-noise ratio in the CT image, $SNR_{\Delta S,CT}$, can be expressed with (Mangard and Hammersberg, 1998):

$$SNR_{\Delta S,CT} = \left(\frac{\sqrt{V}}{c_{noise}} \right) SNR_{\Delta proj} \tag{1-7}$$

where c_{noise} describes the relationship between the noise in the CT image and the noise in the projection data and originates from the data collection and reconstruction procedure. This implies that the maximum detail signal-to-noise ratios in the CT projection data and the CT image are obtained with the same optimum CT-equipment settings.

1.3.1.3. Modulation transfer function

A system can be defined as that which produces a set of output functions from a set of input functions. For a digital radiography or computed tomography system, the input is a set of spatially varying intensities or exposure, and the output image is the same in the case of a radiograph, and for a CT image, is a spatial representation of density or attenuation coefficient. Suppose that the input exposure is a one-dimensional sinusoidal distribution of the form shown in Figure 1-13. This can be defined as (Dainty and Shaw, 1976):

$$f(x) = a + b \cos (2 \pi \omega x + \varepsilon) \tag{1-8}$$

where ω is the one-dimensional spatial frequency, and ε is a measure of the phase. b is the shift in the distribution in the y-axis and a is the half-amplitude. The output, or image, is also sinusoidal with the same spatial frequency as the input, but with a change of amplitude, or modulation (Dainty and Shaw, 1976). The ratio of the output modulation to the input modulation depends on the spatial frequency and is equal to the modulus of the Fourier transform of the line spread function (also known as the point spread function). It is this ratio of output to input modulation that is called the *modulation transfer function*.

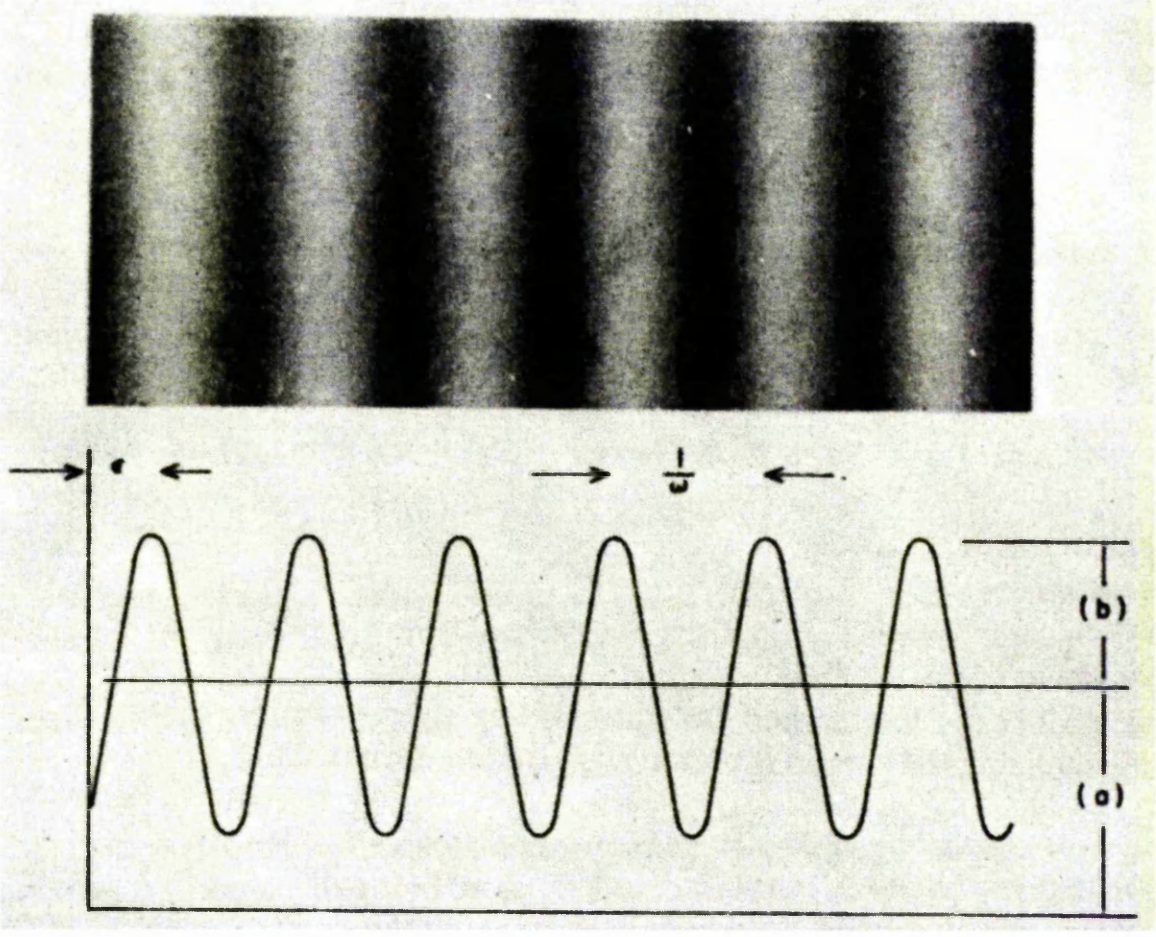

Figure 1-13. A one-dimensional sine wave input, with spatial frequency ω, modulation b/a, and phase ε. (Dainty and Shaw, 1976).

The input modulation is defined by (Dainty and Shaw, 1976):

$$M_{input} = \frac{f_{max} - f_{min}}{f_{max} + f_{min}} = \frac{b}{a} \tag{1-9}$$

The output function, $g(x)$, is also sinusoidal, and has the same frequency as the input:

$$g(x) = a + M(\omega)\, b \cos(2\pi\omega x + \varepsilon + \phi(\omega)) \tag{1-10}$$

where $M(\omega)$ and $\phi(\omega)$ are the modulus and phase of the Fourier transform of the line spread function (see Section 1.4 for an explanation of Fourier transforms). The output modulation is defined by (Dainty and Shaw, 1976):

$$M_{output} = \frac{g_{\max} - g_{\min}}{g_{\max} + g_{\min}} = M(\omega)\frac{b}{a} \tag{1-11}$$

Thus the ratio of the output modulation to the input modulation is equal to $M(\omega)$:

$$M(\omega) = \left| \int_{-\infty}^{+\infty} l(x).e^{-2\pi i\omega x} dx \right| \tag{1-12}$$

The *MTF* is usually normalised to unity at zero spatial frequency:

$$M(0) = \left| \int_{-\infty}^{+\infty} l(x_1) dx_1 \right| = 1 \tag{1-13}$$

The line spread function, $l(x)$, is usually obtained by scanning the image of an edge trace, which is converted from density or transmittance to effective exposure using a macroscopic response curve. Differentiation of this edge response function, $e(x)$, gives the line spread function. The whole scheme is illustrated in Figure 1-14. The main problem in the analysis of edge traces is due to the influence of image noise.

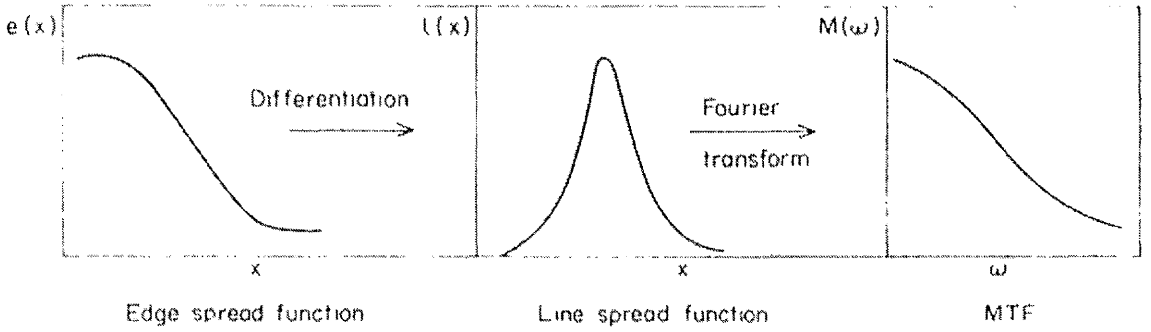

Figure 1-14. Illustrating the process of the derivation of the *MTF* from the edge response function. (Dainty and Shaw, 1976).

1.3.1.4. Detectability

Detectability of details depends on both the imaging quality, in terms of noise, contrast and resolution, and the image observer. In digital images, such as CT images, the number of pixels that represent the imaged detail affect the detectability, and this can be described by the limiting perception factor, G. Investigations have found the value of G to be between 7 and 14 (Cohen and DiBianca, 1979; Sekihara *et al*, 1982). If the detail size, τ, the modulation transfer function of the CT system, MTF_{CT}, and the pixel size, Δp, in the

image are known, it is possible to determine the required value of the detail signal-to-noise ratio, $SNR_{\Delta S,CT}$, for 50% probable detection (Mangard, 2000):

$$SNR_{\Delta S,CT} = \frac{G\Delta p}{\sqrt{2}.\tau.MTF_{CT}\left(\frac{1}{2\tau}\right)} \tag{1-14}$$

In Figure 1-15, a typical detail signal-to-noise ratio detectability curve as a function of detail size is shown (Mangard, 2000).

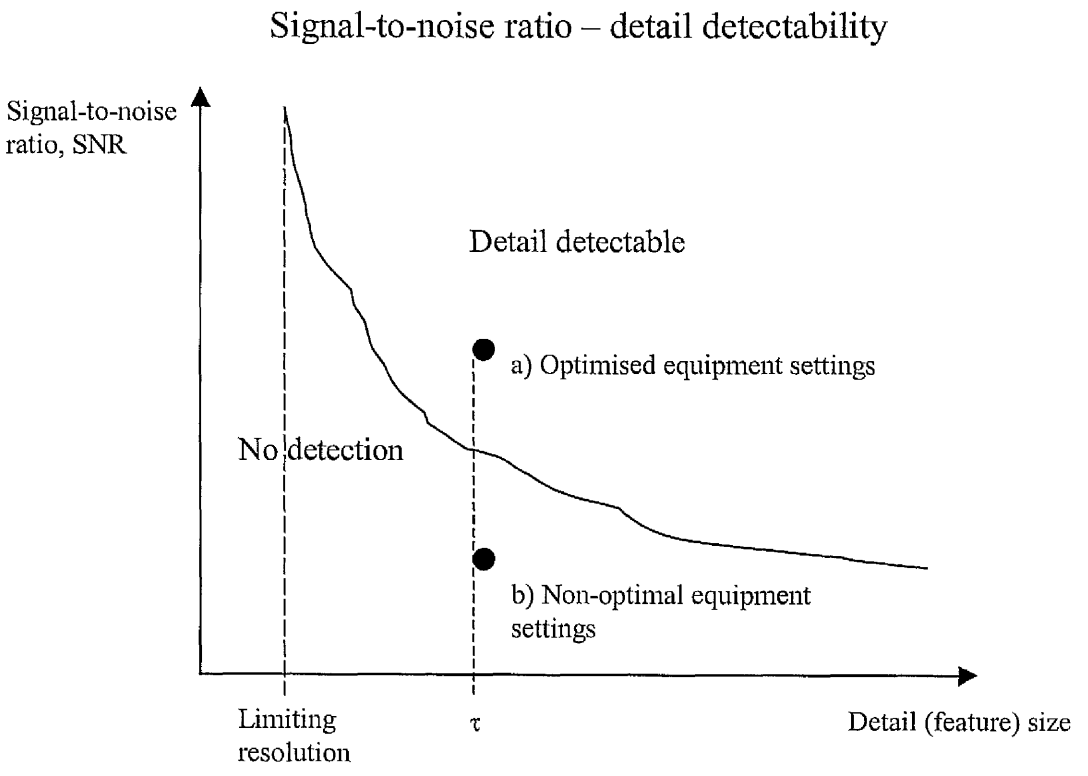

Figure 1-15. Typical $SNR_{\Delta S,CT}$-detail detectability curve. For a detail of size τ, above the curve the detail is detectable (a). On the curve are the details detectable with 50% probability. Below the curve there is no detection (b).

To emphasise the detectability of a defect in the final CT image, the differences in the signals between the defect and the base material must increase. The X-ray spectrum has to be chosen with a tube potential and shaped with filters so that the contrast from a defect within an object increases more than the image noise in the detector. Each individual defect for each individual object material and geometry has its own optimum X-ray tube potential and filter material/thickness, which means that the optimum image equipment settings will change with imaging task and are difficult to find.

1.3.2. Synchrotron X-ray sources

1.3.2.1. Improvement in the signal-to-noise ratio

Synchrotron radiation sources allow exposure times to be reduced, and still improve the signal-to-noise ratio of the reconstructed images compared to a standard X-ray microfocus tube, due to the high flux of such a source. Figure 1-16 illustrates the differences in the signal-to-noise ratio between the images of a vertebra sample obtained using both the synchrotron ID19 beam line microtomography setup and a standard X-ray tube microtomography setup (Ruegsegger *et al*, 1996).

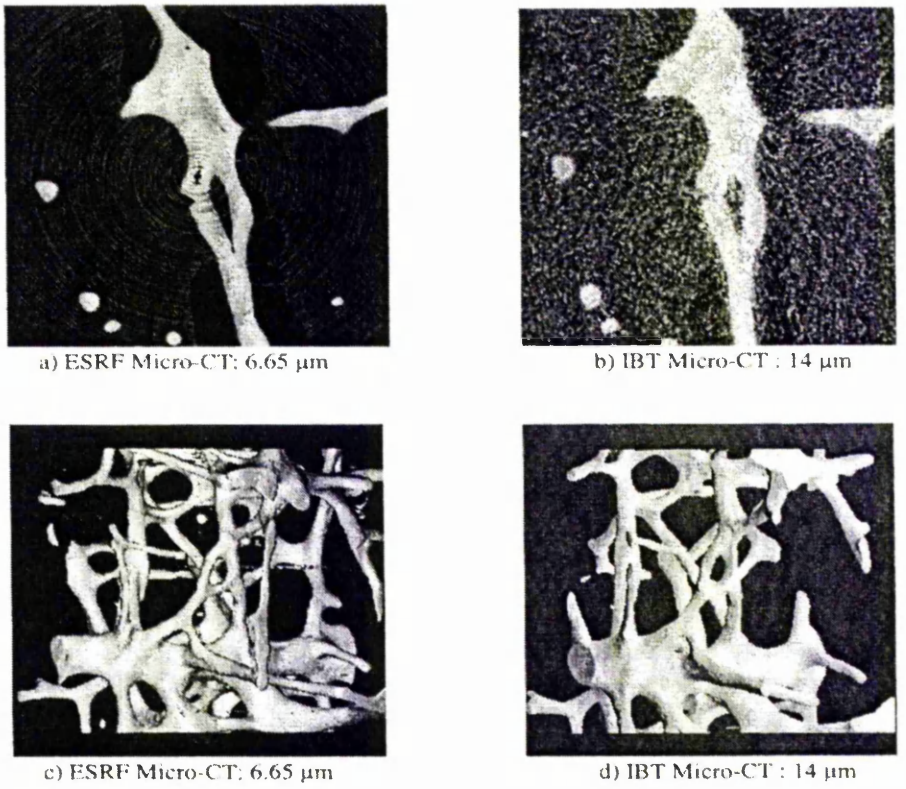

Figure 1-16. Images of a vertebra sample obtained using the ESRF microtomography beam line and a laboratory microfocus CT system, as indicated: (a), (b) 2-D slices extracted from the 3-D images; (c), (d) 3-D rendered displays. (Ruegsegger *et al*, 1996).

Figures 1-16(a) and (b) represent reconstructed slices through the scanned 3-D volumes acquired from the respective setups, as indicated, whose pixel sizes are 6.65 µm and 14 µm respectively. The image obtained at the ESRF is clearly less noisy, and to give an order of magnitude, the signal-to-noise ratio estimated under the assumptions that the noise is stationary and uncorrelated was found to be 70.8 in the synchrotron image and 5.8 in the

X-ray tube image (Ruegsegger *et al*, 1996). These values were derived from the fact that the signal-to-noise ratio is proportional to the detected number of photons. The improvement of the signal-to-noise ratio in the X-ray tube image would be possible if the acquisition time was increased. The differences are smaller in surface rendered displays of the 3-D datasets, as illustrated in Figures 1-16(c) and (d), because the surrounding noise can be suppressed in such a representation.

1.3.2.2. Improvement in the spatial resolution

The availability of intense, parallel and monochromatic beams has made it possible to obtain images from a diverse number of materials, and to reconstruct volumes with a resolution of the order of 0.1 μm (Babout *et al*, 2003; Salvo *et al*, 2003). This is much better than that provided by the polychromatic and divergent beams produced by laboratory microfocus X-ray tubes, which are limited in spatial resolution to about 10 μm. The spatial resolution on a synchrotron beam line is mainly determined by that of the detector, a specially developed CCD camera (see Section 1.2.3), with suitable optical setups (Cloetens *et al*, 1999; Cloetens *et al*, 1997; Espeso *et al*, 1998). Increasing the spatial resolution, while keeping the same signal-to-noise ratio, requires the number of photons to be increased. Under some estimations of the signal-to-noise ratio in a reconstructed image, it can be considered that the required number of photons grows as the third power of the number of pixels in the image (Baruchel *et al*, 2000). Figure 1-17 illustrates the capabilities of micron resolution synchrotron microtomography, representing a reconstructed slice from a three dimensional image of a fetal mouse bone, with a voxel size of 1.8 μm (Baruchel *et al*, 2000). An inferior spatial resolution would not allow the observation of the structure within the bone.

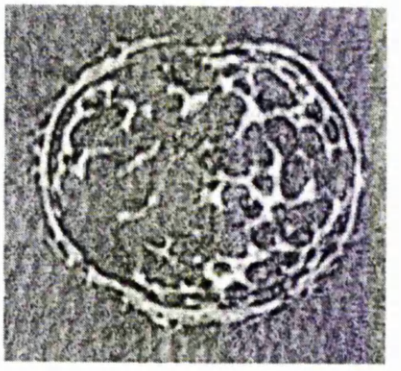

Figure 1-17. Reconstructed slice of a fetal mouse bone with a pixel size of 1.8 μm. (Baruchel *et al*, 2000).

1.3.3. Phase contrast tomography

For medical and industrial imaging, X-ray radiography and tomography both normally rely on the conventional mode of imaging, contrast given by simple *absorption*. This results from the difference between the linear attenuation coefficients of the materials/phases inside an object, so that the larger the difference the better the contrast. With such a mode of imaging, too low a transmission of the beam through the object results in bad photon statistics, whereas too high a transmission results in too low a contrast between phases/elements. A transmission of ~10% has been found to be a good trade off between the two extremes (Flannery and Roberge, 1987; Graeff and Engelke, 1991). This attenuation contrast has been found to be sufficient in the majority of cases, such as the monitoring of fatigue crack closure in Al-Li alloys (Guvenilir *et al*, 1997), the characterisation of void and reinforcement distributions in ZrO_2 particle reinforced Al MMCs (Justice *et al*, 2000) and the study of the porous structure of metallic foams (see Chapters 5 and 6). However, the availability of synchrotron sources has enabled several modes of phase imaging to be taken advantage of (Beckmann *et al*, 1997; Ingal and Beliaevskaya, 1995; Momose, 1995) leading to improvements in the detection of internal structures in the 3-D reconstructions. Phase imaging can be used either in a qualitative way, mainly useful for edge detection (Cloetens *et al*, 1997), or in a quantitative way, involving numerical retrieval of the phase from images recorded at different distances from the sample (Cloetens *et al*, 1999).

1.3.3.1. Qualitative imaging

When an X-ray beam is partially coherent, such as that at a synchrotron source (ESRF), and when the distance between the sample and detector is increased relative to that in absorption mode, a *phase contrast* mode is observed (Cloetens *et al*, 1997). The refractive index of X-rays deviates slightly from unity and an X-ray beam is modulated in its optical phase after passing through an object or through different constituents inside the object. The occurrence of contrast is due to interference, after propagation of the beam through the sample (Cloetens *et al*, 2000) and when the direction of the X-ray beam is tangential to the edge of structures in the sample, between parallel rays passing on each side of an interface between two constituents of the studied material, that have undergone different phase retardation. This phase contrast, due to the phase difference, is superimposed onto the conventional absorption or attenuation contrast. A spatial redistribution of the photons occurs due to deflections (more generally due to Fresnel

diffraction). The overlap or interference between the parts of the wavefront that have suffered slightly different angular deviations is only possible after propagation over a certain distance. The spatial coherence of the X-ray beams produced at synchrotron sources such as the ESRF ensures good contrast in the interference patterns. Phase imaging is in general much more sensitive than absorption imaging. This is crucial when the attenuation contrast is weak, such as in the observation of light materials (polymers), and in being able to distinguish between absorbing constituents with similar X-ray attenuation, such as in Ti/SiC fibre composites (see Section 4.4) or Al/SiC particulate composites (Buffière *et al*, 1999). Density discontinuities appear as dark/light fringes. The technique was initially used in radiography (Cloetens *et al*, 1996; Snigirev *et al*, 1995), and has allowed defects that are smaller than the pixel size to be detected (Cloetens *et al*, 1997). Phase sensitivity has been shown to be an excellent way of improving the detection of cracks in their early development stage, i.e. when they have sub-micron opening (Buffière *et al*, 1999). The detection of isolated features smaller than the spatial resolution of the detector system is possible as the interference fringes that are produced can be larger than the feature itself (Cloetens *et al*, 1997).

Phase sensitivity is obtained by increasing the distance between the sample and the detector, initially resulting in a stronger and broader signature of edges between different materials/phases in an object. At larger distances, these broad Fresnel fringes cover the image, turning it into a hologram with less and less direct resemblance to the object. The image contrast changes tremendously with the sample-detector distance, d, which in turn determines the defocusing distance, D, through the expression $D = (d \times l) / (d + l)$, where l is the source-sample distance (Cloetens *et al*, 2000). In the case of the long beam line at the ESRF ($d \ll l$ = 145 m), the defocusing distance and the sample-detector distance are practically equal. Figure 1-18 shows, as an example, four radiographs of a 0.5 mm thick piece of polystyrene foam at increasing distances of D (Cloetens *et al*, 1999). It is clear that as this distance increases the contrast and width of the Fresnel fringes both increase. Blurring due to source size and detector resolution explains why no interference fringes are observed with laboratory sources, although the propagation distances are also non-zero in projection radiography. Using the same propagation principle, deflection sensitive images have been obtained with polychromatic radiation delivered by laboratory X-ray micro-sources, using edge contrast and dual energy X-ray microtomography (Justice *et al*, 2000). Using such an approach, X-ray absorption is measured at two X-ray energies either side of a critical X-ray absorption edge of an element.

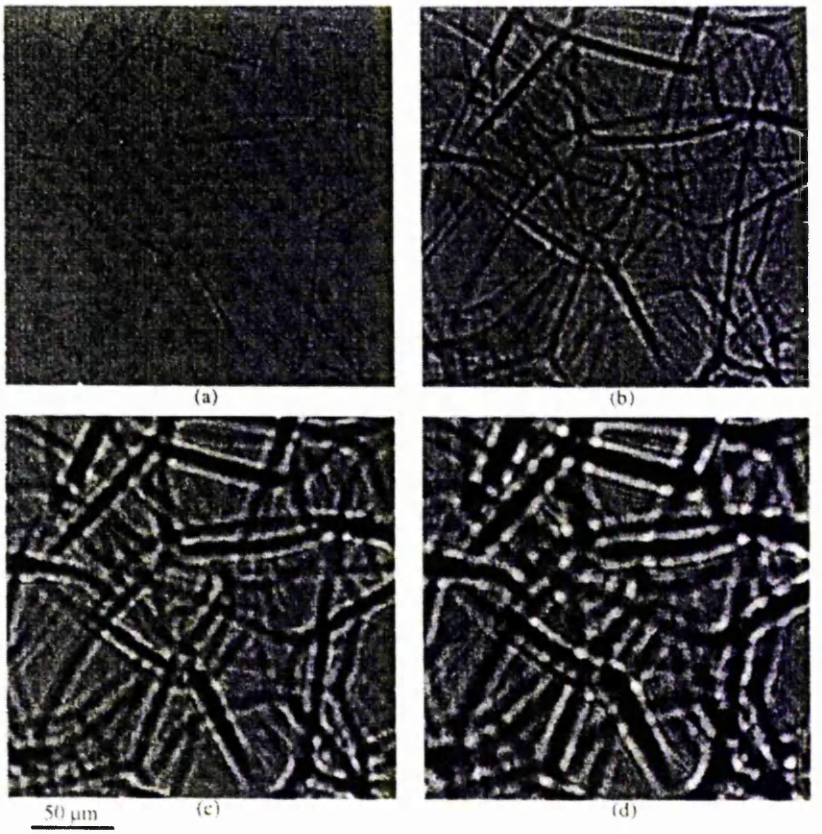

Figure 1-18. Phase sensitive radiographs of a 0.5 mm thick piece of polystyrene foam, with the detector at various distances, *d*, from the sample. X-ray energy = 18 keV. (a) D = 0.03 m, (b) D = 0.2 m, (c) D = 0.5 m, (d) D = 0.9 m. The contrast and the width of the interference fringes increase through the series of images. (Cloetens *et al*, 1999).

1.3.3.2. Quantitative imaging

The edge detection regime does not allow the measurement of the local phase. A more quantitative approach, *holotomography*, has been implemented to extract, using a specific algorithm, the quantitative distribution of the optical phase in two-dimensional projection images, and then turn it into a 3-D reconstruction (Cloetens *et al*, 1999). This phase-retrieval procedure involves using radiographs recorded at different distances of the sample with respect to the detector. When this operation is performed for each projection, and the result is used as input for a tomographic reconstruction, the decrement with respect to unity of the refractive index is reconstructed for each voxel of the sample. This decrement is essentially proportional to the electron or mass density of the material. When the fringes of the phase images are disentangled in a holographic reconstruction, the spatial resolution is limited by the detector. The following describes two examples using this

approach: a non-absorbing polymer foam (Cloetens *et al*, 1999) and an absorbing metal alloy that introduces very large phase shifts (Cloetens *et al*, 2000).

Polymer foam

The cellular structure of a piece of polystyrene foam with a complex 3-D structure was studied, having a cross-section of 0.5×0.7 mm^2 and negligible attenuation (Cloetens *et al*, 1999). Four tomographic scans of 700 images each were recorded at defocusing distances, D, of 0.03, 0.21, 0.51 and 0.9 m. The radiographs for a given angular position are shown in Figure 1-18. The corresponding reconstructed phase map is shown in Figure 1-19, illustrating a projection along the X-ray path of the electron density in the sample (Cloetens *et al*, 1999). Cells with sizes of the order of 100 μm have been revealed.

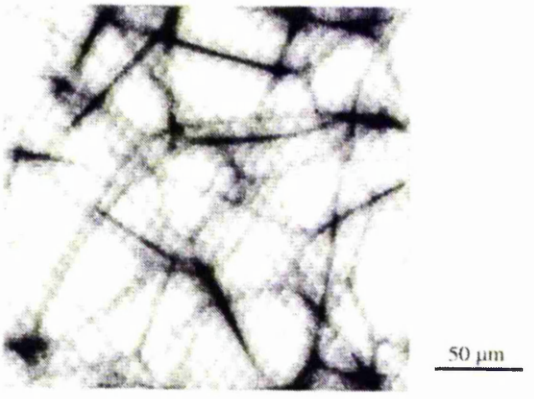

Figure 1-19. Phase map retrieved with an algorithm that combines images recorded at four distances, as shown in Figure 1-18. The sample is a 0.5 mm thick piece of polystyrene. X-ray energy = 18 keV. (Cloetens *et al*, 1999).

The holographic reconstruction was repeated for 700 angular positions of the sample. The phase maps, which are projections of the refractive index decrement, δ, were used to determine the 3-D distribution of δ in the sample with a filtered back-projection algorithm. Figure 1-20(a) shows a slice of the reconstructed volume (Cloetens *et al*, 1999). The grey scale is linear with respect to the index decrement, with darker regions corresponding to a higher electron and mass density. This enables straightforward interpretation of the reconstructed slices, and the contrast of the cell walls of the polymer foam is very clear. This would not be the case in absorption tomography, due to the very low density of the material. Figure 1-20(c) shows a profile of the index decrement along a line segment shown in Figure 1-20(a). It was found that in regions that apparently contain

only polymer the refractive index decrement was 6.6×10^{-7}, corresponding to a mass density of 0.96 g/cm^3, which is in agreement with the expected density value for polystyrene of about 1 g/cm^3 (Cloetens *et al*, 1999). As can be seen, the tomographic slice shown in Figure 1-20(a) intersects a cell of the foam that is completely enclosed by a polymer wall. These thin walls were found not to be evident in the projection images, but they appear correctly after tomographic reconstruction. The shape of the cell is irregular and is very distorted, which is probably due to a crushing process. Thanks to the detector resolution, and also because the holographic reconstruction disentangled the object information from the defocused images, an excellent 3-D isotropic spatial resolution can be obtained, as shown by the magnified portion of the slice in Figure 1-20(b).

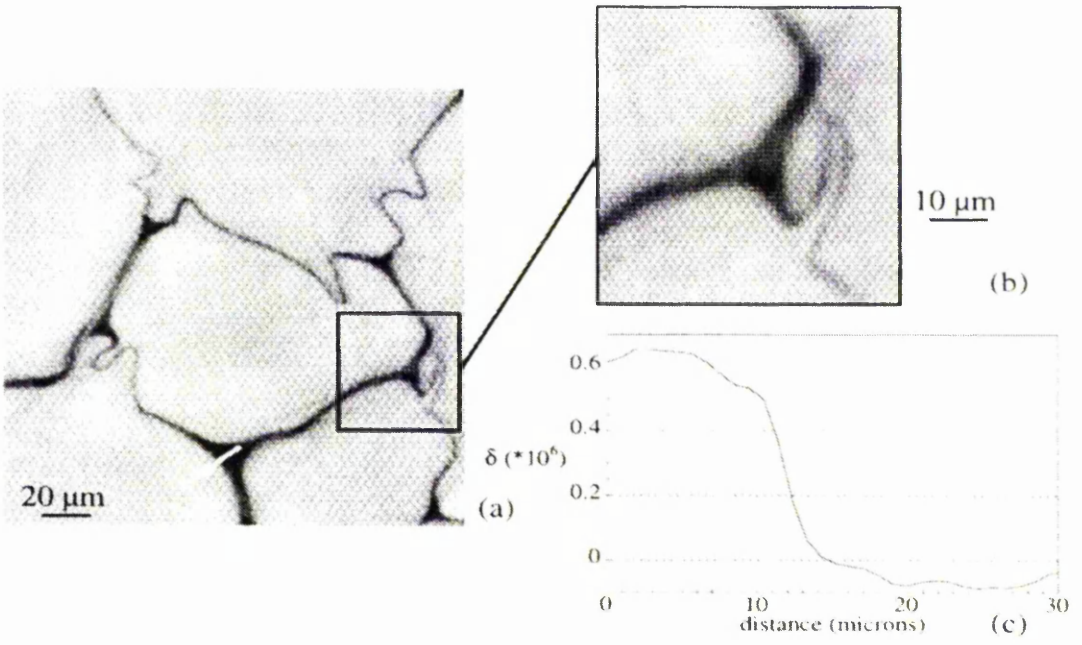

Figure 1-20. (a) A slice of the reconstructed distribution of the refractive index decrement, δ through a polystyrene foam piece. (b) Magnified portion of the reconstructed slice shown in (a). (c) Profile along the arrow shown in (a). E = 18 keV. (Cloetens *et al*, 1999).

Metal alloy

The microstructure of an aluminium-silicon alloy that had been quenched from the semi-solid state was studied (Cloetens *et al*, 2000). With such a technique as holotomography, problems can arise with the thickness of samples. A sample of aluminium with a thickness of 1.5 mm can introduce a large phase shift using an X-ray

energy of 18 keV, resulting in difficulties with reconstructing. Such a phase shift would not occur in a polymer foam because most of it consists of air. As a result, only the phase variations with respect to the phase introduced by a homogeneous matrix were reconstructed (Cloetens *et al*, 2000).

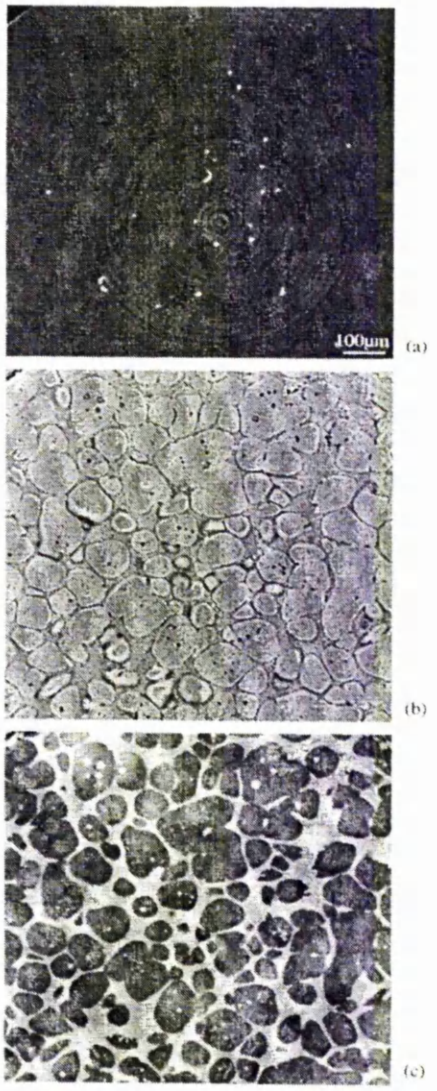

Figure 1-21. Three tomographic slices of an aluminium-silicon alloy quenched from the semi-solid state, obtained using (a) absorption contrast, (b) phase contrast and a single propagation distance and (c) phase contrast and holotomography based on four distances. E = 18 keV. (Cloetens *et al*, 2000).

Figure 1-21(a) shows a tomographic slice recorded at D = 7 mm, sensitive only to variations in absorption. It is impossible to distinguish between the two phases of the material, and some bright spots appear corresponding to iron-rich inclusions.

Figure 1-21(b) shows a tomographic slice obtained for a single distance, D = 0.6 m, revealing density jumps as dark/light fringes. Figure 1-21(c) is a reconstructed map of the variations in the refractive index decrement, clearly showing the slight difference in density of the two phases ($\Delta\rho \approx 0.05$ g/cm^3). The grey phase is the liquid in the semi-solid state and it consists of an aluminium-silicon eutectic. The dark phase is the solid and is essentially pure aluminium with substitutional silicon. The data set consisted of four sets of 800 images recorded at distances of 0.007, 0.2, 0.6 and 0.9 m from the X-ray source.

1.4. Reconstruction

1.4.1. Basis and methods of reconstruction

The purpose of computed tomography (CT) is to create or reconstruct a 2-D or 3-D representation of the internal structure of an object from a set of projection measurements or radiographs acquired from a number of incremented angular views. The projections are a set of measurements of the integrated values of the linear attenuation coefficient, μ, along straight lines through the object, referred to as line integrals. The object can be modelled as a 2-D or 3-D distribution of the X-ray attenuation coefficient and a line integral represents the total attenuation suffered by a beam of X-rays as it travels in a straight line through the object. Several different methods and algorithms exist for the reconstruction of these projections depending on the geometry of the system being used, either parallel (pencil), fan or cone beam setups (as defined in Section 1.2.1), and have been detailed extensively by Kak and Slaney (Kak and Slaney, 1987). The mathematical basis assumes that the acquisition system is able to provide a set of these projections of μ in a so-called 'parallel-beam' geometry, and has the object fixed while a measurement system, composed of a source and a detector, translates and rotates around the object, as shown in Figure 1-22 (Robert-Coutant and Marc, 2000). In most practical laboratory microtomography systems, the source-detector setup is fixed and the object moves, but in order to define the mathematics behind the reconstruction algorithms it is easier to define a reference system attached to the object. Let (x,y) be the coordinates of a point, M, in the reference system, the origin, O, of which is at the axis of rotation. A line integral is defined by the parameters (θ,t) where θ is the angle between the x-axis and the perpendicular to the ray, and t is the algebraic distance from the axis of rotation to the ray.

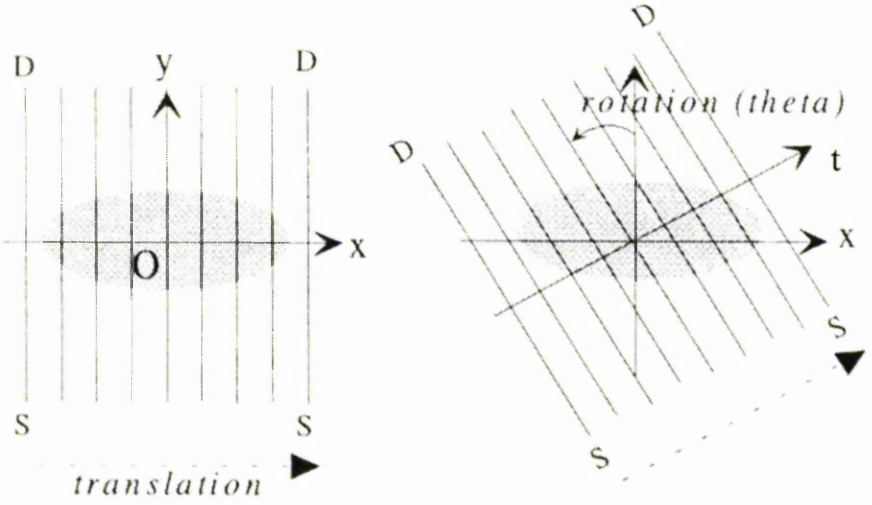

Figure 1-22. Acquisition geometry used to define the mathematical basis of parallel-beam tomography, with object *O*, source *S* and detector *D*. (Robert-Coutant and Marc, 2000).

If ϕ_0 is the number of photons delivered by the source, and ϕ is the number of photons after attenuation by the object, Equation (1-1) gives the Beer-Lambert law as:

$$\phi = \phi_0 \cdot \exp\left(-\int_{M \in ray} \mu(M)\, dM\right) \tag{1-15}$$

If it is assumed that both ϕ and ϕ_0 are measured by the acquisition system, then the projection, $P(\theta,t)$, of μ along a ray, (θ,t), can be expressed as follows (Robert-Coutant and Marc, 2000):

$$P(\theta,t) = \ln\left(\phi_0 / \phi\right) = \int_{M \in ray(\theta,t)} \mu(M)\, dM \tag{1-16}$$

$P(\theta,t)$ is used to define a projection or line integral along a ray given by (θ,t), as shown in Figure 1-24 (Kak and Slaney, 1987). A 'projection' refers to the set of measurements acquired for a single angle of rotation. The set of projections measured over many angles, i.e. 180° or 360°, defines the Radon transform of the function μ (Radon, 1917/1986). In parallel-beam geometry, and when extended to the fan and cone-beam geometries, projection measurements over 180° are sufficient to represent the Radon transform, since $P(\theta,t) = P(\theta+\pi,-t)$. The linear and angular sampling, i.e. the angle between each successive projection measurement, must be fine enough so that the projection data can be mathematically considered as a satisfactory sampled version of the continuous Radon transform. The function μ must be zero outside the circle defined by the acquisition

system when it rotates in order to define a reference for the projection measurements (Kak and Slaney, 1987). Real measurements are not acquired with infinitely thin rays, but each ray has a width that is determined by the focal spot size of the X-ray source, the detector element width, the source-to-object distance and the source-to-detector distance. Accordingly, the translation step used for the acquisition of projections in the pencil beam geometry, must be small enough to be consistent with this ray width and with the size of the structures in the object. It is recommended that the number of angular projections is between $\pi/2$ and $\pi/4$ times the number of linear pixels per projection (Kak and Slaney, 1987), e.g. 1000^2 pixels equals 785-1570 angular increments. Figure 1-23 shows an example of a set of projections over 180° or 'sinogram', which is the name given to the 2-D representation which is obtained if the projections are displayed in grey levels one below the other (Robert-Coutant and Marc, 2000).

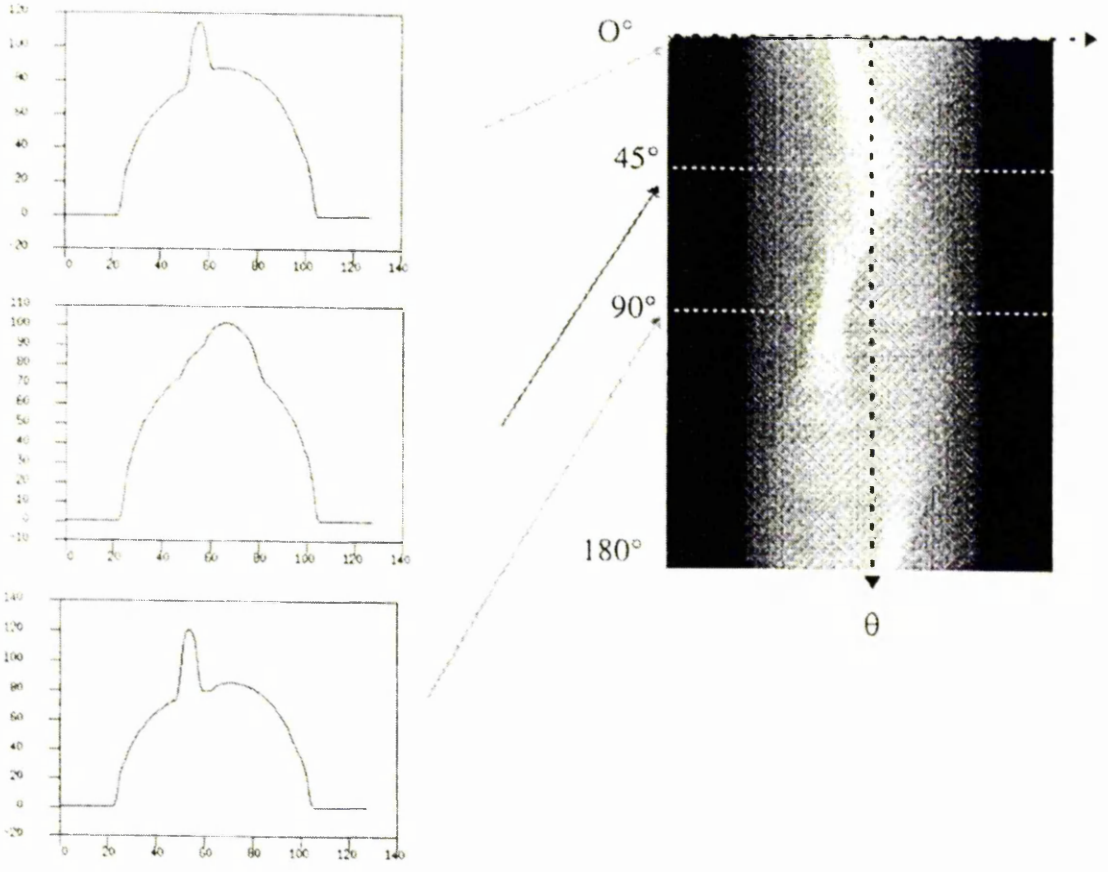

Figure 1-23. Right: a sinogram or set of projections over 180°; left: three projections extracted from the sinogram, with the *x*-axes representing the position across the sample, and the *y*-axes the grey level intensity. (Robert-Coutant and Marc, 2000).

In order to define the mathematical function of the 'Radon transform', the coordinate system defined in Figure 1-24 is used.

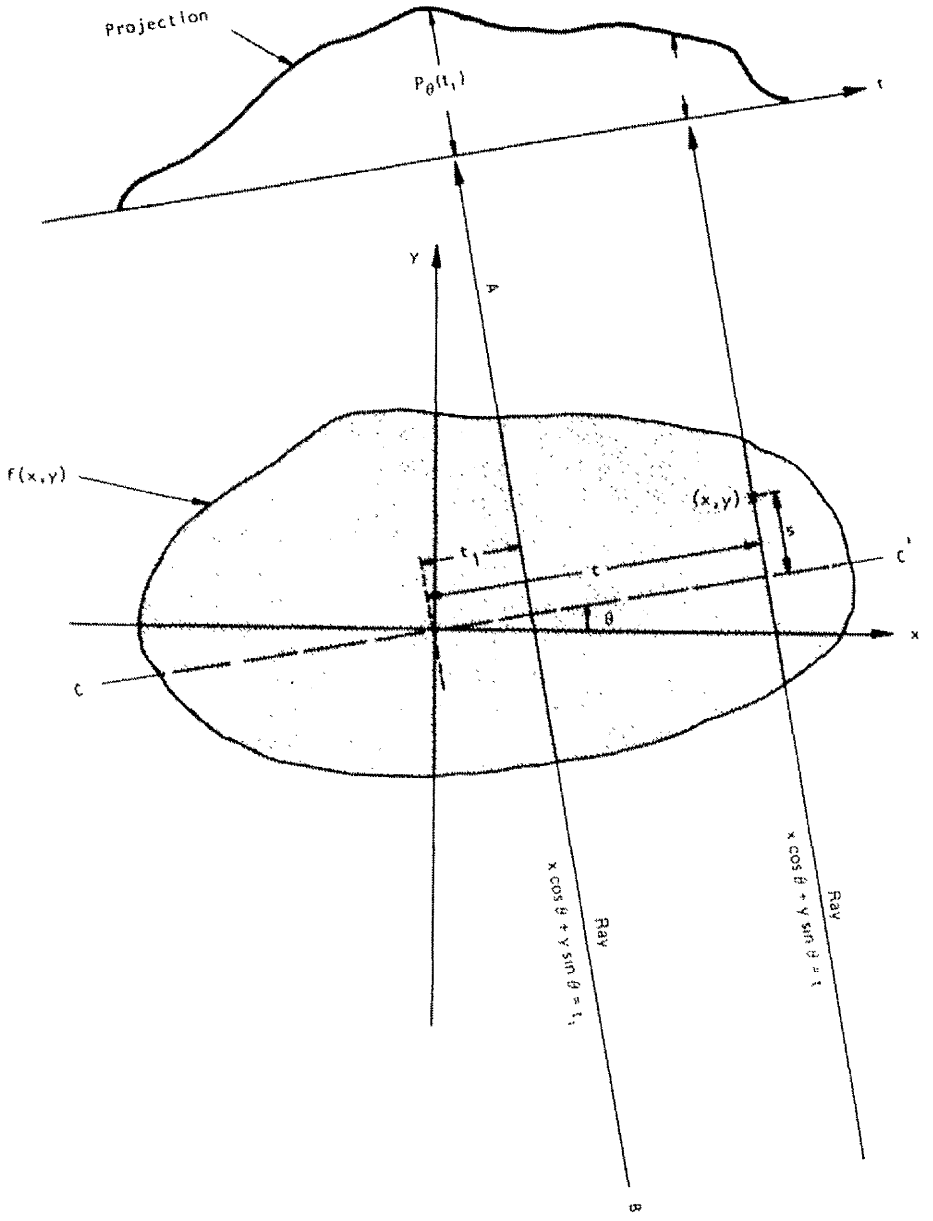

Figure 1-24. The coordinate system for an object, represented by the function f(x,y), and its projection, $P_\theta(t_1)$, are defined for an angle of θ. (Kak and Slaney, 1987).

Referring to Figure 1-24, the object is represented by a two-dimensional function, f(x,y), and each line integral by the (θ,t) parameters (Kak and Slaney, 1987). The equation of the line AB in Figure 1-24 is:

$$x \cos \theta + y \sin \theta = t \qquad (1\text{-}17)$$

and this relationship can be used to define the line integral $P_\theta(t)$ as (Kak and Slaney, 1987):

$$P_\theta(t) = \int_{(\theta,t)line} f(x,y)\, dy \qquad (1\text{-}18)$$

The function $P_\theta(t)$ is known as the Radon transform of the function $f(x,y)$.

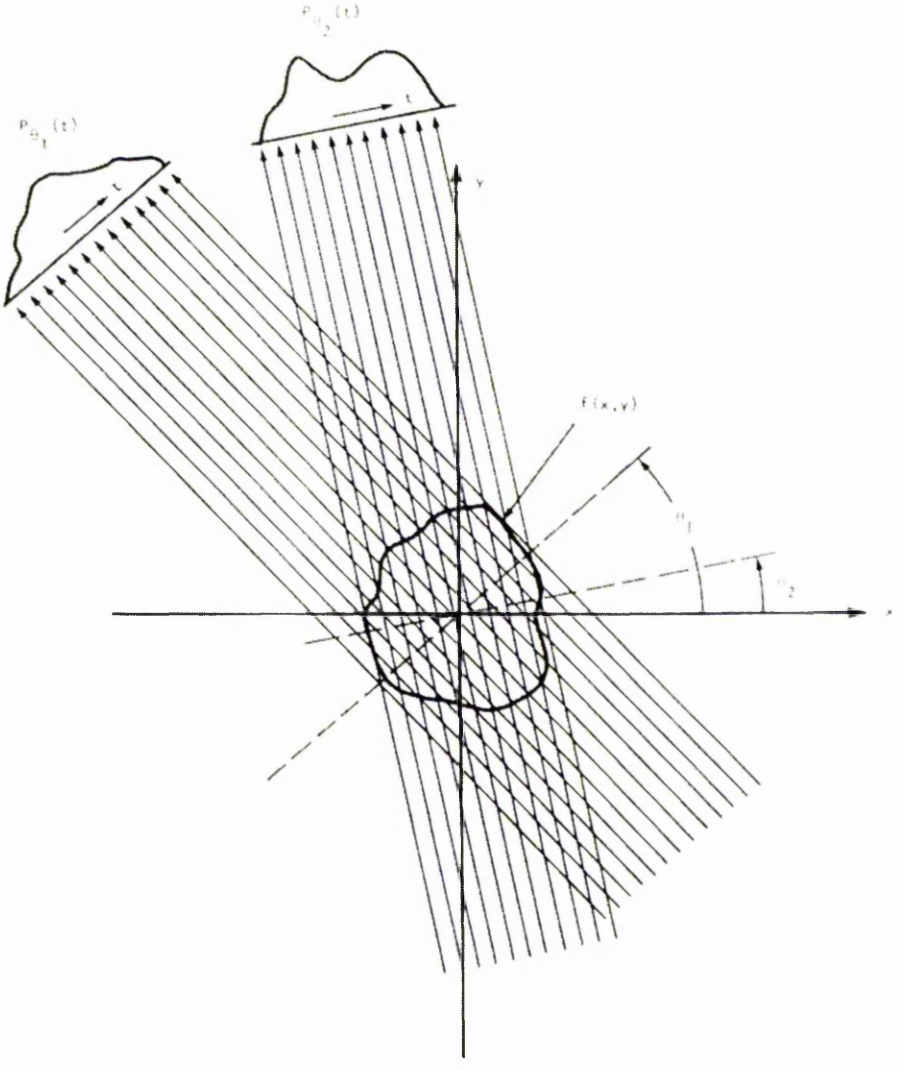

Figure 1-25. Parallel projections are acquired by measuring a set of parallel rays for a number of different angles. (Rosenfeld and Kak, 1982).

A projection is formed by combining a set of line integrals. The simplest projection, for which the mathematical basis has been shown, is a collection of parallel ray integrals, as is given by $P_\theta(t)$ for a constant θ. This is known as a *parallel projection*, illustrated in Figure 1-25 (Rosenfeld and Kak, 1982), and is used at synchrotron sources such as at the ESRF.

Successive projections are measured by rotating the object with respect to the source and detector. Another type of projection is possible if a point source is placed in a fixed position relative to a line of detectors and the line integrals are measured along fans. This is shown in Figure 1-26 and is known as a *fan beam projection* (Rosenfeld and Kak, 1982).

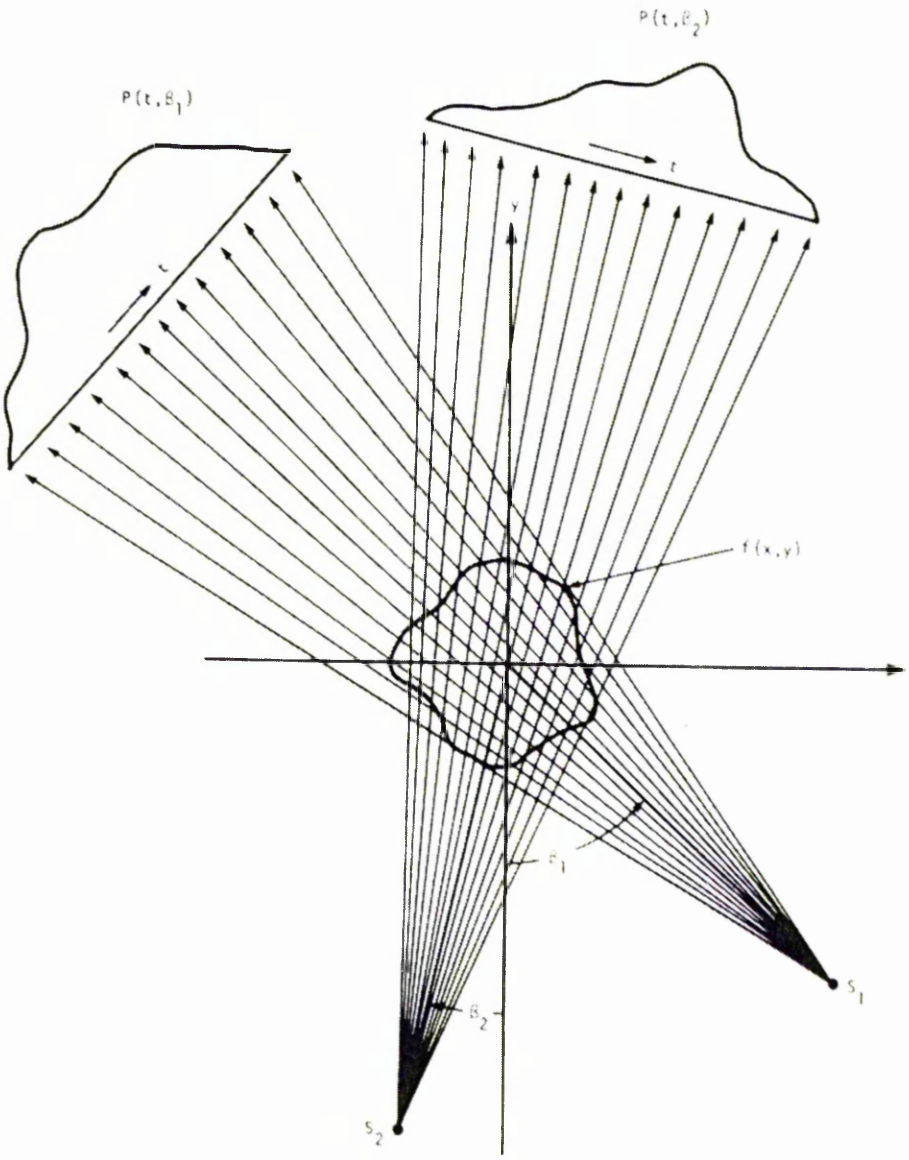

Figure 1-26. A fan beam projection is collected if all the rays from a point source meet at the detector location. (Rosenfeld and Kak, 1982).

Note that a cone beam projection is the volumetric equivalent of a fan beam projection, and used with micro-focus X-ray tube sources.

1.4.2. Reconstruction from parallel projections

Several methods are available for reconstructing a slice, $f(x,y)$, from its projection data, $P_\theta(t)$, depending on the system geometry. The reconstruction algorithm that is widely used for all geometries, and derived initially for the parallel beam geometry, is the filtered backprojection method (Herman, 1980), and is derived using the Fourier slice theorem. Fourier analysis is used to represent the functions of such an algorithm in the frequency domain as opposed to the time or space domain. All of the deviations of the filtered backprojection algorithm for the various geometries rely on the principles of this method.

1.4.2.1. The Fourier slice theorem

One of the important properties of the Radon transform, $P_\theta(t)$, of an object, $f(x,y)$, is its relationship to the Fourier transform, $F(u,v)$, of $f(x,y)$, usually termed the *Fourier slice theorem*. The Fourier slice theorem is the basis of many reconstruction methods. It is derived by taking the one-dimensional Fourier transform of a parallel projection and equating it to a slice of the two-dimensional Fourier transform of the original object. It follows that, given the projection data, it should be possible to estimate the object by performing a two-dimensional inverse Fourier transform. The two-dimensional Fourier transform of the object function is defined as (Kak and Slaney):

$$F(u,v) = \int_{-\infty}^{\infty} \int_{-\infty}^{\infty} f(x,y) \cdot \exp\left[-j 2\pi (ux + vy) \right] dx\, dy \qquad (1\text{-}19)$$

where (u,v) are the coordinates of the object in the frequency domain and (x,y) the coordinates in the space domain, as defined in Figure 1-27 below. j represents the complex number. The Fourier transform, $S_\theta(\omega)$, of a projection, $P_\theta(t)$, at an angle θ is defined as (Kak and Slaney, 1987):

$$S_\theta(\omega) = \int_{-\infty}^{\infty} P_\theta(t) \cdot \exp\left[-j 2\pi \omega t \right] dt \qquad (1\text{-}20)$$

where ω is the spatial frequency. The simplest example of the Fourier slice theorem is given for a projection at $\theta = 0$. Firstly, consider the Fourier transform of the object along a line in the frequency domain given by $v = 0$, shown in Figure 1-27 (Kak and Slaney, 1987). The Fourier transform integral can now be simplified, and the integral can also be split into two parts because the phase factor is no longer dependent on y. From Equation (1-19):

$$F(u,0) = \int_{-\infty}^{\infty} \left[\int_{-\infty}^{\infty} f(x,y)\, dy \right] \cdot \exp\left[-j 2\pi ux \right] dx \qquad (1\text{-}21)$$

From the definition of a parallel projection and its Radon transform, the first term in brackets is the equation for a projection along lines of constant x (Equation 1-18), or:

$$P_{\theta=0}(x) = \int_{-\infty}^{\infty} f(x,y)\, dy$$

Substituting this into Equation (1-21), gives:

$$F(u,0) = \int_{-\infty}^{\infty} P_{\theta=0}(x) \cdot \exp[-j 2\pi ux]\, dx \qquad (1\text{-}22)$$

The right-hand side of this equation represents the one-dimensional Fourier transform of the projection $P_{\theta=0}(x)$ (Equation 1-20). The relationship between a vertical projection and the 2-D transform of the object function is given by (Kak and Slaney, 1987):

$$F(u,0) = S_{\theta=0}(u) \qquad (1\text{-}23)$$

This result is the simplest form of the Fourier slice theorem, and is independent of the orientation between the object and the coordinate system. If, for example, as shown in Figure 1-27, the coordinate system is rotated by an angle θ, the Fourier transform of the projection defined in (1-18) is equal to the two-dimensional Fourier transform of the object along a line rotated by θ.

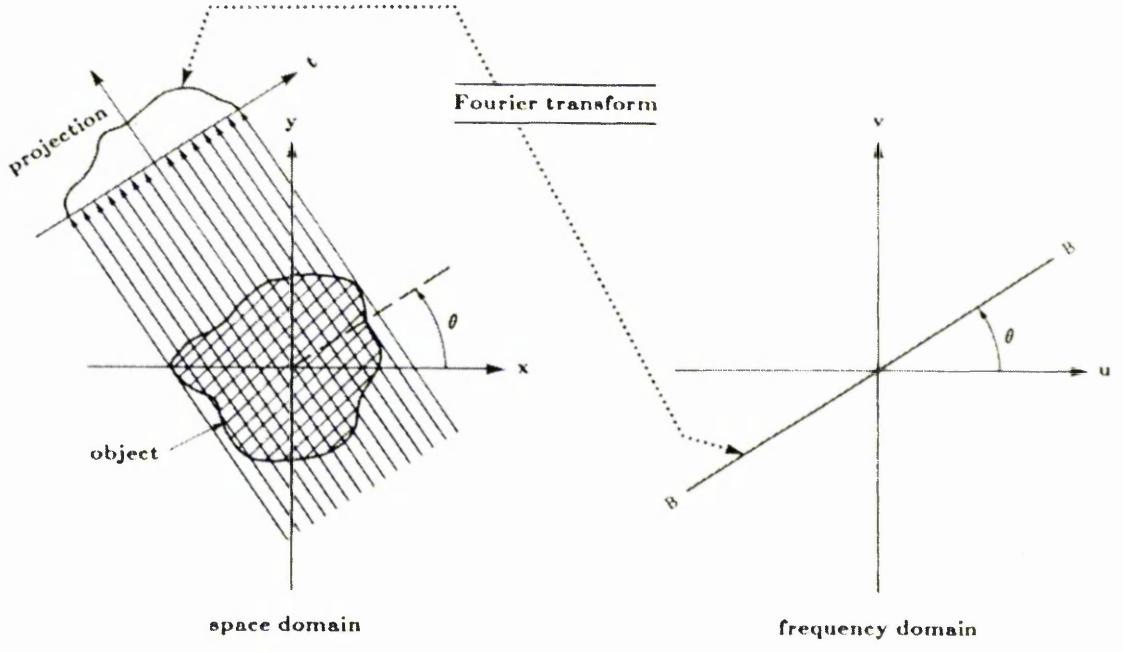

Figure 1-27. The Fourier Slice Theorem relates the Fourier transform of a projection to the Fourier transform of the object along a radial line. (Kak and Slaney, 1987).

The Fourier slice theorem, the result of which is given by Equation (1-23), is stated as:

> The Fourier transform of a parallel projection of an image, $f(x,y)$, taken at an angle θ, gives a slice of the two-dimensional transform, $F(u,v)$, subtending an angle θ with the u-axis. In other words, the Fourier transform of $P_\theta(t)$ gives the values of $F(u,v)$ along the line BB in Figure 1-27.

The above result indicates that by taking the projections of an object function at angles θ_1, θ_2, ..., θ_k and applying a Fourier transform to each, the values of $F(u,v)$ can be determined on radial lines as shown in Figure 1-27. If an infinite number of projections are taken, then $F(u,v)$ would be known at all points in the uv-plane. Knowing $F(u,v)$, the object function, $f(x,y)$, can be recovered by using the inverse Fourier transform, defined by (Kak and Slaney, 1987):

$$f(x,y) = \int_{-\infty}^{\infty} \int_{-\infty}^{\infty} F(u,v) \cdot \exp\left[j 2\pi (ux + vy) \right] du\, dv \qquad (1\text{-}24)$$

Regarding Fourier slice reconstruction, an important point must be noted (Hiriyannaiah, 1997). The Fourier transform, $S_\theta(\omega)$, of $P_\theta(t)$ gives the values of the Fourier transform, $F(u,v)$, of $f(x,y)$ along a radial path at an angle θ in the (u,v) domain, as illustrated in Figure 1-27. For equiangular values of θ, values of $F(u,v)$ are obtained along radial paths in concentric circles. These values then have to be interpolated onto a rectangular grid and the errors associated with this interpolation are not constant. Toward the origin there will be a dense collection of samples and interpolation errors will be small, whereas in the high-frequency regions the samples are sparse and the interpolation errors will be high. Consequently, edges and other high-frequency spatial content in the intensity signal of an image, $f(x,y)$, can be distorted.

1.4.2.2. Filtered backprojection

The algorithm that is currently being used in almost all applications of straight ray tomography is the filtered backprojection algorithm (Herman, 1980). It has been shown to be extremely accurate and amenable to fast implementation and is derived using the Fourier slice theorem (Kak and Slaney, 1987). Recall the formula for the inverse Fourier transform, Equation (1-24), using which enables the object function, $f(x,y)$, to be recovered from the Fourier transform of the set of projections in the frequency domain. Exchanging the rectangular coordinate system in this domain, (u,v), for a polar coordinate system, (ω,θ), by making the substitutions $u = \omega \cos\theta$ and $v = \omega \sin\theta$, and then changing the

differentials by using $du\ dv = \omega\ d\omega\ d\theta$, the inverse Fourier transform of a polar function can be written as (Kak and Slaney, 1987):

$$f(x,y) = \int_{-\infty}^{\infty} \int_{-\infty}^{\infty} F(\omega,\theta) \cdot \exp\left[j 2\pi \omega (x \cos\theta + y \sin\theta) \right] \omega\, d\omega\, d\theta \qquad (1\text{-}25)$$

If the Fourier transform of the projection at an angle θ, $S_\theta(\omega)$, defined by Equation (1-20), is substituted in place of the two-dimensional Fourier transform, $F(\omega,\theta)$, and the expression is simplified by setting $t = x \cos\theta + y \sin\theta$, the following expression is obtained:

$$f(x,y) = \int_{0}^{\pi} \left[\int_{-\infty}^{\infty} S_\theta(\omega) |\omega| \cdot \exp[j 2\pi \omega t]\, d\omega \right] d\theta \qquad (1\text{-}26)$$

The integral in Equation (1-26) can be expressed as (Kak and Slaney, 1987):

$$f(x,y) = \int_{0}^{\pi} Q_\theta(x \cos\theta + y \sin\theta)\, d\theta \qquad (1\text{-}27)$$

where:

$$Q_\theta(t) = \int_{-\infty}^{\infty} S_\theta(\omega) |\omega| \cdot \exp[j 2\pi \omega t]\, d\omega \qquad (1\text{-}28)$$

This estimate of $f(x,y)$, given the Fourier transform of the projection data, $S_\theta(\omega)$, can be interpreted as follows. Equation (1-28) represents a filtering operation, where the frequency response of the filter is given by $|\omega|$. Therefore, $Q_\theta(\omega)$ is called a 'filtered projection'. The resulting projections for different angles, θ, are then added to form the estimate of $f(x,y)$.

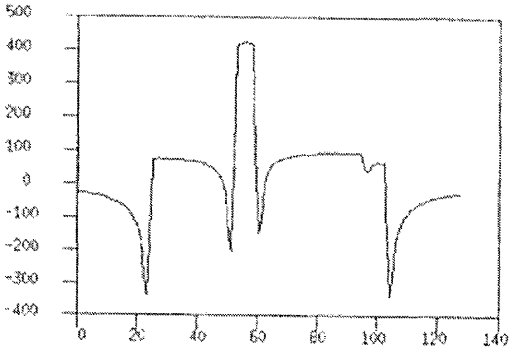

Figure 1-28. A profile of a filtered projection for $\theta = 0°$, the image for which is shown in Figure 1-29. The x-axis represents the position across the sample, and the y-axis the grey level intensity. (Robert-Coutant and Marc, 2000).

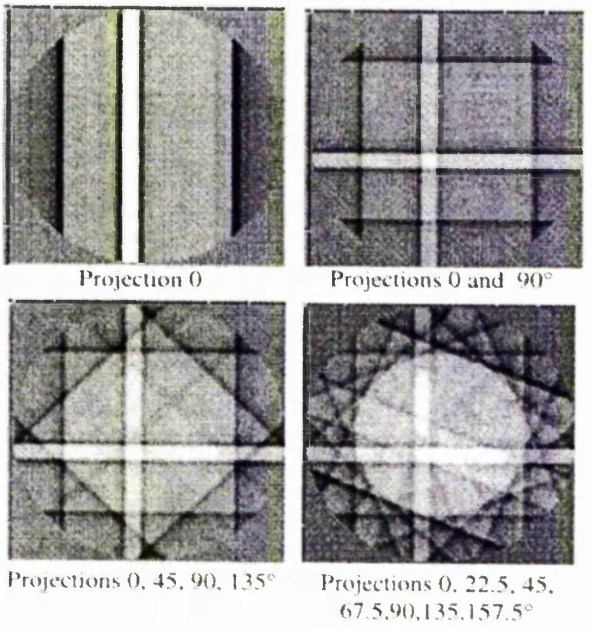

Figure 1-29. Backprojection of filtered projections for 1, 2, 4 and 8 different angles. (Robert-Coutant and Marc, 2000).

The filtering operation has the effect of creating negative components on the filtered projection, as illustrated in Figure 1-28, which compensates for the contribution of other projections in the backprojection step, illustrated in Figure 1-29 (Robert-Coutant and Marc, 2000). Different filters and filtering methods exist. The Ram-Lak filter is the best filter in terms of fine spatial frequency resolution, but it is sensitive to noise and artefacts because of the discontinuity in the frequency domain (Horn, 1978). The Horn filter tends to blur edges while suppressing noise (Horn, 1978). The Shepp-Logan filter lies in-between in performance (Horn, 1978). In practice, filtering methods tend to increase high frequencies, and so the use of a smoothing window, such as a Hanning window, forces high frequencies to decrease smoothly down to zero (Robert-Coutant and Marc, 2000). Such smoothing windows reduce noise but also tend to blur edges and to obtain a compromise it is best to use various linear combinations of these smoothing windows to suit different applications. In order to briefly explain the basis of these filters, Equation (1-28) can be expressed with the use of the filter transfer function, $H(\omega)$, giving (Kak and Slaney, 1987):

$$Q_\theta(t) = \int_{-\infty}^{\infty} S_\theta(\omega)\ H(\omega) \cdot \exp[j\,2\pi\,\omega t]\,d\omega \qquad (1\text{-}29)$$

The impulse response of the filter, h(t), is obtained from the inverse Fourier transform of H(ω), giving (Kak and Slaney, 1987):

$$h(t) = \int_{-\infty}^{\infty} H(\omega) \,.\, \exp[\, j\, 2\pi\, \omega t\,]\, d\omega \qquad (1\text{-}30)$$

Figure 1-30(a) illustrates the frequency response of an ideal filter (Kak and Slaney, 1987). The three filters named above are discrete versions of the filter for which the transfer function is shown in Figure 1-30(b).

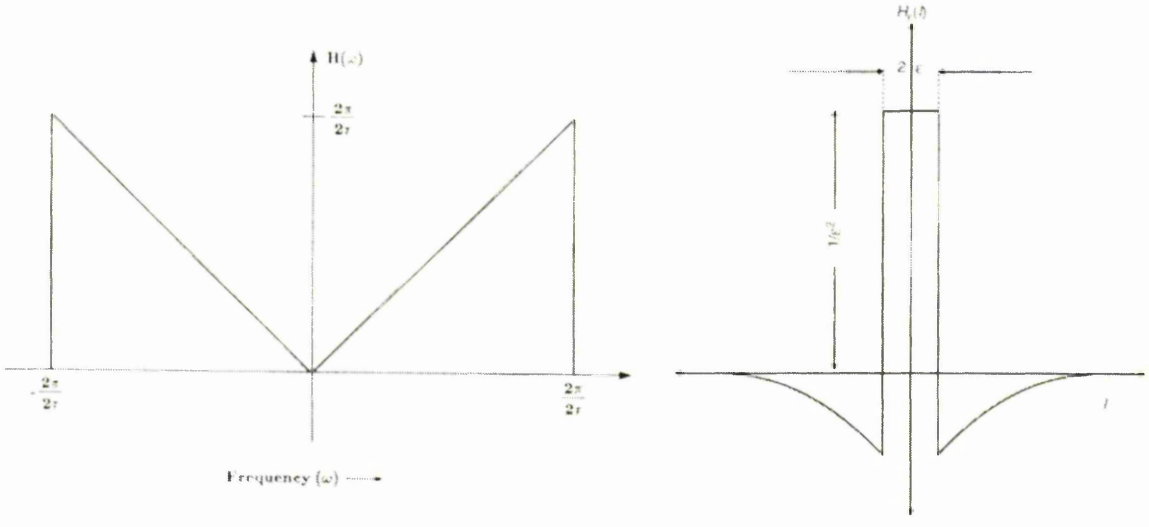

(a) (b)

Figure 1-30. (a) The ideal filter transfer function response with which a projection is processed prior to backprojection. (b) The discrete versions of this filter are the Ram-Lak, Horn and Shepp-Logan kernels. The total area under $H_\varepsilon(l)$ is zero. (Hiriyannaiah, 1997; Kak and Slaney, 1987).

After the filtering operation, Equation (1-27) calls for each filtered projection to be 'backprojected'. To every point, (x,y), in the image plane there corresponds a value of t (= $x \cos\theta + y \sin\theta$) for a given value of θ, and the filtered projection, Q_θ, contributes to the reconstruction its value at t. In other words, each point of the object is assigned the average value of all the projections at the corresponding location, as illustrated in Figure 1-29. This is further illustrated in Figure 1-31 (Rosenfeld and Kak, 1982). For the indicated angle, θ, the value of t is the same for all points, (x,y), on the line LM. Therefore, the filtered projection will make the same contribution to the reconstruction at all of these points. In the reconstruction process, each filtered projection, Q_θ, is smeared back, or

backprojected, over the image plane. It is important to understand that the averaging of all the projections in each pixel of an image, as shown in Figure 1-23, is equivalent to the successive spreading of the projections over the image, as in Figure 1-29. Without pre-filtering of the projections, the backprojected image, when compared with the 'perfect' object, would be highly blurred. As a result of such a 'projection-then-backprojection' process, each pixel contains information about what the object really contains at the pixel location, but this information is added to a blurred version of the rest of the object. The smoothing effect of the pre-filtering of the projections removes this blurring.

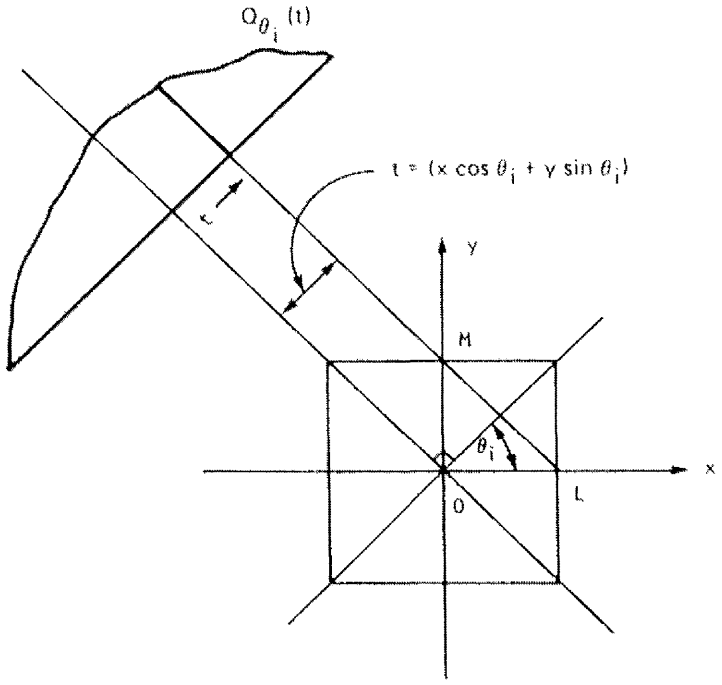

Figure 1-31. During backprojection, a filtered projection is smeared back over the reconstruction plane along lines of constant t. The filtered projection at a point t makes the same contribution to all pixels along the line LM in the x-y plane. (Rosenfeld and Kak, 1982).

A review of the specific algorithms for the fan and cone beam geometries, the latter being a 3-D extension of the former and both based on the principles of filtered backprojection (Feldkamp *et al*, 1984; Kak and Roberts, 1986), can be found in the Appendix.

1.4.3. Reconstruction artefacts

Laboratory or microfocus X-ray computed tomography can offer a number of possibilities in terms of the imaging task. If the aim is simply to resolve features or defects

in an object, such as cracks (Breunig *et al*, 1993; Guvenilir *et al*, 1997; London *et al*, 1990), or to image its internal structure (Benaouli *et al*, 2000; Mummery *et al*, 1995; Salvo *et al*, 2003), then the operating conditions of the system, such as the tube potential and current, must be selected to provide sufficient contrast between the features and the object material. The pixel resolution of the reconstruction must be taken into account in terms of the size of the details being observed. Attention must also be paid to the dynamic range of the camera, which is linked to the operating conditions (see Section 1.3.1.2), and this affects the signal-to-noise ratio in the image (Cendre, 1999). When the issue of CT inspection is the determination of the accurate size of some internal feature (Bernard *et al*, 2000; Justice *et al*, 2000) or the local characterisation of materials, e.g. density distribution (Badel *et al*, 2003; Kriszt *et al*, 2000), then increased attention must be paid to reconstruction artefacts. (Note that only laboratory X-ray tomography studies are referred to due to the relative absence of such artefacts when using synchrotron microtomography, see Section 1.2.3). Physical limitations and problems arise in estimating the line integrals, along which local attenuation measurements are derived and reconstructed, from the projection measurements. These reconstruction artefacts create artificial patterns inside a reconstructed slice, or they locally modify the grey level value of a pixel, and hence the quantitative result (Schneberk *et al*, 1990). The following describes the main types of reconstruction artefacts that can occur in CT slices, and the main physical mechanisms leading to their existence.

1.4.3.1. Beam hardening

When collecting X-ray projection measurements, it is of main importance to determine the physical meaning of the X-ray attenuation coefficient, μ, in the reconstructed images as this determines the observed structure of different phases in the object. The interest of attenuation measurements lies in the fact that μ is dependent on the photon energy being used and is proportional to the density, ρ, of the material being studied. Therefore, for a given material and energy, μ/ρ is a constant. In practice, a problem arises from the fact that the X-ray beam delivered by an X-ray tube consists of photons at different energies, i.e. it is strongly polychromatic. The basic assumption in computed tomography is that a particular voxel representing the object attenuates X-rays in the same way for every projection angle, independent of how much matter the X-rays have penetrated before reaching the voxel. This is true for monoenergetic X-rays, such as those produced at a synchrotron source such as at the ESRF, which uses a beam that is essentially monochromatic (single energy and wavelength). These X-rays are attenuated

through the thickness of an object without any change in the photon energy distribution (spectrum) as the beam propagates. This means that the number of photons taken away from the beam for a particular voxel is not dependent on how deep the voxel lies in the object. With polyenergetic X-ray sources, throughout the path of the X-ray beam as it passes through the sample, the attenuation at a fixed point in an object is generally greater for photons of lower energy, and such components of the energy spectrum are attenuated preferentially. As a result, the spectrum changes (hardens) as it passes through the object, and there is a relative increase of the mean energy along the path of the beam and of the 'hard' components of the spectrum. Such behaviour, called *beam hardening*, causes artefacts in the reconstructed map of μ.

The shape of the spectrum impinging on a voxel is therefore dependent on how deep the voxel lies within the object. As a result, the number of photons taken away from the beam in the same voxel for different projection angles will be different, unless the voxel is located in the centre of a cylindrical object where the X-ray spectra reaching such a voxel has approximately the same shape from all directions. When a voxel is close to the edge of an object on the side turned towards the source, for the first few projections the effective energy of the X-ray spectrum will be lower and the number of photons attenuated from the beam as it passes through the voxel will be larger. This is in contrast to later projections, such as those at ~180°, when the object is turned relative to the X-ray source and there is more object material between the voxel and the source. This causes the effective energy to rise since the low energy photons are taken away from the beam before reaching the voxel. The result is the measurement of a less dense material for the voxel in these later projections than for the early projections, and a false linear attenuation coefficient gradient. Thus, for CT imaging with polychromatic sources, the 2-D pixel values in CT slices are dependent on both the voxel itself, in terms of the 3-D object, and where it is located in the object.

The most common beam hardening artefact is the *cupping effect*, corresponding to measured values of μ that are corrupted, thus preventing the measurement of the 'true' density of the object. The name 'cupping effect' is used to describe this artefact due to the lower measured grey level values at the centre of a cylindrical object, for example, with a uniform density distribution, than at the edges, as shown by Figure 1-32. Figure 1-32(a) shows a reconstructed slice through a uniform density steel rod, and Figure 1-32(b) shows a grey level profile extracted from across the slice, revealing it to be denser at the centre than at the edges. Projections can be corrected by acquiring an image of a step-wedge (a

homogeneous object containing increasing thicknesses of the same material), in such a way so as to correlate the measured attenuation to the true material thickness (see Section 2.5). Beam hardening artefacts can be avoided by assigning to each point the attenuation coefficient of photons at a particular energy. If X-ray beams consisting of photons only at that single energy were used, i.e. monochromatic X-ray beams, photons from different directions would be attenuated in the same way at a fixed point. Tomography using synchrotron radiation rarely generates these artefacts because a monochromator is always used due to the huge X-ray flux.

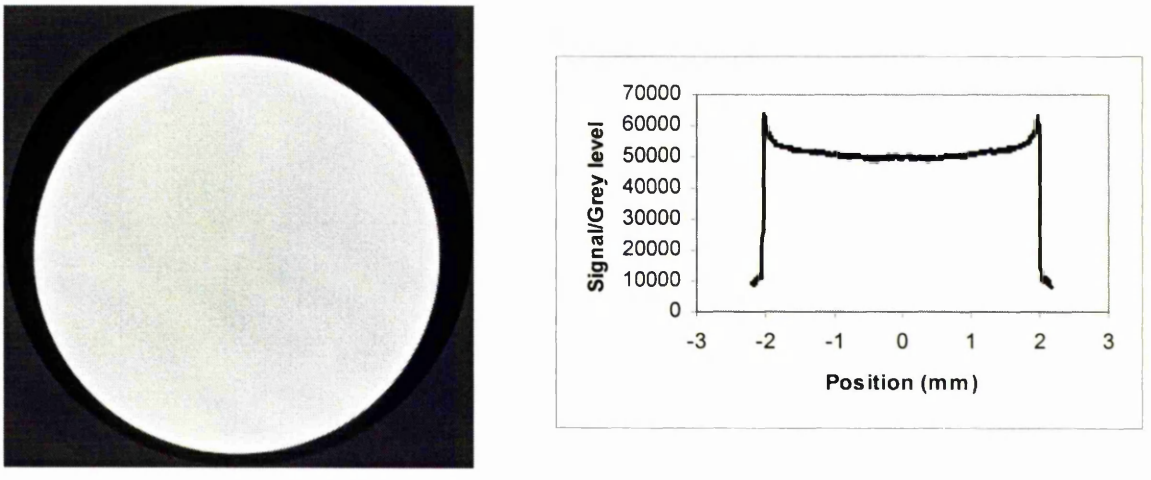

(a) (b)

Figure 1-32. (a) A reconstructed slice through a 4 mm diameter steel rod, showing an apparent density gradient across the object. (b) A grey level profile across the slice in (a) showing the 'cupping effect' across the object.

1.4.3.2. Centre of rotation errors and artefacts

During collection of the raw projection data for a CT scan, there is a defined centre of rotation about which the object rotates. The filtered backprojection algorithm requires accurate knowledge of the detector array location through which the centre of rotation passes for all of the projections. If this value is incorrect by even fractions of a pixel, the backprojection integral can distort the reconstruction. Centre of rotation errors produce two types of characteristic effects in reconstructed CT images, as shown in Figure 1-33 which displays different reconstructed images of a hollow cylinder, where each slice is reconstructed using a different value for the centre of the detector array (Schneberk *et al*, 1990). Distortions to the circularity of the cylinder are observed resulting from incorrect values of the centre of rotation. The reconstructed slices show a discontinuity between the

two halves of the cylinder, with one half being either larger or smaller than the other, and bright and dark 'tails' can be seen running in opposite directions. Only the reconstruction that employs the correct value of the centre of rotation is free from these artefacts. An understanding of the mechanics behind centre of rotation artefacts can be gained by inspecting the backprojection integral (Equation (1-27)). Every reconstructed pixel depends on receiving the correct projected ray value through the variable t (Figure 1-31). If the projected centre is incorrect, the sinusoidal paths through the sinogram (e.g. Figure 1-23) do not include the correct ray-sums. Attenuation measurements that do not intersect at a voxel position in the object are then incorrectly included in the backprojection sum for that reconstructed pixel.

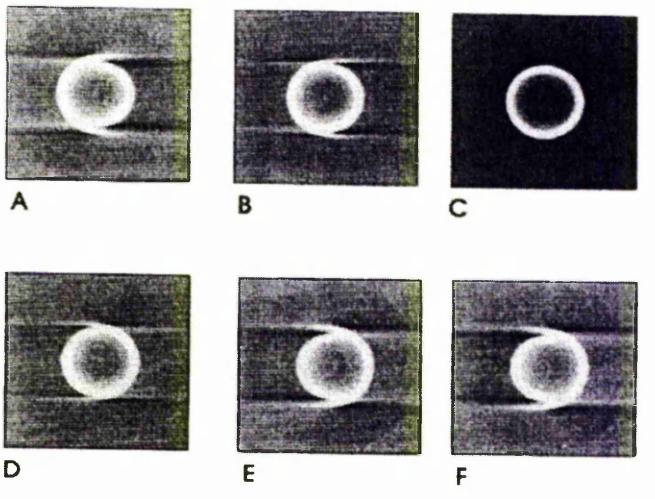

Figure 1-33. Reconstructed images of a slice through a hollow cylinder using different values (in pixels) for the projected centre of rotation. Centre = (a) 134, (b) 137, (c) 140 (correct), (d) 143, (e) 147, (f) 150. (Schneberk *et al*, 1990).

1.4.3.3. Uncalibrated detector arrays

Ring artefacts, faint concentric circles surrounding or centred on the pixel corresponding to the location of the centre of rotation, can result as a consequence of vertical lines in the sinogram being mapped into annular rings in the reconstructed slice. The signal delivered by every sensitive cell of the detector must be linearly spread between the offset level, corresponding to the absence of photons (i.e. black reference image, see Section 2.2), and the gain level, corresponding to the non-attenuated flux (i.e. white reference image). A bad correction of one cell will generate these ring artefacts in the

reconstructed image. Figure 1-34 shows a number of rings visible in an image (Robert-Coutant and Marc, 2000). The phenomenon is a direct result of imbalanced detector elements in a 2-D detector array. The elements of each vertical line in a sinogram, which are ray-sums for the different views of the object, are recorded using the same detector element at each angle. If there is a gain or offset imbalance between elements, vertical lines will emerge in the sinogram and reconstruct into these concentric rings. These rings introduce an additional variation in the image, making the identification of low-contrast features difficult.

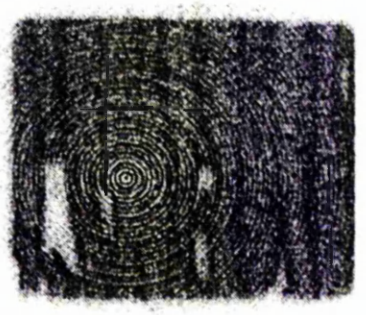

Figure 1-34. Illustrating ring artefacts in a reconstructed image. (Robert-Coutant and Marc, 2000).

1.5. Alternative Characterisation Techniques

While X-ray microtomography is the principal characterisation technique used in the two main studies of this thesis: (1) the observation of damage accumulation and cracking in Ti/SiC_f Metal Matrix Composites (MMCs) and (2) the evaluation of the effect of the internal structure on the compressive deformation of metallic aluminium foams; alternative characterisation techniques exist for the study of such materials. A technique that has long been established for internal structure evaluation of materials is that of metallographic preparation and microscopy, but a major disadvantage of this method over the use of tomography is that it is destructive and only gives 2-D sections. When the characteristics of fibre cracking in composites is the issue of inspection, such a destructive technique can alter the morphology of cracks, while tomography reconstructs exact virtual slices of the state of cracks in fibres inside a sample. The fact that the technique also produces 3-D data directly from a single scan enables the simple viewing of the morphology of such cracks in many directions through their physical entirety. This non-destructively acquired 3-D dataset is important for the study of the undeformed and

deformed structures of foam samples, without which it would be very difficult to establish the true effect of the former structure on the latter. The following briefly describes two other characterisation techniques related to the issues of inspection covered in this thesis, one used for the detection of cracks in fibre composites and the other for the characterisation of deformation bands in cellular metallic foams.

1.5.1. Acoustic emission for damage detection in composites

The principle of *acoustic emission* is to 'listen' to damage events, such as cracks, taking place upon loading of a material, and is an effective means of examining dynamic processes generated in materials. When a failure mechanism is activated, part of the total strain energy is dissipated as a wave that propagates from the failure source through the sample medium. Acoustic emission offers the potential to monitor damage accumulation in real time, and to distinguish between different micro-damage mechanisms (Giordano *et al*, 1998) with the capability of establishing the spatial coordinates of an event (Barney *et al*, 1998). Equipment for acoustic emission measurements involves two piezoelectric transducers or sensors located at the two shoulders of a tensile test-piece specimen. The spatial location of a damage event can be identified approximately by the time delay at each of the two or more sensors. Post-test analyses of damage event amplitude, frequency and duration enable the identification of different sources of acoustic emission and thus different damage events and mechanisms. Spatial filtering using a threshold criterion enables the monitoring of a pre-selected gauge volume free from noise of the grips during the tensile test and the application of load. In order to analyse the spectral frequency characteristic of an acoustic emission signal, it is necessary to perform the acquisition with a wide-band probe. However, such probes are too sensitive to environmental noise, i.e. electrical and electronic. To overcome this, a resonant transducer is used allowing a triggering system for the acquisition of an acoustic signal due to fibre breakage, for example, to be developed. A highly sensitive resonance type transducer (~200-400 kHz) is recommended for amplitude and energy analysis. Acoustic signals due to fibre failure are of very small amplitude with respect to the mechanical and electrical noise, but they are generally characterised by higher frequencies (Giordano *et al*, 1998).

The technique has been used to study cracking in both polymer (Giordano *et al*, 1998) and metal matrix composites (Barney *et al*, 1998), and each microfracture process in a composite has been observed to generate an AE signal. Correlations have been found between the acoustic emission characteristics of the signal, such as the amplitude, duration,

energy (which is essentially the amplitude multiplied by the pulse duration), frequency spectra and counts per event, and the different modes of failure that are known to occur in a composite. These include fibre cracking, matrix cracking and fibre-matrix debonding, and, for example, matrix cracking has been found to produce lower amplitude signals than fibre breakage. The recorded amplitude is the most commonly used characteristic for acoustic emission analysis, but this is related to the test geometry and the propagating medium, as well as to the position of the initial failure event. Attenuation of the signal amplitude with distance can be small (~few dB/m in metals), which means that similar events can give similar amplitudes whatever their location within the gauge volume. Frequency based analysis has the advantage that it is insensitive to the sample-sensor distance or the thickness of the coupling medium, but since each mechanism tends to have a complex frequency spectrum signature which is dependent on specimen geometry, the identification of specific mechanisms in this way is more difficult. With the use of acoustic emission, Barney *et al.* were able to deduce that, during growth of a matrix fatigue crack in a continuous Sigma SiC fibre reinforced Ti-6Al-4V matrix (fibre volume fraction of 31%), individual fibre failure was often followed by another fibre failure within its immediate vicinity under cyclic loading (Barney *et al*, 1998). An advantage of acoustic emission characterisation over X-ray microtomography, concerning cracking in fibre composites, is that damage events can be detected in real-time such that the length of time between them during loading can be deduced. While the spatial location of cracks can also be deduced, tomographic slices through the specimen enable direct measurement of fragment lengths and crack openings, and the visual characteristics of cracks can be observed.

1.5.2. Surface strain mapping for deformation observations in metal foams

The strain field on the surface of a metallic foam resulting from thermomechanical loading can be measured using *surface strain mapping* (Bart-Smith *et al*, 1998). The surfaces of cellular metals are irregular, with the cell membranes or edges appearing as peaks and troughs, allowing *in-situ* optical imaging to be used to provide a map of surface deformation. The technique is based on image correlation analysis and the comparison of pairs of digital images taken by optical microscopy and captured during the compressive deformation history sequence (Chen *et al*, 1993). The images are divided into sub-images, which provide an array of analysis sites across the surface. The relative displacement vectors from these sites are evaluated by means of a 2-D fast Fourier transform (FFT)

comparison of consecutive pairs of sub-images upon taking the inverse of their spectral difference. The method requires surface imaging, for which commercial, digital speckle interferometry software and a video camera with a CCD array of 640 × 480 pixels are used (Bart-Smith *et al*, 1998). A wide numerical aperture lens with extended depth of field and a fibre-optic light source are also used. Since cellular metals exhibit non-uniform, heterogeneous deformation, the field of view should be optimised such that each unit cell can be mapped to approximately 50 pixels in each direction. The analysis can be carried out by applying FFTs to a 32-pixel square array of sub-images, centred at nodal points eight pixels apart, such that the deformation of each unit cell is represented by at least four nodal points in each direction. The method relies on the recognition of surface pattern. The foam surface can be imaged directly, relying on the irregular pattern of surface cell-edges for matching between consecutive frames. Alternatively, a thin, substantially pre-stretched latex film sprayed with black and white emulsion to give a random pattern can be epoxy-bonded to the surface (Bart-Smith *et al*, 1998). During loading, the film follows the cell shape changes without delamination. While the latex film method is more accurate, direct imaging of the surface provides essentially the same continuum deformation field, and is simpler. In both cases, the specimen surface is sprayed with a krylon paint to enhance the speckle pattern.

Deformation histories are visualised as false colour plots of components of strain in the plane of the surface, as illustrated in Figure 1-35 (Bart-Smith *et al*, 1998). These surface strain maps of the incremental distortion with increase in applied load have enabled the formation of localised deformation bands in the material to be revealed. As an example of the information that is contained within such maps, Figure 1-35 reveals the following features, comparing the deformation band formation to the corresponding applied strains on the stress-strain curve (Bart-Smith *et al*, 1998). The strain is non-uniform, and bands are revealed to form at the onset of non-linearity in the stress-strain curve (point 3) and then become essentially inactive. Upon further straining new bands develop in spatially disconnected regions of the foam, and expansion of existing bands occurs. Deformation is observed to start at stress levels far below general yield or plastic collapse. The principal strains reveal that the flow vectors are primarily in the loading direction, normal to the band plane, indicative of a crushing mode of deformation.

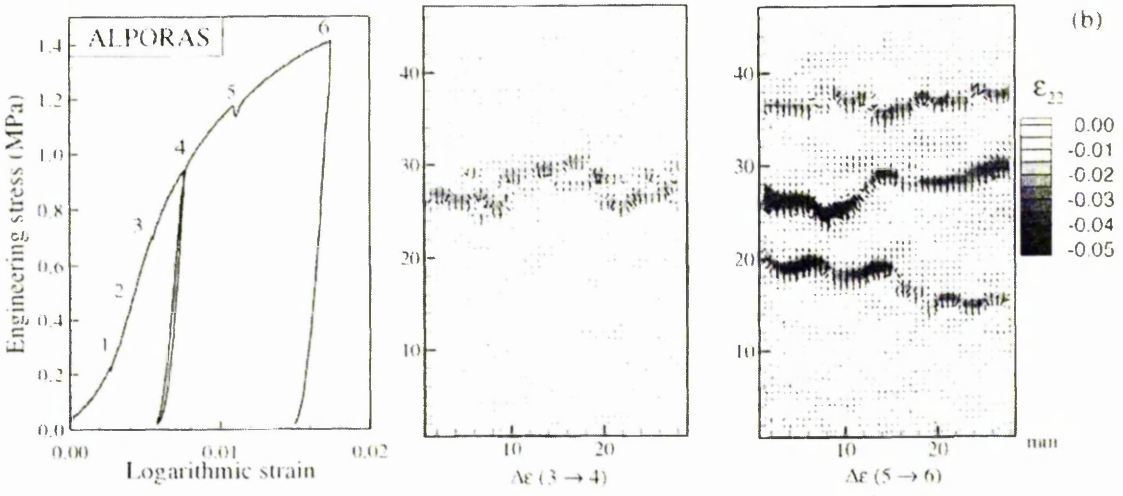

Figure 1-35. Illustrating surface maps of the incremental principal compressive strains and the formation of deformation bands, as the applied load is increased, in a cellular aluminium foam sample. The indicated applied strains correspond to the stress-strain curve. (Bart-Smith *et al*, 1998).

1.6. Summary

The principles behind X-ray microtomography as a powerful characterisation technique for the non-destructive evaluation of the internal structure of materials have been introduced. As a major development of conventional radiography techniques, the information gained from tomography methods revolutionised the field of medical diagnosis. It is now being used increasingly for industrial research of structural materials, and due to its basis on a local material-dependent property, the attenuation coefficient, quantitative, readily interpretable data are obtained. The visual inspection of the interior of structures is possible, enabling the size, shapes and spatial locations of features to be investigated. The possibilities offered by third generation synchrotron X-ray sources have further enhanced the quality of the information that can be obtained in terms of the resolution of the features under inspection. Microtomography using such a source has taken advantage of phase sensitive imaging due to a phase contrast, improving the detection of small features and enhancing the boundaries between phases. It is clear that with the use of such a technique, when the output of the reconstruction algorithms applied to the raw data is in the form of virtual 2-D and 3-D image representations, image quality is an important issue. This is especially so when industrial laboratory based micro-focus sources are used, which are prone to reconstruction artefacts such as beam hardening due to the use of polychromatic radiation. Note that the monochromatic and parallel nature of

a synchrotron source gives 'exact' reconstructions free from such artefacts. The image quality, or detail signal-to-noise ratio, will affect the detection of small features or details in a reconstructed image, while minimisation of beam hardening artefacts is important when quantitative data of phases is to be obtained. The following chapter will outline a brief investigation into the performance of a laboratory microtomography system, based on these two aspects of the quality of the images obtained. The advantages of the technique, i.e. 3-D non-destructive evaluation of internal structures, will then be demonstrated through the investigation of the damage development and deformation mechanisms in two composite structural materials, continuous fibre MMCs (Chapter 4) and cellular metallic foams (Chapter 6).

References

Baaklini, G. Y., Bhatt, R. T., Eckel, A. J., Engler, P., Castelli, M. G. and Rauser, R. W., (1995), 'X-ray microtomography of ceramic and metal matrix composites', *Materials Evaluation*, 1040-1044.

Babout, L., Ludwig, W., Maire, E. and Buffière, J.-Y., (2003), 'Damage assessment in metallic structural materials using high resolution synchrotron X-ray tomography', *Nuclear Instruments and Methods in Physics Research Section B: Beam Interactions with Materials and Atoms*, **200**, 303-307.

Badel, E., Létang, J-M., Peix, G. and Babot, D., (2003), 'Quantitative microtomography: measurement of density distribution in glass wool and local evolution during a one-dimensional compressive load', *Measurement Science and Technology*, **14**, 410-420.

Barney, C., Ibbotson, A. and Bowen, P., (1998), 'Experimental characterisation of fibre failure and its influence on crack growth resistance in fibre reinforced titanium metal matrix composites', *Materials Science and Technology*, **14**, 658-668.

Bart-Smith, H., Bastawros, A.-F., Mumm, D. R., Evans, A. G., Sypeck, D. J. and Wadley, H. N. G., (1998), 'Compressive deformation and yielding mechanisms in cellular Al alloys determined using X-ray tomography and surface strain mapping', *Acta Materialia*, **46**(10), 3583-3592.

Baruchel, J., Boller, E., Cloetens, P., Ludwig, W. and Peyrin, F., 'Microtomography at a third generation synchrotron radiation facility', in Baruchel, J., Buffière, J.-Y., Maire, E., Merle, P. and Peix, G., *X-ray tomography in Materials Science*, HERMES Science Publications, Paris, 2000, 45-59.

Beckmann, F., Bonse, U., Busch, F. and Gunnewig, O., (1997), 'X-ray microtomography (μCT) using phase contrast for the investigation of organic matter', *Journal of Computer Assisted Tomography*, **21**, 539.

Benaouli, A.-H., Froyen, L. and Wevers, M., 'Micro focus computed tomography of aluminium foams', in Baruchel, J., Buffière, J.-Y., Maire, E., Merle, P. and Peix, G., *X-ray tomography in Materials Science*, HERMES Science Publications, Paris, 2000, 139-153.

Bernard, D., Vignoles, G.-L. and Heintz, J.-M., 'Modelling porous materials evolution', in Baruchel, J., Buffière, J.-Y., Maire, E., Merle, P. and Peix, G., *X-ray tomography in Materials Science*, HERMES Science Publications, Paris, 2000, 177-192.

Breunig, T. M., Stock, S. R., Guvenilir, A., Elliott, J. C., Anderson, P. and Davis, G. R., (1993), 'Damage in aligned-fibre Al/SiC quantified using a laboratory X-ray tomographic microscope', *Composites*, **24**(3), 209-213.

Buffière, J.-Y., Savelli, S. and Maire, E., 'Characterisation of MMC_p and cast aluminium alloys', in Baruchel, J., Buffière, J.-Y., Maire, E., Merle, P. and Peix, G., *X-ray tomography in Materials Science*, HERMES Science Publications, Paris, 2000, 103-113.

Buffière, J.-Y., Maire, E., Cloetens, P., Lormand, G. and Fougères, R., (1999), 'Characterisation of internal damage in a MMC_p using X-ray synchrotron phase contrast microtomography', *Acta Materialia*, **47**(5), 1613-1625.

Buffière, J.-Y., Maire, E., Verdu, C., Cloetens, P., Pateyron-Salomé, M., Peix, G. and Baruchel, J., (1997), 'Damage assessment in an Al/SiC composite during monotonic tensile tests using synchrotron X-ray microtomography', *Materials Science and Engineering*, **A234-236**, 633-635.

Cendre, E., 'Conception of a High Resolution X-Ray Computed Tomography Device; Application to Damage Initiation Imaging Inside Materials', in *Proceedings of the 1st World Congress on Industrial Process Tomography*, UMIST, UK, 1999, 362-369.

Chen, D. J., Chiang, F. P., Tan, Y. S. and Don, H. S., (1993), 'Digital speckle-displacement measurement using a complex spectrum method', *Applied Optics*, **32**, 1839-1849.

Cloetens, P., Ludwig, W., Guigay, J.-P., Baruchel, J. Schlenker, M. and Van Dyck, D., 'Phase contrast tomography', in Baruchel, J., Buffière, J.-Y., Maire, E., Merle, P. and Peix, G., *X-ray tomography in Materials Science*, HERMES Science Publications, Paris, 2000, 29-44.

Cloetens, P., Ludwig, W., Baruchel, J., Van Dyck, D., Van Landuyt, J., Guigay, J.,P. and Schlenker, M., (1999), 'Holotomography: Quantitative phase tomography with micrometer resolution using hard synchrotron radiation X-rays', *Applied Physics Letters*, **75**(19), 2912-2914.

Cloetens, P., Pateyron-Salomé, M., Buffière, J.-Y., Peix, G., Baruchel, J., Peyrin, F. and Schlenker, M., (1997), 'Observation of microstructure and damage in materials by phase sensitive radiography and tomography', *Journal of Applied Physics*, **81**(9), 5878-5886.

Cloetens, P., Barrett, R., Baruchel, J., Guigay, J. P. and Schlenker, M., (1996), 'Phase objects in synchrotron radiation hard X-ray imaging', *Journal of Physics D*, **29**, 133-146.

Cody, D. D., McCubbrey, D. A., Divine, G. W., Gross, G. J. and Goldstein, S. A., (1996), 'Predictive value of proximal femoral bone densitometry in determining local orthogonal material properties', *Journal of Biomechanics*, **29**, 753-761.

Cohen, G. and DiBianca, F. A., (1979), 'The use of contrast-detail-dose evaluation of image quality in a computed tomographic scanner', *Journal of Computer Assisted Tomography*, **3**, 189-195.

Copley, D. C., Eberhard, J. W. and Mohr, G. A., (1994), 'Computed Tomography Part 1: Introduction and Industrial Applications', *Journal of Materials*, 14-26.

Cormack, A. M., (1963), *Journal of Applied Physics*, **34**, 2722-2727.

Dainty, J. C. and Shaw, R., *Image Science: principles, analysis and evaluation of photographic-type imaging processes*, Academic Press, London, 1976, 190-275.

Elliott, J. C. and Dover, S. D., (1982), 'X-ray microtomography', *Journal of Microscopy*, **126**, 211-213.

Engelke, K., Graeff, W., Meiss, L., Hahn, M. and Delling, G., (1993), *Investigative Radiology*, **28**, 341-349.

Espeso, J. I., Cloetens, P., Baruchel, J., Härtwig, J., Mairs, T., Biasci, J. C., Marot, G., Salomé-Pateyron, M. and Schlenker, M., (1998), 'Conserving the Coherence and Uniformity of Third-Generation Synchrotron Radiation Beams: the Case of ID19, a `Long' Beamline at the ESRF', *Journal of Synchrotron Radiation*, **5**, 1243-1249.

Feldkamp, L. A., Davis, L. C. and Kress, J. W., (1984), 'Practical cone-beam algorithm', *J. Opt. Soc.*, **1**, 612-619.

Ferrero, M.A., Sommer, R., Spanne, P., Jones, K.W. and Conner, C., (1993), 'X-ray microtomography studies of nascent polyolefin particles polymerized over magnesium chloride-supported catalysts', *Journal of Polymer Science A*, **31**, 2507-2512.

Flannery, B. P. and Roberge, W. G., (1987), 'Observational strategies for three-dimensional synchrotron microtomography', *Journal of Applied Physics*, **62**(12), 4668-4674.

Giordano, M., Calabro, A., Esposito, C., D'Amore, A. and Nicolais, L., (1998), 'An acoustic-emission characterisation of the failure modes in polymer-composite materials', *Composites Science and Technology*, **58**, 1923-1928.

Graeff, W. and Engelke, K., 'Microradiography and microtomography', in *Handbook on synchrotron radiation*, North Holland, 1991, **4**, 361-405.

Guvenilir, A. and Stock, S. R., (1998), *Fatigue and Fracture of Engineering Materials and Structures*, **21**, 439-450.

Guvenilir, A., Breunig, T. M., Kinney, J. H. and Stock, S. R., (1997), 'Direct observation of crack opening as a function of applied load in the interior of a notched tensile sample of Al-Li 2090', *Acta Materialia*, **45**, 1977-1987.

Hammersberg, P., Stenstrom, M., Sandborg, M., Matscheko, G. and Alm-Carlsson, G., (1995), 'A theoretical model for determination of the optimum irradiation conditions for computerised tomography', *Insight*, **37**, 978-985.

Hasnain, S. S., Helliwell, J. R. and Kamitsubo, H., (1994), 'Overview on Synchrotron Radiation', *Journal of Synchrotron Radiation*, **1**, 1-4.

Herman, G. T., *Image Reconstruction from Projections: the Fundamentals of Computerised Tomography*, Academic Press, New York, 1980.

Hirano, T., Usami, K., Tanaka, Y. and Masuda, C., (1995), 'In-situ X-ray CT under tensile loading using synchrotron radiation', *Journal of Materials Research*, **10**, 381-386.

Hiriyannaiah, H. P., (1997), 'X-ray computed tomography for medical imaging', *IEEE Signal Processing Magazine*, **14**, 42-59.

Horn, B. K. P., (1978), 'Density reconstruction using arbitrary ray-sampling schemes', *Proceedings of the IEEE*, **66**(5), 551-562.

Hounsfield, G. N., (1973), 'Computerized transverse axial scanning (tomography). 1. Description of system', *British Journal of Radiology*, **46**, 1016-1022.

Ingal, V. N. and Beliaevskaya, E. A., (1995), 'X-ray plane wave topography observation of the phase contrast from a non-crystalline object', *Journal of Physics D: Applied Physics*, **28**, 2314-2317.

Justice, I., Derby, B., Davis, G., Anderson, P. and Elliott, J., 'Characterisation of void and reinforcement distributions by edge contrast', in Baruchel, J., Buffière, J.-Y., Maire, E., Merle, P. and Peix, G., *X-ray tomography in Materials Science*, HERMES Science Publications, Paris, 2000, 89-101.

Kak, A. C. and Roberts, B., 'Image reconstruction from projections', in *Handbook of Pattern Recognition and Image Processing*, Young, T. Y. and Fu, K. S., Eds., Academic Press, New York, 1986, 649-693.

Kak, A. C. and Slaney, M., *Principles of Computerised Tomographic Imaging*, IEEE Press, London, 1987, 49-134.

Kinney, J. H. and Haupt, D. L., (1997), 'Evidence of critical scaling behaviour during vapour phase synthesis of continuous filament composites', *Journal of Materials Research*, **12**, 610-612.

Kinney, J. H., Lane, N. E. and Haupt, D. L., (1995), *Journal of Bone and Mineral Research*, **10**, 264-270.

Kinney, J. H., Stock, S. R., Bonse, U., Breunig, T. M., Saroyan, R. A., Nusshardt, R., Johnson, Q. C., Busch, F. and Antolovich, S. D., (1990), 'Nondestructive investigation of damage in composites using X-ray tomographic microscopy (XTM)', *Journal of Materials Research*, **5**, 1123-1129.

Kirby, B. J., Davis, J. R., Grant, J. A. and Morgan, M. J., (1997), *Physical and Medical Biology*, **42**, 1375-1385.

Kriszt, B., Foroughi, B., Faure, K. and Degischer, H. P., (2000), 'Behaviour of aluminium foam under uniaxial compression', *Materials Science and Technology*, **16**, 792-796.

Laclare, J. L., (1994), 'Target Specifications and Performance of the ESRF Source', *Journal of Synchrotron Radiation*, **1**, 12-18.

Layton, M. W., Goldstein, S. A., Goulet, R. W., Feldkamp, L. A., Kubinski, D. J. and Bole, G. G., (1988), 'Examination of subchondral bone architecture in experimental osteoarthritis by microscopic computed axial tomography', *Arthritis and Rheumatism*, **31**, 1400-1405.

Lee, S. B., Stock, S. R., Butts, M. D., Starr, T. L., Breunig, T. M. and Kinney, J. H., (1998), 'Pore geometry in woven fibre structures: 0°/90° plain-weave cloth layup preform', *Journal of Materials Research*, **13**, 1209-1217.

Linzer, M., (1996), '21st International Symposium on Ultrasonic Imaging and Tissue Characterisation', *Ultrasonic Imaging*, **18**, 35-75.

London, B., Yancey, R. N. and Smith, J. A., (1990), 'High-resolution X-ray computed tomography of composite materials', *Materials Evaluation*, **48**, 604-608.

Mangard, M., *Optimised performance of industrial high resolution computerised tomography*. Linköping Studies in Science and Technology, No. 659, Linköping, Sweden, 2000.

Mangard, M. and Hammersberg, P., (1998), 'Optimised detail detectability in computerised tomography', *Journal of X-ray Science and Technology*, **8**, 51-73.

Mansfield, P. and Morris, P. G., *NMR Imaging in Biomedicine, Advances in Magnetic Resonance*, Supplement 2, (ed. Waugh, J. S.) Academic Press, N.Y., 1982.

Martin, C. F., Josserond, C., Salvo, L., Blandin, J. J., Cloetens, P. and Boller, E., (2000), 'Characterisation by X-ray microtomography of cavity coalescence during superplastic deformation', *Scripta Materialia*, **42**, 375-381.

Momose, A., (1995), 'Demonstration of phase-contrast X-ray computed tomography using an X-ray interferometer', *Nuclear Instruments and Methods A*, **352**, 622-628.

Mummery, P. M., Derby, B., Anderson, P., Davis, G. R. and Elliott, J. C., (1995), 'X-ray microtomographic studies of metal matrix composites', *Journal of Microscopy*, **177**, 399-406.

Peix, G., Duvauchelle, P. and Freud, N., 'General principles of X-ray tomography', in Baruchel, J., Buffière, J.-Y., Maire, E., Merle, P. and Peix, G., *X-ray tomography in Materials Science*, HERMES Science Publications, Paris, 2000, 15-27.

Radon, J., (1917), Ber. Sächsischen Akad. Wiss., **69**, 262-277. Also (1986), *IEEE Transactions in Medical Imaging*, **MI-5**(4), 170-176.

Robert-Coutant, C. and Marc, A., 'Introduction to reconstruction methods', in Baruchel, J., Buffière, J.-Y., Maire, E., Merle, P. and Peix, G., *X-ray tomography in Materials Science*, HERMES Science Publications, Paris, 2000, 29-44.

Rosenfeld, A. and Kak, A. C., *Digital Picture Processing*, Academic Press, New York, 1982.

Ruegsegger, P., (1996), 'A microtomographic system for the non-destructive evaluation of bone architecture', *Calcif. Tiss. Int.*, **58**, 24-29.

Salvo, L., Cloetens, P., Maire, E., Zabler, S., Blandin, J. J., Buffière, J.-Y., Ludwig, W., Boller, E., Bellet, D. and Josserond, C., (2003), 'X-ray micro-tomography an attractive characterisation technique in Materials Science', *Nuclear Instruments and Methods in Physics Research Section B*, **200**, 273-286.

Schillinger, B., Blümlhuber, W., Fent, A. and Wegner, M., (1999), '3D neutron tomography: recent developments and first steps towards reverse engineering', *Nuclear Instruments and Methods in Physics Research A*, **424**, 58-65.

Schneberk, D. J., Azevedo, S. G., Martz, H. E. and Skeate, M. F., (1990), 'Sources of error in industrial tomographic reconstruction', *Materials Evaluation*, **48**, 609-617.

Sekihara, K., Kohno, H. and Yamamoto, S., (1982), 'Theoretical prediction of X-ray CT image quality using contrast-detail diagrams', *IEEE Transactions on Nuclear Science*, **NS-29**, 2115-2121.

Snigirev, A., Snigireva, I., Kohn, V., Kusnetsov, S. and Schelokov, I., (1995), 'On the possibilities of X-ray phase contrast microimaging by coherent high-energy synchrotron radiation', *Review of Scientific Instruments*, **66**, 5486-5492.

Stock, S. R., (1999), 'X-ray microtomography of materials', *International Materials Reviews*, **44**(4), 141-164.

Stock, S. R., Guvenilir, A., Breunig, T. M., Kinney, J. H. and Nichols, M. C., (1995), *Journal of Materials*, 19-24.

Wang, D. and Doddrell, D. M., (2002), 'MR image-based measurement of rates of change in volumes of brain structures. Part I: Method and validation', *Magnetic Resonance Imaging*, **20**, 27-40.

White, D. N., Clark, G., Carson, J. and White (eds.), *Ultrasound in Biomedicine*, Pergamon Press, 1982.

Chapter 2

Investigation of Computerised Tomography System Performance

2.1. Introduction

The principal aim of this section of the work was to investigate and illustrate the performance of a high-resolution X-ray microtomography system with respect to several points raised in the literature review of Chapter 1. Several objectives were formed based on this main aim:

1. To determine the best possible spatial resolution of the system for when performing non-destructive evaluation;
2. To investigate and optimise the image quality through the use of optimum equipment settings;
3. To investigate procedures for the suppression of CT image reconstruction artefacts such as beam hardening.

When performing non-destructive evaluation using X-ray microtomography, and the purpose is to resolve small features or details in the output reconstructed images, it is important to know the minimum discernible detail size that can be resolved using the technique. This was investigated through the measurement of the maximum spatial resolution of the system, and two different methods were compared. The first method determined the spatial resolution from the sharpness across the edge of a small titanium test-piece of square cross-section, while the second method determined the modulation transfer function (MTF) using the same set of images, through which the spatial resolution of an X-ray system can be quantified. The detectability of features or details in reconstructed CT images is affected by the image quality, which in turn is affected by the CT system settings used during collection of the raw data. The investigation and improvement of image quality has been carried out through the maximisation of the signal-to-noise ratio, $SNR_{\Delta S,CT}$, between a contrasting detail and its surroundings. Changes in the equipment settings for collection of the raw data, such as the X-ray tube potential, and the effect of filter material and thickness, have been investigated for reconstructed images of a

metal matrix composite with the fibres as the detail. With conventional laboratory based CT systems equipped with polyenergetic X-ray sources, the artefact of beam hardening can be a significant problem in reconstructed images, implying false density or composition gradients in the imaged object. The presence of beam hardening has been measured for the same titanium test-pieces as used above, and the use of an experimental method, based on linearisation of the CT data, is illustrated to correct for its effects. While providing only a brief investigation into each of these facets of the performance of a CT system, the following gives a description of important experimental aspects one should consider in order to obtain improved reconstructed CT images for structural and numerical characterisation.

2.2. Instrumentation and Setup of the CT System

2.2.1. Instrumentation

The CT system that was used was a commercially available high-resolution Computerised Tomography and Digital Radiography system (HMXST 225), supplied by X-Tek Systems Ltd. The system comprised:

1. A microfocus X-ray source with a tungsten target, based on the cone beam geometry (see Section 1.2.1). This gave a tube potential in the range 25-225 kV, a tube current in the range 0.01-2 mA and a minimum focus spot size of 5-10 μm for up to 225 Watt target load (aluminium or copper filtration of the beam was possible up to a thickness of 2 mm each);
2. A 4-axis motorised manipulation stage supplied by AEA Technology plc. for sample handling, in order to move and rotate the sample relative to the X-ray source and detector, with a focus-to-object distance of up to 1 m, geometric magnification up to 160× and system magnification up to 400×. The axes included rotation, magnification, horizontal (X) and vertical (Y) movement (the accuracy of the turntable and linear stage was 0.05° and 1-2 μm respectively, with a load capacity of 25 kg;
3. An imaging chain consisting of an image intensifier, optics and digital CCD camera. The image intensifier was a Thomson TH 9464 HX, with a field of view of about 115 mm, a resolution at the centre of 70 lp/cm and a CsI-scintillator

entrance screen. The camera was an Adimec MX12P 12-bit high-resolution digital video CCD camera, with 1024 × 1024 pixels;

4. The image handling and CT reconstruction software package was AEA Technology's TOMOHAWK Version 4, with an angular increment for data collection from 0.185°, pixels in digitised radiographic images up to 1280 × 1024 × 16-bits and pixels in CT images up to 1280 × 1280 × 1280 × 16 bits (for 3-D);
5. The control console consisted of a Pentium PC running Windows NT with 256 Mb RAM, a 20 Gb hard disk for data storage and a 1024 × 1024-pixel image capture board. A 1024 × 1024-resolution display was used to view the results. Control of the X-ray source was with X-Tek Systems' iXS software, while the camera and manipulation stage were controlled with Tomohawk.

Figure 2-1 shows a schematic diagram of the imaging arrangement in the tomography system used, based on the cone beam geometry as described in Section 1.2.1. Pictures of the actual system, illustrating the X-ray gun, the sample manipulation stage and the detector system, are also shown.

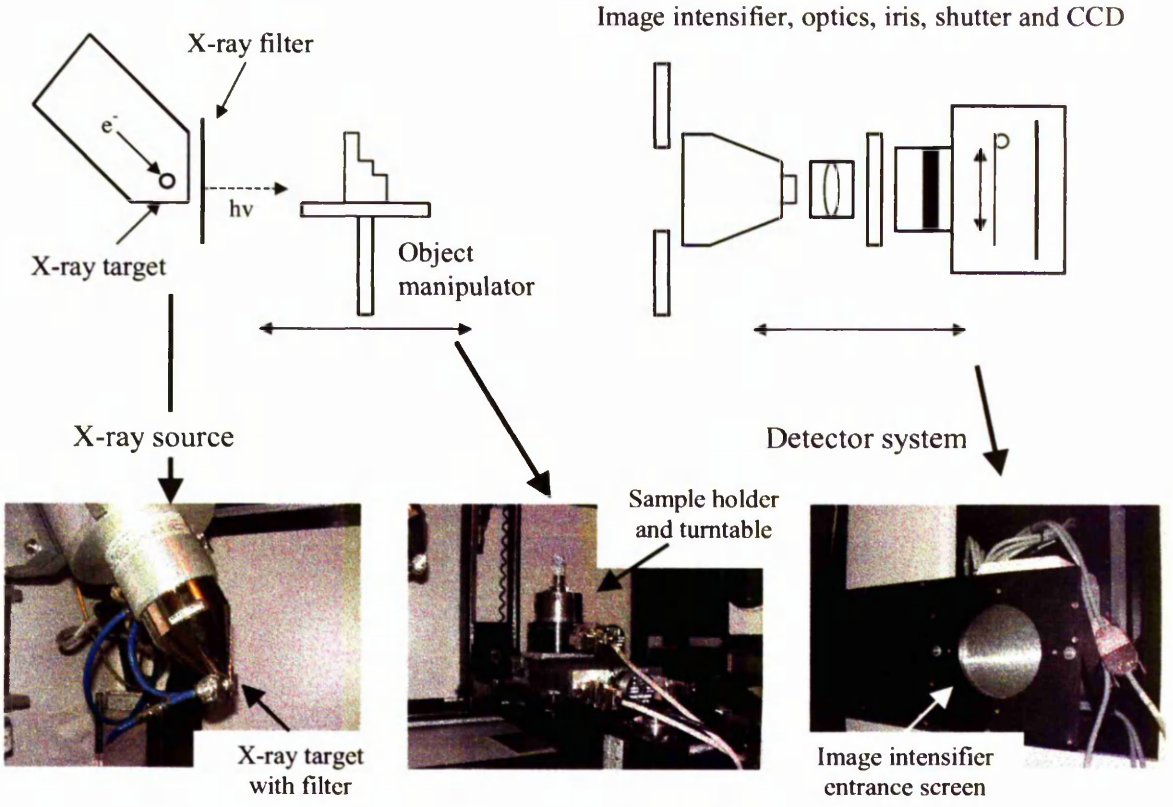

Figure 2-1. Schematic description of the imaging arrangement of the tomography system used, illustrating the three principal components of the instrumentation.

With the cone beam geometry, the voxel resolution of the reconstructed 3-D volume depends on the source-to-object distance, and thus the smaller the sample that is being viewed the better the resolution that can be obtained.

2.2.2. Setup and calibration

In order to generate high quality reconstructed CT images, it was necessary for the imaging instrumentation (X-ray source, sample manipulation stage and image intensifier/CCD camera chain) to be set up accurately, relative to each other. The X-ray source and detector units were aligned, both horizontally and vertically, along the principal axis of the tomography system, defined by the line joining the X-ray focal spot with the centre of the image intensifier entrance screen. It was also important that the axis defining the centre of rotation of the turntable was accurately aligned perpendicular to the principal axis of the system, noting that CT images/slices through an object are derived from horizontal lines through the object extracted from radiographs or projection images representing many views. Prior to calibration of the system, there was an inherent degree of spatial distortion clearly visible in the acquired projection images of a sample due to the non-linearity of the imaging system, which, if not corrected for, would result in reconstruction artefacts, such as ring artefacts (see Section 1.4.3.3), in the CT images/slices. Correction for this spatial distortion was carried out prior to performing a measurement scan, as part of a number of necessary calibration tasks for setting up the system. For measuring the horizontal and vertical non-linearities (distortion) introduced by the imaging system, a linearity plate, containing a grid of horizontal and vertical grooves, was mounted in front of the detector, as illustrated in Figure 2-2. Figure 2-2(a), a projection image of the linearity plate prior to the correction, illustrates the distortion in the horizontal and vertical lines of the plate. This distortion was parameterised from such projection images of the linearity plate using a polynomial fitting routine defined in the CT acquisition and reconstruction software. The coefficients of this routine, related to the linearisation of a distorted (curved) line, were used at the time of CT data acquisition to remove the effects of the horizontal and vertical distortion within each projection radiograph of the scanned object. The resulting projection after the correction was applied to the linearity plate is illustrated as a series of straight lines, as shown in Figure 2-2(b). The grooves on the linearity plate also defined the accurate horizontal and vertical axes of the imaging system.

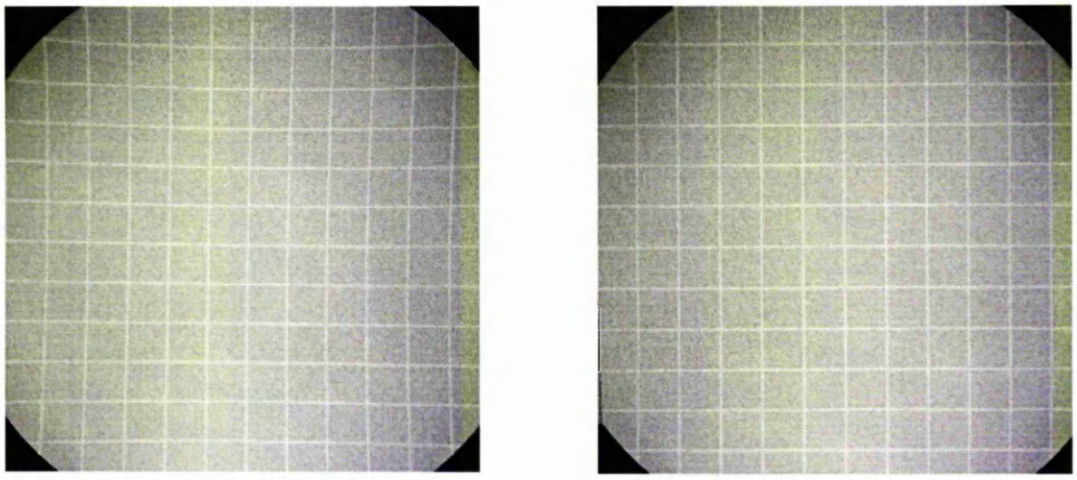

(a) (b)

Figure 2-2. Illustrating X-ray radiographs or projection images of a linearity plate fixed in front of the detector system, with horizontal and vertical grooves used to correct for the effects of spatial distortion, both (a) before, and (b) after, the correction.

The second calibration task was to acquire black (no X-rays) and white (X-rays on, no sample) reference images. It was necessary to know the signal level of X-rays passing beside the object (obtained from the white reference image) to be able to reconstruct a CT image from the projection data, and this depended on the X-ray settings used, i.e. voltage and current. These were used for correction of the projection images acquired during a tomographic scan in order to calibrate the grey levels of the scanned object during reconstruction of the CT images. The third task was to specify the distances between the key components of the system. The distance between the X-ray focal spot and the detector was set at a value of 900 mm for all scans. The distance between the X-ray focal spot and the centre of rotation of the turntable depended on the required magnification of the sample in relation to its size and the necessity of it remaining within the field of view of the detector system during rotation. This distance was calculated automatically by the software from the measured width of the sample, and determined the voxel resolution of the reconstructed volume, an important parameter when carrying out quantitative characterisation of the tomographic data. The fourth and final calibration task was to measure the axis of the centre of rotation of the turntable in the projection images, ensuring it was aligned laterally about (or in line with) the principal axis of the system, with respect to the X-ray source and detector. An accurate centre of rotation is vital for high quality CT images, as pronounced artefacts (see Section 1.4.3.2) are obtained if the centre of rotation is inaccurate. The CT image reconstruction software had algorithms for automatically

deriving the centre of rotation from the raw CT projection data collected during a scan, making this calibration task somewhat less important. The experimental calibration routine automatically derived the centre of rotation using projection images of a thin vertical steel rod, collected at angles of 0 and 180°. Once all of the calibration procedures were complete, collection of the raw projection data could be performed.

2.3. Measurement of the Spatial Resolution of the System

2.3.1. Methods of measurement

Measurements were carried out in order to make inferences of the optimum spatial resolution of the CT system for when performing non-destructive evaluation of details and features inside an object, and two different methods were used. The first method derived a measurement from the sharpness at the well-defined edges in CT slices of a small titanium matrix composite test-piece, giving a direct value in millimetres. The second method also derived the measurement from the edge profiles of the same CT slices of the test-piece, but from the calculation of the modulation transfer function (MTF). The following describes how the two methods were carried out to derive the respective measures of the spatial resolution of the system.

2.3.1.1. Method 1 – Measurement from edge profiles

The tomography system was set up and calibrated according to Section 2.2.2. The test object that was used was a titanium matrix composite test-piece of rectangular cross-section (1.5 mm width × 1.4 mm thickness), of which the damage evolution with applied load was studied in detail and is reported in Chapter 4. Such a test object was chosen for this study due to its small rectangular cross-sectional area, allowing a high magnification of the sample resulting in highly focussed and thus sharp edges for the edge profile measurement. Due to the cone beam geometry of the system, and the fact that a micro-focus X-ray source is used, the primary limitation to the spatial resolution achievable in the radiograph or projection images, and thus the CT slices, was the unsharpness of the imaging system. This was minimised by the use of geometric magnification of the sample. The sample was positioned as close to the X-ray source as possible, thus obtaining magnification, but making sure that the whole of the specimen was visible within the field of view of the imaging system at all rotation angles (i.e. with the cone beam geometry the sample size limits the amount of magnification). At these higher magnifications, the

focussing of the X-ray beam becomes much more sensitive, enabling very sharp edges to be defined. The smaller the test object the higher the magnification that can be achieved, and a CT spatial resolution approaching the limit imposed by the size of the X-ray source itself can be obtained. A tomographic scan was performed on the sample with a voltage setting of 70 kV, used to give sufficient attenuation of the X-rays through the object but not so high as to introduce increased amounts of noise in the projection images. When carrying out the scan it was important that the radiographic density of the sample, or the length of the X-ray path through it, was low enough for adequate penetration of all regions of the sample at the particular energy being used. This was particularly important for angles of rotation giving the greatest effective sample density such as the diagonals of a square cross-sectional prism. The advantage of cylindrical samples is that the X-ray path length is the same at all rotations. If this condition was not fulfilled then artefacts due to inadequate penetration would be obtained in the CT images or slices, regions of which would appear uniformly dark in the projection images. A rotation step of 0.3° was used, improving reconstruction of the sample over a typical step of 0.5°, with 64 frames averaged for acquisition of each projection (using a recommended exposure time for each frame of 120 ms). An increase in the number of frames that were averaged results in less noise in the raw projection images due to a greater sampling. Ten 2-D cross-sectional slices of equal spacing along the length of the scanned volume of the sample were reconstructed at the highest resolution (1024 pixels^2) for analysis purposes, using the filtered backprojection algorithm used for fan beams (Feldkamp *et al*, 1984; Herman, 1980; see Section 1.4. and Appendix).

Each of the reconstructed CT slices was taken and the following applied in order to obtain a representative value of the maximum achievable spatial resolution of the system:

1. The vertical gradient of the original image was derived, which involved effectively differentiating the image and converting the edge response function (which can be represented by a profile across an edge of the object in the original CT slice) into a point spread function (see Section 1.3.1.3). The point spread function describes the amount of distortion there is across an edge.
2. Extracting a profile across an edge of the object in this differentiated image, representing the point spread function, gave the grey level intensity or signal as a function of position across the edge. This was equivalent to differentiating the profile of the edge response function. The characteristic shape of the profile

contained a peak at the position of the edge, and in measuring the full-width-half-maximum (FWHM), a valid measure of the total system resolution was obtained.

2.3.1.2. Method 2 – Calculation of the MTF

The second method of measuring the spatial resolution was essentially an extension of the first in that similar image processing steps were initially undertaken. The same CT images of the composite test-piece used for the first method were used for this analysis. The following steps were applied to the reconstructed CT slices in order to calculate the MTF of the system (see Section 1.3.1.3):

1. A composite profile across an edge of the test object in the original CT slice was generated to obtain the edge response function (ERF), as above. This had the purpose of converting an edge trace from density or transmittance (i.e. the original CT slice) into effective exposure using a macroscopic response curve.
2. The derivative of this ERF profile was then calculated to obtain the point spread function (PSF), as in step 1 of method 1.
3. The amplitude of the Fourier transform of the PSF was then calculated, and the results were normalised to unity at zero frequency to obtain the modulation transfer function (MTF). The frequency at 10% modulation gave a quantitative measure.

2.3.2. Results and Discussion

2.3.2.1. Spatial resolution measurement from edge profiles

Figure 2-3(a) shows a typical reconstructed CT slice through the test object that was subsequently used for the spatial resolution measurement. Note that the image of the composite test-piece shows a single row of fibres within the surrounding titanium matrix. Only the sharp edges of the metal matrix, i.e. the object itself, had a purpose for this part of the study. There are no apparent reconstruction artefacts, as discussed in Section 1.4.3, in the slice of the object, and the edges appear focused and sharp. Figure 2-3(b) shows the corresponding slice with the vertical gradient derived, i.e. the original image of the object was differentiated with respect to the vertical direction in the plane of the image, in order to obtain the point spread function of the grey level distribution in the slice. It is clear from Figure 2-3(b) that this process has had the effect of emphasising the top and bottom edges of the object, effectively illustrating the amount and spread of distortion from each pixel at the edge.

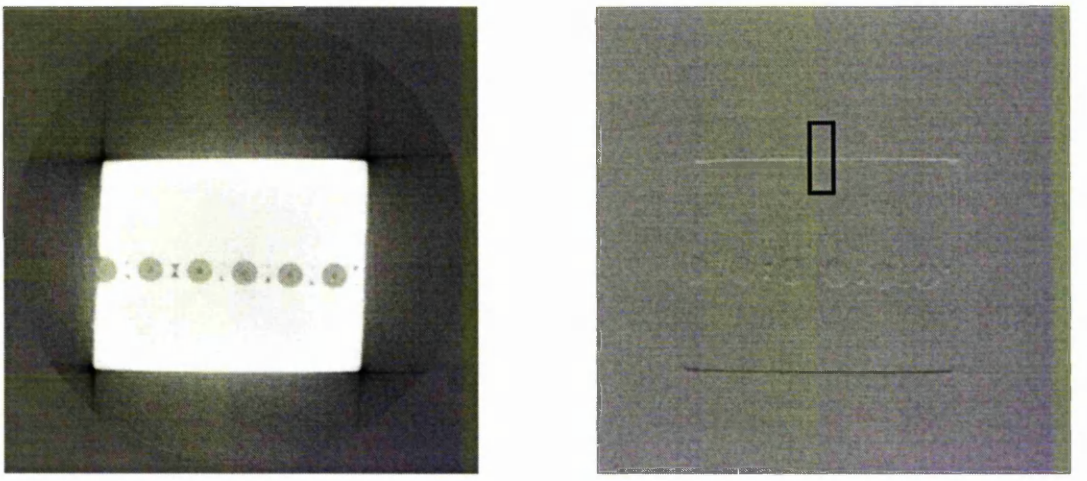

(a) (b)

Figure 2-3. (a) A reconstructed CT slice through the cross-section of the scanned volume of the titanium matrix composite test object (1.5 mm width × 1.4 mm thickness). (b) Corresponding slice with the vertical gradient derived, giving the point spread function of the original slice and emphasising the top and bottom edges of the object.

An intensity or grey level profile was then extracted from across a section of such an edge of the object in the differentiated CT slice, as illustrated in Figure 2-3(b). Figure 2-4 shows an example of such a profile, with the *x*-axis representing position across the sample (edge) in the vertical (perpendicular) direction. The profile illustrates a maximum at the exact position of the edge, corresponding to the centre (or highest point) of the spread of the grey level distribution across the edge. As the distribution is a function of position across the edge, in measuring the full-width-half-maximum of the peak, a valid measure of the spatial resolution of the CT system was obtained (Burch, 2003). A value of 9 μm was inferred. Corresponding intensity or grey level profiles were extracted from across the differentiated edges of the object of the ten cross-sectional CT slices that were reconstructed. Slight differences in this spatial resolution measurement were found across these ten slices, but only by +2 μm, with the value of 9 μm being the highest that was measured. This suggests that, through the analysis of the sharpness of edge traces, the reconstruction algorithm is not uniform for all slices through a scanned 3-D volume. This could be due to a number of reasons. The cone-beam reconstruction algorithm, an extension of the 2-D filtered backprojection algorithm, is an approximation and so some blurring might be expected for slices along the vertical axis of the 3-D volume due to each row of the detector receiving contributions from more than one slice during acquisition of

the raw data (Feldkamp *et al*, 1984; Stock, 1999). Another possible reason lies with the presence of image noise when analysing edge traces, and when linked with the polychromaticity and scattered radiation effects of such an X-ray source, the preferential attenuation of photons with different energies results in non-uniformities in the slices along the vertical axis of the reconstructed 3-D volume (Dainty and Shaw, 1979; Schneberk *et al*, 1990). Also, if the faces of the test object were not perfectly perpendicular with the X-ray beam at all angles during its rotation the resulting reconstruction would not be uniform along its vertical axis. The value of 9 μm is a sensible value for the spatial resolution considering the quoted X-ray source size from the manufacturer of between 5-10 μm. Also, in performing the same routine on a simple projection of a sharp edge, a value of 4.5 pixels was obtained for the full-width-half-maximum of the grey level spread distribution across the differentiated edge. This removed any effects of additional noise from the reconstruction process that might be found in CT images, but multiplying this value by the pixel size of the reconstruction (2 μm) still infers a value of 9 μm.

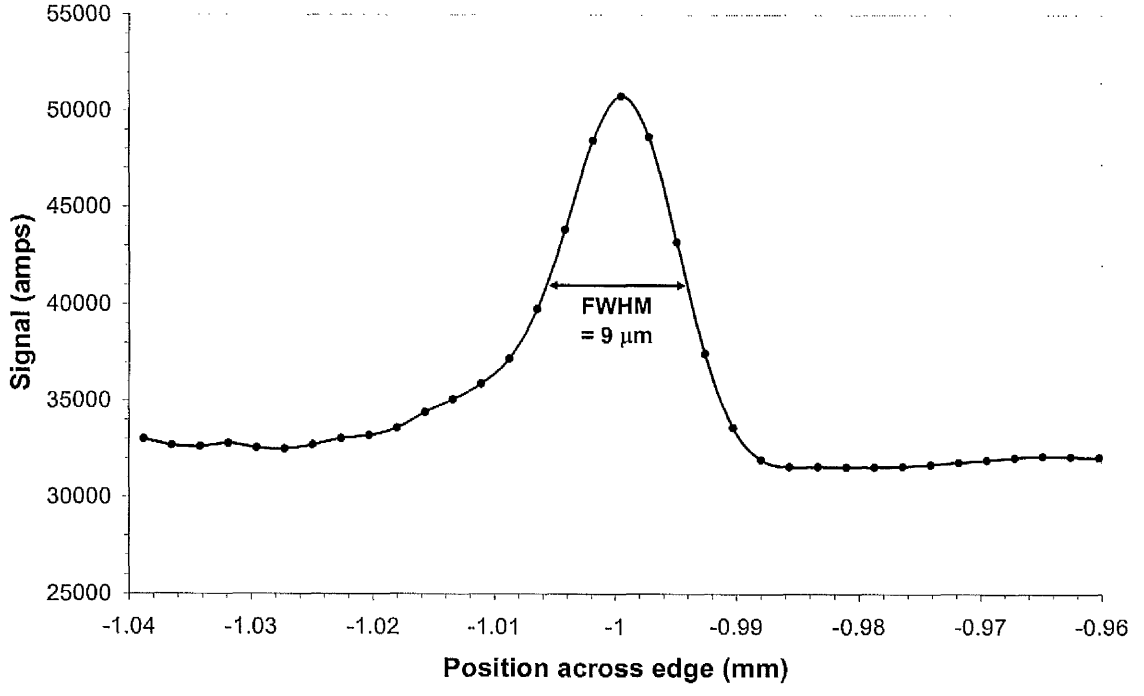

Figure 2-4. A typical profile extracted from across an edge (the position or *x*-axis representing the vertical or perpendicular direction) of the test object in the differentiated CT slice, such as that shown in Figure 2-3(b). The full-width-half-maximum of the distribution infers a measure of the spatial resolution of the CT system. Note that the intensity values of the *y*-axis can equally be interpreted as grey level values.

2.3.2.2. Spatial resolution inferred from the MTF

Using the same reconstructed CT slices as for the previous method, one of which is shown in Figure 2-3(a), the point spread function was derived, as previously, by differentiating this original CT slice, or edge response function profile across an edge, resulting in Figure 2-3(b). The Fourier transform of this intensity or grey level profile across the differentiated edge (PSF), such as that shown in Figure 2-4, was then calculated to give the modulation transfer function (see Section 1.3.1.3). Figure 2-5 shows an example of such an MTF profile, as a function of spatial frequency, after the amplitude of the Fourier transform was normalised to unity at zero frequency (Dainty and Shaw, 1976). The quantitative value of the measured MTF was taken as the frequency at 10% modulation (ASTM Standard E1695, 1995). The spatial resolution inferred from the analysis of all ten reconstructed slices was in the range 75-85 mm^{-1}. The range in the measured values is assumed to be due to the reasons outlined in Section 2.3.2.1. Converting this measurement into an interpretable value in microns gives a maximum spatial resolution of ~11 μm.

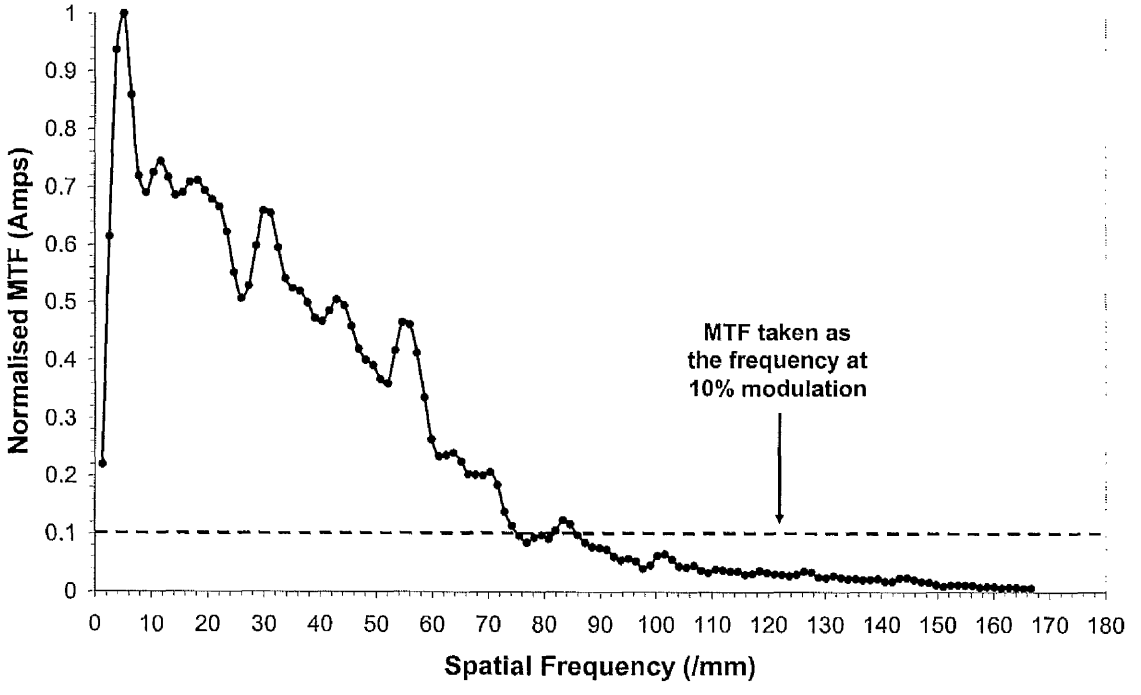

Figure 2-5. An example of a calculated Fourier transform profile from across the differentiated edge of the titanium matrix composite in a reconstructed slice, giving the MTF as a function of spatial frequency.

The two methods give very similar values for the maximum spatial resolution of the CT system, differing only very slightly in terms of the physical values obtained. This is due to the fact that the two measurement techniques are the same up to the generation of the point spread function across the edge. The first method gave a direct measurement of the spatial resolution from the profile across the edge, and as a result of using the full-width-half-maximum of the distribution, while more easily interpretable, the value obtained is more of an approximation of the spatial resolution. The method of calculating the modulation transfer function to quantify the spatial resolution extends this by measuring the Fourier transform of the point spread function across the edge, and so determines the contrast across the edge as a function of spatial frequency. The value obtained from this method is therefore a more quantitative measure of the total unsharpness of the imaging system. The MTF profile of Figure 2-5, and the quantitative value of the spatial frequency at 10% modulation, is in good agreement with measured and modelled values of the work by Mangard and Hammersberg for a test object of similar thickness/diameter and thus geometric magnification, of ~78 mm^{-1} (Mangard and Hammersberg, 1998). They investigated the performance and optimised detail detectability limits of a very similar CT system in terms of its instrumentation and setup, noting that the measure of image quality parameters, such as the MTF, is unique to each individual CT imaging system. Knowing the maximum spatial resolution of a computed tomography system is important for when performing non-destructive evaluation of small features and details within an object, as it gives inferences of the minimum detectable detail size within the object.

2.4. Optimisation of Image Quality and Detail Detectability

2.4.1. Experimental Method

The optimisation of image quality in reconstructed CT images of a test object was investigated in terms of optimising the data collection parameter settings of the CT system. Maximisation of the signal-to-noise ratio, $SNR_{\Delta S,CT}$, between a contrasting detail and its surroundings, which combines measures of both contrast and noise and was used to characterise the image quality, was obtained by optimising the X-ray source tube potential and X-ray filter material and thickness. The object material/detail combination, or test object, that was used was the titanium matrix composite test-piece as used in the spatial resolution investigation (thickness 1.4 mm, see Figure 2-3(a)), but this time with direct

relevance for the silicon carbide fibres, which represented the imaged detail with diameter ~140 μm. Again, such a sample was used for the test object to give a high geometric magnification and therefore accurate focusing of the fibres within the matrix, important for such matrix/detail image quality measurements, using the sharpness of the edges of the sample. The effect of changing the X-ray source tube potential with no X-ray filtration was investigated first of all. The tomography system was set up and calibrated according to Section 2.2.2. Tomography scans were carried out, with X-ray source voltages in the range 60-160 kV, in 10 kV steps, with a rotation step of 0.3° and 64 frames averaged for acquisition of each projection (using a recommended exposure time for each frame of 120 ms). Ten 2-D slices were reconstructed at equal intervals along the sample length from the projection data acquired for each scan, at the highest resolution (1024 pixels^2). This was so that an average measure of the signal-to-noise ratio could be obtained at each X-ray source voltage. An intensity or grey level profile was extracted from across the centre fibre (detail) and the neighbouring regions of matrix (object material) either side of the fibre for each of the reconstructed CT images of the object. Figure 2-6(a) illustrates the region across which profiles were extracted, and an example of one is shown in Figure 2-6(b).

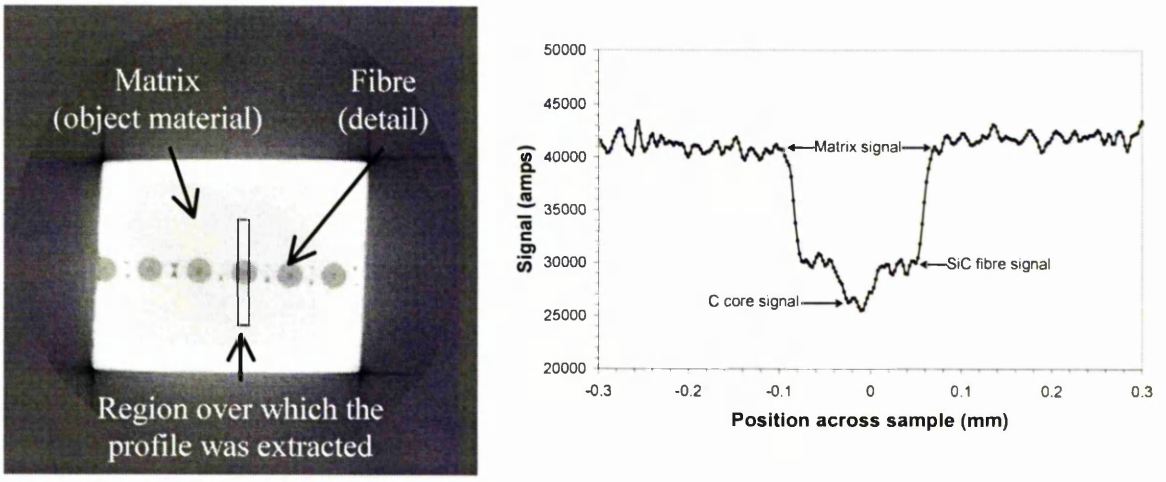

(a) (b)

Figure 2-6. (a) To illustrate the region of a reconstructed CT slice of the test object across which an intensity profile, such as that shown in (b), was extracted for the signal-to-noise ratio calculation. The diameter of a fibre representing the detail was 140 μm.

Such profiles were used to calculate the detail signal-to-noise ratio, $SNR_{\Delta S,CT}$ as defined by Equation (1-4) and Figure 1-10, from the signal differences between the detail and surrounding object. The profile shows significant scatter in the signals from the matrix and fibre, representing the noise in the signals, and the difference between the upper and lower levels, or variance, was used in the calculation according to Equation (1-4). In calculating an average value over the ten reconstructed slices for each scan at a particular X-ray tube potential, the optimum potential setting for the imaging task was found. Note the presence of a trough at the centre of the signal measured from across the fibre, as indicated in Figure 2-6(b). This part of the signal, from the carbon core at the centre of the fibre, was not used in the analysis, which just used the signal from the SiC region.

The effect of using X-ray filters, during data collection, on the image quality of the reconstructed CT slices of the object was also investigated. Sandborg *et al.* presented the benefit to the image quality obtained with X-ray tomography through the use of filters to shape the energy spectrum (Sandborg *et al*, 1994). A range of thicknesses, up to 2 mm, of aluminium and copper X-ray filters were studied, and slotted into a bracket in front of the X-ray source. Tomographic scans and signal-to-noise ratio calculations were carried out in exactly the same way, determining the effect of changing the tube potential at constant filter thickness and filter material, for different filter thicknesses.

2.4.2. Results and Discussion

Figure 2-7 shows plots of the calculated signal-to-noise ratio, $SNR_{\Delta S,CT}$, as a function of X-ray tube potential for the range 60-130 kV, for cases of no X-ray filtration and with the use of 1 mm and 2 mm Al X-ray filters. Figure 2-8 shows similar plots but compares the case of no X-ray filtration with the use of 0.125 mm and 0.25 mm Cu X-ray filters. The plotted values represent the average and the error bars indicate the standard deviation, of the individual values calculated from the ten reconstructed slices for each tube potential. For the case of an unfiltered beam (the lower curve in both figures), a clear trend is observed in terms of an optimum tube potential which maximises the signal-to-noise ratio in the images, measured to be 100/110 kV. The image quality falls away quite significantly either side of these optimum settings. This behaviour can be explained by the fact that at higher tube potentials, the noise in the images increases more significantly than the difference between the effective linear attenuation coefficients of the object and detail materials. At lower tube potentials, the difference between the attenuation coefficients,

and thus the intensity between the two phases in the object, decreases and thus lowers the contrast between the two.

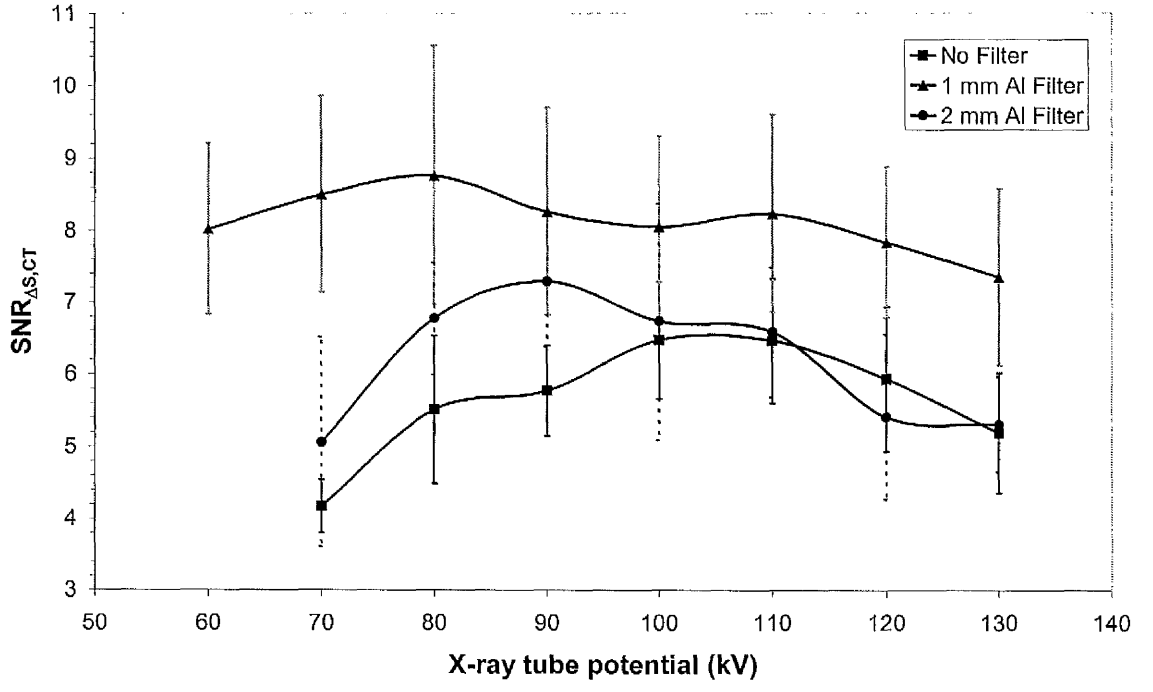

Figure 2-7. Plots of $SNR_{\Delta S,CT}$ as a function of X-ray tube potential for cases of an unfiltered X-ray beam and with the use of 1 mm and 2 mm Al X-ray filters, for the studied Ti/SiC object/detail material combination (sample thickness 1.4 mm).

The main effect of using both X-ray filter materials has been to increase the signal-to-noise ratio across the range of tube potentials investigated. Such high-energy pass filters remove low-energy photons from the polychromatic beam characteristic of such micro-focus tube sources (Sandborg *et al*, 1994). With no X-ray filter, low-energy photons are absorbed more efficiently by the object causing the mean energy of the photon energy spectrum to rise as the beam propagates through the matter (see Section 1.4.3.1). As will be illustrated in Section 2.5, this causes artefacts in the reconstructed CT slices of the object and thus affects the quality of such images due to a large distribution of voxels with different intensities. The removal of these photons with filtration of the beam prior to attenuation through the object thus gives a more uniform distribution of voxel intensities and reduces noise. Regarding Al filters, an increase in the thickness from 1 mm to 2 mm results in a decrease in the contrast between the two phases of the object to a level just above that of the case with no filter. This is due to the fact that an increase in filter thickness causes

absorption of a larger amount of photons from the beam, and reduces the mean energy of the photon energy spectrum reaching the object and therefore the contrast. With the use of Cu filters, this reduction in contrast is larger and more noticeable at lower thicknesses, due to the higher atomic number (and thus density) of Cu compared to Al. The use of a 0.5 mm thick Cu filter was observed to reduce the signal-to-noise ratio below the level of that for the 0.25 mm thickness. Sandborg *et al.* also observed Al to give a smaller reduction in contrast with increasing filter thickness (Sandborg *et al*, 1994). They observed the decrease in contrast with increasing filter thickness to be caused by beam hardening tending to make the beam mono-energetic and the contrast independent of filter thickness at large thicknesses.

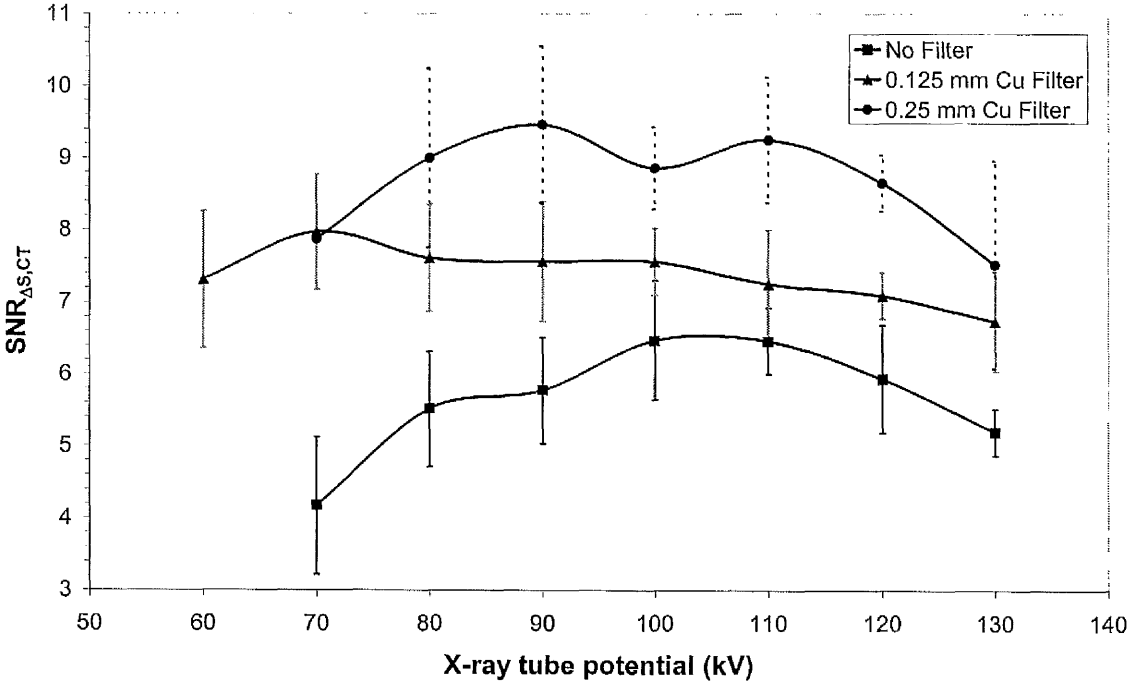

Figure 2-8. Plots of $SNR_{\Delta S,CT}$ as a function of X-ray tube potential for cases of an unfiltered X-ray beam and with the use of 0.125 mm and 0.25 mm Cu X-ray filters, for the studied Ti/SiC object/detail material combination (sample thickness 1.4 mm).

Also suggested are small shifts in the optimum tube potential with the use of filters, suggested to be to slightly lower energies. There also seems to be a less sharp drop in the signal-to-noise ratio from the optimum, as observed for the measurements with 1 mm Al and 0.125 mm Cu filters, indicated by the flatter curves. The validity of such observations is difficult to assess due to the nature of how image quality has been evaluated. It must

also be noted that optimum acquisition parameters are dependent on the imaged object and detail materials and the size of the object, as found by Mangard and Hammersberg who developed a simulation based on system parameters to maximise detail detectability (Mangard and Hammersberg, 1998). Although only two filter materials have been investigated, the effect of using X-ray filters during acquisition of the tomographic data is clearly illustrated, as is the effect of system settings.

2.5. Investigation of Beam Hardening

2.5.1. Method of beam hardening calibration

The effects of beam hardening, a reconstruction artefact inherent in such a computed tomography system using a polychromatic source (see Section 1.4.3), on reconstructed CT images, and an experimental calibration procedure to correct for its presence, was investigated. The calibration method (Badel *et al*, 2003; Hammersberg and Mangard, 1998) involved measuring the X-ray attenuation through the material under investigation as a function of its thickness. To illustrate the method, material of increasing thickness was obtained by placing side-by-side an increasing number of the titanium matrix composite test-pieces (e.g. as illustrated by the CT slices of Figures 2-11, 2-12 and 2-13), for which the correction was to be evaluated. First of all, the transmitted X-ray intensity through each object of increasing thickness was measured, for a particular X-ray energy setting, from simple projection radiograph images. Figure 2-9(a) and (b) shows an example of a projection image of the test object (composite test-piece) under investigation and an intensity (or attenuation) profile calculated from across the centre of the object, respectively. Using the attenuation profiles obtained for each of the object thicknesses, and specifically the measured I/I_0 values, a beam hardening calibration curve was plotted, determining the equivalence between the negative logarithm of the attenuation ratio, I/I_0, and thickness (in mm). A polynomial approximation was fitted to these measured calibration points, the roots of which were used in the reconstruction process resulting in the 'linearisation' of the attenuations from the object (Kak, 1979), and hence correction for beam hardening effects. The purpose of linearisation is to transform raw CT-data values from a curved function (see Section 2.5.2), typical of those collected from polyenergetic X-ray sources, to a value on a linear function, representing monoenergetic CT-data, for the

same object thickness. Rewriting the classical attenuation law (Equations (1-1) and (1-2)) and taking into account the fact that μ/ρ is a constant:

$$\ln\left(\frac{I_0}{I}\right) = \frac{\mu}{\rho}\int \rho(x)dx \tag{2-1}$$

Application of this correction, especially in order to retrieve quantitative data of a phase, ideally requires a homogeneous object of constant density of the material under consideration, as opposed to the two-phase composite material used here. This is since a particular value of the attenuation ratio must correspond to specific material thicknesses in order to be corrected. In the case of a calibration object of constant density, ρ, Equation (2-1) shows the correlation between the I/I_0 ratio and the integral of dx along the X-ray path (i.e. to sample thickness). The method has been evaluated mathematically (Dainty and Shaw, 1976), where it is proposed that the data from a polyenergetic source are best fitted with a polynomial function, third order at most. In order to test the correction on reconstructed CT slices, tomography scans of three different thicknesses of the test objects were carried out. The tomography system was set up and calibrated according to Section 2.2.2. A voltage setting of 100 kV was used due to the calibration being performed at that voltage, with a rotation step of 0.3° and 64 frames averaged for acquisition of each projection (using a recommended exposure time for each frame of 120 ms). A 1 mm thick aluminium filter was also used during data acquisition, simulating the top curve. 2-D slices were reconstructed at the highest resolution (1024 pixels^2).

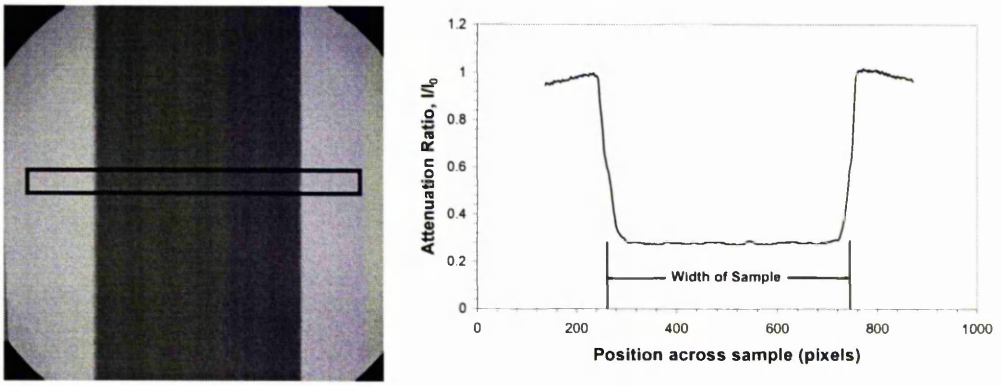

(a) (b)

Figure 2-9. (a) Projection radiograph of the composite test-piece used for the calibration procedure, illustrating the region over which the attenuation profile shown in (b) was extracted. The profile was normalised with the signal collected from the X-ray path beside the object, giving I/I_0 along the y-axis.

2.5.2. Results of calibration/correction

Figure 2-10 shows two calibration curves of the negative logarithm of the measured attenuation ratio as a function of object thickness, using an X-ray energy setting of 100 kV for both. As indicated, one curve was measured with the use of a 1 mm Al X-ray filter and the other with the use of a 1 mm Cu filter in order to compare filtration effects. Both curves are shown fitted with the polynomial approximations and the resulting calculated linearisation curves. It is clear from the two sets of curves that the effect of the Cu filter has been to reduce the beam hardening effect more significantly for a particular thickness, indicated by the fitted curve for the Cu filter being closer to its linearised curve. This is due to the higher atomic number and thus X-ray absorption properties of copper, resulting in the more effective removal of the lower energy photons prior to absorption in the sample, which is partly responsible for the beam hardening artefact. On the other hand, as expected, the Cu filter has also had the effect of reducing the attenuation ratio at all object thicknesses compared to that when using the Al filter.

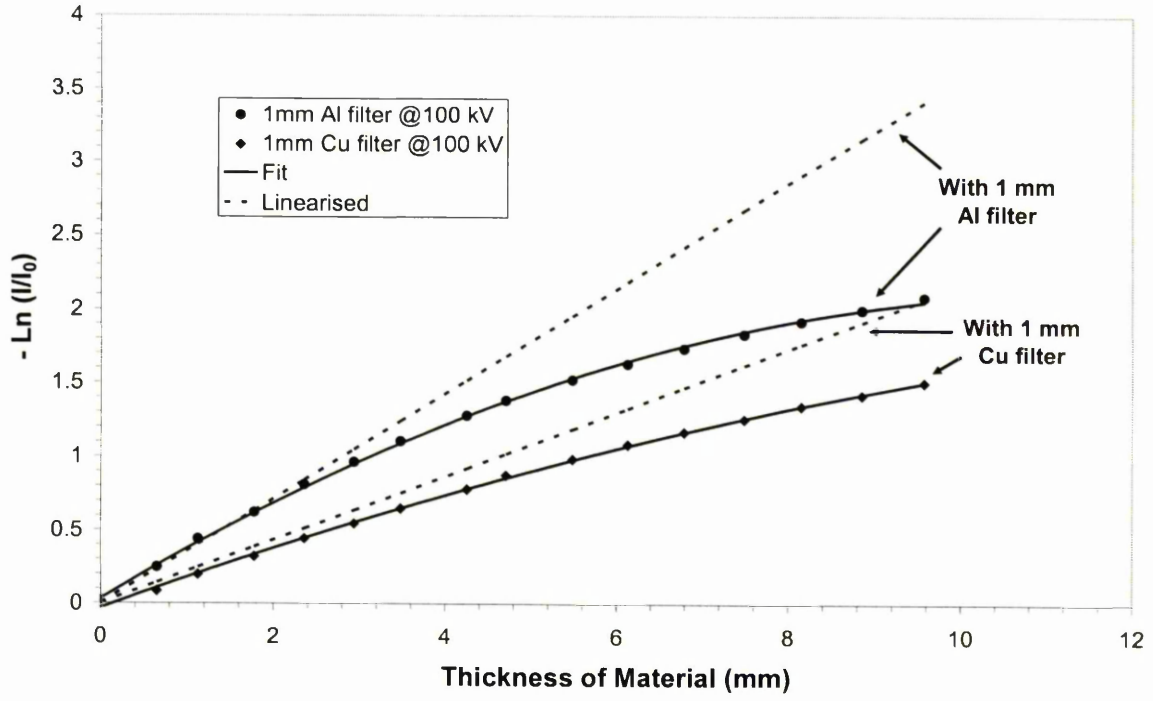

Figure 2-10. Calibration curves of the measured attenuation ratio as a function of object thickness for the composite test-pieces using an X-ray energy of 100 kV. The use of both Al and Cu X-ray filtration is compared, both 1 mm in thickness. The solid lines show the polynomial approximations to the measured data, and the dashed lines show the respective calculated linearised curves.

In order to illustrate the effect of this beam hardening calibration, the roots of the fitted polynomial were used in the reconstruction algorithm and applied to CT scans of three different thicknesses of the test objects. Figure 2-11(a) and (b) shows reconstructed CT slices and the corresponding extracted intensity profiles across the thickness of the object (vertical direction as shown), before and after correction respectively, from a test-piece 1.2 mm in thickness. At this thickness, as shown in Figure 2-10, the measured attenuation ratio is on the linearised curve and so not much of an effect from beam hardening should be observed compared to thicker samples.

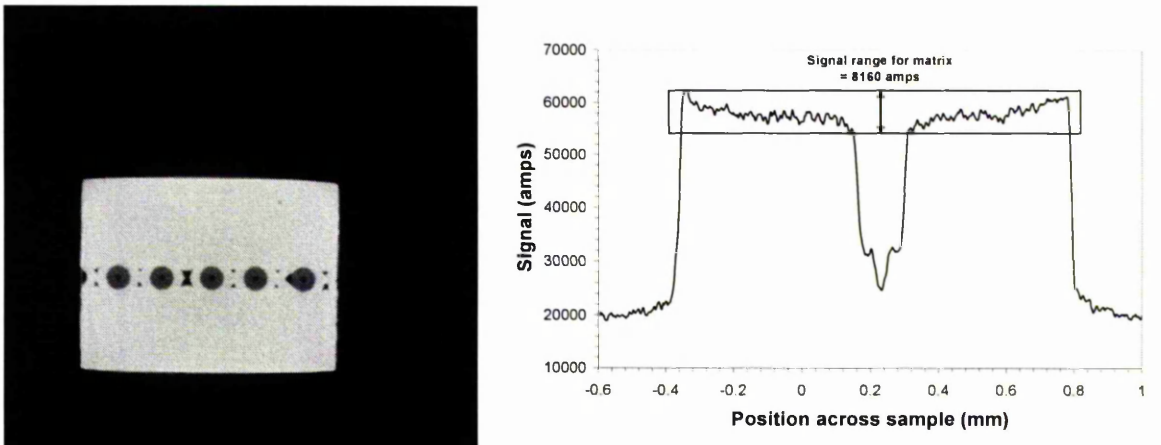

(a)

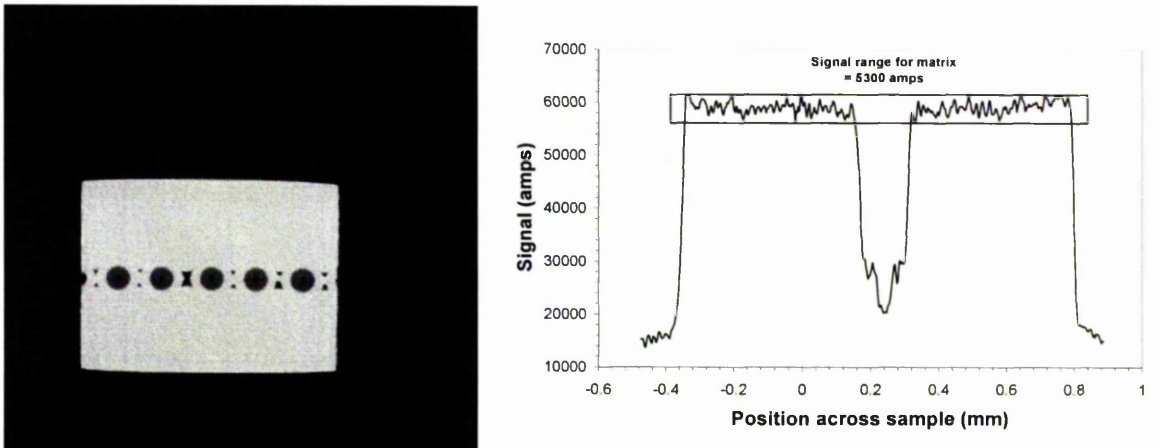

(b)

Figure 2-11. Reconstructed CT slices and corresponding intensity profiles measured across the thickness (vertical direction in plane of images) of a 1.2 mm thick test-piece, (a) before and (b) after correction. The region of interest in the intensity profiles, the signal from the matrix, is highlighted.

There is no distinct effect in the actual slice of the sample when comparing before and after correction. Taking into account only the response from the titanium matrix (as highlighted, and ignoring the sharp trough from the SiC fibre signal), the intensity profile of Figure 2-11(a) shows a slight 'cupping effect', as described in Section 1.4.3. The signal from the corrected slice in Figure 2-11(b) shows a more uniform profile through the thickness, with a reduction in the signal range.

Figure 2-12(a) and (b) shows results from a test object 4.8 mm in thickness.

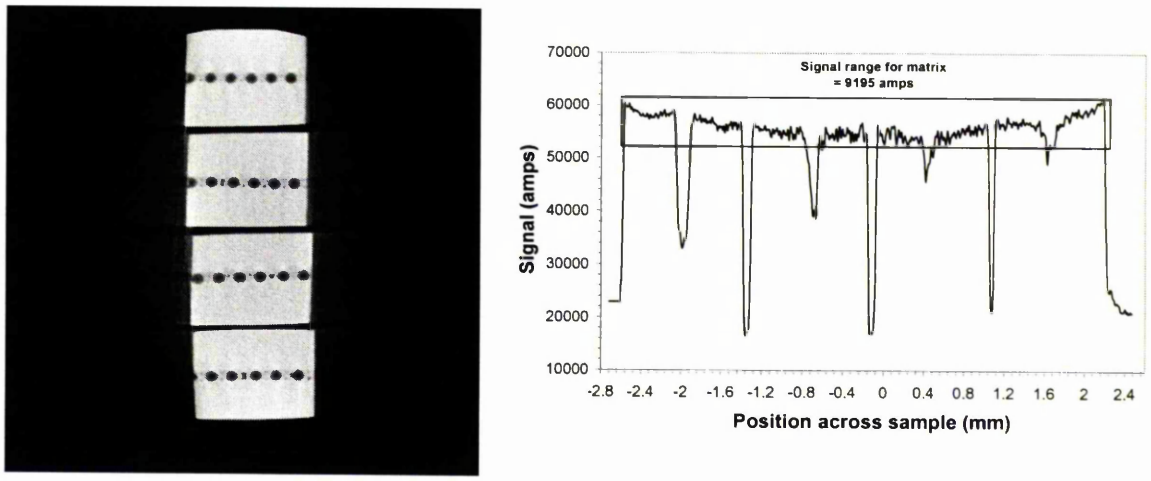

(a)

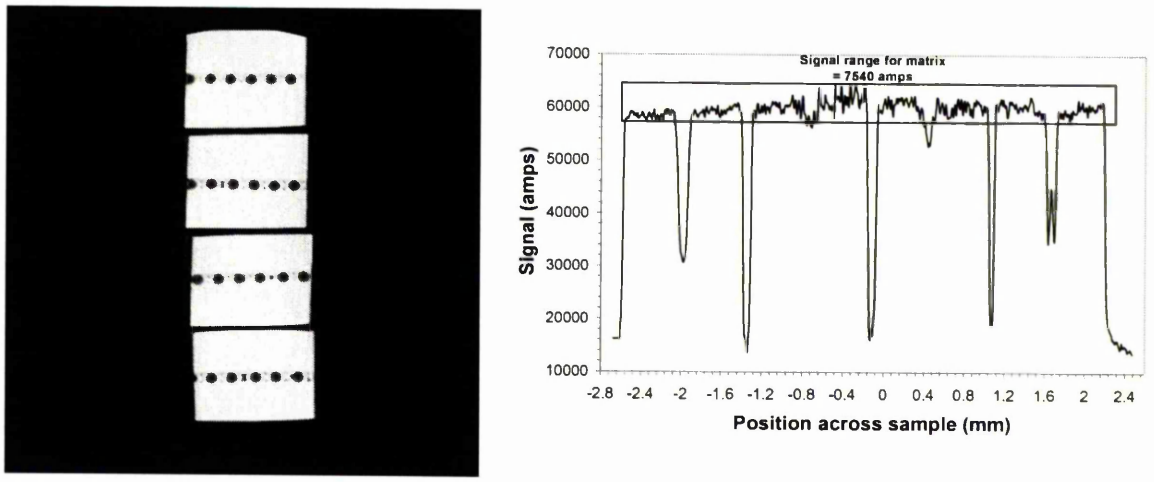

(b)

Figure 2-12. Reconstructed CT slices and corresponding intensity profiles measured across the thickness (vertical direction in plane of images) of a 4.8 mm thick object, (a) before and (b) after correction. The region of interest in the intensity profiles, the signal from the matrix, is highlighted.

The measured attenuation ratio at this thickness is below the linearised curve, and this effect can be seen in the profile before correction by a larger dip of the signal in the middle of the complete object compared to that of the previous sample. It is acknowledged that the gaps between each small sample making up the complete object would have an effect on the attenuation, but the effect of beam hardening is still illustrated. The actual slice before correction is observed to be clearly darker towards the centre, and the corrected image is uniformly grey as shown by the profile.

Figure 2-13(a) and (b) shows results from a test object 6.9 mm in thickness, for which the measured attenuation ratio is well below the linearised curve (Figure 2-10).

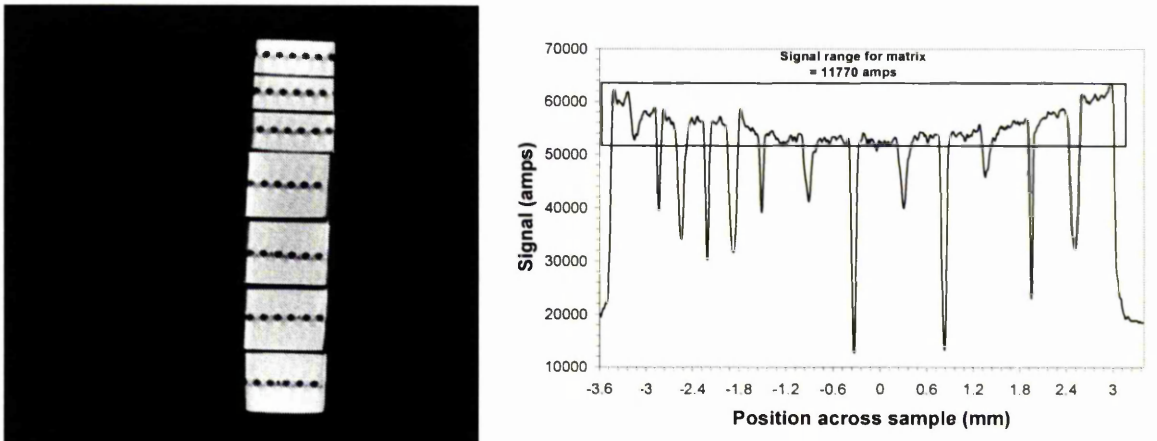

(a)

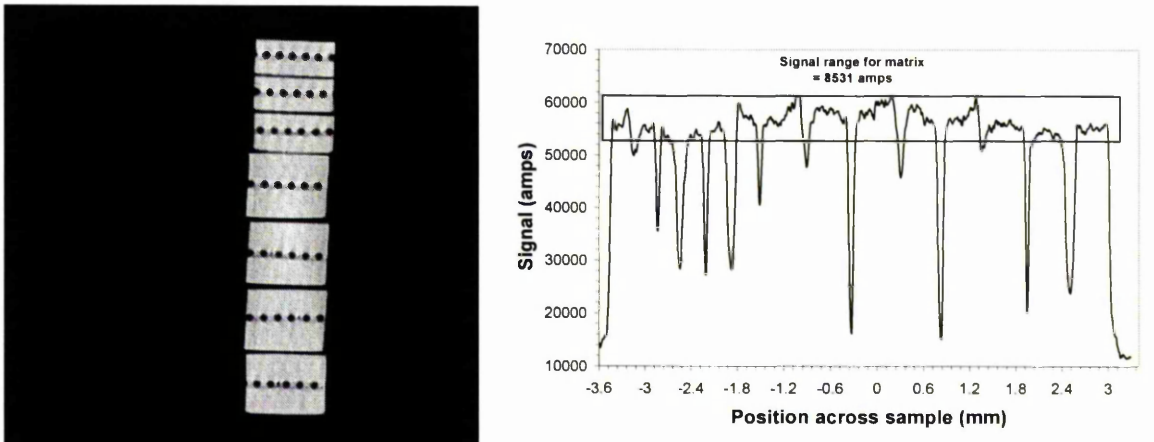

(b)

Figure 2-13. Reconstructed CT slices and corresponding intensity profiles measured across the thickness (vertical direction in plane of images) of a 6.9 mm thick object, (a) before and (b) after correction. The region of interest in the intensity profiles, the signal from the matrix, is highlighted.

The beam hardening effect is very clear in the slice before correction – the image is white at the top and bottom and a clear apparent density change through the middle (when viewing the vertical plane of the image). The cupping effect in the profile is much larger compared to the previous objects, which on correction doesn't give a perfectly straight profile but improves it significantly. The result is a slice that is slightly lighter in the middle of the object than at the edges, suggesting that the calibration procedure over corrects at larger thicknesses due to the beam hardening effect being more significant.

The effect of beam hardening in reconstructed images due to the polychromaticity effects of the microfocus X-ray source used in this study has been illustrated. An experimental correction procedure has been outlined and the results of such a correction have been shown to give improved results in terms of reducing the phenomenon.

2.6. Summary and Conclusions

The performance of a high-resolution X-ray microtomography system has been investigated and illustrated with respect to points raised in the literature review of Chapter 1. A brief investigation into three facets of the performance of a tomography system has been undertaken, giving a description of important experimental aspects one should consider in order to obtain improved reconstructed tomography images for structural and numerical characterisation.

The maximum spatial resolution of the system for when performing non-destructive evaluation has been determined at a value of ~9 μm. It is important to know the minimum discernible detail size that can be resolved using the technique, especially when the purpose is to resolve small features or details in the output reconstructed images. The image quality, which affects the detectability of features or details in reconstructed tomography images, has been investigated through the use of optimum equipment settings. The signal-to-noise ratio between a contrasting detail and its surroundings has been shown to be affected by the tomography system settings, such as the X-ray tube potential, used during collection of the raw data. The effect of using X-ray filters has also been found to improve the quality of images, but only up to a certain thickness. The significance of beam hardening in reconstructed images, inherent to such laboratory based tomography systems equipped with polyenergetic X-ray sources, has been measured and investigated. False density or composition gradients in the imaged object are implied, but its presence can be suppressed by linearisation of the raw tomography data, which has been illustrated.

References

ASTM, 'Standard Test Method for Measurement of Computed Tomography (CT) System Performance', ASTM E1695, 1995.

Badel, E., Létang, J-M., Peix, G. and Babot, D., (2003), 'Quantitative microtomography: measurement of density distribution in glass wool and local evolution during a one-dimensional compressive load', *Measurement Science and Technology*, **14**, 410-420.

Burch, S., AEA Technology plc. Private Communication. Engineering Solutions, AEA Technology plc, E1 Culham Science Centre, Abingdon, Oxon OX14 3ED. 2003.

Dainty, J. C. and Shaw, R., *Image Science: principles, analysis and evaluation of photographic-type imaging processes*, Academic Press, London, 1976, 190-275.

Feldkamp, L. A., Davis, L. C. and Kress, J. W., (1984), 'Practical cone-beam algorithm', *J. Opt. Soc.*, **1**, 612-619.

Hammersberg, P. and Mangard, M., (1998), 'Correction for beam hardening artefacts in computerised tomography', *Journal of X-ray Science and Technology*, **8**, 75-93.

Herman, G. T., *Image Reconstruction from Projections: the Fundamentals of Computerised Tomography*, Academic Press, New York, 1980.

Kak, A. C., (1979), 'Computerised Tomography with X-ray, Emission and Ultrasound Sources', *Proceedings of the IEEE*, **67**(9), 1245-1272.

Mangard, M. and Hammersberg, P., (1998), 'Optimised detail detectability in computerised tomography', *Journal of X-ray Science and Technology*, **8**, 51-73.

Sandborg, M., Alm-Carlsson, G. and Carlsson, C. A., (1994), 'Shaping X-ray spectra with filters in X-ray diagnostics', *Medical & Biological Engineering & Computing*, 384-390.

Schneberk, D. J., Azevedo, S. G., Martz, H. E. and Skeate, M. F., (1990), 'Sources of error in industrial tomographic reconstruction', *Materials Evaluation*, **48**, 609-617.

Stock, S. R., (1999), 'X-ray microtomography of materials', *International Materials Reviews*, **44**(4), 141-164.

Chapter 3

Ti/SiC$_f$ MMCs and Composite Micromechanics

The aim of this chapter is to provide a review of the relevant research that has been carried out regarding the use of metal matrix composites, and in particular Ti/SiC$_f$ MMCs, for aeroengine applications. An understanding of the micromechanical aspects and behaviour of such two phase materials, and the interaction between them, is important to their introduction into such structural applications. An introduction to the development of Ti/SiC$_f$ MMCs for particular aeroengine applications will be given, as will an account of the different processes that exist for their fabrication, which are important when considering the micromechanical performance of the resulting composite material. A review of the models describing both pure elastic interaction and partial debonding between fibres and matrix will be extended to illustrate their use in fibre fragmentation studies of lateral load transfer from matrix to fibres. Such studies enable detailed analysis of interfacial shear strengths. Considerations of fibre strength are important, particularly when fibre fracture results in the redistribution of load. As the main topic of the work covered in Chapter 4, an account of such studies in the literature will be given. An understanding of the phenomenon of fibre bridging of a matrix fatigue crack is also important regarding industrial use in aeroengines and will act as a background to the crack opening measurements made using X-ray microtomography.

3.1. Introduction

Titanium matrix composites being developed for use in aeroengines typically comprise a Ti-6Al-4V alloy matrix reinforced with SiC monofilaments. Titanium MMCs offer increased stiffness and strength combined with the consequent opportunity for weight reduction. Table 3-1 gives a range of material properties for the individual constituents of the Ti/SiC composites under consideration, illustrating the increased stiffness and strength of the reinforcing fibres at reduced density (Clyne and Withers, 1993; Materials Properties Handbook, 1994). Ashby has presented a review of the criteria for selecting the components of composites using materials-selection charts (Ashby, 1993). Figures 3-1 and 3-2 show design charts for lightweight composites – a Young's modulus-density (E-ρ)

chart for stiff composites (Figure 3-1) and a strength-density (σ_f-ρ) chart for strong composites (Figure 3-2), illustrating how these materials improve over monolithic titanium alloys. The use of bounds has been shown to be useful in defining the envelope of properties accessible to a given composite system (Ashby, 1993). These are shown very simply (i.e. no accurate calculation) on the charts for Ti/SiC, illustrating how this composite system can give higher stiffness and strength at lower densities.

Table 3-1. Table of material properties for Ti-6Al-4V and SiC/SCS-6. (Clyne and Withers, 1993; Materials Properties Handbook, 1994).

Material	Young's modulus (GPa)	Tensile strength (MPa)	Poisson's ratio	CTE ($\mu\varepsilon$/K)	Density (Mg/m^3)
Ti-6Al-4V	115	950	0.3	9	4.4
SiC – SCS-6	400	3800	0.17	4	3.29

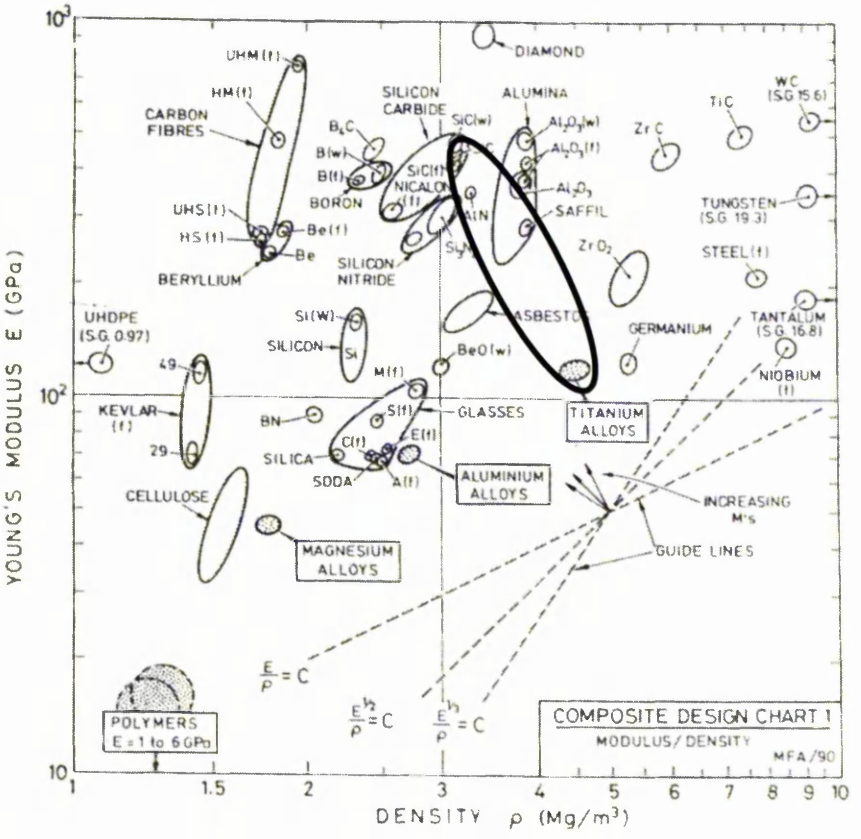

Figure 3-1. Design chart for light, stiff composites. The bound indicated on the chart illustrates the potential of Ti/SiC over monolithic titanium alloys in terms of increased stiffness at lower weight. (Ashby, 1993).

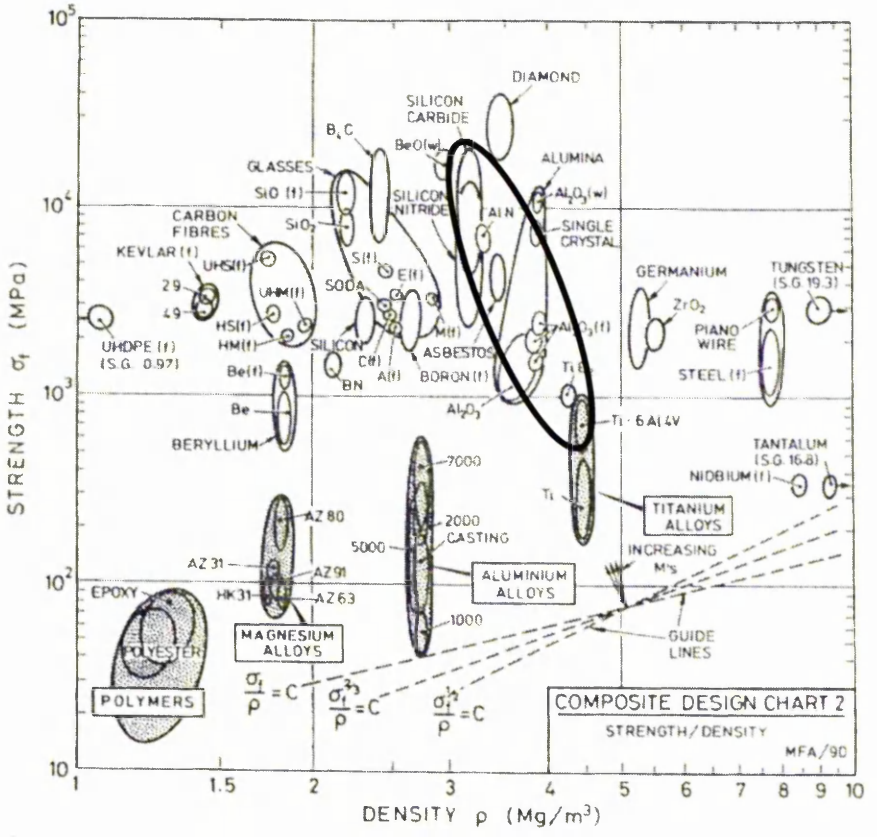

Figure 3-2. Design chart for light, strong composites. The bound indicated on the chart illustrates the potential of Ti/SiC over monolithic titanium alloys in terms of increased strength at lower weight. (Ashby, 1993).

Aeroengine test parts have concentrated on the use of these composites for weight savings in rotors (Hooker and Doorbar, 2000), and giving potential for additional weight reduction in the surrounding static structural parts. In a conventional engine, much of the weight consists of mechanical fixings and spacers, which are independently supported and direct flow through the engine. Figure 3-3 illustrates a series of modifications which could be made so as to reduce weight as a result of the exploitation of the high performance of Ti/SiC composites (Driver, 1989). As it is a rotating system, weight savings at the periphery of the engine are especially helpful because they reduce the necessary radial support. One-piece bladed disks (blisks) reduce the parasitic weight, but much greater savings are possible through the use of composite hoop-wound ring structures. These eliminate the need for weighty support structures through their high circumferential specific strength and stiffness, combined with acceptable radial properties (~50% lower) (Clyne and Withers, 1993). Without Ti/SiC composites it would not be possible to use these new aeroengine composite designs.

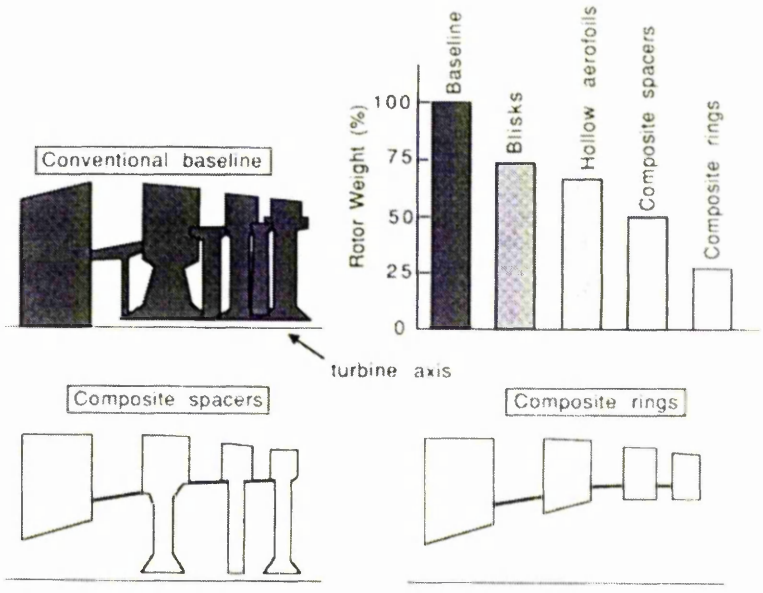

Figure 3-3. Diagram to illustrate that composite rings and spacers can give weight savings of nearly 75%. Conventional and composite bladed disk designs are shown. (Driver, 1989).

Titanium matrices reinforced with continuous SiC fibres, aligned in the direction of principal load, offer massive potential for high-duty aeroengine use (Hooker and Doorbar, 2000). Unidirectional composites show a significant increase in strength and stiffness in the fibre direction, compared with the monolithic matrix alloy, as shown by the UTS and modulus plots in Figure 3-4. Upon incorporation of around 40 vol. % of SiC fibres, the stiffness of Ti can be doubled and its strength improved by 50% (Clyne and Withers, 1993). Transverse stiffness is retained but transverse strength is reduced.

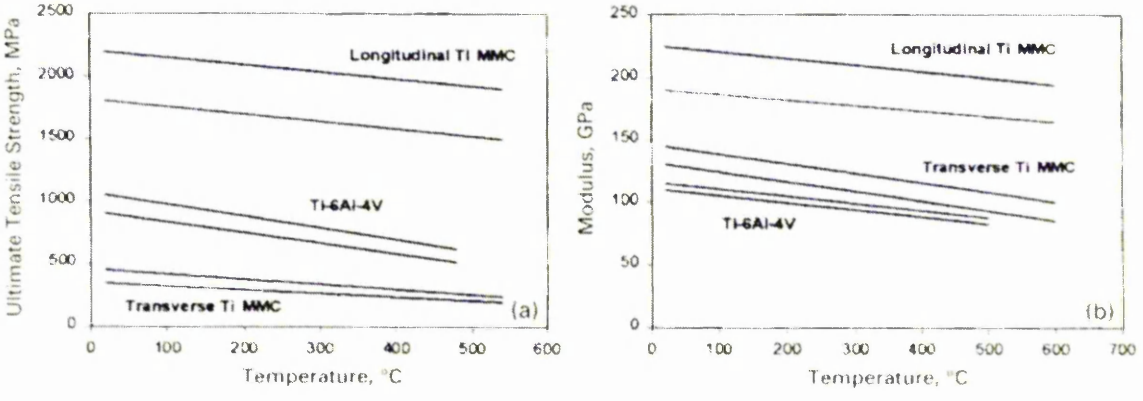

Figure 3-4. Comparisons of (a) tensile strength and (b) modulus for Ti/SiC MMCs containing 35-40 vol. % SCS-6 fibres in a Ti-6Al-4V matrix, with the matrix alloy itself. (Hooker and Doorbar, 2000).

Understanding the behaviour of aerospace components down to the microscale of the materials, and in terms of the behaviour of the constituents of the composite, is of great importance in terms of making the transition from conventional monolithic metals to MMCs a safe one. Influencing the mechanical properties of these composites, and thus their safe use in such an application, is the effect of fibre defects that can be introduced during manufacturing and processing. Low-cycle fatigue properties tend to be the most sensitive to such defects (Hooker and Doorbar, 2000). The effect of gross fibre defects, where several fibre layers in close proximity are broken, is, not surprisingly, the most detrimental to mechanical properties (Gonzalez and Llorca, 2001). When considering the failure of a unidirectionally reinforced fibre composite specimen, where initially all the fibres are intact and able to carry load, as increasing load is applied the weakest fibre will eventually fail. The loads that are shed by the broken fibre near the failure site must then be transferred to neighbouring fibres and possibly to the matrix. How much of the load is transferred depends on parameters including the strength and sliding resistance of the fibre/matrix interface, the fibre to matrix modulus ratio, the yield stress of the matrix and the fibre spacing. After the first break occurs, the load is redistributed and this can cause other fibres to fail and thus shed further load to intact fibres. At some point the composite specimen will be unable to carry additional load and failure of the composite will occur.

A detailed understanding of the effects of fibre defects on neighbouring fibres in terms of the strain induced under load and the transfer of load is vital to the successful use of Ti MMCs in aeroengines. Understanding the characteristics of fibre breaks and cracking sequences as a function of applied load, and also the interaction of matrix crack paths with the fibres, is important so that their effects can be contained as much as possible. X-ray microtomography, as has been reviewed in detail in Chapter 1, is a non-destructive technique that can provide important information about the accumulation of fibre breakages as a function of applied load. A 3-D tomographic scan of a sample or component allows detailed observation of the characteristics of fibre breakage within the metal matrix in terms of crack morphologies. The effect of a defect on neighbouring fibres in terms of the relative positions and numbers of subsequent breaks can be accurately determined. It can also provide explicit visualisation of how the growth of a matrix fatigue crack interacts with the presence of the longitudinal fibres designed to keep its damaging effects to a minimum. Together with the measurement of load redistribution from damaged to intact fibres, such work forms the basis of the investigation detailed in Chapter

4, into the effect of matrix and fibre defects and damage, i.e. cracks, on the performance of Ti/SiC_f composites and thus their successful use in aeroengine applications.

3.2. Fabrication Processes and Thermal Residual Stresses

3.2.1. Background and general microstructural features

More than 30 years have been spent on active research into Metal Matrix Composites (MMCs) since Cheskis and Heckel first started looking at the mechanical and deformation behaviour of the reinforcement of Al and Cu matrices (Cheskis and Heckel, 1970). Initially, attention was concentrated on the improvement of creep resistance of rotor blades through the reinforcement of aluminium with boron or tungsten fibres (Garibotti, 1978; Lilholt, 1977), but poor foreign object damage tolerance proved a serious obstacle. More recently, interest has focused on axisymmetric aeroengine components (Driver, 1989; Hooker and Doorbar, 2000), many of which are ideally suited to the excellent unidirectional properties that can be achieved with hoop-bound titanium-based long fibre reinforced composites. They are now beginning to make a significant contribution to industrial and engineering practice. This has been a consequence of developments in several key areas, including processing methods and advances in the understanding of various structure-property relationships. The term metal matrix composite encompasses a wide range of scales and microstructures, but common to them all is a contiguous metallic matrix, and a reinforcing constituent, normally a ceramic. The composite microstructures may be subdivided according to whether the reinforcement is in the form of continuous fibres, as used in the development of Ti/SiC aeroengine components, short fibres or particles, and further distinctions can be drawn on the basis of fibre diameter and orientation distribution. The main microstructural features to take into account when considering composites for a particular use are mostly linked to fibre/matrix compatibility, and include: fibre volume fraction, fibre diameter, interfacial shear strength, residual stresses introduced during fabrication, and matrix yield strength. Each of these will affect or be affected by the mechanical properties of the composite. For example, the difference in the coefficient of thermal expansion of the two phases will determine the residual stresses introduced during fabrication. Mechanical properties such as Young's modulus, yield strength, work hardening rate, creep resistance, toughness and UTS will be affected by the fibre volume fraction, fibre diameter, interfacial shear strength and matrix yield strength.

3.2.2. Fabrication of Ti/SiC composites

A variety of processing routes have been developed for the manufacture of Ti MMC specimens and components using continuous monofilaments. It is important to note that making the right choice of fabrication procedure is very important in terms of the microstructure and performance of a component.

3.2.2.1. Diffusion bonding of fibre/foils

This technique involves the placement of arrays of fibres between thin metallic foils, often by means of a filament winding operation, followed by a hot pressing operation. This fibre/foil method is the most developed approach and has been used to manufacture a range of component forms. The procedure is attractive for Ti MMCs because: routes involving liquid Ti suffer from rapid interfacial chemical reactions (Wheatley and Wawner, 1985); and Ti is well suited to diffusion bonding operations because it dissolves its own oxide at temperatures above 700°C (Kasakov, 1985). Suitable conditions for composite production have been established and typically involve a few hours at around 900°C (Partridge and Ward-Close, 1989). Additions of Al and V, in Ti-6Al-4V for example, slow the kinetics of interfacial reaction (Smith and Froes, 1984). There can be difficulties in obtaining very high fibre volume fractions and homogeneous fibre distributions. Furthermore, a significant interfacial reaction layer (~1 μm) usually forms during the heat treatment necessary for consolidation. A microstructure is shown in Figure 3-5(a) (Partridge and Ward-Close, 1989). The relative inflexibility of the foil limits the complexity of the shapes that can be considered, which largely restricts its use to 'open-ended' type structures or thin rings.

3.2.2.2. Physical vapour deposition of metal matrix coatings

There is considerable interest in fibre coatings designed to reduce the problems of interfacial attack. With the metal matrix coated fibre technique, which has been developed independently by 3M in the US and DERA in the UK, the metal coating is applied directly to the SiC fibre using an electron beam physical vapour deposition (EBPVD) process. The fibre is passed continuously through a vapour cloud, having a high partial vapour pressure, above a molten pool of Ti alloy. The vapour condenses onto the moving fibre to form a continuous, relatively thick and uniform matrix coating, as shown in Figure 3-5(b) (Ward-Close and Partridge, 1990). Typical deposition rates are ~5-10 μm min^{-1}. Composite fabrication is usually completed by assembling the coated fibres into a bundle and consolidating this in a hot pressing or HIPing operation. Although a slight variation in

coating thickness is sometimes observed, it is evident that the consolidated composite cannot contain touching fibres and has a near perfect fibre distribution, as shown in Figure 3-5(c) (Hooker and Doorbar, 2000). The fibre volume fraction can be accurately controlled via the thickness of the deposited coatings. This technique is particularly suitable for critical rotating components such as compressor blings.

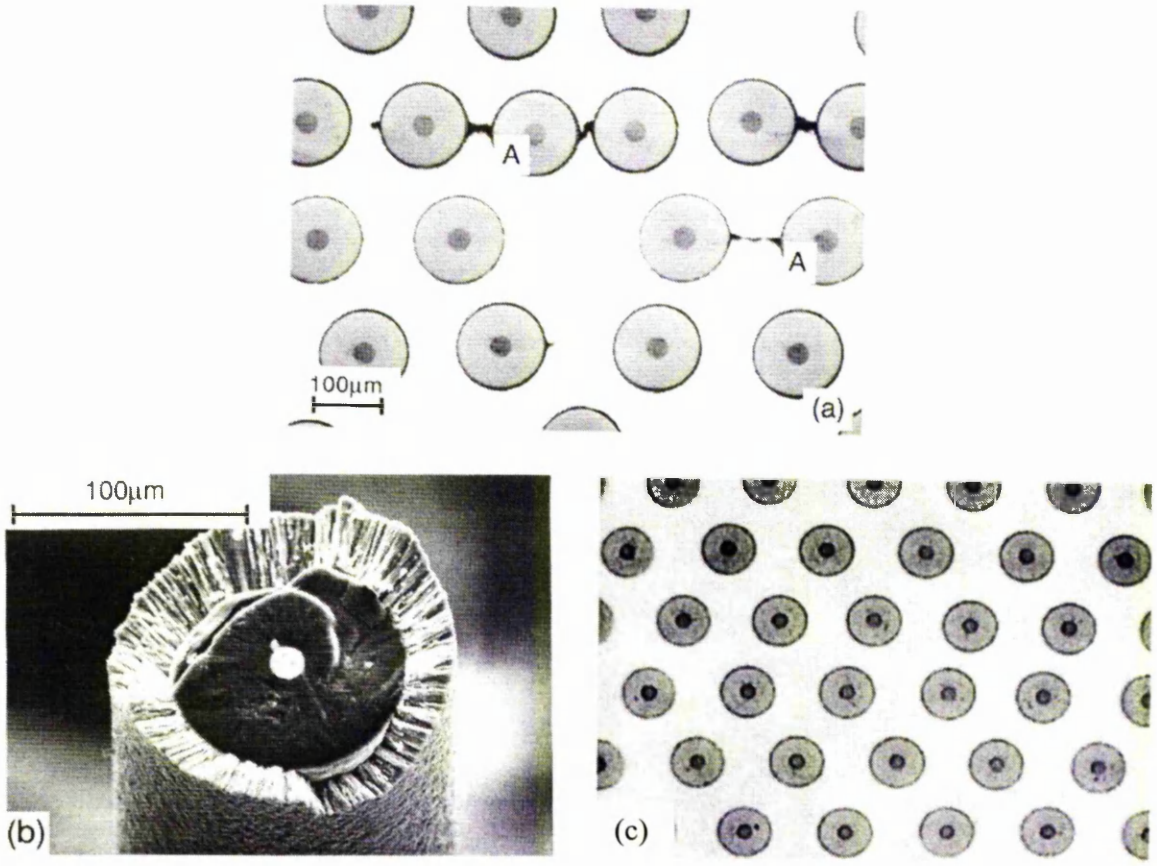

Figure 3-5. (a) Diffusion bonded Ti-6Al-4V with SiC monofilaments, showing residual porosity at points marked 'A' (triple points where two foils meet a fibre). (Partridge and Ward-Close, 1989). (b) A SiC monofilament coated with a 35 μm vapour-deposited layer of Ti-6Al-4V. (Clyne and Withers, 1993). (c) A Ti-6Al-4V/35 vol% SiC composite revealing the distribution of fibres of diameter 140 μm. (Hooker and Doorbar, 2000).

A third fabrication process, the plasma spray process, is capable of producing large sheets of single layer prepreg. A vacuum plasma or induction plasma spray system is used to deposit Ti alloy powder directly onto a drum of wrapped fibre. The resulting sheets are stacked and then consolidated in a similar manner to the fibre/foil process. Impact damage

to the fibre and its coating during spraying has proven to be a problem with this technique and the limited flexibility of the prepreg sheets restricts the type of component that can be manufactured.

3.2.3. Thermal residual stresses in Ti/SiC composites

During cooling to room temperature from the strain free high temperature consolidation process during composite fabrication, which can exceed temperatures of 1000°C, appreciable thermal stresses are induced into the fibres and the matrix (Cox *et al*, 1990; Pickard *et al*, 1995; Withers and Clarke, 1998). This is due to a thermal expansion coefficient mismatch between the two constituents, as revealed in Table 3-1 of the Introduction to Chapter 3, leaving the fibres in axial and radial residual compression and the matrix in residual tension (Covey *et al*, 1995; Materials Properties Handbook, 1994). Quoting characteristic values for SiC fibres, axial and transverse thermal residual stresses of -700 MPa and -300 MPa respectively, have been measured (Withers and Clarke, 1998). Also, an effective stress-free temperature drop of ~600°C has been measured (Withers and Clarke, 1998). These residual stresses can be both detrimental and beneficial. Detrimental aspects include a variety of damage types introduced into the matrix, such as the observation of matrix plasticity below 500°C in Ti-24Al-11Nb/SCS-6 composites where residual stresses have been measured to exceed the matrix yield stress (Ghonem *et al*, 1994). Radial cracks at the fibre matrix interface have been observed in Ti-15V-3Cr/SCS-6 composites, and crack-like consolidation defects at the interface of the fibre and the fibre matrix coating in Ti-6Al-4V/SCS-6, which are thought to reduce the level of fibre clamping caused by the residual hoop matrix stresses (Preuss *et al*, 2002). A beneficial aspect is that compressive radial residual stresses around the fibre play a significant role in fibre/matrix stress transfer, particularly in composites with relatively weak interfacial bonding such as Ti-15V-3Cr/SCS-6. Axial residual stresses can also influence debonding and fibre bridging. For a bonded interface, the applied axial stress on the fibre which is required to debond the interface is modified by the presence of the axial residual stresses. When the interfacial shear stresses induced by both the applied stress and the axial residual stresses are in the same direction, the existence of these axial residual stresses facilitates debonding. When they are in opposite directions, debonding is inhibited by the axial residual stresses. For a partially-bonded interface, axial residual stresses modify the stress distribution in the debonded region and can influence the opening of a matrix fatigue crack, which in turn increase or decrease the bridging traction in the fibres. As a result,

axial residual stresses can affect the damage mode in Ti MMCs. In Ti-β-21S/SCS-6 composites, the level of axial thermal residual stresses is lower than the yield stress of the matrix (Ghonem *et al*, 1994). Thus, when a fatigue crack grows through the matrix it can cause sliding between the fibres and the matrix, and the axial residual stresses may be relieved and allow the fibre to elongate and the matrix to contract.

3.3. Load Transfer between Fibre and Matrix

3.3.1. Interactions between constituents

One of the main objectives for MMCs is to combine the excellent ductility and formability of the matrix (prior to fabrication) with the stiffness and load-bearing capacity of the reinforcement. Composite materials are inherently inhomogeneous, in terms of both elastic and inelastic properties. A consequence of this is that, on applying a load, a non-uniform distribution of stress is set up within the composite. This distribution determines how the material will behave and can be used to explain the superior properties of composites over conventional materials. Central to an understanding of the mechanical behaviour of a composite is the concept of load sharing between the matrix and the reinforcing phase. The stress can vary sharply from point to point, but the proportion of the external load borne by each of the individual constituents can be gauged by volume-averaging the load within them. At equilibrium, the external load must equal the sum of the volume-averaged loads borne by the constituents, e.g. the matrix and the reinforcement. This gives rise to the condition (Clyne and Withers, 1993):

$$(1 - V_f)\,\sigma_M + V_f\,\sigma_F = \sigma^{\Lambda} \qquad (3\text{-}1)$$

which governs the volume-averaged matrix and fibre stresses (σ_M and σ_F respectively) in a composite under an externally applied stress, σ^{Λ}, containing a volume fraction, V_f, of the reinforcement or fibres. For a simple two-constituent MMC under a given applied load, a certain proportion of that load will be carried by the reinforcement and the remainder by the matrix. Provided the response of the composite remains elastic, this proportion will be independent of the applied load and it represents an important characteristic of the material. It depends on the volume fraction, shape and orientation of the reinforcement and on the elastic properties of both constituents (Clyne and Withers, 1993). The reinforcement may be regarded as acting efficiently if it carries a relatively high proportion of the externally applied load. This can result in higher strength, as well as greater stiffness, because the reinforcement is usually stronger, as well as stiffer, than the matrix.

Similarly, the '*Rule of Mixtures*' describes the composite axial stiffness, E_{3C}, as a weighted mean between the moduli of the fibres (E_F) and matrix (E_M), depending on the volume fraction of reinforcement (Clyne and Withers, 1993):

$$E_{3C} = (1 - V_f) E_M + V_f E_F \quad (3\text{-}2)$$

It is derived from the fact that the two constituents must have the same strain in the direction parallel to the fibre axis. This equation is expected to be valid to a high degree of precision, provided the fibres are long enough for the equal strain assumption to apply. Very minor deviations are expected as a result of stresses which arise when the Poisson's ratios of the two constituents are not equal. Prediction of the transverse stiffness, E_{2C}, of a composite from the elastic properties of the constituents is more difficult because, in a real composite, the phases are neither equally stressed nor equally strained. An equal stress assumption gives only a crude approximation (Clyne and Withers, 1993):

$$E_{2C} = \left[\frac{V_f}{E_F} + \frac{(1 - V_f)}{E_M} \right]^{-1} \quad (3\text{-}3)$$

3.3.2. Pure elastic shear stress transfer and the shear lag model

The most widely used model describing the effect of loading a continuous, aligned short-fibre composite is the shear lag model, originally proposed by Cox (Cox, 1952). It centres on the transfer of tensile stress from matrix to fibre by means of interfacial shear stresses. Elastic and debonding theories based on the shear lag model have since been proposed by Piggott (Piggott, 1980) and subsequently modified to apply to a partially debonded system (Bannister *et al*, 1995; Lacroix *et al*, 1992) (see Section 3.3.3). The original shear lag model assumes that both fibres and matrix behave elastically, and that the interface transfers stress from fibres to matrix without yielding or slip. Figure 3-6(a) illustrates a short length of fibre and the surrounding matrix, with the external load applied parallel to the fibre axis. Each fibre is surrounded by other fibres which are packed in an orderly fashion, for example, hexagonally, as shown in Figure 3-6(b). The basis of the model calculations is shown schematically in Figure 3-7, and considers the radial variation of shear stress in the matrix and at the interface (Clyne and Withers, 1993).

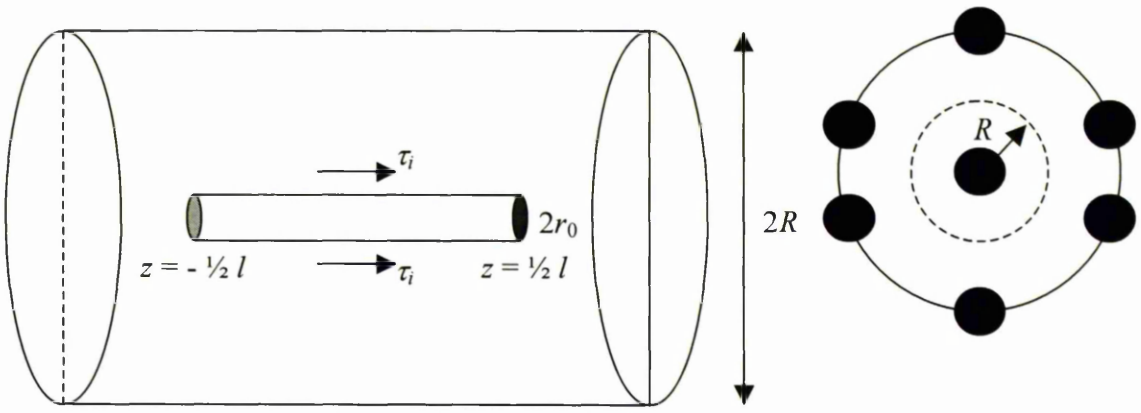

Figure 3-6. (a) Short length of fibre of length l and radius r_0, and the surrounding matrix. (b) Fibre with nearest neighbours, hexagonally packed. R represents the characteristic radius of the influential matrix cylinder around the fibre.

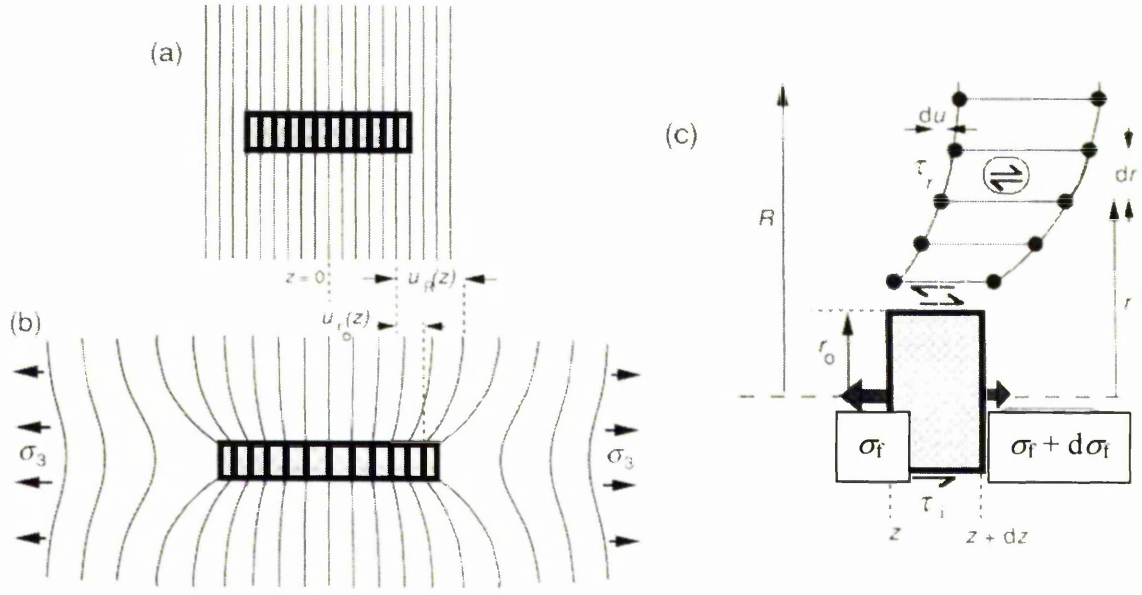

Figure 3-7. Schematic illustration of the basis of the shear lag model, showing (a) the unstressed system, (b) the axial displacements, u, introduced on applying a tensile load parallel to the fibre and (c) the variation with radial location of the shear stress and strain in the matrix. (Clyne and Withers, 1993).

The radial variation of the matrix shear stress, $\tau(r,z)$, at a given axial distance, z, from the fibre mid-point can be calculated by equating the shear forces on neighbouring

annuli (rings, with inner and outer radii r_1 and r_2) of length dz (Figure 3-7(c)) (Clyne and Withers, 1993):

$$2\,\pi\, r_1\ \tau(r_1,z)\,\mathrm{d}z\ =\ 2\,\pi\, r_2\ \tau(r_2,z)\,\mathrm{d}z$$

$$\frac{\tau(r_1,z)}{\tau(r_2,z)}=\frac{r_2}{r_1} \tag{3-4}$$

(Note: Alternatively, shear forces at a distance $r = r_1$ can be equated with those at the fibre surface, $r = r_0$). The shear stress, $\tau(r,z)$, at any radius r, written as τ_r, can be related to that at the interface, radius r_0, written as τ_i, by:

$$\tau_r=\tau_i\left(\frac{r_0}{r}\right) \tag{3-5}$$

The change in the matrix displacement, du, in the z direction, relative to the position with no applied stress, on moving out from the fibre axis by dr, is determined by the shear strain, γ, and the shear modulus, G_m (Clyne and Withers, 1993):

$$\frac{du(r,z)}{dr}=\gamma=\frac{\tau(r,z)}{G_m}=\tau(r_o,z)\frac{r_o}{G_m r} \tag{3-6}$$

Integration of this for a given value of z gives the difference between the displacement of the matrix at a radius R and that of the interface at r_0:

$$u(R,z)-u(r_o,z)=\frac{\tau(r_o,z)r_o}{G_m}\ln(\frac{R}{r_o}) \tag{3-7}$$

The assumption is made that the matrix strain is uniform remote from the immediate vicinity of the fibre. The radius R represents some far field distance where this condition becomes operative, the value of (R/r_0) being related to the proximity of neighbouring fibres and hence to the fibre arrangement and volume fraction, V_f. A hexagonal array leads to (Clyne and Withers, 1993):

$$\left(\frac{R}{r_0}\right)^2=\frac{\pi}{(2V_f\sqrt{3})}\approx\frac{1}{V_f} \tag{3-8}$$

The build-up of tensile stress in the fibre is governed by the distribution of interfacial shear stress, τ_i, parallel to the fibre surface near the ends. Referring to Figure 3-7(c), the fibre stress will change from σ_f to $\sigma_f + \mathrm{d}\sigma_f$ along an element of length dz. For the surface shear forces to be in equilibrium with the tensile forces in the fibre, force balance requires:

$$2\,\pi\, r_0\ \tau_i\,\mathrm{d}z\ =\ -\,\pi\, r_0^{\,2}\,\mathrm{d}\sigma_f \tag{3-9}$$

Rearranging and simplifying:

$$\frac{d\sigma_f}{dz} = -\frac{2\tau_i}{r_0} \tag{3-10}$$

Substituting for the rate of change of fibre stress with the rate of change of fibre strain, the interfacial shear stress can be deduced from:

$$\tau_i = \frac{E_f r_0}{2}\frac{d\varepsilon_f}{dz} \tag{3-11}$$

where E_f is the Young's modulus of the fibre.

Equation (3-7) can be used to relate the variation of τ_i with z to displacements and hence to axial strains (Clyne and Withers, 1993). Assuming perfect interfacial bonding and no variation with radius of the fibre strain (so that within the fibre $u(r,z) = u(r_0,z)$, the displacement of the fibre surface), and substituting for the shear modulus in terms of the Young's modulus and Poisson's ratio, leads to the result:

$$\frac{d\sigma_f}{dz} = \frac{E_m(u(R,z) - u(r_0,z))}{(1+\nu_m)r_0^2 \ln(R/r_0)} \tag{3-12}$$

where E_m and ν_m are the Young's modulus and Poisson's ratio of the matrix. The fibre displacement can be calculated from the fibre stress, since the fibre strain is $\varepsilon_f = du(r_0,z)/dz = \sigma_f/E_f$. That of the matrix at $r = R$ is $du(R,z)/dz = \varepsilon_m = \varepsilon_c$, the overall composite strain. Differentiation of Equation (3-12) and substitution leads to:

$$\frac{d^2\sigma_f}{dz^2} = -\frac{n^2}{r_o^2}(\sigma_f - E_f\varepsilon_c) \tag{3-13}$$

where n is a dimensionless constant given by:

$$n^2 = \frac{E_m}{E_f(1+\nu_m)\ln(R/r_0)} \tag{3-14}$$

The standard solution to this 2nd order linear differential equation (3-13), on applying the boundary conditions $\sigma_f = 0$ at $z = \pm \frac{1}{2}l$, where l is the fibre length, gives:

$$\sigma_f = E_f\varepsilon_c\left[1 - \frac{\cosh(nz/r_o)}{\cosh(nl/2r_o)}\right] \tag{3-15}$$

From this, the variation of interfacial shear stress along the fibre length can be derived using Equation (3-10), to give:

$$\tau_i = \frac{nE_f\varepsilon_c}{2}\frac{\sinh(nz/r_o)}{\cosh(nl/2r_o)} \tag{3-16}$$

The approach used in this basic model does not take account of stress transfer across the fibre ends or the stress concentration at the fibre ends.

Figure 3-8 shows distributions of the internal stress in the fibre (Equation 3-15) and the fibre-matrix interface stress (Equation 3-16) respectively, both as a function of position along a fibre such as that shown in Figure 3-6(a).

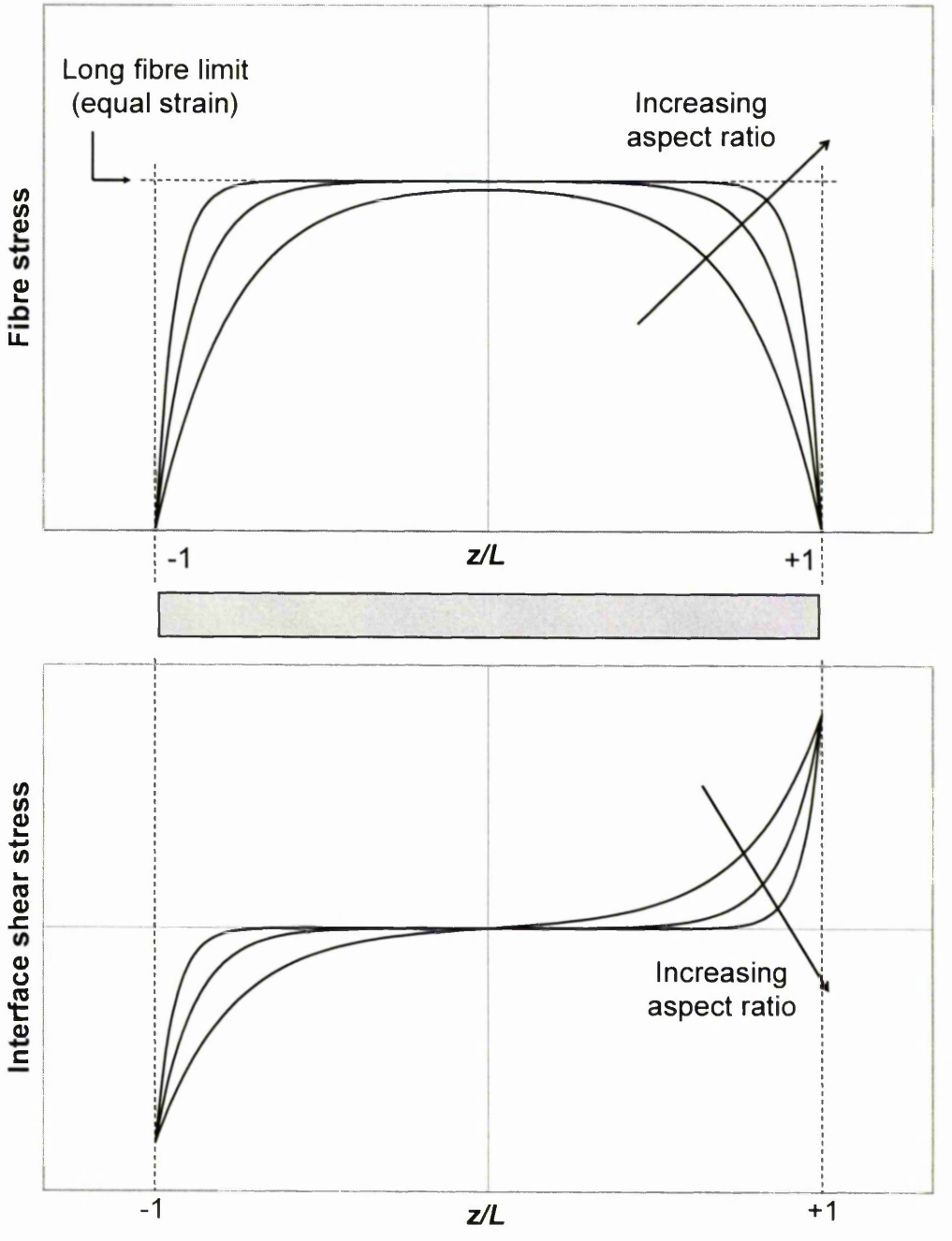

Figure 3-8. The fibre internal stress and the fibre-matrix interfacial shear stress as a function of position along the fibre, normalised by the fibre length, and the fibre aspect ratio, based on Equations (3-15) and (3-16) respectively, for elastic stress transfer.

3.3.3. Frictional shear stress transfer and the partial debonding model

Classical shear stress transfer theory indicates that the interfacial shear stress varies along the fibre length when a load is applied to a composite, as shown in Figure 3-8(b). However, stress transfer between fibre and matrix in single-fibre model composites actually takes place by a combination of frictional shear stress transfer in debonded regions and elastic shear stress transfer in bonded regions, as shown in Figure 3-9. The fibre strain and interfacial shear stress distributions in both regions are described by the partial debonding model (Bannister *et al*, 1995; Lacroix *et al*, 1992). In the case of metal matrices, if work hardening is neglected, and if the fibre-matrix adhesion is perfect, the shear stress will be constant in the sliding regions, as shown in Figure 3-9(c), and equal to the shear yield stress of the metal, τ_{my} (Piggott, 1980). Sliding occurs over a length ml at both ends of the fibre, where m is a dimensionless parameter representing the fraction of the fibre length, l, that is debonded or sliding, and depends on the applied stress. In the case of frictional sliding with a constant frictional shear stress, the fibre strain distribution, $\varepsilon_f(z)$, in the sliding or debonded region is described by (Lacroix *et al*, 1992):

$$\varepsilon_f(z) = \frac{2\tau_f}{E_f r_f}\left(\frac{l}{2} - z\right) \tag{3-17}$$

where τ_f is the interfacial frictional shear strength. Near the fibre mid-section, at ~ $z = 0$, the interfacial shears are generated by elastic interactions. For this bonded region, the fibre strain distribution is (Lacroix *et al*, 1992):

$$\varepsilon_f(z) = \varepsilon_m - \left(\varepsilon_m - \frac{2\tau_f sm}{E_f}\right)\frac{\cosh(nz/r_f)}{\cosh[ns(1-m)]} \tag{3-18}$$

where n is defined by Equation (3-14), ε_m is the applied matrix strain, s is the fibre aspect ratio (= $l/2r_f$), and m is the relative sliding length (= $l_d/2l$, with l_d being the sliding length).

The fibre strain in the sliding region, Equation (3-17), assumes a constant interfacial frictional shear stress. Substituting for ε_f in Equation (3-11) with Equation (3-18) gives the interfacial shear stress variation in the bonded region:

$$\tau_i(z) = n\left(\frac{\varepsilon_m E_f}{2} - \tau_f sm\right)\frac{\sinh(nz/r_f)}{\cosh[ns(1-m)]} \tag{3-19}$$

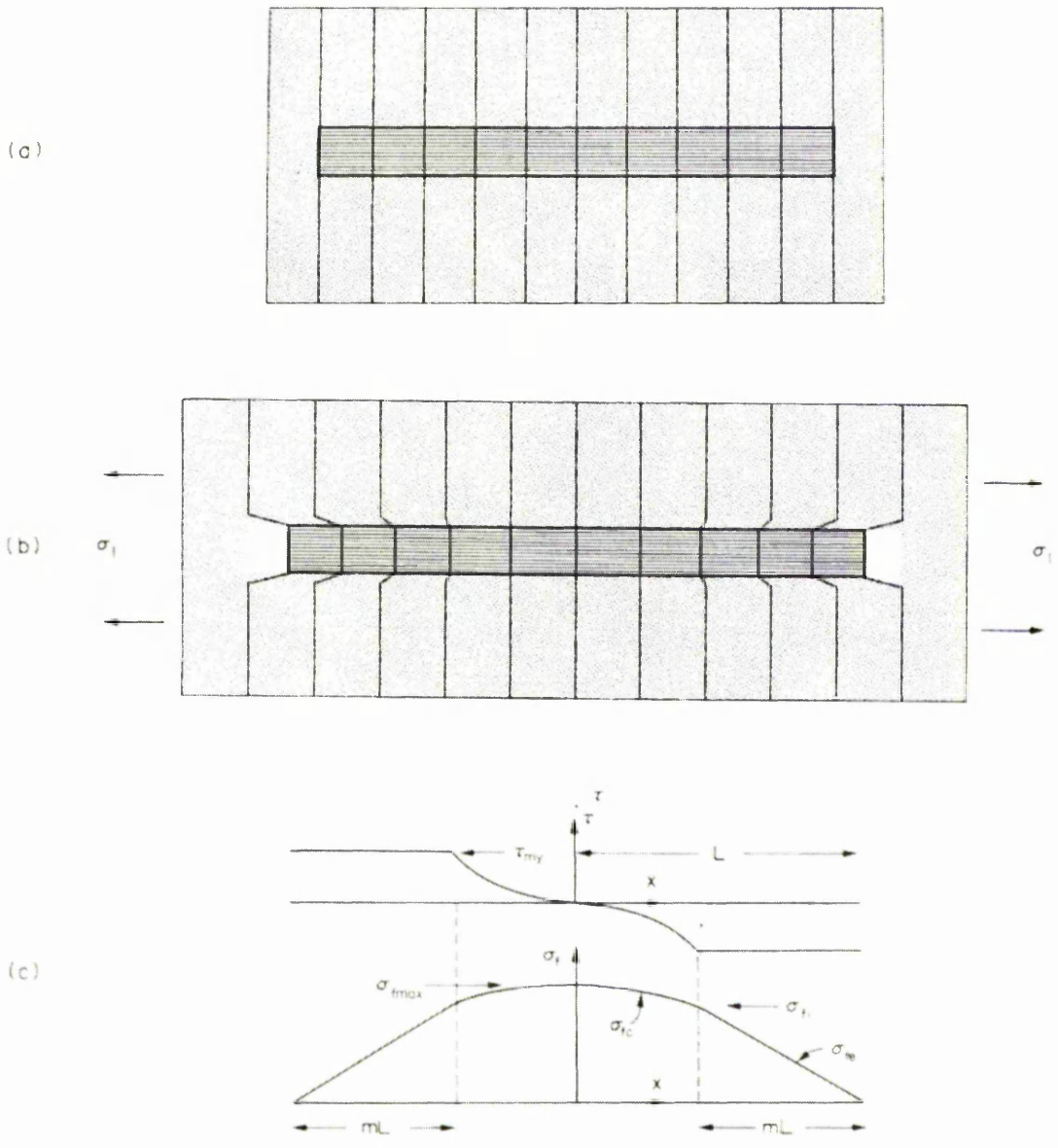

Figure 3-9. Single fibre composite element: (a) unstressed and (b) stressed. (c) shows the fibre-matrix interfacial shear stress and the fibre internal stress for a well-bonded reinforced metal. (Piggott, 1980).

3.4. Single Fibre Fragmentation

3.4.1. Full-fragmentation theory

Crucial aspects of the mechanical behaviour of fibre-reinforced metal matrix composites are dependent on the properties of the fibre-matrix interface and the efficiency of stress transfer from matrix to fibres. For example, the state of the interface determines composite transverse strength through lateral load transfer to neighbouring fibres, and the

extent of crack bridging during fatigue crack growth. In terms of composite strength and creep resistance to loads in the transverse direction a strong interface is desired, while a weak interface encourages fibre pull-out and crack bridging when the material is fatigued under longitudinal loading (Majumdar, 1997; Rauchs *et al*, 2002). Single fibre full-fragmentation tests allow the interfacial shear strength, a key parameter for these materials, to be measured and stress transfer to be studied while the composite material is under tensile load. A characteristic of such tests is that the fibres break *in-situ* while the whole composite is strained moderately. This is not achieved in alternative techniques for interfacial shear strength characterisation, such as the push-out (Yang *et al*, 1990) and pull-out (Kieschke and Clyne, 1990) tests, as they often involve unrepresentative sample/loading geometries, e.g. a compressive load is applied in the push-out test to the free surface of a fibre in a thin composite slice. These stress fields can be quite different from those that would be expected in a service application such as an aeroengine, e.g. in the push-out test a large compressive radial stress is generated at the fibre/matrix interface at the initial point of fibre slippage.

In conventional fragmentation tests (Huang and Young, 1994; Le Petitcorps, 1989; Majumdar *et al*, 1998; Preuss *et al*, 2002) single fibre model composites are subjected to an increasing tensile strain in the direction of the fibre axis. Lateral load transfer from the matrix to the fibre occurs through shear stresses at the fibre/matrix interface such that the fibre fractures into many small fragments, since the fibre failure strain is much lower than that of the matrix. As higher tensile strains are applied the fragmentation process continues until, at a certain level of strain, interfacial stresses are no longer capable of inducing further fracture of the fibre segments. The fragments become too short to allow sufficient tensile stress to build up in any of the remaining fragments to such an extent as to cause further fibre breakage. This allows the critical fibre length to be defined as the length of the smallest fibre segment which can still be broken during the fragmentation test, at a given value of the strain imposed on the specimen. Figure 3-10 shows a schematic of the envisaged fibre strain distribution during and after a fragmentation test.

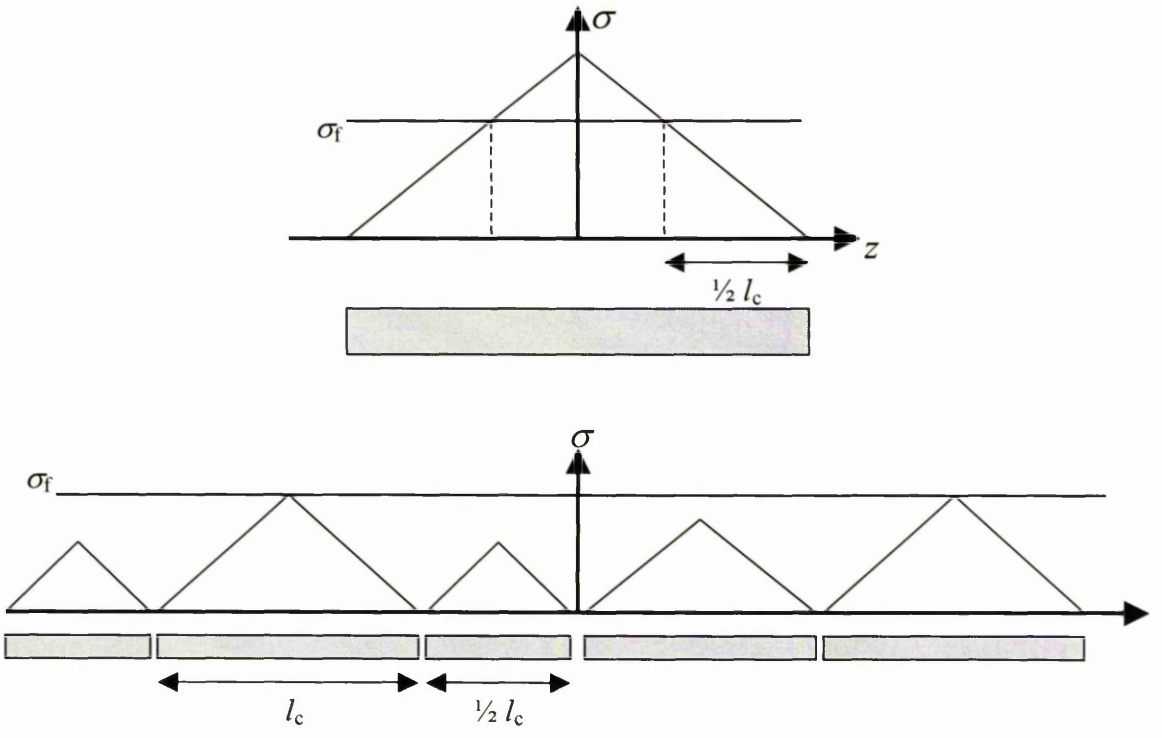

Figure 3-10. Schematic representation of the fibre strain distribution during (top, for a single fragment) and after (bottom, fragmentation complete) a fragmentation test.

The relationship between interfacial shear strength, τ_i, and the critical length, l_c, was first given by Kelly and Tyson for a metal matrix composite with an ideal plastic matrix (Kelly and Tyson, 1965). This relationship was defined through a force balance approach for the build-up of fibre stress from the fibre end (Equation 3-9). The strain in the fibre cannot exceed the strain of the composite, ε_c, so that the fibre stress, σ_f, at a distance z from the end will build up to the value $\varepsilon_c E_f$ provided the fibre is sufficiently long. Since the fibre is loaded up from both ends, a fibre of length l will be long enough to be strained to the strain of the composite, provided that (Kelly and Tyson, 1965):

$$l \geq \frac{r_0 E_f \varepsilon_c}{\tau_i} \tag{3-20}$$

The tensile strain in the matrix occurs due to plastic flow. It will be possible to break a fibre by plastic flow of the matrix provided that the stress in it builds up to the tensile strength of the fibre. If l_c is the critical fibre length for this to occur:

$$l_c = \frac{\sigma_f r_0}{\tau_i} \tag{3-21}$$

where σ_f is the tensile strength of the fibre at the critical length. This equation is based on the assumption that the interfacial shear strength is constant along the fibre fragment and is the same for each fragment. A fragment of length greater than the critical length can break into two fragments with lengths less than l_c. Therefore, the arithmetic mean fragment length, l_f, determined when the fibre is fully fragmented (saturated state), is the median value between $l_c/2$ and l_c, assuming a uniform fragment length distribution (Oshawa *et al*, 1978). The critical fragment length can be expressed as:

$$l_c = \frac{4}{3} l_f \tag{3-22}$$

Substituting for l_c in Equation (3-21) and rearranging for τ_i, gives:

$$\tau_i = \frac{3\sigma_f r}{4l_f} \tag{3-23}$$

3.4.2. Fragmentation analysis of polymer matrix composites

Single fibre fragmentation analysis has been carried out on carbon-fibre/epoxy model composites by means of Raman spectroscopy (Huang and Young, 1994). The interfaces of two carbon fibres in an epoxy matrix were examined to determine the point-to-point variation of fibre strain in the resin. An important breakthrough was obtained by the realisation that Raman spectroscopy, a unique way to determine material properties, could be used to quantify the state of stress and strain in the fibre fragments during a fragmentation test (Di Landro and Pegoraro, 1987). The Raman spectrum is obtained by excitation using a monochromatic light source such as a laser beam and recording the intensity of the inelastic (Raman) parts of the scattered light on a CCD detector. The spectrum is made up of a number of bands of different intensity and position (the Raman shift, $\Delta\nu$ (cm^{-1})), and the application of tensile stress or strain causes a shift in the band position. Monitoring of a particular band and its strain-induced band shift enables the determination of the point-to-point variation of strain under any state of stress or strain, noting that the Raman shift is sensitive to elastic strain. Depth probing, such as the collection of a signal from a fibre embedded within a matrix, is made possible due to the highly monochromatic laser light source which is polarised and focused on the fibre. For the case of the polymer matrix composites used in the following study (Huang and Young, 1994), Raman scattering for the fibre was very strong but very weak for the resin matrix, enabling easy collection of the signal from the fibre without interference from the matrix.

Figure 3-11 shows an example of the elastic fibre strain distributions measured during the fragmentation of a PAN-based carbon fibre embedded in an epoxy resin matrix (Huang and Young, 1994). The fibre diameter is 7.7 μm. Up to about 0.6% strain, the fibre strain distribution follows a Cox-type shear lag distribution, as illustrated in Figure 3-8(a), which predicts that the fibre strain should plateau along the centre of the fibre (Cox, 1952). By 0.8% strain fibre fracture starts to occur, and by 1.0% strain fragmentation saturates, with the strain distribution in the fragments similar to that shown in Figure 3-10. The fragmentation behaviour is observed to be very similar to that envisaged theoretically (Kelly and Tyson, 1965). The fibre is initially continuous and deforms elastically, and it records the same change in strain as would be recorded by an external strain gauge. Therefore, the applied strain of the composite is equal to the maximum strain in the fibre, $\varepsilon_c = \varepsilon_f$, as indicated by the dashed lines marking the composite strain in Figure 3-11. Thus, the composite is observed to obey the equal strain criterion throughout fragmentation.

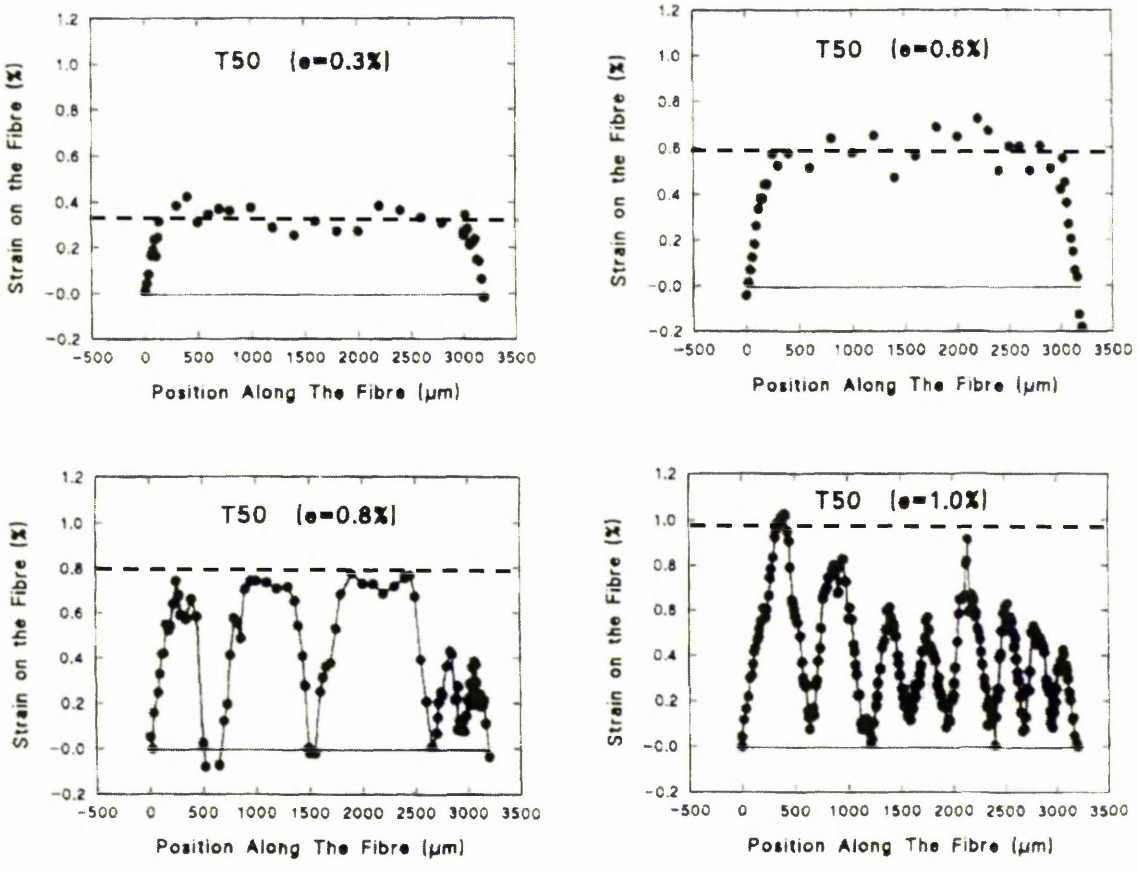

Figure 3-11. Fibre strain distributions, measured under load, determined from stress-induced Raman bandshifts for a PAN-based fibre in an epoxy resin, at different levels of indicated matrix strain. (Huang and Young, 1994).

The interfacial shear stress distribution along this fibre, calculated using the force balance argument culminating in Equation (3-11), is shown in Figure 3-12 (Huang and Young, 1994). The interfacial shear stress (ISS) along the fragments was determined using the rate of change of strain with position along the fibre, the measured data shown in Figure 3-11. Figure 3-12(a) shows that τ_i is a maximum at the ends of the fibres or fragments and falls to zero along the middle, as described by the shear lag approach and shown by Figure 3-8(b) (Cox, 1952). The maximum ISS in the fragments is shown against matrix strain in Figure 3-12(b), the maximum value reaching 40-45 MPa at about 1.4% strain. This behaviour is very similar to that observed for Kevlar fibres in the same resin (Andrews and Young, 1993), where it was shown there to be essentially good bonding between the fibres and the matrix, and the maximum ISS to be the shear yield stress of the matrix (about 43 MPa). This indicates that the strength of the interface is controlled by shear yielding of the matrix resin in the vicinity of the fibre/matrix interface. Similar analysis of a pitch-based fibre in the same epoxy resin matrix revealed the interface to fail through debonding rather than shear yielding (Huang and Young, 1994).

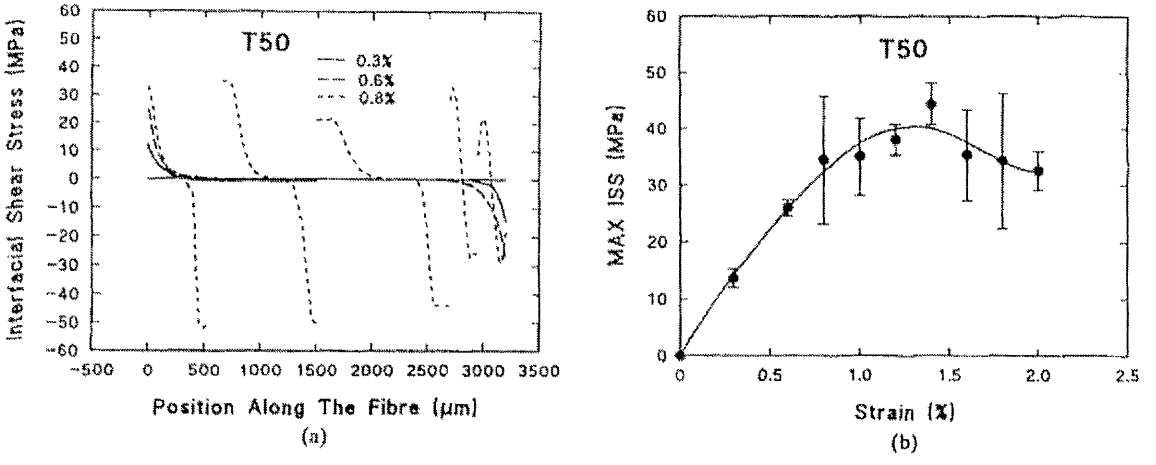

Figure 3-12. Derived interfacial shear stress for the PAN-based fibre fragmentation specimen: (a) variation of ISS with position along the fibre at different levels of indicated matrix strain; (b) maximum derived ISS values as a function of applied matrix strain. (Huang and Young, 1994).

The two micromechanical models that have been widely used to explain stress transfer from matrix to fibre in fibre-reinforced composites, reviewed in Sections 3.3.2 and 3.4.1, are the Kelly-Tyson model (Kelly and Tyson, 1965) and the shear lag approach by

Cox (Cox, 1952). In the Kelly-Tyson model elastic fibres are embedded in an ideally plastic matrix, while in the shear lag approach both fibre and matrix are fully elastic and a perfect bond exists between them. It is the shear lag approach that predicts the experimental data of these polymer matrix systems well. As the applied strain is increased, the interfacial shear stress on the fibre is so high that interfacial debonding, or matrix yielding, occurs when the maximum shear stress reaches the interfacial shear strength, or matrix yield stress, τ_{my} (Lacroix *et al*, 1992; Piggott, 1980). The formation and propagation of the debonding or plastic yielding region tend to relax the stress on the well-bonded region of the fragment. The well-bonded region then becomes too short for the stress to build up for further fragmentation.

3.4.3. Fragmentation analysis of metal matrix composites

Single fibre full-fragmentation analysis has been performed on a model composite of an SCS-6 SiC single fibre in a Ti-6Al-4V matrix, using synchrotron X-ray diffraction (Preuss *et al*, 2002). The composite was made via hot isostatic pressing of an SCS-6 matrix-coated fibre (140 μm diameter, 50 μm layer coating) between two Ti-6Al-4V sheets, consolidated at a vacuum level of 10^{-5} bar and 880°C/20 MPa for 30 minutes. The use of matrix-coated fibres, the coating being applied by physical vapour deposition, has the advantage that, through control of the coating thickness, the desired reinforcement fraction can be achieved. Composite fabrication is important from the point of view of the fibre-matrix interfacial shear strength. The use of matrix-coated fibres ensures a good bond between fibres and matrix, but complete consolidation of the coated fibres within the matrix is important so as cracks between the two are avoided. Diffraction is a well established tool for the evaluation of internal stresses during loading, and both X-ray (Hanan *et al*, 2003; Hanan *et al*, 2002; Lilholt, 1977; Maire *et al*, 2001; Preuss *et al*, 2003) and neutron diffraction (Withers and Clarke, 1998) have been used for the examination of metal matrix composites. The principle involves monitoring changes in the spacing between atomic lattice planes, d_{hkl}, which are deduced from shifts in the diffraction peak angles, θ, when an external load is applied. This enables the associated elastic strain changes of both phases to be resolved, relative to the 'stress-free' state. The 'stress-free' reference value for the lattice spacing was chosen to give zero strain at the fibre ends (or position of cracks, once fibre fracture had begun). The use of an area detector (Hanan *et al*, 2003) as opposed to a point detector (Hanan *et al*, 2002) enables entire characteristic Debye Scherrer diffraction rings (cones) to be collected, revealing substantially more

information about damage evolution in the same metal matrix composite. In the case of the fragmentation test of Preuss *et al*, diffraction profiles were collected with a sampling gauge of 50 μm in the longitudinal (fibre) direction and 150 μm in the direction transverse to the fibre axis, slightly larger than the diameter of the fibre. This enabled 100 diffraction profiles to be taken along the fibre with 50 μm between each measurement point.

Figure 3-13 shows the change in longitudinal strain recorded for the SiC fibre as a function of position and applied load (Preuss *et al*, 2002). Since a completely strain free lattice spacing reference value was not measured, the term 'relative strain' is used to qualify the measurements. The elastic strain experienced by the SiC fibre exceeded 1.5% prior to fracture. The fibre was found to be broken after load step 8, at positions of $z = 2.3$ and $z = 4.2$ mm, these locations corresponding to positions where the elastic strain (stress) was highest in the preceding load step (7). Further fragmentation of the fibre took place as the composite was further strained (shown by steps 9 and 13). By step 13, fragmentation was observed to be complete and a fairly regular distribution of cracks had occurred.

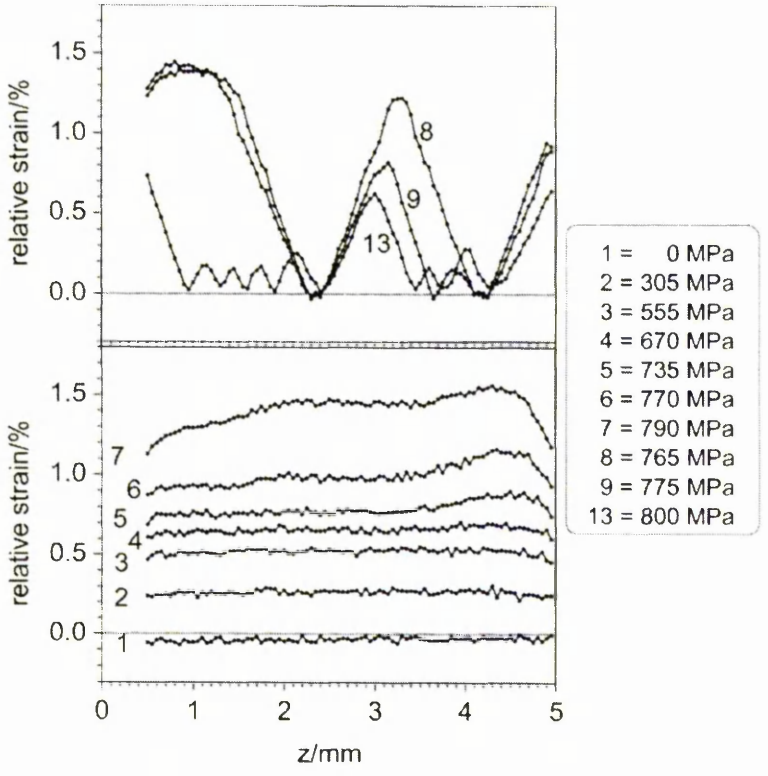

Figure 3-13. Variation in the longitudinal strains of the (110) SiC reflection measured, via diffraction, along the fibre length, under applied load, during a tensile fragmentation test. (Preuss *et al*, 2002).

For the final load step (13), the majority of the peak elastic strains, i.e. those reached between the smallest of the fibre fragments, are around 15% of that originally achieved. This is in contrast to full fragmentation theory, which predicts a range of fragment lengths and peak strains from slightly below the fracture strain (1.5%) to half that value (see Section 3.4.1). An explanation for this could be attributed to damage of the coating and the reaction zone after the initial fracture, as observed by Majumdar *et al* in the same composite system, resulting in lower measured strains in the fragments (Majumdar *et al*, 1998). They observed radial cracks to start at the reaction zone and propagate radially through the coating and end next to the SiC surface. Another possibility is that immediately after fracture the elastic strains are high and they decay to the measured levels within the times between composite straining increments needed for data acquisition. Similar multiple fracture events at fibre strains below the original fracture strain prior to failure have been reported elsewhere (Huang and Young, 1994; Majumdar *et al*, 1998).

Unloading steps were also measured during the fragmentation analysis, and showed some interesting characteristics. Figure 3-14 shows the residual axial fibre strain profile (labelled 10) measured after removal of the applied load after load step (9), and is compared to the initial state (step 1). The residual strain distribution differs significantly from the low level of thermally induced compression originally observed for step 1. The fibre strain shows a characteristic 'W' configuration across the larger of the two fragments, as shown in the highlighted section of the figure.

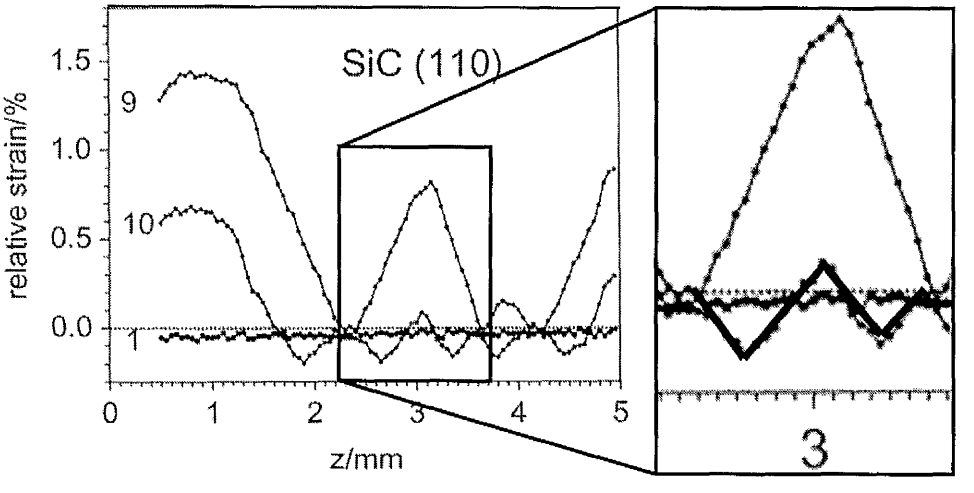

Figure 3-14. The variation in the longitudinal strain of the (110) SiC reflection for the unloaded stage (10), and a highlighted region showing the characteristic 'W' configuration of the strain distribution across a fibre fragment. (Preuss *et al*, 2002).

At the mid-length, where the fibre/matrix interface had remained bonded throughout, the fragment is in residual tension. This is because the neighbouring matrix had been plastically extended during loading, conferring a tensile stress to the fibre. In the vicinity of cracks, however, the relative strain in the fibre reverses into compression. Finite element analysis has indicated this characteristic to be associated with reverse sliding initiating from the fibre ends as the load is removed (Rauchs *et al*, 2002). In regions of unfragmented fibre that remain bonded during unloading, the tensile plastically strained matrix keeps the fibre in tension even though the applied stress is relieved. A study of crack-bridging aramid fibres in a brittle epoxy matrix has also observed compressive strains in the fibre after unloading (Bennett and Young, 1998), with closure of the matrix crack resulting in reverse sliding of the fibres in debonded regions. Figure 3-15 shows relative sliding distances for loaded (cracked) and unloaded states determined from finite element analysis (Rauchs *et al*, 2002). The plot shows the difference in the sliding distance between the loaded and the initial state and the difference between the unloaded and loaded state. A significant amount of interface sliding takes place during loading, whereas during unloading, reverse sliding occurs only in a small region close to the crack, with most of the previously sliding interface reverting to a 'sticking' state. This region is referred to as a slip/stick region, i.e. an interface that was previously sliding, but is now sticking. It can also be concluded from Figure 3-15 that interface reverse sliding starts at, and progresses away from, the fibre crack towards the middle of the fibre fragment.

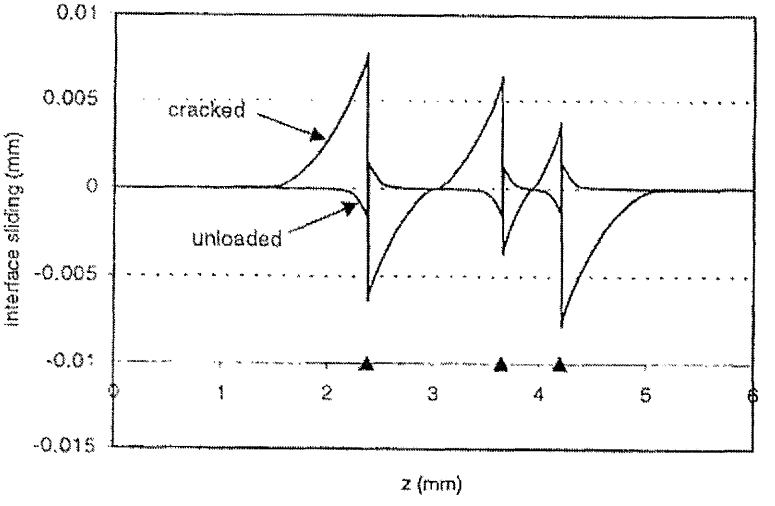

Figure 3-15. Showing the interface sliding distance in the vicinity of three cracks (positions in z along the fibre indicated by triangles), as determined using finite element analysis. Plots with applied load and the unloaded case are shown. (Rauchs *et al*, 2002).

The fibre/matrix interface strength was investigated from the fragmentation test of Preuss *et al.* Figure 3-16(a) shows the strain distribution in the fibre measured at load step 8 (765 MPa), after the first two cracks appeared (Preuss *et al*, 2002). The solid line represents the best fit for the partial debonding model, described by Equations 3-17 and 3-18, to the experimental data. The inferred shear stress distribution derived from the model fit is shown in Figure 3-16(b). The fitted partial debonding model gives an essentially constant interfacial frictional shear strength, τ_f, of about 200 MPa. This is higher than results reported from push-out tests for specimens of the same system made in the same way, where interfacial frictional shear strengths ranging from 90 MPa (Majumdar *et al*, 1998) to 140-160 MPa (Warrier and Majumdar, 1999) have been measured. According to the partial debonding model, a sharp maximum in the interfacial shear strength is inferred at the junction between the sliding and the still bonded regions, giving a maximum interfacial shear strength threshold for the onset of sliding of between 300 and 550 MPa. This is consistent with a value of ~390 MPa measured by Majumdar *et al.* under fragmentation conditions via a post mortem determination of the mean fragment length, as described below. Again, this is much higher than results reported for push-out tests of the same study, which reveal interfacial debonding shear strengths of 160-190 MPa (Majumdar *et al*, 1998; Warrier and Majumdar, 1999).

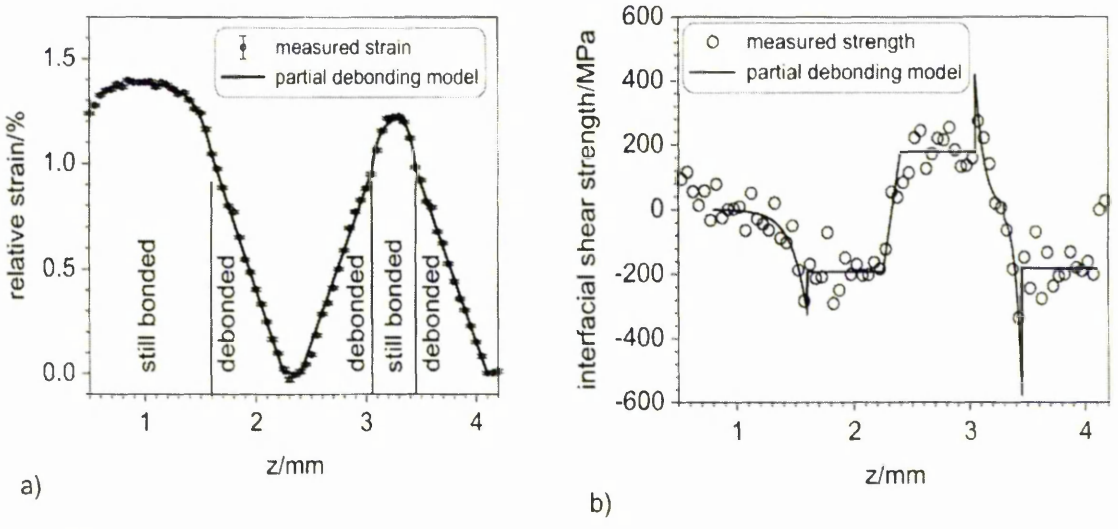

Figure 3-16. (a) Strain distribution of the (110) SiC reflection at an applied load of 765 MPa. The solid line shows the best-fit for the partial debonding model. (b) The derived interfacial shear strength distribution from the strain measurements and the model fit. (Preuss *et al*, 2002).

A likely reason for the higher interfacial shear strength values measured under fragmentation conditions, compared to values obtained by push-out tests, is the greater clamping of the fibre at the location of a break (Carara and McGarry, 1968; Majumdar *et al*, 1998; Nicholas and Ahmad, 1994). Carara and McGarry showed the radial stress to attenuate very rapidly along the length of a fibre from the point of a fibre break. Nicholas and Ahmad, through analysis of a discontinuous fibre, showed the compressive radial interface stress in the immediate vicinity of a break to be the order of the axial stress in the matrix, which is the flow stress in the single fibre fragmentation samples. Calculations of Majumdar *et al.* indicated that in the absence of a fibre break the clamping stress was not significantly different from the residually stressed state, suggesting that the clamping that occurs is very local in nature. Figure 3-17(a) displays a synchrotron X-ray radiography montage, comprising seven single X-ray radiographs, of the fully fragmented single fibre sample, after the fragmentation process had saturated (Preuss *et al*, 2002). This radiograph was used to make a post mortem measurement of the mean fragment length, enabling the interfacial shear strength to be inferred from Equation (3-23). The crack locations agree well with the locations inferred from the dips in the elastic fibre strains measured during the final load step, shown in Figure 3-17(b). The mean fragment length was measured to be 380 ± 60 μm and fragmentation was complete at an applied strain of approximately 7%. The inferred interfacial shear strength, with σ_f = 5100 MPa (Laffargue and Bowen, 2001), was approximately 700 ± 10 MPa, significantly larger than that determined via strain scanning (Figure 3-16(b)). An explanation for this is that the post mortem measurement method assumes that the fragments are formed when the maximum fibre stress is exceeded, whereas, in reality, after the initial fracture the fibre fragmented further at much lower stresses. The extent of the crack openings shown in Figure 3-17(a) reflect the subsequent matrix plastic strain that occurred after each crack so that the largest fissures correspond to the earliest cracks. The crack openings for the two cracks that were first to form, numbers 6 and 10/11, are 90 and 80 μm respectively. In terms of the observed crack morphologies, as illustrated in Figure 3-17(a) and confirmed by 3-D tomographic images, it was found that in some stages single cracks were introduced, whereas in others a number of closely spaced cracks occurred, similar to that observed by Majumdar *et al.* (Majumdar *et al*, 1998; see Section 3.5.2). Cracks showing a wedge morphology, i.e. two cracks connected at one surface of the fibre but radiating outwards as two single cracks, were also observed. Evidence suggested that the first fibre fracture to occur initiated at high stress in the core of

the fibre, giving a conventional mode I fracture morphology, while later cracks occurring at lower stresses were in the form of wedge cracks originated from the surface (Preuss *et al*, 2002). This is consistent with observations on single fibres (Laffargue and Bowen, 2001). This argument is consistent with the fact that crack 10 in Figure 3-17(a) is the initial high stress fracture event followed almost instantaneously by wedge crack 6.

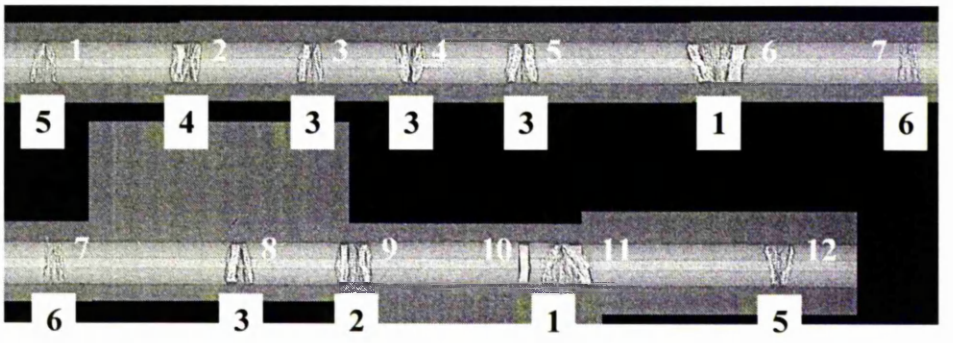

(a)

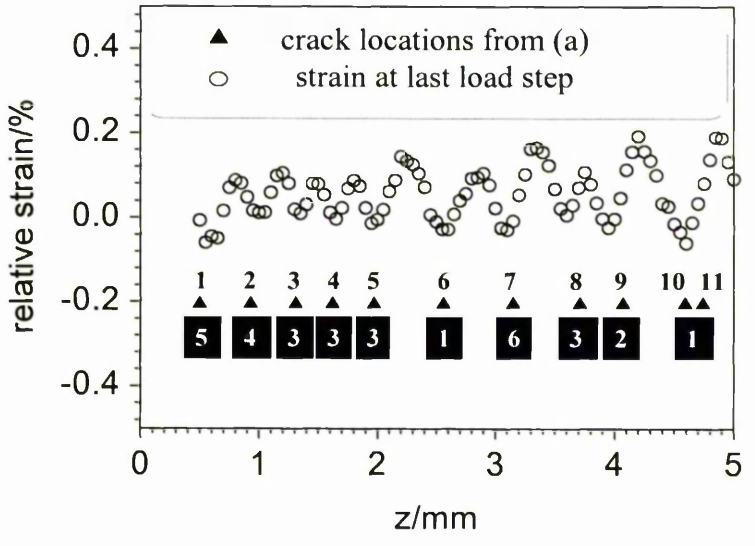

(b)

Figure 3-17. (a) A montage comprising seven single 6 μm resolution synchrotron X-ray radiographs from the single fibre full-fragmentation sample used for strain scanning, after the last load step at which point it fully fragmented (strain 7%, load 900 MPa). The crack morphologies are clearly observed, and the order in which the cracks occurred (lower numbers) is indicated. (b) The corresponding elastic strain profile measured for the last load step, with the crack locations identified from the radiograph marked with triangles. The lower numbers indicate the order in which the cracks occurred. (Preuss *et al*, 2002).

Both of these studies (Huang and Young, 1994; Preuss *et al*, 2002) show how full-fragmentation analysis can be used to provide useful information about interface strengths in two very different composite systems. By means of the measurement of the point-to-point variation in the internal fibre strain, the strength of the fibre-matrix interface can be inferred.

3.5. Fibre Strength and Stress Concentration Effects

3.5.1. Fibre strength – a statistical treatment

When considering the failure of a unidirectionally reinforced fibre composite specimen, where initially all the fibres are intact and able to carry load, as increasing load is applied the weakest fibre will eventually fail. Most reinforcing fibres, including SiC-SCS-6, are brittle and they sustain little or no plastic deformation or damage up to the point when they fail catastrophically. Such materials do not, in general, have a well-defined tensile strength. The stress at which they fail usually depends on the presence of flaws, which may occur randomly along the length of a fibre. The high strength of fibres, compared to the corresponding bulk matrix materials, is often attributable to the absence of large flaws. A population of flaws is nevertheless expected along the length of fibres, resulting in a variation of the strength between individual fibres.

The fibre strength can be treated on a statistical basis. The approach was pioneered by Weibull, and a Weibull distribution is used to describe fibre failure (Weibull, 1951). The approach involves conceptually dividing a length, L, of fibre into a number of incremental lengths, ΔL_1, ΔL_2, etc. When a stress, σ, is applied, the parameter n_σ defines the number of flaws per unit length sufficient to cause failure under this stress. The fibre fractures when it has at least one incremental element with such a flaw. The probability of any given element failing depends on n_σ and on the length of the element. For example, for the first element (Weibull, 1951):

$$P_{f1} = n_\sigma \Delta L_1 \tag{3-24}$$

The probability, P_s, of the entire fibre surviving under this stress is the product of the probabilities of survival of each of the N individual elements which make up the fibre:

$$P_s = (1 - P_{f1})(1 - P_{f2})\ldots(1 - P_{fN}) \tag{3-25}$$

Since the length of the elements can be taken as vanishingly small, the corresponding P_f values must be small. Using the approximation $(1 - x) \approx \exp(-x)$, applicable when $x << 1$, leads to:

$$P_s = \exp\left[-\left(P_{f1} + P_{f2} \ldots + P_{fN}\right)\right] \tag{3-26}$$

Substituting for P_{f1} with Equation (3-24), and the corresponding equations for the other elements, gives:

$$P_s = \exp\left[-L\, n_\sigma\right] \tag{3-27}$$

For an expression for n_σ, Weibull proposed that most experimental data for failure of brittle materials conforms to an equation of the form (Weibull, 1951):

$$n_\sigma L_0 = \left(\frac{\sigma}{\sigma_0}\right)^m \tag{3-28}$$

where m is the *Weibull modulus* and σ_0 is a normalising strength which can be taken as the most probable strength expected from a fibre of length L_0. Making this assumption, the probability of failure of a fibre of length L, for an applied stress σ, is:

$$P_f = 1 - \exp\left[-\left(\frac{L}{L_0}\right)\left(\frac{\sigma}{\sigma_0}\right)^m\right] \tag{3-29}$$

The Weibull modulus is an important parameter for characterising the strength distribution exhibited by a certain type of fibre. If the value of m is large, i.e. > 20, it follows from Equation (3-28) that stresses even slightly below the normalising value, σ_0, would lead to a low probability of failure, while if they were slightly above then a high probability would be predicted. Conversely, a low Weibull modulus, i.e. < 10, would introduce much more uncertainty about the strength of a fibre. Many ceramic materials exhibit a Weibull modulus in the range 2–15 (Hull and Clyne, 1996), representing considerable uncertainty about the stress level at which any given specimen is likely to fail.

Regarding studies of fibre strength, a comparison of the Weibull modulus and strength of SCS-6 fibres has been made between *in situ* single fibre fragmentation tests and fibres extracted from untested specimens (Majumdar *et al*, 1998). For the *in situ* tests of single fibres in a Ti-6Al-4V matrix, values of σ_0 = 3300 MPa and m = 5 were measured for 25.4 mm long fibres. Weibull parameters obtained for SCS-6 fibres that were extracted (by etching out) from the matrix of untested multiple fibre specimens were significantly higher at σ_0 = 4483 MPa and m = 13.6. For the measurements obtained from extracted fibres, the three lowest strengths in the population were eliminated leading to a higher average value of σ_0. This was because previous studies with SCS-6 fibres have shown that the low-strength fibres, which exhibit considerable departure from the average, belong to a separate fibre population (Gambone, 1996; Gambone and Wawner; 1997). Such a

population was found to consist of surface initiated failures (damage related), compared with internally initiated failures in the bulk of the fibres. These studies suggested that if only the data from fibres with surface initiated failures were considered, then the Weibull parameters are in the range σ_0 = 2100–2800 MPa and m = 4–6. Although the strength of virgin SiC fibres can be retained up to 1000°C, evidence of degradation of the strength of the fibres was found due to the processing of the composite and the subsequent heat treatments at high temperatures (Gambone, 1996). The Weibull parameters of the as-received fibres used in the study of Majumdar *et al.* were σ_0 = 4668 MPa and m = 12.7, similar to those of the etched fibres, indicating that the composite consolidation process did not have any significant damaging effect on the strength of the fibres (Majumdar *et al*, 1998). Tensile experiments carried out on single SCS-6 SiC fibres of 10 mm gauge length revealed a mean failure strength of 5106 ± 65 MPa (Laffargue and Bowen, 2001). Liu and Bowen have looked at the effect of fatigue loading on the strength of SCS-6 fibres in a Tiβ21s/35 vol. % SCS-6 composite, compared to that before fatigue, in an attempt to understand the degradation of fibre strength after composite processing and cyclic loading (Liu and Bowen, 2003b). Tensile tests conducted on extracted fibres from as-received specimens showed the fibres to be made up of three subpopulations. A low-strength subpopulation consisted of fibres with strength lower than 2000 MPa, where most of the fibres had surface defects. A medium subpopulation consisted of fibres with strength 2000-3700 MPa, where failure of most of the fibres started from regions close to the carbon core. The high-strength subpopulation, with fibres of strength higher than 3 700 MPa, was found to demonstrate similar Weibull parameters to virgin SCS-6 fibres (Liu and Bowen, 2003b). Cyclic loading was found not to significantly change the mean strength of fibres of either the medium or high strength subpopulations, but it did degrade the strength of some of the SCS-6 fibres at certain levels of applied load range. The percentage of fibres in the high-strength subpopulation was decreased by damage to some fibres which reduced their strength to those of medium- or low-strength fibres. Cyclic loading also fractured some of the individual fibres in the low-strength subpopulation.

3.5.2. Load redistribution upon fibre fracture

The longitudinal tensile failure of metals uniaxially reinforced with brittle ceramic fibres is dictated by the progressive failure of the fibres, whose ductility (typically ≈ 1 %) is much smaller than that of the matrix. As increasing load is applied to the composite the

weakest fibre will eventually fail. The loads that are shed by the broken fibre near the failure site must then be transferred to neighbouring fibres. How much of the load is transferred depends on parameters including the strength and sliding resistance of the fibre/matrix interface, the fibre to matrix modulus ratio, the yield stress of the matrix and the fibre spacing. After the first break occurs, the load is redistributed and this can cause neighbouring fibres to fail sympathetically if the stress concentration is high, and thus shed further load to intact fibres. On the other hand, neighbouring fibres may resist failing if the stress concentration is low. At some point the composite specimen will be unable to carry additional load and final failure of the composite will occur, preceded by random failures of the fibres throughout the gauge length of the composite specimen.

The ultimate tensile strength of a composite depends on the micromechanisms of fracture and two extreme situations, which lead to marked differences in the overall strength (Deve and McCullough, 1995; Jeng *et al*, 1991). These two extremes are Global Load Sharing (GLS) and nearest neighbour Local Load Sharing (LLS). Under GLS conditions the effect of local stress concentrations in neighbouring intact fibres around fibre breaks are neglected, and the stress along a broken fibre recovers to the applied stress linearly from the break or fibre end. The load shed by fractured fibres is distributed equally among the intact fibres in the remaining cross-section. This type of load transfer requires sliding along the fibre/matrix interface and a relatively stiff matrix (Curtin, 1991; Hui *et al*, 1995; Landis and McMeeking, 1999). A GLS composite with a large number of fibres has a stress-strain behaviour that is initially linear, and as fibres progressively fail the material softens until a smooth maximum in the stress is reached. This arises from the competition between the hardening induced by matrix plasticity and fibre deformation and the softening due to fibre fragmentation. The overall strength of the composite is determined from the maximum in the stress-strain curve and depends on this softening process. However, local stress concentrations do affect the damage accumulation in the majority of composites, especially those composites that undergo brittle failure where the material behaves nearly linear elastically up to fracture. These systems are usually associated with LLS conditions (Foster *et al*, 1998; Landis *et al*, 2000; Zhou and Curtin, 1995). Intact fibres experience a stress concentration in the presence of a break, and fibres closest to the break experience the highest stress concentration. In the extreme case, only nearest neighbours experience the stress concentration and other fibres further from the break are unaffected.

The accurate prediction of the composite failure stress requires an accurate determination of the stress concentration function (SCF) around a broken fibre. Shear lag-based micromechanical models of damage evolution have been developed for two- and three-dimensional fibre arrangements in unidirectional composites. The first contribution to the problem was for a square or hexagonal array of fibres (Hedgepeth and Van Dyke, 1967), a unidimensional approximation which presupposes that the matrix has no axial stiffness and transfers load by shear. This early work solved for the stresses and displacements in the fibres and matrix generated by a single row of fibre breaks, and assumed perfect bonding between fibres and matrix. Many studies followed with similar intentions allowing for one or a combination of features, including yielding matrices (Goree and Gross, 1980), interfacial debonding (Nairn, 1988; Ochiai *et al*, 1991), and for matrices that support a portion of the tensile stress (Fukuda and Kawata, 1976; Ochiai *et al*, 1991; Zeng *et al*, 1997). The analysis of Fukuda and Kawata showed that the SCF increases with increasing number of adjacent broken fibres. The introduction of influence superposition techniques enabled the problem to be solved for any arbitrary arrangement of fibre fractures in a composite with an elastic matrix (Beyerlein *et al*, 1996), a plastic matrix and slipping interfaces (Beyerlein and Phoenix, 1996) or a viscoelastic matrix (Beyerlein *et al*, 1998). More recent studies have provided analytical solutions which include the effect of matrix yielding and interface debonding on the SCF (Landis and McMeeking, 1999). Numerical techniques have been used to solve more complex situations, involving uneven fibre spacing, matrix axial stiffness, and multiple fibre cracks (Landis and McMeeking, 1999; Beyerlein and Phoenix, 1996).

Finite element simulations of a representative volume of a studied composite have been used to obtain the SCF around a broken fibre (Gonzalez and Llorca, 2001), who observed the failure mechanism in Ti-6Al-4V/SiC to be dominated by LLS conditions. The fibres in this composite were assumed to be distributed in a hexagonal array, and the centre fibre contained one fibre break. The stress increase in nearest-neighbour fibres as given by the simulation did not exceed 4% for an applied strain of 1% and fibres spaced 1.5 fibre diameters apart. This is compared to a maximum stress concentration in nearest-neighbour fibres of 10% as predicted by the classical shear-lag model for a hexagonal arrangement (Hedgepeth and Van Dyke, 1967). The main cause of the difference is attributed to the relative sliding at the fibre/matrix interface. Hedgepeth and Van Dyke presupposed that the matrix had no axial stiffness, an assumption which is only good for polymer matrices, and transferred load by shear. Perfect bonding between fibre and matrix

was also assumed, and sliding at the interface mitigates the stress concentration around the broken fibre. The study of Gonzalez and Llorca determined the tensile properties and fracture micromechanisms in a Ti-6Al-4V alloy uniaxially reinforced with 35 vol. % Sigma 1140+ SiC monofilaments. They showed that the defect formed by a cluster of several broken fibres grew unstably due to the stress concentrations at the edges of the cluster, with no increase in the applied stress. This was indicated by the composite exhibiting a bilinear stress-strain curve, and damage was localised a few hundred microns above and below the fracture surface, as observed in the micrograph of Figure 3-18 (Gonzalez and Llorca, 2001). Multiple fibre fractures were observed, with the distance between the cracks in each fibre ranging from 100 to 300 μm. Fibre fracture was never observed far away from the fracture surfaces, which suggested a failure mechanism dominated by the formation of an initial cluster of broken fibres. This propagated across the specimen section prior to the development of any global damage. This kind of microscopic damage has been observed elsewhere in Ti/SiC composites (Gundel and Wawner, 1997; Majumdar *et al*, 1998).

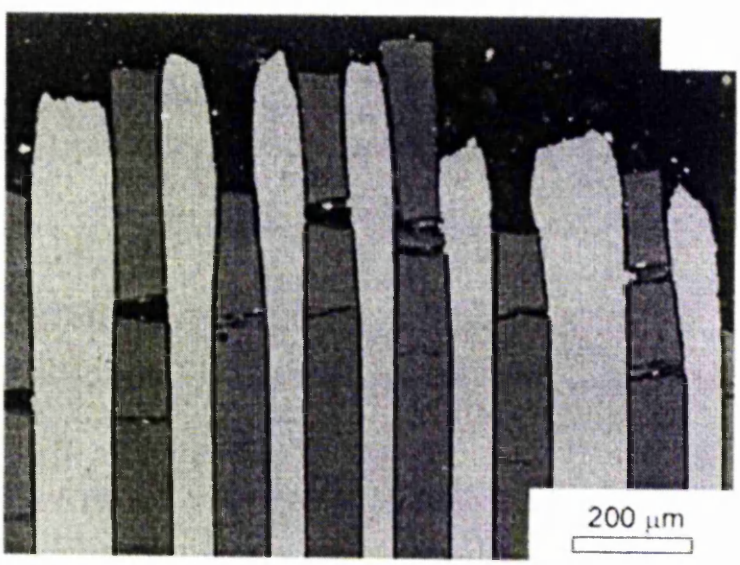

Figure 3-18. Back-scattered scanning electron micrograph showing multiple fibre fracture near the fracture surface of a Ti-6Al-4V alloy uniaxially reinforced with 35 vol. % Sigma 1140+ SiC monofilaments, and tested in tension. (Gonzalez and Llorca, 2001).

Most notably, Majumdar *et al.* observed multiple fractures in Ti-6Al-4V/SCS-6, during a fragmentation test, to consume a total length of up to one fibre radius (Majumdar *et al*, 1998). The crushing and severe fragmentation of the fibre at the position of the break

caused the matrix to cave in, likely increasing the local interface radial stress at the ends of the break. Analysis of the failure of a single-ply composite in the same study, with a fibre separation of 200 μm, showed localised matrix plasticity to be responsible for the cumulative failure of fibres due to a one-to-one correspondence between slip band intersections with the fibres and the fibre break locations. Subsequent fibre breaks were observed to form as the slip bands from existing fibre breaks impinged on an adjacent fibre. Also, the fibres were found to be much more fragmented at the original break locations. As the extent of plastic deformation in each major slip band increased, so did the number of breaks for a fibre within that band. This behaviour suggests a high friction stress. The overall fracture behaviour suggests local load sharing (LLS) for this system.

High energy X-ray diffraction has been employed elsewhere to study load transfer in single ply Ti-6Al-4V/SCS-6 unidirectional fibre composite systems (Hanan *et al*, 2003). The fibres, 140 μm in diameter, were uniformly spaced with an average centre-to-centre distance of 240 μm. In order to observe stress redistribution, the two centre fibres were cut using wire electric discharge machining by plunging the wire into the centre of the composite. Axial fibre strain measurements were made using high energy X-ray diffraction, a measurement method that will be explained in detail in the Experimental Procedure of Chapter 4, under an applied tensile load of 850 MPa. Figure 3-19 shows the measured strain distribution in a broken and intact fibre, revealing a strain concentration of 30-40% across the axial position of the hole in the first intact nearest-neighbour fibres (Hanan *et al*, 2003). A strain concentration of ~10% was measured in next-nearest fibres. These measured strains were compared to predictions of a 'matrix stiffness shear lag' (MSSL) micromechanics model (Beyerlein and Landis, 1999). This model was developed to compute stresses and displacements in two-dimensional, infinitely large, unidirectional fibre composites in response to multiple fibre and matrix breaks. Both the fibres and matrix are able to sustain longitudinal load in contrast to earlier models based on the shear lag concept. The predictions of the MSSL model, which considers both the fibres and matrix as linear elastic and well bonded, compare well with the measured fibre strains in terms of showing the same strain concentration, as observed in Figure 3-19 (Hanan *et al*, 2003). The experimental strain profiles, however, are observed to be broader than those predicted by the model. This is due to plastic deformation in the matrix which may reduce the strength of the interface (Preuss *et al*, 2002), and demonstrates how it distributes the extra load due to the broken fibres away from the damage zone (Hanan *et al*, 2003). This

mechanism of load transfer in MMCs is largely responsible for their enhanced damage tolerance. The results of Beyerlein and Landis showed a significant dependence of fibre failure on the fibre-to-matrix stiffness ratio, $\rho = E_m A_m / E_f A_f$ (Beyerlein and Landis, 1999). The peak fibre stress concentrations decreased and the peak matrix stress concentrations increased as ρ increased. Also, lower stress concentrations were calculated in fibres where the matrix regions between broken fibres and the intact fibres were intact compared to where they were broken.

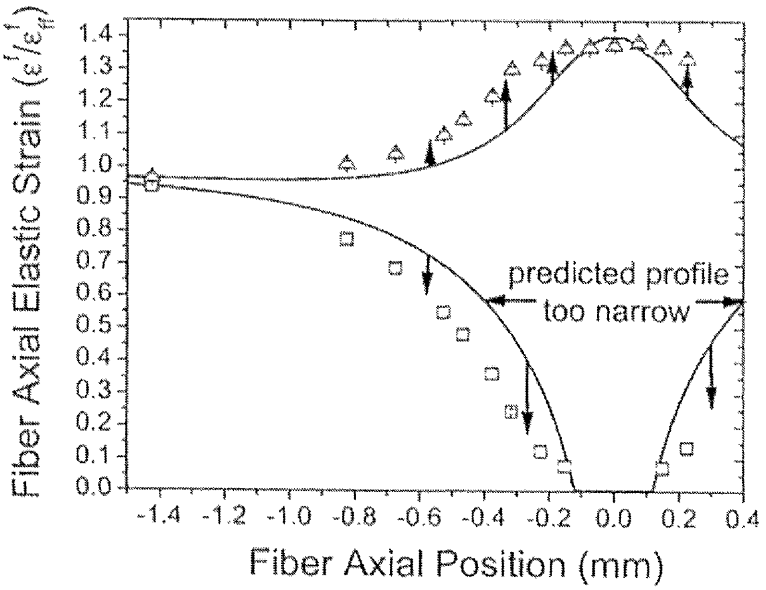

Figure 3-19. Relative axial strain distribution, measured using X-ray diffraction, in a fibre containing a break and the adjacent intact fibre, under an applied load of 850 MPa. The measured strains are compared to model predictions (solid line). (Hanan *et al*, 2003).

The influence of inter-fibre spacing on the stress transfer characteristics around fibre breaks has been investigated for alumina-fibre/epoxy model composites using fluorescence spectroscopy (Mahiou *et al*, 1999). A stress concentration factor (SCF) of 1.21 for an inter-fibre distance of 2.6 fibre diameters was observed. This was found to decrease to a value approaching unity at high inter-fibre distances (12.6 fibre diameters). Similar values were reported by Van den Heuvel *et al.* for a carbon fibre/epoxy microcomposite (Van den Heuvel *et al*, 1997), who found the SCF to decrease from a value of 1.26 at an inter-fibre spacing of 0.8 fibre diameters to a value of 1.06 at an inter-fibre spacing of 10.4 fibre diameters. At higher inter-fibre spacing no significant SCF could be determined. The interfacial shear stress at a fibre adjacent to a break was found to

decrease with inter-fibre spacing exponentially, in the same way as the SCF. Compared to these experimental measurements, the theory and SCF prediction of Hedgepeth and Van Dyke (1.33) is too high, but is only based on elastic stress transfer. Experimentally, local matrix yielding of the interface is observed to occur in the vicinity of a fibre break owing to an interfacial shear stress slightly less than the shear yield stress of the matrix (Mahiou *et al*, 1999; Van den Heuvel *et al*, 1997). Local yielding has been shown to decrease the SCF in adjacent fibres, while matrix cracking and debonding increase and decrease the SCF respectively (Ochiai *et al*, 1991). Also, the fibre strain in fibres beyond a fixed number, i.e. ± 9 fibres, from one containing a break has been found to be uniform (Ochiai *et al*, 1991). Van den Heuvel *et al.* observed that at relatively small inter-fibre spacing the SCF was sufficiently high to cause fibre failure, and 'coordinated' fibre failure took place resulting in the alignment of fibre breaks. At increasing inter-fibre spacing the decrease in the SCF resulted in a decreasing influence of the initial fibre break on the subsequent failure process, which became more random.

3.6. Fatigue Crack Growth Resistance

3.6.1. Physical aspects of fatigue crack growth

Regarding the development and detailed consideration of Ti matrix composites reinforced with SiC monofilaments for applications in turbine engines (as covered in the Introduction to this Chapter), cyclic loading will always occur during such a service operation (Bowen and Hartley, 1994). Many studies have been carried out to characterise the fatigue crack growth behaviour of these composites at ambient and elevated temperatures (Brisset and Bowen, 1998; Cotterill and Bowen, 1996; Cotterill and Bowen, 1993; Jeng *et al*, 1992; Barney *et al*, 1998). These experiments have shown that the improved fatigue crack growth resistance, where the fatigue crack growth rate is observed to decrease with increased crack length (Cotterill and Bowen, 1993), benefits from the bridging effects caused by intact fibres across the crack path. Shielding of the crack-tip by these fibre bridging effects decreases the effective stress intensity at the growing crack tip, leading to crack arrest and an important toughening mechanism in such materials (Marshall *et al*, 1985). The balance between sub-critical crack growth and catastrophic failure is governed primarily by the number of fibres remaining intact within the crack path. Interfacial shear strength is therefore important, which determines whether a fibre fractures or remains intact. Figure 3-20 illustrates a typical fatigue crack growth resistance curve,

measured in three point bending, for a 35% volume fraction SCS-6 SiC fibre reinforced Ti-6Al-4V alloy matrix, with an initial stress intensity range, ΔK = 16.2 MN m$^{-3/2}$, and a load ratio, R = 0.5 (Bowen and Hartley, 1994). Crack arrest (defined by the crack increment per cycle da/dN $\leq 10^{-8}$ mm/cycle) was observed to occur readily under applied stress intensity range conditions that would promote rapid catastrophic failure of the monolithic alloy (Bowen and Hartley, 1994).

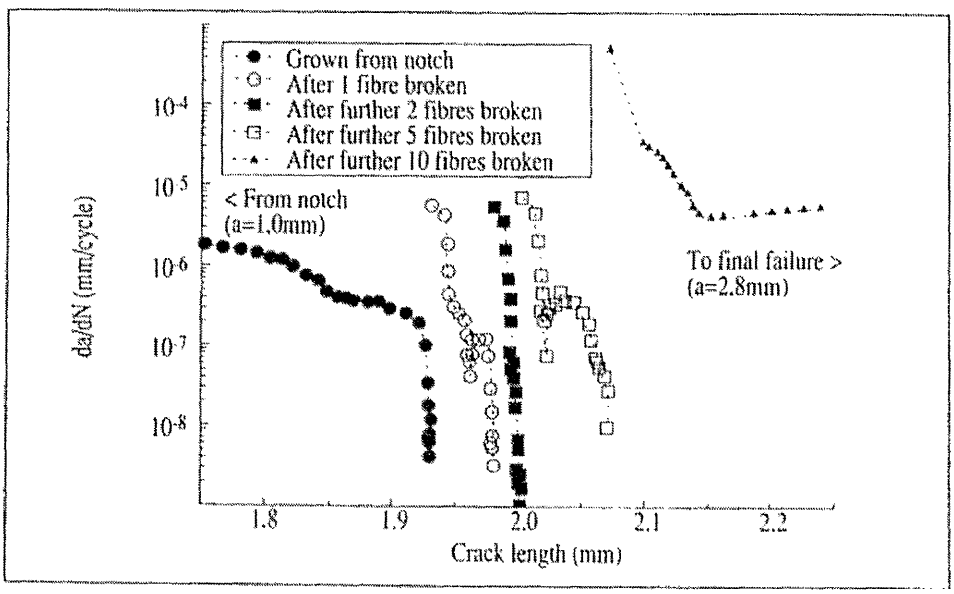

Figure 3-20. A fatigue crack growth resistance curve for a 35% volume fraction SiC fibre reinforced Ti-6Al-4V matrix: initial stress intensity range ΔK = 16.2 MN m$^{-3/2}$, load ratio R=0.5. (Bowen and Hartley, 1994).

The major damage modes which occur during fatigue crack propagation under Mode I loading (applied load normal to direction of crack) are observed to be matrix cracking, fibre bridging, crack bifurcation and crack deflection (Jeng *et al*, 1992). As the fibre is strong enough to withstand the stress concentration at the crack tip, the fatigue crack propagates around the fibre, causing matrix cracking and fibre/matrix interfacial debonding. For composite systems with a relatively strong interfacial shear strength, such as Ti-6Al-4V/SCS-6, fibre/matrix debonding is limited to the matrix cracking region, whereas for composites with weak interfaces, such as Ti-15V-3Cr/SCS-6, crack bifurcation along the fibre matrix interface (Mode II crack growth) is observed (Jeng *et al*, 1992). The damage modes that occur in Ti MMCs are observed to be influenced by several factors, including the applied stress intensity factor, applied stress ratio, fibre strength, fibre/matrix

interfacial debonding shear strength, frictional sliding stress, and the fatigue strength of the matrix (Jeng *et al*, 1992). Investigation of the fatigue crack growth mechanisms in a Ti-15V-3Cr/SCS-6 fibre reinforced composite (Cotterill and Bowen, 1996; Cotterill and Bowen, 1993) has revealed crack propagation behaviour to be critically dependent on the applied load range (or initial ΔK). At low loads crack arrest was observed, whereas at high loads specimen failure occurred, with the specimen life decreasing significantly as the load range was increased. Fatigue crack growth resistance was also found to be significantly reduced at an elevated temperature of 350°C, with fibre failure occurring more readily.

3.6.2. Crack shielding/bridging and crack opening displacement

Crack propagation under Mode I loading is accompanied by interfacial debonding ahead of the crack tip, which eventually leads to fibre bridging in the crack wake. When intact fibres bridge a Mode I crack, the crack driving force is shielded by the load carried by bridging fibres. This shielding of crack tip driving forces occurs in two ways. Firstly, the higher modulus fibre ahead of the crack tip carries a larger fraction of the applied load than the matrix, thus reducing the local stress intensity factor at the crack tip and resulting in a reduced crack growth rate (Warrier and Majumdar, 1999). Warrier and Majumdar also found a more significant crack retardation due to this elastic shielding the higher the interfacial shear strength. Secondly, the mechanism of crack bridging, for which the fibre/matrix interface plays an important role, can dramatically reduce crack growth rates and even arrest crack growth. A higher interfacial frictional shear strength is observed to lower the crack opening displacement, providing that crack bridging is not compromised, and thus reduces the fatigue crack growth rate (Warrier and Majumdar, 1999). However, this also increases the stress magnitude in bridged fibres, resulting in fibre fracture. In order to achieve maximum crack growth resistance, a balance between the interfacial frictional shear strength and fibre bridging must be obtained. Although a weakly-bonded interface is desired for increased fatigue crack growth resistance, it also reduces transverse strength since the transverse strength of composites is determined primarily by the strength of the interface (Gundel *et al*, 1997).

Many attempts have been made to analyse the bridging effects and to predict the effective fatigue crack driving forces at the crack tip. The method employed by most studies to model the effects of fibre bridging is a stress-intensity-factor range approach, by superposition of a crack subjected to a far-field stress and a crack subjected to a bridging traction. It is the determination of this bridging traction that is the key issue in modelling

the bridging effect, and a shear lag approach has been used to predict this theoretically for elastic-elastic situations (Cox and Marshall, 1994; Cox *et al*, 1989; Marshall *et al*, 1985). Models based on such an approach assume that the stress sustained by bridging fibres can be transferred to the matrix by interfacial sliding and can act as a 'pressure' to retard the opening of the crack. The shear-lag approach was originally applied by Marshall *et al.* to ceramic matrix composites (Marshall *et al*, 1985). The principal implications of their analysis concerned the predicted transition to a crack-length-independent matrix-cracking stress (i.e. the first deviation from linearity in the stress-strain curve) for cracks longer than a characteristic length. The analysis indicated that the attainment of steady-state cracking at high stress levels is restricted by the volume fraction of fibres aligned in the principal stress axis, because an increase in V_f beneficially influences all of the parameters that determine optimum steady-state properties. The shear-lag model has also been used to analyse the effects of intrinsic factors, such as fibre strength and fibre strength distributions (Cox *et al*, 1989). Fracture of ceramic matrix composites containing matrix cracks that are fully bridged by fibres was found not to be strongly affected by the width of the fibre strength distribution. Over the range of Weibull shape parameters typically expected for brittle fibres ($m > 1$) the steady-state matrix cracking stress was measured to be within 10% of its value for a single-valued fibre strength ($m = \infty$). At fibre strengths below a certain value the failure mechanism changed from the non-catastrophic mode associated with multiple matrix cracking to a catastrophic mode resulting from simultaneous fibre fracture and matrix crack growth. An increased tendency to a catastrophic mode of failure was found to occur with decreasing values of m.

In MMCs, crack opening displacement (COD) provides a possibility of establishing an experimental based methodology to analyse crack bridging (Buchanan *et al*, 1997; Davidson, 1992). Liu and Bowen investigated the bridging mechanisms in an eight-ply SCS-6 fibre reinforced Tiβ21s/SiC composite by means of COD measurements (Liu and Bowen, 2003). *In-situ* scanning electron microscope (SEM) tensile tests were conducted to measure the COD profiles and to examine interactions between the crack and bridging fibres and the crack-opening procedure at the crack tip. Figure 3-21(b) and (c) shows the half-COD profiles that were measured, at positions indicated in (a), during this test for two samples that were pre-fatigued at different maximum applied loads (Liu and Bowen, 2003).

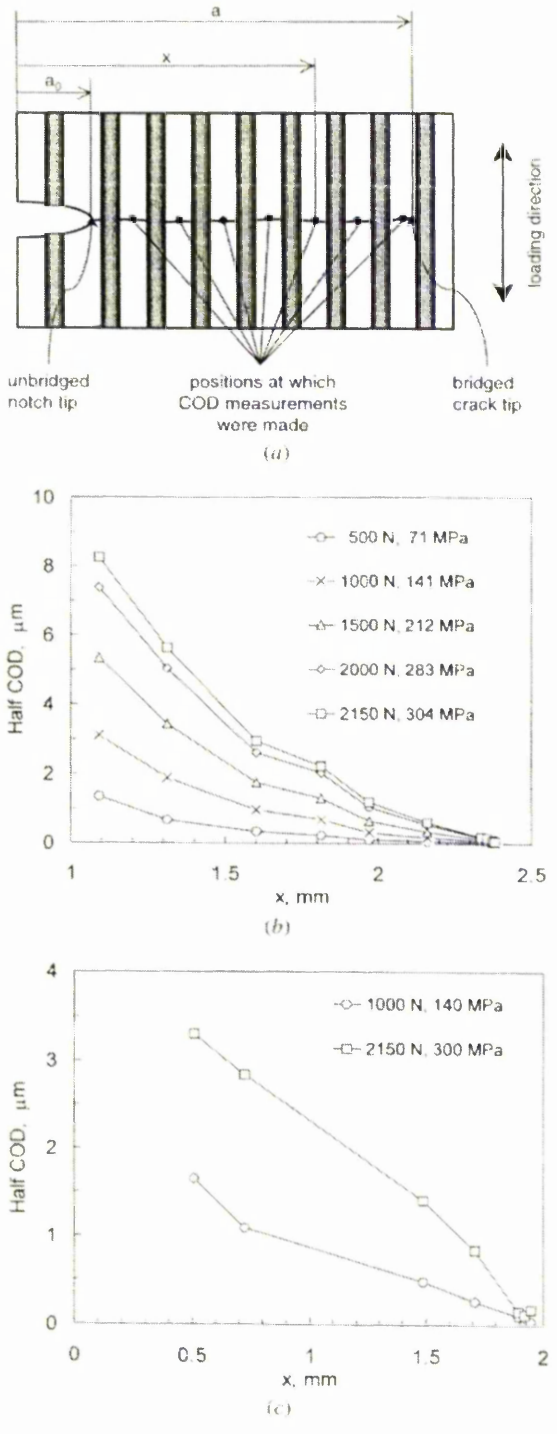

Figure 3-21. Half-COD profiles, measured at positions along the crack path indicated in (a), for specimens under different maximum applied loads: (b) 304 MPa and (c) 563 MPa. The specimen was an eight-ply SCS-6 fibre reinforced Tiβ21s/SiC composite. (Liu and Bowen, 2003a).

The results showed the half-CODs to decrease as the crack tip was approached, and a decrease in the applied stress resulted in a decrease in the magnitude of the half-CODs.

The efficiency of load transfer at the interface was found to be higher at positions close to the crack tip than at positions far away, deduced to be due to the amount of interfacial opening along part of the bridging fibres. When the crack tip was observed to approach the interface, this debonded interface opened further but did not slide when an external load was applied to the specimen. This suggests that the interfacial shear stress applicable during fibre bridging is lower than the interfacial shear strength measured by fibre push-out or pull-out tests. This is in strong agreement with work carried out by Preuss *et al*, who made high spatial resolution diffraction strain measurements to map the strain around a matrix fatigue crack in a Ti-6Al-4V/35 vol.% SCS-6 fibre (140 μm diameter) unidirectional composite specimen under an applied tensile load (Preuss *et al*, 2003). The crack was grown in three-point bending using a constant load range with an applied stress ratio, R, of 0.1 (where $R = K_{min}/K_{max}$ and K_{min} and K_{max} are the minimum and maximum stress intensity factors applied during a fatigue cycle). When loaded to K_{max} (parallel to the fibre direction but perpendicular to the direction of growth of the fatigue crack), the longitudinal strain distribution of the fibres revealed maximum interfacial shear stresses of about 80 MPa (Preuss *et al*, 2003). Such values are lower than those measured from fibre push-out or pull-out tests, due to severe deterioration of the fibre/matrix interface during fatigue and the repeated forward and reverse frictional sliding. In the unloaded stage, the matrix was found to exhibit a small area of tensile strain in front of the crack tip, suggesting that the crack was forced to stay slightly open (Preuss *et al*, 2003). This suggests the frictional resistance of the bridging fibres keeps the crack slightly open. Residual crack opening displacements, due to relaxation of the fibre and matrix residual stresses generated during processing, by passage of the fatigue crack, have also been measured in the same system (Davidson, 1992). Via a matrix removal technique, such measurements inferred fibre debonding to occur over a length of 1 mm, determined from fibre coating damage.

3.7. Summary

A review of the relevant research that has been carried out regarding, in particular, the micromechanical aspects and behaviour of metal matrix composites, and specifically Ti/SiC_f MMCs, for aeroengine applications has been presented. These composite materials are being considered for such applications because, due to the properties of the ceramic SiC constituent (which is typically 30-40% by volume), they offer increased stiffness and strength combined with the consequent weight reduction. It is important to consider the

level of thermal residual stress induced during composite fabrication as such stresses can affect the damage mode in Ti MMCs and can be both detrimental and beneficial. Damage can be introduced into the matrix and crack-like defects can occur at the fibre-matrix interface, while residual stresses can also influence stress transfer at the interface and debonding and thus the bridging effect of fibres towards matrix cracks. An account of the models describing interfacial shear stress transfer between fibres and matrix has been presented. This included the original case of perfect adhesion between fibre and matrix, for which load transfer occurs in a purely elastic manner, and the modification to include the case of fibre/matrix interface debonding, where frictional sliding occurs at a constant interfacial frictional shear stress. Such interfacial behaviour is paramount to the understanding of the micromechanical properties and performance of composite materials, and the fragmentation test has been illustrated as an extremely useful method for the study of stress transfer and interface strength in both polymer and metal matrix systems. For the case of the Ti/SiC composite system, fibre fragments larger than the critical length showed a fully bonded region across their mid-length with sliding occurring over regions (~0.5 mm) adjacent to a crack, inferring an interfacial frictional shear strength of ~200 MPa.

Fibre strength distributions have been shown to be important, particularly when fibre fracture results in the redistribution of load. A significant amount of work has been carried out regarding the stress concentration effects of defects in polymer systems, but there is little experimental work reporting such work in Ti/SiC composites. As the main topic of the work covered in Chapter 4, knowledge of the effect of defects in such composites, and the measurement of the redistribution of load which occurs, is important towards their use in aeroengine components. A brief review of the load sharing models in the literature has been given, and these suggest a local load sharing mechanism to occur. Regarding fatigue crack growth resistance, important when considering cyclic loading, benefits are observed from the bridging effects caused by intact fibres across the crack path. Shielding of the crack-tip by these fibre bridging effects decreases the effective stress intensity at the growing crack tip, leading to crack arrest. The strength of the fibre-matrix interface is important for this mechanism to occur. While mechanisms of interaction between fibres and matrix cracks are quite well understood, direct observations and visualisation is lacking. X-ray microtomography can provide such observations non-destructively, as well as the visualisation of fibre cracking characteristics.

References

Andrews, M. C. and Young, R. J., (1993), *Journal of Raman spectroscopy*, **24**, 539.

Ashby, M. F., (1993), 'Criteria for selecting the components of composites', *Acta Metallurgica et Materialia*, **41**(5), 1313-1335.

Bannister, D. J., Andrews, M. C. and Cervenka, A. J., Young, R. J., (1995), 'Analysis of the single-fibre pull-out test by means of Raman spectroscopy: Part II. Micromechanics of deformation for an aramid/epoxy system', *Composites Science and Technology*, **53**(4), 411-421.

Barney, C., Ibbotson, A. and Bowen, P., (1998), 'Experimental characterisation of fibre failure and its influence on crack growth resistance in fibre reinforced titanium metal matrix composites', *Materials Science and Technology*, **14**, 658-668.

Bennett, J. A. and Young, R. J., (1998), 'The effect of fibre-matrix adhesion upon crack bridging in fibre reinforced composites', *Composites Part A*, **29A**, 1071-1081.

Beyerlein, I. J. and Landis, C. M., (1999), 'Shear-lag model for failure simulations of unidirectional fibre composites including matrix stiffness,' *Mechanics of Materials*, **31**, 331-350.

Beyerlein, I. J. and Phoenix, S. L., (1996), 'Stress concentrations around multiple fibre breaks in an elastic matrix with local yielding or debonding using quadratic influence superposition', *Journal of the Mechanics and Physics of Solids*, **44**, 1997-2039.

Beyerlein, I. J., Phoenix, S. L. and Raj, R., (1998), 'Time evolution of stress redistribution around multiple fibre breaks in a composite with viscous and viscoelastic matrices', *International Journal of Solids and Structures*, **35**, 3177-3211.

Beyerlein, I. J. and Phoenix, S. L. and Sastry, A. M., (1996), 'Comparison of shear-lag theory and continuum fracture mechanics for modeling fiber and matrix stresses in an elastic cracked composite lamina', *International Journal of Solids and Structures*, **33**, 2543-2574.

Bowen, P. and Hartley, M. V., (1994), 'Titanium based composites: exploiting the benefits', *Materials World*, **66**, 2-5.

Brisset, F. and Bowen, P., (1998), 'Fatigue crack growth in fibre reinforced titanium MMC laminate at room and elevated temperatures', *Materials Science and Technology*, **14**, 651-657.

Buchanan, D. J., John, R., Johnson, D. A., (1997), 'Determination of crack bridging stresses from crack opening displacement profiles', *International Journal of Fracture*, **87**, 101-117.

Carara, A. S. and McGarry, F. J., (1968), 'Matrix and interface stresses in a discontinuous fibre composite model', *Journal of Composite Materials*, **2**, 222-243.

Cheskis, H. P. and Heckel, R. W., (1970), 'In-situ measurements of deformation behaviour of continuous fibre MMC materials', *Metallurgical Transactions*, **1**, 1931-1942.

Clyne, T. W. and Withers, P. J., *An Introduction to Metal Matrix Composites*, Cambridge University Press, Cambridge, UK, 1993.

Cotterill, P. J. and Bowen, P., (1996), 'Fatigue crack growth in a Ti-15-3 matrix/SCS-6 fibre metal matrix composite under tension-tension loading', *Materials Science and Technology*, **12**, 523-529.

Cotterill, P. J. and Bowen, P., (1993), 'Fatigue crack growth in a fibre-reinforced titanium MMC at ambient and elevated temperatures', *Composites*, **24**(3), 214-221.

Covey, S. J., Lerch, B. A. and Jayaraman, N., (1995), 'Fiber volume fraction effects on fatigue crack growth in SiC/Ti-15-3 composite', *Materials Science and Engineering*, **A200**, 68-77.

Cox, H. L., (1952), 'The elasticity and strength of paper and other fibrous materials', *British Journal of Applied Physics*, **3**, 73-79.

Cox, B. N., James, M. R., Marshall, D. B. and Addison, R. C., (1990), 'Determination of residual stresses in thin sheet titanium aluminide composites', *Metallurgical Transactions A*, **21A**, 2701-2707.

Cox, B. N. and Marshall, D. B., (1994), 'Concepts for bridged cracks in fracture and fatigue', *Acta Metallurgica et Materialia*, **42**(2), 341-363.

Cox, B. N., Marshall, D. B. and Thouless, M. D., 'Influence of statistical fibre strength distribution on matrix cracking in fibre composites', (1989), *Acta Metallurgica et Materialia*, **37**(7), 1933-1943.

Curtin, W. A., (1991), 'Theory of mechanical properties of ceramic matrix composites', *Journal of the American Ceramics Society*, **74**, 2837-2845.

Davidson, D. L., (1992), 'The micromechanics of fatigue crack growth at 25°C in Ti-6Al-4V reinforced with SCS-6 fibres', *Metallurgical Transactions A*, **23A**, 865-879.

Deve, H. E. and McCullough, C., (1995), *Journal of Materials*, **47**(7), 33.

Di Landro, L. and Pegoraro, M., (1987), 'Carbon fibre – thermoplastic matrix adhesion', *Journal of Materials Science*, **22**, 1980-1986.

Driver, D., 'Towards 2000 – The Composite Engine', 1989, in Clyne, T. W. and Withers, P. J., *An Introduction to Metal Matrix Composites*, Cambridge University Press, Cambridge, 1993.

Foster, G. C., Ibnabdeljalil, M. J. and Curtin, W. A., (1998), 'Tensile strength of titanium matrix composites: direct numerical simulations and analytic models', *International Journal of Solids and Structures*, **35**, 2523-2536.

Fukuda, H. and Kawata, K., (1976), 'On the stress concentration factor in fibrous composites', *Fibre Science and Technology*, **9**, 189-203.

Gambone, M. L., (1996), 'SiC fibre strength after consolidation and heat treatment in Ti-23Al-23Nb matrix composite,' *Scripta Metallurgica*, **34**(3), 507-512.

Gambone, M. L. and Wawner, F. E., (1997), 'The effect of surface flaws on SiC fibre strength in a SiC/Ti-alloy composite', *Journal of Composite Materials*, **31**(11), 1062-1079.

Garibotti, J. F., (1978), 'Trends in aerospace materials', *Astronautics and Aeronautics*, **16**, 70-81.

Ghonem, H., Wen, Y. and Zheng, D., (1994), 'An interactive simulation technique to determine the internal stress states in fiber reinforced metal matrix composites', *Materials Science and Engineering*, **A177**, 125-134.

González, C. and Llorca, J., (2001), 'Micromechanical modelling of deformation and failure in Ti-6Al-4V/SiC composites', *Acta Materialia*, **49**, 3505-3519.

Goree, J. G. and Gross, R. S., (1980), 'Stresses in a three-dimensional unidirectional composite containing broken fibres', *Engineering Fracture Mechanics*, **13**, 395-405.

Gundel, D. B., Warrier, S. G. and Miracle, D. B., (1997), 'The interface debond stress in single and multiple SiC fibre/Ti-6Al-4V composites under transverse tension', *Acta Materialia*, **45**(3), 1275-1284.

Gundel, D. B. and Wawner, F. E., (1997), 'Experimental and theoretical investigation of the tensile strength of SiC/Ti-alloy composites', *Composites Science and Technology*, **57**, 471-481.

Hanan, J. C., Ustundag, E., Beyerlein, I. J., Swift, G. A., Almer, J. D., Lienert, U. and Haeffner, D. R., (2003), 'Microscale damage evolution and stress redistribution in Ti-SiC fibre composites,' *Acta Materialia*, **51**(14), 4239-4250.

Hanan, J. C., Swift, G. A., Ustundag, E., Beyerlein, I. J., Almer, J. D. and Lienert, U., (2002), 'Microscale elastic strain evolution following damage in Ti/SiC composites', *Metallurgical and Materials Transactions A*, **33**, 3839-3845.

Hedgepeth, J. M. and Van Dyke, P., (1967), 'Local stress concentration in imperfect filamentary composite materials', *Journal of Composite Materials*, **1**, 294-309.

Hooker, J. A. and Doorbar, P. J., (2000), 'Metal matrix composites for aeroengines', *Materials Science and Technology*, **16**, 725-731.

Huang, Y. and Young, R. J., (1994), 'Analysis of the fragmentation test for carbon-fibre/epoxy model composites by means of Raman spectroscopy', *Composites Science and Technology*, **52**, 505-517.

Hui, C.-Y., Phoenix, S. L. and Ibnabdeljalil, M. J., (1995), 'An exact closed form solution for fragmentation of Weibull fibres in a single filament composite with applications to fibre-reinforced ceramics', *Journal of the Mechanics and Physics of Solids*, **43**, 1551-1585.

Hull, D. and Clyne, T. W., *An Introduction to Composite Materials*, 2nd Edition, Cambridge University Press, Cambridge, 1996.

Jeng, S.-M., Alassoeur, P. and Yang, J.-M., (1992), 'Fracture mechanisms of fiber-reinforced titanium alloy matrix composites V: Fatigue crack propagation', *Materials Science and Engineeering*, **A154**, 11-19.

Jeng, S.-M., Yang, J.-M. and Yang, C. J., (1991), 'Fracture mechanisms of fibre-reinforced titanium alloy matrix composites', *Materials Science and Engineeering*, **A138**, 169-190.

Kasakov, N. F., *Diffusion Bonding of Materials*, Pergamon Press, Oxford, UK, 1985.

Kelly, A. and Tyson, W. R., (1965), 'Tensile properties of fibre-reinforced metals: Copper/tungsten and copper/molybdenum', *Journal of the Mechanics and Physics of Solids*, **13**, 329.

Kieschke, R. R. and Clyne, T. W., in *Fundamental relationships between microstructures and mechanical properties of metal-matrix composites*, TMS, Indianapolis, USA, 1990, 325-340.

Lacroix, T., Tilmans, B., Keunings, R., Desaeger, M. and Verpoest, I., (1992), 'Modelling of critical fibre length and interfacial debonding in the fragmentation testing of polymer composites', *Composites Science and Technology*, **43**, 379-387.

Laffargue, J. and Bowen, P., IRC in materials for high performance applications. Private Communication. School of Metallurgy and Materials, University of Birmingham, Birmingham BI5 2TT. 2001.

Landis, C. M., Beyerlein, I. J. and McMeeking, R. M., (2000), 'Micromechanical simulation of the failure of fibre reinforced composites', *Journal of the Mechanics and Physics of Solids*, **48**, 621-648.

Landis, C. M. and McMeeking, R. M., (1999), 'Stress concentrations in composites with interface sliding, matrix stiffness and uneven fibre spacing using shear lag theory,' *International Journal of Solids and Structures*, **36**, 4333-4361.

Le Petitcorps, Y., Pailler, R. and Naslain, R., (1989), 'The fibre/matrix interfacial shear strength in titanium alloy matrix composites reinforced by silicon carbide or boron CVD filaments', *Composites Science and Technology*, **35**, 207-214.

Lilholt, H., (1977), 'Hardening in two-phase materials—I. Strength contributions in fibre-reinforced copper-tungsten', *Acta Metallurgica et Materialia*, **25**, 571.

Liu, J. and Bowen, P., (2003a), 'Bridging mechanisms in a Tiβ21s/SCS-6 composite: *In-situ* scanning electron microscopy study', *Metallurgical and Materials Transactions A*, **34A**, 1193-1202.

Liu, J. and Bowen, P., (2003b), 'Strength of SCS-6 fibres in a Tiβ21s/SCS-6 composite before and after fatigue', *Metallurgical and Materials Transactions A*, **34A**, 1203-1213.

Mahiou, H., Beakou, A. and Young, R. J., (1999), 'Investigation into stress transfer characteristics in alumina-fibre/epoxy model composites through the use of fluorescence spectroscopy', *Journal of Materials Science*, **34**, 6069-6080.

Maire, E., Owen, A., Buffiere, J.-Y. and Withers, P. J., (2001), 'A synchrotron X-ray study of a Ti/SiC_f composite during in-situ straining,' *Acta Materialia*, **49**, 153-163.

Majumdar, B. S., Matikas, T. E. and Miracle, D. B., (1998), 'Experiments and analysis of fibre fragmentation in single and multiple-fibre SiC/Ti-6Al-4V metal matrix composites', *Composites Part B: Engineering*, **29**(2), 131-145.

Majumdar, B. S., in *Titanium matrix composites*, Technomic Publications, Lancaster, PA, USA, 1997, 113-168.

Marshall, D. B., Cox, B. N. and Evans, A. G., (1985), 'The mechanics of matrix cracking in brittle-matrix fibre composites', *Acta Metallurgica et Materialia*, **33**(11), 2013-2021.

Materials Properties Handbook, 'Titanium Alloys', ASM International, 1994, 516-924.

Nairn, J. A., (1988), 'Fracture mechanics of unidirectional composites using the shear lag model I: Theory', *Journal of Composite Materials*, **22**, 561-588.

Nicholas, T. and Ahmad, J. A., (1994), 'Modeling fibre breakage in a metal-matrix composite', *Composite Science and Technology*, **52**, 29-38.

Ochiai, S., Schulte, K. and Peters, P. W. M., (1991), 'Strain concentration factors for fibres and matrix in unidirectional composites', *Composites Science and Technology*, **41**, 237-256.

Oshawa, T., Nakayama, A., Miwa, M. and Hasegawa, A., (1978), 'Temperature dependence of critical fiber length for glass fiber-reinforced thermosetting resins', *Journal of Applied Polymer Science*, **2**, 3203-3212.

Partridge, P. G. and Ward-Close, C. M., (1989), 'Diffusion bonding of advanced materials', *Metals and Materials*, **4**, 334-339.

Pickard, S. M., Miracle, D. B., Majumdar, B. S., Kendig, K. L., Rothenflue, L. and Coker, D., (1995), 'An experimental study of residual fiber strains in Ti-15-3 continuous fiber composites', *Acta Metallurgica et Materialia*, **43**(8), 3105-3112.

Piggott, M. R., *Load Bearing Fibre Composites*, Pergamon Press, Oxford, UK, 1980, 83-89.

Preuss, M., Withers, P. J., Maire, E. and Buffière, J.-Y., (2002), 'SiC single fibre full-fragmentation during straining in a Ti-6Al-4V matrix studied by synchrotron X-rays', *Acta Materialia*, **50**, 3175-3190.

Preuss, M., Rauchs, G., Doel, T. J. A., Steuwer, A., Bowen, P. and Withers, P. J., (2003), 'Measurements of fibre bridging during fatigue crack growth in Ti/SiC fibre metal matrix composites', *Acta Materialia*, **51**(4), 1045-1057.

Rauchs, G., Preuss, M. and Withers, P. J., (2002), 'Micromechanical analysis of internal stress development during single-fibre fragmentation testing of Ti/SiC_f', *Acta Materialia*, **50**, 2477-2490.

Rauchs, G., Thomason, P. F. and Withers, P. J., (2002), 'Finite element modelling of frictional bridging during fatigue crack growth in fibre-reinforced metal matrix composites', *Computational Materials Science*, **25**, 166-173.

Smith, P. R. and Froes, F. H., (1984), 'Developments in Ti MMCs', *Journal of Metals*, **36**, 19-26.

Van den Heuvel, P. W. J., Peijs, T. and Young, R. J., (1997), 'Failure phenomena in two-dimensional multi-fibre microcomposites: 2. A Raman spectroscopic study of the influence of inter-fibre spacing on stress concentrations', *Composites Science and Technology*, **57**, 899-911.

Ward-Close, C. M. and Partridge, P. G., (1990), 'A fibre coating process for advanced metal matrix composites', *Journal of Materials Science*, **25**, 4315-4323.

Warrier, S. G. and Majumdar, B. S., (1999), 'Elastic shielding during fatigue crack growth of titanium matrix composites', *Metallurgical and Materials Transactions A*, **30A**, 277-286.

Weibull, W., (1951), 'A statistical distribution function of wide applicability,' *Journal of Applied Mechanics*, **18**, 293-305.

Wheatley, W. J. and Wawner, F. W., (1985), 'Kinetics of the reaction between SiC (SCS-6) filaments and Ti-6Al-4V matrix', *Journal of Materials Science Letters*, **4**, 173-175.

Withers, P. J. and Clarke, A. P., (1998), 'A Neutron diffraction study of load partitioning in continuous Ti/SiC composites', *Acta Materialia*, **46**(18), 6585-6598.

Yang, C. J., Jeng, S. M. and Yang, J. M., (1990), 'Interfacial properties measurement for SiC fiber-reinforced titantum alloy composites', *Scripta Metallurgica et Materialia*, **24**, 469-474.

Zeng, Q. D., Wang, Z. L. and Ling, L., (1997), 'A study of the influence of interfacial damage on stress concentration in unidirectional composites', *Journal of Composite Materials*, **57**, 129-135.

Zhou, S. J. and Curtin, W. A., (1995), 'Failure of fibre composites: a lattice green function model', *Journal of the Mechanics and Physics of Solids*, **43**, 3093-3104.

Chapter 4

Micromechanics of Load Transfer and Damage Development

4.1. Introduction

The objective of the following study was to gain an understanding of the micromechanics of stress and damage development that occur on progressive straining in the vicinity of damaged fibres. Thus, the aim with regards to the fabrication of the composite material and specimens was to make single composite plies containing precisely located fibre defects so that the redistribution of load from damaged fibres to neighbouring ones could be investigated. The defects were induced via laser drilling of the individual fibres in the fibre ribbons according to various configurations of damage, i.e. number and proximity. High spatial resolution synchrotron X-ray strain measurements, carried out via diffraction, and X-ray microtomography have been performed on the damaged Ti/SiC_f composite samples. The distribution of axial strain has been mapped along individual fibres during incremental loading using a small X-ray spot size to obtain strain profiles along each fibre and in the neighbouring matrix. The results obtained aim to give important insights into the build-up of strain around the fibre defects, the interfacial characteristics in these regions, such as the shear stresses at the interface, the lateral transfer of load to neighbouring intact fibres and the subsequent failure sequences. Cracking sequences and the accumulation and characteristics of fibre breakages neighbouring an original crack defect have been monitored and observed in detail by X-ray microtomography as a function of straining. The phenomenon of fibre bridging of a matrix fatigue crack has also been observed using high resolution synchrotron X-ray microtomography. A specimen with six plies of unidirectional fibres and a matrix fatigue crack grown via three-point bending perpendicular to the fibre direction was used to measure crack opening displacements as a function of applied load. The X-ray tomography analysis aims to illustrate the considerable contribution of the technique towards the study and understanding of both types of damage and cracking, i.e. in the fibres and matrix and the interaction between the two. Such an understanding is important in the use of composite materials in structural aeroengine applications.

4.2. Materials and Specimens

4.2.1. Fabrication of composite material

The work regarding fabrication of the composite material was carried out at the University of Cambridge, for which P. Dewey and Professor T. W. Clyne are acknowledged for assistance. Tensile specimens for the axial fibre strain measurements and tomography analysis were designed to include fibre defects within their gauge volume. This was for the purpose of investigating the redistribution of load that occurs from damaged fibres to neighbouring fibres during progressive composite straining. 10 cm long ribbons of 42 SCS-6 coated fibres, each having a diameter of 140 μm with a 45 μm thick physical vapour deposition (PVD) coating of Ti-6Al-4V, were laser drilled so as to induce fibre defects or holes prior to fabrication of the composite specimens. Laser drilling is a non-contact process which produces a relatively small region of damage around the drill site and can produce very fine holes with a high degree of reproducibility. Figure 4-1 shows the experimental arrangement of the laser drilling equipment, including a JK701 GSI Lumonics pulsed Nd:YAG laser (wavelength = 1.06 μm) and a translation stage.

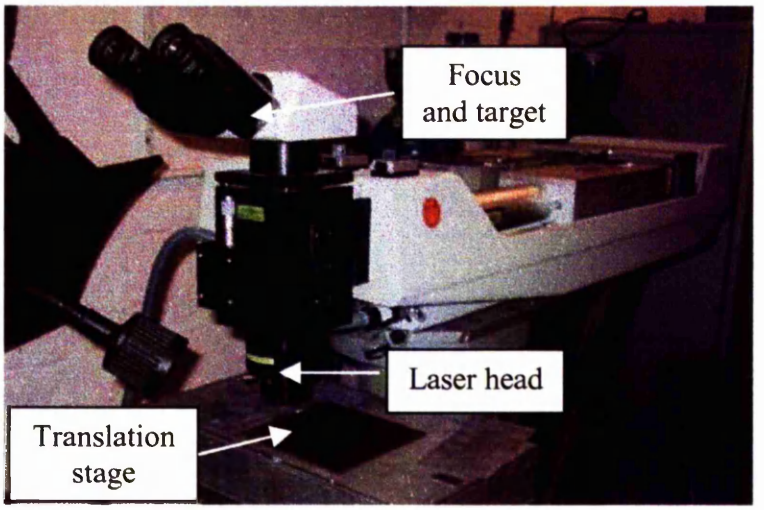

Figure 4-1. Showing the experimental arrangement of the laser drilling equipment at the University of Cambridge, including a pulsed Nd:YAG laser and translation stage.

The laser had an average power of 400 W, and pulses of between 0.5 and 2.5 ms could be produced with energies of up to 20 J. A pulse energy of 0.3 J was used in this case. The fibre ribbons were placed onto the motorised translation stage and the lateral position of each fibre was monitored using the target cross-hairs viewed through the focussing eye-

pieces. The positions of holes along each fibre were chosen and applied by translating the ribbons according to 'patterns' of damage.

In order to study various configurations of damage, for example to investigate the effect of the number and proximity of fibre defects on the micromechanics of stress and damage development, different patterns of defects in the gauge lengths of the tensile specimens were laser drilled. Considering the gauge width of a tensile sample could contain up to 6 fibres and making sure that the damaged fibres were within this gauge width, the central 14 fibres of the ribbons were damaged, making machining of the specimens easier than if only 7 fibres were damaged. Figure 4-2 shows a schematic diagram illustrating two such patterns of defects that were designed, with the short horizontal lines representing damage in the fibres (vertical lines).

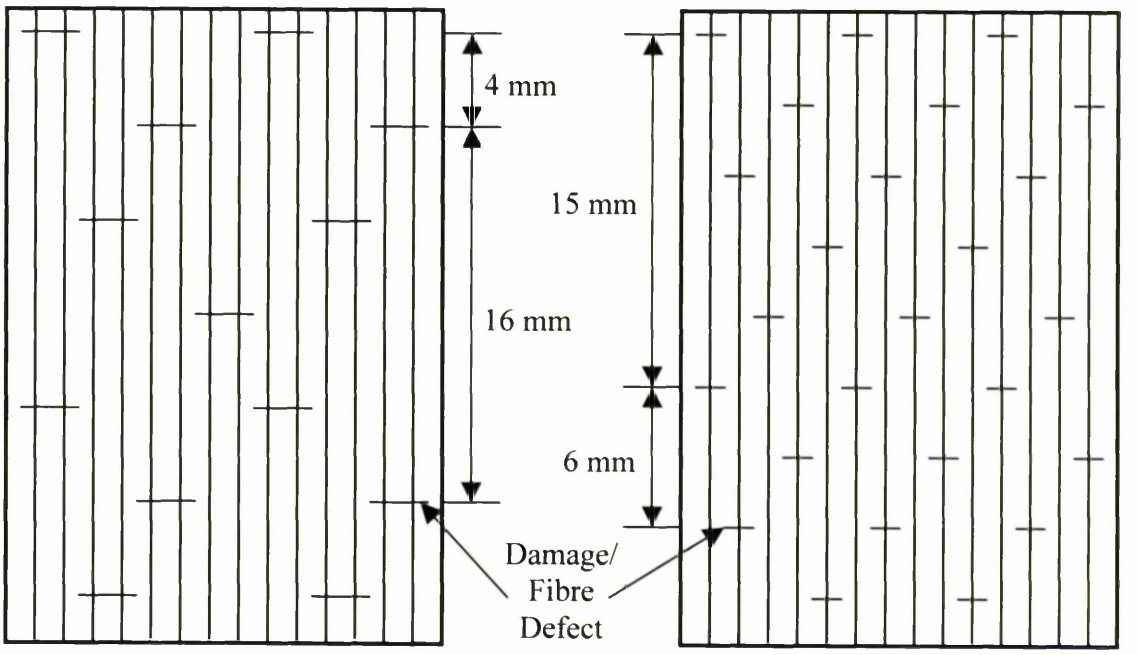

Figure 4-2. Schematic illustration of two such patterns of defects laser drilled into the fibre ribbons. The vertical lines represent the fibres and the short horizontal lines the damage.

Figure 4-2(a) represents a case with two adjacent fibre defects, with the distances between failures in one fibre and the offset of the failures between two fibres being indicated. Figure 4-2(b) represents a case with single isolated defects. Variations of this second case were applied by varying the distance between failures in individual fibres and the offset between adjacent fibres. Radiographs of samples chosen for study are shown in Section

4.2.2. Care was taken to ensure that tensile specimens were cut such that their gauge widths were in the central 14 damaged fibres of the fibre ribbons, but it was difficult to have any control over where the defects were within the gauge length or in which fibres of the resulting gauge width. For this reason, systematic patterns of damage were induced to ensure that the gauge volumes of the specimens did contain at least one set of each of the defect configurations.

Consolidation of the composite material was achieved by hot isostatic pressing or HIPing of the two phases (metal matrix and fibres). Prior to consolidation, four 0.7 mm thick Ti-6Al-4V sheets (80 x 90 mm) and the damaged fibre ribbons were etched (using an etchant containing 5% HF + 40% HNO_3 + 55% H_2O) in order to obtain clean and active surfaces, and to keep the number of surface defects to a minimum. Subsequently, a sandwich of graphite foils (used to prevent contact of the composite materials with the press), metal sheets and the fibre ribbons was placed in a uniaxial vacuum hot press, as illustrated in Figure 4-3.

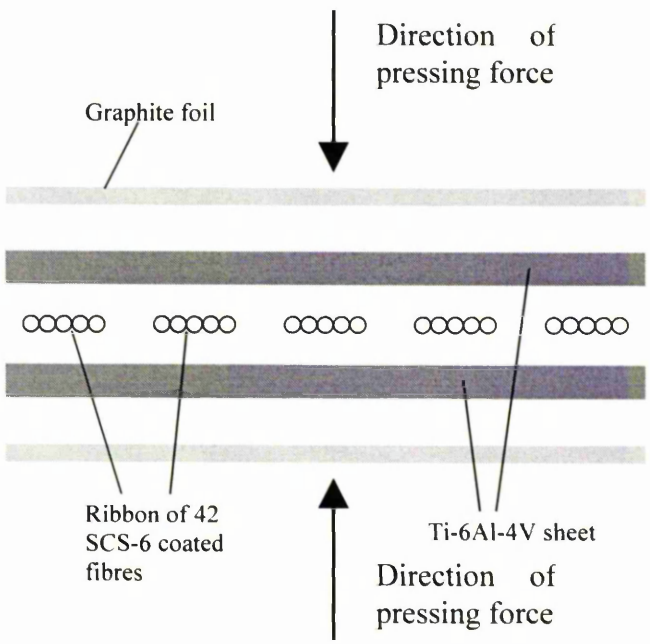

Figure 4-3. Schematic illustration of the lay-up procedure for the composite material fabrication during hot pressing.

The assembled sandwich was consolidated at a vacuum level of 10^{-5} torr and hot-pressed at 900°C/20MPa for 1 hour, followed by furnace cooling. This corresponded to a cooling rate of about 2 K/min. The vacuum hot press was a Clark Scientific unit with RF induction

heating via a graphite susceptor. It had a 10^{-5} torr vacuum capacity (via a diffusion pump system), a 37-tonne hydraulic press and feedback control systems necessary for logging temperatures and applied loads.

Tensile samples were cut from the composite plates by computer controlled electro-discharge machining for which great care had to be taken to ensure that the fibres were aligned parallel with the tensile axis. Figure 4-4 shows the final dimensions of the tensile samples after they had been polished to a thickness of approximately 0.7 mm.

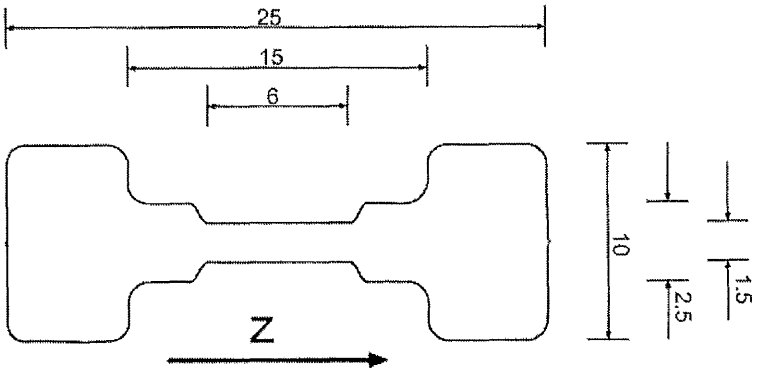

Figure 4-4. Dimensions, all in mm, of the tensile specimens electro-discharge machined from the composite plate. *z* is the tensile axis, parallel to which the fibres are aligned.

4.2.2. Radiography

All of the composite specimens were checked by radiography on beam line (ID19) at the ESRF prior to testing. The optical system used for this experiment gave a pixel resolution of 6 μm and a field of view of 6 mm, the exact length of the gauge region of the specimens. The radiographs were then evaluated to identify samples with different damage characteristics suitable for axial fibre strain analysis. Figure 4-5(a)-(c) shows high-resolution radiographs of three samples chosen for detailed study: (a) a sample with two adjacent fibre defects (sample 1); (b) a sample with two isolated defects in different fibres and separated by a distance along the gauge length (sample 2); and (c) a sample with no defects in its active gauge volume (sample 3).

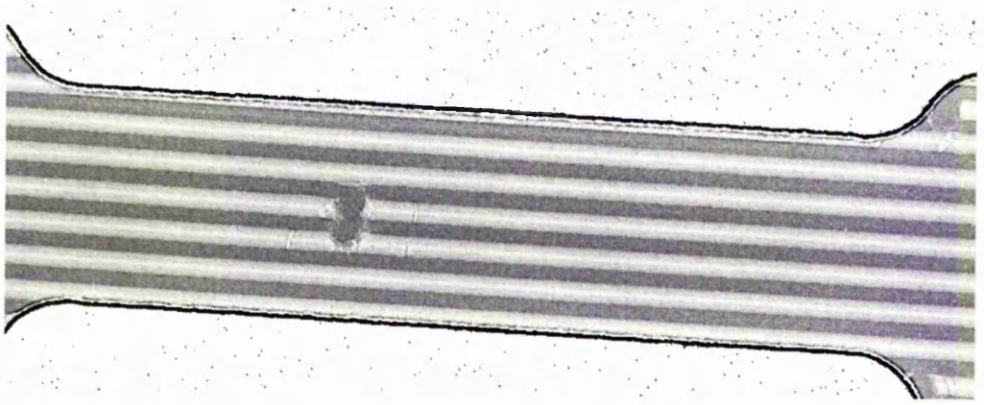

(a)

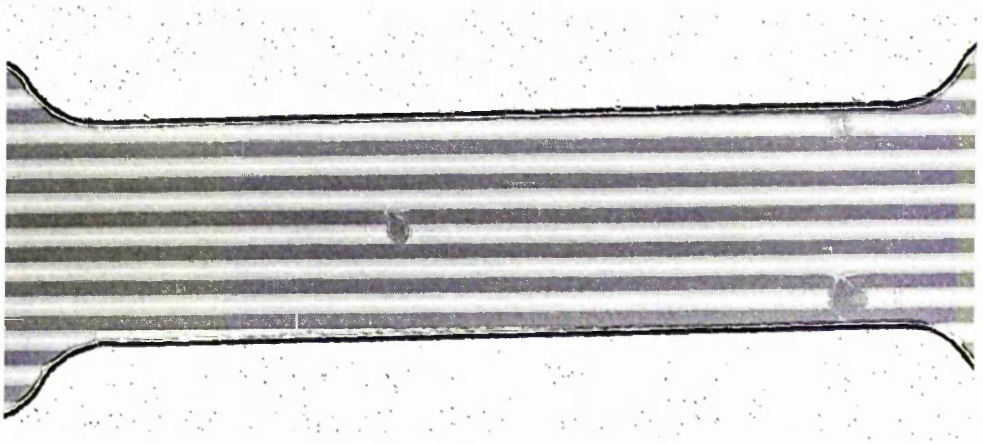

(b)

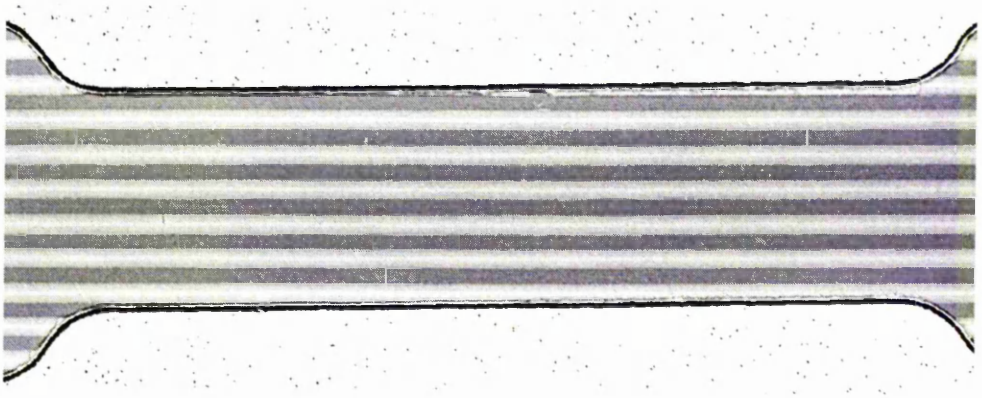

(c)

Figure 4-5. 6 μm pixel resolution radiographs showing the three samples chosen for detailed axial fibre strain measurements, exhibiting (a) two adjacent fibre defects (sample 1), (b) two isolated fibre defects in different regions of the gauge area (sample 2), and (c) no fibre defects (sample 3). The fibre diameter is 140 μm.

4.2.3. Composite microstructure

For microstructural analysis, a region was cut from the grip section of a failed sample after being tested, with the fibre direction normal to the cutting plane. The sample was polished down to a 1 μm colloidal silica suspension and subsequently etched, using Kroll's-etchant, to reveal the microstructure of the metal matrix. Figure 4-6 shows an optical micrograph of the Ti-6Al-4V coated SCS-6 fibres / Ti-6Al-4V sheet composite material after consolidation, magnifying in on two adjacent fibres. The carbon cores of the fibres and the 5 μm thick protective carbon coating on the surface of the SiC fibres are clearly visible. The difference in the microstructures of the PVD Ti-6Al-4V fibre coating and the Ti-6Al-4V sheet material can also be clearly observed. The fibre coating exhibits short α-lamellae with none of the former β grain boundaries that are usually observed in lamella microstructures of α + β titanium alloys. Adjacent to the coating, an equiaxed microstructure of the sheet material is observed. The integrity of the SiC/C/Ti interfaces appears to be good. However, small regions of poor consolidation between the fibre coating and the matrix sheet material were observed in some samples in the form of small holes or cracks, as circled in Figure 4-6, which extended down the length of the samples, as will be shown in the tomography analysis of Section 4.5.3.

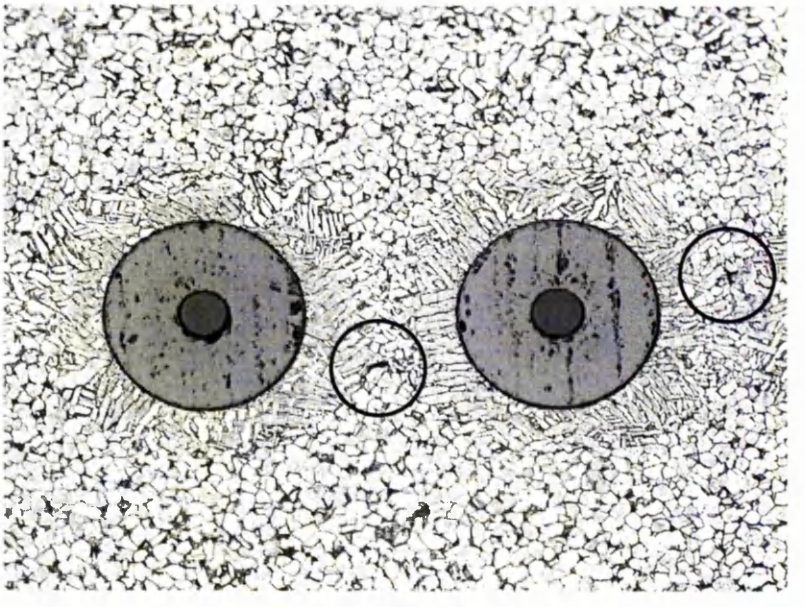

Figure 4-6. Optical micrograph of the microstructure of the consolidated composite material. The different microstructures of the Ti-6Al-4V fibre coating and sheet material are clearly observed. The fibre diameter is 140 μm.

4.3. Experimental Setup and Procedure

4.3.1. Setup of the beam line

Small changes in the Bragg angle, θ, due to the application of an external load can be interpreted as changes in lattice spacing, d_{hkl}, allowing the associated strain changes of the matrix and reinforcing phases to be inferred by diffraction. In order to measure the strain development in the SiC fibres and the Ti-6Al-4V matrix *in-situ*, a 2 kN tensile loading rig was placed with its tensile axis vertical on the sample stage of the ID11 beam line at the ESRF in Grenoble, France. Figure 4-7 shows a schematic diagram of the experimental setup on beam line ID11, and a photograph of the tensile loading rig and CCD camera.

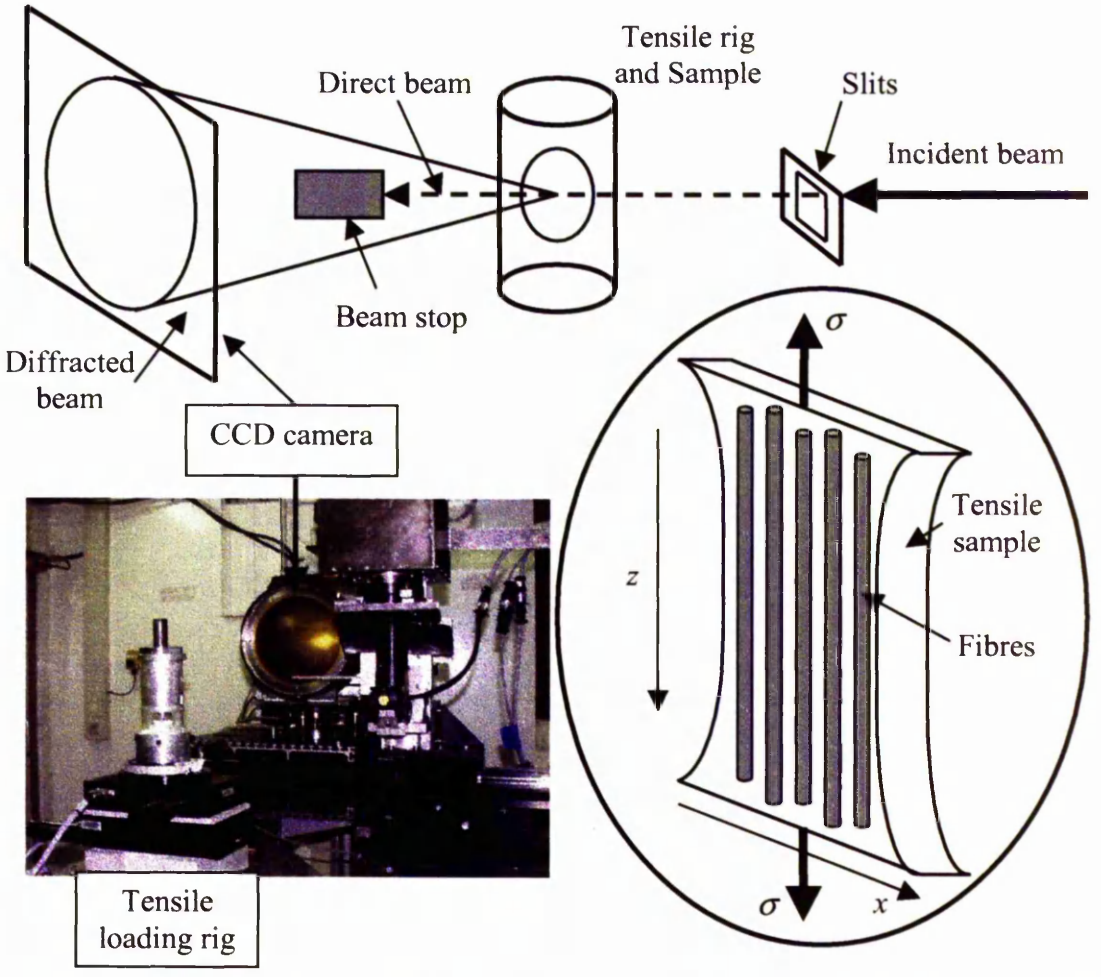

Figure 4-7. Schematic diagram of the beam line setup on ID11 at the ESRF. Also shown is a picture illustrating the tensile loading rig especially designed to allow tomography observations during loading (actually shown on ID19, but also used on ID11).

The tensile rig had been especially designed to allow the observation of damage by tomography during the deformation of materials (Buffière *et al*, 1999), but was also used for the strain scanning experiment. In order to avoid the frame of the machine obscuring the beam during the 180° rotation required for collecting tomographic data, a PMMA tube was used to transmit the load between the upper and lower grips of the tensile rig. The tube had been carefully polished to give uniform absorption for all the collected X-ray radiographs during a tomographic scan.

The radiation source for this beam line is a 24 pole wiggler which is positioned in the storage ring of the facility and has the purpose of bending the beam sharply many times to give more intense photons and thus a greater level of radiation. The measurements were made in transmission geometry. A monochromatic beam of energy 60 keV was used, resulting in a wavelength of 0.2 Å. The spot size of the beam was prescribed by the incident slits to be 75 μm in the longitudinal (z) and 120 μm in the direction transverse to the fibre axis (x). This resulted in a measurement point every 75 μm along a gauge length of 6 mm, and a beam wide enough to cover almost the entire diameter of a fibre. The tensile rig was set on an x, z automated translation stage, which was used to scan the sample through the incident beam along the line of each fibre. The x and z directions with respect to the samples are shown in Figure 4-7. The force and cross-head displacement of the tensile rig were recorded on a computer. A cross-head displacement rate of 150 μm/min was used, corresponding to an initial strain rate of 2.4×10^{-3}/s for a sample having a gauge length of 6 mm. Since the tensile rig was displacement controlled, at high loads the sample would relax slightly when the strain was maintained at a constant level. To avoid the associated stress drop, which typically occurred in the first few minutes, the measurements were started when the stress on the sample had stabilised. Entire diffraction rings were recorded on an area detector, a CCD camera (1024 x 1024 pixels) set to a camera length (distance between the sample and the camera) of approximately 600 mm. A beam stop was inserted to prevent damage of the CCD camera from the direct beam.

4.3.2. Strain mapping procedure

For each sample, prior to straining, five fibres were identified by scanning the sample across the gauge width transverse to the fibres (i.e. across x) at three different z positions and observing the appearance and disappearance of the SiC diffraction ring. Finding the positions of highest intensity enabled the x coordinate of each fibre to be obtained. The fibres were very well aligned along the tensile axis and could be scanned

along their length simply by completing a z-scan along each. To guard against any lateral movement of the sample during the loading procedure, the transverse positions of each of the fibres was also checked, in the same way, between each load step. Six load steps were typically performed for each sample, including the initial residually stressed state and an unloaded step. For each load step, 75 diffraction profiles along each fibre were measured with 75 μm steps between each measurement point. An exposure time of 10 seconds was used for data acquisition for each diffraction profile (or ring as illustrated in Figure 4-7). The complete Debye Scherrer cones were collected on the CCD camera, but only the two polar and equatorial fragments were of interest, providing the axial and transverse strains respectively. In order to improve counting statistics, the diffraction ring data were 'caked' to collapse ± 10° wide segments at the polar and equatorial zones to give simple radial (line) profiles. The centre of each peak in the radial profile was found by Gaussian peak fitting. By determining the position of two opposing poles it was possible to measure the ring diameter, D, for each load step during a complete tensile test. As a result of the application of an external load, small variations in the ring diameters, ΔD, could be translated to changes in the Bragg angle and thus lattice spacing. The strain in the fibres and matrix due to the applied load was calculated from the change in ring diameter, using:

$$\varepsilon = \frac{d - d_0}{d_0} = -\cot\theta \frac{\theta - \theta_0}{\theta_0} \approx -\frac{D - D_0}{D_0} \tag{4-1}$$

Since the embedded fibres and surrounding matrix would be expected to be initially thermally stressed (Withers and Clarke, 1998), it was necessary to deduce the 'stress-free' reference diameters, D_0, for both phases. For the SiC-reflection this was difficult to deduce, even from fibres extracted from the matrix via electropolishing. It was taken to be equal to the diameter recorded to be representative of the fibre ends (once fibre fracture had begun). With the composite under an applied tensile load, the fibre ends must be unstressed axially. However, Poisson strains might mean that this is not a true location of zero strain. The 'stress-free' reference diameters for the matrix reflections were calculated from the stress-balance model when no external stress was applied (load step 1). Since a completely 'stress-free' D_0 value was not measured for either of the phases, the term 'relative strain' is used to qualify the measurements presented. Absolute strain values are of less importance for interfacial shear stress (τ_i) determination since the rate of change of axial fibre strain ($d\varepsilon_f/dz$) is the determining quantity. Equation (3-11) (see Section 3.3.2) was used to infer the interfacial shear stress distribution from the measured strains.

4.4. Results and Discussion of Load Transfer Micromechanics

4.4.1. Strain mapping analysis

The diffraction patterns recorded on the CCD camera of the ID11 beam line comprised several rings of different diameters, each from different lattice planes of the two composite phases. Four α-Ti and one SiC reflection were measured and analysed. The considerable amount of texture in the fine-grained SiC (Nutt and Wawner, 1985) enabled analysis of only one SiC diffraction ring. Reflections (10 $\bar{1}$0), (0002), (10 $\bar{1}$2) and (11 $\bar{2}$0) of the hexagonal titanium phase and the (111) reflection of the silicon carbide phase were used for calculation of the relative strains. Since Ti-6Al-4V is a two-phase alloy with a small amount of β-phase, the (110) and (200) reflections of this phase were also observed. However, the intensity/background ratio was too poor to analyse these reflections with a reasonable uncertainty.

Figure 4-8 shows the applied stress against average axial lattice strain response for the four α-Ti and SiC reflections for the five load steps applied to this particular five-fibre single-ply sample. Only regions of uniform strain along the gauge length of a fibre were averaged, i.e. regions of peaks or troughs in the strain distribution due to defects were not included. Table 4-1 shows the resulting experimental crystalline diffraction elastic stiffnesses (diffraction elastic constants, DEC) of the matrix reflections. Averaged values are shown, considering measurements from two samples. These are compared to previously measured values for Ti-6Al-4V in the literature (Preuss *et al*, 2002; Withers and Clarke, 1998) and theoretical single crystal stiffness reference data (Noyan and Cohen, 1987; Nye, 1985). The measured stiffnesses are observed to lie between the single crystal values and the Young's modulus of the bulk material (115 GPa) for all but the $(10\ \bar{1}2)_{Ti}$ reflection. Of course, the measured value of E_{hkl} would only be expected to lie between E_{bulk} and $E_{single\ crystal}$ for loading of a single phase sample, i.e. unreinforced Ti. The presence of the SiC reinforcement should mean that $E_{hkl,\ Ti\ in\ composite} > E_{hkl,\ Ti\ unreinforced}$ due to stiffening of the matrix phase, except for very low volume fractions of fibres. In this case a $V_f \approx 0.07$ is low enough to observe the values that are shown in Table 4-1. The (0002) reflection is measured to be the stiffest, in line with the single crystal stiffnesses.

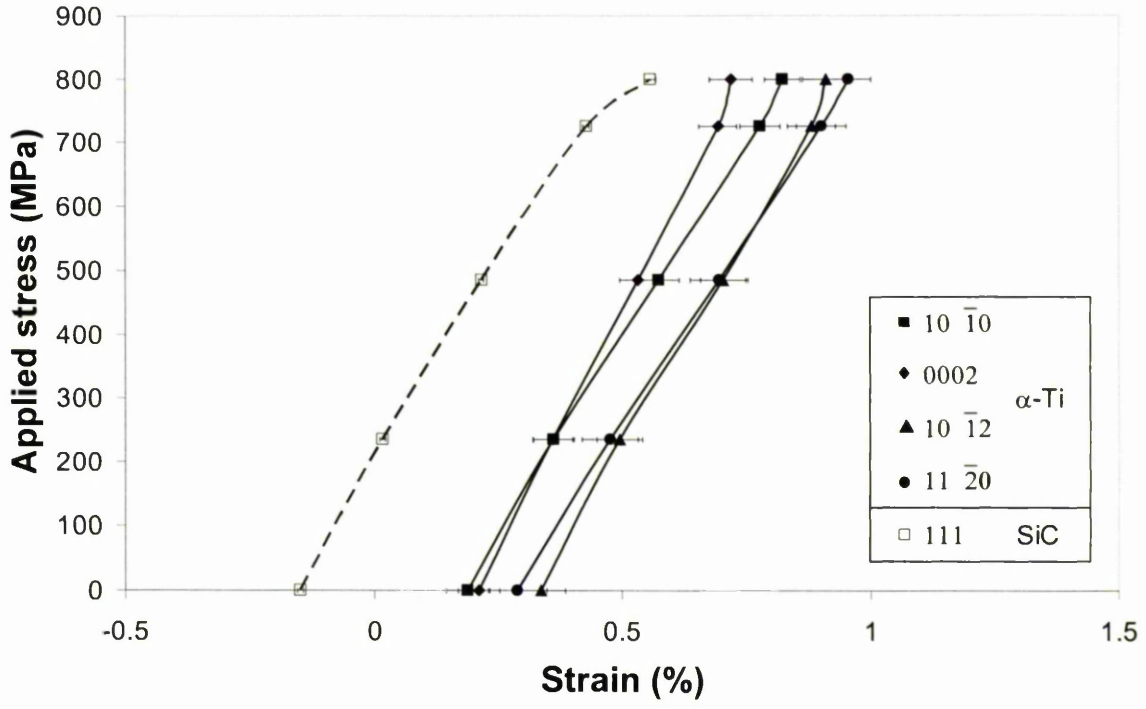

Figure 4-8. The applied stress/average axial lattice strain response for four α-Ti (solid lines) and the $(111)_{SiC}$ (dashed line) reflections measured across the gauge length during the five load steps applied to the sample. The typical uncertainty in the measured matrix strain is 0.04%, and 0.003% in the measured fibre strain.

Table 4-1. Measured axial diffraction elastic constants (all in GPa) for each Ti reflection averaged for two composite samples, as compared to previously measured values for unreinforced Ti-6Al-4V (Preuss *et al*, 2002; Withers and Clarke, 1998) and theoretical single crystal stiffnesses (Noyan and Cohen, 1987; Nye, 1985). The typical error in the measured diffraction elastic constants is ±7 GPa.

Reflection	**{10 $\bar{1}$ 0}**	**{0002}**	**{10 $\bar{1}$ 2}**	**{11 $\bar{2}$ 0}**
Experimental DEC (averaged)	111	137	111	107
Previously measured DEC for Ti-6Al-4V	104	134	108	107
Single Crystal Stiffness	103	145	118	103

Because the SiC monofilaments deform elastically and are continuous, one would expect their elastic strain behaviour to match the response of the specimen, provided the interfaces

remain intact. It can be seen in Figure 4-8 that as loading progresses into the plastic regime, which starts at ~650 MPa and results in plastic flow of the matrix, the lattice strain responses become non-linear, which is indicative of load redistribution towards the fibres. In order to maintain strain balance between fibres and matrix, it is expected that the matrix reflections become compressive, which seems to be the case for all the reflections analysed, bearing in mind that only two loading measurements were made beyond the plastic regime. The transfer of load from matrix to fibre is clear from the increase in strain of the $(111)_{SiC}$ reflection with increasing applied stress once plastic deformation of the matrix has occurred. The bulk elastic response of the matrix is to curve upwards, as seen in Figure 4-8, and reach a limiting value where further increase in load causes no increase in the internal strain, indicating decreasing share of the load. With plastic flow the elastic matrix strains begin to saturate, indicating a poor degree of strain hardening in the material.

Figure 4-8 also reveals the typical thermal residual strains that were measured in a sample before the load steps were applied. Thermal compressive axial residual strains in excess of 0.2% (-2000 microstrain) were measured in the SiC fibres (taking into account all samples measured). This is comparable to expected strains equivalent to a temperature drop, $\Delta T_{effective}$, of around 700°C, suggested by an experiment using neutron diffraction (Withers and Clarke, 1998) in the same composite system but with a fibre volume fraction of 35%, in which thermal residual strains in excess of 0.15% (-1500 microstrain) were measured. As the fibre volume fraction drops the thermal residual strains in the fibre would be expected to increase, and so the values found here agree favourably. The level of axial residual fibre strain was found to vary from sample to sample and even from fibre to fibre (as is observed in the strain profiles of Section 4.4.2). Some fibres are observed to have quite large compressive residual strains while others have very little or none at all. It is thought that this is due to variability in processing, either to the variability in the coated fibres produced by 3M or more probably to the hot-pressing process described in Section 4.2.1. As revealed in the tomographic analysis of Section 4.5.3, consolidation of the composite material was not complete during the hot-pressing process, i.e. the time allowed for hot-pressing (1 hour) was not sufficient for complete consolidation of the matrix around the fibres. This is evidenced in the form of cracks down the length of the sample between fibres, which may have lowered the residual strains in some cases. Also, the hot-pressing force may have affected the stress state during manufacture. Thermal tensile residual strains as high as 0.24% (+2400 microstrain) were measured in the matrix phase, contrasting well with the compressive strains measured in the fibres. This also agrees with

the value of 0.26% (+2600 microstrain) measured by Withers and Clarke for the $(10\ \bar{1}0)_{Ti}$ reflection.

4.4.2. Effect of fibre breaks on the strain distribution

Sample 1

The individual fibre strain distributions for sample 1 over five load steps and one unloading step are summarised in Figure 4-9. Each plot for each individual fibre shows the change in axial fibre strain recorded as a function of position along the fibre and the applied stress. In accordance with the radiograph of the sample, also shown in Figure 4-9, the strain scans reveal the effect of the holes drilled in fibres 2 and 3 at around $z = 3.5$ mm. No (111) SiC reflection is observed in this region where the laser has drilled the holes in these fibres, as indicated by the profiles falling to zero at this position (Figure 4-9). The average uncertainty in the strain measurements was 0.003%.

The strain distributions in the fibres adjacent to the defects for load steps 3, 4 and 5 reveal the extent of load transfer laterally from cracked fibres towards adjacent fibres. Table 4-2 summarises the strain concentrations measured in these intact neighbouring fibres for each of load steps 3, 4 and 5, calculated as the percentage of the measured uniform strain for the corresponding step. For load step 5, the strain concentrations are also represented as a factor of the far-field strain in the corresponding fibres (in parentheses), or SCF, as represented in the literature (Hanan *et al*, 2003; Van den Heuvel *et al*, 1997). After step 3, weak strain (stress) concentrations are apparent in the nearest neighbour fibres (1 and 4). Fibre 5, a 'next-nearest' fibre, remains unaffected after this step. The strain concentrations increase after load steps 4 and 5, and fibre 5 shows lateral load transfer at this stage, although clearly much weaker than in nearest neighbour fibres, indicating localised lateral stress transfer. Of the two nearest neighbour fibres, it is fibre 4 that takes slightly more of the load. One would expect a lower strain concentration in fibres where there are more of them able to carry load due to a greater load sharing capability. In this case, there are two fibres (4 and 5) adjacent to fibre 3, whereas only one (fibre 1) adjacent to fibre 2, but the strain concentration is higher in fibre 4. The expected effect of the load-carrying fibre imbalance is illustrated to some degree by the relative increases in strain concentration between loading steps for each of the fibres. The strain concentration increase between load steps 4 and 5 compared to that between steps 3 and 4 is much greater for fibre 1 (increases of 9% and 35% for load steps 3→4 and 4→5 respectively) than fibre 4 (17% and 29% for load steps 3→4 and 4→5).

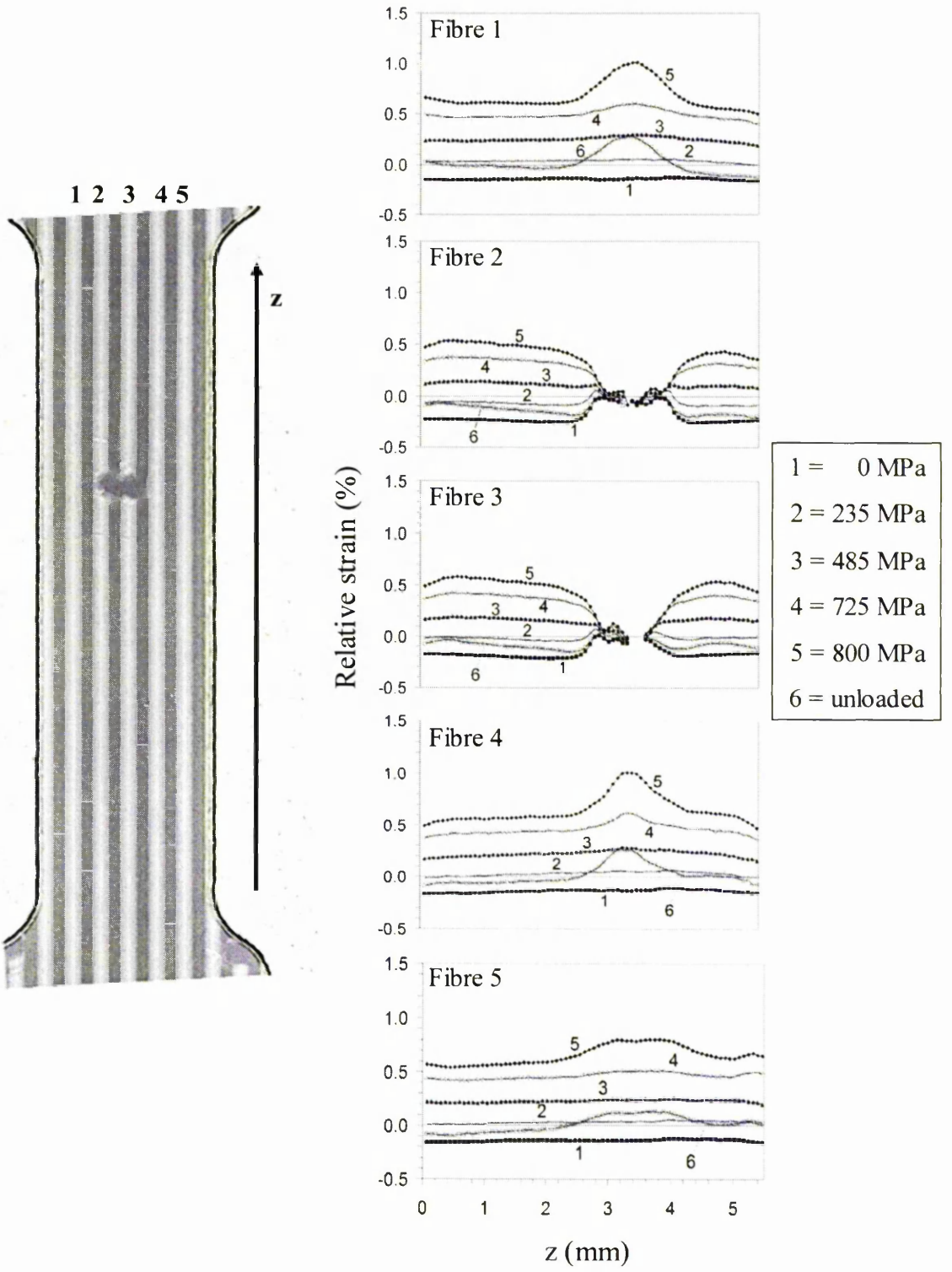

Figure 4-9. Strain profiles, measured using synchrotron diffraction, showing the variation in the longitudinal strains along the five fibres of sample 1, as indicated in the radiograph, for five load steps and one unloading step. Fibres 2 and 3 were damaged at $z = 3.5$ mm.

Table 4-2. Strain concentrations measured in the intact neighbouring fibres to the defects of sample 1 for load steps 3, 4 and 5, calculated as the percentage of the measured uniform strain for the corresponding step. Those for load step 5 are also represented as a stress concentration factor (SCF), or the peak strain as a factor of the far-field value.

Loading Step	Fibre 1	Fibre 4	Fibre 5
3	11%	14%	0%
4	20%	31%	10%
5	55% (1.68)	60% (1.72)	29% (1.42)

Regarding the strain concentration peaks in fibres 4 and 5 for load step 5, illustrated together in Figure 4-10, the peak is much flatter in fibre 5 and dips slightly in the middle by about 0.016% (160 microstrain). This is in contrast to the adjacent, nearest neighbour fibre, fibre 4, for which the strain concentration peak is sharper over the same region (between $z = 3$ and 3.8 mm, overall peak broadness between $z = 2.5$ and 4.4 mm). The rate of change of fibre strain is higher in the centre of the peak, compared to the outer region of the overall peak, showing that fibre 4 is taking a higher proportion of the load in this small region as opposed to the load being extended to fibre 5.

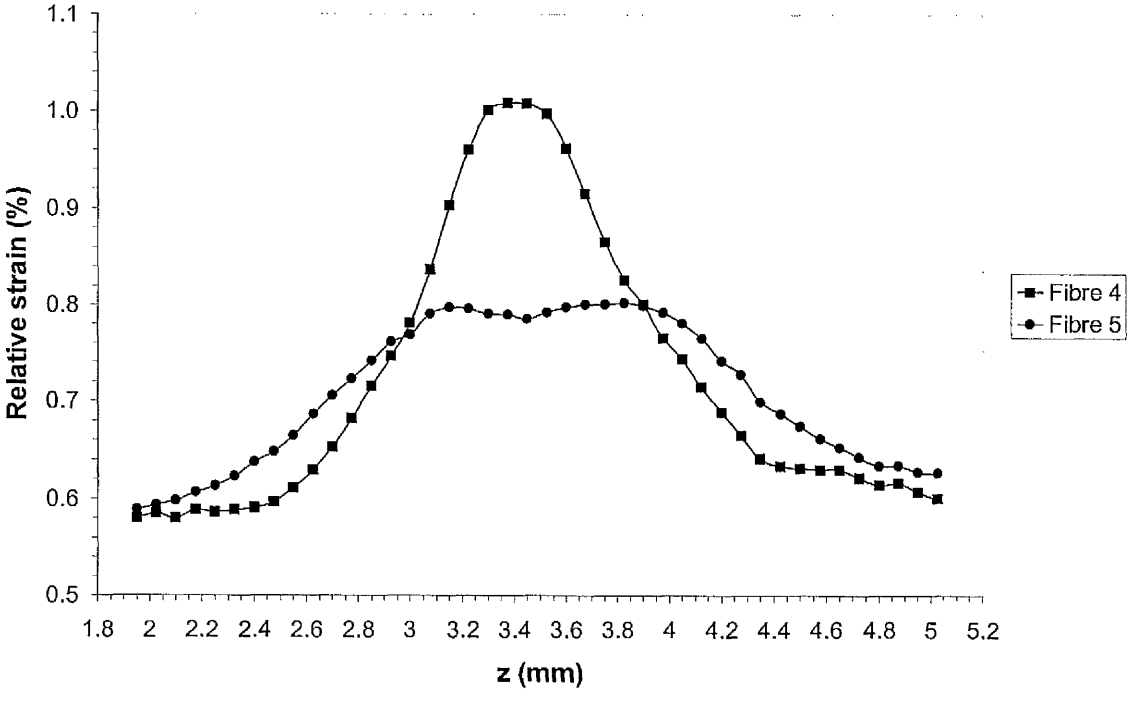

Figure 4-10. Measured strain profiles, taken from Figure 4-9, showing the strain concentration peaks in fibres 4 and 5 of sample 1, as indicated, for load step 5.

During the incremental loading experiment, an unloading step (6) was also monitored. The residual strains differ significantly from those observed originally for step 1. In the two nearest neighbour fibres (1 and 4) the effect of lateral load transfer from the cracked fibres has been to leave these fibres in residual tension and still carrying a concentration of strain over the exact same fibre region as that measured for load step 5. The peak height for the unloading step of fibre 1 is about 0.31% (3100 microstrain) compared to 0.41% (4100 microstrain) after load step 5. The corresponding values for fibre 4 are 0.3% (3000 microstrain) and 0.42% (4200 microstrain), and showing that the residual concentration of strain is about 0.1% (1000 microstrain) lower than that with the applied load. This suggests evidence of fibre slippage during unloading, resulting in the small relaxation in the unloaded strains from the loaded state (see Section 4.4.5 for representative interfacial shear stress values). This marked tensile shift for the unloaded strains of fibres 1 and 4, compared to those observed originally for step 1 and consistent with the presence of the defects in fibres 2 and 3, suggests a significant plastic strain to have occurred in the neighbouring matrix.

Sample 2

The corresponding fibre strain distributions for sample 2 are summarised in Figure 4-11. The radiograph of this sample, also shown in Figure 4-11, reveals this to be another sample containing two fibre defects but at different positions along the gauge length. The strain scans reveal these to be at around $z = 0.4$ mm in fibre 1 and $z = 3.5$ mm in fibre 3.

Regarding first the defect at $z = 3.5$ mm in fibre 3 of sample 2, Table 4-3 summarises the strain concentrations (and SCF values) measured in the neighbouring fibres for load steps 3 and 4. After load step 3, strain concentration is apparent only in fibre 4, while the strain in fibre 2 remains unaffected. After step 4, strain concentrations are apparent in all the fibres. This suggests that the matrix has plastically deformed heterogeneously across the whole gauge width at this axial position. Strain concentration is largest in nearest neighbour fibres, as observed for the previous sample. After further straining (step 5) all of the fibres have failed at approximately $z = 3.5$ mm, the axial position of the break in fibre 3, due to the concentration of strain at this position. This is presumably triggered by failure of fibre 4 first, which is most highly strained in tension (1.1%).

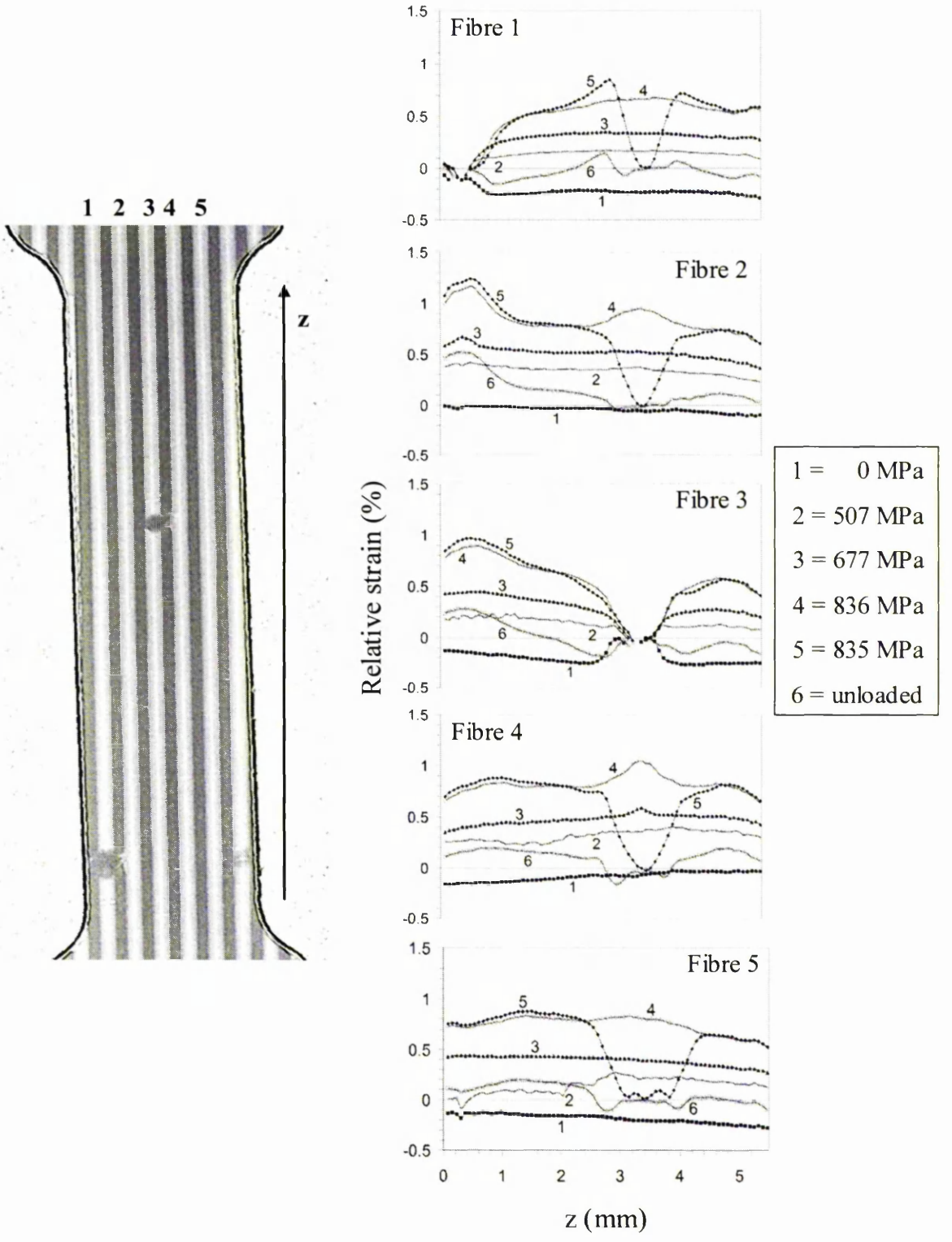

Figure 4-11. Strain profiles, measured using synchrotron diffraction, showing the variation in the longitudinal strains along the five fibres of sample 2, as indicated in the radiograph, for five load steps and one unloading step. Fibre 1 was damaged at $z = 0.4$ mm and fibre 3 at $z = 3.5$ mm.

Table 4-3. Strain concentrations measured in the intact neighbouring fibres to the defect of fibre 3 of sample 2 for load steps 3 and 4, calculated as the percentage of the measured uniform strain for the corresponding step. SCF values are also shown for load step 4.

Loading Step	Fibre 1	Fibre 2	Fibre 4	Fibre 5
3	0%	0%	12%	0%
4	11% (1.16)	22% (1.23)	30% (1.33)	6% (1.07)

The strain profile of fibre 5 for load step 5, illustrated in Figure 4-12 along with that of fibre 4, is indicative of three closely spaced fractures, as opposed to one fracture in fibre 4. These fractures, at z = 3.1 mm, 3.4 mm and 3.8 mm, are too close together to each have occurred at the original failure strain, according to full-fragmentation theory and the inability for the strain in the fibre to build up to such a level so as to cause failure. This indicates that either they formed in one fracture event, or alternatively that the initial fracture process damaged the fibre leading to a much lower subsequent fracture stress.

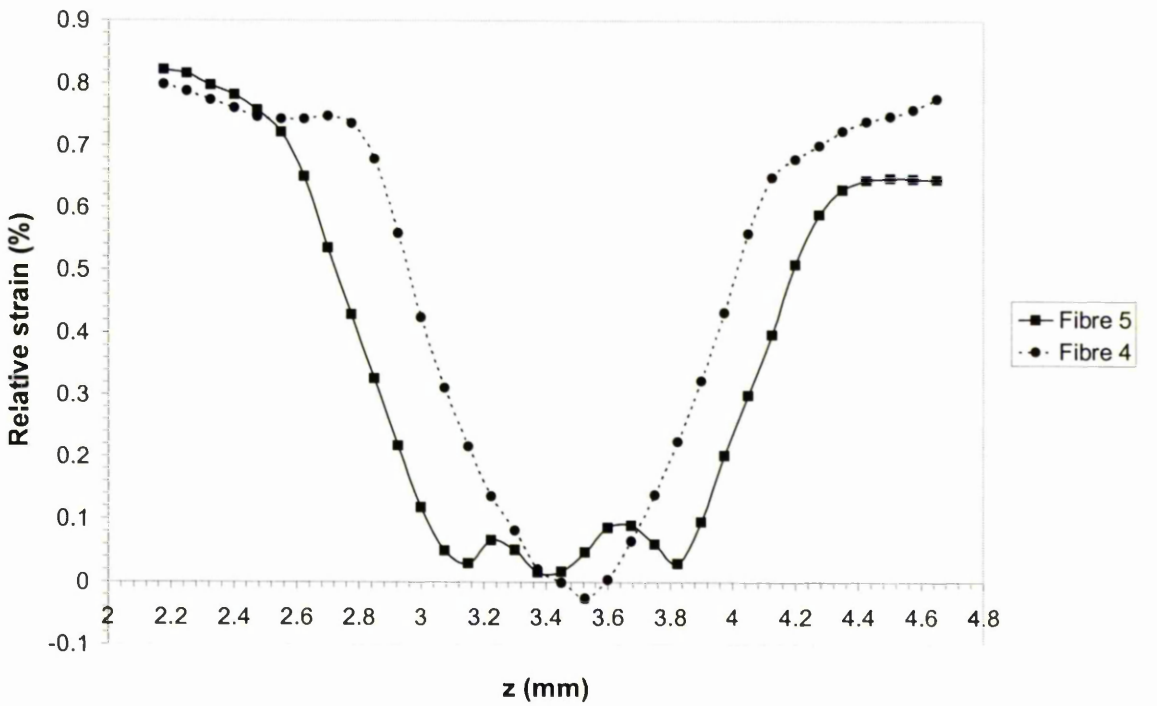

Figure 4-12. Measured strain profiles, taken from Figure 4-11, showing the strain distribution at the fracture position in fibre 5 (three closely spaced fractures, solid line) compared to that of fibre 4 (one fracture, dashed line) in sample 2, for load step 5.

This observation is in agreement with a study of successive fracture during full fibre fragmentation testing (Preuss *et al*, 2002). They observed that, subsequent to the initial fracture, prior to which the elastic strain experienced by the SiC fibre exceeded 1.5%, further fibre fracture appeared to occur at much lower elastic strains and not necessarily at locations of maximum strain. This is presumably because the initial fracture event caused surface damage to the fibre and lowered the subsequent fibre failure stress from around 5800 MPa to around 0.5% × 400 GPa = 2000 MPa. During fragmentation it was found that in some steps single cracks were introduced, whereas in others a number of closely spaced cracks occurred. Similar multiple fracture events have also been reported elsewhere (González and Llorca, 2001; Majumdar *et al*, 1998). Local successive fracture events observed by Majumdar *et al*, spaced sufficiently long in time to discount any dynamically linked events, suggested possible fibre damage along the length of the fibre close to a fibre break, possibly through damage of the coating and the reaction zone. Also noted from Figure 4-12 is the same rate of increase of fibre strain from the fracture positions, despite the difference between the fracture events in the two fibres (see Section 4.4.5 for extraction of representative interfacial shear stress profiles and values).

Regarding the effect of the defect in fibre 1 at $z = 0.4$ mm, Table 4-4 summarises how far the strain concentrations extend to the four neighbouring fibres for load step 3 and the average of steps 4 and 5. After load step 3, strain concentration is only apparent in fibre 2. With increased straining the strain concentration broadens considerably and extends from fibre 2 laterally to fibre 3 and, to a small degree, fibre 4. Fibre 5 remains unaffected for the load steps that were measured. Despite the large tensile strain (1.24% strain) recorded for fibre 2 in this region, fibre fracture does not occur here. Note that the difference between the stress concentrations represented as SCF values for fibres 2 and 3 is smaller than when they are represented as a percentage of the measured uniform strain. A possible reason for this is that the latter takes into consideration the residual strain in the fibres, which is significantly different between these two fibres and also varies along the fibre length (Figure 4-11). The SCF values (in parentheses) are calculated as a factor of the far-field strain under load only in the respective fibre for the particular load step under consideration, and is thus a more representative measure of stress concentration. Also, perhaps more importantly, for the calculation of the stress concentration in fibre 3 it was difficult to define the far-field strain in the fibre due to the presence of a defect and a decrease in strain as soon as it fell away from the peak in the concentration. This strain was taken at the mid-point between the two.

Table 4-4. Strain concentrations measured in the intact neighbouring fibres to the defect of fibre 1 of sample 2 for load step 3 and the average of steps 4 and 5, calculated as the percentage of the measured uniform strain for the corresponding step. SCF values are also shown for the average of load steps 4 and 5.

Loading Step	Fibre 2	Fibre 3	Fibre 4	Fibre 5
3	20%	0%	0%	0%
4 and 5 (average)	51% (1.53)	29% (1.45)	6% (1.05)	0%

In order to compare the stress concentrations measured in the two samples, Figure 4-13 shows the SCF values, i.e. stress concentrations represented as factors of the far-field strain (given in parentheses in Tables 4-2, 4-3 and 4-4), in the intact neighbouring fibres adjacent to defects, for the final load step applied to each sample. The distance from a defect is represented in terms of fibres so that '1' refers to nearest neighbours, '2' refers to next nearest, and so on. Due to the defect configurations, only 3rd and 4th neighbouring fibres were present for the defect of fibre 1 in sample 2, and where there were two nearest neighbours, for example in sample 1, the average value is plotted.

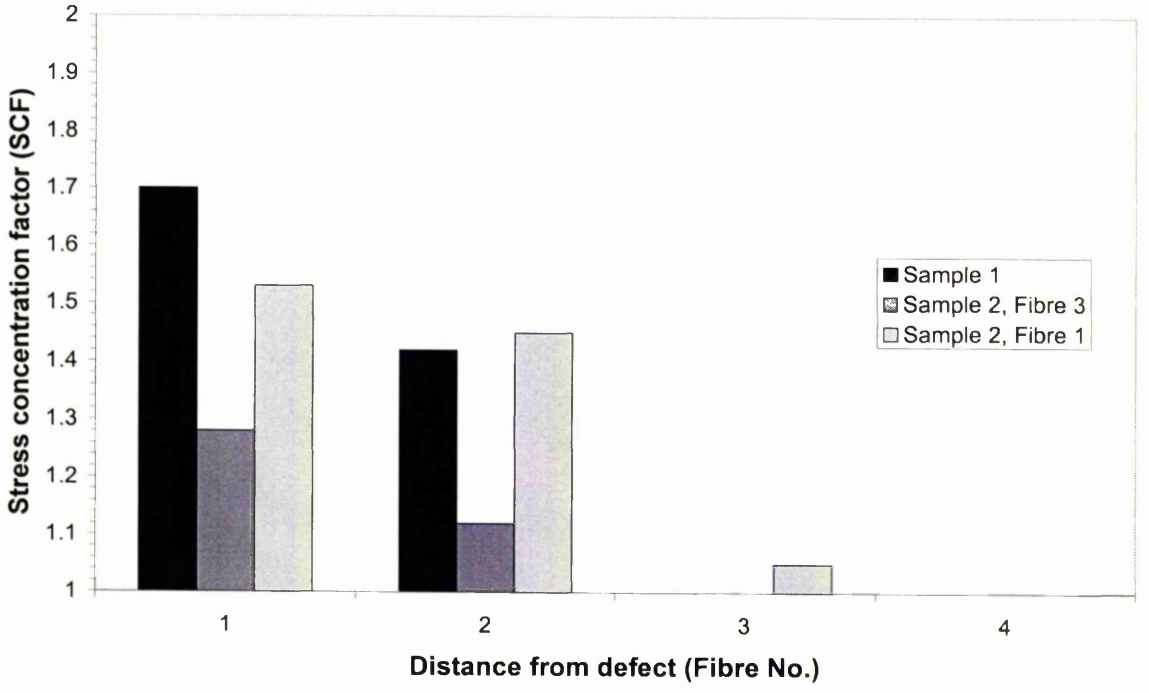

Figure 4-13. Chart illustrating and comparing the SCF values in the neighbouring intact fibres of both samples, the distance represented as the number of fibres from that containing a defect.

A number of observations are noted from the plot of Figure 4-13. Regarding the two defects of sample 2, the strain concentrations for both nearest neighbour and next nearest fibres are much larger at the position of the z = 0.4 mm defect (fibre 1) compared to the one at 3.5 mm (fibre 3). This is presumably due to the fact that the load is shared in both directions for the latter due to the defect being in the centre fibre (3), whereas for the former the load could only be shared one way. Strain concentration is largest in nearest neighbour fibres for all sample/defect cases, indicating the importance of such fibres in bearing the externally applied load in the presence of defects, and thus two nearest neighbours (fibre 3) share the load borne by the one adjacent to fibre 1. The same effect also explains the larger SCF observed in the next nearest fibre relative to the defect of fibre 1. The SCF values exhibited by sample 1 are significantly larger than those measured adjacent to the defect of fibre 3 in sample 2, even though there is still two nearest neighbour fibres relative to the two adjacent fibre defects. A possible suggestion for this lies with the fact that there are fewer fibres able to carry the load (compared to the one defect in sample 2 at the z = 3.5 mm position) thus increasing the concentration of stress. Regarding the effect of the defect in fibre 1 of sample 2, the stress situation 4 fibres away was found not to be influenced by the defect, which equates to a distance of about 6-7 fibre diameters. The fact that fibres closest to the defects in both samples experience the highest stress concentration indicates a local load sharing (LLS) mechanism of failure.

In comparing the stress concentration factors measured here with studies reported in the literature, this concentration of stress in nearest neighbour fibres is in agreement with the modelling results of Gonzalez and Llorca (2001) and Beyerlein and Landis (1999) and experimental results of Hanan *et al.* (2003). In terms of the experimental work carried out and the composite system used, the study of Hanan *et al.* is very similar. The specimen morphology consisted of a single-ply of 30 unidirectional SCS-6 SiC fibres, each 140 μm in diameter with an average centre-to-centre spacing of 240 μm, in a Ti-6Al-4V matrix (average fibre volume fraction of 32%). The two centre fibres were cut such that stress redistribution under an applied load of 850 MPa, measured using X-ray diffraction, revealed a strain concentration factor (SCF) in nearest neighbour fibres of ~1.4. The SCF in the next-nearest neighbours was no greater than 1.1. This is compared to SCF values measured here, having been calculated through normalisation of the maximum strain with respect to the far field strain in the fibre for comparison purposes (and shown in parentheses in Tables 4-2, 4-3 and 4-4), of up to ~1.7 in nearest neighbours and ~1.4 in next-nearest fibres. These values are for sample 1 with two adjacent defects at an applied

load of 800 MPa. When considering those of sample 2 as well, the results become more comparable. Adjacent to the defect in the centre fibre (fibre 3) a SCF of ~1.3 was measured in nearest neighbour fibres and ~1.1 in next-nearest (for an applied load of ~830 MPa). Note that for the calculation of these SCF values for comparison purposes, both here and in the study of Hanan *et al*, the initial residual lattice strains have been subtracted from the total lattice strains due to the applied stress.

Between the two samples for which stress redistribution has been observed (1 and 2), a significant variation in SCF values has been measured, but there is good agreement with Hanan *et al* in that strain is concentrated in nearest neighbour fibres. The fibre volume fraction in the specimens of the study by (Hanan *et al*, 2003) was significantly higher than that of the specimens used here, 32% compared to 7%, and suggests why the measured SCF values, especially for sample 1, are significantly higher. The SCF will depend on the number of fibres in the ply and the number of broken fibres since this determines the level of local and global load sharing. One would expect a lower strain concentration when there are more fibres able to carry load. The fact that the measured results of Hanan *et al.* agree very well when compared with the 'matrix stiffness shear lag' model of Beyerlein and Landis (Beyerlein and Landis, 1999) suggests that the SCF values of sample 1 would be comparable with a larger fibre volume fraction. The work of Beyerlein and Landis found the peak fibre stress concentrations to decrease as the fibre-to-matrix stiffness ratio increased. Also, it was found that as the number of fibre breaks increased, the change in the peak stress concentration increased with the change in stiffness ratio. This suggests a dependence of the SCF on the number of broken fibres, as has been observed between samples 1 (two centre defects) and 2 (1 centre defect) of Figure 4-13. Again, this would be dependent on the number of fibres in the ply. Hanan *et al.* also measured the axial strain in the broken fibres to build up to the far field value, which is effectively the sliding distance of the fibre/matrix interface, over a distance of ~1 mm which agrees well with that measured here (up to ~0.8 mm). Note that the centre-to-centre fibre spacing, another parameter that determines load transfer to intact fibres from neighbouring breaks, is the same as in the work of (Hanan *et al*, 2003).

Work regarding the extent of stress concentration in fibre/epoxy systems, carried out using Raman spectroscopy to evaluate the zone of influence of a damaged fibre, is in good agreement (Mahiou *et al*, 1999; van den Heuvel *et al*, 1997). van den Heuvel *et al* found the strain in fibres adjacent to a break to be concentrated largely in nearest neighbours, as observed here. Investigation of the effect of fibre spacing on the strain

concentration in fibres neighbouring a break found that at small inter-fibre spacings, the large stress concentrations present in adjacent fibres (SCF value of 1.26) initiated fibre fracture (van den Heuvel *et al*, 1997). This interacted fibre failure resulted in the alignment of the fibre breaks, exactly as observed here for sample 2. At large inter-fibre spacings the stress concentrations were very small and the occurrence of coordinated fibre failure was little, resulting in a more random failure. This is in agreement with the work of Beyerlein and Landis, with an increase in the inter-fibre spacing analogous to the investigated increase in the fibre-to-matrix stiffness ratio (Beyerlein and Landis, 1999). The stress situation in a fibre at a distance of 9 fibre diameters away from a fibre break was found not to be influenced by this break, and a transition from coordinated fibre failure to random fibre failure occurred. This infers that a similar observation would be expected here due to the concentration of strain in nearest neighbours.

4.4.3. Fibre cracking and reverse sliding

The fibre strain distributions for the final sample chosen for detailed analysis, sample 3, are summarised in Figure 4-14. The radiograph, also shown in Figure 4-14, reveals no laser-drilled fibre defects within the gauge region.

On loading up to step 5 the strain profiles show fibres 1, 3, 4 and 5 to have fractured at the same position along the gauge width at $z = 2.4$ mm. Only fibre 5 shows a strain concentration for the preceding loading steps prior to fibre fracture, but only 8% of the uniform strain. This strain concentration is possibly due to a fibre defect present in the adjacent edge fibre that was cut during machining of the specimen. Fibre 1 has also fractured at $z = 4$ mm whereas none of the other fibres have at this position, and this has created a fibre fragment 1.6 mm in length with a characteristic strain distribution over this length as observed in fibre fragmentation studies (Preuss *et al*, 2002; Huang and Young, 1994). The measurements suggest a failure strain in excess of 1.2%, in agreement with the results of (Laffargue and Bowen, 2001) who observed a mean failure strain of 1.4% for 10mm gauge length fibres. As indicated by the strain profiles, fibre 2 is observed to be carrying no load at all during the incremental loading steps due to it having fractured into many pieces, presumably during composite fabrication. The profile at zero load (step 1) reveals a number of fragments each showing a compressive thermal residual stress, further illustrating that the fibre had fragmented prior to the loading experiment. Tomographic analysis confirms the fragmentation of this fibre (see Section 4.5.3.2). Fibre 3 shows the presence of two cracks close together at the primary fracture position, separated by 0.4

mm, similar to the multiple fracture event observed in fibre 5 of sample 2. This is again observed in the tomographic analysis (see section 4.5.3.2).

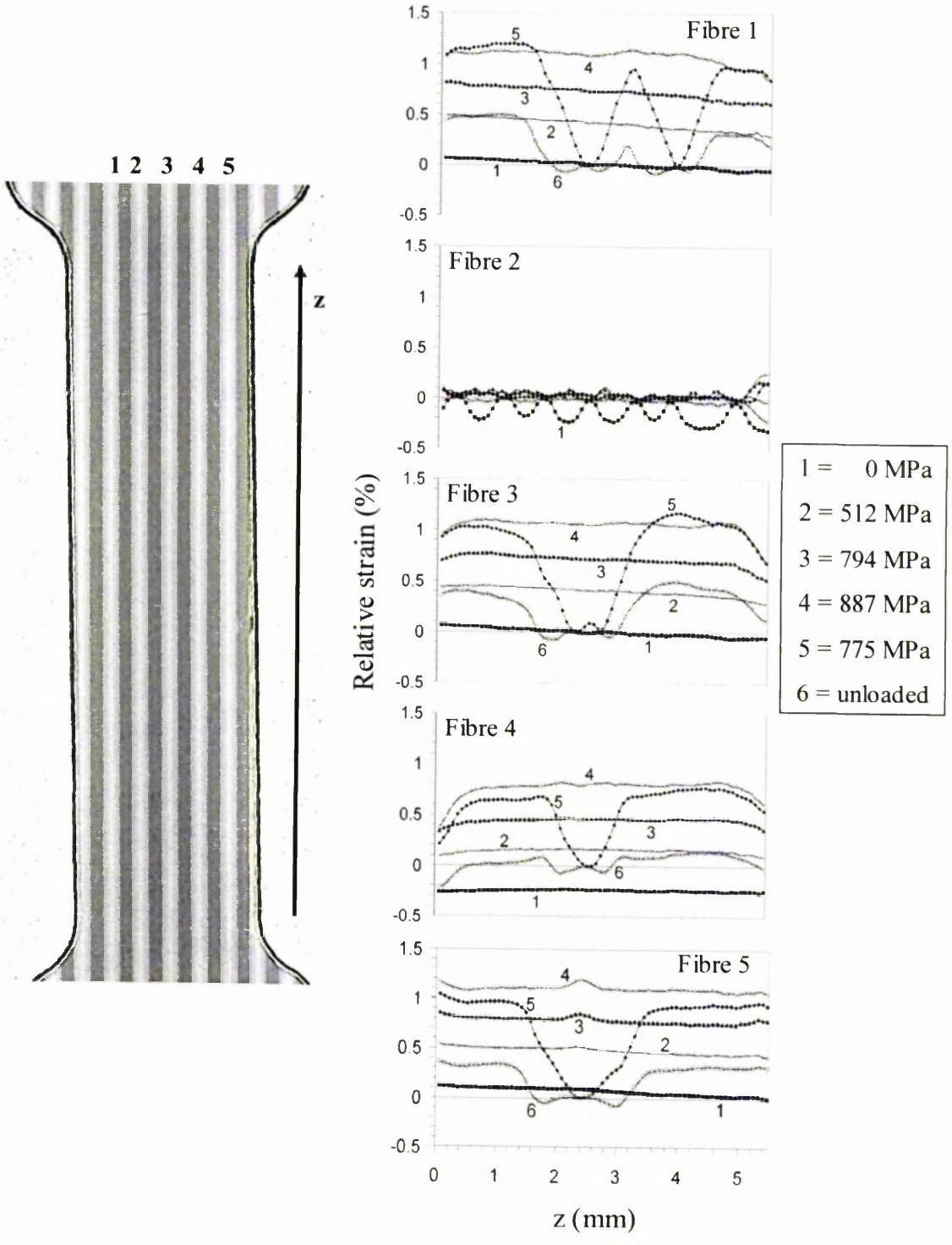

Figure 4-14. Strain profiles, measured using synchrotron diffraction, showing the variation in the longitudinal strains along the five fibres of sample 3, as indicated in the radiograph, for five load steps and one unloading step.

It is interesting to note that fibre 5, the strain profile for which is shown in Figure 4-15, shows a distinct change (increase) or 'kink' in the rate of change of fibre strain with axial fibre position at the point z = 3.1 mm, as shown highlighted in Figure 4-15. This gives some important information about what is happening at the fibre/matrix interface and is possibly indicative of a transition from frictional sliding in a debonded region to a 'still bonded' elastic region. (See Section 4.4.5 for a detailed analysis of interfacial behaviour and for extraction of representative frictional sliding interface stresses for these fibres).

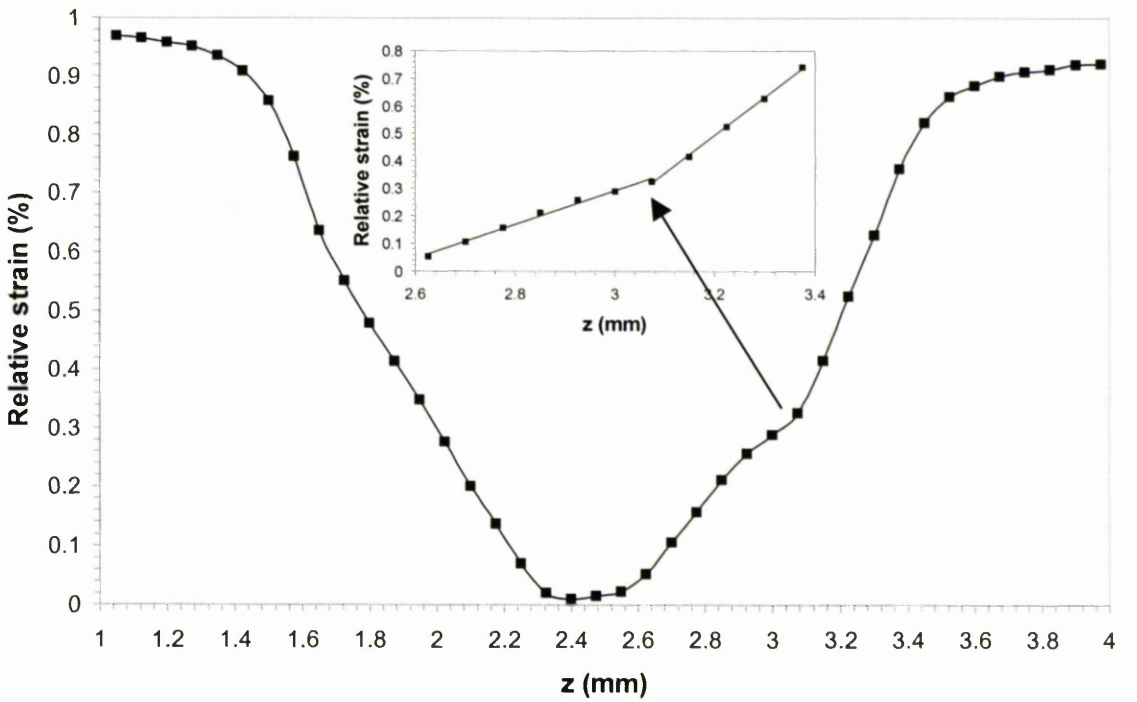

Figure 4-15. Measured strain profile, taken from Figure 4-14, showing the strain distribution at the fracture position in fibre 5 of sample 3, for load step 5. Inset: a highlighted region of the distinct change in the rate of change of fibre strain.

As illustrated in the strain profiles of samples 2 and 3 (Figures 4-11 and 4-14 respectively), differences in the residual strains after unloading were observed, as compared to the initial thermal residual strains, depending on the position relative to a fibre fracture. An example of such a profile is shown in Figure 4-16 for the region of the fracture at z = 2.5 mm in fibre 1 of sample 3, and is observed as a characteristic 'W'-shaped profile (solid line). It is shown together with the corresponding section of the profile for the preceding load step, when the fibre fractured (dashed line). In regions further away from the fibre fracture (> 500 μm), and therefore in regions that have strained

uniformly, the fibre fragments are in residual tension relative to the level of thermal residual strain. This is because the neighbouring matrix has been plastically extended conferring a tensile stress to the fibre. Note that this tensile shift is even more marked in fibres 2 and 3 of sample 2 towards z = 0 mm, suggesting that a more plastic strain has occurred in this region consistent with the presence of the defect in fibre 1 and some resultant plastic bending. This is similar to that observed in fibres 1 and 4 of sample 1 in the region of the defects in fibres 2 and 3. In the vicinity of the fracture, however, the fibre strains reverse into compression.

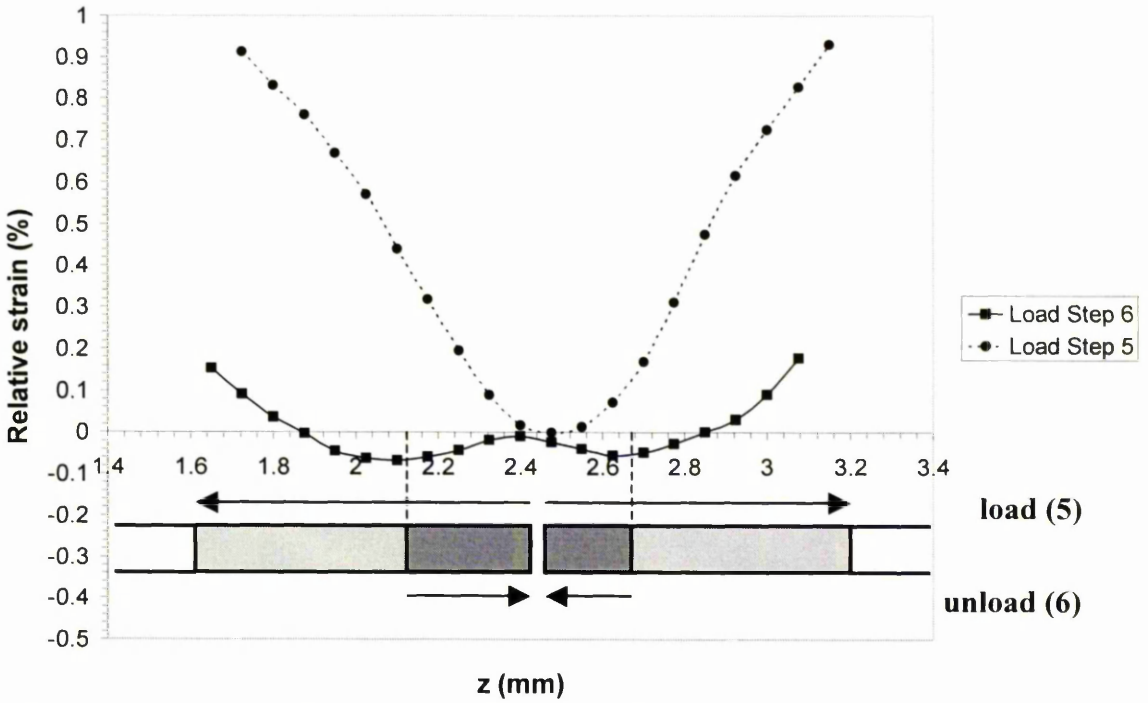

Figure 4-16. Measured strain profiles showing the strain distributions at the fracture position at z = 2.5 mm in fibre 1 of sample 3 for load steps 5 (dashed line) and 6 (unloaded, solid line). The unloaded profile is observed as a characteristic 'W' profile, its shape explained with help from the schematic showing forward and reverse sliding lengths.

The schematic diagram of the fibre shown underneath the fibre strains in Figure 4-16 helps to explain this observation. Under applied load, forward sliding occurs progressively away from the fibre ends over a length of approximately 750 μm (see the interfacial analysis of Section 4.4.5), represented by the lighter grey region in the schematic (which extends from the fibre ends). When the load is removed reverse sliding takes place in the immediate vicinity of the fibre ends over a length of ~300 μm (represented by the darker grey region

in the schematic), putting this region into compression. The remainder of the previously forward sliding interface reverts to a sticking state, this region being referred to as a 'slip-stick' region, i.e. an interface which has previously been sliding, but is now sticking. Results of finite element modelling which predict reverse sliding and mimic this effect have helped to understand this observation and are consistent with this interpretation (Rauchs *et al*, 2002). This observation of the characteristic 'W' profile is consistent with measurements carried out during fragmentation of a single fibre sample of the same composite system (Preuss *et al*, 2002; see Section 3.4.3). Bennett and Young, who studied fibre bridging of high performance fibres in a brittle matrix, also observed compressive strains in the fibre after unloading (Bennett and Young, 1998). They found that matrix crack closure during unloading resulted in reverse sliding of the fibres in the debonded region and that the reverse sliding followed a 'slip-stick' type pattern, with sticking points occurring consistently at each level of crack closure. The micromechanics of unloading resemble that originally envisaged by Marshall (Marshall, 1992).

4.4.4. Matrix response to incremental loading

Selected axial matrix strain distributions for the incremental loading stages applied to each of samples 1, 2 and 3 are summarised in Figure 4-17(a)-(c) respectively. As a hexagonal material, titanium might be expected to generate considerable intergranular strains (Pang *et al*, 1999) and thus exhibit marked plastic anisotropy, i.e. the shifting of the residual strains with plastic strain (Bache *et al*, 1998). The $(10\ \bar{1}0)_{Ti}$ reflection is analysed in what follows (Figure 4-17) because previous work in bulk Ti-6Al-4V (Withers and Clarke, 1998) has suggested that it has the least sensitivity to plastic anisotropy, even at large plastic strains. For example, the study of Withers and Clarke found both the (0002) and $(10\ \bar{1}1)$ reflections to be sensitive to the extent of plastic straining, evidenced by the curvature of the responses at high loads and the residual strains upon unloading. This arises from the generation of plastic misfits and hence stress between neighbouring grains. It is potentially more severe in hexagonal materials than cubic ones because of the limited number of slip systems available for the maintenance of plastic strain compatibility. The strain distributions of each sample in Figure 4-17(a)-(c) show the same load steps as indicated for the corresponding fibre strain profiles in Figures 4-9, 4-11 and 4-14 respectively. The average uncertainty in the strain measurements was 0.04%.

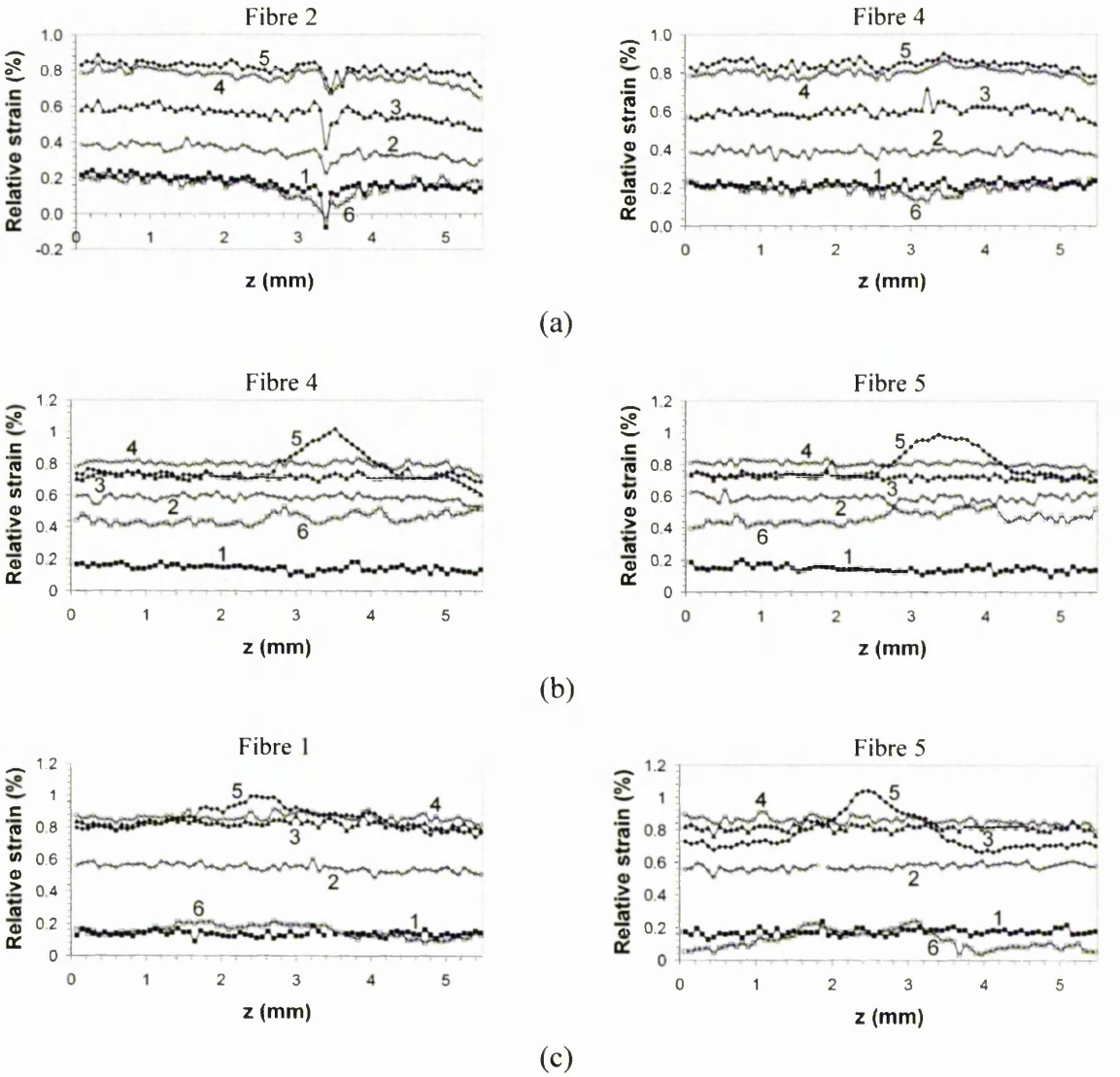

Figure 4-17. Development of the axial matrix strain measured for the (10 $\bar{1}$0) reflection, neighbouring, respectively, (a) fibres 2 and 4 of sample 1, (b) fibres 4 and 5 of sample 2 and (c) fibres 1 and 5 of sample 3.

After fibre fracture occurs, such as in sample 2 (Figure 4-11) and sample 3 (Figure 4-14), pronounced maxima are observed in the matrix strain distributions for load step 5, near the fibre failure locations. No strain maxima are observed for the preceding load step, prior to fracture. An increase in the matrix strain is to be expected due to the matrix having to bear the entire load locally in the regions where the fibre has cracked. In sample 3 all fibres fractured at the same point ($z \approx 2.4$ mm) and the two matrix strain profiles shown for this sample (Figure 4-17(c)) observe a local concentration in this region. Fibre 1 of sample 3 also fractured at the same load step at $z \approx 4$ mm, but only a small degree of strain

localisation is measured in the matrix at this point (19% of the uniform strain compared to 28% for the strain concentration at $z \approx 2.4$ mm). A strain concentration of 55% is measured for the matrix strain maximum neighbouring fibre 5 of sample 3 (Figure 4-17(c)), much higher than that measured for fibre 1. The two matrix strain maxima of fibre 1 can also be observed as one very large broad peak with a lower strain concentration compared to that of fibre 5. The matrix maximum of neighbouring fibre 5 seems to show two levels of strain corresponding to the change in the rate of change of fibre strain with axial fibre position observed in the strain distribution of this fibre (Figure 4-15). The two matrix strain profiles of sample 2, Figure 4-17(b), show strain concentrations of 55% and 43% for measurements along fibre 4 and fibre 5 respectively. This difference could possibly be due to the fact that fibre 4 is a nearest neighbour to the fibre with the original defect and thus the more load borne by the nearest neighbour fibre over the next nearest is also borne by the neighbouring matrix. The fracture of fibre 5 of sample 2 showed several closely spaced fractures (Figures 4-11 and 4-12) and the strain peak of the neighbouring matrix is observed to be much broader than that of fibre 4, for example, corresponding to the multiple fracture region. Note that the matrix strain distributions of sample 1 show no strain localisation due to the absence of any fibre fractures during the loading of this sample.

The relative strain peaks observed in the matrix for samples 2 and 3 would be expected to be less pronounced, compared to those in the fibres, due to the nature of how the X-ray measurements were carried out (in transmission). The results provide a through-thickness average of the strain along the line of sight including the fibre. The matrix volume fraction (93%) is much higher than the fibre volume fraction (7%) which, combined with the fact that the matrix stress would be expected to vary with radial position, would tend to level out the local matrix strain peaks. Large variations in the $(10\ \bar{1}0)$ matrix strain during single fibre fragmentation testing of the same fibre/matrix system have been measured (Preuss *et al*, 2002). Finite element modelling (Rauchs *et al*, 2002) indicated that the observed load repartitioning would lead to relatively small variations in matrix strain, such as those measured by Preuss *et al* for the (0002) matrix reflection. The origin of the large measured variations is believed to be due to the generation of tensile intergranular strains as a result of the increased local matrix plasticity occurring in the fibre fracture regions (Withers and Clarke, 1998). Majumdar *et al* showed this localised matrix plasticity to be responsible for the cumulative failure of fibres due to a one-to-one correspondence between slip band intersections with the fibres and the fibre

break locations (Majumdar *et al*, 1998). Subsequent fibre breaks were observed to form as the slip bands from existing fibre breaks impinged on an adjacent fibre.

4.4.5. Interfacial shear strength analysis

For weakly bonded systems, i.e. systems for which the interface shears before matrix yielding, stress transfer between fibre and matrix takes place by a combination of frictional shear stress transfer in debonded regions and elastic shear stress transfer in bonded regions. For the single fibre fragmentation test, elastic and debonding theories based on the shear lag model were proposed by Piggott to predict the distribution of fibre strain and interfacial shear stress, τ_i, in embedded fibres (Piggott, 1980). These models have been shown to fit data well when compared with point-to-point strain distributions, such as those measured using various techniques such as Raman and fluorescence spectroscopy (Bannister *et al*, 1995; Bennett and Young, 1998) and synchrotron strain mapping (Maire *et al*, 2001; Preuss *et al*, 2002). The theories and models have subsequently been modified (Bannister *et al*, 1995; Lacroix *et al*, 1992) to apply to a partially debonded system, with the distribution of strain across the debonded and bonded regions of the fibre given by Equations (3-17) and (3-18) respectively. The maximum value of τ_i is equivalent to the interfacial shear strength as long as it is determined when the interface is in a state of full loading. For the case where interfacial bonding is purely frictional, the modified shear lag theory proposes that τ_i will be constant along the frictionally bonded length or interfacial sliding region (unless the normal clamping force varies). For the case where the embedded fibre changes from frictional to perfect bonding (never having slid) along part of its length (i.e. partial debonding), τ_i will increase along the perfectly bonded region until it reaches a maximum value at the point of transition. Because the value of τ_i is limited to a maximum value, further increases in interfacial shear stress would cause the transition point between frictional and perfect bonding to move along the interface, increasing the debonded length (Rauchs *et al*, 2002).

Equation (3-11) demonstrates that, by balancing stress across a section of fibre, the variation in interfacial shear stress is directly proportional to the rate of change of fibre strain with axial position, and thus can be inferred from this. Accordingly, the interfacial shear stress distribution along fibre 1 of sample 3 for load step 5, calculated from the measured fibre strain distribution shown in Figure 4-18, is shown in Figure 4-19.

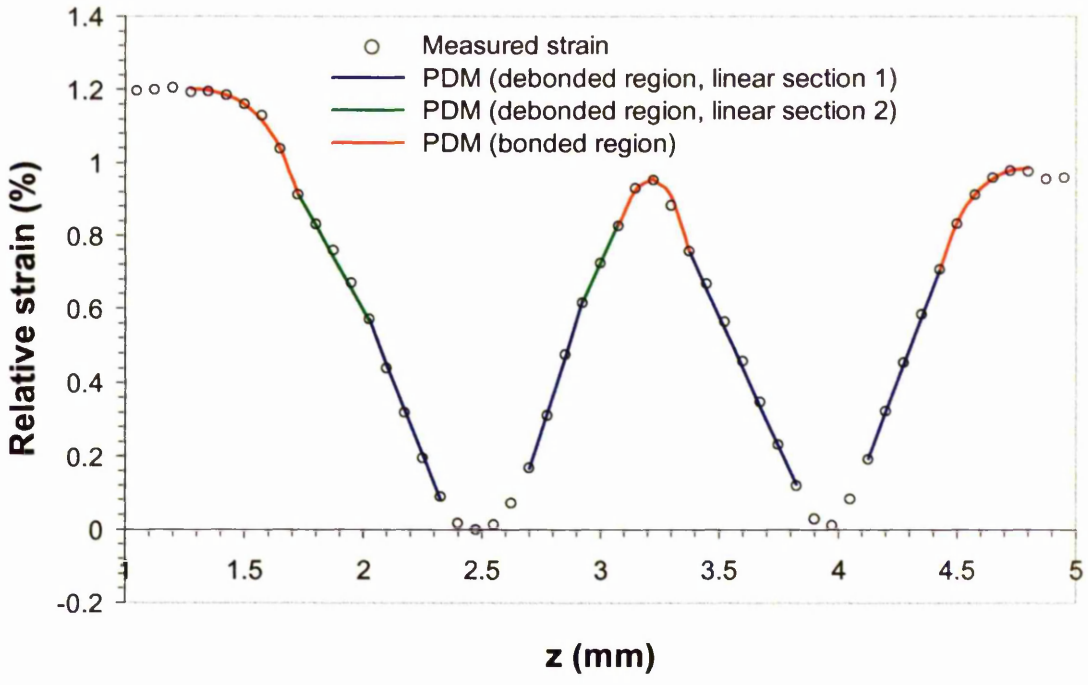

Figure 4-18. The measured strain distribution along fibre 1 of sample 3 for load step 5, shown fitted with the calculated strains for the debonded (linear) and bonded regions according to the partial debonding model (PDM).

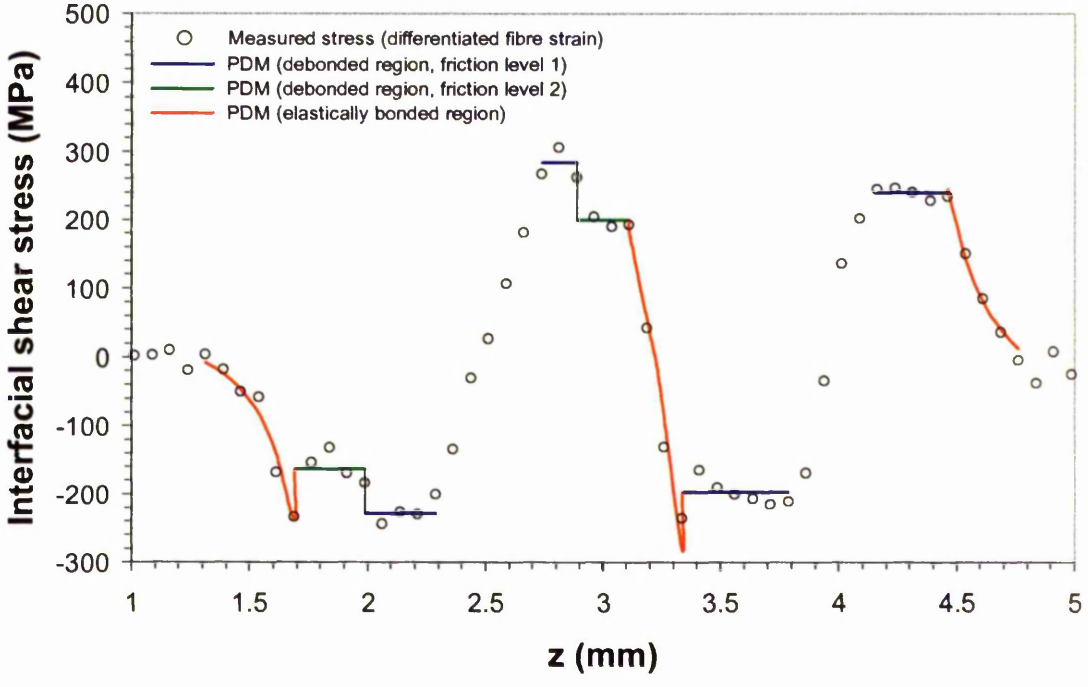

Figure 4-19. Derived (differentiated) interfacial shear stress distribution from the measured strains along fibre 1 of sample 3, and the indicated debonded (sliding) and bonded regions inferred from the model fit. The fibre is broken at z = 2.4 mm and 4 mm.

The measured (differentiated) values of interfacial shear stress shown in Figure 4-19, while quite scattered, reveal essentially the four regions of constant τ_i along the frictionally bonded lengths of the fibre fragments. These interfacial sliding regions are inferred to be 600-750 μm in length from the fibre ends. This is fairly consistent with experimental observations during the single fibre fragmentation case (Preuss *et al*, 2002) for which a value of ~500 μm was measured, and equal to that obtained from FE modelling of the single fibre case (Rauchs *et al*, 2002). The solid lines through the measured points of the fibre strain distribution of Figure 4-18 represent the best fit for the partial debonding model to the experimental data. This was described for the fragmentation (embedded fibres) case by Lacroix *et al.* for frictional sliding (Equation 3-17) and bonded (Equation 3-18) regions, into which the strain distribution either side of a crack can be divided. For the strain calculations using these expressions, values for the Young's modulus of the fibre, E_f (400 GPa), and the radius of the fibre, r_f (140 μm), were used. The value of m, the relative sliding length (= $l_d/2l$), was calculated from the measured sliding length, l_d, equal to 750 μm. For the calculation of n, values for the Young's modulus, E_m (115 GPa), and the Poisson's ratio, ν_m (0.3), of the matrix were used, and the characteristic radius of the matrix cylinder around the fibre, R, was based on the fibre spacing (~110 μm). The calculated shear stress distribution, using Equation (3-11), derived from the model fit is shown alongside the differentiated values for the sliding and bonded regions as corresponding solid lines in Figure 4-19.

Considering first the sliding or debonded regions, these occur from the fibre ends either side of a fibre crack and are marked by linear profiles in the strain distribution of Figure 4-18. Stress transfer in these regions is controlled by friction. The fitted model reveals an essentially constant interfacial frictional shear strength, τ_f, of 200-250 MPa, similar to that measured for the single fibre fragmentation case of ~200 MPa (Preuss *et al*, 2002). This interfacial shear strength is important considering that for fatigued interfaces during fibre bridging, such as those that would be expected for the material during cyclic loading in-service, lower interfacial shear stresses are applicable, measured to be ~80 MPa (Preuss *et al*, 2003). It is interesting to note that, for both the fibre ends enclosing the crack at z = 2.4 mm, the model and the differentiated experimental data infer frictional sliding at two significantly different values of the interfacial shear strength. Two linear sections are evident in each debonded region of the strain profile either side of this crack (marked by blue and green lines), indicating that the fibre may be subjected to different

levels of friction. These two levels are revealed in the interfacial shear stress profile (Figure 4-19) as two regions of constant shear stress. The upper level (blue line) is immediately adjacent to the crack on both sides, and calculated to be as high as 280 MPa (on the right-hand side of the crack). The shear stress then reduces significantly to the lower level, calculated to be just over 160 MPa on the left-hand side of the crack. Overall, the interfacial shear stress values calculated from the four frictional sliding regions are significantly higher than results reported from push-out tests (Majumdar *et al*, 1998; Warrier and Majumdar, 1999). These studies revealed an interfacial frictional shear strength ranging from 90 MPa (Majumdar *et al*, 1998) to 140-160 MPa (Warrier and Majumdar, 1999). A possible reason for the higher measured values here compared to push-out tests lies with the nature in which the interfacial shear stresses are calculated in both cases. Calculations based on the build-up of fibre strain adjacent to a crack might be expected to be higher due to a greater clamping action on the fibre at the location of a break, increasing the local interface radial stress at the fibre ends of the break (Carara and McGarry, 1968; Majumdar *et al*, 1998). Majumdar *et al.* showed this to be due to localised matrix plasticity during tensile loading of the specimen. This clamping action would not occur during a push-out test. More comparable, other than those of Preuss *et al*, are values reported from conventional full fragmentation testing by Le Petitcorps *et al*, who measured an interfacial frictional shear strength of ~180 MPa (Le Petitcorps *et al*, 1989).

In regions corresponding to those expected for a fibre that remains bonded to the matrix, the strain increases to a plateau in a manner defined by shear lag theory (Cox, 1952; see Section 3.3.2). The model fit to such regions of the strain profile, assumed to hold in the central part of a fibre fragment and adjacent to the sliding regions, is shown in Figure 4-18 and marked by red lines. The interface lengths (half lengths) that remain bonded are inferred to be between 150 and 400 μm, considerably smaller (about half the length) than the sliding regions and agreeable with single fibre fragmentation observations (half length ~250 μm; Preuss *et al*, 2002). In terms of the interfacial shear stress distribution inferred from the model fit to the bonded elastic regions (Figure 4-19), a sharp maximum is suggested for the fit to two of the regions and occurs at the junction between the sliding and elastic regions. This jump in shear stress is also inferred from the differentiated data even though it is quite scattered. This gives a maximum interfacial shear strength threshold for the onset of sliding of between 250 and 280 MPa. It is important to note that the sampling gauge length used for consecutive measurement points

during the strain mapping procedure in the longitudinal fibre direction was 75 μm, causing the results to be smeared out. This is especially so for the two bonded regions at the centre of the fragment (at $z \approx 3.3$ mm) enclosed by the two cracks, each fitted over only three data points. As a result, maxima in the interfacial shear stress for the bonded region are difficult to discern with any real confidence. In order to prove or disprove the existence of such a sharp maximum in the interfacial shear stress, a sampling gauge length an order of magnitude smaller would have to be used such that the measurement data points are much closer together. As mentioned earlier, the interface shear stresses extracted by differentiation from the experimental strain profile show a considerable level of scatter. This is due to the fact that experimental errors are strongly enhanced by the numerical differentiation of the experimental data. Partial sliding analysis of the single fibre fragmentation case showed a discernible 'still bonded' region at the centre of a fibre fragment (Preuss *et al*, 2002). This inferred a maximum interfacial shear strength threshold for the onset of sliding of between 300 and 550 MPa, using a 50 μm sampling gauge length. Even with reducing the sampling gauge length compared to that used here, there was still difficulty in discerning such a sharp maximum, but its existence was proved more convincingly.

The interfacial shear stress distribution along fibre 5 of sample 3 for load step 5, calculated from the measured fibre strain distribution shown in Figure 4-20, is shown in Figure 4-21. A distinct change or 'kink' in the rate of change of fibre strain with axial position was observed in this fibre on the right-hand side of the crack (see Section 4.4.3 and Figure 4-15), as illustrated by the transition from the blue/green regions to the yellow region in Figure 4-20. As shown in Figure 4-21, this is inferred as a significant change in the interfacial frictional shear strength along the sliding region of this fibre segment. Three different levels of friction have been modelled in the sliding region, ranging from an interfacial shear stress as low as 65 MPa (95 MPa adjacent to the fibre end) to one of 190 MPa, which is similar to values measured for fibre 1. This results in an extended sliding region equal to 900 μm. The one level inferred on the left-hand side of the crack gave an interfacial shear stress of 130 MPa, which is quite low compared to values observed for fibre 1. A possible reason for such a significant difference in the interfacial shear stress in the same region could be due to wear of the interface brought about by the instantaneous energy release upon fibre cracking. The maxima in the interfacial shear stress inferred

from the bonded regions are similar to those observed for fibre 1. A significant increase from debonded to bonded is observed on the left-hand side of the crack.

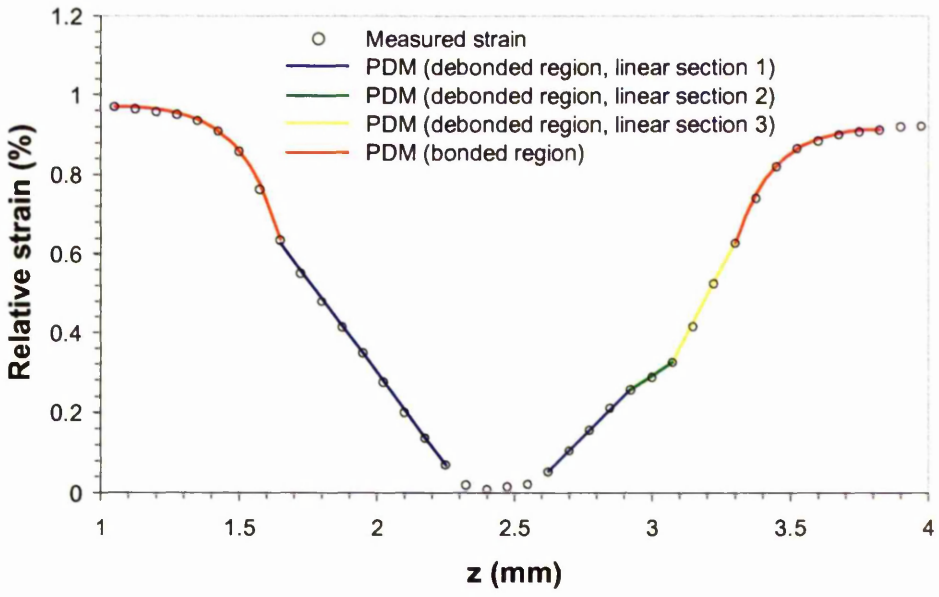

Figure 4-20. The measured strain distribution along fibre 5 of sample 3 for load step 5, shown fitted with the calculated strains for the debonded (linear) and bonded regions according to the partial debonding model (PDM).

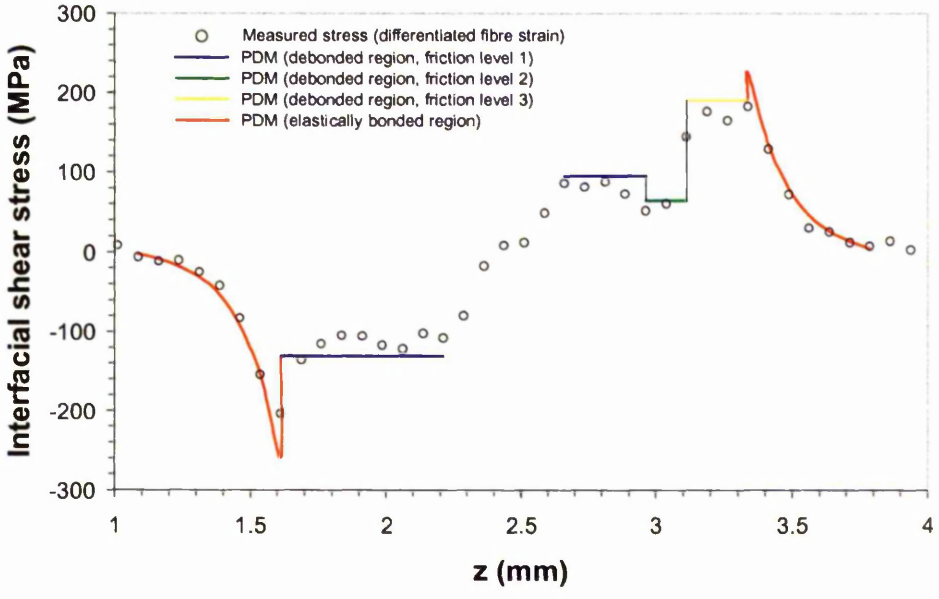

Figure 4-21. The derived (differentiated) interfacial shear stress distribution from the measured strains of Figure 4-20 and the indicated debonded (sliding) and bonded regions inferred from the model fit. The fibre is broken at $z = 2.4$ mm.

In the same way that critical interfacial shear strengths have been inferred from the fibre strain distributions at the fibre ends resulting from instantaneous cracks during a loading experiment, those from distributions at the fibre ends resulting from the laser drilled holes have been analysed. The interfacial shear stress distribution along fibre 3 of sample 2 for load step 5, calculated from the measured fibre strain distribution shown in Figure 4-22, is shown in Figure 4-23. The fitted model reveals an interfacial frictional shear strength, τ_f, of ~100-150 MPa, but dropping to as low as 50 MPa in the lower friction level of the two on the left-hand side of the hole. As expected, this is significantly lower than typical values measured adjacent to cracks that occurred during loading. Firstly, since laser hole drilling is a very localised but severe thermal heating process, a lower interfacial shear strength across fibre ends adjacent to these holes is not surprising. Secondly, one might expect the interfacial shear stress to be higher at the fibre ends of a crack resulting from a fully loaded state due to the instantaneous release of energy (if sliding is dynamic). For fibre ends present prior to the loading history, sliding is possibly more progressive as the load is increased. The maximum interfacial shear stress inferred from the bonded elastic region on the right-hand side of the hole is, as expected, comparable to values measured for the load-induced cracks, at ~250 MPa.

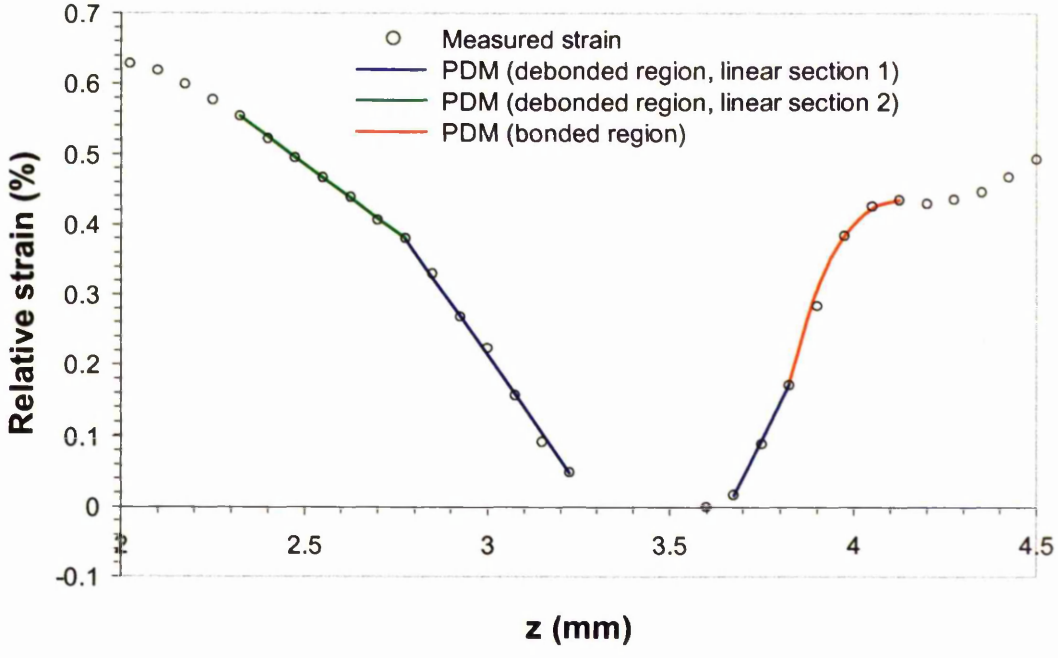

Figure 4-22. The measured strain distribution along fibre 3 of sample 2 for load step 5, shown fitted with the calculated strains for the debonded (linear) and bonded regions according to the partial debonding model (PDM).

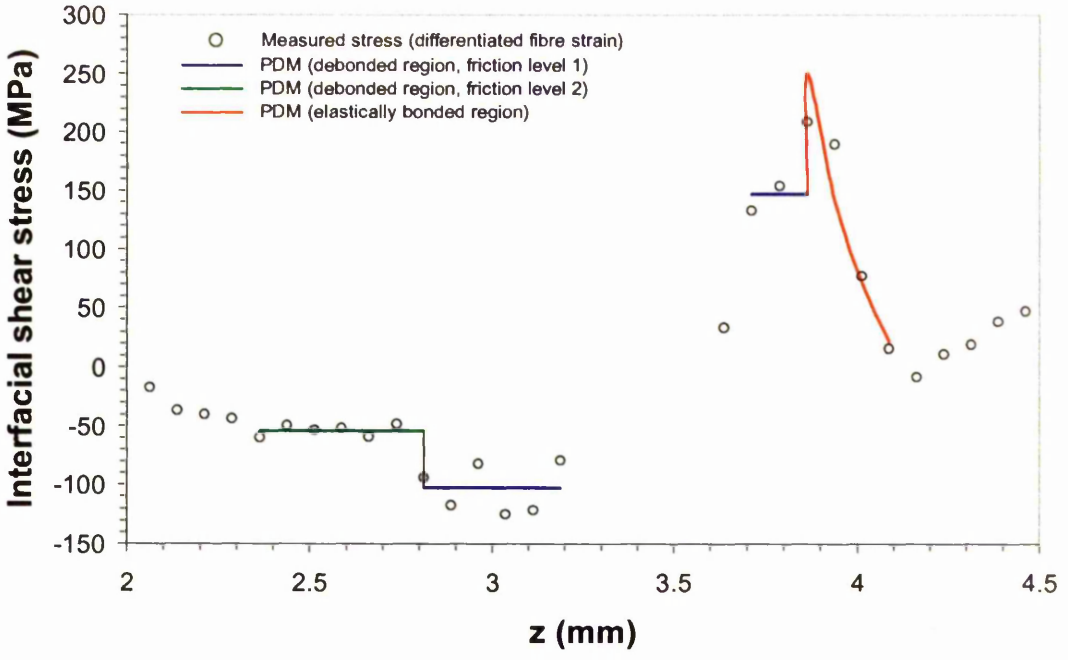

Figure 4-23. The derived (differentiated) interfacial shear stress distribution from the measured strains of Figure 4-22 and the indicated debonded (sliding) and bonded regions inferred from the model fit. The laser drilled hole is at $z \approx 3.5$ mm.

To show the interface shear stresses that occur during unloading, Figures 4-24 and 4-25 reveal the measured strain distribution along fibre 1 of sample 3 for load step 6 and the derived interfacial shear stress distribution, respectively. The crack positions are marked in each figure together with the reverse sliding regions, as illustrated in Figure 4-16. As revealed by the interfacial shear stress distribution (differentiated fibre strains) of Figure 4-25, an interfacial shear stress of ~40 MPa is inferred for the onset of reverse sliding. This only occurs in the immediate vicinity (~300 μm) either side of the cracks. According to finite element analysis (Rauchs *et al*, 2002), the remainder of the forward sliding regions remain stuck during unloading, and an interfacial shear stress of 160-210 MPa is inferred, similar to values inferred for the frictional sliding regions of the fibre under load (step 5, Figure 4-19). The distribution does actually reveal discernible regions (~300 μm) adjacent to the reverse sliding regions of shear stress values in between the values inferred for the reverse sliding and sticking regions, of ~70 MPa. This perhaps suggests a lower interfacial frictional shear strength region, adjacent to the reverse sliding region, before the interface reverts to a sticking state. Finite element analysis also reveals that in the vicinity of a crack (~100 μm), the interface does not transfer any stress, but due

to a measurement sampling gauge in the longitudinal fibre direction of 75 μm it was not possible to measure such a region.

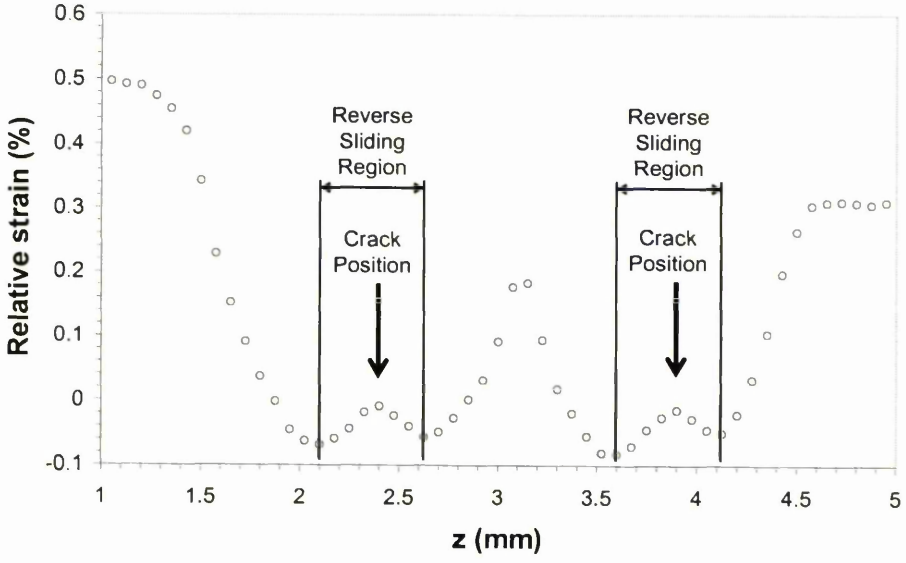

Figure 4-24. The measured strain distribution along fibre 1 of sample 3 for the unloaded step (step 6). The positions of the cracks are shown, at $z = 2.4$ mm and $z = 3.9$ mm.

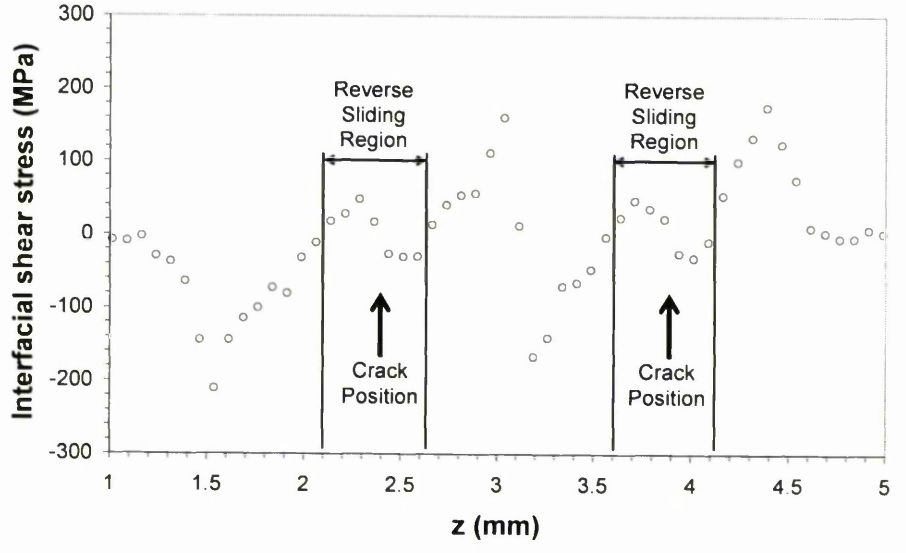

Figure 4-25. The derived (differentiated) interfacial shear stress distribution from the measured strains of Figure 4-24. The fibre is broken at $z = 2.4$ mm and $z = 3.9$ mm.

Figures 4-26 and 4-27 show the interfacial shear stress distributions giving rise to the stress concentrations in fibres 1 and 4 of sample 1 respectively, adjacent to the breaks of fibres 2 and 3, derived by differentiation of the corresponding fibre strain distributions

shown inset in each Figure (load step 5). An interfacial shear stress of ~70-90 MPa is inferred along fibre 1 in the region neighbouring the defect of fibre 2. The interfacial shear stress distribution along fibre 4 in the region neighbouring the defect of fibre 3 infers a shear stress as high as 120 MPa. These τ_i values for both fibres are similar to values giving rise to stress build-up across fibre ends induced by laser drilling (Figure 4-23). The larger shear stress observed for fibre 4 is consistent with the slightly larger stress concentration in this fibre compared to that in fibre 1 (see Table 4-2). It is interesting to note that the τ_i distribution along the neighbouring fibre 4 infers bonded regions of varying shear stress, as would be expected and indicated in the plot of Figure 4-27. The central bonded region immediately either side of the peak in the strain due to the neighbouring defect can be described by the fact that when the fibre is strained from both ends, the fibre doesn't slide one way or the other, resulting in the concentration of strain. The regions of constant shear stress between the bonded regions on either side of the strain maximum are not understood, but suggest regions of interfacial sliding. However, considering interfacial shear stresses of ~50-60 MPa in these regions, much higher interfacial frictional shear strengths of ~200 MPa are inferred from the analysis above. It is possible that the laser drilling process has caused damage to the interface, resulting in these low sliding stresses.

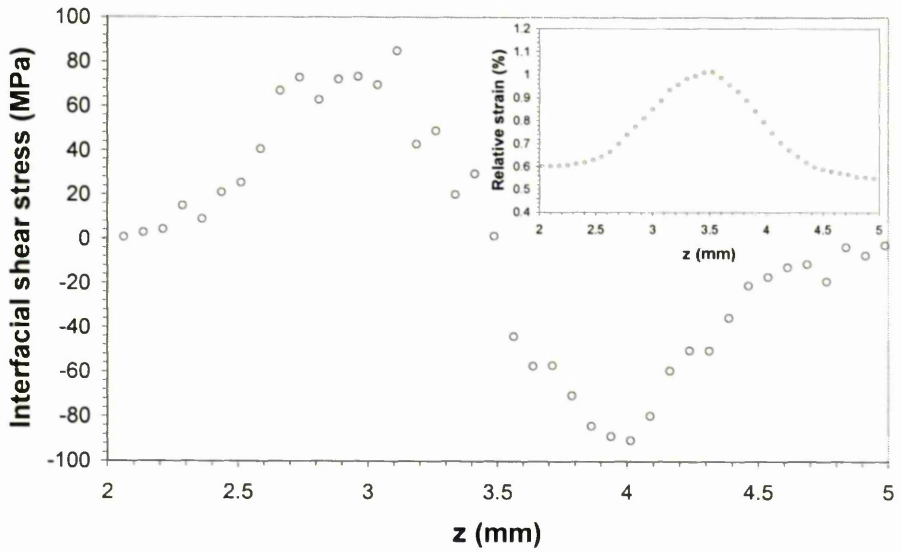

Figure 4-26. The derived (differentiated) interfacial shear stress distribution from the measured strains along fibre 1 of sample 1 (load step 5), shown inset. The maximum of the stress concentration is at z = 3.5 mm.

The phenomenon could also be due to an effect of the time taken between measurement points, such as the occurrence of backsliding. A smaller gauge volume between measurement points would be needed to confidently describe the effect. Stress concentration investigations in polymer matrix composites infer sharp Gaussian-like peaks in the τ_i distribution in adjacent intact fibres (Mahiou *et al*, 1999; van den Heuvel *et al*, 1997).

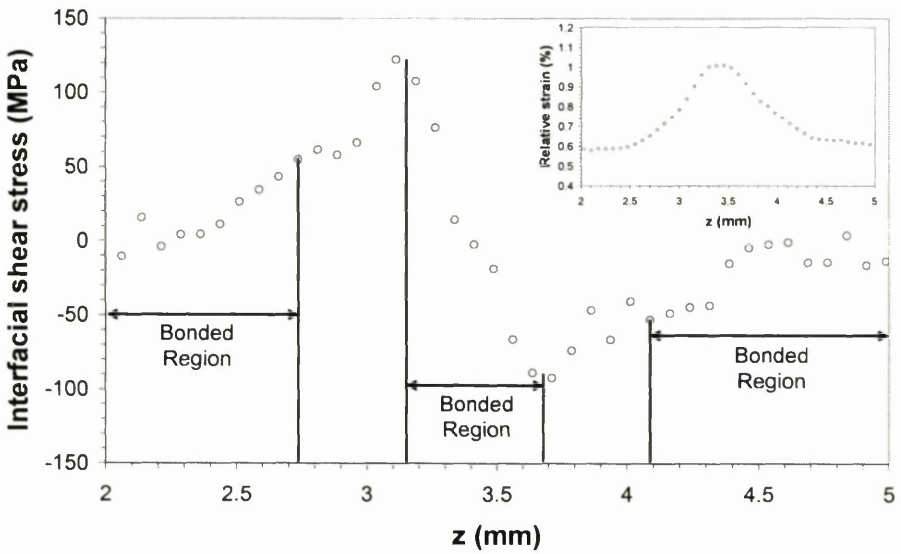

Figure 4-27. The derived (differentiated) interfacial shear stress distribution from the measured strains along fibre 4 of sample 1, shown inset. The maximum of the stress concentration is at $z = 3.5$ mm.

4.5. Results and Discussion of Damage Development Observations

4.5.1. Materials and specimens

4.5.1.1. Specimen types

In order to monitor cracking sequences and to observe the accumulation and characteristics of fibre breakages, such as those measured in the previous strain mapping section, via X-ray tomography, similar single-ply samples to those shown in Figure 4-5 were used. Again, in order to study the effect of a damaged fibre on the occurrence of subsequent failure of its neighbours, samples containing laser-drilled fibre defects were studied. In order to study the morphology and interaction of a fibre bridging fatigue crack, a multiple ply composite sample comprising 6 plies of SCS-6 SiC fibres and a matrix

fatigue crack was also fabricated. (Dr. T. Doel of the University of Birmingham is acknowledged for the fabrication of the multi-ply composite sample). As for the single-ply samples, the SiC fibres were 140 μm in diameter with a carbon core, and were coated with Ti-6Al-4V to control interfibre spacing. The volume fraction of fibres was 35%. Both sides of the composite were clad with a 0.15 mm layer of monolithic Ti-6Al-4V prior to consolidation. This multi-layer fibre composite material was fabricated by the fibre/foil process in which alternate layers of Ti-6Al-4V foil and SCS-6 fibres were laid up and subsequently subjected to a hot isostatic pressing (HIPing) consolidation process. The final thickness of the composite was about 1.5 mm. Pieces measuring 50 x 5 x 1.5 mm were cut out from the composite plate, to which a spot weld was applied to one of the clad surfaces of the test-piece to act as a crack initiator.

4.5.1.2. Mechanical testing

During the tomography experiment, the single-ply samples, as for the strain mapping experiment, were subjected to uniaxial tension using a 2 kN tensile rig especially designed to allow the observation of damage by tomography during the deformation of materials (Buffière *et al*, 1999; see Section 4.3.1). The multi-ply sample had undergone fatigue tests prior to the tomography experiment in order to grow a matrix crack so that fibre bridging and crack opening displacements could be observed (Dr. T. Doel of the University of Birmingham is again acknowledged for the fatigue testing). Fatigue testing was carried out using an Instron servo-hydraulic testing machine, and was load controlled, i.e. the maximum and minimum loads were kept constant during the test. The fatigue tests were carried out using three-point bending geometry, with an applied load ratio, R, of 0.1 (where R is the ratio between the minimum and maximum loads applied during a fatigue cycle), a maximum load of 224 N and a frequency of 5 Hz. The matrix fatigue crack was grown perpendicular to the loading (fibre) direction and had propagated about 0.5 mm through the thickness of the sample, causing two plies of fibres to bridge the crack. A tensile specimen, the dimensions of which are defined in Figure 4-4, was electro-discharge machined from this piece cut from the original composite plate, so as to contain a straight region of the fatigue crack. During the tomography experiment, the sample was loaded to K_{min} and K_{max} (where K is the stress intensity factor at the crack tip, corresponding to the minimum (56 MPa) and maximum (560 MPa) applied loads respectively during the fatigue cycle as explained above) in-situ on the tomography beam line (ID19).

4.5.2. X-ray tomography procedure

As described in Chapter 1, X-ray tomography is a non-destructive technique that allows the reconstruction of the internal structure of samples in 3-D, allowing, for this case, the position and morphology of damage in both the fibres and the matrix to be determined. A schematic diagram of the experimental set-up used at the ESRF on beam-line ID19 was shown in Figure 1-8 of Section 1.2.3. The large distance between the source and the experimental hutch (~150 m) leads to a beam that is essentially parallel and exhibits a high lateral coherence of the photons. The synchrotron radiation white beam passes through a set of two parallel silicon single crystals to select photons of energy 33 keV (wavelength 0.4 Å) and produce a monochromatic beam for imaging. The distance between the sample and the CCD detector was set to about 120 cm. The sample, which was placed inside the tensile loading rig fixed to the rotation stage throughout the experiment to allow for in-situ measurements, was rotated in the beam to provide a set of 900 radiographs (one radiograph collected every 0.2°). A detector comprising a camera, together with an optics system, giving an effective pixel size of 2 μm was used, a parameter which depends on the cross-sectional area of the sample. The radiographs were analysed using reconstruction software to give a 3D attenuation contrast image of the object using backprojection algorithms (see Section 1.4). From this 3D volume it is possible to view 2D slices for any section through the volume. The large sample-detector distance combined with the high lateral coherence of the photons enabled a 'phase contrast' effect to be taken advantage of, which superimposes on the regular attenuation contrast. This leads to an improvement in the detection of phase features like cracks due to the presence of Fresnel fringes, as described in Section 1.3.3.

4.5.3. Tomography of fibre cracking sequences and damage characteristics

4.5.3.1. Observation of fibre crack accumulation

Cracking sequences were observed and monitored as a function of applied load for sample 4, the initial radiograph of which is shown in Figure 4-28(a). The sample can be seen to contain a defect in fibre 1, with its effect on subsequent failure of its neighbours being studied. Figure 4-28(b)-(d) shows a sequence of tomographs of the sample, scanned at increasing levels of applied load, illustrating the evolution of damage that has occurred due to the presence of the defect in fibre 1. The images show representations of the 3-D volumes rendered so as to show the crack features through the entirety of the sample at the

different stages, i.e. the matrix and fibres have been rendered transparent leaving the outline of the fibres and the fibre cracks visible.

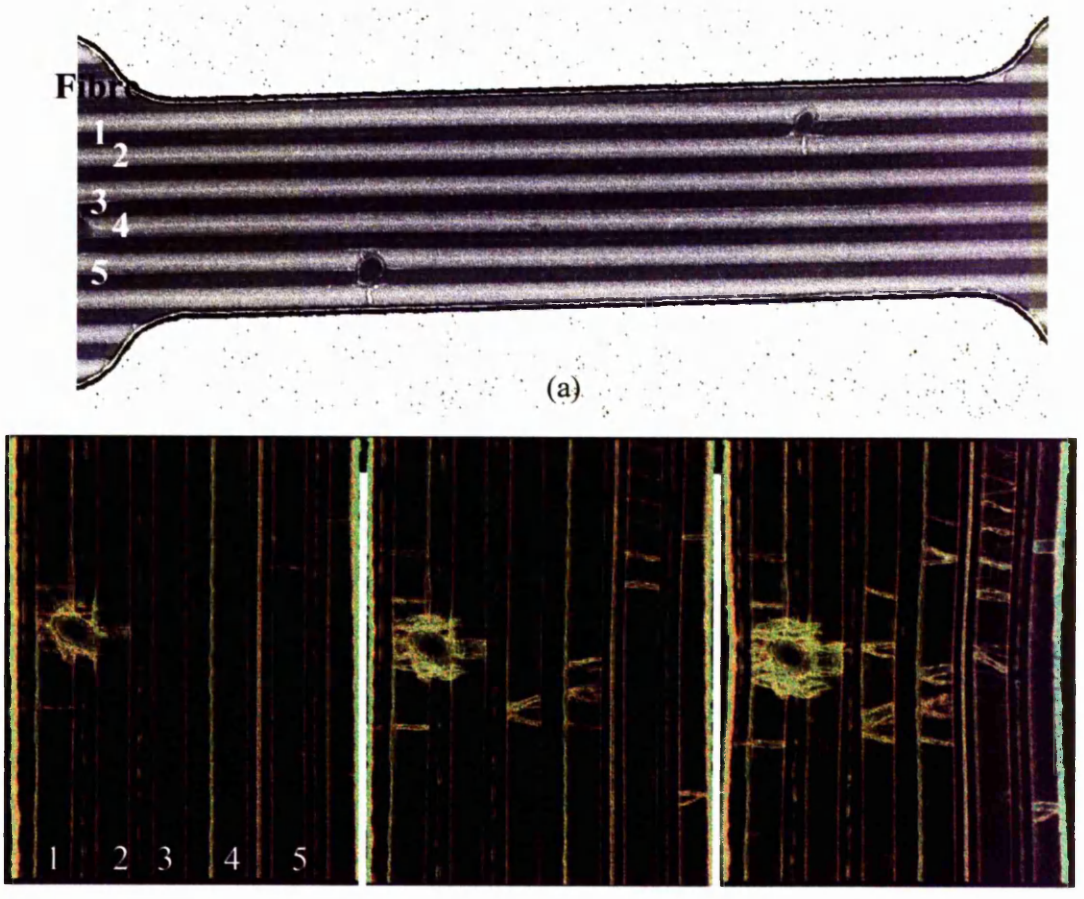

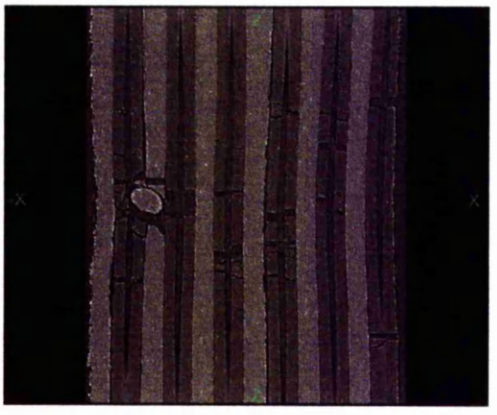

Figure 4-28. (a) Initial radiograph of sample 4 showing the defect in fibre 1. A sequence of 3-D tomographic representations, at 2 μm resolution, illustrating the evolution of damage in the sample, at applied loads of (b) 200 MPa, (c) 890 MPa and (d) 960 MPa. (e) A 2-D virtual slice of the sample volume through the *X-Z* plane, corresponding to the 3-D image in (d). The fibre diameter is 140 μm.

Figure 4-28(b), showing the sample at an applied load of 200 MPa, indicates the laser drilled hole observed in the radiograph (which has been in-filled with Ti) lying slightly to the right of fibre 1. This has introduced damage into fibres 1 and 2, most notably the crack in fibre 2, adjacent to the defect, which has opened slightly due to the small applied load. Fabrication of the composite material has caused fibre 5 to fracture in two places. On reaching 890 MPa (Figure 4-28(c)), all of the cracks apparent in the previous step have now opened (note the crack in fibre 2 and the one in fibre 1 below the defect) – evidence of considerable sliding between the fibre and matrix. Additionally, new cracks have formed, most notably in fibres 3 and 4, neither of which showed cracks after the first loading step. Note that, unlike the initial cracks, these new cracks have a characteristic wedge-shape (see Section 4.5.3.2) also observed in the single fibre fragmentation study of the same system (Preuss *et al*, 2002). Fibre 5 has broken into many small fragments. On increasing the load to about 960 MPa, the sample at this step being shown in Figure 4-28(d), existing cracks have widened significantly and, again, new cracks have formed. In some regions (e.g. the crack in fibre 2) the carbon core has pulled out of the fibre segments. This can be seen more clearly in the equivalent 2-D slice (*X-Z* plane) through the centre of the sample volume at the same loading step, Figure 4-28(e). Measuring directly from this image using simple measurement tools provided by the visualisation package Volview (from Kitware), the crack in fibre 2 had an opening of 30 μm at 200 MPa whereas at 960 MPa the opening of the crack had increased to 130 μm. Note that while the two fragments of fibre 2 slipped by a combined distance of 100 μm (roughly two thirds of a fibre diameter) further cracking did not occur. In contrast, fibres 3 and 4 have developed a large number of cracks to give a number of very small fragments. In addition to the characteristic wedge-shaped cracks, a smaller number of single cracks have formed perpendicular to the loading axis. The occurrence of multiple fibre failures leading to very short fibre fragments indicates a considerable weakening of the fibre strength after initial fibre failure, in agreement with the strain measurements of (Preuss *et al*, 2002). Gonzalez and Llorca have also observed multiple fibre fractures to occur in close proximity to each other, with the distance between cracks ranging from 100-300 μm (Gonzalez and Llorca, 2001). They also found that fibre fracture was never observed far away from the fracture surfaces, which suggested a failure mechanism dominated by the formation of an initial cluster of broken fibres. The effect of the defect in fibre 1 of Figure 4-28(b) has been to concentrate subsequent fibre failures in its neighbours within 600 μm along the fibre length either side of the defect position.

Majumdar *et al.* showed localised matrix plasticity to be responsible for the cumulative failure of fibres (Majumdar *et al*, 1998). They observed a one-to-one correspondence between slip band intersections with the fibres and the fibre break locations, and subsequent fibre breaks were observed to form as the slip bands from existing fibre breaks impinged on an adjacent fibre.

4.5.3.2. Characteristics of fibre cracking

A number of different fibre crack characteristics were observed in the samples scanned during the tomography experiment. Figure 4-29(a) shows a 3-D tomograph representation of sample 3 used during the strain mapping experiment, illustrating the state of fibre cracks after the final loading step. The corresponding 2-D slice through the centre of the sample volume is shown in Figure 4-29(b). The images show the 2 mm section of the sample gauge length in the region of the fibre fractures that were measured, during the strain mapping experiment, across the sample at $z = 2.4$ mm (see Figure 4-14).

The cracks measured during the strain scanning experiment at this position are observed to be the characteristic wedge cracks observed during the loading of sample 4. Slight bending of the sample is observed in Figure 4-29(a), something that is also very evident in the final loading step of sample 4 (Figure 4-29(d)). This is due to a combination of necking and, in sample 4, the fact that the early damage was not symmetrically distributed about the sample centre line. This may suggest that a bending moment encourages these wedge cracks to form, and it is highly likely that surface defects introduced during the initial fibre failure event play an important role. Spowart and Clyne observed similar crack morphologies caused by propagation of shear- or bend-induced cracks during compressive loading (Spowart and Clyne, 1999). It is possible that wedge cracks originate at a defect on the surface of a fibre, which then radiates outwards as two cracks grow. This is illustrated in Figure 4-29(c), which shows a magnified 3-D representation of a typical wedge crack (from fibre 1) and three 2-D slices revealing the morphology of the wedge crack at different stages through the *Y-Z* plane of the fibre, as indicated by the coloured dashed lines. These 2-D slices show that such a crack morphology comprises two main cracks, with debris in-between, that have radiated outwards from a point of connection on the opposite fibre surface. It is worth noting that the strain measurements suggested a fibre failure strain in excess of 1.2% which equates to a stress of ~5000 MPa and a lot of stored strain energy prior to fibre fracture.

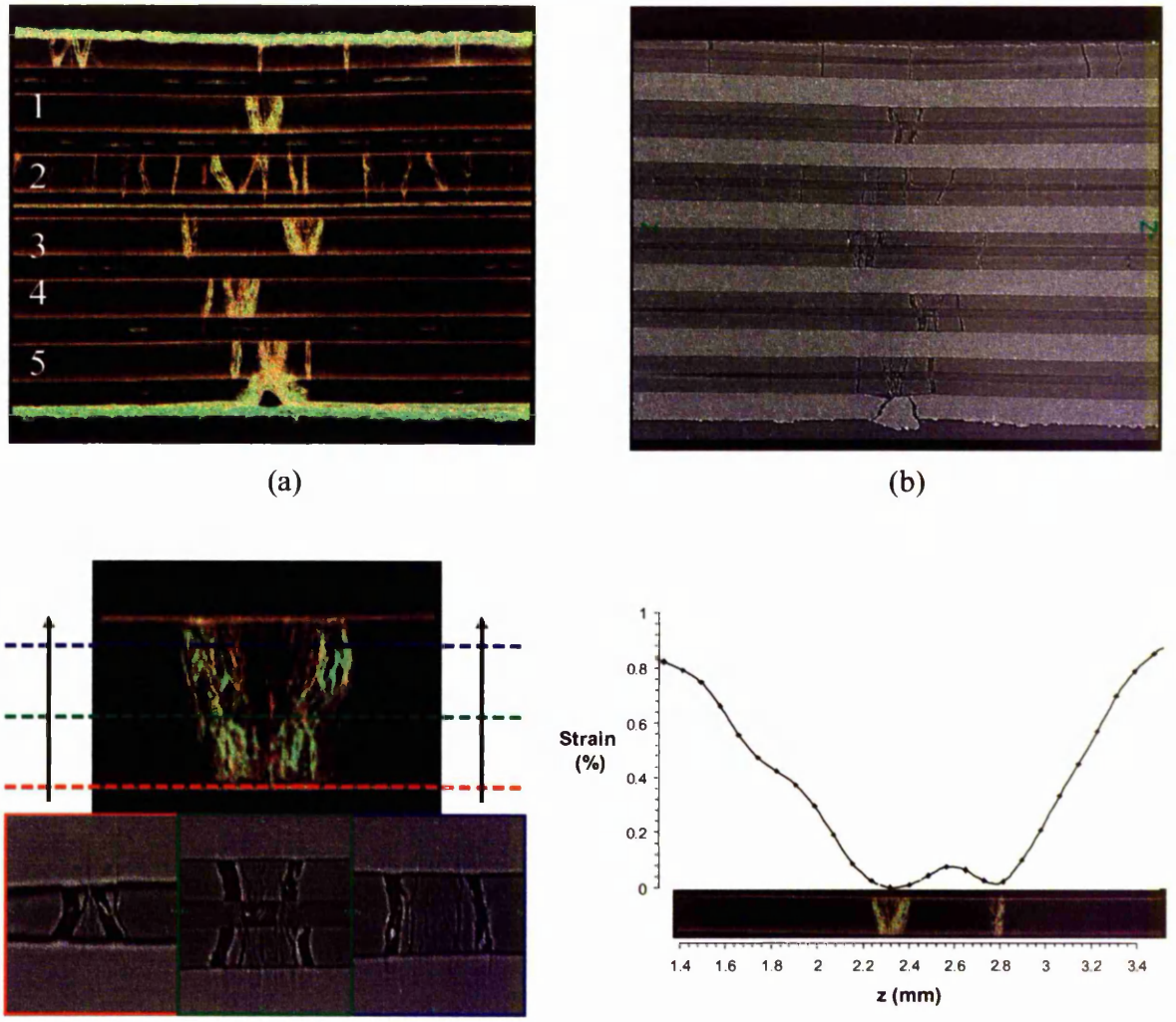

Figure 4-29. (a) 3-D tomograph representation of the state of fibre cracks in sample 3 after the strain mapping experiment and (b) a virtual 2-D slice corresponding to the image in (a). (c) Magnified 3-D representation of the wedge crack in fibre 1, together with virtual 2-D slices showing the wedge crack in the *Y-Z* plane near the two surfaces and in the middle of the fibre diameter, as indicated by the coloured dashed lines. (d) Illustrating the equivalence of the strain profile from loading step 5 along fibre 3 (from Figure 4-14) together with the tomograph of the same fibre. The fibre diameter is 140 μm.

Also, given that the fibre failure stress drops to ~40% of the initial strength (Preuss *et al*, 2002), it is likely that the shockwave or recoil of the fracturing fibre caused by the first high stress fracture event, itself consisting of a straight crack morphology, introduces surface damage from which the wedge cracks form. This is consistent with experimental

observations during failure of individual single fibres (Laffargue and Bowen, 2001), which suggest that high failure stresses are often associated with fracture initiation from the SiC core, whereas lower stress failures originate from the surface. It is interesting to note that all of the wedge cracks observed in Figure 4-29(a) originate at the bottom surface of each fibre (as viewed in the figure) and that they all conform to the characteristic shape in the same viewing plane, again adding to the argument that such a fracture event might be aided by a bending component. The fact that many of the multiple fibre failures observed in samples 3 and 4 are wedge cracks nucleating from the surface corroborates the hypothesis that the considerable weakening of the fibre strength after initial fibre failure is due to the introduction of surface flaws. Figure 4-29(d) illustrates the equivalence of the crack positions measured by the strain mapping experiment and the actual observation of the cracks in 3-D, shown for fibre 3 of sample 3. The tomograph also confirms that fibre 2 has fragmented into many pieces, as measured in the strain mapping experiment through no load being carried by this fibre (Figure 4-14).

A similar sample, sample 5, the radiograph of which is shown in Figure 4-30(a), was strained continuously and radiographs acquired every half a second until failure of the sample in order to create an animation. Figure 4-30(b) shows a 3D rendered tomograph of one half of the failed sample, with both colour and greyscale representations. Failure occurred across the sample at the position of the fibre defects observed in the radiograph, the position of these defects corresponding to the right-hand side of the tomograph as indicated by the fibre numbers. The interesting feature to note is the zig-zag or spiral effect to the cracks in fibre 3, shown highlighted from the colour representation in the greyscale representation. It seems that a crack has initiated and this has spiralled down the fibre. On first inspection the sequence of radiographs suggested a zig-zag type defect, and therefore a series of neighbouring wedge cracks, that occurred down the fibre in one 'event'. Careful analysis of the tomographic volume actually reveals it to be a spiral crack, which is shown by a magnified greyscale representation of the region of interest of the fibre in Figure 4-30(b). Taking a series of virtual 2-D slices through the 3-D volume, Figure 4-30(c)-(e) each shows such a slice from the centre of the fibre (Figure 4-30(d)) and slices from both in front of (Figure 4-30(c)) and behind (Figure 4-30(e)) this centre slice. This set of slices reveals a characteristic spiral 'staircase' crack morphology and infer that the cracks penetrated the fibre. This was confirmed by metallographic sectioning and Figure 4-30(f), which shows a polished section from behind the core of the fibre and a series of diagonal cracks that have penetrated fibre 3, rather than just simply spiralling

around the outside of it or in the coating. It is not understood why such an unusual fibre crack morphology should occur.

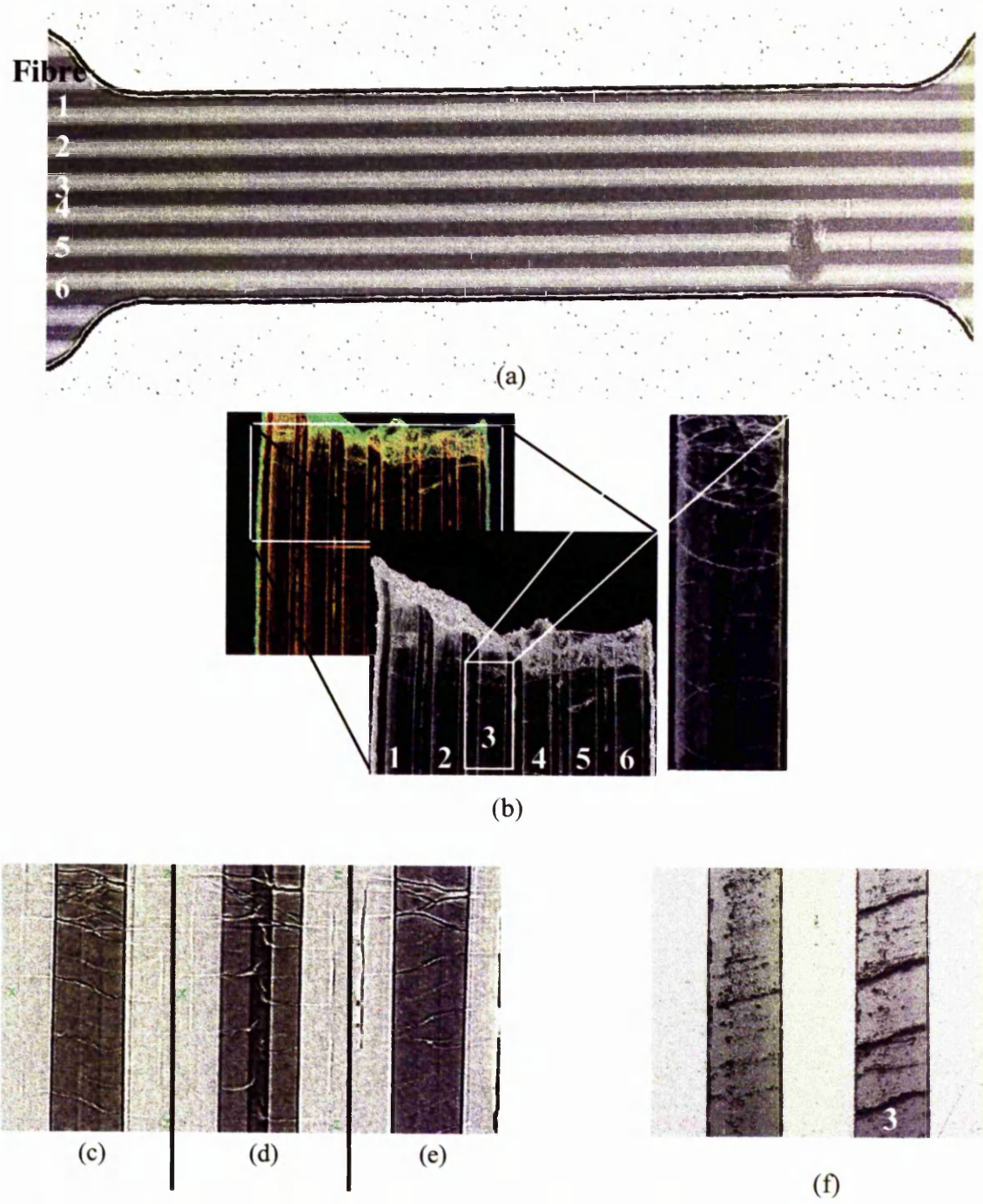

Figure 4-30. (a) Radiograph of sample 5, showing the defects in fibres 5 and 6 where the sample failed. (b) 3-D tomograph representations of the failed sample, highlighting the section of fibre 3 showing the spiral crack morphology. 2-D virtual slices taken from (c) in front of the centre slice, (d) through the centre of the fibre and (e) behind the centre slice. (f) A metallographically polished section from behind the core and showing a series of diagonal cracks in fibre 3. The fibre diameter is 140 μm.

4.5.4. Tomography of a fibre bridging fatigue crack

The aim of this section of the work was to study, entirely through the use of X-ray tomography, the interaction of a matrix fatigue crack with the longitudinal SiC fibres, and in particular, the extent of crack bridging by the fibres during growth of the fatigue crack. As is shown in what follows, the technique allowed detailed observation of the physical mechanisms that occurred and measurement of parameters such as the crack opening displacement (COD) at different stages of applied load.

4.5.4.1. Fibre/matrix-crack interaction

The fabrication of this fatigue cracked multi-ply sample is described in Section 4.5.1. Figure 4-31 shows two 3-D representations of the section of the sample containing the matrix crack (Figure 4-31(a)) and two 2-D virtual slices through the volume in both the *Y-Z* (Figure 4-31(b)) and *X-Y* (Figure 4-31(c)) planes, as indicated by the dashed white lines. In the second of the two 3-D representations, the matrix has been rendered partly transparent to reveal the longitudinal fibres and fatigue crack. The location of the spot weld is visible in the centre of the 3-D volume from which the matrix crack has grown. The extent of growth of the crack is suggested by the 2-D slices, which is measured to be ~0.6 mm into the sample from the spot-welded face (sample thickness 1.5 mm).

Figure 4-32(a) and (b) shows 3-D rendered images of the fatigue crack sample scanned with applied loads of 56 MPa (K_{min}) and 560 MPa (K_{max}) respectively. For both these tomographic volumes the opacity of regions of differing attenuation has been varied in order to show the crack plane through the sample, revealing the extent of growth of the matrix crack (low density region) which is represented by the grey regions. The higher density regions, such as the fibres and matrix, have been rendered transparent. The fibre/matrix interfaces, visible as rings, are also in high contrast due to the presence of Fresnel fringes in the original radiographs, originating from the beam line setup as explained in Sections 1.2.3/1.3.3. Comparison of the two images reveals that at K_{max} the tip of the crack appears to be further advanced, presumably due to the fact that, at a higher applied load, the crack has been opened up making it easier to image. Note that the 'speckled' contrast of the crack region at K_{min} compared to K_{max}, is suggestive of some face to face contact, although this may be partly a consequence of the 2 μm resolution of the detector used. One would expect the sliding action of the bridging fibres during loading to mean that the crack face is held open upon unloading. It appears as if the left most fibre near the crack front in Figure 4-32(b), circled in red, has cracked, and a search

through the individual slices has revealed that this occurred near the crack plane during loading from K_{min} to K_{max}. Figure 4-32(b) also suggests that the matrix crack has advanced furthest in regions free from fibres.

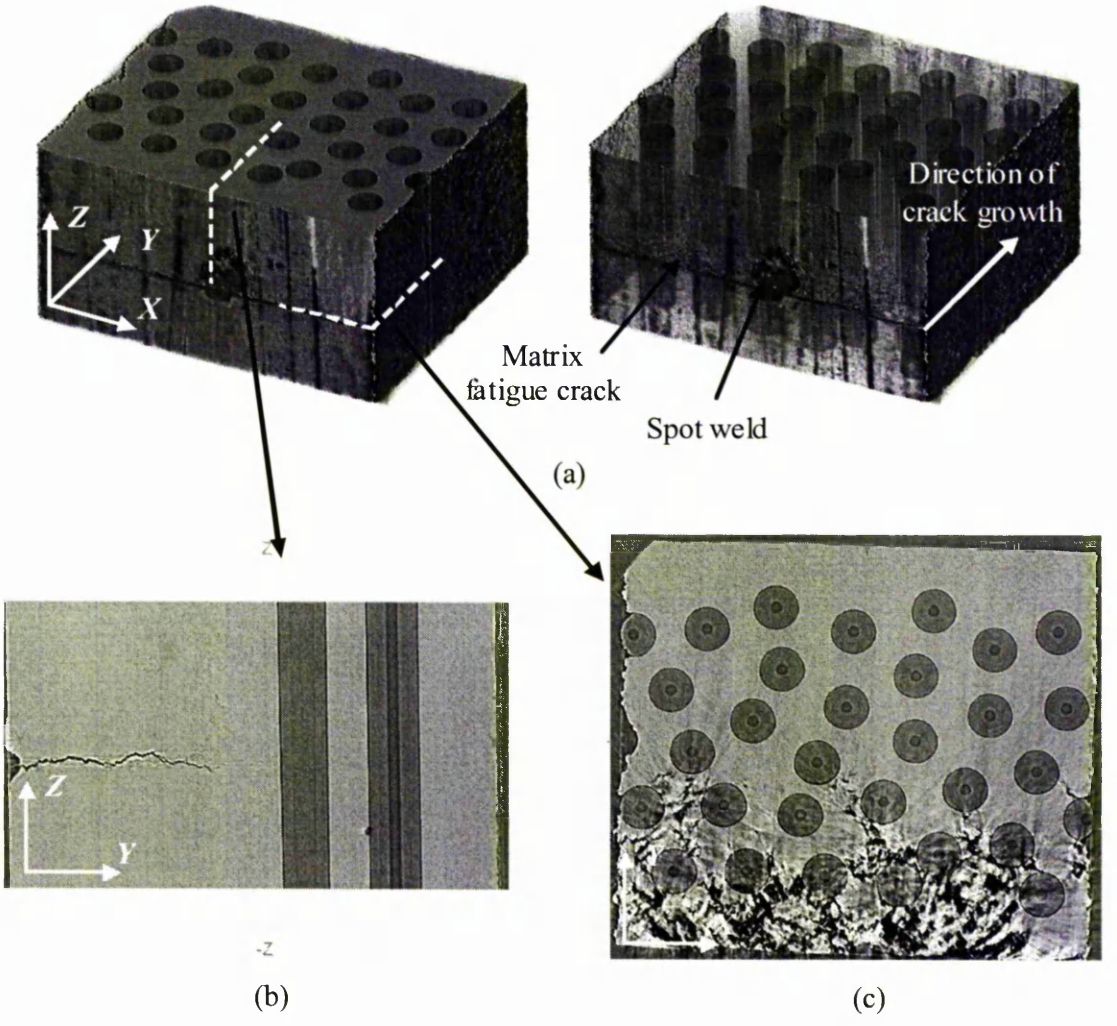

Figure 4-31. (a) A 2 μm resolution 3-D rendered representation showing the section of interest of the gauge area of the fatigue crack sample. (b) and (c) 2-D virtual slices through the volume (XY and YZ, respectively) showing the layout of the fibres and the morphology of the matrix crack. The fibre diameter is 140 μm.

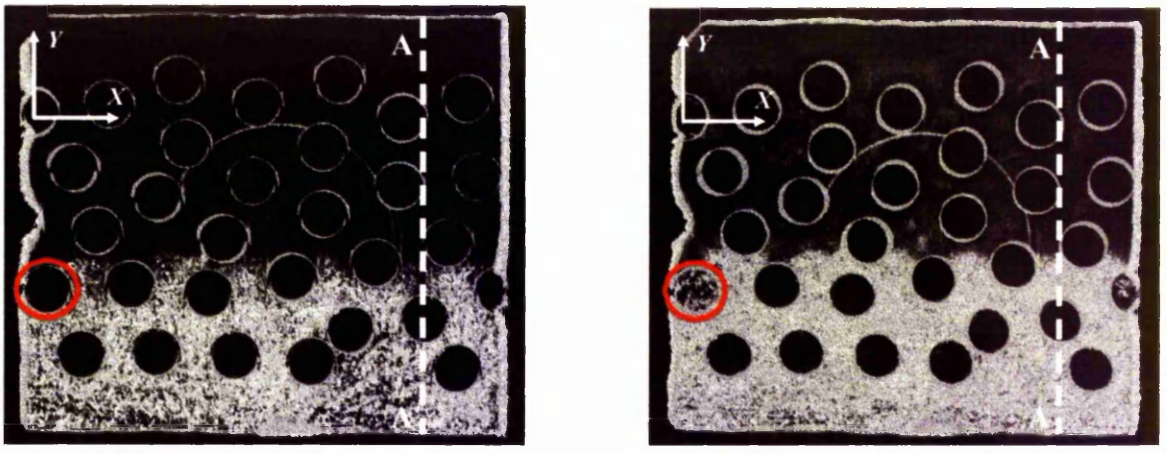

(a) (b)

Figure 4-32. 2 μm resolution 3-D rendered tomographic representations of the fatigue crack sample showing the extent of crack growth (grey regions) as observed at (a) K_{min} and (b) K_{max}. The location of the slices shown in Figure 4-33 are indicated by the dashed lines AA. The fibre diameter is 140 μm.

In terms of viewing the crack front, virtual 2-D slices through the reconstructed volume can be more instructive. Figure 4-33(a) and (b) shows two equivalent 2-D slices through the tomographic volumes at K_{min} and K_{max} respectively, and corresponding to the location indicated by the dashed lines marked AA in Figure 4-32. It is clear from the image at K_{max} (Figure 4-33(b)) that the crack is very much more open compared to that at K_{min} (see the crack opening displacement (COD) analysis of Section 4.5.4.2). Furthermore, the crack has bifurcated to form two cracks on growing past the fibre, the dominant crack assumed to be the lower of the two as shown in the image due to its greater prominence. This is probably caused by the fact that the crack grows around the fibre at different heights on either side so that the crack fronts do not rejoin downstream of the fibre. There is some evidence that there are two cracks slightly upstream of the fibre. At the point the matrix crack first reaches the fibre there is some evidence of interfacial debonding of the fibre from the matrix. A raised section is observed at this point when compared to a point on the interface away from the matrix crack region, although the resolution of 2 μm is insufficient to prove the observation conclusively. This is consistent with fibre and matrix crack opening strain maps collected for similar samples which indicate a sliding region of about 1mm either side of the crack plane having very low

interface stresses (Preuss *et al*, 2003). It is this sliding of the interface that reduces the stress intensity felt by the fibre in the crack plane. This reduces the tendency for fibre cracking and allows the crack to grow around the fibre rather than causing fracture of the fibre. The resulting crack bridging fibres shield the crack front from the full applied stress intensity leading to crack arrest (Liu and Bowen, 2003). There is some suggestion in the images that the fibre has cracked, but a more detailed look at the slices immediately in front and behind have revealed that this is not the case. The crack-like feature is an artefact introduced by the back-projection reconstruction algorithm.

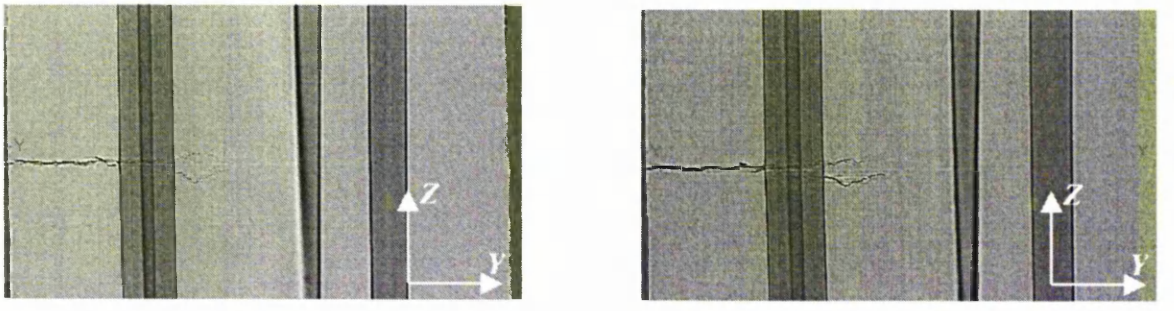

(a) (b)

Figure 4-33. 2-D virtual slices through the 3-D tomographic volumes of the sample at (a) K_{min} and (b) K_{max}, corresponding to the location indicated by the dashed lines in Figure 4-32. The crack bridging effect of the fibre is illustrated. The scale of the images can be inferred from the fibre diameter (140 μm).

4.5.4.2. Crack opening displacement (COD) profiles

Using the 3-D tomographic volumes of the fatigue cracked multi-ply sample, for which 3-D representations and 2-D slices were shown in the previous section, crack opening displacement (COD) profiles were measured. Profiles were obtained for four different applied loads, namely those of K_{min} (applied load of 56 MPa) and K_{max} (560 MPa) as observed previously, and also K_{mid} (308 MPa) and $1.2\times K_{max}$ (672 MPa). Due to the measurements being performed on virtual slices of the sample, care was taken in order to make them as accurate as possible. This involved mapping the intensity values of the pixels making up the original slice to the full range of values of the colormap, i.e. 0 to 255, such that the crack was fully distinguished from the matrix material in which it is contained. The high intensity and parallel nature of the synchrotron beam, and the setup of the beamline allowing phase contrast to be obtained, as described in Sections 1.2.3 and

1.3.3, ensured a high contrast between the feature (crack) and the surrounding matrix material in the reconstructed images. Figure 4-34 illustrates a typical image used to make COD measurements, taken from the tomographic volume at K_{max}, with the matrix crack appearing as blue and low intensity due to it being effectively air, and the matrix material appearing as yellow. The boundary surfaces of the crack show as red due to the phase contrast, or Fresnel fringe effect, discussed in Section 1.3.3, and therefore the opening of the crack is easily distinguished up to the crack tip. The contrast level across the boundary or edge from the crack (low) to the matrix material (high) therefore has a sharp increase and is not smoothed, as defined in Figure 1-9 of Section 1.3.1. COD measurements were made at intervals of 20 μm along the crack from the crack tip, giving ~25 measurement points along its length. For each measurement point, the opening was measured as the number of adjoined 'blue' pixels between the two boundaries, and the results were averaged for the same position over 15 slices for each of the four tomographic datasets (applied loads). This averaging was carried out in order to reduce the scatter in the measured profiles inherent to such a measurement procedure of crack opening. The excellent definition of the boundaries of the crack within the matrix enabled this simpler method of measurement to be used. This is in contrast to a study of Guvenilir *et al.* who measured crack opening in an Al-Li alloy as a function of applied load using tomography datasets (Guvenilir *et al*, 1999). Because of the lack of sufficient contrast between the crack and the matrix, crack openings were measured through the definition of a threshold linear attenuation coefficient relative to an average value of that of the matrix.

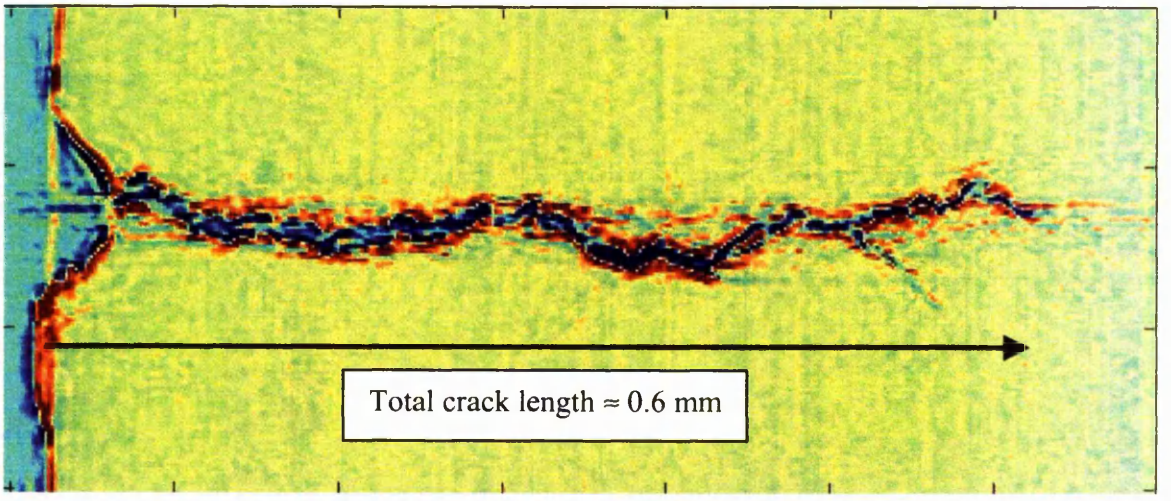

Figure 4-34. Typical image of a slice through a 3-D tomographic dataset used to make COD measurements, with the crack (blue) clearly distinguishable from the matrix.

Figure 4-35 shows the COD profiles measured from the tomographic datasets for the four different loads that were applied to the sample, as a function of distance from the notch tip. Figure 4-36 shows the same profiles as in Figure 4-35 but as a function of the square root of the distance – such a functional form has been found to fit the data better than a linear relation (Davidson, 1992). The averaged results are shown for slices (through the respective volumes) not containing any fibres in the crack path, such as that shown in Figure 4-34, due to the fact that the COD could not be measured where a fibre was in the way. It is important to note that the resolution or pixel size of the tomographic reconstructions was 2 μm, and therefore a crack opening of less than 2 μm could not be measured and similarly only openings of multiples of 2 μm could be measured with the camera that was used. This is especially important regarding crack openings in the crack tip region. The crack tip was assumed to be one pixel wide. It is clear from the profiles that the CODs decrease as the crack tip is approached, and an increase in the applied stress results in an increase in the magnitude of the CODs. This, and the overall shape of the measured profiles, is in agreement with *in-situ* SEM COD measurements in Tiβ21s/35 vol. % SCS-6 composites (Liu and Bowen, 2003 (see Section 3.6.2); Kaya, 2003).

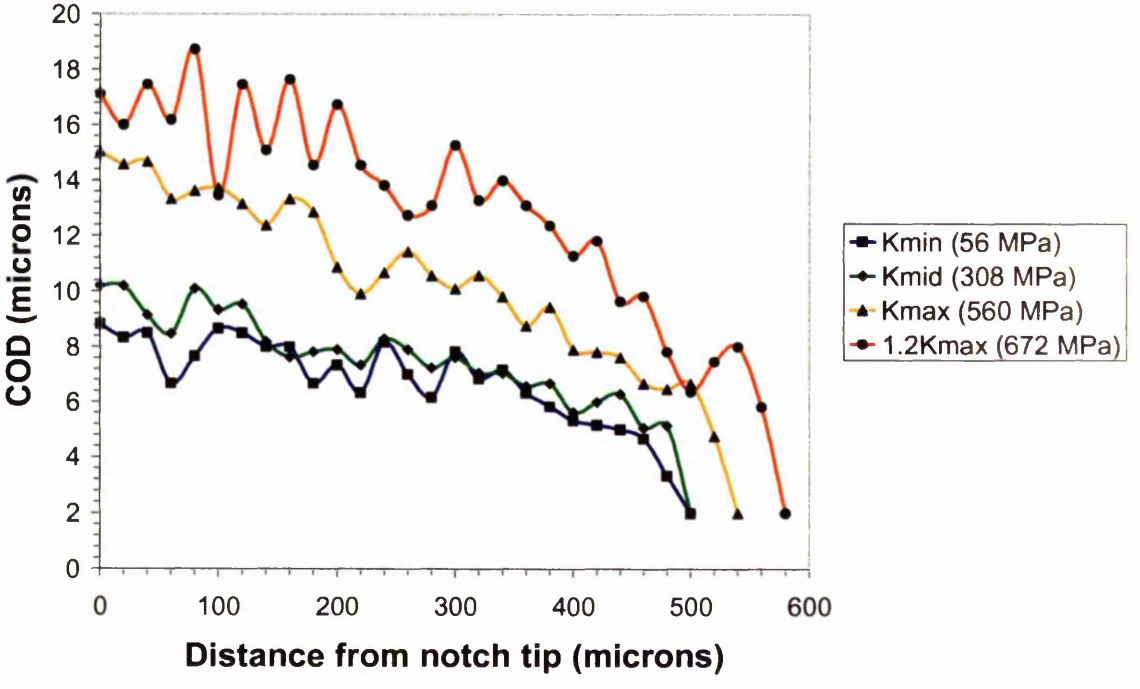

Figure 4-35. COD profiles along the crack path, measured as the distance from the notch tip, under different applied loads, measured from virtual slices through the corresponding 3-D tomographic volumes such as that in Figure 4-34.

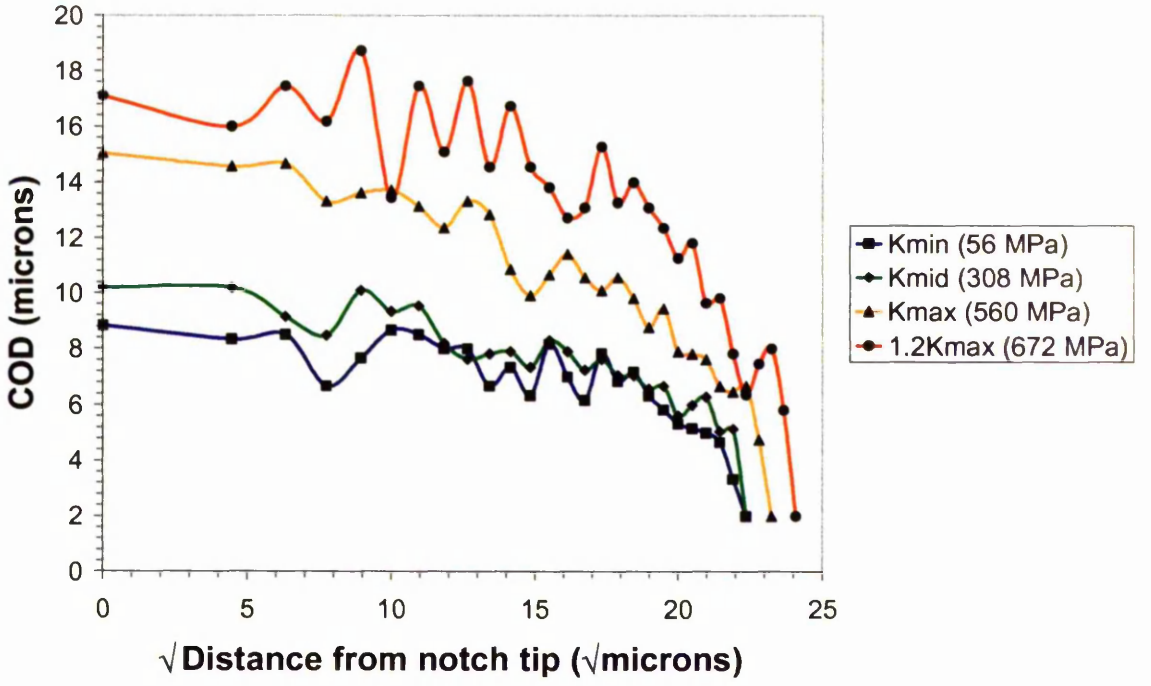

Figure 4-36. COD profiles as in Figure 4-35 but plotted against √distance along the crack path, measured from the notch tip.

Both of these studies report a residual crack opening in the unloaded state, measured to be ~1-2 μm, which would have been undetectable here due to the pixel resolution of the images used for the measurement. Residual crack opening displacements (CODr) are caused when the passage of a fatigue crack breaks the matrix and causes sliding between the fibre and matrix, thus relieving the axial residual stresses present in the two phases from fabrication of the material (see Section 3.2.3), allowing the fibre to elongate and the matrix to contract. CODr is proportional to the residual stress and the slip distance, and values as high as 5 μm have been measured, using stereo-imaging, for the Ti-6Al-4V/SCS-6 composite system containing 42 vol.% fibres (R = 0.1) (Davidson, 1992). From the CODr measurements, slip lengths up to 1 mm from the crack plane were suggested, similar to values measured adjacent to cracks for the single-ply samples (see Section 4.4.5). The CODr measurement of Davidson is comparable to the COD profile of Figure 4-35 for a small applied load (K_{min}, 56 MPa), which reveals a maximum COD of ~8 μm. Under an applied load of 175 MPa, Davidson measured COD values up to ~8 μm, comparable to values shown in Figure 4-35 for the applied loads at K_{min} and K_{mid}, which sandwich said applied load (Davidson, 1992). Davidson also estimated an average fibre-matrix sliding stress, from the COD and the fibre stress, at ~245 MPa, but with shear stresses ranging

from 15 to 580 MPa. This value is much higher than τ_i values of Preuss *et al.* (~80 MPa) measured from the longitudinal fibre strain distribution around a matrix fatigue crack in a Ti-6Al-4V/35 vol.% SCS-6 fibre composite (Preuss *et al*, 2003), a sample very similar to the one used for the COD measurements of Figure 4-35. One would expect a lower interfacial shear stress during fibre bridging (Liu and Bowen, 2003a) due to the interfaces being fatigued, while that suggested by Davidson is similar to the shear stresses measured during fibre cracking in the single-ply samples (see Section 4.4.5). A number of measurement errors were suggested for the variation in COD and interfacial shear stress measurements of Davidson, associated with the measurement technique and the process of matrix removal.

Analysis of the tomographic volumes indicated that all except one of the fibres remained intact, and this fractured fibre is located near the edge of the specimen as revealed in Figure 4-32. This suggests that all of the fibres in the sample are bridging the fatigue crack. The profiles of Figure 4-35 seem to confirm this due to the absence of an increase in the rate of crack opening at distances further away from the crack tip. The measurements of Liu and Bowen (Liu and Bowen, 2003) and Kaya (Kaya, 2003) show a significant increase in this rate at distances greater than ~1 mm from the crack tip. This suggests the crack opens without constraint due to the presence of fractured fibres within this range. Intact fibres located from the crack tip up to ~1 mm were shown to be bridging the fatigue crack. From this it can be concluded that fibre bridging constrains the crack opening and decreases the effective stress intensity factor at the crack tip. As observed in the COD profiles, the crack extends further for the higher applied loads, i.e. at K_{max} and above. This shows that crack closure is observed in the vicinity of the crack tip, and when an external load is applied, the closed crack tip opens. Also, Kaya reported experimental values of COD to fall well below those of a completely unbridged crack, calculating an unbridged crack opening of 30 μm compared to a measurement of 6 μm for the bridged case (and 8 μm as measured here), both with an applied load of ~60 MPa.

4.6. Summary and Conclusions

High spatial resolution diffraction strain measurements and X-ray tomography have been carried out to study the micromechanics of stress and damage development that occurs on progressive straining in the vicinity of damaged fibres in Ti/SiC_f composite samples. Samples were designed to contain these damaged fibres, which were induced via

laser drilling of the fibre ribbons prior to the composite fabrication process. Regarding the strain measurements, information regarding the stress concentrations apparent in fibres adjacent to a fibre defect while under load has been obtained. In addition, the state of the interface has been determined via the calculation of interfacial frictional shear strengths. Via X-ray tomography, cracking sequences and the characteristics of cracks have been observed. The interaction between the fibres and a matrix crack has also been observed, enabling representative crack opening displacement profiles to be measured as a function of applied load, non-destructively. The important findings are summarised as follows:

1. Thermal compressive axial residual strains in excess of 0.2% (-2000 microstrain) have been measured in the SiC fibres and thermal tensile residual strains as high as 0.24% (+2400 microstrain) have been measured in the matrix phase. These are in agreement with an equivalent temperature drop, $\Delta T_{effective}$, of around 700°C, suggested by (Withers and Clarke, 1998). In some cases small or essentially no initial thermal residual strains were measured in the fibres or neighbouring matrix, which is thought to be due to a variability in processing.
2. Load redistribution from a broken fibre increases that in its nearest neighbours by about 40% of the uniform strain, and that in next nearest fibres by about 20% (average values), causing successive fractures to occur near the original defect through a local load sharing (LLS) mode of failure. This is observed to be dependent on the number of broken and unbroken fibres in the ply. Localised matrix plasticity has been suggested as contributing to the cumulative failure of neighbouring fibres.
3. Fibre fracture occurs at strains in excess of 1.2%, in agreement with the results of (Laffargue and Bowen, 2001) who observed a mean failure strain of 1.4% for 10mm gauge length fibres. Multiple fibre cracks were also measured in some cases (also observed during tomography), and observed to occur at strains below the original fracture strain. This is thought to be due to surface damage to the fibre during the initial fracture, or damage of the fibre coating and/or reaction zone.
4. Reverse sliding occurs during unloading in the immediate vicinity of the fibre ends over a length of ~300 μm, giving rise to a characteristic compressive residual strain in these regions. In regions further away from the fibre ends, the fibre fragments are in residual tension due to the neighbouring matrix having been plastically extended conferring a tensile stress to the fibre. The remainder of the previously forward sliding interface reverts to a sticking state. Sliding is also suggested to

occur in an unbroken fibre neighbouring a defect, inferring an interfacial shear stress of ~50-60 MPa.

5. The fibre strains are measured to build-up from fibre ends adjacent to a crack over a distance of ~750 μm, which is the frictional sliding length. Interfacial frictional shear strengths in the region 200-250 MPa have been measured across fibre ends resulting from load-induced cracks. In most cases, the fibres are subjected to different levels of friction. These values are significantly higher than those measured from push-out tests, presumably due to the greater clamping force around a fibre break compared to the nature of the push-out measurements (Majumdar *et al*, 1998). Shear strengths in the range 100-150 MPa are measured across fibre ends adjacent to laser drilled holes.
6. Fibre breakages are mainly in the form of characteristic wedge shaped cracks, which are assumed to originate at a defect on the surface of a fibre. It is likely that the shockwave or recoil of the fracturing fibre caused by the first high stress fracture event, itself consisting of a straight crack morphology, introduces surface damage from which the wedge cracks form. This is consistent with experimental observations during failure of individual single fibres (Laffargue and Bowen, 2001), which suggest that high failure stresses are often associated with fracture initiation from the SiC core, whereas lower stress failures originate from the surface. Spiral-like defects have also been observed, although their origin is unknown.
7. In the fibre bridging fatigue crack sample, no fibre breakages were observed for the interior fibres, revealing that all fibres bridge the crack. The crack front showed a number of characteristic features, including preferential advancement in fibre-free regions, crack bifurcation near fibres and different crack plane heights upstream and downstream of fibres. It is clear from the measured COD profiles that the CODs decrease as the crack tip is approached, and an increase in the applied stress results in an increase in the magnitude of the CODs, in agreement with *in-situ* SEM COD measurements of (Liu and Bowen, 2003).

References

Bache, M. R., Evans, W. J., Randle, V. and Wilson, R. J., (1998), 'Characterisation of mechanical anisotropy in titanium alloys', *Materials Science and Engineering*, **A257**(1), 139-144.

Bannister, D. J., Andrews, M. C. and Cervenka, A. J., Young, R. J., (1995), 'Analysis of the single-fibre pull-out test by means of Raman spectroscopy: Part II. Micromechanics of deformation for an aramid/epoxy system', *Composites Science and Technology*, **53**(4), 411-421.

Bennett, J. A. and Young, R. J., (1998), 'The effect of fibre-matrix adhesion upon crack bridging in fibre reinforced composites', *Composites Part A*, **29A**, 1071-1081.

Beyerlein, I. J. and Landis, C. M., (1999), 'Shear-lag model for failure simulations of unidirectional fibre composites including matrix stiffness,' *Mechanics of Materials*, **31**, 331-350.

Buffière, J.-Y., Maire, E., Cloetens, P., Lormand, G. and Fougères, R., (1999), 'Characterisation of internal damage in a MMC_p using X-ray synchrotron phase contrast microtomography', *Acta Materialia*, **47**(5), 1613-1625.

Cox, H. L., (1952), 'The elasticity and strength of paper and other fibrous materials', *British Journal of Applied Physics*, **3**, 73-79.

Davidson, D. L., (1992), 'The micromechanics of fatigue crack growth at 25°C in Ti-6Al-4V reinforced with SCS-6 fibres', *Metallurgical Transactions A*, **23A**, 865-879.

González, C. and Llorca, J., (2001), 'Micromechanical modelling of deformation and failure in Ti-6Al-4V/SiC composites', *Acta Materialia*, **49**, 3505-3519.

Guvenilir, A., Breunig, T. M., Kinney, J. H. and Stock, S. R., (1999), 'New direct observations of crack closure processes in Al-Li 2090 T8E41', *Phil. Trans. R. Soc. Lond. A*, **357**, 2755-2775.

Hanan, J. C., Ustundag, E., Beyerlein, I. J., Swift, G. A., Almer, J. D., Lienert, U. and Haeffner, D. R., (2003), 'Microscale damage evolution and stress redistribution in Ti-SiC fibre composites,' *Acta Materialia*, **51**(14), 4239-4250.

Huang, Y. and Young, R. J., (1994), 'Analysis of the fragmentation test for carbon-fibre/epoxy model composites by means of Raman spectroscopy', *Composites Science and Technology*, **52**, 505-517.

Kaya, PhD Thesis, University of Birmingham, 2003.

Lacroix, T., Tilmans, B., Keunings, R., Desaeger, M. and Verpoest, I., (1992), 'Modelling of critical fibre length and interfacial debonding in the fragmentation testing of polymer composites', *Composites Science and Technology*, **43**, 379-387.

Laffargue, J. and Bowen, P., IRC in Materials for High Performance Applications, School of Metallurgy and Materials, University of Birmingham, Birmingham, B15 2TT. Personal Communication, 2001.

Le Petitcorps, Y., Pailler, R. and Naslain, R., (1989), 'The fibre/matrix interfacial shear strength in titanium alloy matrix composites reinforced by silicon carbide or boron CVD filaments', *Composites Science and Technology*, **35**, 207-214.

Liu, J. and Bowen, P., (2003), 'Bridging mechanisms in a Tiβ21s/SCS-6 composite: *In-situ* scanning electron microscopy study', *Metallurgical and Materials Transactions A*, **34A**, 1193-1202.

Mahiou, H., Beakou, A. and Young, R. J., (1999), 'Investigation into stress transfer characteristics in alumina-fibre/epoxy model composites through the use of fluorescence spectroscopy' *Journal of Materials Science*, **34**, 6069-6080.

Maire, E., Owen, A., Buffiere, J.-Y. and Withers, P. J., (2001), 'A synchrotron X-ray study of a Ti/SiC_f composite during in-situ straining,' *Acta Materialia*, **49**, 153-163.

Majumdar, B. S., Matikas, T. E. and Miracle, D. B., (1998), 'Experiments and analysis of fibre fragmentation in single and multiple-fibre SiC/Ti-6Al-4V metal matrix composites', *Composites B: Engineering*, **29**(2), 131.

Marshall, D. B., (1992), 'Analysis of fibre debonding and sliding experiments in brittle matrix composites', *Acta Metallurgica et Materialia*, **40**, 427-441.

Noyan, I. C. and Cohen, J. B., *Residual Stress, Measurement by Diffraction and Interpretation*, New York: Springer-Verlag, 1987.

Nutt, S. R. and Wawner, F. E., (1985), 'Silicon carbide filaments: microstructure', *Journal of Materials Science*, **20**, 1953-1960.

Nye, J. F., *Physical Properties of Crystals*, Oxford University Press, Oxford, 1985.

Pang, J. W. L., Holden, T. M., Turner, P. A. and Mason, T. E., (1999), 'Intergranular stresses in Zircaloy-2 with rod texture', *Acta Materialia*, **47**(2), 373-383.

Piggott, M. R., *Load Bearing Fibre Composites*, Pergamon Press, Oxford, UK, 1980, 83-89.

Preuss, M., Rauchs, G., Doel, T. J. A., Steuwer, A., Bowen, P. and Withers, P. J., (2003), 'Measurements of fibre bridging during fatigue crack growth in Ti/SiC fibre metal matrix composites', *Acta Materialia*, **51**(4), 1045-1057.

Preuss, M., Withers, P. J., Maire, E. and Buffière, J.-Y., (2002), 'SiC single fibre full-fragmentation during straining in a Ti-6Al-4V matrix studied by synchrotron X-rays', *Acta Materialia*, **50**, 3175-3190.

Rauchs, G., Preuss, M. and Withers, P. J., (2002), 'Micromechanical analysis of internal stress development during single-fibre fragmentation testing of Ti/SiC_f', *Acta Materialia*, **50**, 2477-2490.

Spowart, J. E. and Clyne, T. W., (1999), 'The axial compressive failure of titanium reinforced with silicon carbide monofilaments', *Acta Materialia*, **47**, 671-687.

Van den Heuvel, P. W. J., Peijs, T. and Young, R. J., (1997), 'Failure phenomena in two-dimensional multi-fibre microcomposites: 2. A Raman spectroscopic study of the influence of inter-fibre spacing on stress concentrations', *Composites Science and Technology*, **57**, 899-911.

Warrier, S. G. and Majumdar, B. S., (1999), 'Elastic shielding during fatigue crack growth of titanium matrix composites', *Metallurgical and Materials Transactions A*, **30A**, 277-286.

Withers, P. J. and Clarke, A. P., (1998), 'A neutron diffraction study of load partitioning in continuous Ti/SiC composites', *Acta Materialia*, **46**, 6585-6598.

Chapter 5

Mechanics and Characterisation of Metallic Foams

The aim of this chapter is to provide a review of the theoretical and experimental considerations on the use of closed-cell metallic foams in energy absorption applications. With particular reference to aluminium foams, one of the most significant properties of such materials is the amount of energy absorbed during deformation, which is directly related to the mechanisms of collapse in compression. An account of the deformation mechanisms observed in a typical compressive stress-strain curve and the model theoretical equations that have been derived based on these mechanisms will be given. A number of different production processes exist for the fabrication of metallic foam materials, and are based on the two main routes of liquid-state and powder metallurgy. A description of these different processes will be given. These processes affect the resulting cellular distributions and therefore the compressive behaviour, which is the main topic of the work covered in Chapter 6. A review of existing characterisation studies of closed-cell foams will then be given, describing model investigations into the effect of defects and imperfections in the cellular structure and cellular arrangement, on the compressive properties and deformation behaviour. These will act as a background to the experimental X-ray microtomography investigation of Chapter 6.

5.1. Introduction

Metallic foams are cellular solids made up of an interconnected network of solid struts or plates which form the edges and faces of cells. If the solid of which the foam is made is contained in the cell edges only, so that the cells connect through open faces, the foam is said to be open-celled. If the faces are solid too, so that each cell is sealed off from its neighbours, it is said to be closed-celled. Some foams are partly open and partly closed. The most important feature of a foam is its relative density, ρ^*/ρ_s; the density of the foam material, ρ^*, divided by that of the solid from which the cell walls are made, ρ_s. In general, cellular solids, and more specifically metal foams, have relative densities of less than about 0.3, resulting in porosities of greater than 70% (Gibson and Ashby, 1997).

In the past few years there has been a considerable increase in industrial interest in metal foams, especially of aluminium or its alloys. Closed-cell aluminium foams have unique properties, including excellent stiffness-to-weight ratio when loaded in bending, low density with good shear and fracture strengths, good mechanical and vibrational damping capacity, and have exceptional ability to absorb energy and impact at almost constant pressure and load (Ashby *et al*, 2000). Figure 5-1 shows a Young's modulus, E, versus density, ρ, material property chart for available metal foams (Ashby *et al*, 2000), shown in relation to the full range of values for all engineering materials (Ashby, 1999). The numbers in parentheses are the foam density in Mg/m^3. The broken lines show the indices E/ρ, $E^{1/2}/\rho$ and $E^{1/3}/\rho$ (defined further in Figure 5-3 below). Metal foams have attractively high values of the last of these indices, suggesting their use as light, stiff panels, and as a way of increasing natural vibration frequencies (Ashby *et al*, 2000). Figure 5-2 shows a metal foam property chart of compressive strength, σ_c, plotted against density, ρ (Ashby *et al*, 2000), again shown in relation to other engineering materials (Ashby, 1999). Note that the chart for the metal foams plots compressive strength. For the general engineering materials chart, yield strength is plotted for metals and polymers (same in tension and compression for most practical purposes), crushing strength in compression for brittle ceramics, tear strength for elastomers and tensile failure strength for composites. The broken lines in this case show the indices σ_c/ρ, $\sigma_c^{2/3}/\rho$ and $\sigma_c^{1/2}/\rho$. High values of the last of these indices suggest the use of metal foams as light, strong panels (Ashby *et al*, 2000). As is observed in Figures 5-1 and 5-2, in terms of both specific stiffness and specific strength, metal foams show similar values to the woods, a naturally occurring cellular material that has been made use of by man for centuries, mainly in the structural construction industry. The reduction in density over other structural materials, such as the engineering alloys, is clear, whilst still retaining appreciable stiffness and strength.

When selecting a material for a specific application, if axial stiffness and strength are needed, then measures of E/ρ and σ_c/ρ respectively are important. If bending stiffness and strength are sought then $E^{1/2}/\rho$ and $\sigma_c^{2/3}/\rho$ (beams) or $E^{1/3}/\rho$ and $\sigma_c^{1/2}/\rho$ (panels) are the important measures (Ashby *et al*, 2000). To illustrate this, Figure 5-3(a)-(c) shows E/ρ vs. σ_c/ρ, $E^{1/2}/\rho$ vs. $\sigma_c^{2/3}/\rho$ and $E^{1/3}/\rho$ vs. $\sigma_c^{1/2}/\rho$ selection charts respectively for currently available metal foams.

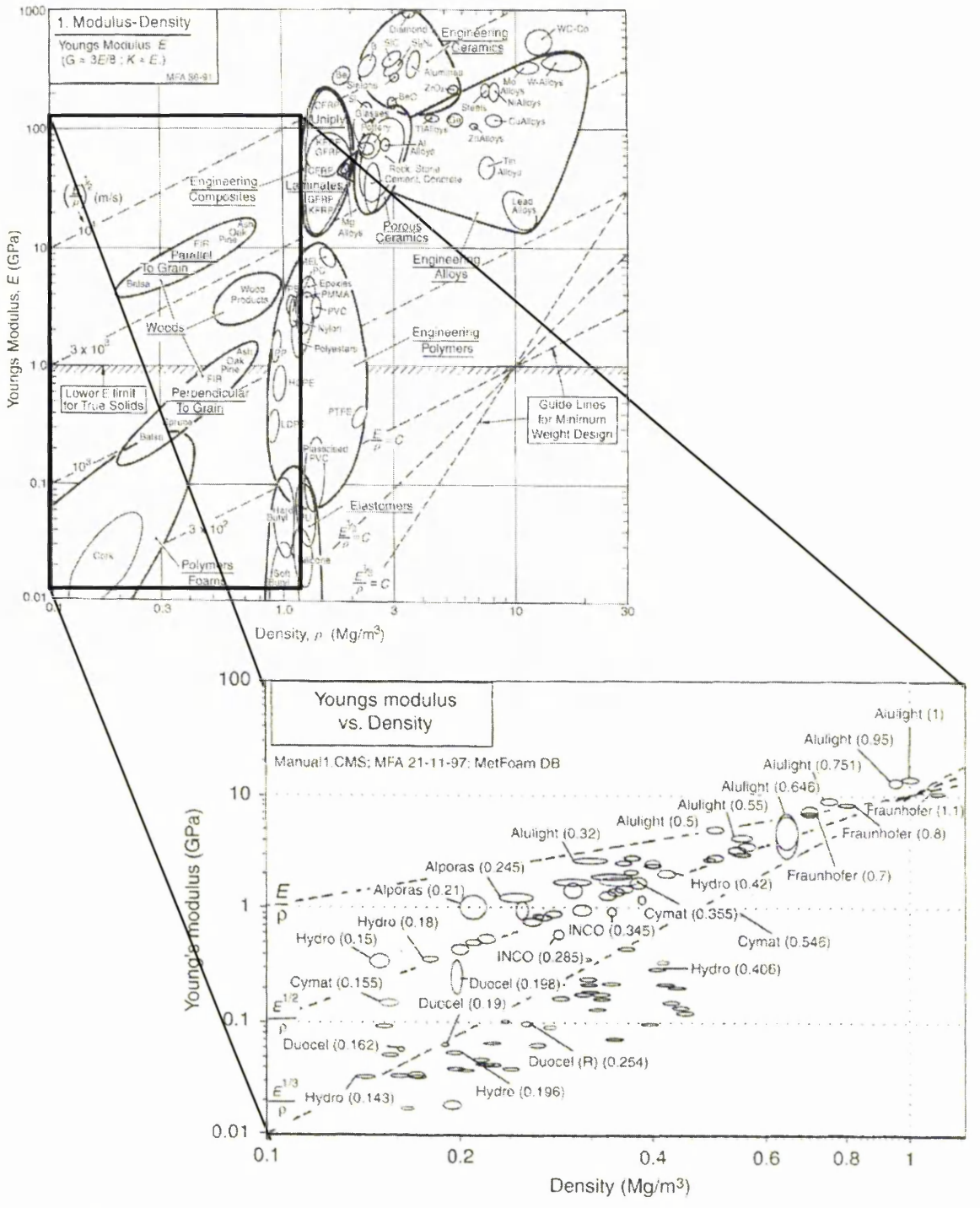

Figure 5-1. Material property chart showing Young's modulus plotted against density for currently available metal foams (Ashby *et al*, 2000), illustrated in relation to the same region of such a chart for all engineering materials (inset; Ashby, 1999).

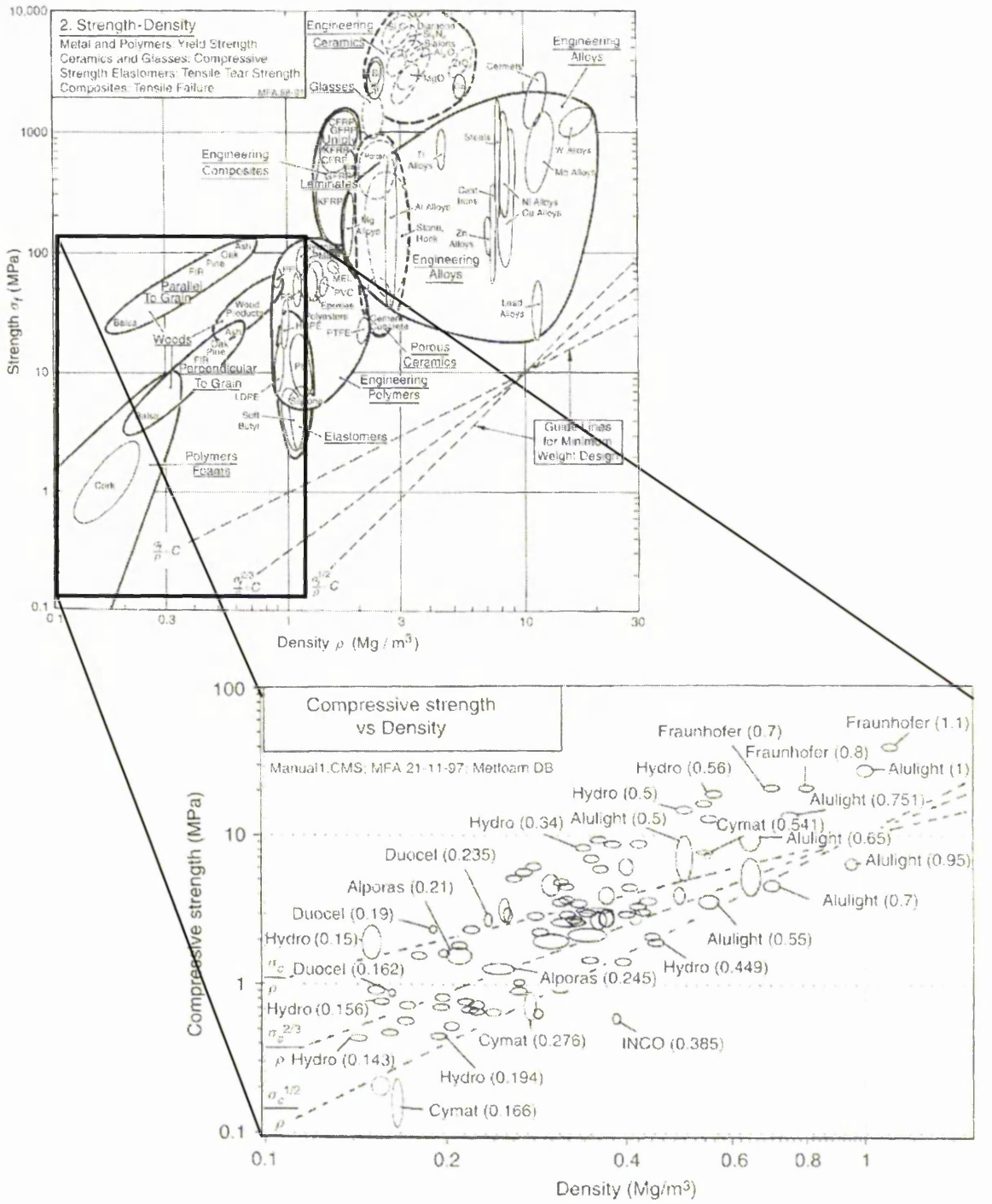

Figure 5-2. Material property chart showing compressive strength plotted against density for currently available metal foams (Ashby *et al*, 2000), illustrated in relation to the same region of such a chart for all engineering materials (inset; Ashby, 1999).

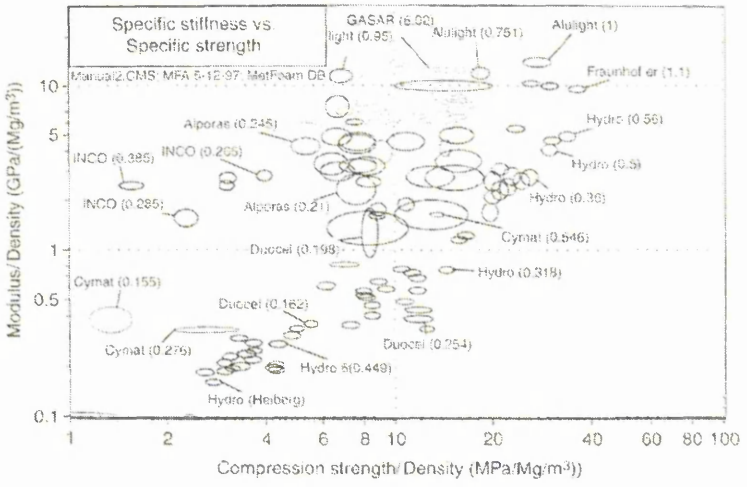

(a)

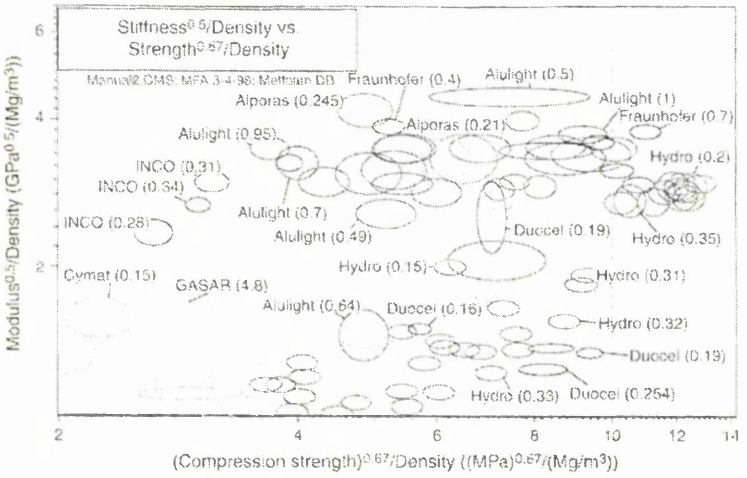

(b)

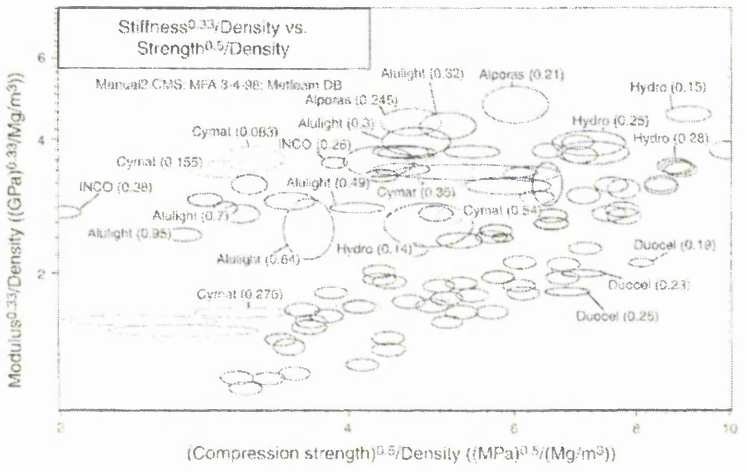

(c)

Figure 5-3. Showing the properties (a) specific modulus E/ρ plotted against specific strength σ_c/ρ, (b) $E^{1/2}/\rho$ vs. $\sigma_c^{2/3}/\rho$ and (c) $E^{1/3}/\rho$ vs. $\sigma_c^{1/2}/\rho$, for a range of metal foams. (Ashby *et al*, 2000).

Considering Figure 5-3(a), for reference, the value of E/ρ for structural steel is 25 GPa/(Mg/m^3) and that of σ_c/ρ is 24 MPa/(Mg/m^3). The values for the 1000 series aluminium alloys are almost the same. It is clear that metal foams have lower values of these two properties compared to steel and aluminium. Figure 5-3(b) shows $E^{1/2}/\rho$ plotted against $\sigma_c^{2/3}/\rho$. Values for steel are 1.8 GPa/(Mg/m^3) and 4.3 MPa/(Mg/m^3) respectively, while those for aluminium are 3.1 GPa/(Mg/m^3) and 6.2 MPa/(Mg/m^3). Metal foams can surpass conventional engineering materials in this case. While for the properties of $E^{1/3}/\rho$ and $\sigma_c^{1/2}/\rho$, shown plotted in Figure 5-3(c), metal foams easily surpass steel (0.7 GPa/(Mg/m^3) and 1.8 MPa/(Mg/m^3) respectively) and aluminium (1.5 GPa/(Mg/m^3) and 3.7 MPa/(Mg/m^3)). This illustrates how metal foams can have improved properties over other conventional engineering materials for a specific application, in this case for bending stiffness and strength in panels.

It is also worth noting the properties of open-cell metallic foams. These have a large accessible surface area and a high cell-edge conduction giving exceptional heat transfer ability. Figure 5-4 gives information about thermal properties of foams, showing the thermal conductivity, λ, plotted against the specific heat per unit volume, $C_p\rho$. Added to this are contours of thermal diffusivity, $a = \lambda / C_p \rho$.

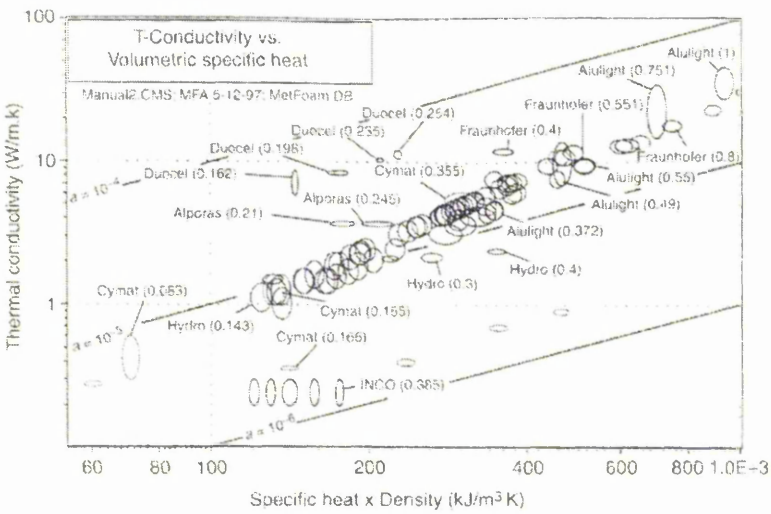

Figure 5-4. Thermal conductivity, λ, plotted against volumetric specific heat, $C_p\rho$, for currently available metal foams. Contours show the thermal diffusivity, $a = \lambda / C_p \rho$, in units of m^2/s. (Ashby *et al*, 2000).

Thermal conductivity is a measure of steady-state heat response; thermal diffusivity is a measure of transient response. Foams are remarkable for having high values of thermal conductivity. Note that the open-cell aluminium foams (e.g. Duocel) have relatively high thermal diffusivities.

As a result of these collective properties, aluminium foams are candidate materials for use in many high technology industries such as the automotive and aerospace industries (Ashby *et al*, 2000; Baumeister *et al*, 1997; Evans and Hutchinson, 1999). They are currently used in applications such as lightweight structures, e.g. the cores of sandwich panels, for energy/impact absorbers and in packaging, for acoustic absorption, and in heat exchangers, filters and electrodes. The efficient use of closed-cell foams in structural applications requires detailed understanding of their mechanical behaviour. For example, one of the most significant properties of aluminium foams, the amount of energy absorbed during deformation, is directly related to the mechanisms of collapse in compression. Simple equations relating their structural features and the properties of the material from which they are made have been derived (Gibson and Ashby, 1997; see Section 5-3). At present, no robust, quantitative methods for characterising the 3-D microstructure exist, and thus the intrinsic relationships between processing conditions, structure and properties cannot be developed. X-ray microtomography can provide detailed 3-D descriptions of the internal microstructure of a metal foam non-destructively (which cannot be achieved with commonly used 2-D characterisation techniques, such as serial sectioning). While monitoring the structural evolution under an applied compressive strain, important relations between the 3-D cellular structure and the mechanisms of deformation within the foam material can be investigated. Such work forms the basis of the investigation detailed in Chapter 6. Here the effect of the cell structure and density distributions on the local concentration of deformation during compression of different closed-cell metallic foams, and thus their efficient use in energy absorption applications is studied.

5.2. Fabrication Processes of Aluminium Foam

The mechanical properties of metal foams have been shown to depend upon the properties of the solid metal of the cell walls and the relative density (Gibson and Ashby, 1997). Thus, the production route will have a significant effect on the mechanical response and behaviour of the material. Aluminium foam can be produced by various methods, the main ones being (Ashby *et al*, 2000; Davies and Zhen, 1983):

- Bubbling a gas through molten Al-SiC or Al-Al_2O_3 alloys.
- By stirring a foaming agent (typically TiH_2) into a molten Al alloy and controlling the pressure while cooling.
- Consolidation of Al powder with a particulate foaming agent (TiH_2) followed by heating into the mushy state when the foaming agent releases hydrogen, expanding the material.
- Manufacture of a ceramic mould from a wax or polymer-foam precursor, followed by burning-out of the precursor and pressure infiltration with molten Al or Al powder slurry which is then sintered.

Production processes can generally be divided into liquid-state and powder metallurgical routes for closed-cell foams and casting processes for open-cell. It can be recognised from even this cursory description of the fabrication processes that, with the exception of the casting method, they are all highly stochastic and difficult to control. This means that consistent and reproducible microstructures are not easy to obtain. Various problems can be encountered during stabilisation and solidification of the cellular material.

5.2.1. Common problems during cell formation

Before a detailed account of each of the main fabrication processes listed above is given, there are two main processing control issues to consider: drainage, and defects. Successful processing is reliant on controlling both of these properties.

5.2.1.1. Drainage of foams

With foams made by liquid routes, processes which determine drainage are important as the foam goes from liquid to solid. At the junction of cell faces in a cell edge, surface tension causes the liquid-gas interface to be curved in an arc of constant radius called a Plateau border (Plateau, 1873). The surface tension forces acting along the Plateau border cause the fluid pressure in the cell edge to be lower than that in the cell face. The drainage pattern in a wet foam is from the cell face into the adjacent cell edges, where the Plateau border regions form channels through which gravitational forces drain the liquid over time. In a liquid foam with no impurities, the cell faces will drain until they burst due to the strong surface tension forces. In order for a liquid foam to become stable and solidify, the liquid-gas interface must be altered either by introducing a surfactant that reduces surface tension or by increasing the viscosity of the surface layer (Walstra, 1989). A cell face in a liquid foam that is stabilised in this way will drain down to some critical thickness and then stop further drainage. The drainage pattern of a liquid metal foam can

affect the structure of the resulting solid foam in two ways. If the excess liquid is not allowed to drain away sufficiently before solidification, a density gradient results causing a high degree of material heterogeneity and anisotropy, as has been noted in some foams (Beals and Thompson, 1997). Drainage also has an influence on the distribution of liquid between the cell faces and the Plateau borders at solidification. As a stable liquid foam drains, the radii of curvature of the Plateau borders and the fraction of total liquid contained within them decrease. A significant effect of the solid distribution in the cell faces relative to that in the cell edges on the strength and stiffness of idealised cellular structures has been investigated (Simone and Gibson, 1998a; see Section 5.4).

5.2.1.2. Defects in cell walls

Studies have shown that metallic foams with a low relative density ($\rho^*/\rho_s < 0.15$) exhibit particularly poor properties compared to idealised models (Andrews *et al*, 1999; Simone and Gibson, 1998b). Closed cell foams deform through two basic mechanisms: the bending of cell edges; and in-plane axial stretching of cell faces (see Section 5.3). Because the cell faces of conventional low relative density metallic foams are often curved or corrugated (Andrews *et al*, 1999) their contribution to the structural performance of the foam is less than optimum, leading to poor mechanical properties. Curved cell walls can result from pressure differences between cells in the liquid metal foam before solidification (Simone and Gibson, 1998c). For a given liquid foam, smaller cells generally have a higher internal gas pressure than larger ones. The liquid cell face separating two adjacent cells has a curvature which is proportional to the difference in internal gas pressure of the cells. Air convection within the cells can also cause cell faces to be curved in the direction of gas rise. Corrugations in cell walls are the result of handling of the liquid foam during solidification, and are found primarily in low density foams produced by the Alcan process (Prakash *et al*, 1995; see Section 5.2.2.1). The corrugations in these foams have been found to be preferentially oriented perpendicular to the thickness of the panel (Prakash *et al*, 1995). The yield strength of solid aluminium alloys at two-thirds of the liquidus temperature can be as little as 10% of that at room temperature (Metals Handbook Vol. 2, 1990), suggesting that even mild mechanical manipulations of an aluminium foam during and immediately following solidification can result in cell face buckling. The lowering of the gas pressure within the closed cells as the foam cools could also be a contributing factor. Lower density foams with large cells are more susceptible to cell face wrinkling due to the low thickness-to-edge length ratio of their cell faces.

5.2.2. Liquid-state processes for closed-cell foams

5.2.2.1. Melt gas injection (air bubbling)

Pure liquid metals cannot easily be caused to foam by bubbling a gas into them – drainage of liquid down the walls of the bubbles usually occurs too quickly to create a foam that remains stable long enough to solidify, as explained in Section 5.2.1.1. The addition of small, insoluble, or slowly dissolving particles, such as aluminium oxide or silicon carbide, raise the viscosity of the aluminium melt and impede drainage in the bubble membrane, thus stabilising the foam (Prakash *et al*, 1995). Gas-injection processes are easiest to implement with aluminium alloys because they have a low density and do not excessively oxidise when the melt is exposed to air or other gases containing oxygen. The method is illustrated in Figure 5-5 (Ashby *et al*, 2000).

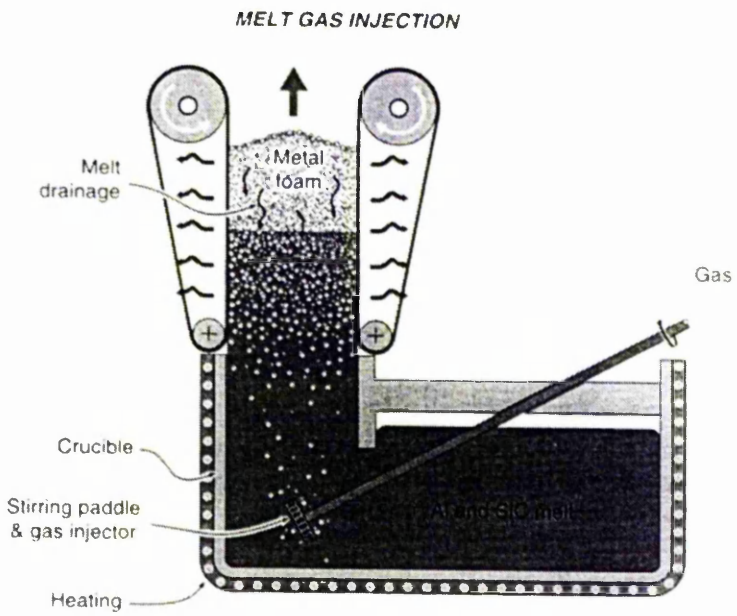

Figure 5-5. A schematic illustration of the method of manufacture of aluminium foam by the melt gas injection method (Alcan/Cymat and Hydro processes). (Ashby *et al*, 2000).

In this process, pure aluminium or an aluminium alloy is melted and gas is dispersed into small bubbles in the melt by rotor impellers. The walls of the created bubbles are stabilised by adding 5-15 wt. % of the ceramic particles, avoiding coalescence between them. The most common particles, typically 0.5-25 μm in diameter, are silicon carbide or alumina. A variety of gases can be used to create bubbles within liquid aluminium – air is most commonly used but carbon dioxide, oxygen, inert gases, and even water can be

injected into liquid aluminium to create bubbles. Bubbles formed by this process float to the melt surface where they accumulate, drain and then begin to solidify. The accumulated foam on the melt surface is transferred to a conveyor belt where it solidifies and cools. The thermal gradient in the foam determines how long the foam remains liquid or semi-solid, and thus the extent of drainage. Low relative density, closed-cell foams can be produced by carefully controlling the gas-injection process and the cooling rate of the foam. Foam material with typical relative densities of 0.1-0.5 can be produced by this method, the density mainly being controlled by the speed of the rotor, the gas flow through the rotor and the amount of particles in the melt (Prakash *et al*, 1995). Norsk-Hydro and Cymat (using a process developed by Alcan) supply foamed aluminium alloys made this way. This method is the least costly to implement.

5.2.2.2. Gas-releasing particle decomposition in the melt

Metal foams can be made by adding a foaming agent to the melt instead of injecting gas into it. When the foaming agent is heated, it decomposes and releases gas. For example, a widely used foaming agent, titanium hydride (TiH_2), begins to decompose into titanium and hydrogen when heated above about 465°C. Large amounts of H_2 gas are rapidly released, creating aluminium bubbles that solidify leading to a closed cell foam. Figure 5-6 shows the fabrication procedure (Ashby *et al*, 2000). The first step consists of adding 0.2-8 wt. % calcium into an aluminium melt between 670-690°C. The melt is stirred for several minutes when its viscosity is raised due to the formation of calcium oxide (CaO) and calcium-aluminium oxide ($CaAl_2O_4$) (and maybe Al_4Ca intermetallics), which thicken the liquid metal. After the desired viscosity is reached, the foaming agent, TiH_2, is added (typically 1-3 wt. %) and gas is rapidly released into the hot viscous liquid. The melt soon starts to expand slowly and isothermally at constant pressure. After cooling the vessel below the melting point of the alloy, the liquid foam turns into solid aluminium foam and can be taken out of the mould for further processing. The volume fraction of added calcium and titanium hydride control the relative density, and the cooling conditions determine the cell size. Aluminium foam produced in this way (tradename Alporas) gives relative densities in the range 0.08-0.2. The method is only suitable for aluminium alloys because hydrogen embrittles many metals and because TiH_2 decomposes too quickly in higher melting point alloys.

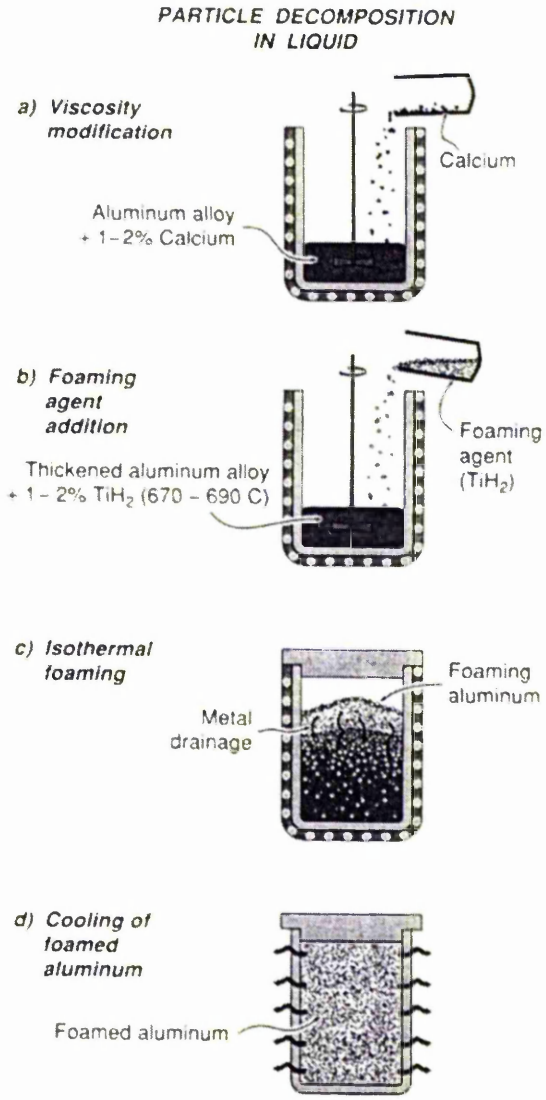

Figure 5-6. The process steps used in the manufacture of aluminium foam by gas-releasing particle decomposition in the melt (Alporas process). (Ashby *et al*, 2000).

5.2.3. Powder metallurgical process for closed-cell foams

Gas-releasing particle decomposition in semi-solids

Foaming agents can be introduced into metals in the solid state by mixing and consolidating powders. The decomposition temperature of titanium hydride (465°C) is well below the melting point of pure aluminium (660°C) and of its alloys. This raises the possibility of creating a foam by dispersing the foaming agent in solid aluminium using powder metallurgy processes and then raising the temperature sufficiently to cause gas release and partial or full melting of the metal, allowing bubble growth. Cooling then stabilises the foam. The process is based on the Fraunhofer and the Alulight processes,

and several groups, including IFAM in Bremen, Germany and LKR in Randshofen, Austria have developed the approach. A schematic diagram of the manufacturing sequence is shown in Figure 5-7 (Ashby *et al*, 2000).

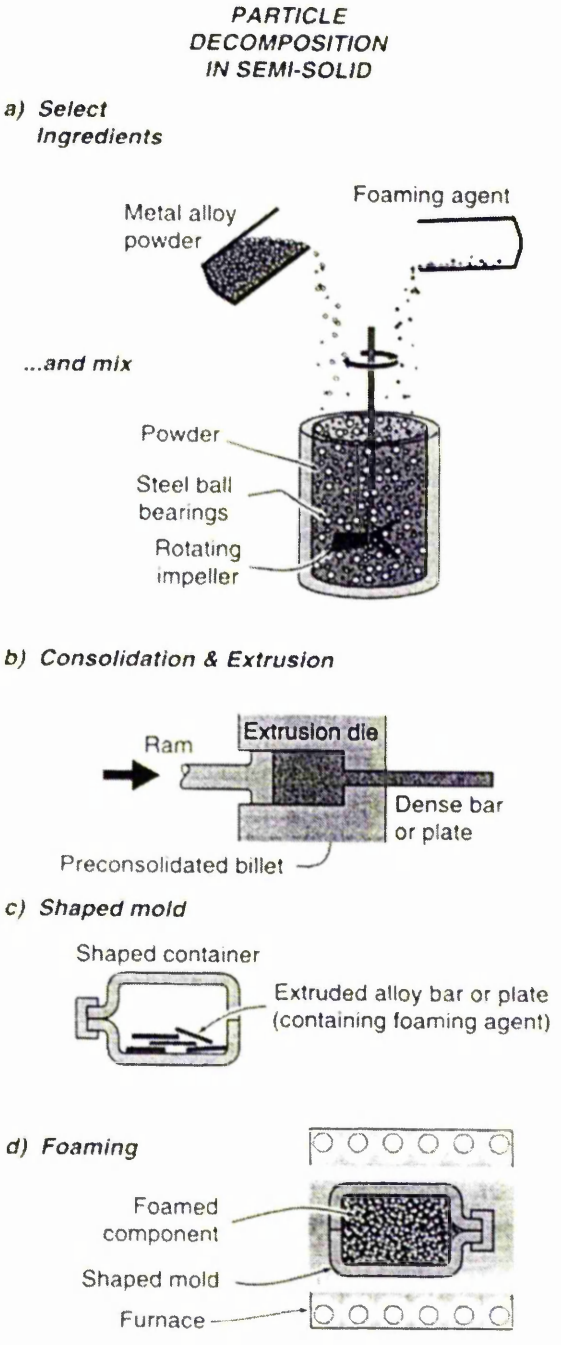

Figure 5-7. Sequence of powder metallurgy steps used to manufacture metal foams by gas-releasing particles in semi-solids (Fraunhofer and Alulight processes). (Ashby *et al*, 2000).

The process begins by combining particles of TiH_2 with an aluminium alloy powder. The content of the foaming agent depends on the desired density. After the ingredients are thoroughly mixed, the powder is cold compacted and then extruded into a bar or plate of near theoretical density. A semi-finished product is obtained in which the foaming agent is homogeneously distributed within a dense, virtually non-porous metallic matrix. This foamable, 'precursor' material is chopped into small pieces of the desired shape by rolling or cutting, placed inside a sealed split mould, and heated to just above the solidus temperature of the alloy. The metal melts and the TiH_2 decomposes, releasing gas in a controlled way and creating voids with a high internal pressure. These expand by semi-solid flow and the aluminium slowly swells, creating a foamy mass that fills the mould. The foaming takes place inside simple closed moulds which are completely filled by the foam, and when filled the process is stopped by simply allowing the mould to cool to a temperature below the melting point of the metal. The density of the metal foam is controlled by adjusting the content of foaming agent and by varying the heating conditions. The process results in components with the same shape as the container and having closed outer skins which can be removed by cutting them into samples of the desired dimensions. Relative densities as low as 0.08 can be achieved.

5.2.4. Casting process for open-cell foams

Open-cell polymer foams with low relative densities and a wide range of cell sizes can be used as templates to create investment-casting moulds into which aluminium alloys can be cast. This method is used by ERG Duocel, and is illustrated in Figure 5-8 (Ashby *et al*, 2000). An open-cell polymer foam mould template with the desired cell size and relative density is first of all selected. This can be coated with a mould casting (ceramic powder) slurry which is then dried and embedded in casting sand. The mould is then baked both to harden the casting material and to decompose (and evaporate) the polymer template, leaving a negative image of the foam. This mould is subsequently filled with aluminium alloy and allowed to cool. The use of moderate pressure during melt infiltration can overcome the resistance to flow of the liquid metal. After directional solidification and cooling, the mould materials are removed leaving behind the metal equivalent of the original polymer foam. The method gives open-cell foams with relative densities as low as 0.05.

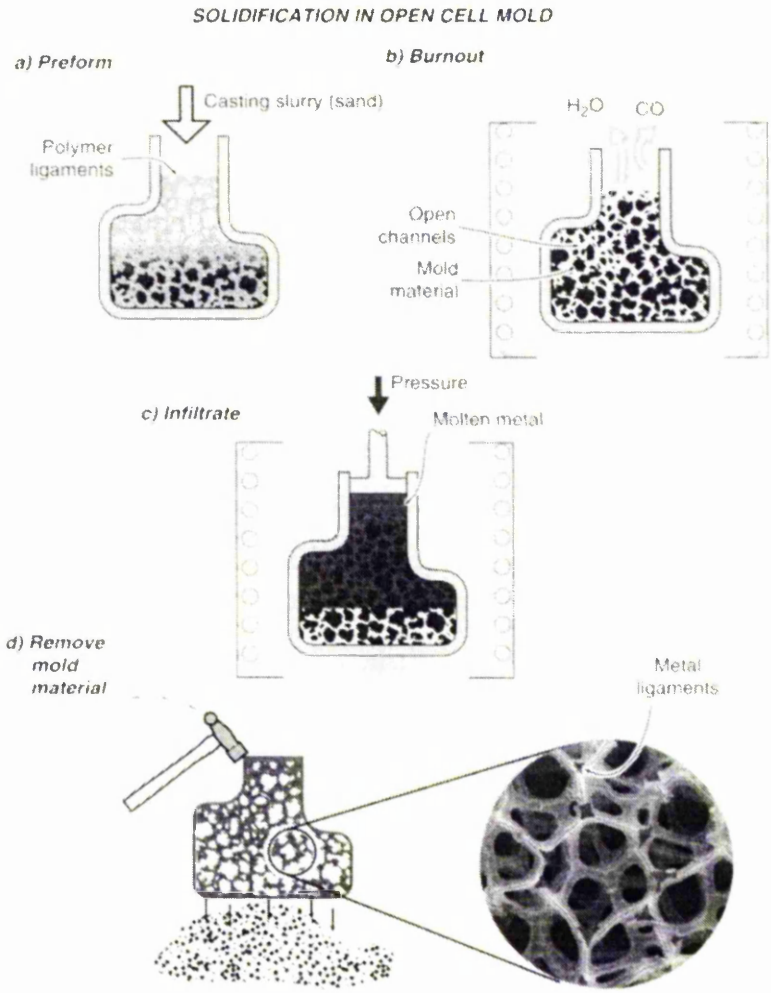

Figure 5-8. Investment casting method used to manufacture open-cell foams (ERG Duocel process). (Ashby *et al*, 2000).

5.3. Mechanics of Foams

Regarding the application of closed-cell foams for energy absorption, the deformation that they experience is directly related to the mechanisms of collapse in compression. Their efficient use requires detailed understanding of these mechanisms and their overall mechanical behaviour under an applied compressive load. Simple equations describing the compressive stiffness and strength of model porous structures, related to their structural features and the properties of the material from which they are made, have been derived for both open and closed-cells (Gibson and Ashby, 1997). The following will give an account of the deformation mechanisms observed during typical compressive loading and the model theoretical equations that have been derived based on these mechanisms.

5.3.1. Compressive deformation mechanisms in metallic foams

Figure 5-9 shows a stress-strain curve generated during a compression test of a closed-cell aluminium foam sample (Alporas material), and, inset, a schematic of an ideal curve with various properties defined. The curve shows three distinct regions:

- Linear elasticity at low stresses – controlled by cell edge/wall bending and, in the case of closed-cell foams, by cell face stretching.
- A long collapse plateau – associated with the collapse of cells by the formation of plastic hinges (compared to elastic buckling in elastomeric foams and brittle crushing in brittle foams). It is this region of the curve that is exploited for energy absorption applications.
- When the cells have almost completely collapsed, opposing cell walls touch and further strain compresses the solid metal itself, giving the final region of rapidly increasing stress or densification.

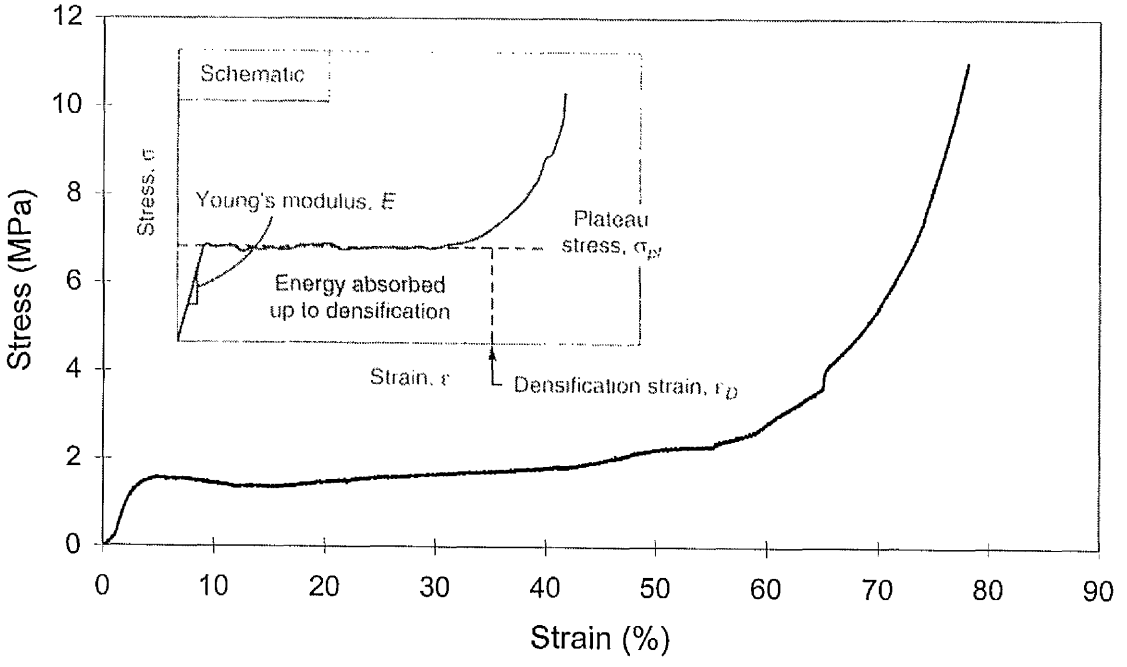

Figure 5-9. Stress-strain curve measured from a compression test of a closed-cell aluminium foam sample (Alporas material), having a relative density of 0.1. Inset, the ideal shape with the various properties defined. (Ashby *et al*, 2000).

Increasing the relative density of the foam increases the Young's modulus, raises the plateau stress, and reduces the strain at which densification starts. Ideal energy absorbers have a long, flat stress-strain curve: the absorber collapses plastically at a constant plateau

stress, σ_{pl}, up to the densification strain, ε_D (inset in Figure 5-9). Energy absorbers for packaging and protection are chosen so that the plateau stress is just below that which will cause damage to the packaged object; the best choice is then the one which has the longest plateau, and therefore absorbs the most energy before reaching ε_D. The energy a foam can absorb is measured from the area under the stress-strain curve up to densification, as illustrated inset in Figure 5-9. In crash protection the absorber must absorb the kinetic energy of the moving object without reaching its densification strain – then the stress it transmits never exceeds the plateau stress.

The stress-strain behaviour of open cell foams, in terms of the shape of the curve, is very similar to that of closed-cell foams, but there are obvious differences regarding the micromechanisms of deformation, as is observed in the next section. The analysis of Gibson and Ashby of the response of both open- and closed-cell foams to load uses simple mechanics and avoids difficult geometries by using scaling laws (Gibson and Ashby, 1997).

5.3.2. Mechanical properties of foams in compression

5.3.2.1. Linear elasticity

At low relative densities, open-cell foams deform primarily by cell edge bending (Warren and Kraynik, 1988). As the relative density increases ($\rho^*/\rho_s > 0.1$) the contribution of simple compression of the cell edges becomes more significant (Warren and Kraynik, 1988). Fluid flow through an open cell foam usually only contributes to the elastic modulus if the fluid has a high viscosity or the strain-rate is exceptionally high. In closed-cell foams the cell edges both bend and extend or contract, while the membranes that form the cell faces stretch, increasing the contribution of the axial cell wall stiffness to the elastic modulus (Christensen, 1986). If the membranes do not rupture, compression of the cell fluid which is trapped within the cells also increases the foam's stiffness.

Open cells

An open-cell foam can be modelled as a simple cubic array of members of length, l, and square cross-section of thickness, t, as illustrated in Figure 5-10(a) (Gibson and Ashby, 1997). Adjoining cells are staggered so that their members meet at their mid-points. The relative density of the cell and the second moment of area of a member, I, are related to the dimensions t and l by (Gibson and Ashby, 1997):

$$\rho^* / \rho_s \propto (t/l)^2 \tag{5-1}$$

$$I \propto t^4 \tag{5-2}$$

The Young's modulus of the foam is calculated from the linear-elastic deflection of a beam of length, l, loaded at its mid-point by a load, F. Standard beam theory (Timoshenko and Goodier, 1970) gives this deflection, δ, as proportional to Fl^3/E_sI, where E_s is the Young's modulus of the solid material of the beam. When a uniaxial stress is applied to the foam so that each cell edge transmits a force, F, as shown in Figure 5-10(b), the edges bend, and the linear-elastic deflection of the structure as a whole is proportional to Fl^3/E_sI. The force, F, is related to the remote compressive stress, σ, by $F \propto \sigma l^2$, and the strain, ε, is related to the displacement, δ, by $\varepsilon \propto \delta/l$ (Gibson and Ashby, 1997). It follows that the Young's modulus of the foam is given by:

$$E^* = \frac{\sigma}{\varepsilon} = \frac{C_E E_s I}{l^4} \tag{5-3}$$

from which, using equations 5-1 and 5-2:

$$\frac{E^*}{E_s} = C_E \left(\frac{\rho^*}{\rho_s} \right)^2 \tag{5-4}$$

C_E, the prefactor for this scaling law, includes all of the geometric constants of proportionality and ≈ 1 (Gibson and Ashby, 1997).

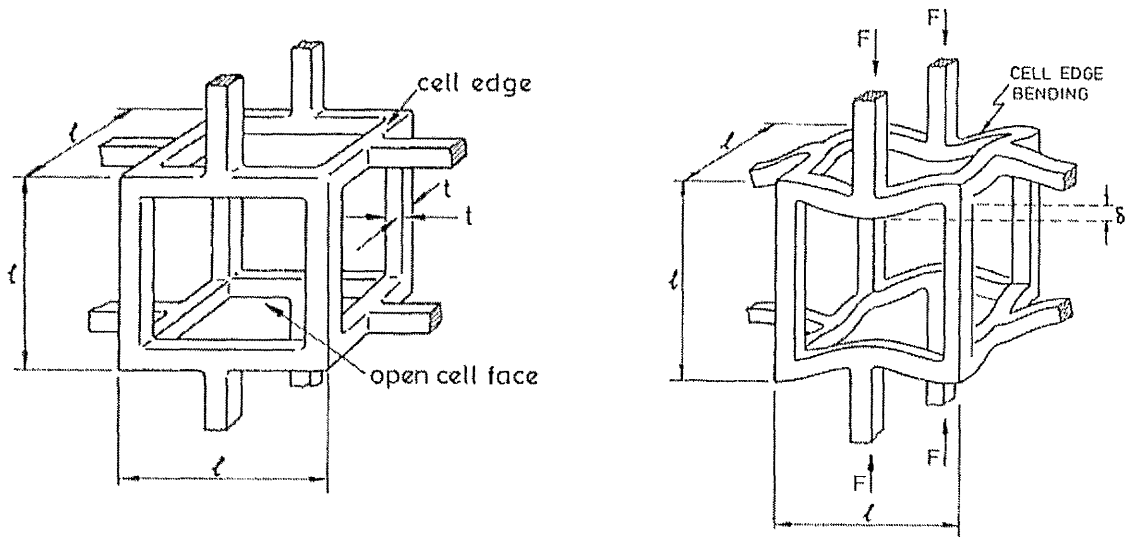

(a) (b)

Figure 5-10. (a) A cubic model for an open-cell foam showing the edge length, l, and the edge thickness, t. (b) Cell edge bending during linear-elastic deformation, deflected by an amount, δ. (Gibson and Ashby, 1997).

Closed cells

When foams are made from liquid components, such as some metallic foams (as explained in Sections 5.2.1 and 5.2.2), surface tension can draw material into the cell edges, leaving only a thin membrane across the faces of the cell which can rupture easily. In the extreme case, although there will be cells which are initially closed, the stiffness may derive entirely from that of the cell edges, resulting in a modulus that is closer to that of an open-cell foam (Gibson and Ashby, 1997). This can be explained by the fact that a closed-cell foam derives its additional stiffness over that of an open-cell from membrane stresses in the cell faces. If these faces are ruptured then this stiffness is removed, leaving that from cell edge bending as for an open-cell foam. Experimental studies have shown that Alulight foam behaves in an open-cell manner up to a relative density of about 0.2, due to cracks and voids observed in most cell faces (McCullough *et al*, 1999).

Consider a closed-cell foam in which a fraction, ϕ, of the solid is contained in the cell edges, which have a thickness, t_e; the remaining fraction, $(1-\phi)$, is in the faces which have a thickness, t_f, as illustrated in Figure 5-11 (Gibson and Ashby, 1997). The ratios t_e/l and t_f/l are related to the relative density, by (Gibson and Ashby, 1997):

$$t_f / l = 1.4 (1 - \phi) (\rho^* / \rho_s) \qquad t_e / l = 0.93 \phi^{1/2} (\rho^* / \rho_s) \tag{5-5}$$

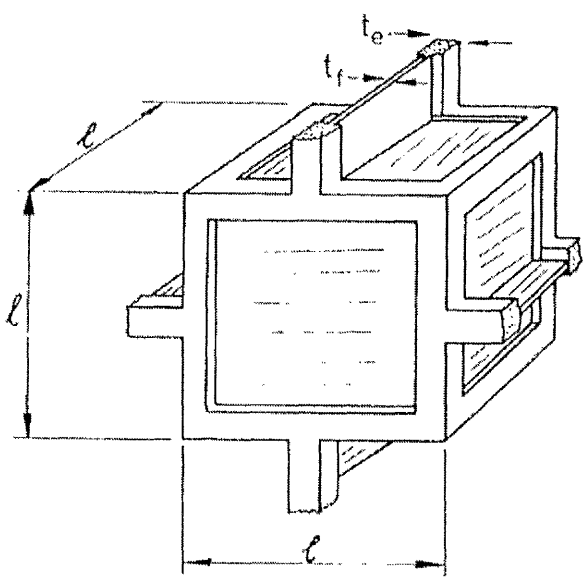

Figure 5-11. A cubic cell model for a closed-cell foam, showing the edge thickness, t_e, and the face thickness, t_f. (Gibson and Ashby, 1997).

The Young's modulus of a closed-cell foam is the sum of three contributions. The first is the contribution of cell edge bending, equal to the modulus calculated for the open-cell foam (Equation 5-4).

The second contribution is that caused by compression of the cell fluid, i.e. the gas contained within the cells (Skochdopole and Rubens, 1965). This contribution is calculated by considering a sample of foam of volume, V_0, and relative density, ρ^*/ρ_s, the cells of which contain a gas. If the sample is compressed axially by a strain, ε, its volume decreases from V_0 to V, where:

$$V / V_0 = 1 - \varepsilon (1 - 2\nu^*) \tag{5-6}$$

ν^* is the Poisson's ratio of the foam. The gas occupies the cell space and is excluded from the volume occupied by the solid cell edges and faces, so its volume decreases from V_g^0 to V_g, where:

$$\frac{V_g}{V_g^0} = \frac{1-\varepsilon(1-2\nu^*)-(\rho^*/\rho_s)}{1-(\rho^*/\rho_s)} \tag{5-7}$$

The contribution to the modulus is calculated from Boyles Law. If the initial gas pressure is p_0 (usually atmospheric pressure) then the pressure, p, after a strain, ε, has been applied, is given by $pV_g = p_0V_g^0$. The pressure which must be overcome by the applied stress is $p'=(p-p_0)$. Using these expressions and Equations 5-6 and 5-7, it is found (Skochdopole and Rubens, 1965):

$$p' = \frac{p_0\varepsilon(1-2\nu^*)}{1-\varepsilon(1-2\nu^*)-(\rho^*/\rho_s)} \tag{5-8}$$

The modulus due to compression of the gas contained in the cells (taking the limit at small ε), is:

$$E_g^* = \frac{dp'}{d\varepsilon} = \frac{p_0(1-2\nu^*)}{1-(\rho^*/\rho_s)} \tag{5-9}$$

When p_0 is atmospheric pressure (0.1 MPa), the contribution is small. If p_0 is much larger than atmospheric pressure, or the cell fluid is not air but a liquid (for which the almost incompressible response of the fluid requires additional cell wall stretching), then the contribution of the cell fluid cannot be neglected.

The third contribution to the stiffness of closed-cell foams is derived from membrane stresses in the cell faces (Christensen, 1986). When a closed-cell foam is loaded the bending of the cell edges causes the cell faces to stretch, as illustrated in Figure 5-12 (Gibson and Ashby, 1997).

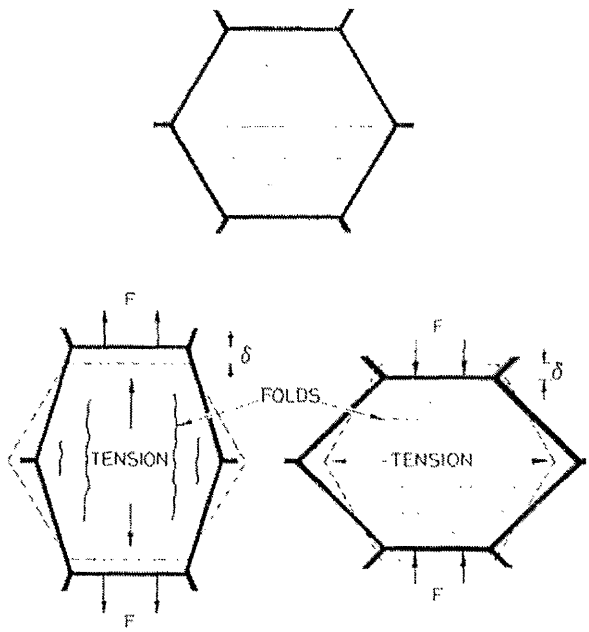

Figure 5-12. Illustrating the stretching of the faces of a closed-cell foam in compression and tension, due to an applied force, F, causing a deflection, δ. (Gibson and Ashby, 1997).

The stretch direction, when the loading is compressive, is at 90° to that when the loading is in tension, but the magnitude is similar in both cases. The applied force, F, causes the cell edge to deflect by δ. The structure is linearly-elastic – work, defined by $\frac{1}{2}F\delta$, is done against the restoring force caused by cell edge bending and cell face stretching (Christensen, 1986). That from cell edge bending is proportional to $\frac{1}{2} S \delta^2$, where S is the stiffness of the cell edge ($S \propto E_s I/l^3$). That caused by cell face stretching is proportional to $\frac{1}{2}E_s\varepsilon^2 V_f$, where ε is the strain caused by stretching of a cell face and V_f is the volume of solid in a cell face ($\varepsilon \propto \delta/l$ and $V_f \propto l^2 t_f$ where the thickness of the edges, t_e, is distinguished from that of the faces, t_f). It follows that (Christensen, 1986):

$$\frac{1}{2}F\delta = \frac{\alpha E_s I \delta^2}{l^3} + \beta E_s \left(\frac{\delta}{l}\right)^2 l^2 t_f \tag{5-10}$$

where α and β are constants of proportionality. Using $I \propto t_e^4$ and $E^* \propto (F/l^2)/(\delta/l)$, gives:

$$\frac{E^*}{E_s} = \alpha'\left(\frac{t_e^4}{l^4}\right) + \beta'\left(\frac{t_f}{l}\right) \tag{5-11}$$

Substituting for t_e and t_f from Equations (5-5):

$$\frac{E^*}{E_s} = C_1\phi^2\left(\frac{\rho^*}{\rho_s}\right)^2 + C_1'(1-\phi)\left(\frac{\rho^*}{\rho_s}\right) \tag{5-12}$$

C_1 and C_1' are constants of proportionality related to the cell geometry. This equation gives the Young's modulus of a closed-cell foam, including membrane stresses, describing the combined effect of cell edge bending and cell face stretching. When the compression of the gas contained within the cells is important, the relevant contribution (Equation 5-9) should be added to this.

The dimensional arguments used to obtain this equation assume that the cell edges and faces are of uniform thickness and do not account for the Plateau borders observed in real foams due to drainage (see Sections 5.2.1 and 5.2.2). Simone and Gibson have used finite element analysis to estimate the elastic modulus of 3-D periodic, closed-cell tetrakaidecahedral foams as a function of relative density and the distribution of solid material in the cell walls/faces relative to the cell edges (Simone and Gibson, 1998a). Their simulations of cells with flat faces of uniform thickness, give:

$$\frac{E^*}{E_s} = 0.32\left(\frac{\rho^*}{\rho_s}\right)^2 + 0.32\left(\frac{\rho^*}{\rho_s}\right) \tag{5-13}$$

for relative densities less than 0.2. For such low relative densities, the second linear density term dominates, implying that cell face stretching is the more significant mechanism of deformation in closed-cell foams.

In terms of experimental measurements of the elastic modulus of a foam, due to stress concentrations caused by defects and local inhomogeneities in the cell structure, such as cell wall curvature and corrugations, a small amount of plastic deformation (or local yielding) can occur almost immediately on loading (Simone and Gibson, 1998b; Sugimura *et al*, 1997). The slope of the loading stress-strain curve has therefore not been found to be a true representation of the elastic modulus. The unloading slope, however, remains roughly constant until the foam has been loaded to its plastic collapse stress, and represents a truer measure of the elastic modulus.

5.3.2.2. Plastic collapse and densification

Foams made from materials that have a plastic yield point, such as metals, collapse plastically when loaded beyond the linear-elastic regime. Plastic collapse gives a long horizontal plateau to the stress-strain curve, as illustrated in Figure 5-9, though the strain is no longer recoverable on unloading. In the generalised case, failure is normally localised in a band transverse to the loading direction which propagates throughout the foam with increasing strain (Vaz and Fortes, 1993). Note that it is the characterisation of and deviation from this uniform behaviour in 3-D that this study is concentrated on. By

analogy with the compressive deformation mechanisms in ductile honeycombs, for which Gibson and Ashby suggest are paralleled by those of foams (Gibson and Ashby, 1997), it is expected that this localisation is associated with a local maximum in the stress-strain curve of a unit cell. The long stress plateau is exploited in foams for crash protection and energy absorbing systems. The amount of energy absorbed during deformation is directly related to the mechanisms of collapse in compression.

Open cells

Plastic collapse occurs when the moment exerted on the cell walls by a force, F, exceeds the fully plastic moment of the cell edges (Thornton and Magee, 1975a; Thornton and Magee, 1975b), creating plastic hinges such as those illustrated in Figure 5-13 (Gibson and Ashby, 1997).

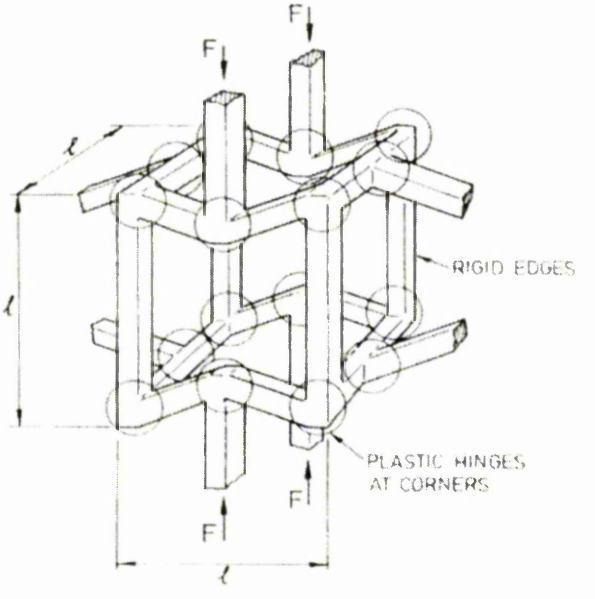

Figure 5-13. Illustrating the formation of plastic hinges in an open-cell foam due to the application of a compressive force, F. (Gibson and Ashby, 1997).

For a beam with a square section of side, t, this moment is defined as (Timoshenko and Goodier, 1970):

$$M_p = \tfrac{1}{4}\,\sigma_{ys}\,t^3 \qquad (5\text{-}14)$$

where σ_{ys} is the yield strength of the cell wall material. If the applied force has a component normal to the cell edge, of length l, the maximum bending moment is proportional to Fl. The stress on the foam is proportional to F/l^2. Combining these results gives the plastic collapse strength of the foam:

$$\sigma_{pl}^* \propto M_p / l^3 \qquad (5\text{-}15)$$

Substituting for M_p with Equation (5-14) and using Equation (5-1) for open cells:

$$\frac{\sigma_{pl}^{*}}{\sigma_{ys}} = C_{\sigma}\left(\frac{\rho^{*}}{\rho_{s}}\right)^{3/2} \tag{5-16}$$

The constant, C_{σ}, the prefactor for this scaling law, contains all the constants of proportionality and is ≈ 0.3 (Gibson and Ashby, 1997).

Closed cells

Closed cells have membranes spanning their faces – plastic collapse causes these membranes to crumple in the compression direction, and as they are thin, the force required to crumple them is small. At right angles to this the membranes are stretched, and the plastic work required to extend them contributes significantly to the yield strength of the foam. This is assessed by calculating the work done in an increment of deformation and equating it to the plastic dissipation in bending and stretching of the cell walls.

Consider the collapse of a cell such as that shown in Figure 5-14 (Gibson and Ashby, 1997).

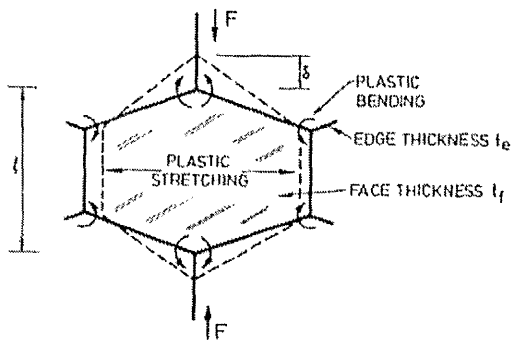

Figure 5-14. Illustrating the plastic stretching of the cell faces of a closed-cell foam due to the application of a compressive force, F. (Gibson and Ashby, 1997).

The cell edges and faces have thicknesses t_e and t_f respectively, which are related to the fraction of solid in the edges, ϕ, by equations (5-5). A compressive plastic displacement, δ, of one cell allows the applied force, F, to do work, $F\delta$. The angle of rotation at the four plastic hinges is proportional to δ/l, where l is the distance between two opposite plastic hinges in the compression direction, and the plastic work done at these hinges is proportional to $M_p(\delta/l)$. The cell face is stretched by a distance which is proportional to δ, doing work which scales as $\sigma_{ys}\delta t_f l$. Equating these expressions, gives (Gibson and Ashby, 1997):

$$F\,\delta = \alpha M_p\,(\,\delta / l\,) + \beta\,\sigma_{ys}\,\delta\,t_p\,l \tag{5-17}$$

where α and β are constants. Replacing F with σl^2, and substituting for M_p with Equation (5-14), with $t = t_e$, gives:

$$\frac{\sigma_{pl}{}^*}{\sigma_{ys}} = \frac{\alpha}{4}\left(\frac{t_e}{l}\right)^3 + \beta\left(\frac{t_f}{l}\right) \tag{5-18}$$

Using Equations (5-5) for t_e and t_f:

$$\frac{\sigma^*_{pl}}{\sigma_{ys}} = C_2\left(\phi\frac{\rho^*}{\rho_s}\right)^{3/2} + C_2'(1-\phi)\left(\frac{\rho^*}{\rho_s}\right) \tag{5-19}$$

C_2 and C_2' are constants of proportionality, again related to the cell geometry. The work of Simone and Gibson on finite element simulations of 3-D periodic, closed-cell tetrakaidecahedral foams, and the distribution of solid material in the cell walls/faces relative to the cell edges (Simone and Gibson, 1998a), gives the plastic collapse strength for relative densities less than 0.2, as:

$$\frac{\sigma^*_{pl}}{\sigma_{ys}} = 0.33\left(\frac{\rho^*}{\rho_s}\right)^2 + 0.44\left(\frac{\rho^*}{\rho_s}\right) \tag{5-20}$$

Densification

Large plastic strains in compression cause opposing cell walls to crush together, resulting in a steep rise in the stress-strain curve to a limiting strain, ε_D, given by (Gibson and Ashby, 1997):

$$\varepsilon_D = 1 - 1.4\,(\rho^* / \rho_s) \tag{5-21}$$

5.4. Characterisation of Foams and their Compressive Behaviour

As observed from Sections 5.2 and 5.3, the relationship between the structure of metallic foams and their global mechanical properties is an important one due to the random and stochastic nature of the distribution of cells within the material. For a complete understanding of this relationship, two different aspects should be studied: the microstructure of the solid material of the cell walls; and perhaps more importantly for the use of metallic foams for structural applications, the microstructure of the cellular material itself. Regarding the latter of these, it is important to understand the effect of the size, morphology and arrangement of the solid and gaseous phases of the foam on its resulting compressive behaviour, for example. X-ray tomography has become a powerful tool for the characterisation of the microstructure of materials, and has been used in a number of studies for the characterisation of metallic foams (Benouali and Froyen, 2001; Bart-Smith

et al, 1998; Degischer *et al*, 2000; Elmoutaouakkil *et al*, 2002; Kriszt *et al*, 2000; Maire *et al*, 2003; Olurin *et al*, 2002). The advantage of this technique over other methods, such as serial sectioning, is that large deformations can be imaged non-destructively, allowing important bending, buckling and fracture events to be visualised throughout deformation. While these X-ray tomography studies describe and extract key quantitative parameters for the cellular structure, with the exception of Degischer *et al.* and Kriszt *et al*, most do not relate these parameters to the observed compressive behaviour. Several approaches have been investigated regarding the modelling of this behaviour of cellular structures, and the effect of imperfections on the mechanical behaviour, and these will be reviewed in the following sections.

5.4.1. Effect of imperfections at the scale of the cellular microstructure

Regarding the effect of the cellular structure on the compressive behaviour of metallic foams, scaling laws have been applied to describe the mechanical properties of ideal, homogeneous, open- and closed-cell materials (Gibson and Ashby, 1997; Warren and Kraynik, 1997; see Section 5.3.2). These laws showed the relative density to be the most important parameter, and correlate the mechanical properties of the cellular structure to those of the bulk solid material. The dominating deformation mechanisms on a microscopic scale were assumed to be bending stretching and buckling of the cell walls. The approach of Gibson and Ashby has proved to be very efficient in allowing a general understanding of the effect of density on the Young's modulus and strength, although disagreement is observed between these laws and experimental values of real foams produced by the processes outlined in Section 5.2 (Andrews *et al*, 1999; Simone and Gibson, 1998b; Sugimura *et al*, 1997). These discrepancies are attributed to the difference between the ideal geometry assumed in the models and the perturbed and random structures observed in the actual materials. It is clear that the structure of a metallic foam has a strong effect on its behaviour, but the modelling methods proposed originally by Gibson and Ashby do not fully capture this effect and the mechanical properties cannot simply be explained based on cells with an idealised morphology.

The experimental discrepancies have been shown to be caused by imperfections and defects in the cell walls of real foams, such as the distribution of solid relative to the cell edges (Simone and Gibson, 1998a; Warren and Kraynik, 1997) and curvature and corrugations in the cell faces (Grenestedt, 1998; Simone and Gibson, 1998c). Simone and Gibson presented estimations of the relative elastic modulus and relative plastic collapse

strength via finite element analysis of 2-D honeycomb, and 3-D periodic, closed-cell tetrakaidecahedral foams as a function of relative density and the distribution of solid material in the cell walls/faces relative to the cell edges (Simone and Gibson, 1998a). The expressions for the modulus and strength estimated for tetrakaidecahedral cells with faces of uniform thickness are given in Sections 5.3.2.1 and 5.3.2.2 respectively. Most relevant to a study of this type are the mechanisms which determine the drainage pattern present in a foam made by liquid-state processes during its evolution from a wet, or undrained, foam to a dry, or drained, foam (see section 5.2.1). Warren and Kraynik found analytically that the elastic modulus of a low density ($\rho^*/\rho_s < 0.15$) honeycomb is increased when material is shifted away from the mid-span of a member towards the nodes (Warren and Kraynik, 1987). Simone and Gibson extended this analysis to honeycombs of a higher relative density. Honeycombs deform primarily by bending of the cell edges, with the maximum bending moment occurring at the ends of a member (Gibson and Ashby, 1997; Simone and Gibson, 1998a). Moving material away from the cell edges into Plateau borders at the vertices was found to initially increase the modulus and peak stress of the honeycomb by increasing the moment of inertia at the ends of the members where the bending moments are highest (Simone and Gibson, 1998a). In moving more material, the increase in the moment of inertia was found not to compensate for the reduction of moment of inertia in the cell edge, causing a reduction in mechanical properties. As described in Section 5.3.2.2, closed-cell foams deform primarily by in-plane stretching of cell faces. Moving material from the cell faces into Plateau borders along the edges was found to have little effect on the modulus but caused a reduction in the peak stress. As the volume fraction of solid moved to the edges was increased to the point where almost all the solid material was in the edges rather than the faces, behaviour analogous to that of an open-cell foam was found, as analysed by Warren and Kraynik (Warren and Kraynik, 1988). Changing the shape of the edge cross-section from circular or square to a Plateau border configuration was found to increase the stiffness by 60-70%.

Metallic foams with high relative density ($\rho^*/\rho_s > 0.2$) have been produced that have a modulus comparable to that of the idealised tetrakaidecahedral foam with no Plateau borders (Kunze *et al*, 1993). The peak stress values of these foams are, however, significantly below the idealised values. Most metallic foams, and especially those with lower relative density, have both modulus and peak stress values far below the idealised behaviour (Andrews *et al*, 1999; Simone and Gibson, 1998b; Sugimura *et al*, 1997). Cell edges in these foams generally have small Plateau borders, although localised regions of

higher relative density and large Plateau borders have been observed in many foam samples (Simone and Gibson, 1998b). In general, material distribution was found not to have a significant effect on the modulus of the foams, but contributes to a reduction in the peak stress (Simone and Gibson, 1998a). The poor mechanical properties of low relative density foams are more likely attributable to the presence of curvature and corrugations in the cell faces (Andrews *et al*, 1999; Prakash *et al*, 1995; Simone and Gibson, 1998b; Simone and Gibson, 1998c). Again, finite element analysis of idealised 2-D hexagonal honeycombs and 3-D tetrakaidecahedral foams has been used to estimate the influence of cell face curvature and cell face corrugations on the elastic modulus and plastic collapse stress (Simone and Gibson, 1998c). In each case, both the axial stiffness and the flexural rigidity of the curved or corrugated structural members were reduced. Face curvature and face corrugations were found to significantly reduce the modulus and peak stress of the two model foams, by up to 32 and 20% (curvature) and 56 and 38% (corrugations), respectively for a foam with a relative density of 0.1. Similar results were found by considering changes in the effective stiffness of individual corrugated beams and plates (Grenestedt, 1998). These reduction factors are representative of an idealised monodisperse foam structure in which each cell has faces with the same curvature or corrugation pattern. Real foams have a distribution of cell sizes, number of cell faces and the degree of cell face curvature or corrugation, which create localised heterogeneity and stress concentrations, and thus direct comparison with the models is difficult. Nevertheless, the results have shown that face curvature and corrugations can significantly reduce the modulus and peak stress of a foam. These local effects have a more significant effect on the peak stress than the modulus because the modulus incorporates deformation through an entire specimen while the peak stress measures the strength of the weakest cross-sectional plane of a specimen.

5.4.2. Effect of imperfections at the scale of cell arrangement

Thus far, imperfections or defects at the scale of a cell (the microstructure scale) have been used to explain experimental discrepancies of the elastic modulus and plastic collapse strength from the idealised values. Imperfections on a mesoscopic scale, or the scale of cell arrangement in a foam, include non-periodic distributions of cell morphologies or sizes (Fazekas *et al*, 2002; Grenestedt and Tanaka, 1999; Silva and Gibson, 1997; Silva *et al*, 1995; Zhu *et al*, 2001) and inhomogeneous density distributions (Beals and Thompson, 1997; Gradinger and Rammerstorfer, 1999; Kriszt *et al*, 2000).

Silva and Gibson have developed models that can be used to quantify the influence of microstructural variability on the mechanical properties of cellular materials (Silva and Gibson, 1997; Silva *et al*, 1995). This included the analysis of the effects of the non-periodic arrangement of cell walls on the elastic properties of two-dimensional cellular solids or honeycombs (Silva *et al*, 1995). This method was based on finite element analysis of non-periodic arrays of Voronoi cells, and the results indicated that the elastic properties of Voronoi honeycombs were, on average, no different to those of periodic honeycombs (determined by unit cell analysis). The effect of non-periodic microstructure on failure properties, i.e. compressive strength, of two-dimensional cellular solids, and the effect of defects, such as missing or fractured cell walls, has also been analysed (Silva and Gibson, 1997). This was brought about by Gibson and Ashby reporting that their unit cell models typically overestimated the compressive strengths of metallic honeycombs by as much as 50% (Gibson and Ashby, 1997). Papka and Kyriakides also found that the strengths predicted by finite element models of honeycombs with periodic, hexagonal cells were approximately 15% greater than the corresponding experimental values obtained from tests on aluminium honeycombs (Papka and Kyriakides, 1994). In addition to imperfections and defects in the cell walls as sources of discrepancies between experimental and idealised values, in both of these studies, the authors concluded that differences between the predicted and measured strengths were due, in part, to variations in cell geometry that were not accounted for by their models.

The work of Silva and Gibson indicated that isotropic, Voronoi honeycombs with random variations in cell wall arrangement were approximately 20-40% weaker than isotropic, periodic honeycombs of the same density (Silva and Gibson, 1997). Similarly, anisotropic Voronoi honeycombs were, on average, approximately 35% weaker than periodic honeycombs of corresponding density and anisotropy. Defects introduced by removing cell walls at random locations were found to cause a sharp decrease in the effective mechanical properties of both Voronoi and periodic honeycombs, these reductions being approximately 2-3 times greater than those caused by equivalent reductions in density by uniform thinning of cell walls. A 5% reduction in density due to defects caused a 30% reduction in strength of the Voronoi honeycombs, equal to the typical reduction in strength caused by the non-periodic arrangement of cell walls. Figure 5-15 illustrates the effect of defects on failure localisation for a Voronoi honeycomb with relative density 0.15 (Silva and Gibson, 1997).

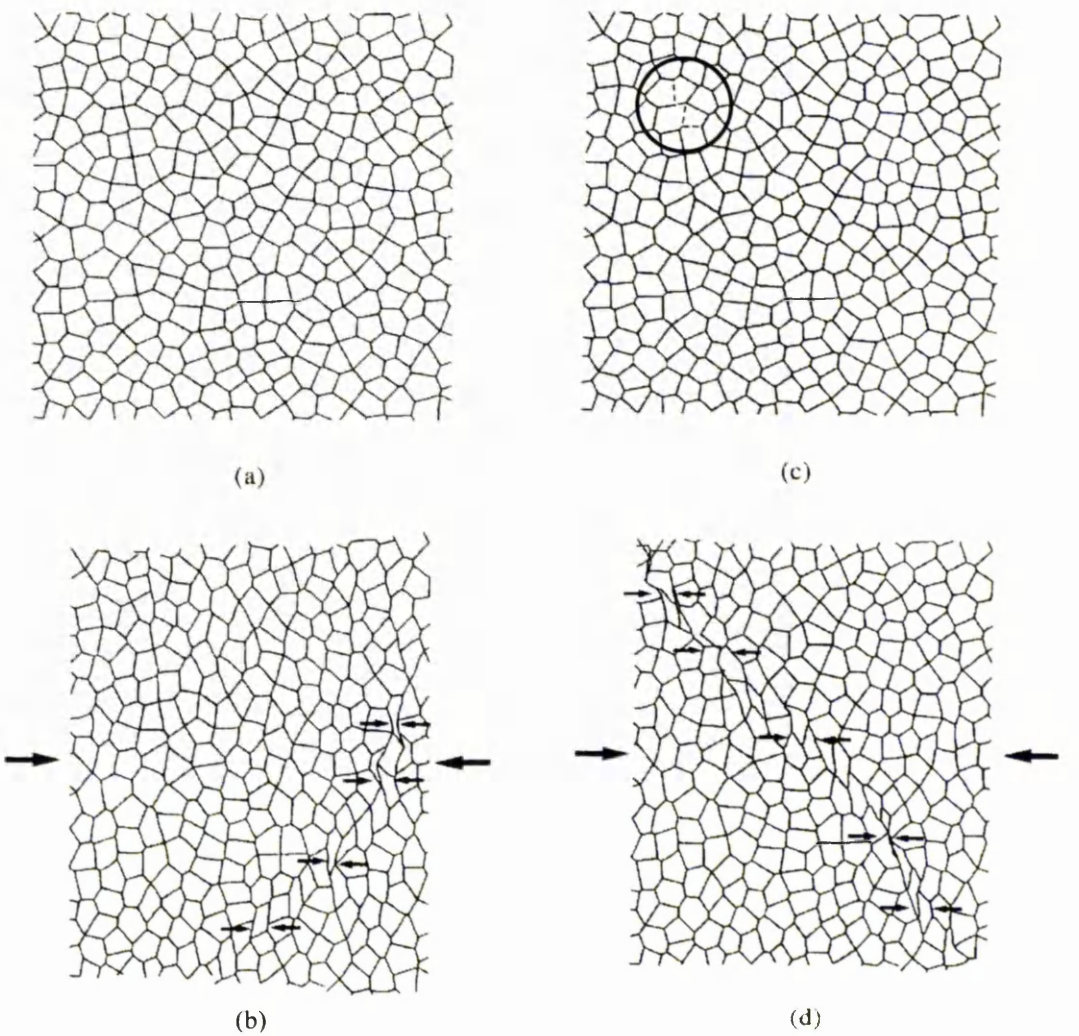

Figure 5-15. Illustrating the effect of defects on failure localisation for a Voronoi honeycomb with relative density 0.15. (a) Undeformed Voronoi honeycomb with no defects. (b) Deformed structure of that in (a) with failure locations indicated by small arrows and loading direction by large arrows. (c) Undeformed Voronoi honeycomb with four adjacent defects, as indicated. (d) Deformed structure of that in (c) illustrating the failure localisation band passing through the defects. (Silva and Gibson, 1997).

Figures 5-15(a) and (b) show undeformed and deformed meshes of an intact (no defects) Voronoi honeycomb, the latter with failure localisation regions indicated. Defects within this region caused the localisation band to become even more narrowly defined. Interestingly, when one or two cell walls were removed away from the original failure band, as illustrated in Figure 5-15(b), the band did not shift. When four or more adjacent

cell walls were removed from the Voronoi honeycomb, effectively resulting in an isolated large cell surrounded by cells around one fifth its size, as illustrated in Figure 5-15(c), the localised band of cell collapse passed through the defect site, as shown in Figure 5-15(d), reducing the strength (Silva and Gibson, 1997). This indicates that small defects and larger cells can alter both the failure pattern and the effective properties. Note that the elastic moduli of Voronoi honeycombs have been reported to be the same as periodic, hexagonal ones (Silva *et al*, 1995), while their strengths are not equal (Silva and Gibson, 1997). This difference between the elastic and failure behaviour is attributed to the wider distribution of local strain for the Voronoi honeycomb, leading to failure at a lower effective stress (or strain) than for the periodic case (Silva and Gibson, 1997). The effective elastic behaviour of the Voronoi honeycomb was found to be unchanged by the higher local strains since these strains are offset by lower strains elsewhere in the structure, and the effective strain for a given stress is unchanged. In general, this study has shown that cellular materials with microstructural variations in the arrangement of cell walls will be weaker than those of the same density that have uniform microstructures. Defects in terms of broken or removed cell walls, effectively producing larger cells, further reduce the strength, altering the patterns of localisation.

A limitation of the study of Silva and Gibson, addressed to some degree by the removal of cell walls, is that the microstructural variability was limited to that produced by the Voronoi approach, resulting in honeycombs with hexagonal cells with approximately uniform size. Such an approach leads to Gaussian-like cell size distributions, which may not be suitable to describe some foams (Elmoutaouakkil *et al*, 2002). The presence of large cells may lead to bimodal distributions with various fractions of large and small cells, which cannot be modelled with traditional Voronoi tessellations. A generalisation of this approach was proposed by Fazekas *et al.* where cells were created from sphere packing, allowing the spatial distribution of cell sizes to be accounted for, and the effect of microstructural heterogeneities on the mechanical properties to be investigated (Fazekas *et al*, 2002). The most common approach for cell generation is based on Voronoi tessellation, as described and used by Silva *et al.* (Silva *et al*, 1995) and Silva and Gibson (Silva and Gibson, 1997), for which meshes are illustrated in Figure 5-15. In this approach the cells are created from a distribution of nucleation points and the positions of the points lead to various structures, from regular to fully random ones. A random distribution of nuclei can be used where a minimum distance between them is specified (Silva *et al*, 1995; Zhu *et al*, 2001). Another possibility is to start with a regular distribution of points

corresponding to a hexagonal structure (see Figure 5-16(a)), and then apply a random small displacement to each nucleus in a restricted area around the initial position (Fazekas *et al*, 2002). The size of this area normalised by the distance between two initial nuclei defines a perturbation coefficient, α. Figure 5-16(b) and (c) illustrates the effect of this variable, for $\alpha = 0.2$ and $\alpha = 0.5$ respectively. A fully random microstructure, where there is no restriction on the displacement, is illustrated in Figure 5-16(d).

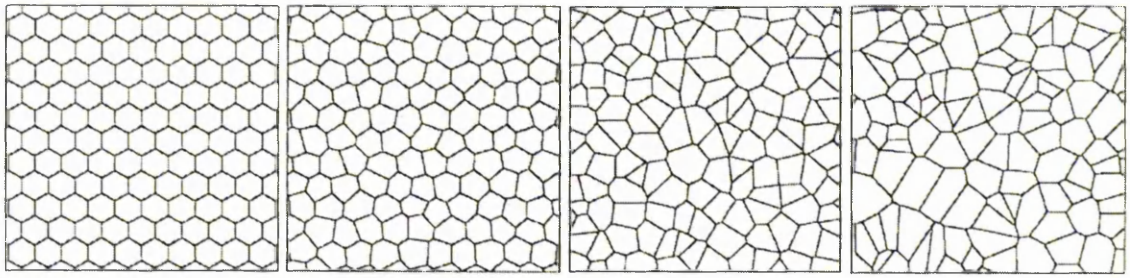

Figure 5-16. Four examples of Voronoi microstructures: (a) regular structure; (b) perturbation coefficient of $\alpha = 0.2$; (c) perturbation coefficient of $\alpha = 0.5$; (d) fully random structure. (Fazekas *et al*, 2002).

In order to create 2-D microstructures exhibiting controlled cell size distributions, Fazekas *et al.* used an extension of the Voronoi tessellation approach, based on radical plane construction (Gellatly and Finney, 1982; Richard *et al*, 1998). This procedure of cell generation starts with the packing of circular cylinders, and the separation plane between two cylinders is defined as the radical plane, i.e. the points with equal tangency to the two cylinders. When performing this construction to each pair of cylinders, polyhedral convex cells are generated, as illustrated in Figure 5-17. Various 2-D microstructures produced with this method are illustrated in Figure 5-18. Monomodal microstructures can be created from packings where a slight variation in the radii of the cylinders is introduced to avoid crystal like arrangements (see Figure 5-18(a)). Figure 5-18(b) and (c) correspond to bimodal distributions with, respectively, radii ratios $R/r = 2$ and 4, where R and r are the radii of the cylinders to create large and small cells respectively. Multimodal distributions can also be obtained (see Figure 5-18(d)). In all cases it is possible to change the relative area fraction of large cells, f_{sl}, by controlling the relative proportion of large and small cylinders.

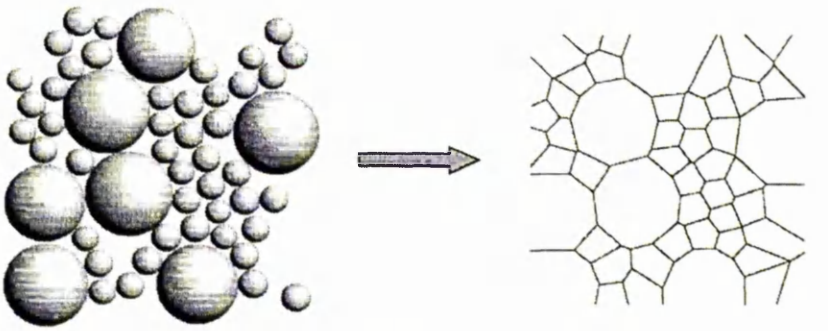

Figure 5-17. Illustrating the initial packing of circular cylinders and the corresponding structure obtained with the radical plane construction approach. (Fazekas *et al*, 2002).

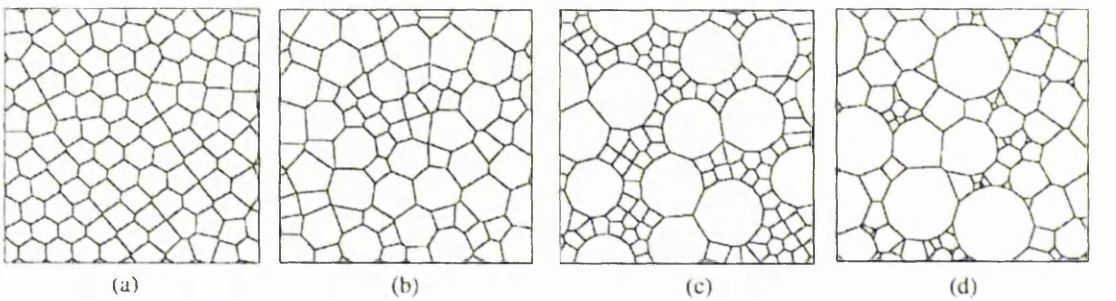

Figure 5-18. Four examples of microstructures generated with the radical plane construction method: (a) monomodal cell size distribution; (b) bimodal cell size distribution with a radii ratio of $R/r = 2$; (c) bimodal cell size distribution with a radii ratio of $R/r = 4$; (d) multimodal cell size distribution. (Fazekas *et al*, 2002).

The effect of structure topology and disorder on the stiffness and strength of 2-D cellular microstructures produced by Voronoi tessellation and the sphere packing method, both outlined above, has been investigated using finite element analysis (Fazekas *et al*, 2002). For the two types of microstructure, the dependence of the relative Young's modulus, E^*/E_s, and the relative yield strength, σ^*/σ_{ys}, upon relative density was explored for low relative densities ($0.005 \leq \rho^*/\rho_s \leq 0.05$) through the application of the scaling laws $E^*/E_s = C_E(\rho^*/\rho_s)^3$ and $\sigma^*/\sigma_{ys} = C_\sigma(\rho^*/\rho_s)^2$ respectively. These laws are directly linked to the only mechanism of deformation that was considered at such low densities, i.e. cell edge bending, and the effect of the different cell structures on the prefactors C_E and C_σ was investigated. Disorder obtained by perturbation of regular honeycombs, or Voronoi tessellation, resulted in a 20% increase in the prefactor, C_E, compared to the regular structure (Fazekas *et al*, 2002). Zhu *et al*. observed a similar effect for similar Voronoi

structures, where the prefactor, C_E, increased significantly for a perturbation coefficient of 0.5, representing equal distributions of regular and random cells, and then saturated for larger values of α (Zhu *et al*, 2001). A bimodal cell size distribution, obtained by packing cylinders of different radii, gave a maximum increase for C_E of 60% above the value for a monomodal structure, for an R/r range of 1-8 (Fazekas *et al*, 2002). For values of R/r of 2 and 4, microstructures illustrated in Figures 5-18(b) and (c) respectively, the maximum value of C_E was obtained for an area fraction of large cells, f_{sl}, of around 0.6, representing an equal bimodal distribution of large and small cells (or slightly more large cells). This suggests that microstructural heterogeneities are beneficial in terms of stiffness of cellular structures, while they were found to be detrimental in terms of strength. C_σ was found to decrease drastically once the microstructure lost regularity in both cases, reaching a value four times lower than for the regular case for perturbed hexagonal structures at a relatively low perturbation coefficient of 0.3. For structures obtained by packing of bimodal cells, for an R/r of 4, C_σ was found to decrease by about 20% to a minimum value for f_{sl} between 0.4 and 0.6, again representing a roughly equal bimodal distribution of large and small cells. Due to the wider distribution of local stress and strain for a non-regular structure, the first plastic hinge appears at a lower global stress than for regular structures. Numerical analysis of similar 2-D cellular structures carried out by Chen *et al.* looked at the effect of cell wall imperfections on yielding, and results indicated a similar decrease at low levels of irregularity compared to a regular structure with perfect cell walls (Chen *et al*, 1999).

The studies of Silva *et al.* and Fazekas *et al.* illustrate the significant effect that imperfections on a mesoscopic scale, or the scale of cell arrangement, have on the mechanical properties and compressive deformation behaviour of 2-D model cellular structures. Non-periodic arrangements of cell walls and defects in terms of isolated large cells have been shown to localise failure and decrease the strength of the structures (Silva *et al*, 1997). The effect of large cells in a bimodal cell size distribution has also been found to be deleterious to the compressive strength of cellular structures (Fazekas *et al*, 2002). However, the stress state, and therefore the mechanical properties and compressive deformation behaviour, can be expected to be completely different in an actual three-dimensional mesh compared to a simplified two-dimensional one (Maire and Buffière, 2000). Also, a difficulty arises in that idealised cells such as those used in the studies outlined above do not completely represent experimental observations. The advantage of using models based on tomographic data is that such models would describe perfectly and

in three-dimensions the complexity of the actual structure of cellular materials (Maire *et al*, 2003). Inhomogeneities in the density distribution, effectively linked to local distributions of cell sizes in 3-D, have also been observed to be a key factor in determining the failure behaviour of metal foams (Beals and Thompson, 1997; Gradinger and Rammerstorfer, 1999; Kriszt *et al*, 2000). Kriszt *et al.* studied the relationship between inhomogeneous density distribution and deformation for Alulight foam material, fabricated by a powder metallurgical route (Figure 5-7), using the 3-D density distribution obtained directly from computed tomography data (Kriszt *et al*, 2000). The local density for each voxel of the sample dataset was calculated by averaging the CT data over a specified surrounding voxel volume or averaging volume. The CT dataset is represented by grey levels for each voxel based on the linear attenuation coefficient of X-rays for the material at that location, i.e. whether the voxel is situated within a cell or inside an aluminium cell wall. In this sub-resolution or binning method, the grey level of the replacing sub-voxel is recalculated as the average of the grey levels of the surrounding group of voxels (Degischer *et al*, 2000). This approach transformed the discrete structural features of the foam into a continuum medium, with the resolution of the walls and struts being lost due to a voxel grouping much larger than the voxel resolution of the cell walls of the foam. For such low resolutions the tomographic dataset reflects the fluctuation of the density of the solid phase in the cellular structure. This dataset was used as a smaller sub-mesh providing easier calculations as input data to a 3-D finite element model (Kriszt *et al*, 2000), enabling the mechanical properties of each element to be described by its density using the scaling laws of Ashby and Gibson as presented in Section 5.3.2 (Gibson and Ashby, 1997).

The work of Kriszt *et al.* found a significant influence of the density distribution on the mechanical properties of the Alulight foam due to a strongly inhomogeneous distribution (Kriszt *et al*, 2000). Figure 5-19 shows the density distributions, through both the *X-Y* and *X-Z* planes of the calculated datasets of two samples, A and B, of the same foam material, together with the stress-strain curves measured from compression tests of the two samples (Kriszt *et al*, 2000). The density distributions were averaged over columns having the thickness of the samples (20 mm) and a cross-section of 5 × 5 mm (sample height 40 mm), with the largest extension of the columns oriented in the *Y*-direction for *X-Z* mapping and in the *Z*-direction for *X-Y* mapping.

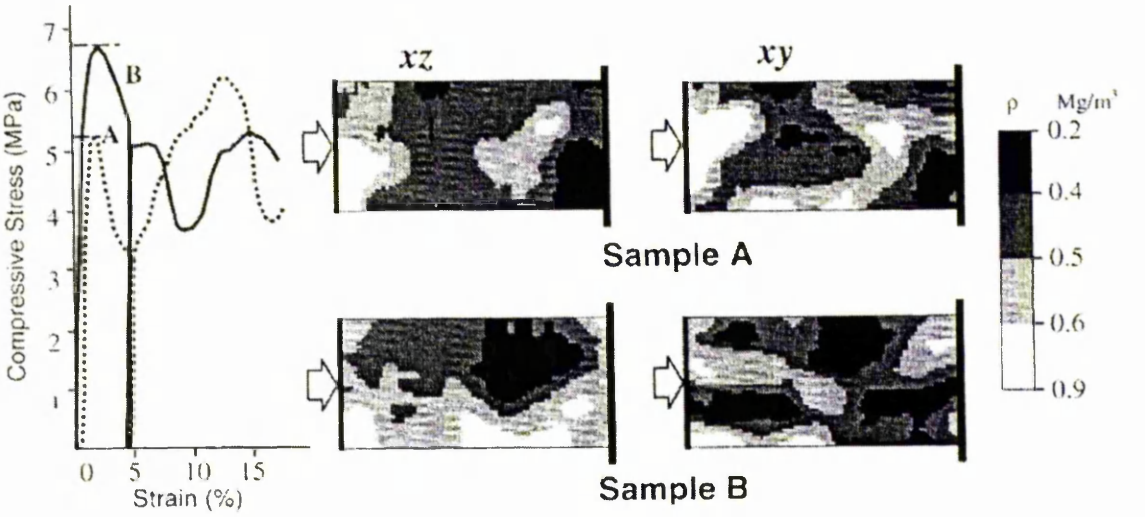

Figure 5-19. Showing compressive stress-strain curves of two Alulight samples, both having an average density of 0.48 Mg/m^3 but different density arrangements as shown by density mappings of these samples. (Kriszt *et al*, 2000).

The yield strength of the two samples is observed to differ by about 20%. Sample A is characterised by a lower yield stress and a zone of low density oriented perpendicular to the compression direction, while sample B has a higher strength and a zone of high density parallel to the loading direction. Correlating low density to low strength and high density to high strength according to the scaling laws of Gibson and Ashby, it is clear from this study how density arrangements can influence the strength of foam samples. The observed compressive deformation behaviour suggests the low strength zones of low density, and their locations with respect to zones of high density, result in the formation of deformation bands and the localisation of failure in these regions. The arrangement of these density zones therefore has an effect on the macroscopic anisotropic and mechanical behaviour of foams (Kriszt *et al*, 2000). Using the calculated 3-D density distribution as input to an FE model, a clear correlation was found between the location of the low density regions and the positions of calculated maximum strain (Kriszt *et al*, 2000). The model was also used to calculate the stiffness and yield strength of the samples, giving a relative error in the stiffness of less than 10%, while the yield strength was underestimated by 20-30% due to the model not taking into account any hardening mechanism. An improved version of this developed model allowed large deformations up to 50% global strain to be simulated (Foroughi *et al*, 2001). Comparison with experimental data showed that the stress-strain

behaviour derived from the model was in good agreement so that if the density distribution of foamed materials is known, the model can predict the mechanical properties.

Beals and Thompson reported experimentally that density gradients existent in Alcan aluminium foam, fabricated by a liquid-state process (Figure 5-5), have a significant effect on compression properties (Beals and Thompson, 1997). Compressive failure of the foam in the through-thickness direction was observed to be sequential, initiating in the lowest density region in a plane of cells perpendicular to the loading direction and progressing to higher density regions only when significant deformation of this low density region had occurred. Through-width tested specimens, with the density gradient perpendicular to the loading direction, had failure of cells occurring in several planes at the same time, resulting in three times the increase in strength. The correlation between predicted, using the relationships derived by Gibson and Ashby (Gibson and Ashby, 1997; Section 5.3.2), and experimental results was closest when the influence of the density gradient was minimised. The strength behaviour was therefore dictated by the performance of the weakest, lowest density plane. The energy absorption characteristics of the foam were also found to be strongly dependent on the density gradient. The energy absorption efficiency, calculated as the ratio of the actual amount of energy absorbed to an ideal total based on the allowable peak stress, decreased with an increasing variation in the density. This was due to an increase in the density and density gradient influencing (increasing) the slope of the collapse region and decreasing the densification strain. The stress-strain curve shown inset in Figure 5-9 illustrates an ideal curve with maximum energy absorption efficiency. In agreement with the finding of Beals and Thompson, the analysis of crush energy absorption in aluminium foam by Gradinger and Rammerstorfer revealed that mesoscopic inhomogeneities in density lead to strain localisation (Gradinger and Rammerstorfer, 1999).

5.5. Summary

A review of the theoretical and experimental considerations on the use of closed-cell metallic foams, and aluminium foams in particular, in energy absorption applications has been presented. Such materials show, among other properties, excellent stiffness-to-weight ratio when loaded in bending and have exceptional ability to absorb energy and impact at almost constant pressure and load. An account of the main fabrication processes of aluminium foam has been given and, particularly regarding liquid-state processes,

successful processing is reliant upon controlling both drainage and defects. These processes are stochastic and can be difficult to control, meaning that consistent and reproducible microstructures are not easy to obtain. The production route will therefore have a significant effect on the mechanical response and behaviour of the material. Regarding the application of closed-cell foams for energy absorption, the deformation that they experience is directly related to the mechanisms of collapse in compression. Their efficient use requires detailed understanding of these mechanisms and their overall mechanical behaviour under an applied compressive load. An account of the deformation mechanisms observed in a typical compressive stress-strain curve and the model theoretical equations that have been derived based on these mechanisms has been given.

Studies regarding modeling of cellular structures have shown that imperfections in the cellular structure and on the scale of cell arrangement in a foam influence their mechanical behaviour. As the main topic of the work covered in Chapter 6, experimental knowledge of the effect of the cellular structure on how the material deforms under a compressive load is important. X-ray microtomography can provide detailed characterisation of foams, enabling such observations to be made non-destructively, and more importantly, in three-dimensions.

References

Andrews, E., Sanders, W. and Gibson, L. J., (1999), 'Compressive and tensile behaviour of aluminium foams', *Materials Science and Engineering*, **A270**, 113-124.

Ashby, M. F., Evans, A. G., Fleck, N. A., Gibson, L. J., Hutchinson, J. W. and Wadley, H. N. G., *Metal Foams: A Design Guide*, Butterworth-Heinemann, Oxford, 2000.

Ashby, M. F., *Materials Selection in Mechanical Design*, 2nd Edition, Butterworth-Heinemann, Oxford, 1999.

Bart-Smith, H., Bastawros, A.-F., Mumm, D. R., Evans, A. G., Sypeck, D. J. and Wadley, H. N. G., (1998), 'Compressive deformation and yielding mechanisms in cellular Al alloys determined using X-ray tomography and surface strain mapping', *Acta Materialia*, **46**(10), 3583-3592.

Baumeister, J., Banhart, J. and Weber, M., (1997), 'Aluminium foams for the transport industry', *Materials and Design (UK)*, **18**(4-6), 217-220.

Beals, J. T. and Thompson, M. S., (1997), 'Density gradient effects on aluminium foam compression behaviour', *Journal of Materials Science*, **32**, 3595-3600.

Benouali, A.-H. and Froyen, L., 'On the mechanical and microstructural characterisation of aluminium foams', in *Cellular Metals and Metal Foaming Technology*. Banhart, J., Ashby, M. and Fleck, N. eds., MIT-Verlag, 2001, 269-272.

Chen, C., Lu, T. J. and Fleck, N. A., (1999), 'Effect of imperfections on the yielding of two-dimensional foams', *Journal of the Mechanics and Physics of Solids*, **47**, 2235-2272.

Christensen, R. M., (1986), 'Mechanics of low density materials', *Journal of the Mechanics and Physics of Solids*, **34**, 563-578.

Davies, G. J. and Zhen, S., (1983), 'Metallic foams: their production, properties, and applications', *Journal of Materials Science*, **18**, 1899-1911.

Degischer, H. P., Kottar, A. and Foroughi, B., 'Determination of local mass density distribution', in Baruchel, J., Buffière, J.-Y., Maire, E., Merle, P. and Peix, G., *X-ray tomography in Materials Science*, HERMES Science Publications, Paris, 2000, 165-176.

Elmoutaouakkil, A., Salvo, L., Maire, E. and Peix, G., (2002), '2-D and 3-D characterisation of metal foams using X-ray tomography', *Advanced Engineering Materials*, **4**(10), 803-807.

Evans, A. G. and Hutchinson, J. W., 'Multifunctionality of cellular metal systems', in *Metal Foams and Porous Metal Structures*, MIT – Verlag, Bremen, 1999, 45-56.

Fazekas, A., Dendievel, R., Salvo, L. and Brèchet, Y., (2002), 'Effect of microstructural topology upon the stiffness and strength of 2-D cellular structures', *International Journal of Mechanical Sciences*, **44**, 2047-2066.

Foroughi, B., Kriszt, B. and Degischer, H. P., 'Modelling of mechanical properties of inhomogeneous cellular materials', in Banhart, J., Ashby, M. and Fleck, N., *Cellular Metals and Metal Foaming Technology*, MIT – Verlag, Bremen, 2001, 265-268.

Gellatly, B. J. and Finney, J. L., (1982), 'Characterisation of models of multicomponent amorphous metals: the radical alternative to the Voronoi polyhedron', *Journal of Non-Crystalline Solids*, **50**, 313-329.

Gibson, L. J. and Ashby, M. F., *Cellular Solids: Structure and Properties*, 2nd edition, Cambridge University Press, Cambridge, UK, 1997.

Gradinger, R. and Rammerstorfer, F. G., (1999), 'On the influence of meso-inhomogeneities on the crush worthiness of metal foams', *Acta Materialia*, **47**(1), 143-148.

Grenestedt, J. L., (1998), 'Influence of wavy imperfections in cell walls on elastic stiffness of cellular solids', *Journal of the Mechanics and Physics of Solids*, **46**, 29-50.

Grenestedt, J. L. and Tanaka, K., (1999), 'Influence of cell shape variations on elastic stiffness of closed cell cellular solids', *Scripta Materialia*, **40**(1), 71-77.

Kriszt, B., Foroughi, B., Faure, K. and Degischer, H. P., (2000), 'Behaviour of aluminium foam under uniaxial compression', *Materials Science and Technology*, **16**, 792-796.

Kunze, H. D., Baumeister, J., Banhart, J. and Weber, M., (1993), *Powder Metallurgy International*, **25**(4), 182.

Maire, E., Fazekas, A., Salvo, L., Dendievel, R., Youssef, S., Cloetens, P. and Letang, J.-M., (2003), 'X-ray tomography applied to the characterisation of cellular materials. Related finite element modelling problems', *Composites Science and Technology*, **63**, 2431-2443.

Maire, E. and Buffière, J.-Y., 'X-ray tomography of aluminium foams and Ti/SiC composites', in Baruchel, J., Buffière, J.-Y., Maire, E., Merle, P. and Peix, G., *X-ray tomography in Materials Science*, HERMES Science Publications, Paris, 2000, 115-125.

McCullough, K. Y. G., Fleck, N. A. and Ashby, M. F., (1999), 'Uni-axial stress-strain behaviour of aluminium alloy foams', *Acta Materialia*, **47**, 2323-2330.

Metals Handbook Vol. 2: Properties and Selection: Nonferrous Alloys and Special Purpose Materials, 10th edn. American Society of Metals, Metals Park, Ohio, 1990.

Olurin, O. B., Arnold, M., Korner, C. and Singer, R. F., (2002), 'The investigation of morphometric parameters of aluminium foams using micro-computed tomography', *Materials Science and Engineering*, **A328**, 334-343.

Papka, S. D. and Kyriakides, S., (1994), 'In-plane compressive response and crushing of honeycombs', *Journal of the Mechanics and Physics of Solids*, **42**, 1499-1532.

Plateau, J. A. F., *Statique Experimentale et Teorique des Liquides Soumis aux Seules Forces Moleculaires*, Gauthier-Villiard, Paris, 1873.

Prakash, O., Sang, H. and Embury, J. D., (1995), 'Structure and properties of Al-SiC foam', *Materials Science and Engineering*, **A199**, 195-203.

Richard, P., Oger, L., Troadec, J. P. and Gervois, A., (1998), 'Tessellation of binary assemblies of spheres', *Physica A*, **259**, 205-221.

Silva, M. J. and Gibson, L. J., (1997), 'The effects of non-periodic microstructure and defects on the compressive strength of two-dimensional cellular solids', *International Journal of Mechanical Sciences*, **39**(5), 549-563.

Silva, M. J. and Gibson, L. J. and Hayes, W. C., (1995), 'The effects of non-periodic microstructure on the elastic properties of two-dimensional cellular solids', *International Journal of Mechanical Sciences*, **37**(11), 1161-1177.

Simone, A. E. and Gibson, L. J., (1998a), 'Effects of solid distribution on the stiffness and strength of metallic foams', *Acta Materialia*, **46**(6), 2139-2150.

Simone, A. E. and Gibson, L. J., (1998b), 'Aluminium foams produced by liquid-state processes', *Acta Materialia*, **46**(9), 3109-3123.

Simone, A. E. and Gibson, L. J., (1998c), 'The effects of cell face curvature and corrugations on the stiffness and strength of metallic foams', *Acta Materialia*, **46**(11), 3929-3935.

Skochdopole, R. E. and Rubens, L. C., (1965), *Journal of Cellular Plastics*, **1**, 91.

Sugimura, Y., Meyer, J., He, M. Y., Bart-Smith, H., Grenestedt, J. and Evans, A. G., (1997), 'On the mechanical performance of closed cell foams', *Acta Materialia*, **45**, 5245-5259.

Thornton, P. H. and Magee, C. L., (1975a), 'The deformation of aluminium foams', *Metallurgical Transactions*, **6A**, 1253-1263.

Thornton, P. H. and Magee, C. L., (1975b), 'Deformation characteristics of zinc foam', *Metallurgical Transactions*, **6A**, 1801-1807.

Timoshenko, S. P. and Goodier, J. N., *Theory of Elasticity*, 3rd Edition, McGraw-Hill, New York, 1970.

Vaz, M. F. and Fortes, M. A., (1993), 'Characterisation of deformation bands in the compression of cellular materials', *Journal of Materials Science Letters*, **12**, 1408-1410.

Walstra, P., in *Foams: Physics, Chemistry and Structure*, ed. A. J. Wilson. Springer-Verlag, London, 1989.

Warren, W. E. and Kraynik, A. M., (1997), 'Linear elastic behavior of a low-density kelvin foam with open cells', *Journal of Applied Mechanics*, **64**, 787-794.

Warren, W. E. and Kraynik, A. M., (1988), 'The linear elastic properties of open-cell foams', *Journal of Applied Mechanics*, **55**, 341-346.

Warren, W. E. and Kraynik, A. M., (1987), 'Foam mechanics: the linear elastic response of two-dimensional spatiallly periodic cellular materials', *Mechanics of Materials*, **6**, 27-37.

Zhu, H. X., Hobdell, J. R. and Windle, A. H., (2001), 'Effects of cell irregularity on the elastic properties of 2-D Voronoi honeycombs', *Journal of the Mechanics and Physics of Solids*, **49**, 857-870.

Chapter 6

Microstructural Characterisation and the Compressive Deformation of Al Foams

6.1. Introduction

The principle aim of the following study was to gain an understanding of the effect of the 3-D cellular structure on the mechanisms of deformation during compression of two different closed-cell aluminium foams and their subsequent mechanical properties. The two foams were fabricated by different liquid-state processes so that the effect of the fabrication procedure on the subsequent compressive deformation behaviour could be investigated. X-ray microtomography has been employed to generate 3-D images of samples of these closed-cell aluminium foam materials, enabling the internal structure, in terms of individual cells, to be characterised in three-dimensions. By performing *in situ* compressive deformation studies within this imaging/characterisation framework, the structural evolution of the cellular materials was investigated in terms of the mapping of deformation bands within the 3-D tomographic virtual microstructures. The results obtained aim to give important insights into the effect of, in particular, cell size and density distributions on the mode of deformation, and the influence of the production method on the structural performance of the foam materials. Also, the effect of both of these aspects on the stress-strain response of the materials has been investigated. Such an understanding is important in the use of cellular metallic foams for energy absorption and crash protection applications.

6.2. Materials and Specimens

A sheet of Alporas closed-cell aluminium foam, fabricated by Shinko Wire, was obtained for the principal 3-D deformation study, from which the necessary samples for the *in situ* compression tests were cut. The production of this foam material was described in Section 5.2.2.2. Figure 6-1 illustrates a simple diagram of the foam sheet or panel and, more importantly, defines the directions used in the subsequent analysis. The sheet had a thickness of 50 mm, defining the principal axis, *Z*. It must be noted that the relationship

between the defined and actual directions of the cast ingot are not known. Both cylindrical samples and samples of square cross-section, as illustrated in Figure 6-1, were cut from the as-received foam panel. Cylindrical samples of 25 mm diameter were cut by electric discharge machining. Two different heights of sample were used in the study in order to distinguish any differences in the compressive deformation modes between two different sample dimensional aspect ratios, 1:1 (25 mm height) and 2:1 (50 mm height). Larger samples of square cross-section, with dimensions of 50 mm cubed, were also used in the analysis in order to determine behaviour on a more global scale and to extract representative stress-strain curves. As explained in the following section, the sample size (diameter or width) had an effect on the achievable resolution of the reconstructed 3-D datasets, and also the measured stress-strain response of a sample. The relative density of the Alporas samples, calculated from the measured mass and volume of each of the samples tested, was ~0.1 (~0.25 g/cm^3).

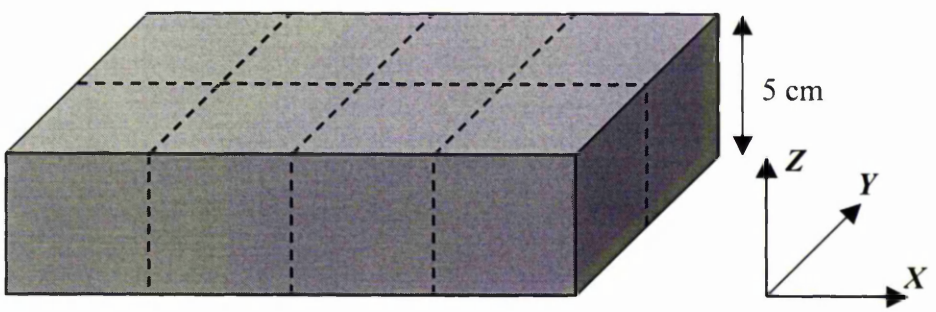

Figure 6-1. Defining the three directions with respect to the as-received foam panel, from which 25 mm diameter cylindrical samples and 5 cm cubed samples were cut. *Z* represents the principal direction and the thickness of the foam panel.

A comparison between the 3-D cell structure and density distributions, and the resulting compressive deformation modes, was made with another closed-cell aluminium foam material, produced by Cymat using an alternative liquid-state process as described in Section 5.2.2.1. The as-received panel of this foam material was in the same form as shown in Figure 6-1 but had a thickness of 25 mm, which again represented the *Z*-direction and the principal axis to which samples will be referred. Cylindrical samples of 25 mm diameter and 25 mm height were used for the *in situ* compression tests and cut by electric discharge machining. The relative density of the Cymat samples was calculated to be ~0.2 (~0.47 g/cm^3).

6.3. Experimental Methods

6.3.1. X-ray microtomography

In order to characterise the internal structure of the two types of aluminium foam, and to study the structural evolution of the materials *in situ* as a function of the applied compressive strain, X-ray microtomography was used to provide virtual 3-D datasets of the samples. This enabled the characterisation of individual cells, the distribution of solid metal, and also the mapping of deformation bands, in three-dimensions. A comprehensive review of the technique was given in Chapter 1, and of laboratory-based computed tomography in Section 1.2. A detailed description of the system instrumentation and the setup and calibration of the system was given in Section 2.2. A schematic diagram of the imaging arrangement of the system was given in Figure 2-1, which employs a cone beam geometry as described and illustrated in Section 1.2.1 and Figure 1-6(d).

As the *in situ* imaging and compression tests were interrupted, so that the samples could be imaged after each compression step, the sample holder was designed so that the bottom of the sample and its rotational start position were the same for each imaging step. This was so that, for the purposes of comparison between the compression steps during image processing and visualisation, the reconstructed datasets of a sample were all in the same orientation. The sample holder was a steel cylinder of the same diameter as the samples (25 mm), with a protruding pin out of the side so that it sat at the same position in the 3-jaw chuck of the sample manipulator, used to set the centre of rotation relative to the source and detector of the system. The samples were glued to the top of this cylindrical sample holder. The pixel resolution of the reconstructed sample datasets depended on the magnification of the sample relative to the X-ray source, a distance which was maximised to achieve the highest possible resolution. This therefore depended on sample size. Also, due to computational limitations on the dataset size for the subsequent image processing steps, reconstructions were processed using resolutions of either 256 × 256 or 384 × 384 pixels in the *X*- and *Y*-directions. In the *Z*-direction, representing the sample height, the dataset size was calculated by keeping the pixel size the same in all directions. As a result, the tomography datasets of the smaller Alporas and Cymat samples (of aspect ratio 1:1) had a pixel size of ~80 μm, while those of the taller samples (height:diameter aspect ratio of 2:1) had a pixel size of ~100 μm. The datasets of the larger cube samples had a pixel size of ~180 μm. An X-ray voltage of 80 kV was used to acquire the images, filtered using

a copper X-ray filter of thickness 0.1 mm. A rotation step of 0.5° was used, whilst averaging 32 frames for each projection.

6.3.2. Mechanical testing

In order to study the structural evolution of the foam materials during compression and to relate this to the microstructural characterisation, samples were compressed in small steps and imaged after each step. This enabled an accurate determination and observation of the formation of deformation bands, and the structural deformation mechanisms that occur at small strains. Interrupted uniaxial compression tests were performed on an Instron 4505 load frame with a 10 kN load cell. The samples were placed between two platens, as illustrated in Figure 6-2, which were lubricated to reduce the effects of friction during compression of the samples. The cross-head displacement speed was set to 0.5 mm/min. The tests were interrupted when the desired height reduction was reached, measured from the cross-head displacement, to give the required applied sample strain. Samples were compressed in steps of typically 5 or 10% applied sample strain (height reduction), apart from several samples which were compressed in a sequence of steps consisting of 1%, 3%, 6% and 10% applied sample strain. This latter sequence of compression steps was carried out to discern the level of cell wall bending or buckling at low strains.

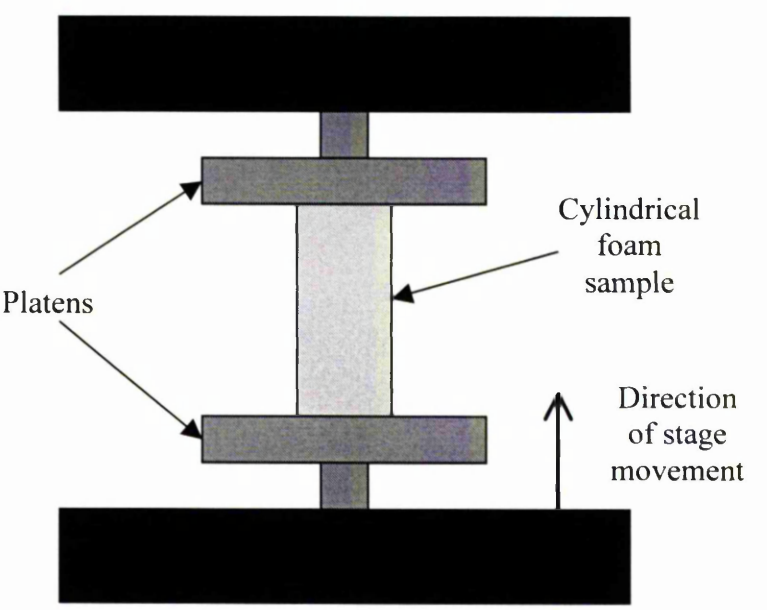

Figure 6-2. The compression of a foam sample in the Instron testing machine.

The elastic modulus, plastic collapse stress, and overall compressive stress-strain response during linear elastic loading, collapse, and densification were measured and recorded for

each sample by piecing together the individual parts of the curves from each compression step. Uniaxial compression tests without interruptions were performed for the Alporas foam on the samples of square cross-section in order to acquire representative stress-strain curves. Such samples were also tested in each of the three orthogonal directions of the as-received foam panel, as defined in Figure 6-1, in order to observe any difference in the stress-strain response and therefore mechanical properties (Young's modulus and compressive strength) with orientation. Two samples were tested in each direction. Andrews *et al.* and Onck *et al.* have looked at the effect of sample size relative to the cell size on the measured stress-strain response (Andrews *et al*, 2001; Onck *et al*, 2001). These studies indicated that the minimum sample size required to avoid edge effects, which reduce the measured values of Young's modulus and compressive strength, is an edge length/diameter of least seven times the cell size. The mechanical properties were found to increase to a plateau level at this ratio of sample size to cell size. This was taken into account for all samples tested. Alporas material has an average cell diameter of ~3 mm (Simone and Gibson, 1998b), and thus cylindrical samples for the interrupted compression tests had a diameter (25 mm) just above this minimum requirement so that the sample size could be kept as small as possible to enable maximisation of the magnification and thus pixel resolution during the tomography scans. The cubic samples for obtaining representative stress-strain curves had an edge length of double this (50 mm). The Cymat foam was tested in the thickness direction of the as–received panel only, with representative stress-strain data being collected from cubic samples measuring 25 mm cubed. Due to stress concentrations caused by defects in the cellular structure (cell walls) of the aluminium foams, a small amount of plastic deformation can occur even at a very low stress levels (Kunze *et al*, 1993). These defects include density variations and imperfections, such as cell wall curvature and corrugations in the cell faces, the effects of which have been analysed in detail (Andrews *et al*, 1999; Simone and Gibson, 1998a; Simone and Gibson, 1998c; see Section 5.4). The slope of the loading stress-strain curve is therefore not a true representation of the elastic modulus. The unloading slope, however, remains roughly constant until the foam has been loaded to its plastic collapse stress (Simone and Gibson, 1998b; Sugimura *et al*, 1997). The elastic modulus for each of the samples tested was taken as the unloading modulus measured at 1% applied strain, well below the plastic collapse stress, σ_{pl}, of the foams. The plastic collapse stress was measured as the peak stress reached before the onset of plastic collapse.

6.3.3. Microstructural characterisation

In order to provide a three-dimensional characterisation of the internal structure of samples of the two foam materials throughout their compression history, the reconstructed 3-D tomographic datasets for each compression step were analysed using a visualisation and volume rendering package called Volview, by VTK. Using a Pentium PC with a specific VolumePro graphics board, this enabled true 3-D manipulation of the tomographic data, and detailed observation of the internal structural evolution as a function of applied compressive strain. The deformation modes present and the characterisation of deformation bands through the three orthogonal directions of the samples could therefore be observed. Digital image analysis of the raw tomographic data representing the sample structures was used to characterise the distribution of the structures of individual cells within a sample quantitatively in three-dimensions. This required a number of image processing steps to be applied to the raw data, carried out using the comprehensive image processing toolbox of the mathematics package Matlab, by Mathworks. The segmentation image processing steps that were applied in order to produce a representative dataset of the original sample containing individually labeled cells, for the purposes of making quantitative measurements, were as follows:-

1. A program was written to read the raw grey-level tomographic dataset into Matlab, from which any slice through each of the three orthogonal directions could be viewed. Figure 6-3 shows such a slice through the original dataset of an Alporas sample, showing a plane perpendicular to the *Z*-direction of the cylindrical sample.

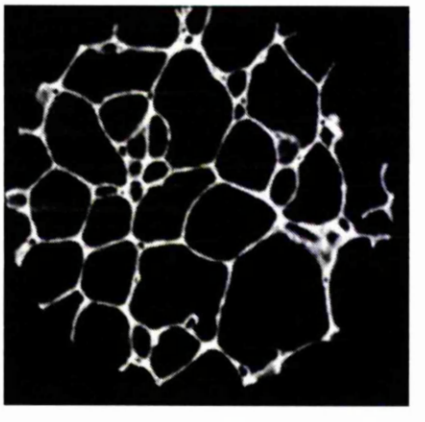

Figure 6-3. A slice through the original raw grey-level dataset of a typical sample used for analysis. The image represents a plane perpendicular to the *Z*-direction. The scale of the image can be deduced from the sample diameter of 25 mm.

The distance between each slice is defined by the pixel size of the reconstruction. The image represents a map of grey levels based on the attenuation coefficient of each voxel or pixel.

2. After each slice of the dataset was adjusted to extend the brightness/contrast levels to the full range of values, i.e. between 0 and 1, the 3-D dataset was segmented by thresholding. Values above a certain threshold level were taken to give a binary dataset required for further processing, and pixel values of 0 and 1 representing a pore and the metal phase respectively. The equivalent binary slice of that in Figure 6-3 after thresholding is illustrated in Figure 6-4.

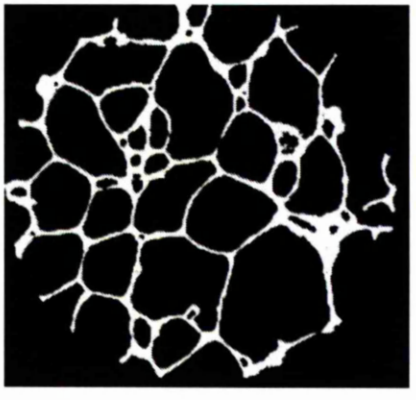

Figure 6-4. The equivalent binary slice of that in Figure 6-3 after the dataset had been thresholded, giving pixel values of 0 (pore) and 1 (metal).

3. The cell walls of the metal foam in each segmented or thresholded slice of the dataset were then morphologically eroded and dilated, as illustrated in Figure 6-5, in order to complete partial boundaries. Such boundaries were present due to defects in the cell walls, especially in the Cymat foam. Erosion removed isolated pixels, while dilation added layers of pixels around important original boundaries. This biased dilation step was also necessary for where the walls were thin, as the subsequent labeling step required thick cell walls in order to identify boundaries and isolated cells in the sample dataset for characterisation purposes. The presence of small pores was not smeared over in this step due to dilation because the subsequent labeling step used the original image (Figure 6-4) as a reference.

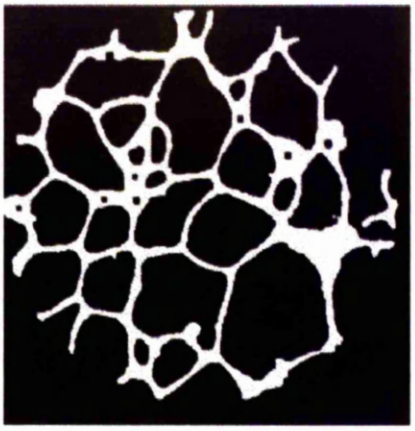

Figure 6-5. The morphological erosion and biased dilation of the cell walls of the metal foam in the segmented slice of Figure 6-4.

4. After inverting the pixel values of the morphologically processed dataset, making the background (pores) white and the metal cell walls black, a Euclidean distance map was calculated from the binary dataset. This essentially assigned a brightness value to each pixel equal to its distance from the nearest boundary (the nearest pixel in the background), and defined the boundaries of the cells for labeling. The equivalent slice through such a dataset is shown in Figure 6-6.

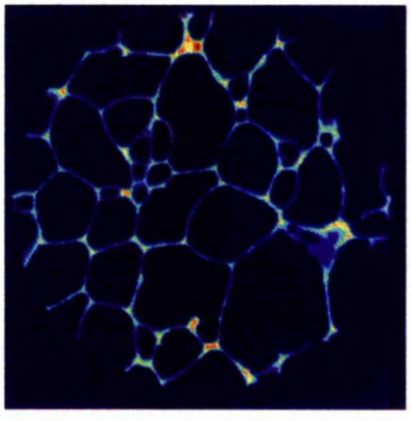

Figure 6-6. The equivalent slice through the dataset after a Euclidean distance map had been calculated, defining the boundaries of the cells for labeling.

5. Using the calculated distance transform, a watershed segmentation algorithm was then applied to the dataset to create one consisting of individual, separated objects/cells. This algorithm effectively identified the peaks (and troughs) of the brightness values across a boundary and joined the peak values to create isolated objects. Each cell was then labeled, as shown in the slice of Figure 6-7 and

represented by different colours, to enable quantitative measurements to be made. The labeling algorithm returned the number of connected objects from the watershed algorithm, based on the connectivity of individual voxels in 3-D.

Figure 6-7. Individually labeled cells in the slice after application of the watershed segmentation algorithm and the labeling procedure, enabling quantitative measurements to be carried out.

The image processing and characterisation procedure was applied to the 3-D dataset of each sample, resulting in cells labeled as 3-D objects. Note that the large cell bottom right of the sample as it is viewed in Figure 6-6 has not been labeled in Figure 6-7. This is a consequence of the labeling algorithm and its required connectivity in 3-D. Any object that is connected to the background relative to its structure in 3-D, i.e. considering every single slice, is not considered and therefore is not labeled. The specified connectivity refers to the connection of surrounding pixels relative to a centre element/pixel.

The principal quantitative measurement value that was obtained for each individual cell in a sample dataset was its volume in 3-D, calculated as the number of voxels contained within each labeled object. A typical Alporas sample (25 mm diameter, 50 mm height) contained ~400 cells. Also, for the purposes of obtaining a measure of how much a cell was compressed at a particular level of strain, the dimensions of a 3-D bounding box created around each cell were calculated. The axes of this box were in the three orthogonal directions representing the dataset, and the width of the box along each dimension represented the smallest box that a cell could fit into. These two region properties represented 3-D measurements. 2-D measurements were also calculated for each of the cells intersecting individual slices that created a sample dataset. An advantage of using the 3-D tomographic data over the serial sectioning method of cell measurements, in terms of

calculating 2-D measurements, is that a 3-D dataset is made up of many slices (typically 256 or 384 slices depending on the reconstruction resolution). The measurement procedure and data collection can thus be applied to all cells of all slices in all three planes of the labeled dataset, providing information about cell sizes and structures in 3-D. The principal axes of each cell were calculated as the directions of maximum and minimum moments of inertia about the calculated centroid of their measured 2-D areas. The 'best-fit' ellipse for each cell was then defined as the ellipse having the same area and second-moments of inertia about the calculated principal axes. The major and minor axis lengths of this ellipse, a and b, and the major axis orientation, θ, measured with respect to the compression axis, were recorded. Variations in cell structure were investigated using properties such as the equivalent diameter, $(ab)^{1/2}$, and the aspect ratio, a/b. The 3-D and 2-D quantitative data was used to identify the distributions of cell volume and morphology.

In addition to 2-D and 3-D distributions of cell size and structure, 3-D mass density distributions in the foam samples were also determined directly from the raw tomographic data, effectively revealing the distribution of the volume fraction of metal within a sample. This was carried out using a routine written for an image processing package called ImageJ (Java), for which Luc Salvo of GEPPM2 in Lyon, France is acknowledged for writing the routine. The local density of an arbitrary point (voxel) in a sample was calculated by averaging the tomographic data, i.e. the reconstructed grey level of each voxel determined from the attenuation coefficient during tomographic data acquisition, over a certain surrounding volume (averaging volume). This approach transformed the discrete structural features of the foam into a continuous function, enabling regions of higher or lower local density to be determined and correlated with the cell volume measurements to describe the positions of deformation band formation in the two foam materials.

In order to assess the validity of microstructural characterisation using virtual tomography slices, a simple comparison was carried out with measurements made using 'true' sectioned slices. As with the reconstructed tomographic datasets, digital image analysis was used to characterise the structure of individual cells of a series of sectioned 2-D images of the two foam types under analysis, using the serial sectioning technique (Simone and Gibson, 1998b). The foam samples, cylindrical specimens of 25 mm diameter, were sectioned using a diamond saw to introduce minimal damage at the cut surface. The cellular structure was then infiltrated with a resin to create the required contrast between the metal walls and the air of the cells, and to provide binary images necessary for measurement purposes. About 10 images were created in this way for each

foam in two perpendicular planes normal to the cylindrical plane. Each image contained about 100 cells, and was digitised using a digital optical microscope.

6.4. Results and Discussion

6.4.1. Microstructural characterisation

Typical 2-D slices through the reconstructed tomographic volumes of an Alporas and a Cymat foam sample are shown in Figure 6-8(a) and (b) respectively, representing views through both the *X-Z* and *Y-Z* planes for each. The *Z*-direction represents the height of the slices as they are shown in Figure 6-8 and the thickness of the respective foam panels as defined in Figure 6-1.

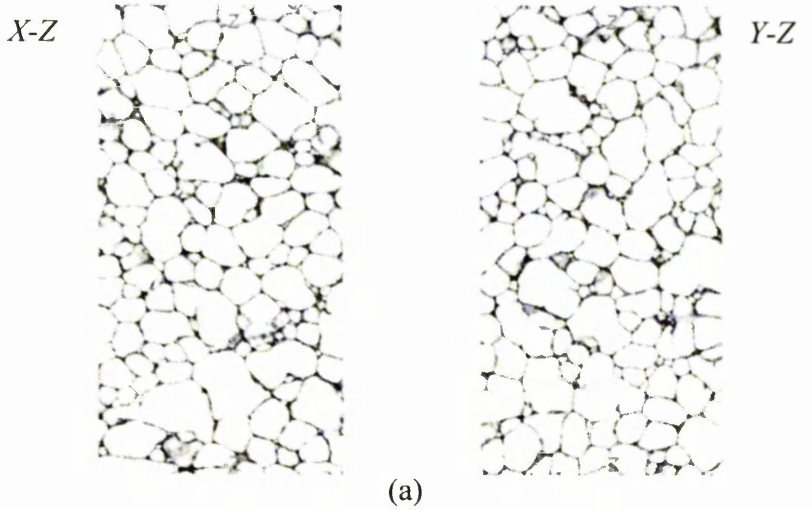

(a)

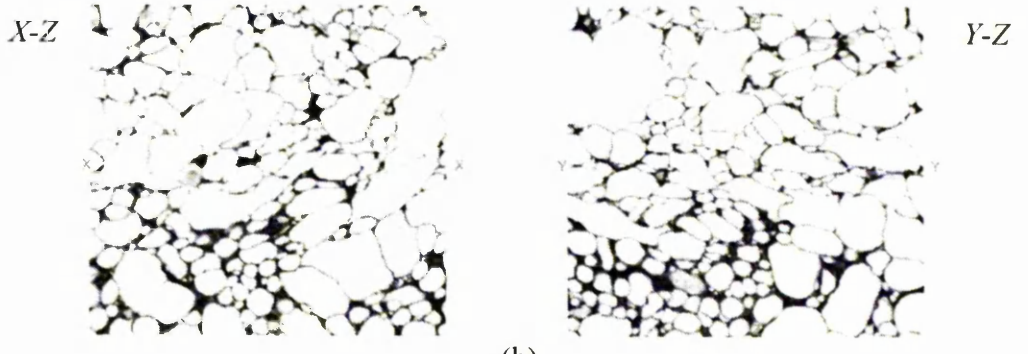

(b)

Figure 6-8. 2-D reconstructed tomographic slices of (a) Alporas Al-Ca-Ti and (b) Cymat Al-SiC foams, representing views through the *X-Z* and *Y-Z* planes respectively (with *Z* the compression direction). The scale of the images can be deduced from the sample diameters (both 25 mm).

The Alporas foam by eye does not exhibit any obvious variation in cell structure through the panel thickness, but maybe shows a dispersion of larger isolated cells. In comparison, the Cymat foam does exhibit a discernible gradient in cell size and distribution of metal in the cell edges through the thickness of the foam. There are clearly two distinct sub-regions here.

The variation in structure of the two foam types in terms of the 3-D cell volume distribution was investigated first of all, using labeled CT datasets, as described in Section 6.3.3, to measure the number of voxels comprised in the individual cells. This was converted to a measurement in mm^3 using the calculated voxel size from the reconstruction. Histograms of the cell volume of individual cells provide insight into the size distribution in the foam samples. Characterisation of the size distributions was made using the standard moments in order to describe the shapes of the distributions. The j^{th} moment, μ_j, of a set of n measurements, x_i ($i = 1 \ldots n$), is defined as:

$$\mu_j = \frac{\sum_{i=1}^{n} (x_i - \bar{x})^j}{n} \tag{6-1}$$

where $\bar{x}$ is the arithmetic mean of all measurements. The skewness, a_3, and the kurtosis, a_4, of a distribution are defined by the third and fourth moments, respectively, and the standard deviation (the square root of μ_2),

$$\sigma = \sqrt{\frac{\sum_{i=1}^{n} (x_i - \bar{x})^2}{n}} \tag{6-2}$$

by

$$a_3 = \frac{\mu_3}{\sigma^3} \tag{6-3}$$

and

$$a_4 = \frac{\mu_4}{\sigma^4} \tag{6-4}$$

The skewness of a distribution indicates the direction and magnitude of skew, reflecting the degree to which the tail of the distribution is lengthened, i.e. the greater its value the more the tail will be lengthened. If the distribution is symmetrical, $a_3 = 0$; if $a_3 < 0$, the left tail of the distribution is lengthened; and if $a_3 > 0$, the right tail of the distribution is lengthened. The kurtosis of a distribution indicates the peakedness, with $a_4 < 3$ indicating a flattened, or platykurtic distribution, and $a_4 > 3$ indicating a highly peaked, or leptokurtic

distribution. It reflects the degree to which the population is distributed in the tails – the more positive it is the more data is concentrated around the mean. These moments have been used in areas such as process control in order to monitor the shapes of distributions during production. For example, skewness and kurtosis values have been used to monitor the effect of cold rolling on the surface roughness and quality of steel (Ma *et al*, 2002).

Alporas foam

Figure 6-9 shows a histogram of the distribution of cell sizes in the Alporas sample of Figure 6-8(a). The mean, standard deviation, skewness and kurtosis values are shown. This is a typical distribution of that measured for the Alporas material, with data acquired from a sample of over 400 cells.

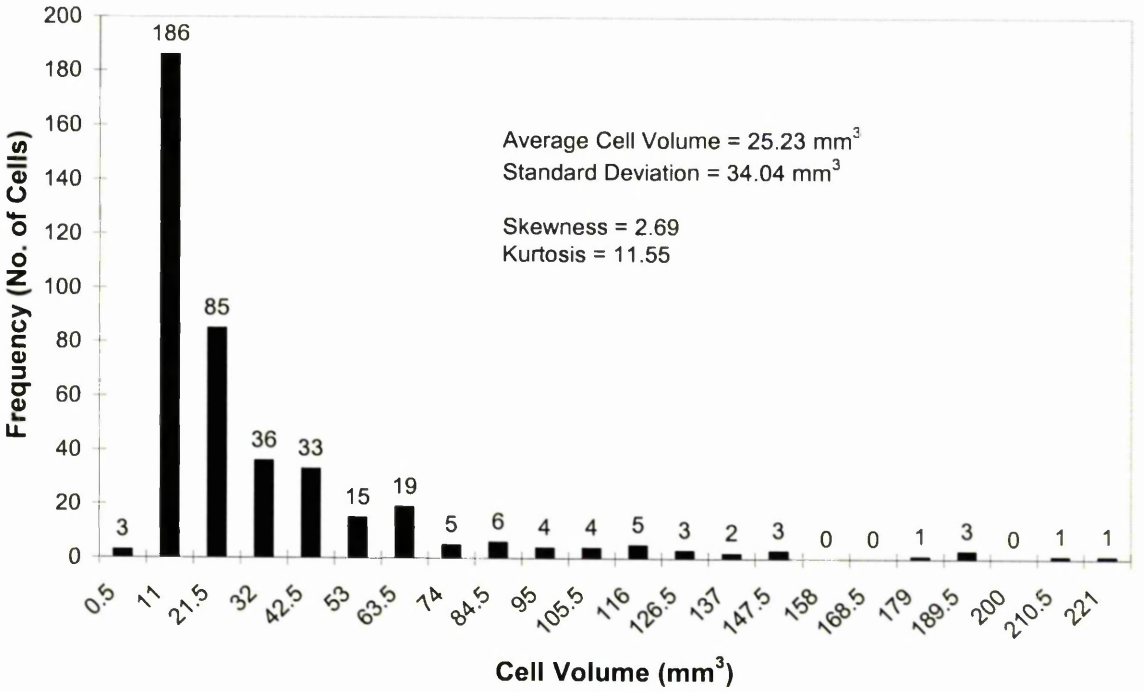

Figure 6-9. Histogram of the cell volume distribution in an Alporas sample (25 mm in diameter and 50 mm in height) containing 415 cells. The values of the mean, standard deviation, skewness and kurtosis are shown.

The distribution shows quite a few cells towards the larger sizes, lengthening the right-hand tail to over 200 mm^3, therefore giving a small but positive skewness value. Because there are a number of cells at the larger sizes in relation to the mean value, the kurtosis value is quite small, correlating with the small skewness value. The histogram reveals a monomodal cell volume distribution and confirms the presence of larger cells dispersed

throughout the foam, which are observed to be very important for the compressive behaviour of the material, analysed in Section 6.4.3. The magnitude of the skewness and kurtosis values calculated here will be put into better context when used to describe the cell volume distributions of other Alporas specimens in Section 6.4.4, and used as 'descriptors' to help describe and predict the general mode of deformation of a sample.

In order to obtain information on the typical shape distribution of cells in the Alporas material, 2-D measurements of equivalent diameter and aspect ratio of a best-fit ellipse representing a cell in a 2-D slice were calculated, as described in Section 6.3.3. These measurements were made for each of the three orthogonal planes with respect to the scanned sample volume and results will be shown for the same sample as that for which the 3-D cell volume distribution is shown in Figure 6-9. The major and minor axis lengths of the best-fit ellipse were calculated for all cells intersecting every slice in the labeled volume, except for the ones cut by the edges of the sample. Therefore, since each cell intersects more than one slice, the maximum value for each of the two lengths was used in the parameter calculations for each cell. These lengths were then used to calculate and plot 2-D distributions of the equivalent diameter of cells, providing further information on the distribution of cell sizes, and more importantly in terms of cell shape, the aspect ratio of each cell in the sample volume. Calculating and comparing the aspect ratio and equivalent diameter of cells from slices through each of the three orthogonal directions of the foam dataset aims to provide inferences of the shape of cells in three-dimensions. Figure 6-10 shows the equivalent diameter distributions for the *X-Y* and *Y-Z* planes of the Alporas sample, representing and comparing planes both parallel and perpendicular to the thickness of the foam panel, while statistical data extracted from all three planes are shown in Table 6-1. Data for only two planes are compared in the actual histogram just to illustrate how differences in the skewness and kurtosis values are reflected in the distributions. The extracted data of Table 6-1 provides the principal comparison. A characteristic to note of the distributions is that they are relatively symmetrical about a diameter of ~3 mm, but indicate a bias in the tail of the distribution towards larger cell diameters, as found previously in the 3-D cell volume distribution. All three distributions have an average diameter of just over 3 mm, and skewness values of around 1, indicating only a small extension of the right-hand tails. The skewness value of cell diameters through the *Y-Z* plane is slightly higher than that of the other planes due to more cells present at these higher diameters. As illustrated in Figure 6-10, the distribution of the *X-Y* plane is slightly more extended than that of the *Y-Z* plane, albeit only for two larger cells. The fact that the

X-Y distribution is also extended for lower cell diameters explains the differences in skewness and the lower value of the *X-Y* plane. In terms of the kurtosis, that for the *X-Z* plane is smallest, indicating a larger number of higher diameter cells (cells in the tail of the distribution), which contributes to the slightly higher mean value.

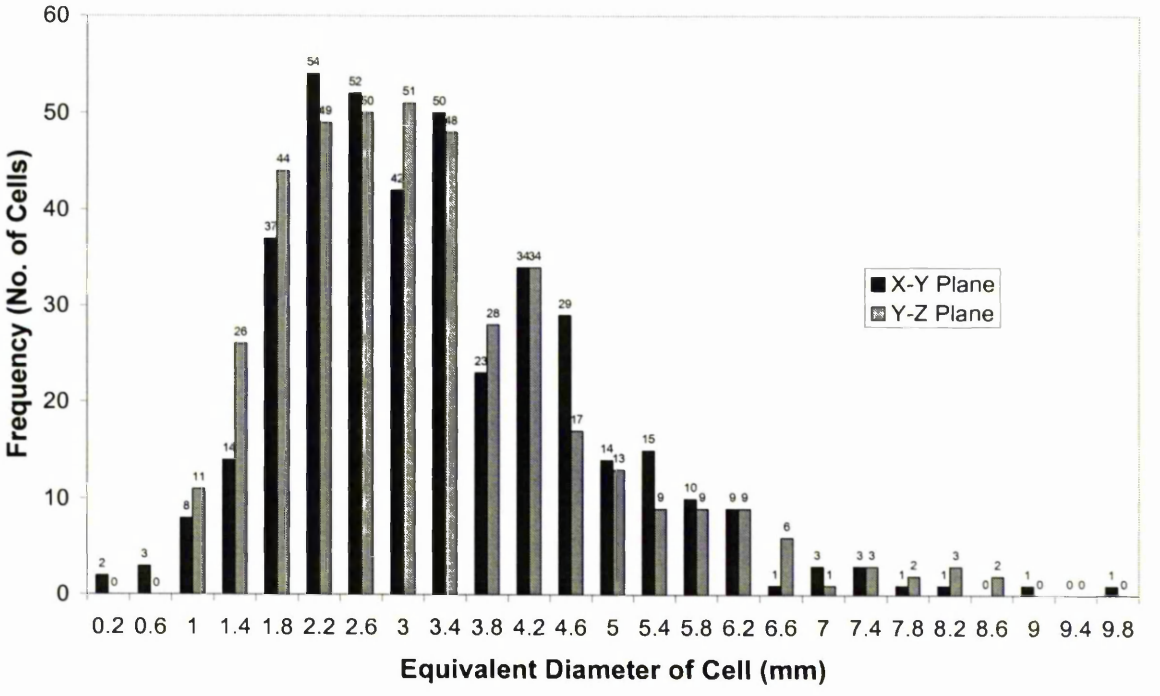

Figure 6-10. Histogram of the equivalent diameter distributions for the *X-Y* and *Y-Z* planes of the Alporas sample considered earlier in Figure 6-9.

Table 6-1. Statistical data extracted from the 2-D equivalent diameter distributions through the three orthogonal planes of the Alporas sample shown in Figure 6-8(a).

	Average (mm)	St. Dev. (mm)	Skewness	Kurtosis
X-Y	3.14	1.44	0.86	4.07
Y-Z	3.06	1.47	1.07	4.19
X-Z	3.23	1.39	0.85	3.59

Overall, there is no significant difference between the three measurement planes, which infers a uniform cell shape in three-dimensions with cells having the same diameter in the three orthogonal planes. Small differences in the statistical moments of the distributions are observed between the three planes, which may indicate a small effect of directional stabilisation and solidification of the cells in the through-thickness *Z*-direction of the foam

panel and samples. These small differences may also be important when comparing the compressive behaviour of the material in the three directions (see Section 6.4.7).

Note that the mean value of ~3.1 mm for the equivalent cell diameter agrees well with 2-D measurements acquired using the serial sectioning technique, which was used as a 'true' comparison in order to determine the level of confidence in the tomographic measurements. The average equivalent diameter measured from ~300 cells using metallographically polished sections, which were then digitized to give binary images, through a different sample taken from the same foam panel, was ~3.0 mm. Therefore, a high degree of confidence can be taken from the fact that measurements from the virtual slices of the tomographic volumes are representative of 'true' sections through the foam. The results also agree well with those of Simone and Gibson (Simone and Gibson, 1998), also carried out using serial sectioning.

Figure 6-11 shows the cell aspect ratio distributions for the *X-Y* and *Y-Z* planes of the same Alporas sample as reported earlier in Figure 6-8, while statistical data extracted from all three planes are shown in Table 6-2.

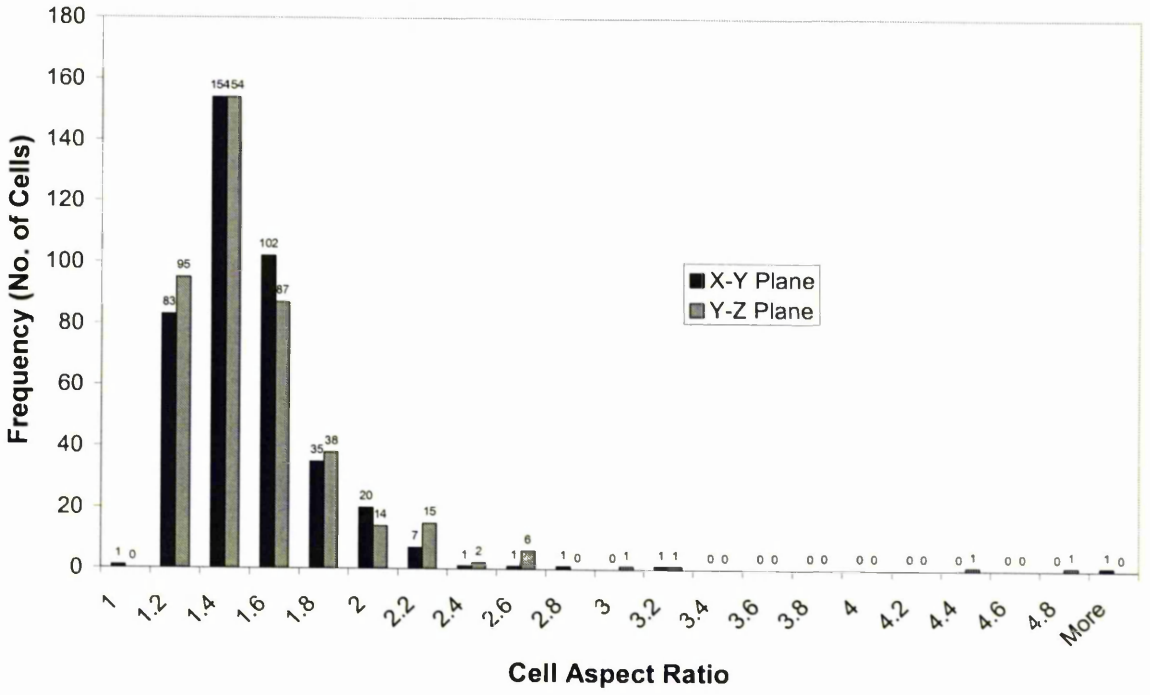

Figure 6-11. Histogram of the cell aspect ratio distributions for the *X-Y* and *Y-Z* planes of the same Alporas sample considered earlier in Figures 6-9 and 6-10.

Table 6-2. Statistical data extracted from the 2-D cell aspect ratio distributions through the three orthogonal planes of the same Alporas sample for which the cell diameter data are shown in Table 6-1.

	Average	**St. Dev.**	**Skewness**	**Kurtosis**
X-Y	1.41	0.48	12.21	203.63
Y-Z	1.42	0.37	3.75	27.15
X-Z	1.53	0.47	3.12	18.13

The distributions are concentrated around an aspect ratio value of ~1.4 for all three planes, and the high kurtosis values indicate a very high concentration around this mean value. This is especially so for the aspect ratio measurements from the *X-Y* plane, for which the kurtosis is very large due to the extension of the right-hand tail for just one cell (indicated as 'more' on the plot). This also results in a much higher skewness value for this plane. Again, measurements from the *X-Z* plane show a lower kurtosis and therefore a slightly larger mean aspect ratio of cells. Orientation measurements were also made, calculated as the angle between the major principal axis and the vertical axis of the sample. The data suggests the presence of cells with their long axis preferentially oriented along the *Z*-direction during stabilisation and solidification of the foam. The measured mean cell aspect ratios of ~1.4-1.5 for all planes, noting that a value of 1 represents a perfect circle or sphere, suggests that the cell structure in terms of shape is relatively uniform or equiaxed, with no significant number of elongated cells. The statistical data further suggests that this is fairly homogeneous throughout the sample of cells.

Cymat foam

In the same way, the cell size and structure distributions for the Cymat material were analysed. Figure 6-12 shows a histogram of the distribution of cell volumes in the Cymat sample shown in Figure 6-8(b). The mean value is much lower than that for the Alporas sample owing to a much higher proportion of cells in the modal bin range, not larger than ~10 mm^3 (80% compared to 45% for the Alporas material), and only a very few distributed in the tail up to ~110 mm^3. As a result, a higher skewness is observed (the tail of the distribution is extended, labeled 'more' in the plot, for a cell measuring 190 mm^3), and a much higher kurtosis, due to the degree to which the cells are all concentrated around the mean. Such initial statistical analysis of a number of representative samples from each foam type has suggested the Cymat material to have a more homogeneous cell size

distribution compared to Alporas, due to many more cells concentrated around the lower mean value. As will be observed in the more detailed analysis of Section 6.4.6, sub-regions through the thickness of this Cymat material reveal significant differences between the cell size distributions in each.

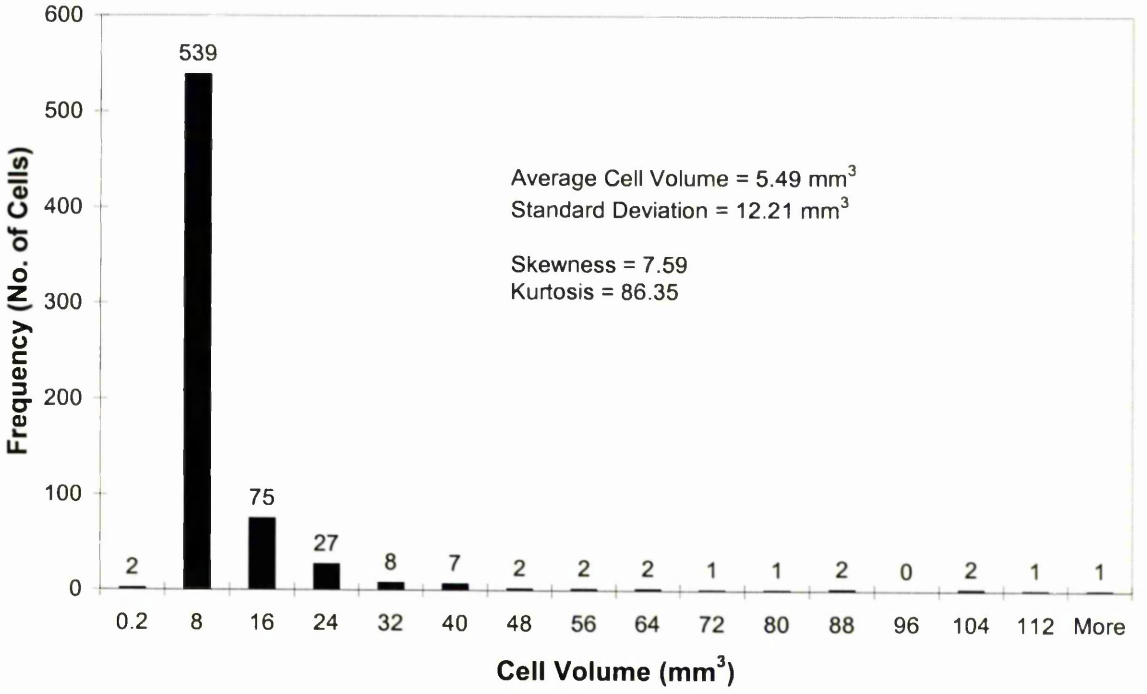

Figure 6-12. Histogram of the cell volume distribution in a Cymat sample (25 mm diameter and 25 mm height) containing 672 cells. The values of the mean, standard deviation, skewness and kurtosis are shown.

As for the Alporas material, 2-D distributions of the equivalent diameter and aspect ratio were measured. Figure 6-13 compares equivalent diameter distributions measured from the *X-Y* (perpendicular to thickness of foam panel) and *X-Z* (parallel to thickness of foam panel) planes of the sample. Table 6-3 shows the statistical data extracted from the distributions through all three planes. The distribution for the *X-Y* plane contains noticeably higher numbers of the larger cell diameters, i.e. > 2 mm, whereas that for the *X-Z* plane contains significantly more cells of diameters less than this. This leads to an average cell diameter of 2 mm compared to 1.8 mm for both the *X-Z* and *Y-Z* planes, both of which are smaller than that of the Alporas material. The *X-Y* and *Y-Z* planes have a slightly higher skewness due to the presence of more cells in their extended tails (shown as a comparison between *X-Y* and *X-Z* in Figure 6-13), and also a higher kurtosis indicating

more cells around the mean values and less distributed in the tails. Whereas the data for the Alporas foam showed an equiaxed structure, larger differences are observed in the directions of the Cymat foam regarding the fact that the data in one plane (*X-Y*) is significantly different from the other two. This suggests that stabilisation of the foam during fabrication has an effect on the cell structure resulting in cells that are ellipsoidal.

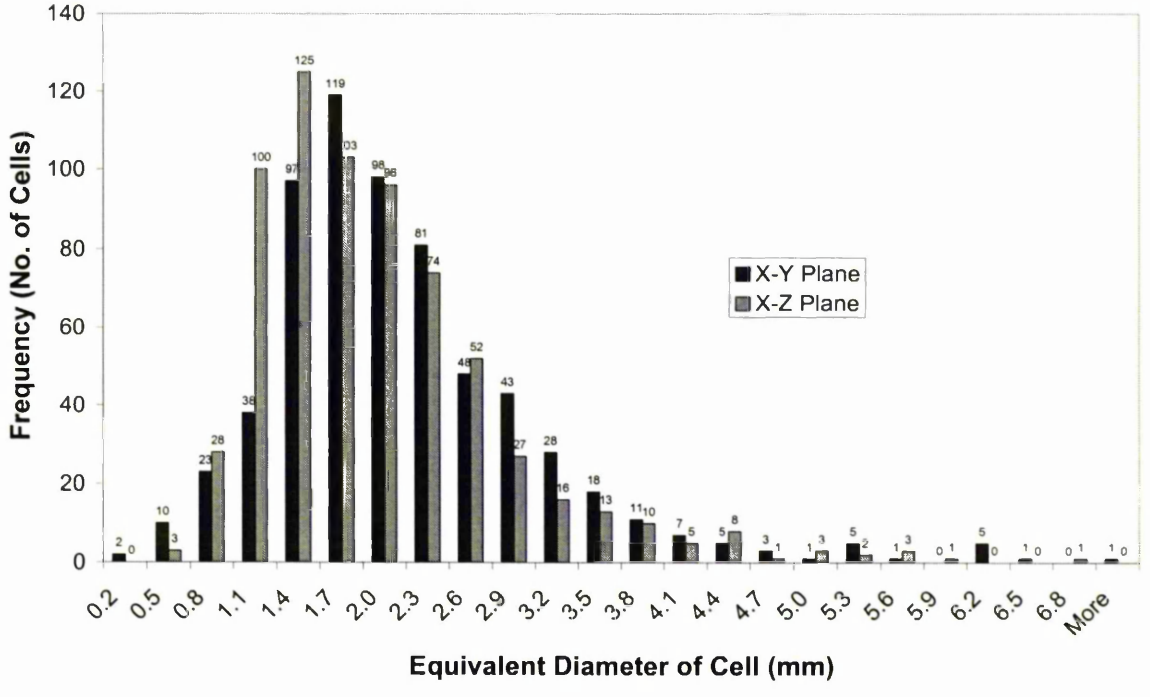

Figure 6-13. Histogram of the equivalent diameter distributions for the *X-Y* and *X-Z* planes of the Cymat sample considered earlier in Figure 6-12.

Table 6-3. Statistical data extracted from the 2-D equivalent diameter distributions through the three orthogonal planes of the Cymat sample shown in Figure 6-8(b).

	Average (mm)	St. Dev. (mm)	Skewness	Kurtosis
X-Y	1.99	0.98	1.93	10.73
Y-Z	1.80	0.89	1.97	10.59
X-Z	1.80	0.87	1.64	7.07

Figure 6-14 shows the cell aspect ratio distributions for the *X-Y* and *X-Z* planes of the same Cymat sample, and the statistical data extracted from all three planes are shown in Table 6-4. A significant difference between the two distributions of Figure 6-14 is observed. The distribution for the *X-Y* plane is concentrated towards the lower aspect ratio

values, showing significantly more cells up to an aspect ratio of ~1.6 and none above ~4.6. Combined with the fact that the distribution of the *X-Z* plane is extended up to ~9, this results in a lower average aspect ratio for the *X-Y* plane. The difference in aspect ratios between the *X-Y* plane and the other two planes confirms the suggestions of the equivalent diameter measurements, that the cells of this Cymat foam have different structures parallel and perpendicular to the thickness of the foam panel. Recalling the average cell aspect ratio of 1.4 for the Alporas material, the cells of the Cymat foam are thus more elongated.

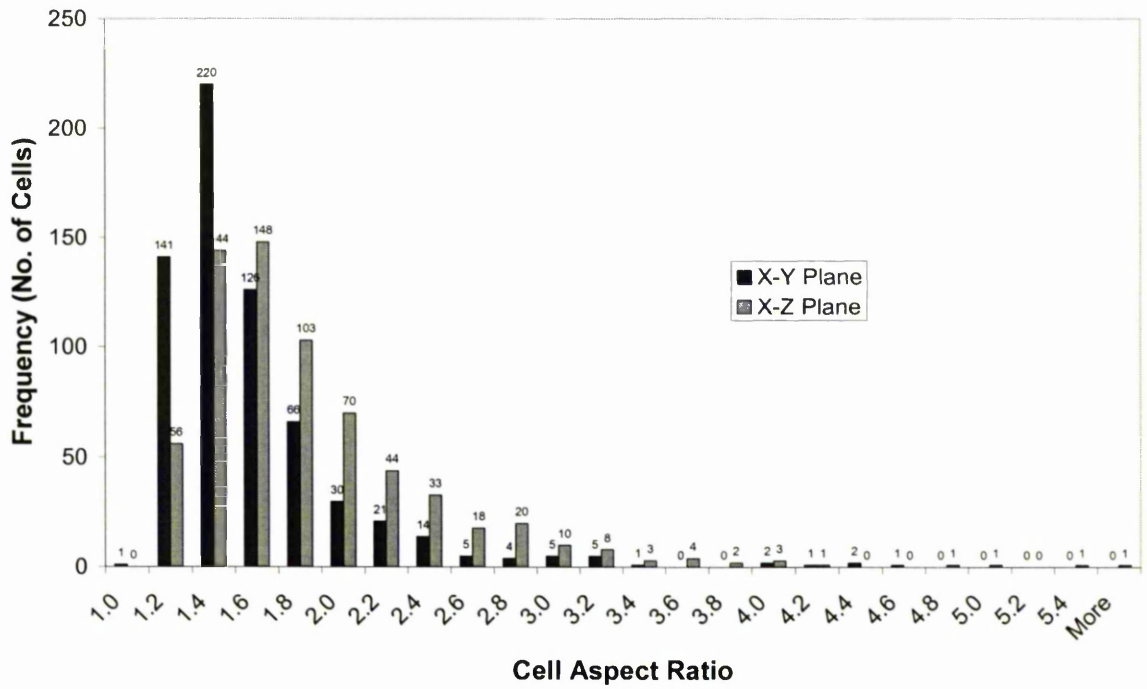

Figure 6-14. Histogram of the cell aspect ratio distributions for the *X-Y* and *X-Z* planes of the same Cymat sample considered earlier in Figures 6-12 and 6-13.

Table 6-4. Statistical data extracted from the 2-D cell aspect ratio distributions through the three orthogonal planes of the same Cymat sample for which the cell diameter data are shown in Table 6-3.

	Average	**St. Dev.**	**Skewness**	**Kurtosis**
X-Y	1.49	0.45	2.87	14.73
Y-Z	1.70	0.62	4.22	38.74
X-Z	1.74	0.63	3.72	32.58

6.4.2. Compressive deformation of Alporas material

Samples of the Alporas foam material were initially compressed in steps of 10% height reduction to study the progression of deformation and the influence of the cellular structure on the formation of deformation bands. A sequence of slices through the centre of tomographic volumes during compression of Alporas foam sample 1 is shown in Figure 6-15.

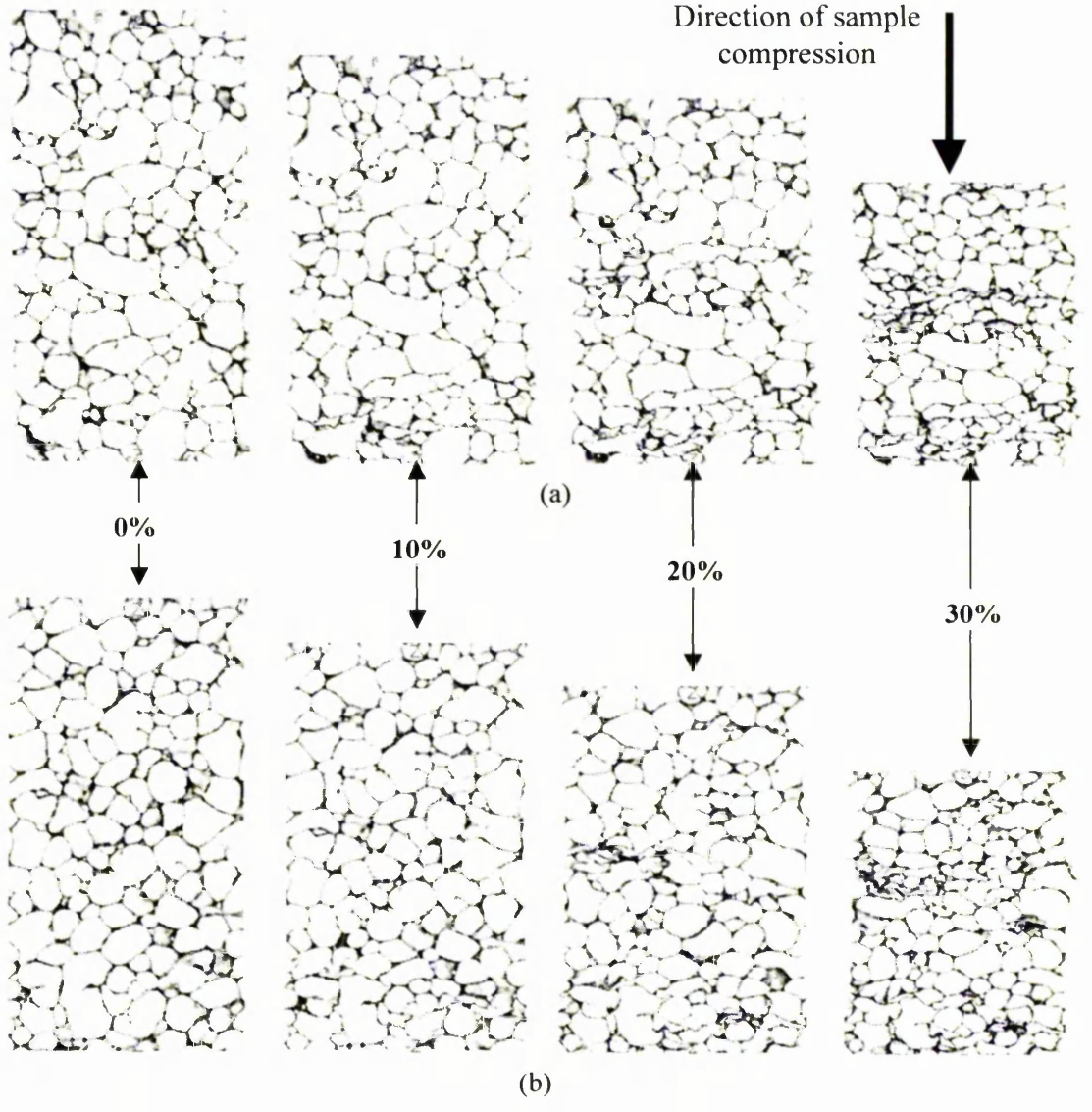

Figure 6-15. Sequence of slices through the centre of tomographic volumes, showing the compression of Alporas sample 1 at 0, 10, 20 and 30% height reduction. Slices through both the (a) *X-Z* and (b) *Y-Z* planes are shown. The specimen diameter is 25 mm and the original height 50 mm.

The sequence illustrates a uniform distribution of localised deformation, in terms of bands across the sample width, in two perpendicular planes, *X-Z* (Figure 6-15(a)) and *Y-Z* (Figure 6-15(b)), of the foam panel as defined in Figure 6-1. Detailed observation of the compression sequence reveals the sample to exhibit multiple minor deformation bands throughout its loading history. By 30% height reduction, progressive collapse has occurred by the expansion of these bands resulting in two visually discernible regions of localised deformation, or crushed regions, across the sample, perpendicular to the direction of applied load. A similar mode of deformation was observed by Simone and Gibson (Simone and Gibson, 1998b). Bart-Smith *et al.* also observed this heterogeneous deformation via surface strain mapping and the propagation of a band across the specimen with increase in load (Bart-Smith *et al*, 1998). They found that in some cases, several bands were found to initiate within the specimen gauge length, while in others the band initiated at one of the loading platens. Both cases have been observed for this sample. Note that up to the 10% height reduction step applied to sample 1 (Figure 6-15), cells outside the highly deformed bands retain their original shape, suggesting that they deform only elastically. Conversely, it is clear that cells within the bands exhibit permanent plastic deformation at 10% strain. The fact that deformation is observed to be very localised in this and all samples tested in the same way suggests that the cell structure, and its relation to those of neighbouring cells, has a significant effect on where deformation occurs. Such analysis will be described in Section 6.4.3. First of all, investigations into cell wall/edge interactions and deformations at smaller strains will be described, enabling observations to be made on the elastic and plastic regimes.

In order to gain information about the modes of deformation that occur at lower strains, such as those in the cell walls and cell edges, several samples were compressed in smaller steps. Figure 6-16 shows a sequence of tomographic slices through the centre of the *X-Z* plane of Alporas sample 2, compressed up to 6% height reduction. Shown highlighted are equivalent regions of the foam sample indicating how a cell wall common to two adjacent cells has buckled at 6% strain compared to the initial state. At 1% strain this cell wall shows some slight bending, more significant bending at 3% strain, and by 6% strain the wall has buckled. Given the major role of bending in determining the compressive load bearing capacity of cellular solids (Gibson and Ashby, 1997), the susceptibility of such a cell wall to bending, and eventually buckling, might be expected to be quite high as its orientation is only ~15° to the compression axis (Bart-Smith *et al*, 1998). Note that this would also depend on the relative movements of the cell edges at

each end of this wall as the foam is compressed, which are also common to other cells, and thus compatibility of deformation with surrounding cells is needed for large displacements. The length span of a cell wall (related to the size of adjacent cells) is important in bending. The distribution of solid material along the length of a cell wall has been shown to affect the stiffness and strength of cellular foams significantly (Simone and Gibson, 1998a), as have curvature and corrugations in the cell walls (Simone and Gibson, 1998c). Such buckling of cell walls is typical of the deformation modes that occur within a deformation band such as those shown during the compression of sample 1 (Figure 6-15).

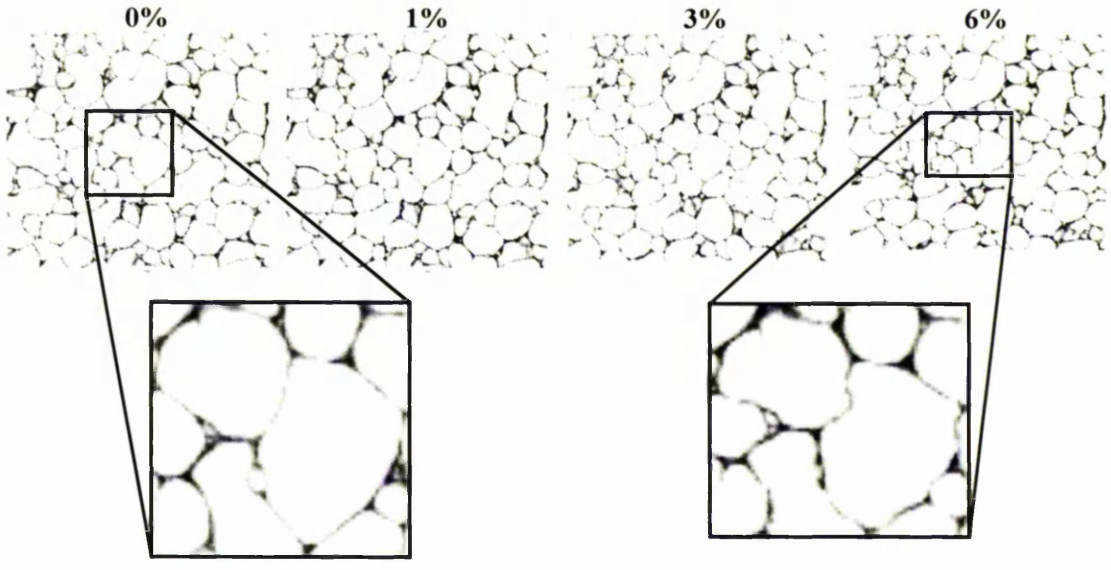

Figure 6-16. Sequence of slices showing the compression of Alporas sample 2 in the *X-Z* plane, at 0, 1, 3 and 6% height reduction. The specimen height and diameter is 25 mm. Highlighted are equivalent regions of the foam at 0 and 6% strain, showing the buckling of a cell wall.

In addition to the yielding of cells by cell wall buckling, further analysis of the displacements of locations within cell walls reveals a particular cell morphology that exhibits permanent deformations within a deformation band. Figure 6-17 illustrates the compression at small strains of ellipsoidal cells with T-shaped cell wall intersections. Equivalent regions of the foam at 0, 6 and 10% strain are highlighted, with the points of interest circled, showing how cell interactions and cell wall displacements result in deformation band formation. This sequence of compression slices is from sample 2, as in Figure 6-16, but now in the *Y-Z* plane. The cell wall intersections are approximately parallel with the load direction, and they are observed to punch into the cells causing large

displacements in the compression direction at the point of intersection. These deformations are appreciable at 6% strain and significant at 10%. Simulations of intersections meeting such cell wall morphologies have shown appreciable curvature of a cell wall to be more susceptible to yielding (Bart-Smith *et al*, 1998). For example, elliptical cells, when oriented with their major axis at 90° to the compression direction, have cell walls that are straighter at the top and bottom of the cell (i.e. straight beams), but significantly curved at the left and right-hand sides. It is clear that an interaction between cells is necessary for deformation to take place within narrow bands and this co-operation is emphasised when cells of the morphologies described are present.

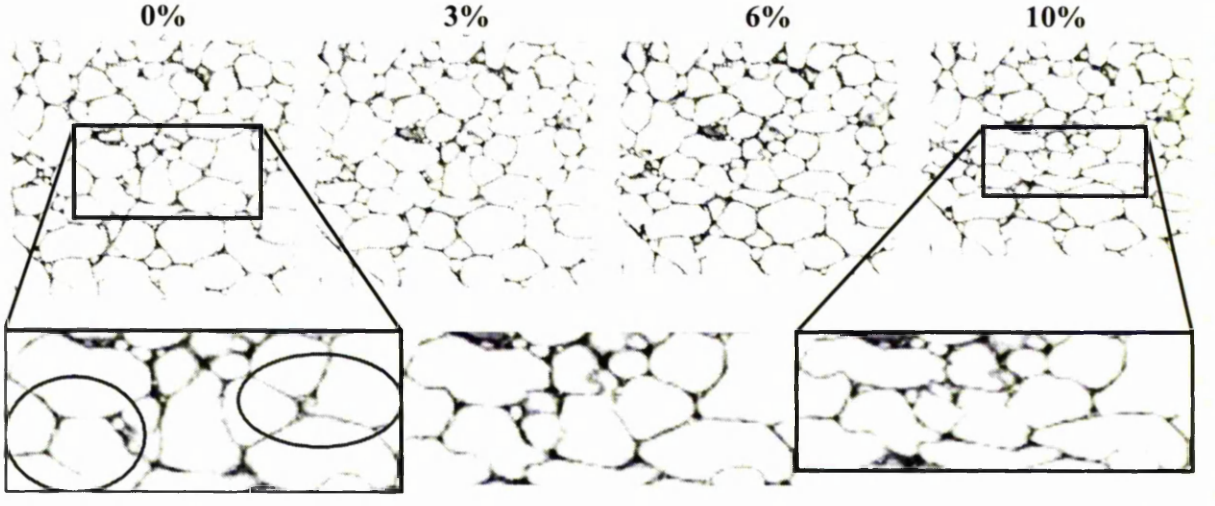

Figure 6-17. Sequence of slices showing the compression of Alporas sample 2 in the *Y-Z* plane, at 0, 3, 6 and 10% height reduction. Shown highlighted are equivalent regions of the foam at 0, 6 and 10% strain, indicating the cell wall displacements leading to deformation band formation.

For an applied strain of ~2%, below the plastic collapse strain measured from the stress-strain response (which was found to be ~4%, see Section 6.4.7), the surface strain mapping results of Bart-Smith *et al.* revealed average strains within the elastic range for regions outside the deformation bands. Within the bands, strain increments exceeded the average by a factor of 10, indicative of cell collapse. The deformation bands defined for these results constituted the very start of cell yielding and collapse, which was found to occur even in the elastic regime due to stress concentrations caused by defects in the cell walls (Andrews *et al*, 1999; Kunze *et al*, 1993; Simone and Gibson, 1998c).

6.4.3. Correlation between 3-D cell volume and deformation bands

Knowing the deformation modes that occur at small levels of applied strain in terms of displacements of the cell walls, the effect of the cell volume distribution on the location of deformation bands was then investigated. Each cell of a 3-D sample dataset scanned at zero applied load was labeled according to the process explained in Section 6.3.3, and mapped to a colour range based on its size. This quantitative value was converted from the number of voxels in the object (cell) to a value in mm^3 according to the voxel size of the tomographic dataset. Viewing any 2-D slice through this cell volume labeled dataset therefore gives the 3-D volume of all cells intersecting that slice and a meaningful observation of the distribution of cell sizes both through a sample and the thickness of the foam panel. Figures 6-18(a) and 6-19(a) show such slices through the *X-Z* and *Y-Z* planes respectively of the cell volume labeled dataset of Alporas sample 1, together with the colourmaps indicating the size range. The value of this approach, compared to the observation of just the 2-D slices as shown to the left in both figures, is observed when considering the circled cells of the volume-labeled colour plot in *X-Z* (Figure 6-18(a)). These cells appear small in the 2-D slice but their volumes are actually two of the largest in the sample. Thus some uncertainty in determining the role of cell size on deformation is removed.

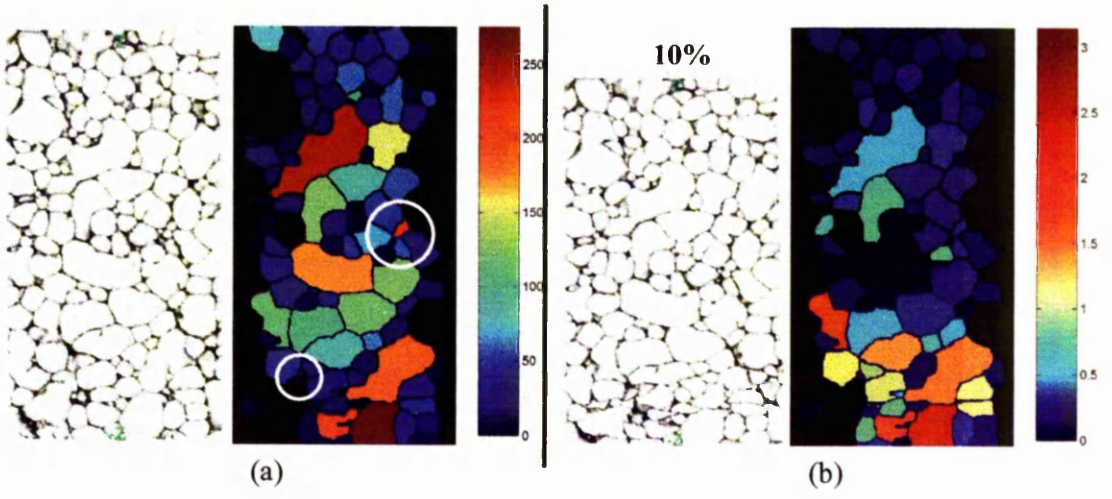

Figure 6-18. Slices in the *X-Z* plane of the dataset of Alporas sample 1, labeled with (a) the cell volume (in mm^3) and (b) the amount a cell had compressed up to 10% applied strain (in mm). The plots are mapped to the respective colour bars shown. The 2-D virtual slices at 0 and 10% applied strain are shown in (a) and (b) respectively.

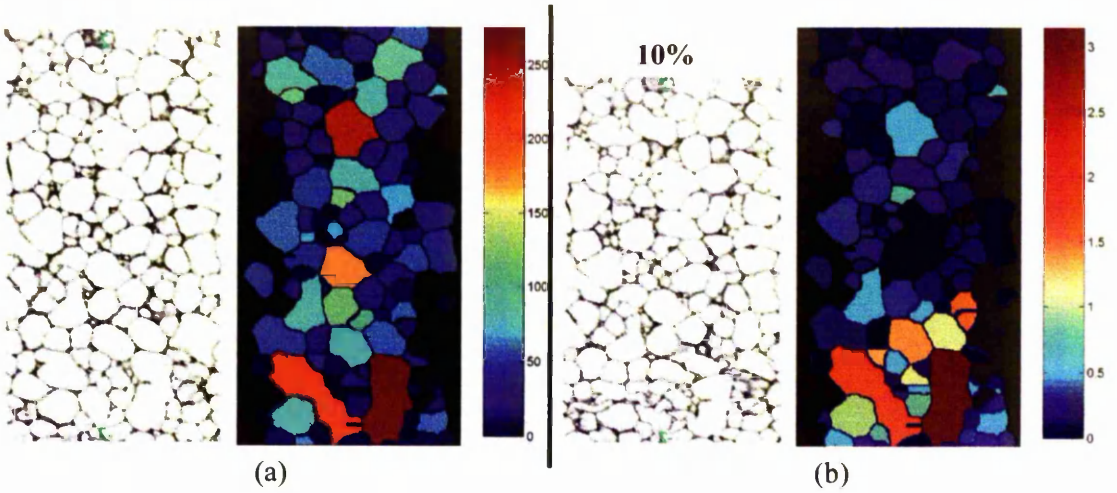

(a) (b)

Figure 6-19. Slices in the *Y-Z* plane of the dataset of Alporas sample 1, labeled with (a) the cell volume (in mm^3) and (b) the amount a cell had compressed up to 10% applied strain (in mm). The plots are mapped to the respective colour bars shown. The 2-D virtual slices at 0 and 10% applied strain are shown in (a) and (b) respectively.

To correlate the information gained from these plots, i.e. the spatial distribution of cell volumes throughout a sample dataset, with the formation of deformation bands, the amount each cell compressed at a particular level of applied sample strain was calculated. 3-D bounding boxes were created around each labeled cell of the datasets at applied strains of up to 20%, and the *Z*-dimensions (compression direction) of the corresponding boxes of equivalent cells were compared in order to obtain a measure of the compression of a cell at a particular level of applied strain. These values were assigned to the corresponding cells of the dataset at no applied load as a colourmap in the same way as for the cell volumes, to illustrate the deformation of cells, and therefore the deformation bands, as colour plots. Figures 6-18(b) and 6-19(b) show the same intersecting *X-Z* and *Y-Z* slices of the corresponding volume labeled plots, showing the amount each cell had compressed (in mm) up to 10% applied sample strain.

The volume-labeled colour plots of Figures 6-18 and 6-19 provide a direct visualisation of the distribution of cell sizes, as opposed to the analysis of just statistical distribution data. A large amount of information can be gained from these volume and deformation plots on the compressive characteristics of the foam material. The sequence of compression slices of Alporas sample 1, shown in Figure 6-15, ultimately reveals four distinct deformation regions at 30% applied sample strain. These are observed as alternate layers, from a crushed zone at the bottom of the sample to an uncrushed zone at the top.

Analysis of the volume-labeled slices through the dataset, with one slice through each plane shown in Figures 6-18(a) and 6-19(a), shows a direct correlation between the position of these two significant deformation bands and the positions of the largest cells that were measured in this sample. A typical histogram for this Alporas material, shown in Figure 6-9, reveals cells at both extremes of the distribution, with a large proportion in the low size band (~45%) and a decreasing number throughout all subsequent bands up to a high of over 200 mm^3 (average ~20 mm^3). Regarding first of all the deformation band at the bottom of sample 1, three cells over 180 mm^3 are present in this region. The immediate surrounding distribution shows cell sizes below 100 mm^3 and mostly below 50 mm^3. Primarily, the compression of these large cells is observed to result in the deformation band at this position, shown by the compression labeled plots (Figures 6-18(b) and 6-19(b)) at an applied sample strain of 10%. The largest cells are observed to compress the most in terms of displacement in the *Z*-direction (1.5-2.5 mm), but the immediate surrounding cells also show significant compression (~1 mm). This suggests that the smaller cells surrounding a large cell have a significant effect on the local deformation. The compression displacements are compared to an overall sample displacement of 5 mm, which is accounted for by the fact that all cells in the sample, outside this deformation band, experience a small displacement of up to 0.2 mm. It must be noted that measurements made using tomographic datasets, such as these displacements and the cell volume measurements, are limited by the pixel resolution, which in this case was ~100 μm. This is sufficient for measuring such displacements in the deformation bands, but would ideally be an order of magnitude smaller for measurements outside the bands. Also, note that a large cell at the bottom of the sample has been cut by the bottom surface and is not a complete cell. Such cells were not considered during the calculation of sample cell statistics, such as in Section 6.4.1, but, especially for one so large, do represent voids that have an effect on neighbouring cells, as is observed in the compression sequence of Figure 6-15. Regarding the deformation band just above halfway of the sample height observed at 30% strain (Figure 6-15), an interesting point to note is that up to an applied strain of 10% the compression of cells within this band is only very small. Slightly higher displacements are calculated than for cells outside the two deformation bands, at up to ~0.7 mm, but this is only for a few cells, significantly the largest of the region. This band, therefore, forms after the one at the bottom of the sample, confirming that the Alporas material shows a progression of cell collapse during loading. There are two large cells with sizes greater than 200 mm^3 at the position where this deformation band has formed,

again showing the position of the largest cells to be very important in the compressive behaviour of the material.

To illustrate the compression of cells in the deformation bands in a more meaningful way, these displacements were converted to a measure of the strain experienced by each individual cell relative to the original *Z*-dimension of its equivalent bounding box. Figure 6-20(a) and (b) shows the same *X*-*Z* slice as in Figure 6-18 but labeled and mapped to a colour range based on these calculated strain values, for an applied strain of 10% and 20% respectively. Figure 6-21(a) and (b) shows the equivalent strain-labeled maps of the same slice through the *Y*-*Z* plane as in Figure 6-19. The corresponding volume-labeled slices and the 2-D virtual slices are shown again for comparison purposes. These strain-labeled colourmaps reveal that up to an applied sample strain of 10% height reduction, the cells at the bottom of the sample have experienced strains of ~0.25. The strains experienced by cells in the second deformation band at this stage, of which the largest showed a discernible displacement compared to those surrounding, are observed to be no more significant than those of cells outside the two deformation bands (a strain of ~0.05).

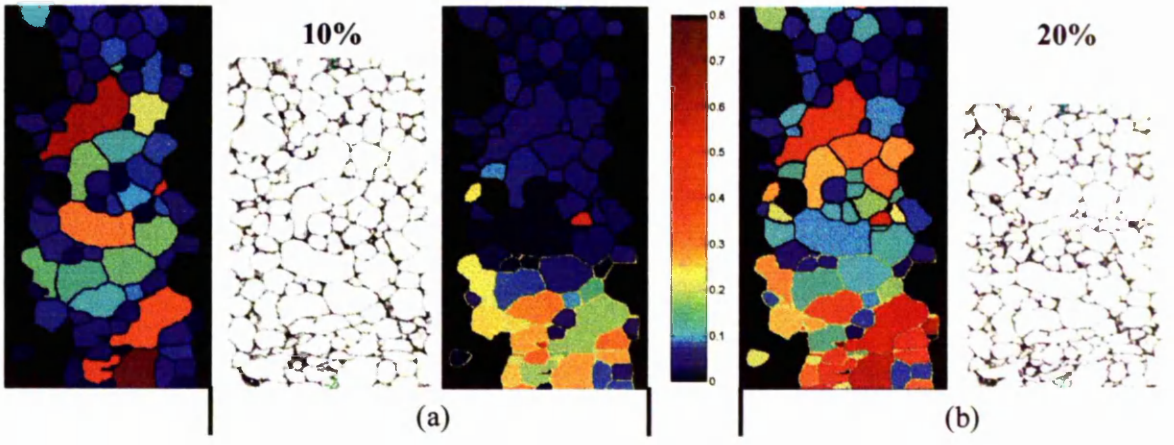

Figure 6-20. Colour plots of the equivalent slice through the *X*-*Z* plane of the dataset of Alporas sample 1, labeled with the strain each cell experiences at an applied sample strain of (a) 10% and (b) 20% height reduction, and mapped to the colour bar shown. The corresponding 2-D virtual slices of the microstructure, and the equivalent volume-labeled slice (left, the colour map for which is in Figure 6-18) are also shown.

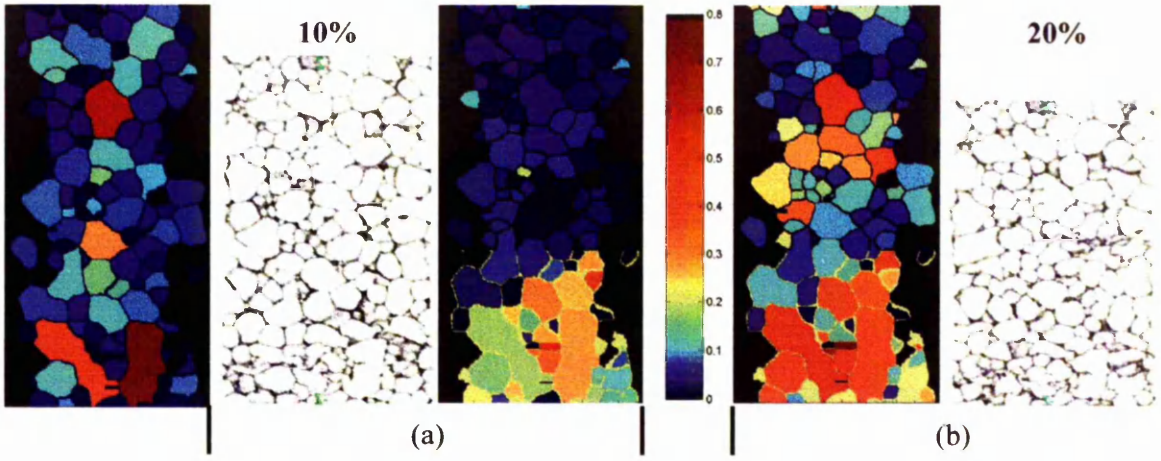

Figure 6-21. Colour plots of the equivalent slice through the *Y-Z* plane of the dataset of Alporas sample 1, labeled with the strain each cell experiences at an applied sample strain of (a) 10% and (b) 20% height reduction, and mapped to the colour bar shown. The corresponding 2-D virtual slices of the microstructure, and the equivalent volume-labeled slice (left, the colour map for which is in Figure 6-19) are also shown.

Increasing the applied sample strain to 20% height reduction (Figures 6-20(b) and 6-21(b)) results in an increase in the strains experienced by the cells in the bottom deformation band, to ~0.3-0.4, and even slightly higher for the largest cells. Also at this stage, the upper deformation band is clearly revealed and comprises cells experiencing strains of ~0.25-0.3. Note that the largest cell in this region is observed to experience a strain of 0.4, suggesting it to be responsible for deformation in this region, which is in agreement with behaviour already observed. The interaction between neighbouring cells of different sizes during compressive straining is illustated by this upper deformation band. The cells directly beneath the largest, ranging from ~50-100 mm^3 in volume, have experienced significant strains (0.25-0.3), while that of the adjacent cell (150 mm^3) has not exceeded 0.1. This again illustrates the significance of the smaller cells (below 100 mm^3) surrounding a large cell, and depending on location and interaction, it is not necessarily the larger cells that experience the largest deformations. It is interesting to note that the significant formation of the upper deformation band observed between the 10% and 20% compression stages gives rise to reduced compressive displacements of cells in the lower band between the same steps (increase in strains of 0.05-0.15), relative to the 0 to 10% step (a strain of 0.25). This illustrates the progression of cell collapse that occurs in this foam material and the higher local strains induced to create a band of deformed cells compared to expanding such a band once significant collapse has been defined. The very simple

representation that has been used here to discuss quantitatively the strains experienced by cells in deformation bands is given support by the surface strain mapping results of Bart-Smith *et al.* (Bart-Smith *et al*, 1998). Although only analysing small deformations in the elastic regime up to an applied sample strain of ~2%, compared to deformations in the collapse regime as analysed here, compressive strains of up to 0.05 in regions where deformation bands formed were measured. These strains were found to be indicative of cell collapse even before the plastic collapse strain was reached, presumably due to defects in the cell walls.

It is necessary to note a few limitations of the analysis used to calculate strains shown in the colour plots. Firstly, as mentioned above, the measured strains are strongly dependent on the pixel resolution of the dataset (~100 μm). For strain calculations of individual cells, this results in an error of 0.03 based on an average cell diameter of 3 mm. It must also be noted that, due to the significant compression of the lower deformation band at 20% applied sample strain, some difficulty was encountered in mapping these cells during the labeling routine, resulting in the merging of cells. A detailed analysis of all slices through the colour plots revealed this to be applicable only to a very few cells, and did not affect the general observations.

The relationships between cell size distribution and the formation of deformation bands were also observed for a more global sample of cells. With the aim of confirming the observations above for such a case, samples of size 50 mm^3 were tested in the same way. Figure 6-22(a) and (b) shows virtual 2-D slices through the *X-Z* and *Y-Z* planes respectively of Alporas sample 3, for applied sample strains of up to 30% height reduction. These are related to three volume-labeled slices through each of the two planes of the dataset, shown in Figure 6-23(a) and (b) respectively. Note that the pixel resolution of this dataset was 180 μm. One might expect such a significant difference in the resolution to affect quantitative measurements such as cell volume, relative to values observed for cylindrical samples used in the characterisation analysis of Section 6.4.1 and the cell volume/compressive deformation correlation above. The average volume of cells within this larger cube sample was calculated to be ~28 mm^3, compared to ~25 mm^3 for the cylindrical samples. It is difficult to extract anything definitive from this difference in terms of the effect of measurement resolution. The larger cube sample contains several significantly larger cells than the largest that were measured in the sample for which the distribution of cell volumes is shown in Figure 6-9. This could equally be due to the fact that, as a consequence of the two sample sizes, these significantly larger cells were cut

during sample preparation of the smaller cylindrical samples. The overall distributions are very similar, as shown in Figure 6-24 which compares the cell volume distributions of Alporas samples 1 (cylinder) and 3 (cube). A notable difference is that the distribution of the cube sample has an extended tail up to a cell size of ~700 mm^3, labeled as 'more' in Figure 6-24, for a few significantly larger cells. The significant extension of the tail towards larger cell volumes for the cube sample is revealed by the higher skewness and kurtosis values, indicated for both samples in Figure 6-24. Also, the higher kurtosis shows that a much higher proportion of the distribution is concentrated around the mean value.

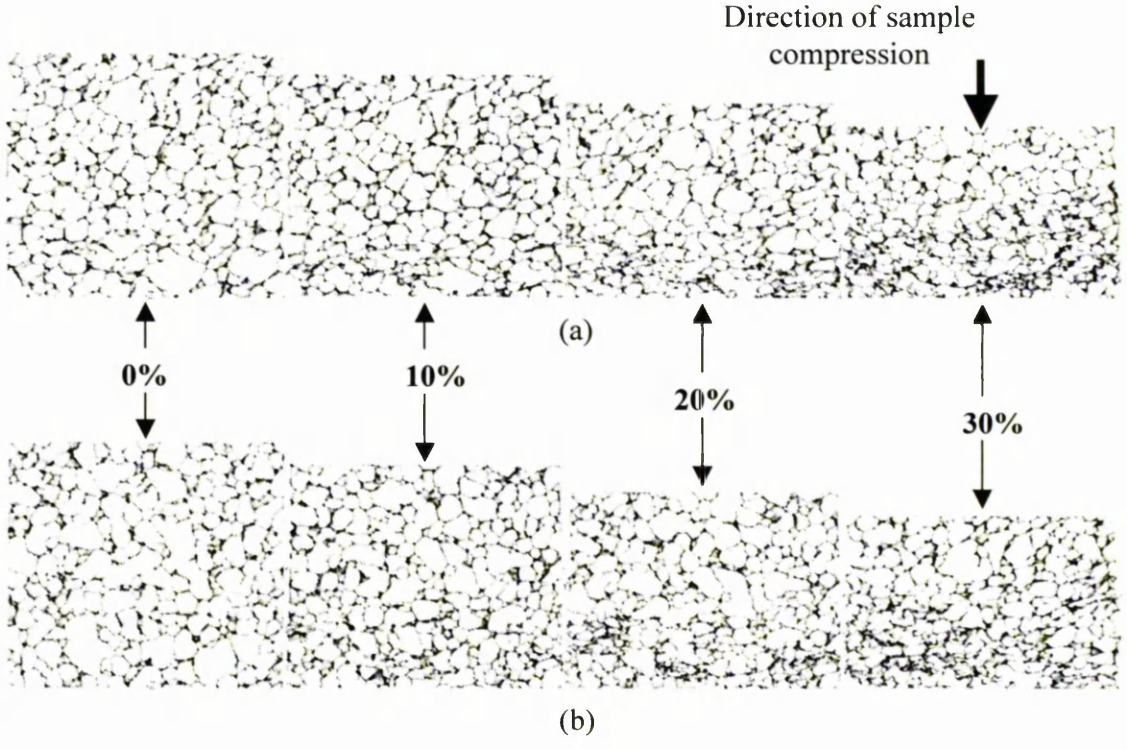

Figure 6-22. Sequence of slices through the centre of the respective tomographic volumes, showing the compression of Alporas sample 3 at 0, 10, 20 and 30% height reduction. Slices in both the (a) *X-Z* and (b) *Y-Z* planes are shown. The specimen is a cube of dimensions 50 mm^3. The height of the sample represents the thickness of the foam panel.

Olurin *et al.* looked at the effect of measurement and analysis parameters, including the measurement resolution, on different geometric structural parameters such as cell volume (Olurin *et al*, 2002). They concluded that the effect of resolution on the quantitative structural parameters is small as long as the feature size is considerably larger than the measurement resolution. A resolution dependence of ± 5% up to an investigated resolution

of 40 μm was observed for measurements of cell size. For two samples scanned using a slightly higher pixel resolution of 80 μm, an average cell volume of ~23 mm^3 was measured, which does suggest a small effect of the resolution on the measured cell volume, relative to that for a 100 μm pixel resolution. Note that the measured cell diameter of ~3 mm (see Section 6.4.1), which is in agreement with destructive, optical serial sectioning measurements, is at least 15 times the size of the lowest pixel resolution used.

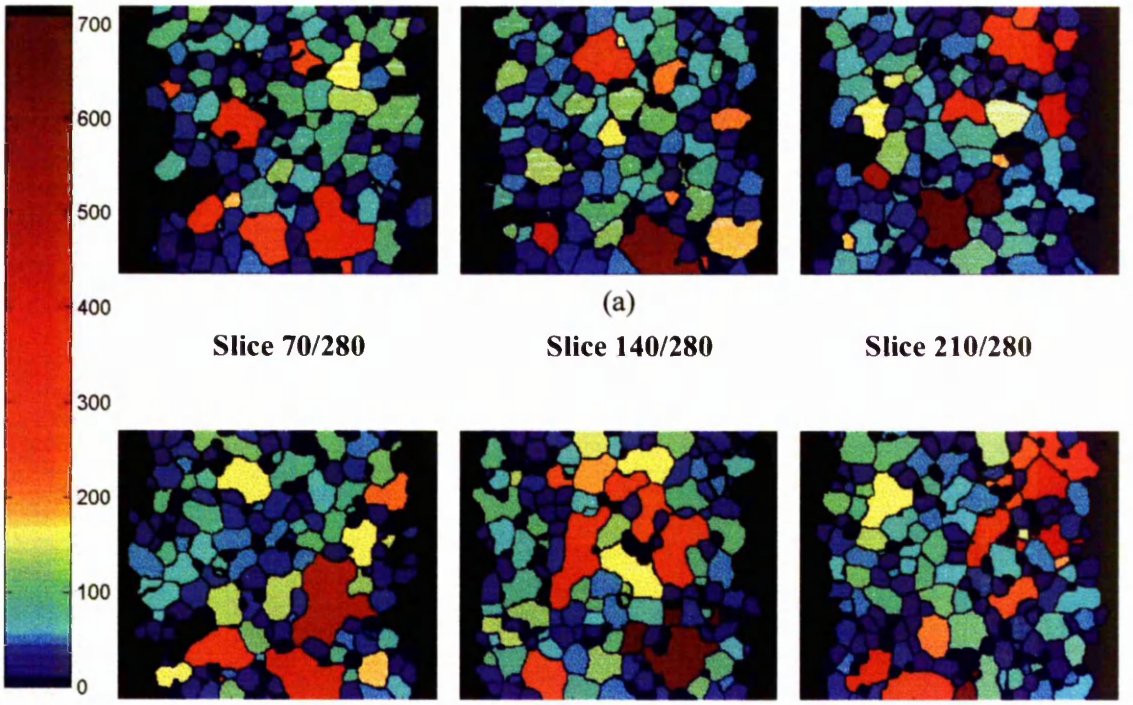

Figure 6-23. Volume-labeled (in mm^3) slices through the (a) *X-Z* and (b) *Y-Z* planes of the dataset of Alporas sample 3, coloured in accordance with the colour scale shown. Three slices in each plane are shown, with the slice positions indicated.

It is clear from Figure 6-22, and from the analysis of all such slices through the sample, that up to an applied strain of 30% height reduction the sample deforms significantly in the bottom half. Deformation is observed to start at the very bottom and progress upwards as the applied strain is increased. In agreement with the behaviour observed above, this is in accordance with the largest cells mostly positioned at the bottom of the sample, as illustrated in Figure 6-23. Bart-Smith *et al*, via inspection of 2-D tomographic images, suggested no obvious preference for larger cells to be more susceptible to permanent deformations (Bart-Smith *et al*, 1998). The advantage of 3-D

quantitative characterisation used here is thus shown in that large cells are observed to undergo preferential permanent deformations, even at applied strains of ~6% used in the test of Bart-Smith *et al.* As touched upon during the analysis of Alporas sample 1, a common characteristic found from the samples that were tested is that an isolated large cell will be crushed significantly, but not when surrounded by moderately sized (50-150 mm^3) cells. A greater influence of the larger cells on localised deformation is observed when they are isolated, i.e. cells of size ~200 mm^3 and greater surrounded by cells of size ~50 mm^3 and below. Figure 6-23 shows the larger cells at the bottom of the sample to be much more isolated than those above. This is observed particularly for slices 140 and 210 in the *Y-Z* plane (Figure 6-23(b)), where aggregates of cells of size greater than 150 mm^3 are present at the top of the sample. It is also interesting to note that in aggregates of large (cells >150 mm^3) and moderately (50-150 mm^3) sized cells it was not necessarily the largest ones that were observed to crush the most. Again, the distribution of cell sizes surrounding a large cell is observed to be very important.

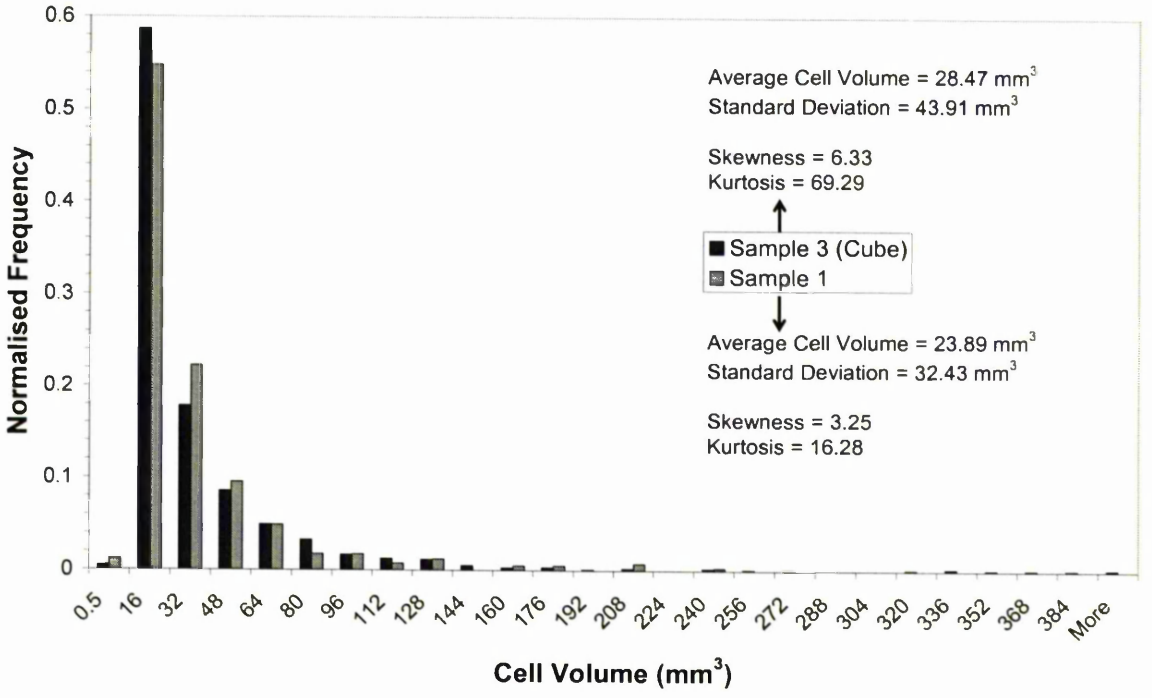

Figure 6-24. Histogram comparing the cell volume distributions in Alporas samples 1 (cylindrical sample of dimensions 25 mm diameter and 50 mm height) and 3 (cube sample of dimensions 50 mm cubed). Normalised frequency values are plotted, based on the number of cells in each sample (407 and 1992 cells respectively). The statistical values of the mean, standard deviation, skewness and kurtosis are shown for each.

Several 2-D simulations of closed cell structures have been performed using finite element analysis (Silva and Gibson, 1997; Silva *et al*, 1995) to predict the effect of the microstructure on the Young's modulus and plastic collapse strength of the compressive stress-strain curve. In these studies, periodic honeycomb structures were compared to random, non-periodic Voronoi honeycombs for a range of relative densities (0.05-0.3). The results showed that the Young's modulus is only slightly affected by the variation in microstructure, while the non-periodic Voronoi structure results in a 30% decrease in the peak stress compared to a periodic structure. The removal of four adjacent cell walls, effectively creating a cell five times the size of those surrounding, caused a localised band of cell collapse to pass through the defect site and reduced the strength. This is analogous to and in agreement with the effect observed above regarding isolated cells of large volume and the fact that localisation of deformation is observed in such regions. A generalisation of this approach was applied by Fazekas *et al*, who created cellular structures from sphere packing, allowing cell size distributions to be accounted for (Fazekas *et al*, 2002). Their results showed that, for the case of idealised bimodal microstructures, the prefactors in the scaling laws for the Young's modulus (E^* / E_s) and plastic collapse strength (σ^* / σ_{ys}), C_E and C_σ respectively (see Section 5.3.2), depended on the area fraction of large cells. For a relative density of 0.1, the strength was found to be reduced by ~20% for an area fraction of large cells of 0.5. Although a mono-modal distribution is observed for the Alporas material (Figures 6-9 and 6-24), there is a dispersion of larger cells throughout the material that have been observed to have a significant effect on its collapse.

6.4.4. Comparison of different behavioural modes

In Section 6.4.3, uniform compressive deformation behaviour was illustrated. Uniform distributions of localised deformation were observed at positions of isolated large cells or aggregates of larger and moderately sized cells. Departures from this behaviour were observed in other samples tested. This resulted in differences in the macroscopic deformation mode of the samples during compression. Using the analysis developed in Section 6.4.3, informed predictions can be made of how a sample will deform. For example, Figure 6-25(a) shows two volume-labeled slices both in the *X-Z* plane of the dataset of Alporas sample 4. This had a sample height to diameter ratio of 1:1 (as opposed to 2:1 for sample 1) so that the localisation of deformation could be observed at an improved measurement resolution (~80 μm). The two slices through the *X-Z* plane are separated by about 4 mm and illustrate the presence of moderate to large cells (>60 mm^3)

separated by about 4 mm and illustrate the presence of moderate to large cells (>60 mm^3) through this plane, situated primarily bottom left of the sample and, to a lesser extent, top right. It can be predicted that significant deformation will occur at the positions of these aggregates of cells. This is indeed the case, as illustrated by the equivalent strain-labeled slices at applied strains of 5 and 10%, shown in Figure 6-25(b) and (c) respectively. At an applied strain of 5%, most of the cells have experienced a small compressive strain of ~0.05-0.1, which is in agreement with the results of Bart-Smith *et al.* (compressive strain of 0.05 at an applied strain of 2%) measured from surface strain mapping of the Alporas material (Bart-Smith *et al*, 1998). It is difficult to identify any significant deformation bands at this stage, but the cluster of cells bottom left of the sample is observed to experience larger strains when compared to any other region. At 10% applied strain (Figure 6-25(c), significant bands are now observed to have formed corresponding to the aggregates of larger cells as predicted, experiencing strains between ~0.15-0.2 with a maximum of 0.3. Note that, if the small cells (size <40 mm^3) that have been cut at the top and bottom of the sample are discounted, the largest cells have not experienced the highest strains, in agreement with predictions of the behaviour of larger cells within aggregates of moderately sized cells.

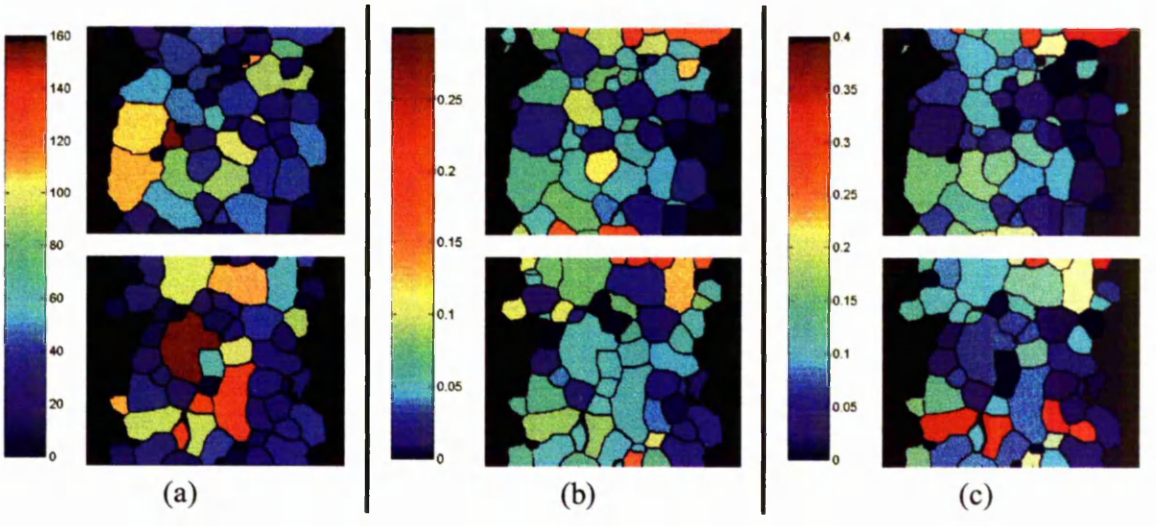

Figure 6-25. Colour plots of two slices in the *X-Z* plane of the dataset of Alporas sample 4, labeled with (a) the volume of each cell, and (b),(c) the strain each cell experienced at an applied sample strain of (b) 5% and (c) 10% height reduction. The plots are coloured in accordance with the colour scales shown for each case.

While sample 1 was observed to have deformed primarily in two significant bands across the whole sample width, the sequence of 2-D tomographic slices of sample 4, shown in Figure 6-26, confirms that, by 30% height reduction, this sample had deformed significantly in opposite corners of the sample (circled). This was predicted from Figure 6-25. As a consequence of the distribution of cell sizes, no clearly defined single deformation band was developed, but multiple minor deformation bands which, in this case, combine through cells in the centre of the sample width resulting in uniform crushing. The local distribution of cell volumes can have a pronounced effect on the macroscopic deformation mode.

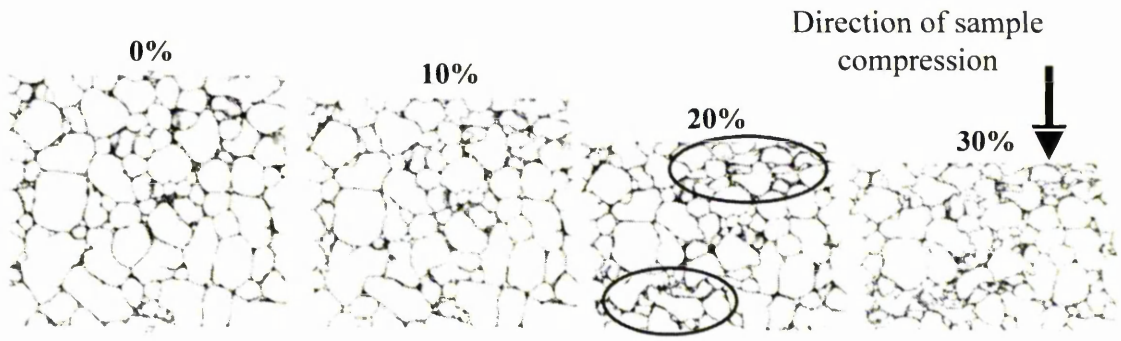

Figure 6-26. Sequence of 2-D virtual slices in the *X-Z* plane of the respective tomographic volumes, showing the compression of Alporas sample 4 at 0, 10, 20 and 30% height reduction. The two regions of significant deformation are circled at 20%. The specimen diameter is 25 mm and the original height 25 mm.

Figure 6-27(a) and (b) illustrates volume-labeled plots in the *X-Z* and *Y-Z* planes respectively of Alporas sample 5. Figure 6-27(a) shows three large cells in the bottom half of the sample, with a very large cell of size ~360 mm^3 on the left and two cells each of half this size on the right-hand side, one on top of the other. One can now predict that, due to the isolated nature of the largest cell, which is up to 8 times the size of its nearest neighbours, the sample will deform significantly at this position compared to the right-hand side where the two other large cells are adjacent to each other. Again, the sequence of virtual 2-D slices during compression of the sample, shown for each plane in Figure 6-27(a) and (b) respectively, confirms this. This is in agreement with the modelling observations of Silva and Gibson (Silva and Gibson, 1997; see Section 5.4.2). It is clear from observations in the *X-Z* plane that the large cell crushes significantly, resulting in the extreme anisotropic buckling of the sample structure in this plane, i.e. the sample walls do not remain straight or parallel to the compression direction. In the *Y-Z* plane, the largest

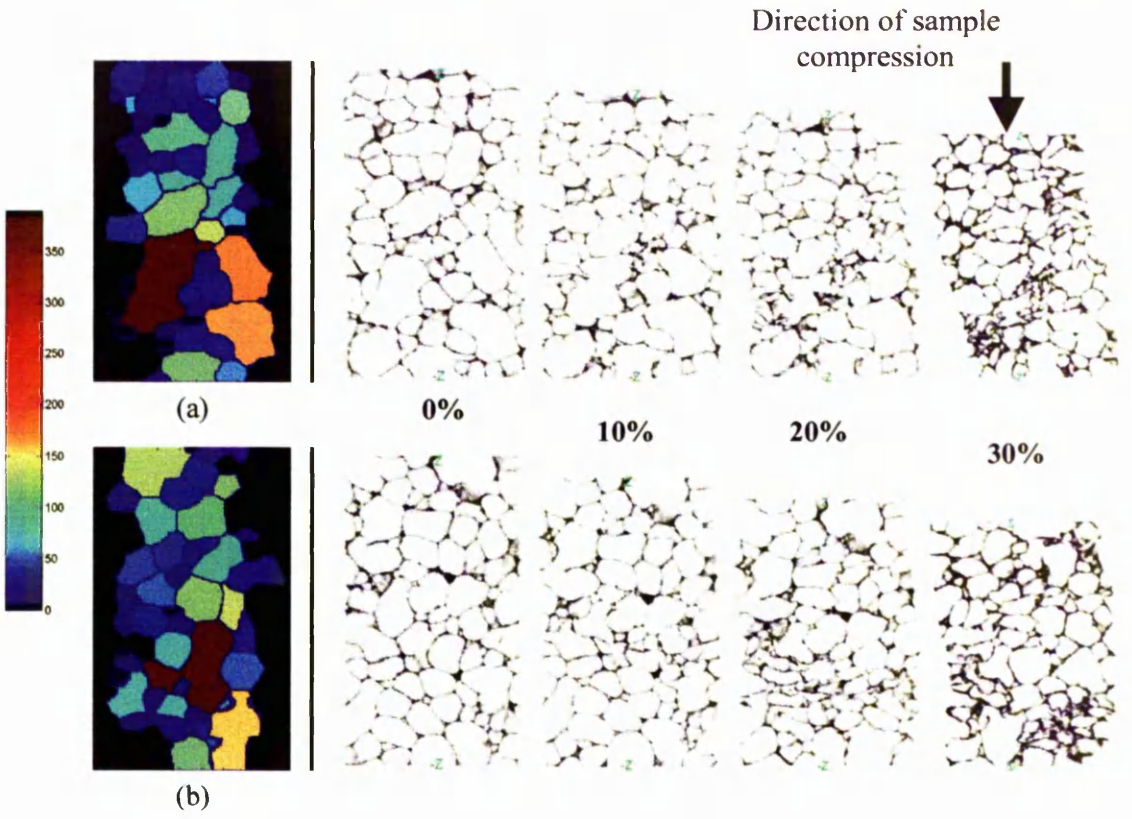

Figure 6-27. Cell volume-labeled slices (in mm^3) in the (a) *X-Z* and (b) *Y-Z* plane of the dataset of Alporas sample 5, coloured in accordance with the colour scale shown, help to illustrate why the sample deformed in a buckled manner. Sequences of virtual 2-D slices showing the compression of the sample, at 0, 10, 20 and 30% height reduction, are also shown for each plane. The specimen diameter is 20 mm and the original height is 30 mm.

The deformation behaviour observed on compression of the samples illustrates the role of the larger cells on the position of deformation bands and indicates the importance of the distribution of cells surrounding a large cell. The deformation of large cube samples (Figures 6-22 and 6-23) has been carried out to gain an understanding of the effect of the distribution of cell volumes on a more global sample of cells. With such large samples it is difficult to analyse the deformation modes that occur locally. Smaller samples, of dimensional aspect ratios of both 2:1 and 1:1, were thus compressed, while still showing similar cell volume distributions as the cube samples and complying with the minimum specimen-to-cell size ratio of seven suggested by Andrews *et al.* (Andrews *et al*, 2001). The macroscopic behaviour of the structure of samples during compression has also shown either uniform deformation behaviour in bands perpendicular to the compression direction, or has exhibited anisotropic buckling, as shown in Figure 6-27. While one might expect

either uniform deformation behaviour in bands perpendicular to the compression direction, or has exhibited anisotropic buckling, as shown in Figure 6-27. While one might expect the dimensional aspect ratio of the sample to have a more significant effect on its macroscopic deformation behaviour, the sample distortion during compression was observed in samples of both geometries.

In order to try to rationalise these differences, statistical techniques have been used to develop descriptors for the behaviour in terms of the cell volume distribution. Because of the experimentally observed dependence on the distribution of cell volumes, the moments of such distributions, such as the skewness and kurtosis, have been investigated to see if there is a correlation between these properties and deformation behaviour.

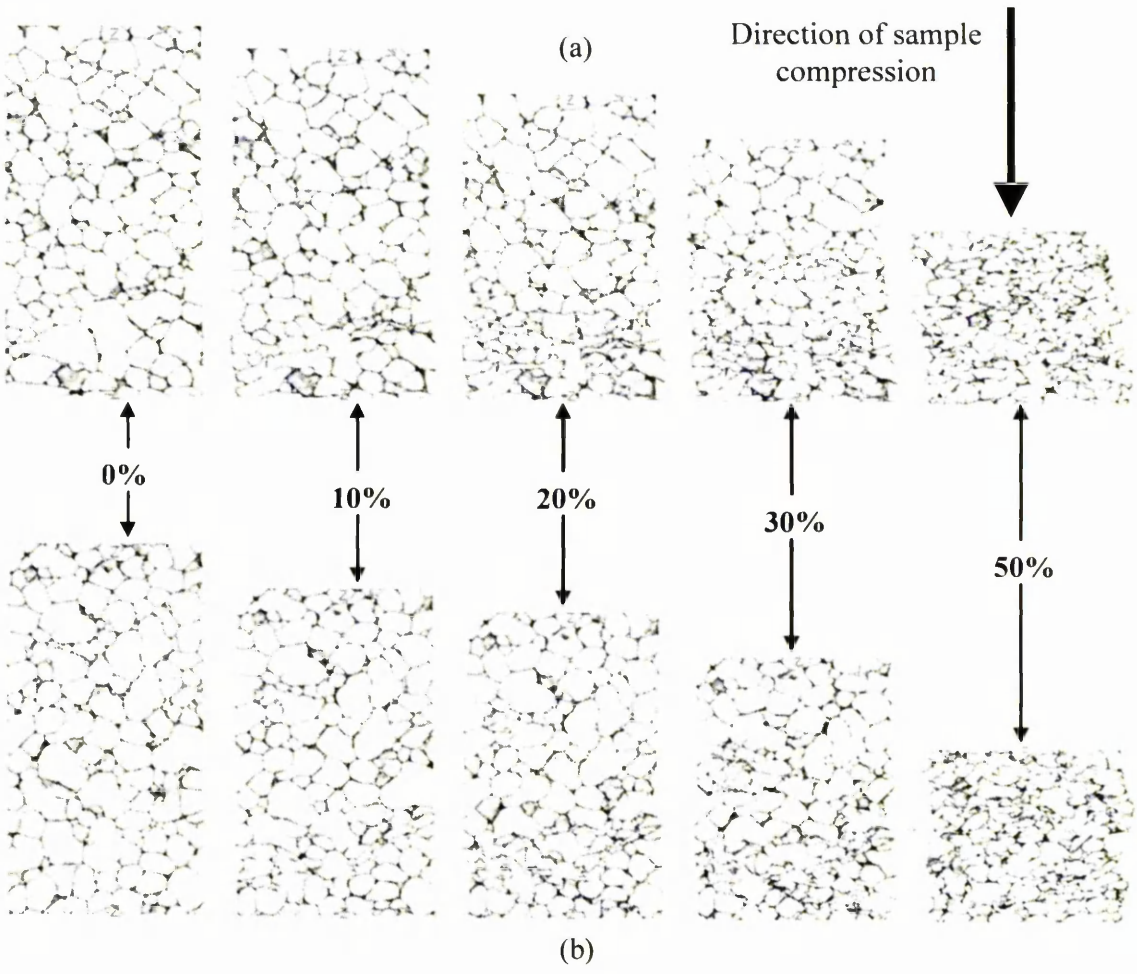

Figure 6-28. Sequence of slices of the compression of Alporas sample 6 at 0, 10, 20, 30 and 50% height reduction. Slices in the (a) *X*-*Z* and (b) *Y*-*Z* planes are shown. The specimen diameter is 25 mm and the original height 50 mm. The sample shows slightly slanted walls in *X*-*Z* at 50% height reduction but no anisotropic buckling.

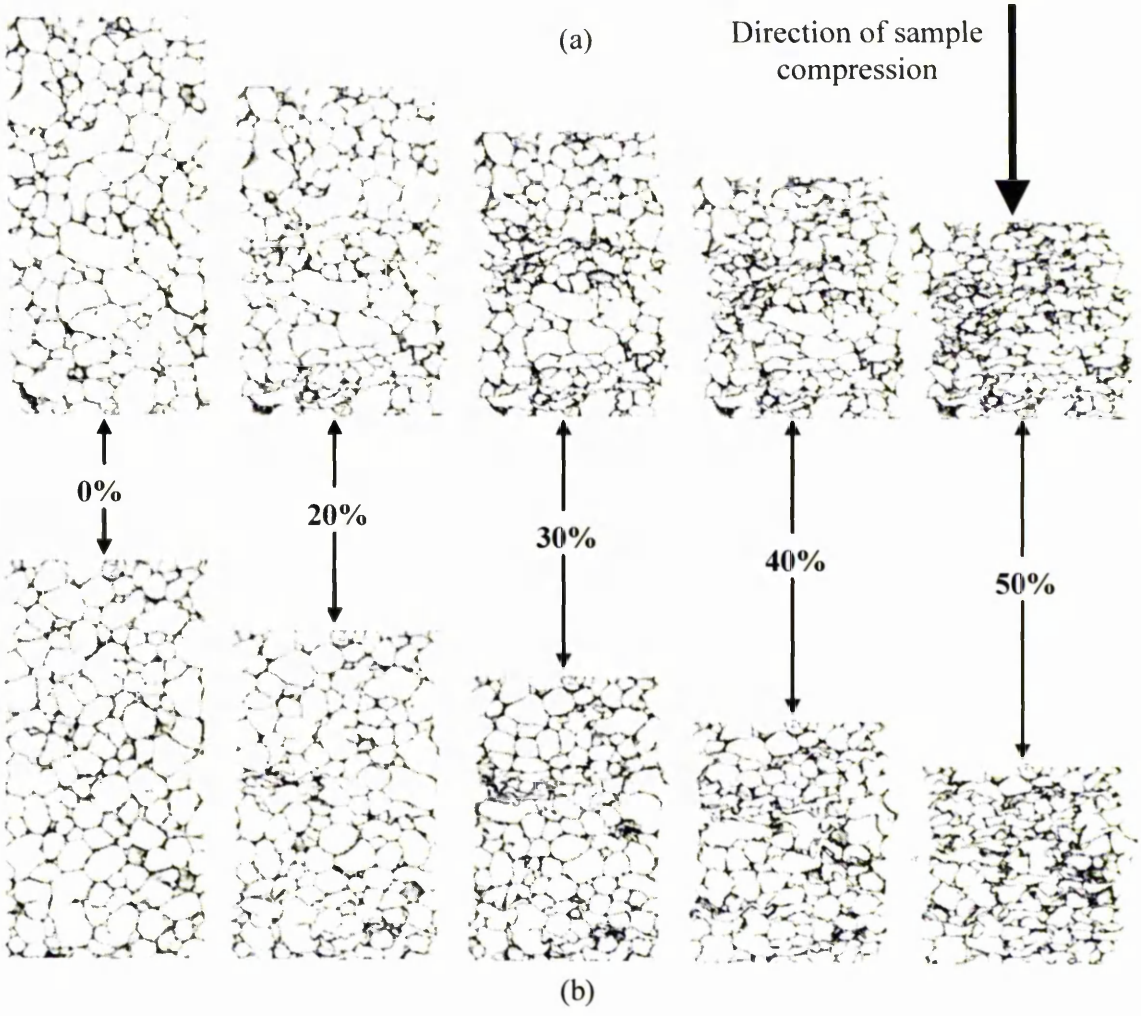

Figure 6-29. Sequence of slices of the compression of Alporas sample 1 at 0, 20, 30, 40 and 50% height reduction. Slices in the (a) *X-Z* and (b) *Y-Z* planes are shown. The specimen diameter is 25 mm and the original height 50 mm. Anisotropic buckling of the sample structure is observed.

To illustrate this, Figures 6-28 and 6-29 show sequences of virtual 2-D slices illustrating the compression of, respectively, Alporas sample 6 and sample 1 up to 50% height reduction. While the two samples have the same geometry, they deform quite differently. Sample 6 (Figure 6-28) shows a uniform distribution of deformation regions in both planes and thus compresses quite uniformly up to 50% height reduction. Sample 1 has buckled at the position of the upper deformation band at the 30-40% height reduction stage (Figure 6-29). The cell volume distributions for these two samples are shown in Figure 6-30, normalised by the number of cells (~400 in both cases) for comparison purposes, and Table

6-5 shows statistical data extracted from the two distributions. Small differences in the skewness and kurtosis values indicate that the distribution of sample 1 is extended to slightly larger volumes (higher skewness), as illustrated in the histogram of Figure 6-30, but also that it is distributed more about the mean value (higher kurtosis). Sample 1 is therefore suggested to contain fewer and therefore isolated larger cells, compared to sample 6 which is indicated to have a higher proportion of larger cells, i.e. aggregates of large and moderately sized cells. It is these isolated larger cells that have been observed to cause significant deformation (see Section 6.4.3). This suggests that the anisotropic buckling behaviour of the sample structure observed during the compression of sample 1 is promoted by a distribution with a larger skewness and kurtosis. Sample 5 also fits this model (Table 6-5). This sample, as shown in Figure 6-27, had a large buckling or distortion of its structure and has a much larger skewness and kurtosis.

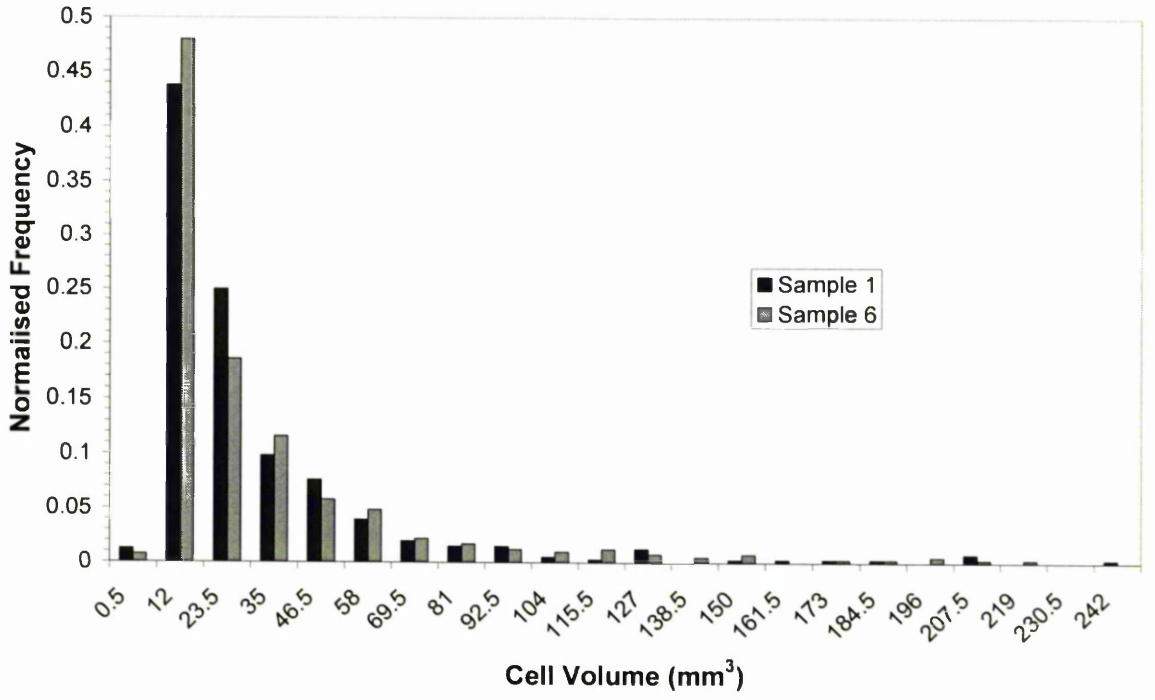

Figure 6-30. Histogram of the cell volume distributions of Alporas samples 1 and 6, each containing ~400 cells. The distributions are fairly similar, but that of sample 1 is extended, and the statistical data of Table 6-5 reveals small differences.

Table 6-5. Statistical data extracted from the 3-D cell volume distributions of samples 1 and 6. The data for sample 5 are also shown.

	Average (mm^3)	St. Dev. (mm^3)	Skewness	Kurtosis
Sample 1	23.89	32.43	3.25	16.28
Sample 6	25.23	34.04	2.67	11.53
Sample 5	22.55	44.88	4.35	31.36

A similar trend was observed with samples of dimensional aspect ratios of 1:1. Figure 6-31(a) and (b) shows a sequence of slices illustrating the compression of Alporas sample 7 in the *X-Z* and *Y-Z* planes respectively.

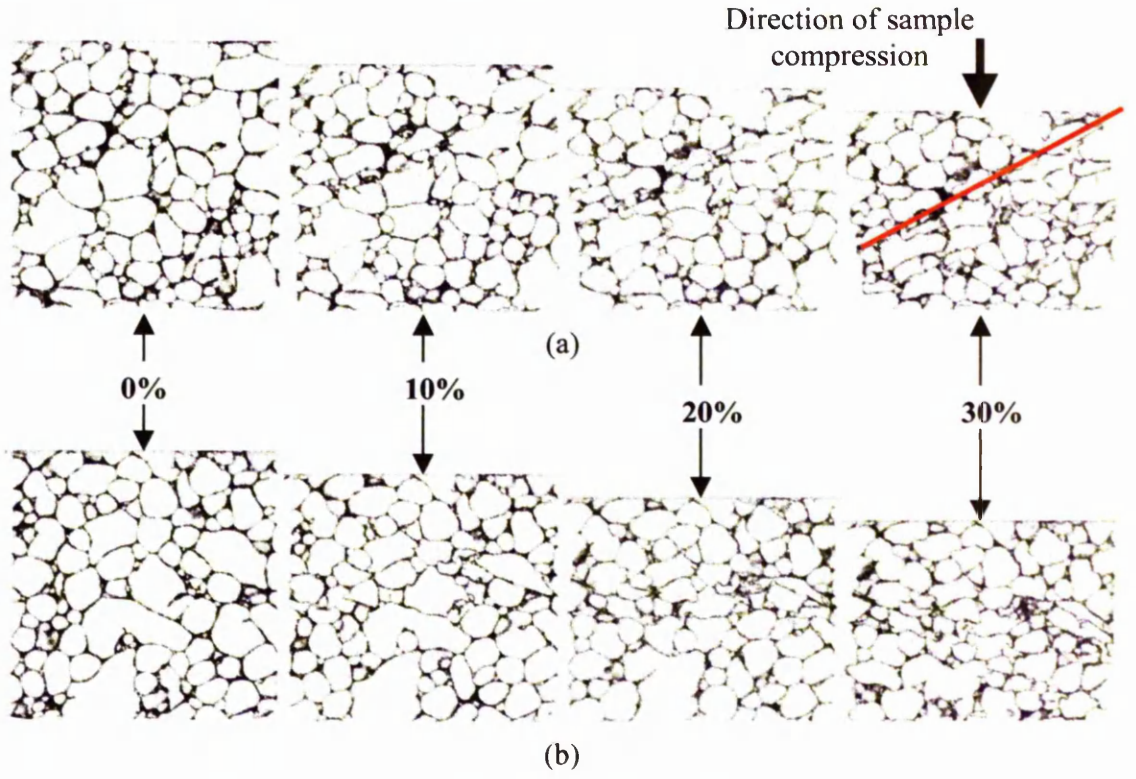

Figure 6-31. Sequence of slices of the compression of Alporas sample 7 at 0, 10, 20 and 30% height reduction. Slices through the (a) *X-Z* and (b) *Y-Z* planes are shown. The specimen diameter is 25 mm and the original height 25 mm. At 30% height reduction the sample shows an irregular deformation band in the *X-Z* plane, resulting in the slight buckling of the structure.

In comparing the compression of this sample with that of sample 4 (Figure 6-26) up to 30% height reduction, it is observed that sample 4 develops slanted walls and deforms in

two clear bands in opposite corners, but ultimately deformation is observed to be quite uniform. Sample 7, however, deforms in a band at an angle to the direction perpendicular to the compression direction, as indicated, and the structure of the sample has buckled slightly at the position where the band meets the left-hand wall. Again, comparing the cell volume distributions (Figure 6-32) and the extracted statistical data (Table 6-6) for the two samples suggests that a larger skewness and kurtosis gives rise to a non-uniform, buckling mode of deformation, in agreement with the observations above. Sample 4 is observed to have more cells through the larger volumes of the distribution, while sample 7 shows fewer, isolated, large cells observed to cause significant crushing and, ultimately, buckling of the sample. It is recognised that the observed anisotropic buckling behaviour is more pronounced in samples of larger aspect ratio, as would be expected. But such behaviour is observed in both specimen geometries.

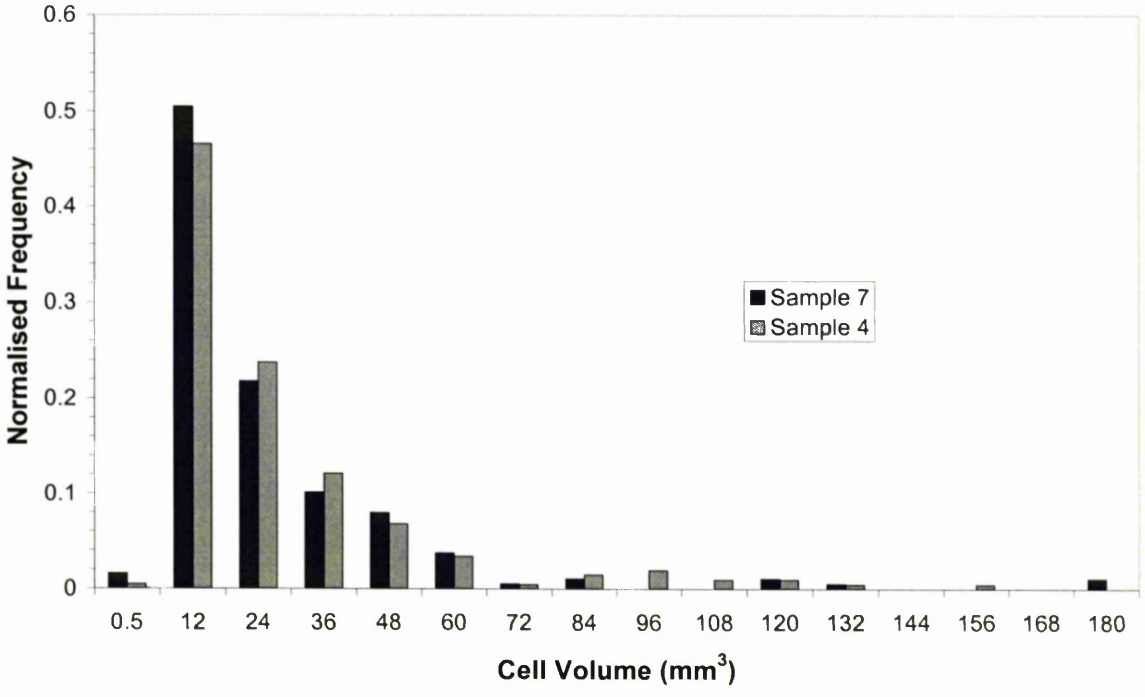

Figure 6-32. Histogram of the cell volume distributions of Alporas samples 4 and 7, each containing ~200 cells. The distribution of sample 7 is extended over that of sample 4, which contains more cells through the larger volumes.

Table 6-6. Statistical data extracted from the 3-D cell volume distributions of samples 4 and 7.

	Average (mm^3)	St. Dev. (mm^3)	Skewness	Kurtosis
Sample 4	21.28	25.12	2.59	10.45
Sample 7	20.03	25.92	4.12	25.93

A direct correlation is observed between the mode of deformation and the extracted moments of the cell volume distributions. Statistical analysis has been found to predict quite robustly the type of behaviour that might be observed, based on the 20 or so samples that were tested. Of course, this hypothesis is suitable only for predicting behavioural modes of the sample sizes that have been studied. But, in terms of cell deformations, this behaviour can be assumed to be analogous to that observed locally in larger samples.

6.4.5. Effect of the 3-D density distribution on deformation

The distribution of cell volumes has been used to describe and to model the compressive deformation behaviour of the Alporas foam material. The tomographic datasets were also used to calculate a measure of the 3-D density distribution of metal within the foam structure, providing a measure of the heterogeneity of the material and a method of characterising the effect of metal distribution on the compressive behaviour. From the scaling laws of Gibson and Ashby (see Section 5.3.2), it is noted that the relative density is the most important parameter when correlating the mechanical properties of the foam to those of the bulk material (Gibson and Ashby, 1997). This implies that, while observations of the cell volume distribution provide explicit information of the role of cell size on local deformation, 3-D density distribution maps can provide direct predictions of the mechanical behaviour. Using the density distribution obtained from CT investigations, Kriszt *et al.* have also studied the relationship between inhomogeneous density distributions and deformation (Kriszt *et al*, 2000).

3-D density distribution maps, calculated as the volume fraction of metal distributed throughout a sample, were obtained by averaging the grey level values, representing the metal, over a certain surrounding volume of each voxel of the reconstructed 3-D raw tomographic dataset. This gave a measure of the local distribution (or volume fraction) of metal relative to the size of the averaging volume (which includes empty pores) at the location of the central voxel of the averaging volume. The size of the

averaging volume that was used for the calculations was chosen for each foam material under analysis using the following expression:

$$R.D. = \frac{\frac{4}{3}\pi r^3}{a^3} \tag{6-5}$$

where $R.D.$ is the relative density of the foam material (~0.1 for Alporas), r is the radius of the equivalent sphere representing a pore/cell of the material (taken as 1.55 from Section 6.4.1), and a is the dimension of the cube representing the averaging volume. Using this expression, a volume of 50 pixels^3 was used for averaging the Alporas material. The expression in (6-5) considers the volume of the equivalent sphere representing a cell/pore relative to the volume of the averaging box via the density of the foam material under consideration. This was found to give a sensible value to use for the dimensions of this averaging volume as it is based on the structure of the foam material under consideration. Note that the colourmaps shown in the analysis that follows are based on the volume fraction of metal distributed throughout the samples.

Figure 6-33(b) shows the distribution of the volume fraction of metal for three slices in the X-Z plane of the 3-D dataset, and is compared to virtual 2-D slices through the foam at 0 and 30% height reduction in Figure 6-33(a). The solid lines divide the sample into four regions representing the crushed and uncrushed zones that are visible in the sample at 30% height reduction. It is clear from the metal distribution through the dataset of the sample, and represented by the three slices, that zone 1 at the top has the highest density and thus little deformation is observed here. Zone 2 shows a significantly compressed band of cells, and this is due to a large region of low density, visible in slice 172, which is coupled with regions of high density above and also below, analogous to the behaviour observed for a very large cell surrounded by lots of small cells. Note that a possible cause of the buckling of this sample, observed in Figure 6-29, is the presence of some very low density regions on the left of the sample in zone 2 of slice 258. The density distribution observed in slice 172 also shows a low density in zone 3 and yet a compression band has not formed here, presumably due to it being evident in fewer slices through the entire distribution of the dataset, compared to that of zone 2. The absence of a compression band here can also be explained by the fact that the zone shown by slice 172 contains a collection of lowest density regions in the middle of the sample width, but with high-density regions either side, providing strength. Analysis of Sections 6.4.3 and 6.4.4

reveals that an aggregate of moderately sized cells, shown by a collection of lowest density regions in zone 3 of slice 172, tended not to be crushed significantly.

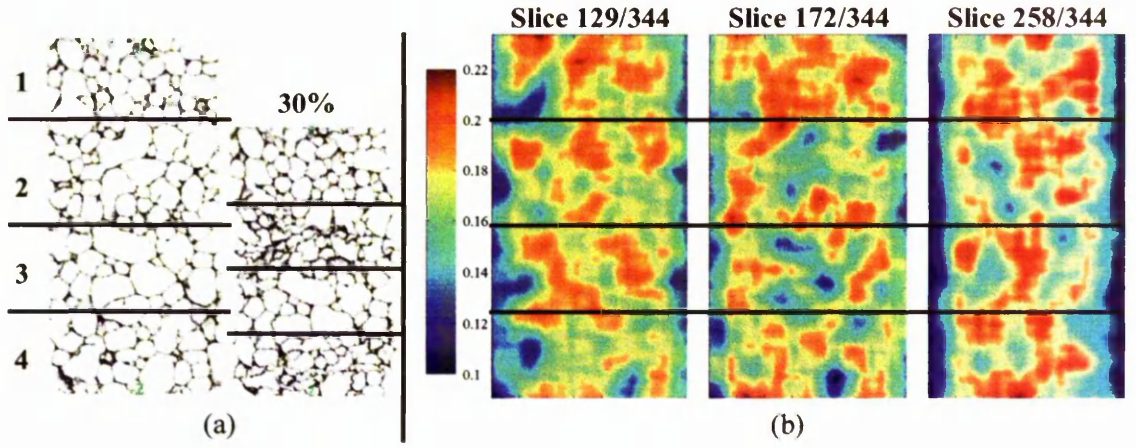

Figure 6-33. (a) Comparing the compression of Alporas sample 1 up to 30% height reduction, with (b) density distribution maps showing the initial volume fraction of metal of three slices in the *X-Z* plane of the sample dataset, as indicated, based on an averaging box size of 50 pixels^3 (5.75 mm^3). The solid lines through the images divide the sample into 4 regions in terms of its compressive behaviour.

Small local heterogeneities in the distribution of metal have been observed to have an effect on the local deformation behaviour of Alporas sample 1. Distribution maps such as those of Figure 6-33 can be used to describe directly where deformation bands will be concentrated, through the correlation of low-density regions with those of weakest strength, as described by Gibson and Ashby. In order to observe the distribution of metal over a more global region of this material, and its effect on the compressive deformation behaviour of such a region, Figure 6-34(b) shows slices in the *X-Z* and *Y-Z* planes of the dataset of Alporas sample 3. The compression of this sample was shown in Figure 6-22 and is shown again at zero and 30% applied sample strain in Figure 6-34(a). Figure 6-23 showed a higher proportion of larger cells in the bottom half of this sample and the volume fraction distribution confirms the presence of larger regions of lower density in the bottom of the sample, illustrated most clearly in slice 74 in the *Y-Z* plane. As a result, deformation is concentrated in this region, revealing that the deformation behaviour is dictated by the weakest, low density regions as described by the relationships of Gibson and Ashby (Gibson and Ashby, 1997). The density distribution maps do indicate lower density regions in the top half of the foam, such as in slice 140 of the *Y-Z* plane, but these are

smaller and aggregated together, analogous to the effect of aggregates of large and moderately sized cells as opposed to isolated large cells.

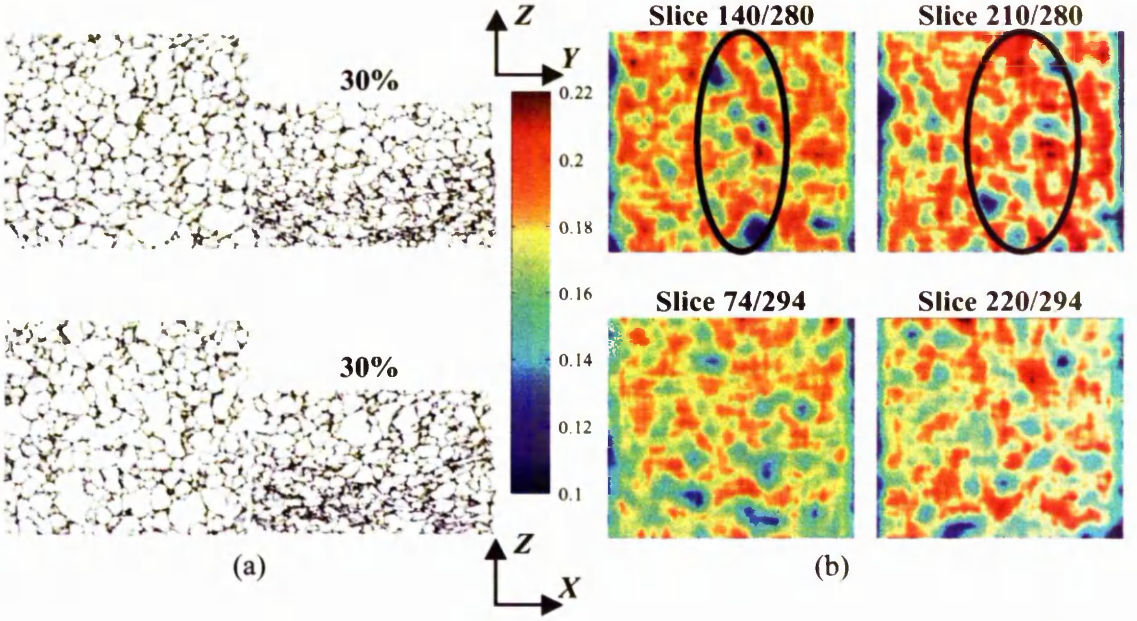

Figure 6-34. (a) Comparing the compression of Alporas sample 3 up to 30% height reduction, with (b) density distribution maps showing the initial volume fraction of metal of two slices in both the *X*-*Z* and *Y*-*Z* planes of the sample dataset, as indicated, based on an averaging box size of 20 pixels^3 (3.7 mm^3).

It is of interest also to observe, and thus compare with that of Figure 6-34, the distribution of metal in an alternative direction in order to make inferences of the effect of the density distribution on the likely mechanical compressive stress-strain response in different directions. Accordingly, Figure 6-35 shows slices through the calculated metal distribution dataset of a second cube sample, for which the characteristic compression axis (or vertical axis) is represented by the *Y*-direction of the original foamed metal sheet of Figure 6-1. A comparison between the two samples will centre on the metal distribution relative to the vertical principal axes as viewed in Figures 6-34 and 6-35, i.e. the *Z*- and *Y*-directions respectively. As a characteristic of this Alporas material, the metal distribution was observed to be quite uniform throughout the three orthogonal planes of the foam panel, as illustrated by the two cube samples. However, small differences in the distribution, particularly the low-density regions, with respect to the two principal axes were observed. Bands of adjacent low density regions were observed to be primarily

oriented perpendicular to the *Y*-direction of the material, and were observed across the width of the sample as indicated by the highlighted regions in Figure 6-35. In contrast, such regions in the sample for which the principal axis is the *Z*-direction (Figure 6-34(b)) were observed to run parallel to this direction, with high-density regions either side down the entire sample height, shown in the slices through the *Y-Z* plane. Another observation centred on the relative distribution of metal throughout the two directions. There were more low-density regions in the *Y* planes than the *Z* planes. This is also shown by slices through the metal distribution of a cylindrical sample representing the *Y*-direction (Figure 6-35), and analogous to this, a sample that was observed to contain a slightly higher distribution of larger cells. Such differences in the distribution of metal in the different directions would be expected to have an influence on the stress-strain response, analysis of which is shown in Section 6.4.7.

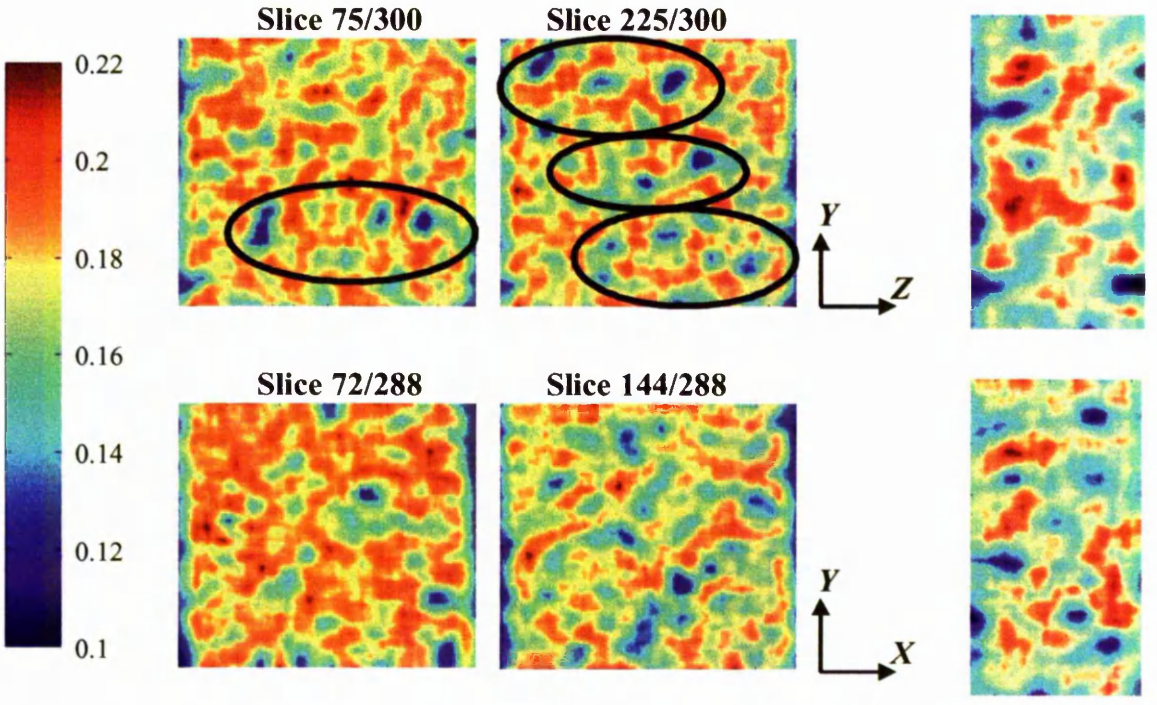

Figure 6-35. Density distribution maps showing the initial volume fraction of metal for two slices in both the *X-Y* and *Z-Y* planes of the sample dataset of a second cube sample, based on an averaging box size of 20 pixels^3 (3.7 mm^3). A slice in each of the same planes of the dataset of a cylindrical sample is also shown on the right-hand side.

Kriszt *et al.* studied the influence of density distribution on the compressive behaviour of Alporas foam (Kriszt *et al*, 2000), and found it to have a uniform density distribution

characterised by a standard deviation of ~2% relative to the average density. This was also found to lead to a more uniform deformation of the foam, with significant bands only being developed at high strain, as observed in the analysis of Section 6.4.3. See Section 6.4.7 for the relation of density distribution to mechanical stress-strain response.

Mapping the local 3-D distribution of metal throughout a sample can help to explain and ultimately provide predictions of the local deformation of the foam material, and shows quite clearly how local regions of heterogeneity of this foam material are linked to this. Using the density distribution as a quantitative description of this heterogeneity may provide a more direct correlation with the mechanical compressive behaviour as it is based on an average over a local volume, rather than observation of individual cell volumes. As the mechanical properties of foams are strongly dependent on their density, it may provide a more direct link to models of behaviour.

6.4.6. Compression of Cymat material

The compressive deformation behaviour of the Alporas foam material has been studied in detail. Generally, a fairly uniform mode of deformation occurs throughout the material due to a relatively homogeneous cell size and shape distribution in the plane parallel to the thickness of the foam panel and the principal direction of testing. Deviations from this uniform mode have been observed due to localised heterogeneity of isolated large cells and the non-uniform distribution of metal.

The structure of the other foam material that was studied, Cymat, showed a much more significant gradient in the cell structure through the thickness of the panel (Figure 6-8(b)) and two clear sub-regions were discernible. A sequence of slices illustrating the effect of this gradient in cell structure on the compression of a Cymat sample in steps of 10% height reduction, in the *X-Z* and *Y-Z* planes of the dataset, is shown in Figure 6-36(a) and (b) respectively. By 30% height reduction, it is clear that deformation has been concentrated significantly in the upper sub-region of the foam panel. Cell collapse was observed to initiate in a localised band at the bottom of this upper sub-region, which then progressed outwards as the band of initially collapsing cells approached densification. In most cases, the band was observed to be perpendicular to the compression direction, but in some cases was also observed to follow the contour of the lower sub-region, suggesting the density of the solid metal in this lower region to be an important factor.

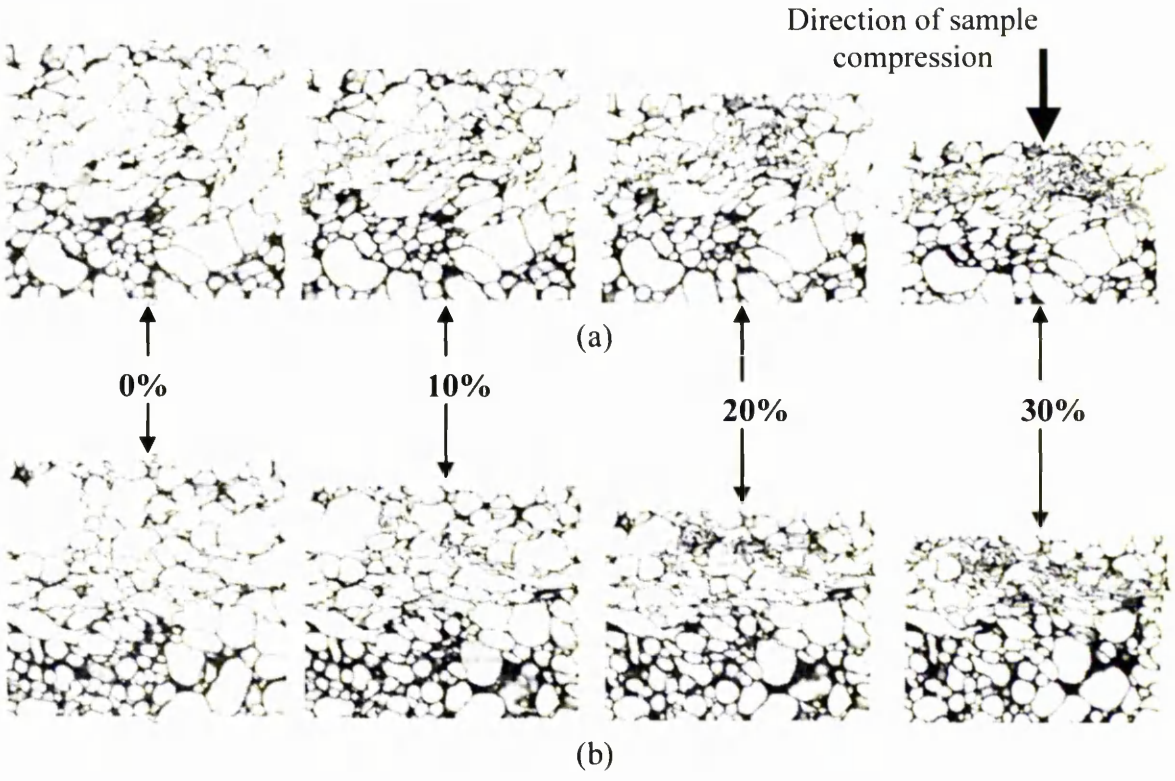

Figure 6-36. Sequence of slices through the centre of the tomographic volumes, showing the compression of a Cymat sample at 0, 10, 20 and 30% height reduction. Slices in both the (a) *X-Z* and (b) *Y-Z* planes are shown. The specimen diameter is 25 mm and the original height 25 mm.

Before describing the effect of the 3-D structure distribution, i.e. distributions of cell volume and density in the two distinct sub-regions, on the compressive behaviour observed in Figure 6-36, it is important to observe the deformation modes occurring in the cell walls at smaller applied strains. Figure 6-37 illustrates such modes occurring on the scale of individual cells and in cell walls at the early stages of formation of the deformation band. The cell wall deformation modes are similar to those of the Alporas material, but an important point to note about the cell walls in the Cymat foam, primarily in this upper sub-region, is that there were a significant number that were already bent before any load had been applied. This presumably occurred during handling of the foam in its liquid state and during solidification. For this reason, in contrast to the Alporas material, significant buckling of the cell walls has occurred by 6% height reduction, as illustrated in the highlighted region of the sample in Figure 6-37. The effect of T-shaped cell wall intersections is also illustrated. Significant punching of the cell walls into other cells

occurs, as seen in the cell at the bottom of the highlighted region. The amount of solid metal in the cell walls in the lower sub-region of the foam is visibly much higher and so there is little, if any, bending or buckling, even at the larger applied strains.

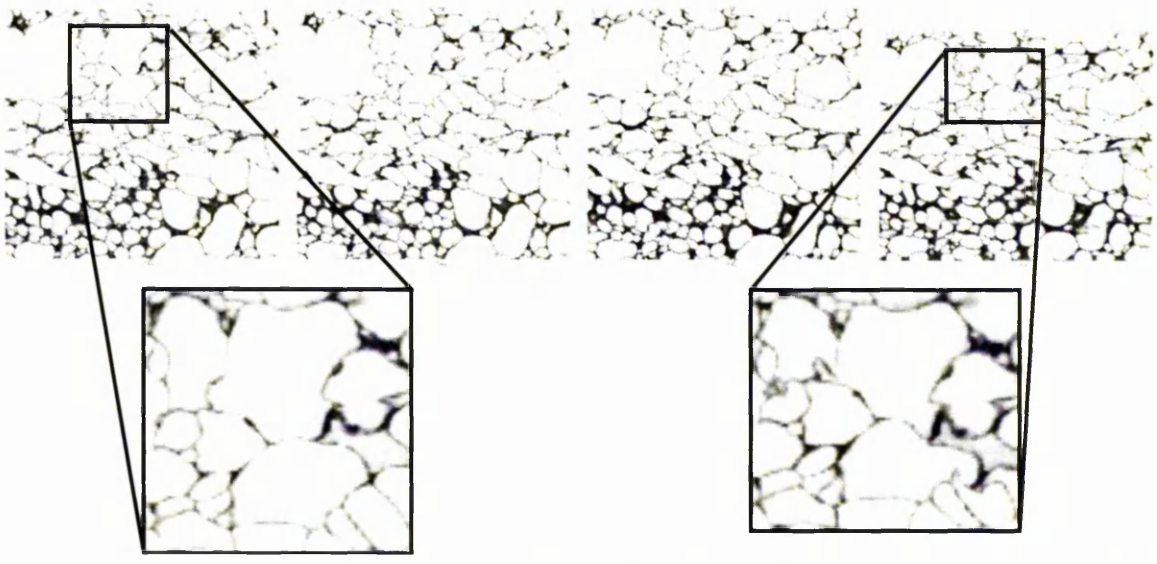

Figure 6-37. Sequence of slices of the compression of the Cymat sample of Figure 6-36, at 0, 1, 3 and 6% height reduction. The specimen height and diameter are 25 mm. Highlighted are equivalent regions of the foam at 0 and 6% height reduction, indicating a small region that goes on to form part of the highly deformed region.

Microstructural characterisation analysis of the Cymat material representing the entire thickness of the foam panel revealed a high proportion of cells (~80%) with volumes in the modal range of the distribution (Figure 6-12), and thus a very high kurtosis as the distribution is mostly concentrated around the mean. The distribution also shows isolated cells down in the tail of the larger volume ranges, resulting in a high skewness compared to the Alporas material. The visible structure and compressive behaviour of the Cymat material observed in Figures 6-36 and 6-37 suggests a significant difference in the cell volume distributions of each sub-region. Figure 6-38 is a histogram comparing the cell volume distributions in the upper and lower sub-regions of the foam sample. Note that, as for the full distribution, only complete cells were considered in each of the two sub-regions, and so cells in the labeled volume that intersected the boundary line between the two were discounted. The statistical data extracted from the two distributions, shown in Table 6-7, do show differences in the cell volumes. The mean values are similar, albeit higher for the upper sub-region, due to the large number of small cells overall, but the

standard deviation is also larger for the upper sub-region indicating larger cells within. The histogram of Figure 6-38 illustrates this best, showing a few cells down in the tail of the distribution (11 cells greater than ~40 mm^3 compared to 2 in the lower region). The statistical values therefore show a higher skewness and kurtosis (both ~1.5 times) for the lower sub-region due to the extended tail for the two larger cells but with the distribution being concentrated largely around the mean.

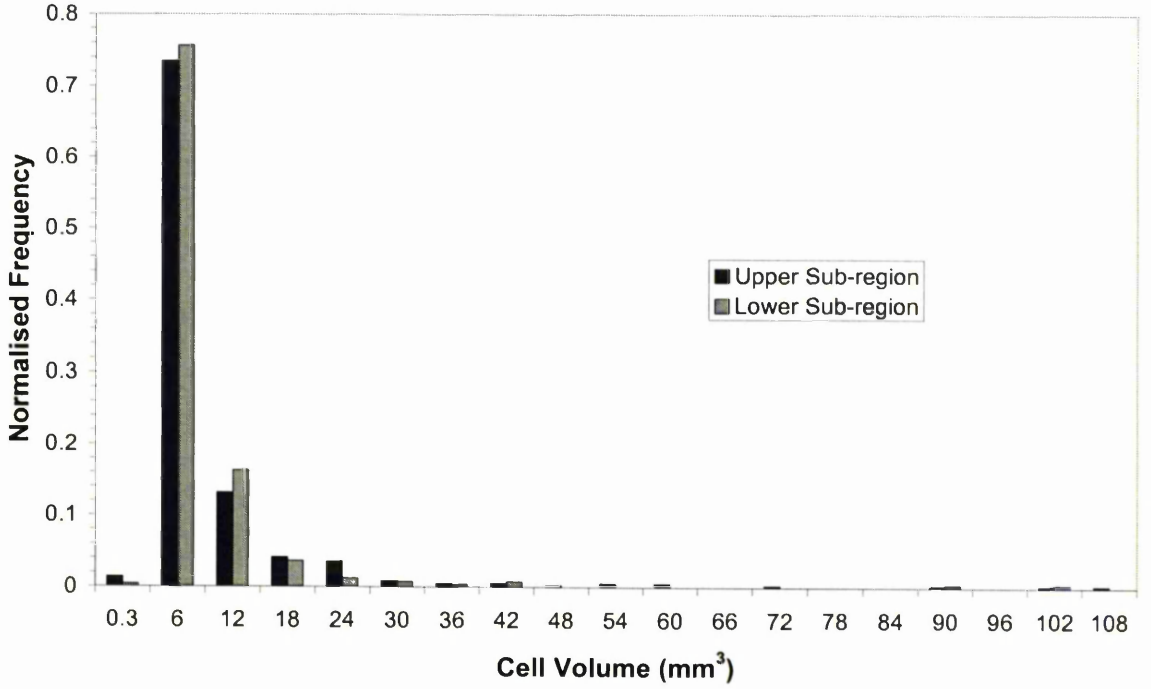

Figure 6-38. Histogram of the cell volume distributions of the upper and lower sub-regions of the Cymat sample, the compression sequence for which is illustrated in Figures 6-36 and 6-37. The distributions have been normalised with the number of cells in the corresponding region. The total population distribution is shown in Figure 6-12.

Table 6-7. Statistical data extracted from the 3-D cell volume distributions of the upper and lower sub-regions of the Cymat sample (Figure 6-38) for which the total population distribution is shown in Figure 6-12.

	Average (mm^3)	St. Dev. (mm^3)	Skewness	Kurtosis
Upper	5.39	11.25	5.32	37.23
Lower	4.56	8.44	7.00	65.76

The compressive behaviour of the Cymat material can be related, in part, to the cell structure characterisation through its thickness. The higher distribution of larger cells in the upper sub-region of the sample has resulted in the initiation of deformation in this region, which continued until densification. Note that this behaviour was typical of that observed in all Cymat samples tested. 2-D serial sectioning of Alcan (Cymat) foam samples carried out by Simone and Gibson revealed the cell size to increase from the bottom of the sample to the top (Simone and Gibson, 1998b). They also observed the cell orientation to rotate from nearly horizontal at the bottom of the panel to nearly vertical at the top, which would have an effect on the compression of cells. Considering the relative weakness of cell walls in the upper sub-region compared to the bottom, and the presence of defective cell walls, the fact that they are oriented parallel to the compression direction suggests their buckling might occur much more easily.

The fact that the compression of the upper sub-region of the Cymat material continued until densification while the lower sub-region remained visually unaffected (Figure 6-36) suggests that the distribution of solid metal has a significant effect. The density distribution, or volume fraction of metal, was therefore calculated from the 3-D dataset of the Cymat sample using an averaging box size of 30 pixels^3 (3 mm^3). Two slices through this distribution are shown in Figure 6-39(b) for both the *X*-*Z* and *Y*-*Z* planes, and are compared with the virtual slices through the foam at zero and 30% applied sample strain (Figure 6-39(a)). It is clear that there is significant heterogeneity in the distribution of metal through the thickness of the foam panel, and locally there are virtually no high-density regions (defined as red) in the upper sub-region, resulting in significant crushing. This conforms to the relationships of Gibson and Ashby for which the strength of a foam is dependent on the relative density (Gibson and Ashby, 1997), and the effect of the significant density gradient on the failure sequence is clearly illustrated in Figure 6-39. The distribution of metal in the Alporas foam was uniform with very small heterogeneities in terms of larger cells, and therefore a lower metal distribution. The Cymat foam shows a significant density gradient through the thickness due to drainage of the molten metal through the structure during stabilisation and solidification, resulting in a lower volume fraction of metal at the top and thus larger cells. This could also be a consequence of a variation in SiC particle content, which would subsequently affect stabilisation during cell coarsening. There is also a density gradient present in the lower sub-region, with significant low-density regions also being observed here. Beals and Thompson studied the effects of the density gradient in the Alcan (Cymat) foam material using video collected

images of the compression sequence, and also observed initial failure to correspond to a plane of connected cells in the lowest density region (Beals and Thompson, 1997). As deformation continued, cells above this initial plane were observed to collapse upon it, with the lower high-density area remaining unaffected until significant deformation had occurred. The strength behaviour was also found to be dictated by the performance of the weakest, lowest density region, confirming observations of the compression sequence above. A 3-D elastic-plastic model developed by Kriszt *et al*, based on the calculated density distribution (Kriszt *et al*, 2000), confirmed a clear correlation between this and localised deformation and collapse bands in Alulight foam material, showing a similar density gradient to the Cymat foam. At an applied sample strain of 2%, local compressive strains as high as 14% were observed in the low-density region.

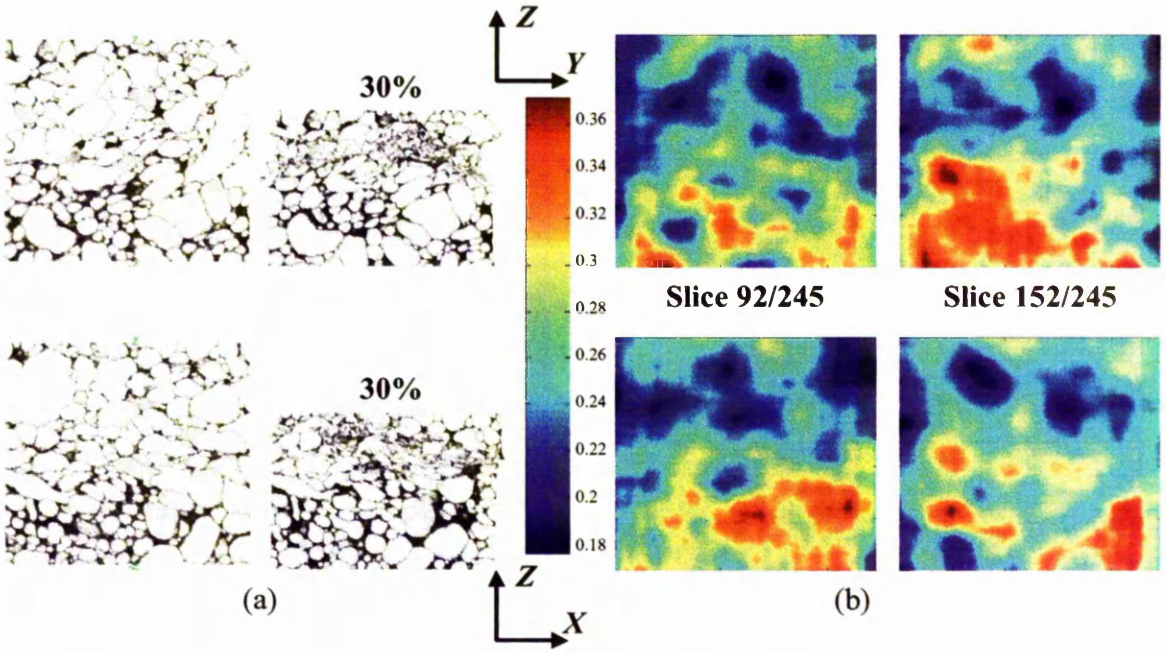

Figure 6-39. Comparing (a) the compression of the Cymat sample up to 30% height reduction (as in Figure 6-36), with (b) density distribution maps showing the initial volume fraction of metal for two slices in both the *X-Z* and *Y-Z* planes of the sample dataset, based on an averaging box size of 30 pixels^3 (3 mm^3). The distinct gradient in density is clear.

The significant differences in the microstructures of the Alporas and Cymat foams are largely a function of the behaviour of liquid aluminium foam prior to solidification, as described in Section 5.2.1.1. The Alporas foam is observed by eye to have cell walls of uniform thickness, and a nearly uniform cell wall thickness distribution has been observed

by Simone and Gibson using digitized optical images of sections through the foam (Simone and Gibson, 1998b). The wall thickness was found not to vary with spatial position. For the Cymat foam, as observed in Figure 6-39, a significant difference in the cell wall thickness exists between the top and bottom regions, due to accumulation of the drained liquid at the bottom. The Plateau borders are also much larger. In terms of the wall thickness distribution of this foam, Simone and Gibson observed an upper region where the wall thickness was roughly constant, and a lower region where the wall thickness rapidly increased as the panel bottom was approached (Simone and Gibson, 1998b). As a consequence, the density distribution as shown in Figure 6-39 is observed. Regarding the factors determining the critical thickness to which a foam drains, when surface viscosity is the stabilising force, the thickness of the viscous surface layers is presumably important, and their interaction as the lower viscosity liquid drains from between them (Walstra, 1989). The heterogeneity and anisotropy of the cellular structure in this Cymat foam can be attributable to the processing methods used in its production, and to straining of the liquid foam prior to solidification. Liquid foams can be deformed elastically through the distortion of individual cells, or plastically through the reordering of cells (Reinelt and Kraynik, 1990). Also, the relative size of adjacent cells in a liquid foam is inversely related to their relative internal gas pressure. When the stabilised liquid foam is conveyed mechanically from the melt, the greater weight carried by cells at the bottom of the liquid foam slab causes increased pressure and a smaller cell size and flattened cell shape (Simone and Gibson, 1998b).

6.4.7. Stress-strain behaviour

Figure 6-40 compares typical stress-strain curves measured from the compression of Alporas and Cymat samples in the thickness (Z) direction. Figure 6-40(a) shows the stress-strain response of the two foam materials up to an applied strain of 5%, illustrating the elastic and initial plastic collapse regions as defined in Section 5.3.1, while Figure 6-40(b) shows the full collapse plateau regions of the two foams approaching densification. Also, shown inset in Figure 6-40(b) is the normalised stress, by the plastic collapse stress of each sample, in each curve for comparison purposes. Note that the relative density of the Cymat foam (0.2) is double that of the Alporas foam (0.1). According to the scaling laws of Gibson and Ashby, one would expect the material of higher relative density to have a higher Young's modulus and compressive plastic collapse strength (Gibson and Ashby, 1997; see Section 5.3.2). This is observed to be the case (see Table 6-8), but there is still a

significant difference between the characteristics in the stress-strain behaviour of the two foam materials. Analysis and observations of the structures and resulting compressive deformation behaviour of the two foams, as carried out in the preceding sections, can help to explain these observed differences.

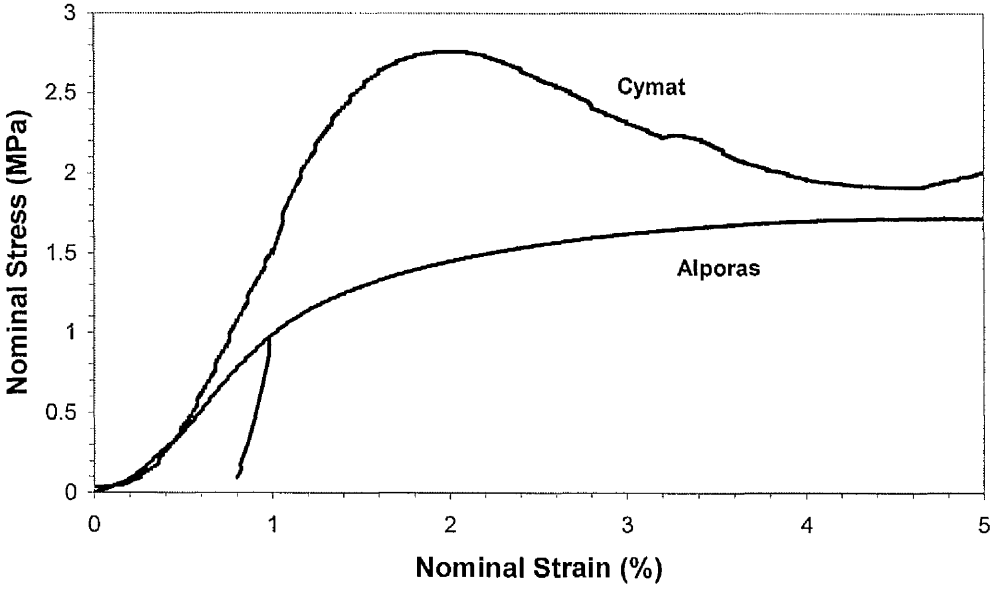

(a)

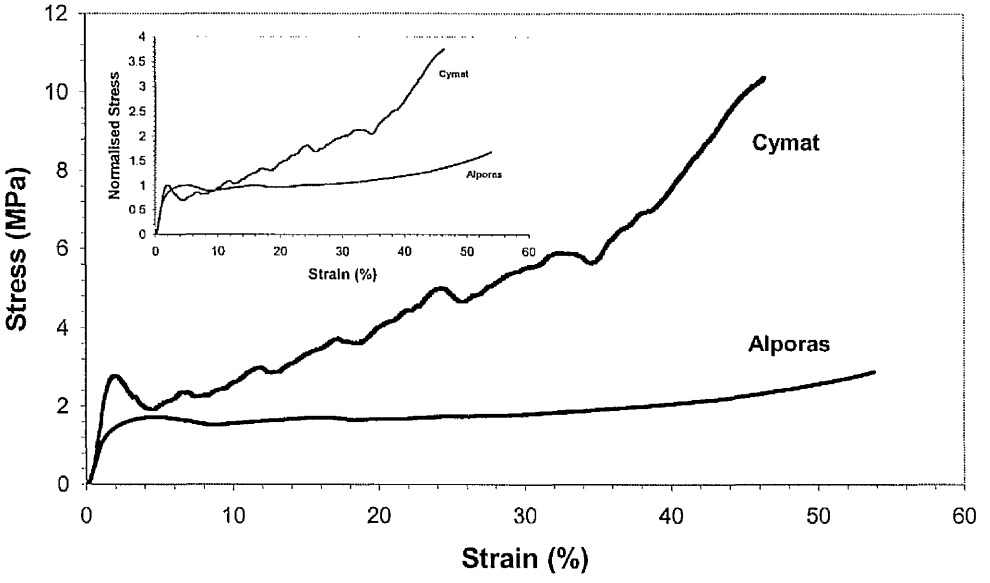

(b)

Figure 6-40. Typical compressive stress-strain curves for Cymat ($\rho/\rho_s = 0.2$) and Alporas ($\rho/\rho_s = 0.1$) foams, loaded to (a) 5% strain and (b) near to densification. Inset in (b) shows, for comparison purposes, the two curves normalised by the plastic collapse stress or peak stress of the sample.

First of all, the peak stress defining plastic collapse is reached at a strain of ~2% for the Cymat foam compared to ~5% for the Alporas material, indicating a more ductile cell wall deformation behaviour in the Alporas foam. The Cymat foam therefore has a higher Young's modulus (see Table 6-8), which can also be explained by the larger local regions of higher density (and the higher overall relative density), especially in the lower sub-region shown in Figure 6-39. Immediately after the onset of plastic collapse, the load resistance of the Cymat foam drops significantly, while that of the Alporas material remains constant. The strong load drop can be explained by the occurrence of damage to the cell walls of the Cymat material within the localised deformation band of the foam (Figure 6-36), once plastic collapse is reached. Significant buckling of a small number of cell walls was observed at these low strains, presumably enhanced by significant corrugations in the cell walls of this foam prior to loading (see Figure 6-37) as analysed by Simone and Gibson (Simone and Gibson, 1998b; Simone and Gibson, 1998c).

In the collapse plateau region, after the load drop, the load resistance in the Cymat foam continuously increases with applied strain, due in part to the higher stiffness and strength of the solid cell wall material. The rate of increase in load resistance increases at around 35% strain as the deformation band progresses towards densification. The stress plateau of the Cymat foam is also serrated (Figure 6-40(b)), and the behaviour of this foam material in the cell collapse region is typical of one where the mechanism of cell collapse is brittle in nature. The serrations correspond to progressive fracture of the cell walls resulting in the densification of the collapse band as the damaged cell walls come into contact. This has been observed by Andrews *et al.* (Andrews *et al*, 1999). Because of the brittle Al-Si eutectic in the microstructure of the Cymat solid cell wall material, as shown in Figure 6-41(a), brittle fracture of the cell walls is favoured (Markaki and Clyne, 2001; Simone and Gibson, 1998b). Small deflections in the cell walls lead to the formation of cracks which propagate through cells, resulting in their subsequent crushing (Kriszt *et al*, 2000). As shown in Figure 6-36, and confirmed in Figure 6-39, significant progressive collapse of the single deformation band in the low-density upper sub-region of the Cymat material occurred. Due to the observed density distribution, significant densification of this band occurred before the strength of the high-density lower sub-region was reached, resulting in a variation of collapse resistance through the thickness and the continuously increasing collapse region of the stress-strain curve. This shows that the strength behaviour is dictated by the performance of the weakest, lowest density plane, in agreement with Beals and Thompson (Beals and Thompson, 1997).

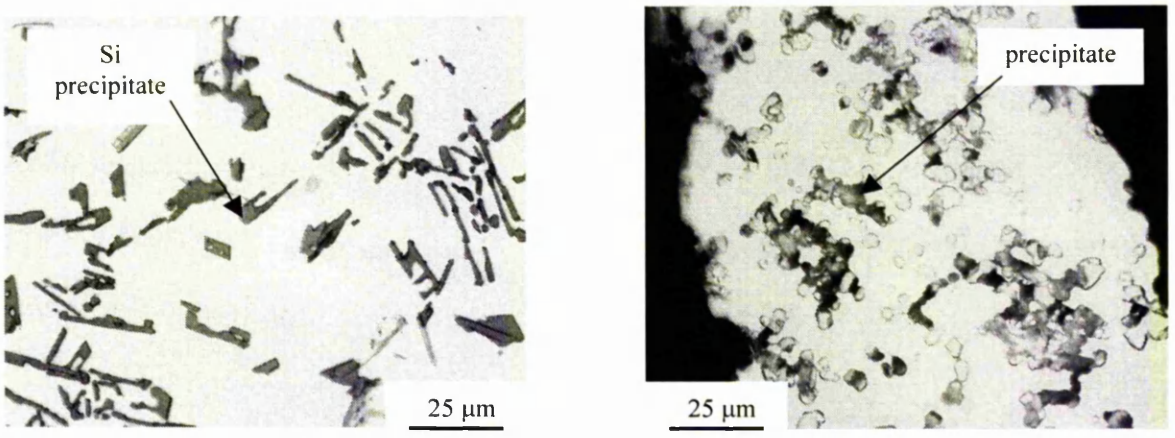

(a) (b)

Figure 6-41. Optical micrographs showing the cell wall microstructure of the (a) Cymat and (b) Alporas foams.

In contrast, the multiple minor deformation bands exhibited throughout the Alporas foam help to explain why the plateau stress remains more or less constant after plastic collapse up to densification. Deformation was observed to be spatially inhomogeneous due to local distributions of large cell volumes with surrounding small cells. However, progressive collapse was observed as deformation bands propagated from an initial site to the rest of the structure. The mechanism of cell collapse was ductile in behaviour because of the different microstructure (Al-Ca-Ti eutectic) of the cell walls, as shown in Figure 6-41(b). Thus only a very small increase in the load resistance in the collapse region of the curve is observed (Figure 6-40(b)). The dominant local deformation mechanism in the cell walls was by the forming of plastic hinges caused by bending, followed by plastic crushing of cells (Gibson and Ashby, 1997). Because of this plastic deformation of the cell walls during collapse, the softening due to damaged cell walls is not as significant as if they fracture. Thus a smooth collapse plateau is observed as opposed to the serrated one observed for the Cymat material (Figure 6-40(b)). The observed cell size and density distributions in this Alporas material (Figures 6-32 and 6-33) are relatively uniform through the thickness of the foam panel, in contrast to the Cymat foam, resulting in an almost constant collapse stress plateau. Using a continuum mesoscopic model developed by Kriszt *et al*, based on finite elements of averaged local mass density obtained from X-ray tomography measurements (Kriszt *et al*, 2000; see Section 5.4.2), Foroughi *et al*, for the Alporas material, simulated large deformations of a sub-domain or some elements in a sub-domain which caused local densification (Foroughi *et al*, 2001). This resulted in slow

hardening of the whole specimen in the collapse plateau regime, and with an increasing number of elements progressively densifying, a simulated stress-strain response in very good agreement with experimental measurements (Figure 6-40(b)) was obtained. This simulated response mirrors and helps to explain the observations of progressive collapse of this foam through the formation and propagation of many deformation bands.

Figure 6-42 compares stress-strain curves measured from compression tests of cubic (5 cm^3) samples of the Alporas foam material in the three orthogonal directions defined in Figure 6-1. A typical curve is shown for each of the three directions. Table 6-8 shows average values of the Young's modulus and plastic collapse strength calculated from two samples tested in each direction. The Young's modulus was calculated from an unloading curve, as illustrated in Figure 6-40(a), at 1% strain. 2-D measurements of cell diameter and aspect ratio from each of the three orthogonal planes (see Section 6.4.1; Simone and Gibson, 1998b) have inferred a relatively uniform and equiaxed cell structure and shape of the Alporas cells in three-dimensions. However, the mechanical properties are observed to depend on loading direction, in agreement with other studies of this foam (Andrews *et al*, 1999; Simone and Gibson, 1998b). This could be due to the presence of bulk variations in the density distribution in the three planes.

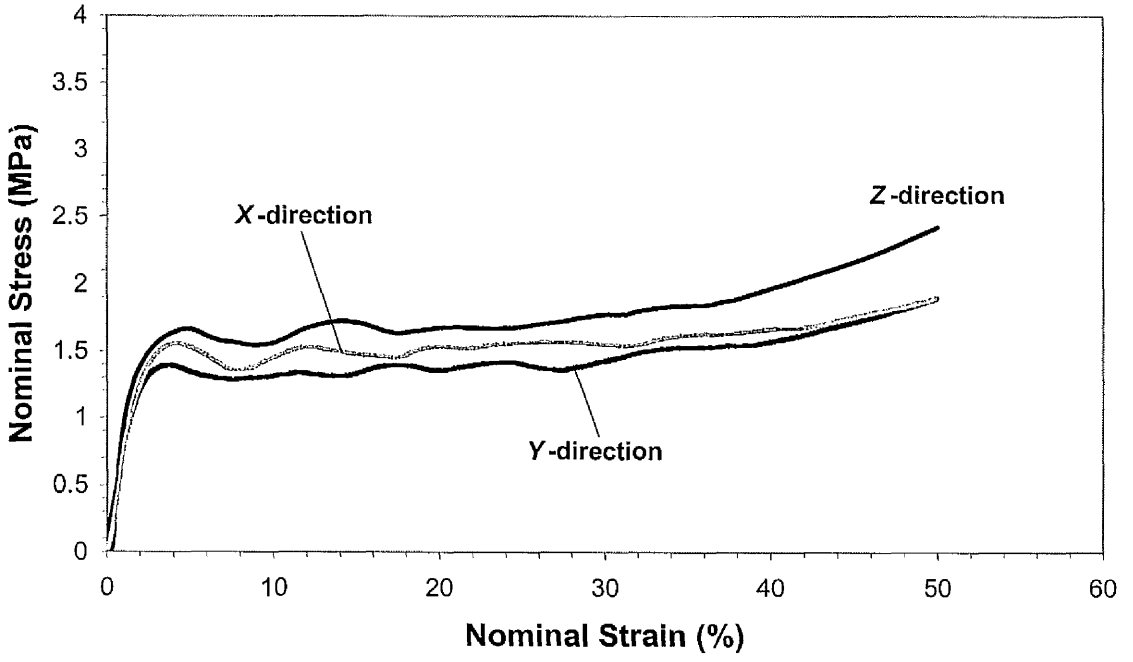

Figure 6-42. Stress-strain curves measured from uniaxial compression tests in three orthogonal directions. The *X* and *Y* directions are perpendicular and the *Z* direction parallel to the sheet thickness.

Table 6-8. Compressive Young's modulus and plastic collapse strength results for samples tested in the three orthogonal directions of the as-received Alporas foam sheet and the thickness direction of the Cymat foam sheet.

	Alporas-*X*	**Alporas-*Y***	**Alporas-*Z***	**Cymat**
Young's modulus (MPa)	535	580	675	891
Strength (MPa)	1.36	1.39	1.75	2.76

The Z-direction, representing the thickness of the foam panel, is observed to have the highest Young's modulus and compressive strength (or collapse strength). Simone and Gibson reported the Alporas material to be anisotropic with moduli and strengths of 870 and 1.60 MPa in one direction and 1210 MPa and 1.36 MPa in the other (Simone and Gibson, 1998b). Andrews *et al.* measured moduli and strengths of 1000 MPa and 1.84 MPa in one direction and 1140 and 1.46 MPa in the other (Andrews *et al*, 1999). While the measured strengths of Table 6-8 agree with those in the literature (Andrews *et al*, 1999; Simone and Gibson, 1998b), the values of the Young's modulus are significantly different. It must be noted that a comparison of the mechanical properties in the specific directions with results in the literature is difficult due to the lack of knowledge of the directions defined in these studies.

The 2-D equivalent diameter and aspect ratio measurements for the Alporas material, for which a typical sample set is observed in Section 6.3.1, did not infer any significant difference in the shape of a cell between the three measurement planes, and therefore in three-dimensions. The mean cell aspect ratio of ~1.4 does suggest the presence of slightly elliptical cells, and the fact that the equivalent diameter measurements and their distributions are slightly larger through a Z (panel thickness) plane suggests they are oriented primarily in this direction. This would therefore affect the mechanical properties in this plane as a consequence of curvature in the cell walls that run parallel to the loading direction (Andrews *et al*, 1999; Simone and Gibson, 1998c). A cell with its longer axis in this direction, and thus longer and less curved walls, would be expected to be more difficult to compress than one that is flatter with its long axis perpendicular and cell walls showing more appreciable curvature. Of course, the cell volume and the distribution of surrounding cells compressing above and below is important, as illustrated in the compression of samples 4 and 5 (Figures 6-26 and 6-27 respectively). The fact that the cell shape is very similar in each of the three orthogonal directions suggests that it is the

cell volume that has the most significant effect on the observed anisotropic mechanical behaviour of the material. The distribution of cell volumes, and the resulting density distribution, was observed to have a significant effect on the concentration of deformation and the formation of deformation bands in a sample (see Sections 6.4.3 to 6.4.5). The scaling laws of Gibson and Ashby outlined in Section 5.3.2, used to describe the mechanical properties of metal foams, identify the relative density as the most important structural parameter affecting such properties (Gibson and Ashby, 1997). Correlating low density to low strength and high density to high strength according to the scaling laws, it becomes evident how density arrangements influence the strength. The density distribution observed in Section 6.4.5 can thus help to explain the observed differences in compressive strength and Young's modulus (Figure 6-42; Table 6-8) between the samples tested in different directions. Figures 6-34 and 6-35 illustrate the volume fraction of metal distributed throughout samples tested in the *Z* and *Y* directions respectively. The fact that the *Z*-direction shows increased mechanical properties can be explained by low density regions being aligned parallel with the compression direction for the sample tested in this direction, as indicated in Figure 6-34, with high density regions either side down the sample height. This provides greater strength and stiffness compared to the compression of a sample with low density regions running across its width, perpendicular to the compression direction, as found in the sample tested in the *Y*-direction (see Figure 6-35). As seen in the compression and density analysis of sample 1 (Section 6.4.5 and Figure 6-33), the result of the latter of the two observed distributions is the crushing of the low-density band between two higher density ones. Also, as mentioned in Section 6.4.5, the *Y* planes (*X*-*Y* and *Z*-*Y*) were observed to contain more low-density regions than the *Z* planes. Comparisons between cylindrical samples representing the two directions (Sample 1 of Figure 6-33 and that for which two slices through the metal distribution dataset are shown in Figure 6-35) showed a similar characteristic. These lower strength regions are assumed to contribute to the observed differences in the stress-strain response.

The measured values of the Young's modulus and compressive plastic collapse strength for both the Alporas and Cymat foams, as shown in Table 6-8, lie well below values predicted by the models of Gibson and Ashby, and Simone and Gibson from finite element analysis of ideal, periodic, closed-cell tetrakaidecahedral cells with faces of uniform thickness (Simone and Gibson, 1998a; Equations 5-13 and 5-20 of Section 5.3.2). Using this model, and values for the relative densities, ρ^*/ρ_s, of 0.1 (Alporas) and 0.2 (Cymat), the density of the cell wall solid, ρ_s (2.7 g/cm^3) and moduli of the cell wall solid,

E_s (Andrews *et al*, 1999), of 69 GPa (Alporas) and 93 GPa (Cymat), gives values of the Young's modulus (Equation 5-13) of 2183 MPa and 5900 MPa for the Alporas and Cymat foam respectively. Similarly, for the compressive strength (Equation 5-20), using values for the yield strength of the cell wall solid (Simone and Gibson, 1998b) of 172 MPa (Alporas) and 390 MPa (Cymat), gives 7.3 MPa and 32.7 MPa for Alporas and Cymat respectively. Finite element calculations have suggested that cell wall curvature can produce significant reductions in modulus and strength below the ideal values for a perfect structure (Simone and Gibson, 1998c). This effect of cell wall curvature was estimated by assuming that the modulus was related to the average curvature in the cell walls, while the strength was related to the weakest cells with the most cell wall curvature. Average modulus and strength reductions resulting from cell wall curvature, for both Alporas and Cymat have been measured to be 0.67 and 0.42, respectively (Andrews *et al*, 1999), while similar values have been suggested by Simone and Gibson (Simone and Gibson, 1998c). Note that the measured values for both properties still lie below those representing the closed cell model corrected for cell wall curvature, and significantly so for the Cymat foam. This suggests that other imperfections in the cellular structure, such as the effects of solid distribution and the cell size/shape distribution, play an important role. Also, as seen in Section 6.4.2, the Cymat foam contained fractured or incomplete cell walls which would significantly reduce the mechanical properties. Note that excellent agreement between predicted and experimental results has been found when the influence of the density gradient was minimized, i.e. through-width tests and sectioned samples of the upper sub-region (Beals and Thompson, 1997). The Cymat foam has been observed to perform worse than an open-cell foam, indicating that the cell faces are not effectively contributing to the foam stiffness (Simone and Gibson, 1998b). The structural performance of both foams can be improved by reducing cell wall defects such as curvature and corrugations (Silva and Gibson, 1997; Simone and Gibson, 1998c). The former can be prevented by reducing the size distribution of cells (which cause pressure differences, see Section 5.2.1.2), while the latter, present especially in the Cymat foam, can be avoided by reducing the stresses applied to the foam immediately after solidification. Note that Alporas and Cymat foams produced by these liquid-state methods have been shown to fall short of the performance of those produced by more expensive production methods based on powder metallurgy (Simone and Gibson, 1998b), such as the Fraunhofer process (see Section 5.2.3). These foams approached the theoretical limit of foam stiffness, while all closed-cell foams performed poorly with respect to peak stress.

The compressive stress-strain behaviour observed for the two aluminium foam types (Figure 6-40(b)), which is directly related to their cellular microstructure and any inhomogeneities, is important for their potential for energy absorption applications. Accordingly, an estimate of the energy absorbed during compression of the two foams up to densification was calculated from the area under the stress-strain curves. For each of the two foam materials, the strain, for calculation purposes, was defined as the strain at which the stress was equal to 1.5 times the stress at 20% strain. Although somewhat arbitrary and not representing the true densification strain of the materials, this gave a strain of ~35% for the Cymat foam, defining the transition point in the rate of increase of the load resistance. This also provided a consistent method, giving a strain for the Alporas material of ~50%. Average values of the energy absorption are given in Table 6-9. It is clear that, under the method used, the Cymat foam has a higher energy absorption capacity, although its densification strain is lower. This is because higher stresses are required for the Cymat foam to densify owing to its higher density and the cell wall material being harder and more brittle. On the other hand, the energy absorbing characteristics of the Alporas foam, i.e. a long flat stress-strain curve where the foam collapses plastically at a constant plateau stress, appear more attractive in practical terms. Such behaviour, in which plastic deformation occurs at relatively low plateau stresses, has been observed to ensure more uniform and efficient collapse of the material.

This can be quantified by defining an energy absorption efficiency value for the two foams (Beals and Thompson, 1997), which is the ratio of the actual amount of energy absorbed to an ideal total based on the stress at the densification strain considered. The efficiency at an allowable peak stress can therefore be defined, minimising damage to the impacting body. These values are also given in Table 6-9. It can be seen that the efficiency of the Alporas foam is higher and therefore its compressive behaviour is more advantageous for energy absorbing applications. It is clear from the stress-strain curves of the two materials (Figure 6-40(b)) that the Alporas foam has a high energy-absorption efficiency throughout its deformation history owing to the more uniform density distribution and thus efficient collapse and a flat plateau stress. In contrast, the observed density gradient in the Cymat foam contributes to a lower energy absorption efficiency throughout due to the influence of the high-density lower sub-region and a continuously increasing plateau stress. This is in agreement with the work of Beals and Thompson, who observed significantly higher collapse plateau gradient values for full through-thickness samples and sectioned lower sub-regions of the Cymat foam (Beals and Thompson, 1997).

When used in a direction independent of the density gradient, i.e. through-width, an efficiency of 85% was obtained. This shows that the energy absorption efficiency will be decreased with an increasing density gradient. Regarding compressive loading rates representative of the use of foams in impact systems, Tan *et al.* investigated the high rate compressive behaviour of closed-cell Norsk Hydro aluminium foam fabricated by a similar route to the Cymat foam (Tan *et al*, 2001). Local density variations were observed to have a significant effect on the dynamic peak forces measured, with cell deformation still being confined to the low-density zone as observed in the analysis of Section 6.4.6. The efficiency and performance of the Cymat foam could almost certainly be improved by making the cellular structure more isotropic and homogeneous and by reducing the density gradient. This could be accomplished through modification of the processing methods and by allowing more complete drainage before solidification. Because of density gradient effects, the level of drainage which occurs before solidification is important. This also determines the distribution of solid material between the cell face and cell edge, which has been shown to affect the structural performance (Simone and Gibson, 1998a).

Table 6-9. Energy absorption properties measured for the Alporas and Cymat samples up to applied sample strains of 49% and 35% respectively.

	Energy absorption ($MJ\ m^{-3}$)	Efficiency (%)
Alporas	0.88	71.9
Cymat	1.28	65.8

Recall the different types of compressive behavioural modes that have been observed locally in the Alporas samples due to the distribution of cell volumes, as analysed in Section 6.4.4. Whether a sample deforms uniformly or shows anisotropic buckling of its structure can have a significant effect on the stress-strain behaviour and thus the energy absorbing characteristics of the material. For example, Figure 6-43 compares the stress-strain curves measured during the compression of Alporas samples 1 and 6, which had very similar densities. The compression sequence of tomographic slices for sample 1, up to 50% sample strain (Figure 6-29), illustrated a buckling of its structure between 30 and 40% applied sample strain. This is observed to correspond to a load drop in the stress-strain response of this sample, as indicated in Figure 6-43, compared to the ideal flat or

uniform response of sample 6. While there is only a small drop in the load resistance, the effect of heterogeneities in the cell volume or density distributions is clear. Localised buckling due to such heterogeneities reduces the area under the stress-strain curve and therefore has consequences for potential uses in impact applications if such local regions of weakness are apparent. Again, the effect is only small, and the presence of globally uniform cell volume and density distributions for this material ensures efficient collapse regions throughout a sample, compensating for any local inhomogeneities. These observations are in agreement with those of Gradinger and Rammerstorfer, who studied the influence of meso-inhomogeneities on the compression of metal foams (Gradinger and Rammerstorfer, 1999). Such inhomogeneities were observed to lead to strain localisations and, consequently, to a decrease of the initial plateau stress and to increasing ascents in the plateau regime, both reducing the energy absorption efficiency as observed significantly in the Cymat foam above. Foroughi *et al.* have shown by simulations of actual foam structures that the inhomogeneity in the density distribution can well describe the phenomena of inhomogeneous deformation and strain localisation (Foroughi *et al*, 2001).

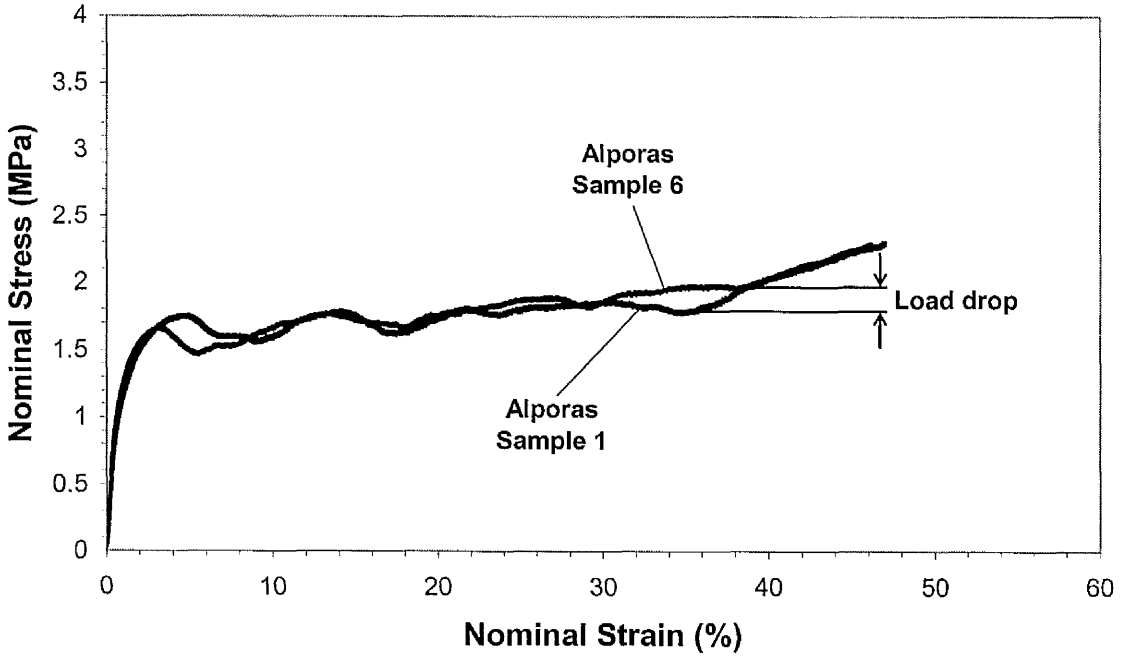

Figure 6-43. Typical compressive stress-strain curves of Alporas samples 1 and 6, at an applied strain rate of 0.5 mm/min. Tomographic 2-D slices illustrating the compression sequences of the two samples up to 50% applied sample strain are shown in Figures 6-29 and 6-28 respectively.

6.5. Summary and Conclusions

X-ray microtomography has been employed to study the effect of the 3-D cellular structure of aluminium foam samples on the compressive deformation behaviour of the material. Two types of closed-cell aluminium foam samples were studied, both fabricated by different liquid-state processes. The generated 3-D tomographic images or datasets were characterised in terms of the distribution of 3-D cell volumes and metal density. In conjunction with performing *in situ* compressive deformation studies, correlations between such characteristic distributions and the position of deformation bands within the samples have been found. The influence of the fabrication method on the structural performance of the foam materials has also been investigated. The important findings are summarised as follows:

1. Microstructural characterisation of the structures of the two foam types in three-dimensions, representing sample sets of cells through the entire thickness of the respective foam panels, revealed significant differences between the distributions of sizes and shapes of cells in each. In terms of cell volume, cells in the Alporas material were observed to be much larger with a significant proportion of larger cell sizes within this distribution. Those in the Cymat material were largely concentrated around a lower mean value. In terms of cell shape in 3-D, made by comparing cell diameters and aspect ratios in the three orthogonal planes, Alporas cells were observed to be relatively uniform and equiaxed. The Cymat cells were more elongated in the plane of the thickness of the foam panel.
2. Compression of the Alporas material was characterised by the formation of multiple minor deformation bands throughout the loading history, with progressive collapse occurring by the expansion of existing bands and the formation of new ones. The positions of the largest cells in a sample were observed to be very important regarding the concentration of deformation bands. The distribution of cells surrounding a large cell was shown to be important. An isolated large cell, i.e. with small surrounding cells, was more significant for concentrating stress than an aggregate of large or moderately sized cells together.
3. The distribution of cell volumes within a sample, described in (1), had a significant effect on its mode of deformation. Anisotropic buckling of a sample structure was promoted for a distribution of cell sizes with a larger skewness and kurtosis, and therefore the presence of isolated large cells. Although only a small effect, such a

deformation mode was shown to be detrimental to the energy absorption properties of the material and therefore its efficient use in such an application.

4. The density distribution, or more appropriately the volume fraction of metal, revealed more effectively the effect of structure on deformation behaviour of the Alporas material. Although quite uniform, small heterogeneities in the distribution dictated where deformation initiated, analogous to the effect of the distribution of large cells. Initiation sites were primarily at locations of low density, correlating with the scaling laws of foam behaviour.
5. The Cymat foam had a significantly inhomogeneous density distribution, due to drainage of the material during stabilisation and solidification, and two clearly distinct sub-regions. Deformation occurred significantly in the lower density sub-region, with the higher density one remaining relatively unaffected until its densification. This, together with the brittle nature of the cell wall solid, had a clear effect on the stress-strain behaviour of the material, characterised by a continuously increasing and serrated post yield behaviour. The ductile solid cell walls of the Alporas material resulted in a flat plateau stress, and a higher energy absorption efficiency more suited to such applications.

References

Andrews, E., Sanders, W. and Gibson, L. J., (1999), 'Compressive and tensile behaviour of aluminium foams', *Materials Science and Engineering*, **A270**, 113-124.

Andrews, E. W., Gioux, G., Onck, P. R. and Gibson, L. J., (2001), 'Size effects in ductile cellular solids. Part II: experimental results', *International Journal of Mechanical Sciences*, **43**, 701-713.

Bart-Smith, H., Bastawros, A.-F., Mumm, D. R., Evans, A. G., Sypeck, D. J. and Wadley, H. N. G., (1998), 'Compressive deformation and yielding mechanisms in cellular Al alloys determined using X-ray tomography and surface strain mapping', *Acta Materialia*, **46**(10), 3583-3592.

Beals, J. T. and Thompson, M. S., (1997), 'Density gradient effects on aluminium foam compression behaviour', *Journal of Materials Science*, **32**, 3595-3600.

Fazekas, A., Dendievel, R., Salvo, L. and Brèchet, Y., (2002), 'Effect of microstructural topology upon the stiffness and strength of 2-D cellular structures', *International Journal of Mechanical Sciences*, **44**, 2047-2066.

Foroughi, B., Kriszt, B. and Degischer, H. P., 'Modelling of mechanical properties of inhomogeneous cellular materials', in Banhart, J., Ashby, M. and Fleck, N., *Cellular Metals and Metal Foaming Technology*, MIT – Verlag, Bremen, 2001, 265-268.

Gibson, L. J. and Ashby, M. F., *Cellular Solids: Structure and Properties*, 2nd edition, Cambridge University Press, Cambridge, UK, 1997.

Gradinger, R. and Rammerstorfer, F. G., (1999), 'On the influence of meso-inhomogeneities on the crush worthiness of metal foams', *Acta Materialia*, **47**(1), 143-148.

Kriszt, B., Foroughi, B., Faure, K. and Degischer, H. P., (2000), 'Behaviour of aluminium foam under uniaxial compression', *Materials Science and Technology*, **16**, 792-796.

Kunze, H. D., Baumeister, J., Banhart, J. and Weber, M., (1993), *Powder Metallurgy International*, **25**(4), 182.

Ma, B., Tieu, A. K., Lu, C. and Jiang, Z., (2002), 'An experimental investigation of steel surface characteristic transfer by cold rolling', *Journal of Materials Processing Technology*, **125-126**, 657-663.

Markaki, A. E. and Clyne, T. W., (2001), 'The effect of cell wall microstructure on the deformation and fracture of aluminium-based foams', *Acta Materialia*, **49**, 1677-1686.

Olurin, O. B., Arnold, M., Korner, C. and Singer, R. F., (2002), 'The investigation of morphometric parameters of aluminium foams using micro-computed tomography', *Materials Science and Engineering*, **A328**, 334-343.

Onck, P. R., Andrews, E. W. and Gibson, L. J., (2001), 'Size effects in ductile cellular solids. Part I: modeling', *International Journal of Mechanical Sciences*, **43**, 681-699.

Reinelt, D. A. and Kraynik, A. M., (1990), 'On the shearing flow of foams and concentrated emulsions', *Journal of Fluid Mechanics*, **215**, 431-455.

Silva, M. J. and Gibson, L. J., (1997), 'The effects of non-periodic microstructure and defects on the compressive strength of two-dimensional cellular solids', *International Journal of Mechanical Sciences*, **39**(5), 549-563.

Silva, M. J. and Gibson, L. J. and Hayes, W. C., (1995), 'The effects of non-periodic microstructure on the elastic properties of two-dimensional cellular solids', *International Journal of Mechanical Sciences*, **37**(11), 1161-1177.

Simone, A. E. and Gibson, L. J., (1998a), 'Effects of solid distribution on the stiffness and strength of metallic foams', *Acta Materialia*, **46**(6), 2139-2150.

Simone, A. E. and Gibson, L. J., (1998b), 'Aluminium foams produced by liquid-state processes', *Acta Materialia*, **46**(9), 3109-3123.

Simone, A. E. and Gibson, L. J., (1998c), 'The effects of cell face curvature and corrugations on the stiffness and strength of metallic foams', *Acta Materialia*, **46**(11), 3929-3935.

Tan, P. J., Harrigan, J. J. and Reid, S. R., 'Influence of cell size and morphology on the dynamic compressive strength of aluminium alloy foams', in Banhart, J., Ashby, M. and Fleck, N., *Cellular Metals and Metal Foaming Technology*, MIT – Verlag, Bremen, 2001, 345-350.

Walstra, P., in *Foams: Physics, Chemistry and Structure*, ed. A. J. Wilson. Springer-Verlag, London, 1989.

General Summary and Conclusions

X-ray microtomography has been applied to the investigation of damage development and deformation mechanisms occurring in two different microstructured materials, namely Ti/SiC_f MMCs and Al foams. Tomography has been shown to be a powerful characterisation technique to study the structural evolution of these materials under an applied external load. Virtual reconstructions of their 3-D internal structures have provided important information, non-destructively, that would not have been possible with any other characterisation technique. The important aspects of the work that tomography has enabled for the study of the two material types are summarised as follows:

1. Tomography has enabled detailed observations of the interaction between longitudinal SiC fibres and a matrix fatigue crack. Virtual reconstructions of the full 3-D morphology of the crack showed fibre bridging to occur. Crack opening displacement measurements as a function of applied load were performed directly using tomography slices of the matrix crack profile through the 3-D reconstructed volumes of the samples. The CODs were observed to decrease as the crack tip was approached, and an increase in the applied stress resulted in an increase in the magnitude of the CODs. The technique also provided information of the characteristics of fibre fractures occurring near pre-induced defects, due to the local redistribution of load that was measured to occur from strain mapping measurements made along individual fibres using X-ray diffraction.
2. Tomography has enabled detailed observations of the effect of the cellular structure of closed-cell aluminium foam samples on the compressive deformation behaviour of the material. 3-D reconstructions of the samples allowed cell volume and density distributions to be characterised in three-dimensions, such characterisation only previously possible in 2-D using sectioning techniques. These distributions were observed to be very important as to where deformation bands occurred during compression, with regions of large cell volume and low density acting as sites of stress concentration. The technique also showed the significant difference in the internal structures of foams produced by different methods.

It has also been shown that it is important to consider image quality when performing X-ray tomography measurements, as various artefacts can infer false features or density gradients in the images. System settings can be optimised to give improved quality.

Further Work

In Chapters 4 and 6, the use of X-ray microtomography to study damage development and deformation mechanisms in Ti/SiC composites and Al foams was described. The following suggests further work to be investigated in both cases to gain an improved understanding of the behaviour of the materials.

Ti/SiC Long Fibre Composites

- An idealised study of the effect of defects in Ti/SiC composites has been undertaken where the stress concentration resulting from, at the most, two pre-induced fibre breaks in a ply of five fibres has been investigated. This has given important information on the level of stress concentrated in adjacent intact fibres, by using X-ray diffraction to map the strain along each individual one, but it is important to understand the effects of larger numbers of breaks in plies containing more fibres. Chapters 3 and 4 suggest that the load sharing mechanisms depend on the numbers of broken and intact fibres.
- Perhaps more critically, it is important to understand the effect of fibre defects in composites containing hexagonal arrays of fibres, where the number of nearest neighbour fibres is greater. Such morphologies or arrangement of fibres (multi-ply as opposed to single-ply) are representative of those being considered for aero-engine use due to the improved fatigue crack growth resistance properties of such arrangements. Further investigation would centre on observations of the effect of pre-induced fibre breaks on the subsequent cracking of surrounding clusters of fibres. High-resolution X-ray microtomography would provide invaluable information of failure sequences and crack morphologies as a function of applied load in such an arrangement. Due to the presence of six nearest neighbour fibres, as opposed to two for a single-ply arrangement, one would expect the level of stress concentration in adjacent intact fibres to reduce compared to the values observed in Chapter 4. Further strain measurement analysis would be carried out to see if this is the case.
- The resolution of the tomographic datasets used to make crack opening displacement measurements was 2 μm. For analysis of the displacements at the crack tip, this was observed to be too large. With the development of cameras

down to resolutions of 0.5 μm, which are now in use at the ESRF, the measurement of CODs at such an improved resolution would provide important information of crack tip displacements.

- An important operating condition not accounted for in the work of Chapter 4, but would be experienced in-service in an aero-engine, is performance at high temperatures. Knowledge of interfacial characteristics, and more specificly the interface stresses, in such environments would be invaluable, to see whether interfacial shear stress values fall below the values measured in Chapter 4, and if so by how much.

Al Foams

- The effect of the cellular structure on the compressive deformation of Al foams has been investigated experimentally using small samples and at low loading rates. While this has given important information about the progression of cell collapse, and the cell volume and density distributions responsible for this, the work can be further extended to investigate loading rates more representative of impact conditions which are important for energy absorption applications. The two foams that have been investigated clearly behave very differently because of their structures, and it is important to know if this behaviour is the same at higher velocities of crushing via impact testing.
- It would be of interest to measure local strains occurring in the three-dimensional foam structures, and relate this to the observed cell structure distributions. A very simple measure of the strain that each cell experiences, from a measure of how much it compresses, has been made. The development of 3-D volume strain mapping and image correlation techniques could measure small deformations and strains experienced by cell edges, for example, more accurately. Such a 3-D measurement is important due to the observed cell volume distributions throughout a foam material and their effect on deformation.
- Models have been developed to describe the mechanical properties of these foams, but due to imperfections in the cellular structures and the arrangement and distribution of cells, they do not adequately describe experimental observations. A 3-D model based on the accurate cellular structure, rather than simplified continuum models, obtained from tomography measurements would be developed

to simulate actual observations. This could be further extended to investigate different aspects such as larger sample sizes representative of those that might be used for crash protection applications for example.

- Perhaps most importantly with regards to the structural characterisation work that has been carried out, more automated and robust descriptors for immediate prediction of local deformation would be developed. At present, where deformation is localised is effectively inferred by looking at the structure in 3-D. Ideally, one would like to make a simple measurement or interrogation of an image or 3-D dataset, and know from that one observation where failure would initiate and whether the mechanical properties would fall outside a standard or design criteria. This would be important for quality control as to whether or not the material passes such criteria.

Regarding the investigation of the performance of a tomography system, further studies would be carried out regarding optimisation of image quality. The effects of a wider range of filter materials, and also detail and specimen materials and sizes, would be studied with the aim of simulating the optimum equipment settings for a particular application.

Appendix

Reconstruction from fan projections

When considering laboratory micro-focus sources, a disadvantage of the pencil-beam geometry (see Section 1.2.1) is the very long scanning times. In generating such projection data, the sample has to be translated to enable a source-detector combination to linearly scan over the length of a projection (to cover the t dimension, as defined in Figure 1-20 of Section 1.4.1), then rotated through a specified angular interval, and translated to scan linearly over the length of the next projection, and so on. This usually results in times that are as long as a few minutes for collecting the data for a single projection. Fan-beam tomography alleviates this problem. A much faster way to generate line integrals is by using fan beams such as those illustrated in Figure 1-24 of Section 1.4.1. In this setup, the X-ray beam is collimated so that a thin, planar fan-shaped beam of rays extends from the X-ray point source and passes through the object before being collected by a detector array, used to make all the measurements in one fan simultaneously. The object then rotates about an axis perpendicular to the fan beam. (In an equivalent motion, the X-ray source and detector array rotate around the object to generate the desired number of fan projections). The fan beam completely covers the object at all positions, as shown by Figure 1-24. There are two main detector configurations for such a geometry, and therefore two types of fan projections depending upon whether a projection is sampled at equiangular or equispaced intervals. The two types are illustrated in Figure 1 (Hiriyannaiah, 1997).

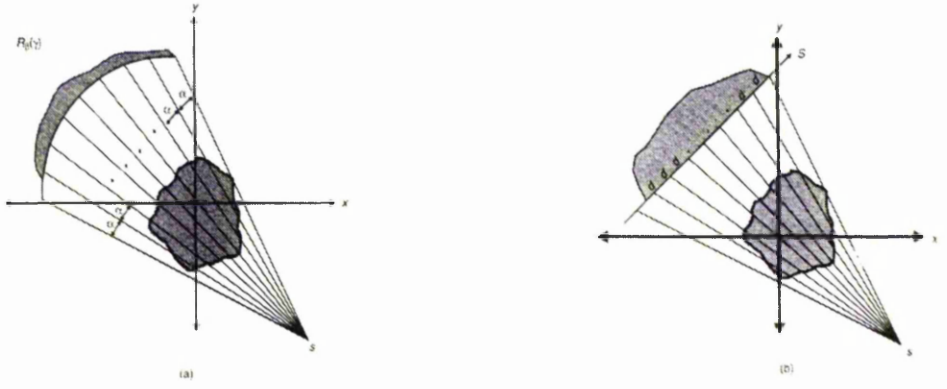

Figure 1. (a) Equiangular fan-beam. The detector elements lie on an arc of a circle with angular spacing, α. (b) Equidistant detector fan-beam. The detector elements are collinear with uniform sampling distance, d. (Hiriyannaiah, 1997).

Figure 1(a) shows an equiangular fan beam, for which the detector array lies on a circular arc (or a complete circle as in present-day scanners) such that the angle subtended between two detectors is constant. Figure 1(b) shows an equispaced or equidistant collinear detector fan beam for which the detector elements lie on a straight line and are equidistant from each other. Of the two configurations, it is the linear detector array setup (Figure 1(b)) that is used most commonly in industrial CT systems. This is due to the convenience of having the object rotating about its axis rather than having the source-detector assembly moving around the object, as used for the circular detector array setup. It is also easier to place the detectors in a linear array rather than along a ring. Let $R_\beta(s)$ denote a fan projection as shown in Figure 2 (Rosenfeld and Kak, 1982).

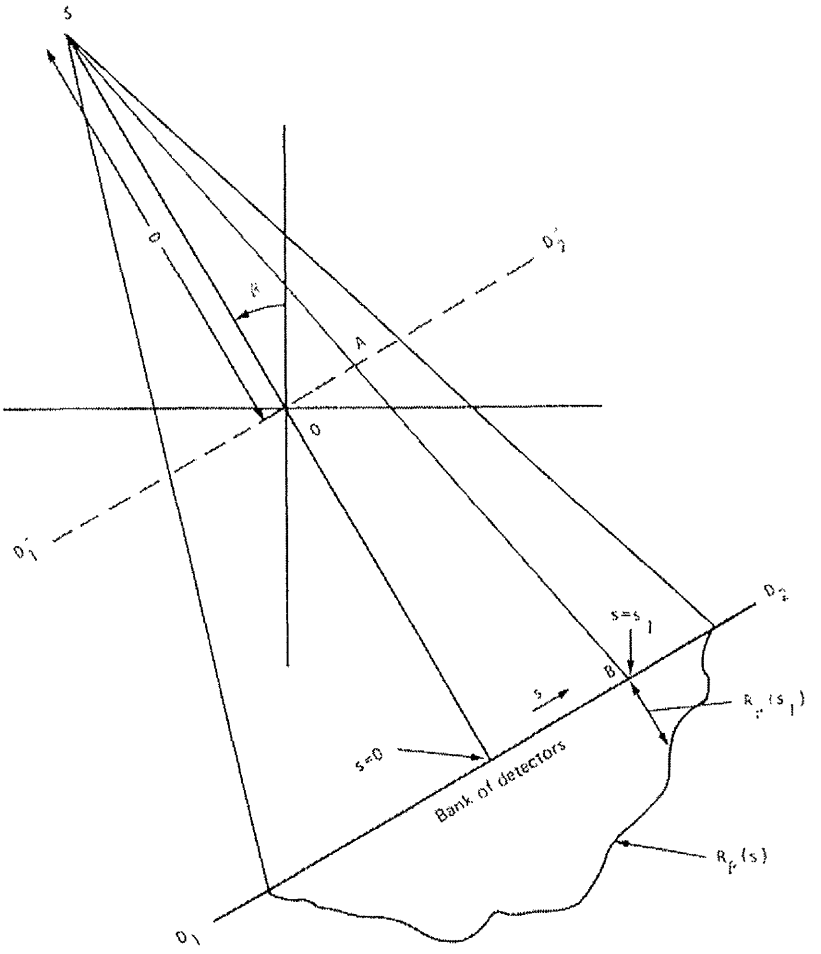

Figure 2. For the case of equispaced detectors on a straight line, such as that indicated by D_1D_2, each projection is denoted by the function $R_\beta(s)$. (Rosenfeld and Kak, 1982).

Uniform sampling of the fan projections is carried out in the (β,s) domain, analogous to the (θ,t) domain used for parallel projections. The detector array is usually at a distance from the origin and projections are measured on a line such as D_1D_2 in Figure 2, with the value s being the perpendicular distance along this line from the source-detector axis. However, for theoretical purposes, it is more efficient to consider the detector array to be placed on a straight line passing through the origin, and to associate the ray integral along the line SB with point A on the line $D_1'D_2'$, as defined in Figure 3, as opposed to point B on D_1D_2 (Figure 2). Figure 3 associates a fan projection, $R_\beta(s)$, with the imaginary detector line, $D_1'D_2'$ (Rosenfeld and Kak, 1982).

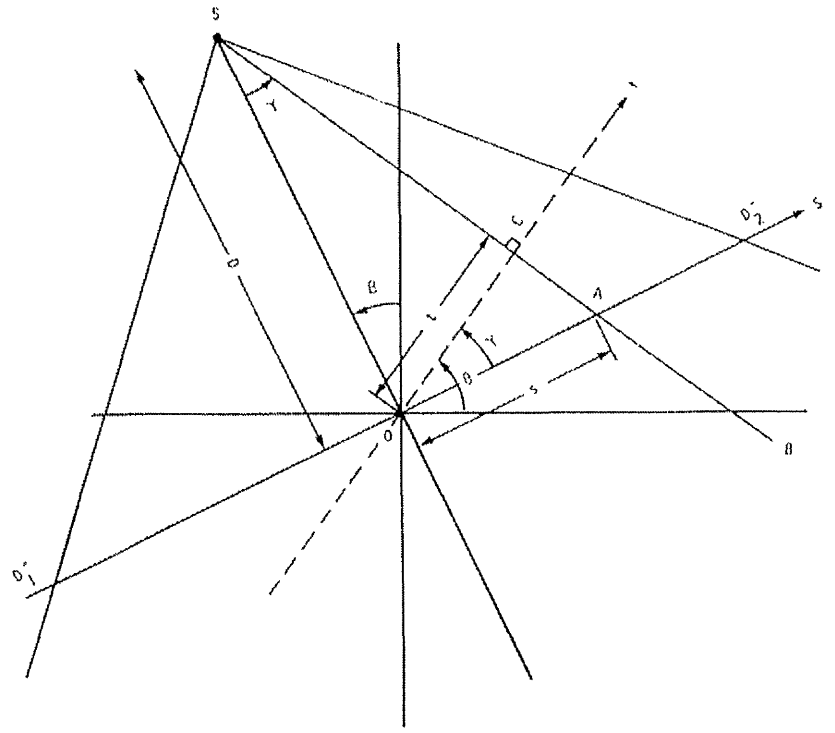

Figure 3. Illustrating the parameters used in the derivation of the reconstruction algorithm for equispaced detectors, and the imaginary detector line, $D_1'D_2'$, with which fan projections are associated. (Rosenfeld and Kak, 1982).

Considering a ray SA in Figure 3, the value of s for this ray is the length of OA. If parallel projection data were generated for the object under consideration, the ray SA would belong to a parallel projection, $P_\theta(t)$, with θ and t as defined in Figure 3. The relationship between s and t and β and θ for the case of a parallel projection is given by (Kak and Slaney, 1987):

$$t = s\cos\gamma \qquad \theta = \beta + \gamma$$
$$t = sD / \sqrt{(D^2 + s^2)} \qquad \theta = \beta + \tan^{-1} s/D \tag{1}$$

where D is the distance of the point source, S, from the origin, O, and γ is the angle between the line $D_1'D_2'$ and the line defining the parallel projection case for the ray SA. Recall the expression for a reconstructed image of an object, $f(x,y)$, in terms of parallel projection data, $P_\theta(t)$ (Hiriyannaiah, 1997):

$$f(x,y) = \tfrac{1}{2} \int_0^{2\pi} \int_{-t_m}^{t_m} P_\theta(t)\ H_\in (x\cos\theta + y\sin\theta - t)\, dt\, d\theta \tag{2}$$

where t_m is the value of t for which $P_\theta(t) = 0$ with $|t| > t_m$ for all projections. This expression uses parallel projections generated over 360°. The point (x,y) can be expressed in polar coordinates, (r,ϕ), where $x = r\cos\phi$ and $y = r\sin\phi$. The expression in (2) can now be written as:

$$f(r,\phi) = \tfrac{1}{2} \int_0^{2\pi} \int_{-t_m}^{t_m} P_\theta(t)\ H_\in (r\cos(\theta - \phi) - t)\, dt\, d\theta \tag{3}$$

where $H_\in(t)$ is the inverse Fourier transform of the frequency response of the filter, $|\omega|$, in the frequency domain (Kak and Slaney, 1987):

$$H_\in(t) = \int_{-\infty}^{\infty} |\omega| . \exp(j\,2\pi\,\omega t)\, d\omega \tag{4}$$

In Equation (3), $f(r,\phi)$ represents a reconstructed image of an object in polar coordinates. In order to express this in a filtered backprojection form, two new variables, U and s', need to be introduced, and are defined in Figure 4 (Rosenfeld and Kak, 1982):

$$U = (D + r\sin(\beta - \phi)) / D$$
$$s' = D\left[\ (r\cos(\beta - \phi)) / (D + r\sin(\beta - \phi))\ \right] \tag{5}$$

U is defined as the ratio of SP to the source-to-origin distance for each pixel, (x,y), where SP is the projection of the source-to-pixel distance, SE, on the central ray defined in Figure 4. s' is denoted as the value of s for the ray that passes through the pixel, (r,ϕ), under consideration, and is given by the distance OF (Figure 4). Using the expressions given in (5) in the reconstruction equation (Equation (3)), the derived expression is given by (Kak and Slaney, 1987):

$$f(r,\phi) = \int_0^{2\pi} 1/U^2 \int_{-s_m}^{s_m} R_\beta(s)\ H_\epsilon(s'-s)\ (D/(D^2+s^2)^{1/2})\, ds\, d\beta \qquad (6)$$

This expression can be interpreted as a weighted filtered backprojection algorithm. The inner integral is the standard backprojection filtering operation on a weighted projection dataset using the weighting factor $D / \sqrt{(D^2 + s^2)}$. The backprojection operation, denoted by the outer integral, is weighted by the factor for each ray.

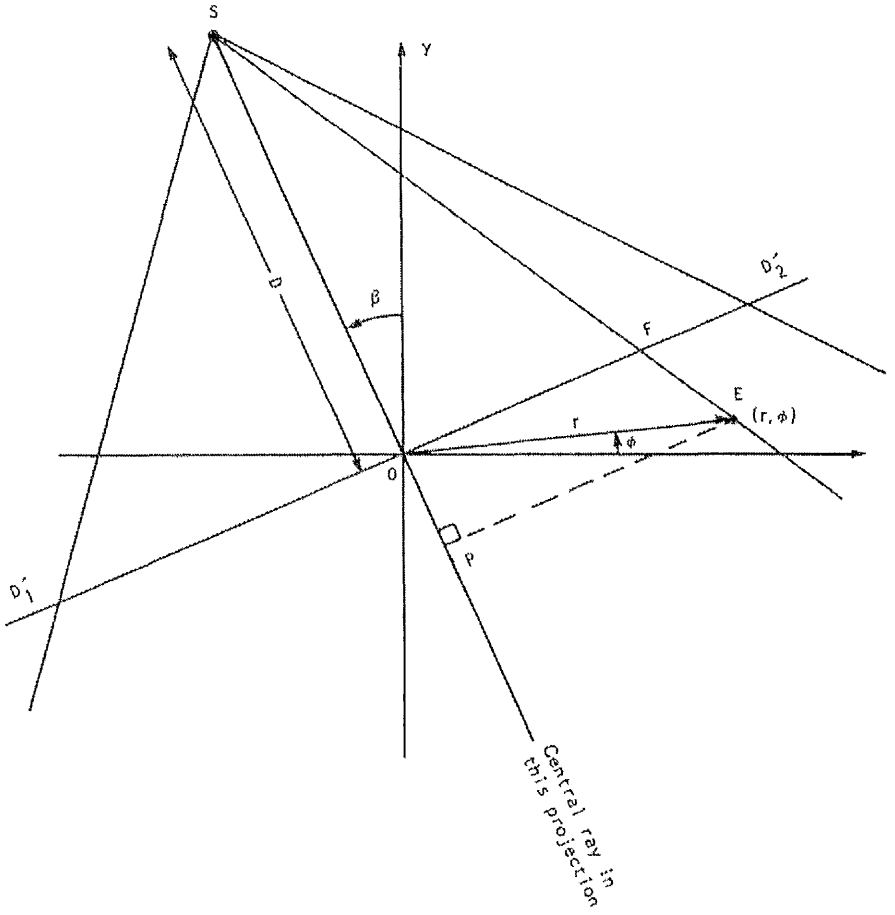

Figure 4. Used to define the parameters U and s' (distance OF) with respect to the central ray and the ray that passes through the pixel (r,ϕ). (Rosenfeld and Kak, 1982).

Equation (6) defines the following steps to be carried out (Kak and Slaney, 1987):

1. Assume that each projection, $R_\beta(s)$, is sampled with a sampling interval of a. The known data are then $R_{\beta i}(na)$ where n takes integer values, with $n = 0$ corresponding to the central ray passing through the origin. β_i are the angles for which fan

projections are known. The first step is to generate, for each fan projection, $R_{\beta i}(na)$, the corresponding modified projection $R'_{\beta i}(na)$, given by:

$$R'_{\beta i}(na) = R_{\beta i}(na) \,.\, (D / \sqrt{(D^2 + n^2a^2)}) \tag{7}$$

2. Convolve each modified projection, $R'_{\beta i}(na)$, with $g(na)$ to generate the corresponding filtered projection:

$$Q_{\beta i}(na) = R'_{\beta i}(na) \,.\, g(na) \tag{8}$$

where the sequence $g(na)$ is given by the samples of $g(na) = \frac{1}{2} H_{\epsilon}(na)$.

3. Perform a weighted backprojection of each filtered projection along the corresponding fan. The sum of all the backprojections is the reconstructed image.

$$f(x,y) = \sum_{i=1}^{M} \frac{1}{U^2(x, y, \beta_i)} \; Q_{\beta i}(s') \tag{9}$$

s' identifies the ray that passes through (x,y) in the fan for the source located at angle β_i.

Cone-beam CT – three-dimensional reconstruction

Three-dimensional projections

A conventional way to obtain a three-dimensional image of an object is to illuminate successive planes within the object with a narrow fan-beam of X-rays. A two-dimensional reconstruction algorithm such as that outlined above can then be used to reconstruct each plane, which when stacked up result in a three-dimensional reconstruction. A more efficient approach is to use a computed tomography system based on the cone-beam geometry, the reconstruction algorithms for which are a generalisation of the two-dimensional fan beam algorithms based on filtered backprojection (Feldkamp *et al*, 1984). Instead of illuminating a slice of the object with a fan of X-rays, the entire object is illuminated with a beam of X-rays that form a cone originating from a point source, and the X-ray flux is measured on a plane. The main advantage of cone-beam tomography over fan beam is the reduction in data collection time. With a single source, ray integrals are measured through every point in the object, and collected on the opposite side by a 2-D array of detectors, in the time it takes to measure a single slice in a conventional two-dimensional scanner.

In three-dimensions, the projection data, $R_{\beta}(t,r)$, are now a function of the source angle, β, and horizontal and vertical positions on the detector plane, t and r. The Radon transform is obtained by integrating along planes. If a plane is represented by (β,l), where

β is a unit 3-D vector in a unit sphere representing the orientation of the plane with respect to the coordinate axes and l represents the distance of the plane from the origin, all the planes that intersect the object are considered and the planar integral of a point in the object, f(x,y,z), along that plane is obtained. This result gives the Radon transform of the projection data in 3-D. A three-dimensional parallel projection of an object, f(x,y,z), is expressed by the following integral (Feldkamp *et al*, 1984; Kak and Roberts, 1986):

$$P_{\theta,\gamma}(t,r) = R_{\beta}(p,\zeta) = \int_{-s_m}^{s_m} f(t,s,r)\, ds \qquad (10)$$

The new coordinate system, (t,s,r), is obtained by two rotations of the original (x,y,z) axes, as defined in Figure 5 (Feldkamp *et al*, 1984; Kak and Roberts, 1986). The first rotation, as in the two-dimensional case, is by θ degrees about the z-axis to give the (t,s,z) axes. A second rotation is then applied out of the (t,s) plane about the t-axis by an angle of γ. Four variables are used to specify the desired ray: (t,θ) specifies the distance and angle in the x-y plane and (r,γ) in the s-z plane.

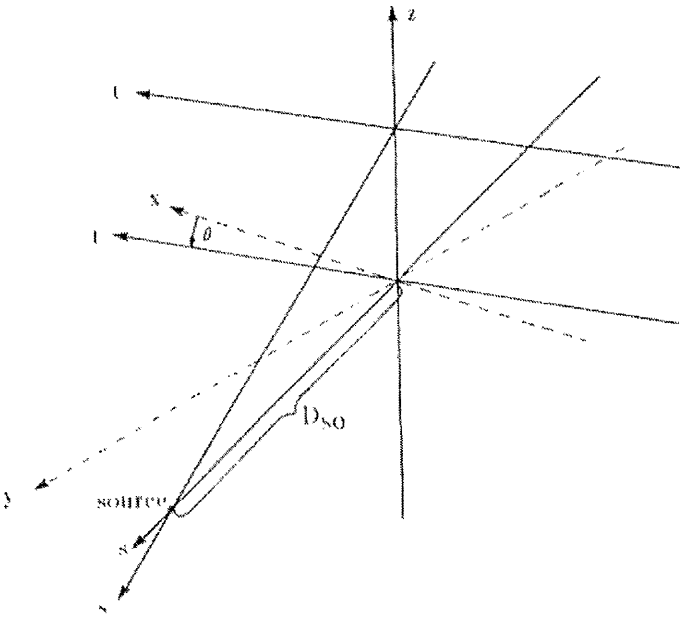

Figure 5. In order to define the cone beam reconstruction, the original (x,y,z) coordinate system is rotated by two angles to give the (t,s,r) axes. The r-axis is not shown but is perpendicular to the t- and s-axes. (Feldkamp *et al*, 1984; Kak and Roberts, 1986).

In a cone beam system, the source is rotated by β and ray integrals are measured on the detector plane as described by $R_\beta(p,\zeta)$. For a given cone beam ray, $R_\beta(p,\zeta)$, the parallel projection ray is given by (Feldkamp *et al*, 1984; Kak and Roberts, 1986):

$$t = p\,(D_{SO} / \sqrt{(D_{SO}^2 + p^2)}$$
$$\theta = \beta + \tan^{-1}(p / D_{SO}) \qquad (11)$$

where t and θ locate a ray in a given tilted fan. D_{SO} indicates the distance from the centre of rotation to the source. r and γ can also specify the location of a tilted fan (Feldkamp *et al*, 1984; Kak and Roberts, 1986; see Equation (10)):

$$r = \zeta(D_{SO} / \sqrt{(D_{SO}^2 + \zeta^2)})$$
$$\gamma = \tan^{-1}(\zeta / D_{SO}) \qquad (12)$$

Three-dimensional filtered backprojection

Reconstruction using cone beam filtered backprojection algorithms involves filtering and backprojecting a single plane within the cone. Each elevation within the cone is considered separately and the final three-dimensional reconstruction is obtained by summing the contribution to the object from all the tilted fan beams (Feldkamp *et al*, 1984; Kak and Roberts, 1986). The algorithm is derived by starting with the filtered backprojection algorithm for equispatial rays, Equation (6). In a three-dimensional reconstruction, each fan is angled out of the source-detector plane of rotation, leading to a change of variables in the backprojection algorithm. It is first of all necessary to consider the two-dimensional fan beam reconstruction formula for the point (r,ϕ). Equation (6) can be simplified by replacing the (r,ϕ) coordinate system with the rotated coordinates, (t,s), as defined above, recalling that (t,s) is the location of a point rotated by the angular displacement of the source-detector array. In a cone beam reconstruction it is necessary to tilt the fan out of the plane of rotation, and thus the size of the fan and the coordinate system of the reconstructed point change. Another coordinate system is defined that represents the location of the reconstructed point with respect to the tilted fan. Because of the changing fan size, both the source distance, D_{SO}, and the angular differential, β, change. The new source distance is given by $D_{SO}'^2 = D_{SO}^2 + \zeta^2$, where ζ is the height of the fan above the centre of the plane of rotation. Also, the increment of angular rotation, $d\beta'$, becomes $d\beta' = d\beta\, D_{SO} / (\sqrt{(D_{SO}^2 + \zeta^2)})$. Substituting these new variables into Equation (6), writing the projection data as $R_\beta'(p,\zeta)$, and then returning the reconstruction back to the original (t,s,z) coordinate system, the derived expression of the reconstruction algorithm becomes (Feldkamp *et al*, 1984; Kak and Roberts, 1986):

$$g(t,s) = \tfrac{1}{2} \int_0^{2\pi} D_{SO}^2 / (D_{SO} - s)^2 \int_{-\infty}^{\infty} R_\beta(p,\zeta)\ H_\epsilon((D_{SO}\, t / (D_{SO} - s)) - p)\ (D_{SO} / \sqrt{(D_{SO}^2 + \zeta^2 + p^2)})\ dp\ d\beta \qquad (13)$$

A more comprehensive breakdown of the derivation is given in the literature (Feldkamp *et al*, 1984; Kak and Slaney, 1987; Kak and Roberts, 1986). The cone beam reconstruction algorithm can be broken down into the following three steps:

1. Multiply the projection data, $R_\beta(p,\zeta)$, by the function $(D_{SO} / \sqrt{(D_{SO}^2 + \zeta^2 + p^2)})$ to find $R_\beta'(p,\zeta)$.
2. Convolve this weighted projection, $R_\beta'(p,\zeta)$, with $H_\epsilon(p)/2$ by multiplying their Fourier transforms with respect to p. This convolution is done independently for each elevation, ζ. The result is $Q_\beta(p,\zeta)$.
3. Finally, each weighted projection is backprojected over the three-dimensional reconstruction grid:

$$g(t,s,z) = \int_0^{2\pi} D_{SO}^2 / (D_{SO} - s)^2\ Q_\beta\left[\ (D_{SO}\, t / (D_{SO} - s))\ ,\ (D_{SO}\, z / (D_{SO} - s))\ \right] d\beta \qquad (14)$$

   The two arguments of the weighted projection, Q_β, represent the transformation of a point in the object into the coordinate system of the tilted fan.

Only those points of the object that are illuminated from all directions can be properly reconstructed. In a cone beam system, this region is a sphere of radius $D_{SO} \sin(\Gamma_m)$ where Γ_m is half the beam width angle of the cone. Outside this region a point will not be included in some of the projections and thus will not be correctly reconstructed.

Feldkamp, L. A., Davis, L. C. and Kress, J. W., 'Practical cone-beam algorithm', *J. Opt. Soc.*, 1984, **1**, 612-619.

Hiriyannaiah, H. P., 'X-ray computed tomography for medical imaging', *IEEE Signal Processing Magazine*, 1997, 42-59.

Kak, A. C. and Roberts, B., 'Image reconstruction from projections', in *Handbook of Pattern Recognition and Image Processing*, Young, T. Y. and Fu, K. S., Eds., Academic Press, New York, 1986.

Kak, A. C. and Slaney, M., *Principles of Computerised Tomographic Imaging*, IEEE Press, London, 1987, pp. 49-134.

Rosenfeld, A. and Kak, A. C., *Digital Picture Processing*, Academic Press, New York, 1982.